

# **Characterization and Catalyst Development**



# Characterization and Catalyst Development

## An Interactive Approach

**Steven A. Bradley**, EDITOR  
*UOP Research Center*

**Mark J. Gattuso**, EDITOR  
*UOP*

**Ralph J. Bertolacini**, EDITOR  
*Amoco Oil Company*

Developed from a symposium sponsored  
by the Division of Petroleum Chemistry, Inc.,  
and by the D-32 Committee of ASTM  
at the 196th National Meeting  
of the American Chemical Society,  
Los Angeles, California,  
September 25-30, 1988



American Chemical Society, Washington, DC 1989



### Library of Congress Cataloging-in-Publication Data

Characterization and catalyst development: an interactive approach.  
Steven A. Bradley, Mark J. Gattuso, Ralph J. Bertolacini, editors.  
p. cm.—(ACS Symposium Series, 0097-6156; 411).

“Developed from a symposium sponsored by the Division of Petroleum Chemistry, Inc., and by the D-32 Committee of ASTM at the 196th National Meeting of the American Chemical Society, Los Angeles, California, September 25-30, 1988.”

Includes bibliographic references.  
ISBN 0-8412-1684-3

1. Catalysts—Analysis—Congresses.  
I. Bradley, Steven A., 1949- . II. Gattuso, Mark J., 1944- . III. Bertolacini, Ralph J. IV. American Chemical Society. Division of Petroleum Chemistry, Inc. V. ASTM Committee D-32 on Catalysts. VI. American Chemical Society. Meeting (196th: 1988: Los Angeles, Calif.). VII. Series

TP159.C3C46 1989  
660'.2995—dc20

89-1777  
CIP

The paper used in this publication meets the minimum requirements of American National Standard for Information Sciences—Permanence of Paper for Printed Library Materials, ANSI Z39.48-1984.



Copyright © 1989

American Chemical Society

All Rights Reserved. The appearance of the code at the bottom of the first page of each chapter in this volume indicates the copyright owner's consent that reprographic copies of the chapter may be made for personal or internal use or for the personal or internal use of specific clients. This consent is given on the condition, however, that the copier pay the stated per-copy fee through the Copyright Clearance Center, Inc., 27 Congress Street, Salem, MA 01970, for copying beyond that permitted by Sections 107 or 108 of the U.S. Copyright Law. This consent does not extend to copying or transmission by any means—graphic or electronic—for any other purpose, such as for general distribution, for advertising or promotional purposes, for creating a new collective work, for resale, or for information storage and retrieval systems. The copying fee for each chapter is indicated in the code at the bottom of the first page of the chapter.

The citation of trade names and/or names of manufacturers in this publication is not to be construed as an endorsement or as approval by ACS of the commercial products or services referenced herein; nor should the mere reference herein to any drawing, specification, chemical process, or other data be regarded as a license or as a conveyance of any right or permission to the holder, reader, or any other person or corporation, to manufacture, reproduce, use, or sell any patented invention or copyrighted work that may in any way be related thereto. Registered names, trademarks, etc., used in this publication, even without specific indication thereof, are not to be considered unprotected by law.

PRINTED IN THE UNITED STATES OF AMERICA

**American Chemical Society**  
Library  
1155 16th St., N.W.  
Washington, D.C. 20036

# ACS Symposium Series

**M. Joan Comstock, *Series Editor***

## *1989 ACS Books Advisory Board*

**Paul S. Anderson**  
Merck Sharp & Dohme Research  
Laboratories

**Alexis T. Bell**  
University of California—Berkeley

**Harvey W. Blanch**  
University of California—Berkeley

**Malcolm H. Chisholm**  
Indiana University

**Alan Elzerman**  
Clemson University

**John W. Finley**  
Nabisco Brands, Inc.

**Natalie Foster**  
Lehigh University

**Marye Anne Fox**  
The University of Texas—Austin

**G. Wayne Ivie**  
U.S. Department of Agriculture,  
Agricultural Research Service

**Mary A. Kaiser**  
E. I. du Pont de Nemours and  
Company

**Michael R. Ladisch**  
Purdue University

**John L. Massingill**  
Dow Chemical Company

**Daniel M. Quinn**  
University of Iowa

**James C. Randall**  
Exxon Chemical Company

**Elsa Reichmanis**  
AT&T Bell Laboratories

**C. M. Roland**  
U.S. Naval Research Laboratory

**Stephen A. Szabo**  
Conoco Inc.

**Wendy A. Warr**  
Imperial Chemical Industries

**Robert A. Weiss**  
University of Connecticut

## Foreword

The ACS SYMPOSIUM SERIES was founded in 1974 to provide a medium for publishing symposia quickly in book form. The format of the Series parallels that of the continuing ADVANCES IN CHEMISTRY SERIES except that, in order to save time, the papers are not typeset but are reproduced as they are submitted by the authors in camera-ready form. Papers are reviewed under the supervision of the Editors with the assistance of the Series Advisory Board and are selected to maintain the integrity of the symposia; however, verbatim reproductions of previously published papers are not accepted. Both reviews and reports of research are acceptable, because symposia may embrace both types of presentation.

# Preface

**W**ORLD-WIDE CATALYST SALES for 1989 are expected to exceed \$5 billion. In the United States, the market is in excess of \$2 billion. Proper preparation, characterization, and evaluation of industrial catalysts are prerequisites for the development and commercial use of these materials. New preparative techniques and novel materials have generated many highly active and selective catalysts. Proper testing procedures to measure chemical and physical properties have accelerated commercialization. Sophisticated new instrumentation has increased our knowledge about the nature of catalytic sites and species, leading to a better understanding of the molecular processes that take place in a catalytic reactor. The need for standardization of test procedures for physical and chemical evaluation of catalysts resulted in the formation in 1975 of the ASTM D-32 Committee on Catalysts. The symposium on which this volume is based sought to focus attention on these important topics, with special emphasis on updating the progress made in the preparation, testing, and characterization of catalysts.

As demonstrated throughout this volume, catalyst development is much more than just plant testing. Rejecting a hypothesis because of poor plant performance and not determining whether the catalyst was improperly prepared or treated can inhibit a breakthrough. Similarly, characterizing only the catalysts that give excellent performance so as to understand the system may cause researchers to miss the critical variable.

The chapters in *Characterization and Catalyst Development: An Interactive Approach*, assembled from both academic and industrial contributors, give a unique perspective on catalyst development. Some chapters thoroughly characterize the catalyst prior to plant evaluation, whereas others utilize characterization to explain performance variances. Some new types of catalysts incorporated into this volume include the preparation of novel catalyst supports based on alumina and hydrous titanates. Attrition-resistant catalysts and ultrafine ceramics were prepared by modified spray-drying methods. New catalyst compositions based on vanadium-containing anionic clays were proposed for oxidation. A recently commercialized catalyst based on magnesium spinel was proposed for use in the abatement of sulfur oxide pollutants in fluid

catalytic cracking. A large variety of instrumental techniques have been applied to the characterization of catalysts and results correlated to performance. These include infrared, nuclear magnetic resonance, scanning transmission electron microscopy, X-ray absorption fine structure, magic angle spinning nuclear magnetic resonance, microporosity techniques, and temperature desorption methods. These techniques are being used to characterize zeolites and oxide supports as well as reforming, desulfurization, and cracking catalysts. Standardized procedures developed by ASTM tell how to test catalysts for important physical properties such as crushing strength and attrition resistance. Standard reference samples are available for calibration for some ASTM methods.

The editors acknowledge the contributions of Susan Lambert, Secretary for the Program Committee of the ACS Division of Petroleum Chemistry, Inc., and our cosponsors, the Division of Petroleum Chemistry, Inc., and the D-32 Committee of ASTM. We also thank the cross-listing Divisions of Fuel Chemistry and of Industrial and Engineering Chemistry, Inc. Robert Koros, Chairman of the ASTM D-32 Committee on Catalysts, and staff manager Bruce Klotz of ASTM were most helpful. We also thank G. E. Dolbear, J. Longenback, and C. A. Audeh for organizing the poster session. We are indebted to Allied Signal, UOP, and Amoco Oil for allowing us to participate in this project and for providing valuable secretarial support. The views and conclusions expressed herein are those of the authors, whom we sincerely thank for the prompt return of their manuscripts and for their excellent presentations. Finally, we thank all of the scientists and engineers who devoted many valuable hours to the critical reviewing of these manuscripts.

STEVEN A. BRADLEY  
UOP Research Center  
Des Plaines, IL 60017

MARK J. GATTUSO  
UOP  
Des Plaines, IL 60017

RALPH J. BERTOLACINI  
Amoco Oil Company  
Naperville, IL 60566

July 18, 1989



# Chapter 1

## The Role of Catalyst Characterization in Process Development

Vladimir Haensel and Hertha Skala Haensel<sup>1</sup>

Department of Chemical Engineering, University of Massachusetts,  
Amherst, MA 01003

### Part I: Introduction

Catalyst characterization, if properly utilized, can be both the cornerstone of the science of catalysis and the "catalyst in its own right for industrial progress". As a long term research endeavor, its goal should be an understanding of the catalytic act on a molecular level, a clear elucidation of the nature of the individual catalyst sites and of their interdependence and interaction with each other as well as with the reactants. It must also provide a stimulus for the development of instrumental capabilities and instrumental and chemical techniques which are the tools for this research effort. A basic knowledge of catalysis and the ability to conceptualize a working hypothesis is a most desirable prerequisite for such studies.

A discerning activity test in a well designed microreactor must be an integral part of the overall approach to develop the means for correlating physical, chemical and electronic properties of the catalyst with activity, selectivity and stability.

Such studies, when well designed, provide for a more fundamental understanding of catalysis. Catalytic concepts and models are thereby developed and "catalysts by design" come within the realm of reality. This area of catalyst characterization is exciting, complex and requires researchers of many talents. This is where the issue of true fundamental interest, the structure and associated energetics of the transition state should be identified as a major challenge.

In industrial catalysis it is the application of catalyst characterization to catalyst development and process trouble shooting which also require researchers of many talents. This is where the overall task of a catalyst diagnostician is to fit together a jigsaw puzzle wherein individual pieces must not only fit into a proper place but they must be a part of the total picture, a picture sufficiently defined even though many pieces

<sup>1</sup>Consultant. Mailing address: 83 Larkspur Drive, Amherst, MA 01002

are still missing. In long range catalyst research we have the luxury of choosing the missing pieces in a specific area of the picture. In application of catalyst characterization to industrial catalyst development and process trouble shooting it is the specific piece which will make the biggest contribution to defining the picture which must be found simply because there is a time limit. It is this aspect of a choice of focus and technique which makes it such a difficult undertaking.

This is where management participation becomes critical because allocation of resources, both manpower and equipment, for long range research, catalyst development and trouble shooting emergency research becomes an exceptionally difficult task.

We have divided this presentation into seven parts. In this first part we point out that it would serve little purpose to enumerate and discuss the modern surface science techniques which have been developed in recent years. This is not the purpose of this presentation, nor is it within our most recent expertise to discuss techniques which will be so ably covered in subsequent presentations. Thus, we contacted some of the leaders in surface science and catalysis and asked them what they consider to be the most important breakthroughs in the area of catalyst characterization and what are the challenges of the future. We spoke with Michel Boudart, Wayne Goodman, Wolfgang Sachtler and John Sinfelt. None of these experts has requested either anonymity or immunity. This is described in Part II.

The third part deals with a brief history of catalyst characterization during the era of its most productive cooperation with catalyst-process development. Unfortunately, largely due to increased extent of sophistication in both areas, there has been a decrease in cooperation and an increase in polarization.

The fourth part addresses the real world of the industrial demands for better catalysts. It is the world which is willing to finance highly sophisticated equipment as well as expensive research talent to improve our catalytic knowledge and apply it to develop better catalysts. Even though such research is given considerable lip service, it is the most vulnerable to termination and/or transfers to more pressing problems.

The fifth part deals with an even more real world, relating to the emergency catalyst characterization problems. Many workers in this area have experienced this terrible pressure - "don't do research, just solve our problem". In this instance we have drawn extensively upon our own experience.

The sixth part returns to the main theme of technological cooperation, in this instance understanding the relationship between the catalyzed reaction and the catalyst surface.

The last part deals with a somewhat humorous experience that the senior author had in connection with catalyst characterization.

#### Part II: View from the Top

As indicated earlier, we have contacted a number of experts in catalysis and asked them about breakthroughs and challenges in catalyst characterization. The replies were not unexpected - each expert provided an answer that to him was of paramount importance.

Michel Boudart felt that the "most universally useful tool is synchrotron radiation which can handle all elements, valences and atomic structure in situ, even in liquid phase". The challenge is "ability to handle and understand catalyst deactivation at molecular and microscopic levels".

Wayne Goodman commented as follows: The development of chemisorption techniques for the characterization of active catalytic surfaces has provided a mechanism for defining specific catalytic activity, thus separating true catalytic activity from the ambiguities of catalytic activity derived from catalyst formulation. As a consequence, chemisorption has allowed the development of relationships between catalyst structure and activity/selectivity. Furthermore, chemisorption has provided a framework which has allowed the surface science of supported metal particles and the surface science of single crystal catalysts to be interrelated.

The emergence of potent structural technique such as EXAFS as well as the application of UHV surface science techniques to catalytic problems has and will play a pivotal role in the development of a fundamental understanding of the science of catalysis. An enhanced understanding inevitably leads to scientific and technological breakthroughs.

With respect to challenges, Wayne Goodman stressed the development of sensitive surface diagnostics for in situ characterization of working catalysts to establish an unambiguous relationship between surface (electronic) structure at the atomic level and catalytic activity/selectivity and first principles design of catalytic materials for specific chemical and fuels applications.

Wolfgang Sachtler's comments on breakthroughs and challenges are considered in terms of: The experimental techniques which helped him most to understand adsorption and catalysis are: Infra-Red Spectroscopy, Field Electron Microscopy and Temperature Programmed Reduction and Desorption (TPR, TPD). In the case of TPR and TPD the principle is old, but modern electronic techniques and computers are required to obtain the needed sensitivity and reproducibility. Professor Sachtler further indicates that this does not mean that he would like to live without GRC, XRD, EXAFS, XPS, Auger or electron microscopy, but if he could design by black magic a futuristic tool, he would like to have some instrument which has the same resolution power as the field ion microscope but can be applied to a working catalyst at the temperature and pressure characteristic for its steady state.

John Sinfelt feels "that the most generally valuable tool for a long time has been the measurement of adsorption isotherms, including the BET method for determination of total surface area and various selective chemisorption methods for determining the amount of surface associated with particular component. The BET method has been widely used by catalytic chemists for almost half a century for the characterization of catalytic materials. It is among the foremost developments in surface science during the twentieth century".

John Sinfelt continues "with respect to EXAFS this has the virtues of great generality regarding structural information, but

it is very difficult to obtain instrument time". He then warns "don't be too enamored of specialized techniques - sometimes simple chemical titration procedures can be very helpful and informative". With respect to challenges for catalyst characterization "look for surface science tools to discern dispersions created in true catalytic environment".

All of the above comments have a commonality - a high appreciation for the new techniques but, at the same time, they emphasize that adsorption - desorption techniques remain indispensable tools for catalyst characterization.

### Part III: Historical

The authors of this paper have spent a combined total of some seventy years in process development and catalyst characterization. We have found the work in these areas as a most interesting and rewarding experience. We firmly believe that catalyst characterization must play an integral and major role in advancing both the science and technology of catalysis. We can go a step further and state that from our experience the interdisciplinary approach is the key to a rapid and successful commercialization of a catalytic process, involving not only most branches of chemistry, surface science, chemical engineering and chemical physics but, as another key ingredient, complete support from the management which can put the whole effort together. A very important function of the management is to bring catalyst characterization personnel into all discussions relating to catalyst and process development from the very beginning of the project.

It is interesting to trace briefly the history of catalyst characterization. Initially the situation was very simple: a catalyst was prepared and characterized by its performance as a catalyst for the reaction of interest. If the performance was not sufficiently good, new formulations were tried. Although nowadays people may look upon this as an exercise in empiricism it certainly was not. The changes which were made required a great deal of chemical thought combined with a certain amount of gut feeling, but it was never of the "taking things off the shelf" variety. The important point is that one examined very carefully the actual catalytic results - that is changes in product composition and quality followed by correlating them with whatever changes were made in catalyst preparation. In early days of our work we did not have the luxury of an almost immediate product analysis. Now we take this for granted, and yet the painstaking time consuming analyses gave time for a more judicious selection of future experiments. Each result was very precious - now we frequently suffer from too much data and too little thought. A bit more philosophy - "treat each individual data point as if this were the end result and draw conclusions". In "Science", Feb. 26, 1988 one finds a concurring statement by Yuri A. Osipian, Director of the USSR Institute for Solid State Physics, who conceded there was a lack of computers in the Soviet Union. However, he also said "sometimes it is a blessing. If you have less science equipment you have more time to think".

The early thinkers in catalysis were enamored of an idea of a unified theory of catalysis, such as the electronic theory of Volkenstein. This was preceded and followed by other ideas but over a period of time it was realized that so many different factors are involved so that a single explanation was most unlikely. But, as pointed out by two of the "greats" in catalysis, Ipatieff and Tropsch, that "to try to understand catalysis you must know a lot of chemistry". This need to know a lot of chemistry applies particularly to catalyst diagnosticians.

The early physical and physico-chemical methods evolved around surface area measurements, catalyst acidity, hydrogen and carbon monoxide titrations. These became essentially standard catalyst characterization tools. Nevertheless, the Herman Pines School maintained that, paraphrasing Gertrude Stein, "a catalyst is a catalyst is a catalyst" and this School was quite successful in selecting suitable test reactions in characterizing catalysts and effects of compositional changes. Over a period of time both schools progressed very successfully in that catalyst surfaces are no longer so mysterious as they were before and, much more was learned of the mechanisms of many reactions.

#### Part IV: The Real World

As surface science tools became more sophisticated it became abundantly clear that nearly all tools required extremely clean surfaces and high vacuum techniques. Michel Boudart has pointed out a number of times the need to bridge the gap between the high vacuum spectroscopic techniques and the real world of catalytic reactions.

The real world is tremendously interested in catalyst structure with respect to:

- (a) In the case of metal containing catalysts, the distribution of the metal function as ensembles, clusters, rafts or even individual atoms. The extent of metal support interaction and the variation in the strength of such interaction. The accessibility of the metal function, its stability, and, most importantly, its activity and selectivity.
- (b) In the case of bifunctional catalysts, involving both acidic and metal sites, the questions deal with relative concentration of the two types, relative location and extent of their interaction, their compatibility with the total catalyst structure and, most importantly, the activity and selectivity of the entire composite.

The composite of all this information is only a part of the total interdisciplinary effort that we spoke about earlier.

Let us return to the catalyst characterization. We can ask the question, "which catalyst do you wish to characterize?" Is it a catalyst which is just about ready to be put into a reactor, or one that has been exposed to the reactants for a few seconds, or a few minutes or hours or months? Or is it a catalyst that has undergone occasional or periodic regenerations? The basic question of catalyst characterization is not that of a fresh catalyst per se, but how can we discern or characterize in a fresh

catalyst those properties and capabilities which can stand up to the subsequent vagaries of commercial reaction environment?

This is where we have to emphasize that a scientist involved in catalyst characterization must be thoroughly knowledgeable not only in his or her own expertise of spectroscopic and other analytical techniques, but that same scientist must also be thoroughly familiar with chemical and engineering particulars of the process which uses this catalyst.

#### Part V: An Even More Real World

A really superb person in catalyst characterization has an analogy in the medical world - a really superb general practitioner - who not only can diagnose but who also knows the specialists who can be called upon. Just like the task of a medical diagnostician, much catalyst characterization is detective work trying to establish what caused catalyst deactivation in a commercial unit - an emergency situation - with much money at stake, particularly when the unit shuts down. Our early experience with the poisoning of the Platforming catalyst confirmed the need for a superb catalyst diagnostician. The first commercial Platforming unit at the Old Dutch Refinery in Muskegon Michigan started in November 1949 and, despite some initial problems, ran successfully and became a show place for potential licensees. By 1952 Platforming units were being licensed at an average rate of a new unit every two weeks, and this continued for many years. Every unit was carefully monitored at the start-up, and those of us who have been involved in process development and catalyst characterization were kept informed of the operation of each new unit, but particularly when trouble arose. We did hit real trouble with an early unit in the Mid-Continent area (Bell Oil and Gas Company) which exhibited the typical platinum poisoning symptoms, a progressive decline in the endothermicity of reaction, first in the top section of the first reactor and then progressively downward and then to the top of the second reactor. Before long, the catalyst in the first reactor became virtually inactive and, amidst much consternation, all possible forces were called upon to diagnose the problems and, most importantly, to provide a solution, preferably one that would be quick, simple and cheap. A sample of catalyst from the top of the first reactor was thoroughly analyzed. We had also obtained samples of feedstock to the unit. The catalyst analysis showed unmistakable signs of poisoning by arsenic, probably one of the most potent poisons for platinum. Next came the analysis of the feedstock, and by extreme care it was shown that the feedstock contained 35 parts per billion of an arsenic compound. Nowadays, it may seem simple to determine such a minute concentration, but go back some 37 years. At that time we only had a "gut feeling" from our previous work where we tested a large number of catalyst additives in minute traces and did show a particularly irreversible poisoning with arsenic. However, to find any poison on the catalyst sample by X-ray required some very ingenious work until finally some very faint X-ray lines were detected showing arsenic. To find arsenic in the feedstock, Dr. E. Bicek, who did the X-ray work on the catalyst, extracted large amounts of

feedstock with sulfuric acid and concentrated the arsenic compound until a positive analysis was finally achieved.

Whenever you have troubles with a commercial unit you invariably get some "gleeful" comments from competition who claim that their newly developed catalyst is arsenic resistant. What has happened is that the competitors fell into the same original trap as we did. When we added minute quantities of an alkylarsine compound to the feedstock the catalyst was not poisoned. Then it dawned on us that a laboratory unit has a tremendous surface to volume ratio as compared to a minute surface to volume ratio in a commercial unit and, in the laboratory, we were losing the poison on the walls prior to contact with the catalyst. Next, we inserted a tiny particle of arsenic on a wire above the catalyst and in less than an hour the catalyst was dead.

At that point we knew the reason and it took a very short time for Dr. J. Murray, head of our analytical facilities, to show that a bed of clay removed the arsenic completely. This was installed and the unit ran perfectly.

The lesson is that the catalyst diagnostician must not only be able to diagnose the problem but must be in a position to solve the problem in a relatively short period of time.

This initial experience which dates some years ago is not unusual, for it has been repeated many times over whenever catalysts are used. Most recently, we have had discussions with Dr. Burkhard Wagner, Research Associate at Unipol Systems Department, Union Carbide. It is interesting to note that Dr. Wagner has also drawn an analogy to the emergency room medical treatment. In his case, the process is gas phase polymerization of ethylene and when there is a suspected catalyst problem, the first approach is to narrow down the realm of possibilities, thus allowing more concentrated effort within the time frame. In this approach, a rapid component analysis is used to test the gross distribution of catalyst components. If the "gross-chemistry" is O.K., the next step will involve an imbedding technique for particles (sizes 30 microns) into polyethylene and cryogenically microtoming. The sliced plug goes into SEM to obtain a visual observation of atomic concentration over the entire particle or sections thereof. If one catalyst component is found to be maldistributed the catalyst manufacturing facilities are immediately contacted.

An outgrowth of the "emergency room procedure for a quick fix" is the concept of "doing it right the first time". This involves stripping the problem to its bare essentials and then start putting things together again in order to find out what is the real problem. In this instance Burkhard Wagner advocates the use of a task force approach rather than team approach. The authors of this paper have advocated this approach in their work, since a task force is more flexible and more direct.

#### Part VI: Happenings on the Surface

Despite the great emphasis on sophisticated tools which we admire and appreciate, we would like to make a case for simple, though not necessarily easier, chemical reasoning and techniques which

provided much of the input in earlier days and should again play a more prominent part.

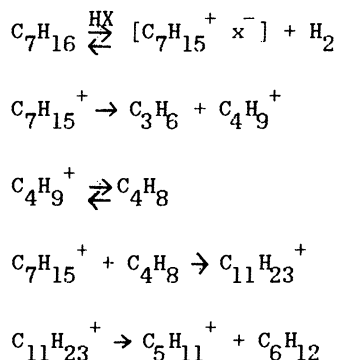
What we are concerned with is the need to understand a reaction mechanism, which, after all is the "guts" of a catalytic reaction. In line with this let us now recall how we tried to deduce what is happening on the surface of a catalyst and how does the surface participate in this occurrence. A simple example is that of hydrocracking normal heptane over a dual-functional catalyst (nickel on silica-alumina) at about 250°C. (Table 1). Hydrocracking is a well established process wherein higher boiling crude oil fractions are subjected to cracking in the presence of hydrogen at relatively high pressures and relatively low temperatures (as compared to catalytic cracking) to produce saturated lower boiling components which are then used directly or are fed to a catalytic reforming step to increase the aromatic content.

In the case of normal heptane it is immediately observed that there is something wrong stoichiometrically - whereas the moles of propane and butane produced are nearly equivalent, there is a substantial discrepancy between the moles of methane and hexane as well as between the moles of ethane and pentane. It is inevitable that the first step is to check the analysis - any departure from stoichiometry is initially inconceivable. But the analysis is correct and this is where the interdisciplinary forces must come to the rescue - ability to understand what is happening on the surface and what is the effect of the composition of the surface upon the series of reactions that must take place. What is happening has been very aptly named by Professor Burwell as "organometallic Zoo". This is shown in figure 1. It is the intermediate formation of butyl and propyl carbonium ions on the surface which can then react with adjacent heptyl carbonium ions to produce C<sub>10</sub> and C<sub>11</sub> carbonium ions. These can then split to give C<sub>5</sub> and C<sub>6</sub> carbonium ions which are then hydrogenated off the surface. What does this explanation have to do with the efforts of the characterization person? We can easily answer: "A great deal". Somehow the surface must allow for adjoining occupancy or proper push-pull migration. Furthermore, it is the extent of occupancy or concentration of hydrogenating sites which, depending upon their distance from the carbonium ion holding sites, will determine whether or not the smaller carbonium ions formed initially will be saturated immediately or be allowed to react with heptyl ions on an adjoining acid site.

Table 1 Hydrocracking of n-Heptane, 17.8% conversion

Product Distribution, Mol%			
CH <sub>4</sub>	0.2	C <sub>6</sub> H <sub>14</sub>	4.3
C <sub>2</sub> H <sub>6</sub>	0.2	C <sub>5</sub> H <sub>12</sub>	9.6
C <sub>3</sub> H <sub>8</sub>	40.5	C <sub>4</sub> H <sub>10</sub>	45.2



Figure 1. Hydrocracking of *n*-heptane.

It is obvious that somehow the distance between the sites of the same species and the distance between sites of different species must be very important. In their early elegant work, Weisz and Swegler have studied the effect of mechanically separating the sites of different species upon a reaction which mechanistically requires the presence of a dual functional catalyst. The result of their findings was that if the particle size of the two species was 5  $\mu\text{m}$  (or less) the dual functionality approached that of an impregnated catalyst.

The catalyst diagnostician can justifiably inquire if the carbonium ion participation and migration by some push-pull mechanism is the only mechanism on which catalyst construction can be based, or do we have some alternatives. Up to the present no alternatives have been published, however, the relatively simple mechanism described above, can be modified in that the initial reaction of carbonium ion formation can be also looked upon as a two step process, whereby a paraffin is first dehydrogenated and the resulting olefin promptly forms a carbonium ion. The overall result is the same.

In some later work at UOP it was shown that in isomerization and hydrocracking of normal decane the reaction of hydrocracking could be virtually stopped if one operates at very high pressures (up to 1500 atmospheres), however, as the pressure is increased, it is the isomerization reaction which is stopped last. These results reinforce the sequential carbonium ion mechanism, wherein each transformation can be reversed by excessive hydrogen pressure.

It is results of this nature and obvious questions that reinforce the importance of the interdisciplinary cooperation among the chemists and engineers involved in new process development, catalyst preparation and catalyst characterization. When species migrate across the catalyst surface how can the transport be facilitated? What is the minimum number of active sites that must be present? Is there an ensemble, and, most importantly how uniform is the size and distribution of such ensembles? The catalyst characterization symposium to follow will

describe some of the most modern tools for catalyst characterization as well as the newer concepts on metal support interaction, catalyst morphology, migration of active sites and transport of reacting species on the catalyst surface. Some fascinating work has been done in these areas and yet one of the most elusive and difficult tasks ahead is to develop methods of catalyst preparation which will increase substantially the turnover frequencies now observed in most of our catalytic processes. This is where the real link between catalyst preparation and catalyst characterization becomes most important.

#### Part VII: Some Humorous Recollections

In the historical part of this presentation we stressed the importance of management support and management participation in bringing together a real team and making sure that all players perform. In our discussion of "An even more real world" we mentioned the first Platforming unit and should have indicated that it was through the full support of Mr. David W. Harris, UOP's President and CEO, that within six months of our laboratory indications of the potential of the process more than fifty percent of the entire R&D effort was put on the project.

When it was time to start the unit in November 1949 the senior author of this paper had a call from Mr. Harris. It went something like this: "Val, this is David Harris. Before you go to Old Dutch for the start-up of the Platforming unit I would like you to prepare a good sized special catalyst sample to be put in the control room. Let me know when you have it ready." So the senior author did as he was told and called Mr. Harris. He said: "Val, please put this sample into a half-gallon jar, fill it near the top and put on a screw cap, but don't seal it. In a few weeks I plan to visit Old Dutch and will see the sample. Incidentally, label it UOP Catalyst with whatever number you wish to put on it."

Upon Mr. Harris' return the senior author received another call from him. "Val, I am very pleased with the way Old Dutch is running; congratulations to you and your coworkers. We have had more interested visitors than we expected. Strangely enough, the catalyst level in the jar appears to be very low; you might have to prepare another sample. By the way, did you characterize this catalyst?" The senior author replied: "Not really, Mr. Harris, only by input." The always cautious David Harris then asked: "What if it really works?" The senior author replied: "Mr. Harris, if it really works, which we have not tried, it will set the science of catalysis either ten years back or ten years forward, but I don't know which." David Harris said: "That is good enough for me - thanks again."

In conclusion, a bit of philosophy; people who have worked in catalyst characterization find that there is nothing more rewarding than observing the images from SEM and STEM revealing the abstract beauty of symmetry as well as lack of it and, at the same time, recognizing that what one observes are images of the forces which are busily lowering the activation energies. This is one time where one cannot help but marvel at nature.

## Chapter 2

# Rationale for Catalyst Characterization

Kamil Klier

Department of Chemistry, Lehigh University, Bethlehem, PA 18015

This volume provides a good cross section of current effort aiming at the design and development of heterogeneous catalysts for desired, mostly industrially important, reactions and processes. The goal of virtually all catalysis research is to select, using ideas, hypotheses, previous empirical knowledge, and surface materials science, a catalyst that drives a desired reaction with minimum amount of side products economically, i.e., at high rates and with a long lifetime. What is sought in terms of scientific principles are "structure-function" relationships, selective utilization of different "reaction channels," and chemical paths that give high overall reaction rates. The word "structure" implies both the local geometric arrangement of atoms in and around that portion of the catalyst surface (or pore) which is called the active site and, equally if not more importantly, the chemical nature of the active site that is determined by the energy levels, distribution, and symmetry of valence electrons, i.e., the "electronic structure." Further, the active sites co-exist with the rest of the surface and bulk of the heterogeneous catalyst, and there is keen interest in determining the relationship between the bulk, surface, and active site structure in any given catalytic system.

Catalyst characterization thus has multiple tasks which must be linked together in order to understand why catalysts are active and selective. It has been recognized for some time that these tasks will be attacked successfully neither by a single experimental tool nor cheaply in terms of professional standards and instrumentation requirements in research departments that deal with catalyst development. However, the payoffs are substantial. First, catalyzed processes are the backbone of petroleum and chemical industry and amount annually to trillion dollar business worldwide. Second, the science is at the forefront of materials science: where microelectronic devices currently have functional elements of micrometer to just submicrometer size, catalysts used in industrial practice have particles of nanometer size and active centers of molecular, i.e., subnanometer, size. Third, the fundamental issues of chemical reactivity appear most prominently in catalysis: how is the activation energy of a reaction lowered by bonding of intermediates to the catalyst, what are the conditions for channeling the energy released in an exothermic step into an endoenergetic step, making thereby the latter possible, and how can an undesirable side reaction be stopped by providing a high barrier for it by a shape constraint or an increase of its activation energy.

One of the important areas of catalyst characterization is to provide information on the bulk and surface properties in relation to the preparation methods, including precursors, calcined, prerduced, or otherwise pretreated catalysts. Other, no less important areas pertain to catalysts in their active working state and to post-mortem analysis of gradually or suddenly deactivated catalysts. There is no greater incentive for a rapid catalyst characterization than a 1,000-ton reactor making a \$400,000/day product going down due to a catastrophic catalyst deactivation.

Although both the laboratory and industrial scale materials science of catalysts requires an integrated approach as already mentioned above, it is customary to classify the characterization methods by their objects and experimental tools used. I will use the object classification and direct the introductory comments to analysis, primarily elemental and molecular **surface analysis**, determination of **geometric structure**, approaches toward the determination of **electronic structure**, characterization by **chemisorption and reaction studies**, determination of pore structure, **morphology**, and texture, and, finally, the role of **theory** in interpreting the often complex characterization data as well as predicting reaction paths.

### Surface Analysis

Commencing with surface analysis of catalysts, excellent tools are available, although few are used in a quantitative manner. Elemental surface analysis by Auger spectroscopy, XPS (ESCA), and SIMS is well established; in many cases the combination of core level XPS and Auger spectroscopy also gives information on the valence states of the elements present in the surface but often monochromatic X-ray sources must be used in XPS that are provided in-house by crystal monochromators (e.g., 1) or at synchrotron sites. Among the more advanced developments with increasing use in microelectronics surface materials science is the "small spot," or "imaging" ESCA (e.g., 2) that has now been pushed to some 20  $\mu\text{m}$  lateral resolution – still far from being useful in catalysis research for mapping the distribution of surface elements.

Electron microscopy (EM), in particular in modern scanning transmission (STEM) instruments, has analytical resolution down to 1 nm, but within that lateral resolution, local bulk rather than surface analysis is provided. The semi-quantitative analytical capabilities are impressive:  $10^{-14}$  g (small spot ESCA or SIMS), or  $5 \times 10^{-20}$  g (analytical STEM) of matter.

Molecular species are analyzed with great sensitivity by temperature programmed desorption (TPD) methods that employ detection by mass spectrometry, provided that the molecules desorb without decomposition in an accessible temperature range. Less sensitive is IR spectroscopy, which, however, has the advantage of analyzing molecular species and intermediates in the adsorbed state and is thus widely used for in situ analysis of adsorbates. In the experience of this writer, IR spectroscopy could be used in a quantitative manner upon careful calibration and proper use of optics in scattering media, but this is not routinely done. Also, not routinely exploited is the overtone and combination spectral region of 4,000–10,000  $\text{cm}^{-1}$ , which contains a wealth of information, particularly on hydrogen-containing adsorbates. Still lower sensitivity to adsorbed species is obtained in Raman spectroscopy, but its information content regarding the catalyst structure down to thin layers is significant.

Surface science that is carried out under clean, ultrahigh-vacuum conditions utilizes with advantage the high resolution electron energy loss spectroscopy (HR EELS) that excels with its high sensitivity, but this technique does not match the energy resolution of IR or Raman spectroscopies. For adsorbates on real catalysts, therefore, the long time used IR spectroscopy, nowadays practiced almost exclusively in its Fourier transform mode (FTIR), is still the method of choice.

Selective chemisorption methods have been used with success for the determination of metal surface area and particle size in supported catalysts, and for titration of acid sites on silica-alumina and zeolite catalysts. The chemisorption methods are sometimes neglected in the quest for a more physical description of the catalyst surface, possibly with the penalty of missing an important and quantitative piece of information about the catalyst surface.

### Structural Analysis

Structural analysis of catalysts relies on diffraction and selected spectroscopic methods. The fascination with zeolites, their shape selectivity, controlled acidity, and ion exchange behavior, no doubt arises from our knowledge of their structure. A combination of X-ray crystallography and knowledge of chemical composition and pore size allowed many zeolite and related phosphoaluminate structures to be resolved even where these materials are not available as single crystals. Magic angle spinning solid state NMR made its impact in determining the order of aluminum and silicon, location of cations, and structures of intracavitary sorption complexes. However, the most reliable structures are still obtained by diffraction on single crystals; a sufficient crystallite size for X-ray crystallography is 0.1  $\mu\text{m}$  on edge.

To obtain a first overall picture of a catalyst structure, X-ray powder diffraction is perhaps the most commonly used method: crystalline phases are readily identified and particle sizes determined with some degree of accuracy. A difficult subject is that of "X-ray amorphous" materials, i.e., those not showing discernible powder pattern. Often the "X-ray amorphous" materials show good crystallinity, albeit of small particles, upon examination by electron diffraction in the electron microscope. The reason for this is that electron microscopy permits examination, in several modern instruments, of very small individual particles by convergent beam diffraction (CBD) or microdiffraction techniques on spots as small as 2 nm, thereby enhancing the signal-to-noise ratio of the diffracted beams and their observability. Even if the particles are "amorphous," electron scattering can in principle be analyzed for atomic positions by computer and optical simulation of the scattering patterns based on geometric models, comparison with the observed patterns, and refinement. Since multiple scattering phenomena play a non-negligible role, the crystallography in the electron microscope (I am referring to methodology developed primarily by A. Klug and applied with success to biological molecules) is a sophisticated science; however, potential payoffs for catalysis have yet to materialize.

A "direct" observation of individual atoms is achieved in atomic resolution transmission electron microscopes (AR-TEM), in the scanning tunneling microscope (STM), and in the atomic force microscope (AFM) (3, 4). While AR-TEM are large machines with very high voltage ( $6 \times 10^5$  to  $10^6$  volts) applied to an electron-transparent small object, STM and AFM are small devices with ultrasensitive tip positioning mechanics that is suited for flat or near-flat objects and will

initially likely make inroads in studies of model, rather than real microdispersed, catalysts.

A method that yields local structural information is EXAFS which utilizes the scattering of photoelectrons emitted from specific atomic core levels for determining the interatomic distances and counting the near neighbors (but does not determine the directions between the emitting atom and its neighbors).

In a related development, the feasibility of determining local structures in ESCA has been demonstrated utilizing both photoelectron diffraction and the so-called forward-directed-focusing (FDF). The FDF utilizes photoelectrons emitted from subsurface atoms as a spherical wave that is refocused by the positive potential of neighboring surface atoms, giving rise to angular peaks whose positions are independent of the incident X-ray wavelength and uniquely determine the relative positions of the surface and subsurface atoms (5, 6). As imaging ESCA makes further advances, it is expected that FDF will be used for structure determination in the imaged areas.

The low energy electron diffraction (LEED) crystallography is also a method where multiple scattering is not negligible (although it is often neglected), and the resolved structures of single crystal surfaces have been summarized in a package available for microcomputers (7). Among spectroscopic tools applied to structural analysis, FTIR is routinely used for both bulk structure and identification of adsorbates. Laser Raman spectroscopy is a less widely used but nevertheless an outstanding tool for resolving structures of oxides; in the laser Raman microprobe, where the laser source light is passed through an optical microscope, a lateral resolution of the order of 1  $\mu\text{m}$  is obtained. A particularly successful characterization of titanias, vanadias, molybdenas, rhenias, hydroxycarbonates, and other inorganic catalysts and precursors has been made by laser Raman spectroscopy.

### **Electronic Structure**

Electronic structure of catalysts and their active sites is the subject of a number of experimental and theoretical investigations. In fact, all experiments that probe into the electronic structure are critically dependent on theoretical interpretation based on quantum mechanics. Among the electron spectroscopies, XANES (or NEXAFS) deals with core-level-to-excited valence level transitions, and a good theory is required for the understanding of the upper states, the core levels being simpler. Currently the scattered wave X- $\alpha$  (SWX $\alpha$ ) method originated by Slater is most widely used for interpreting the XANES spectra (8). UPS and valence band XPS deal with electron transitions from highest occupied levels to vacuum and probe the energies, densities of states, and symmetries of valence bands of solids including catalysts. Optical transitions usually occur between the highest occupied and lower unoccupied levels, such as the d-d\* excitations in transition metal oxides and aluminosilicates (9), valence band-to-conduction band transitions in oxides and sulfides, and intraband transitions in metals. EPR and magnetic moment measurements determine the spin and orbital momentum in catalytic compounds and have been used to resolve the ground states of sorption and catalytic centers and their association with molecules. Spin-polarized XPS resulted in discovering surface ferromagnetism in otherwise diamagnetic metals such as chromium.

### **Reactor Studies**

In all of the catalyst characterization techniques, reactor studies have a central

role in that they determine whether a catalyst or a class of catalysts is worthy of a detailed structural and surface analysis. The results of characterization in turn provide feedback for improved preparation of the catalysts. Examination of a catalyst by EM often reveals which preparation methods ensure the desired fine and uniform dispersion of metal particles on the support, surface analysis unravels the presence of impurities that may accumulate from both the bulk of the catalyst and the gas or liquid phase, and chemisorption methods determine whether all metal particles seen in the electron microscope are accessible to reactants. **Pore structure** analysis that is usually obtained by sorption methods allows engineers to estimate whether the catalyst works in kinetic or mass transfer limited regime. **Hardness and attrition resistance tests** are useful predictors of the durability of a catalyst in fluid beds.

### Summary

It is evident from the above discussion that catalyst characterization is an activity important for scientific understanding, design, and troubleshooting of catalyzed processes. There is no universal recipe as to which characterization methods are more expedient than others. In the opinion of the writer, we will see continued good use of diffraction methods and electron microscopy, surface analysis, IR spectroscopy, and chemisorption methods, increased use of combined EM and ESCA analyses for determining the dopant dispersion, increased use of MAS-NMR and Raman spectroscopies for understanding of solid state chemistry of catalysts, and perhaps an increased use of methods that probe into the electronic structure of catalysts, including theory.

Science of catalysts has much to learn from materials science of metals, alloys, ceramic materials, and semiconducting materials. In turn, because catalytic science is practiced on a molecular nanostructure and surface submonolayer scale, it is one that is at the cutting edge of materials science in general and will no doubt have its impact on the technology of new, catalytic and non-catalytic materials. This symposium volume demonstrates that the field is well and alive and that progress toward a scientific catalyst design is substantial.

### Literature Cited

1. Gelius, U., Asplund, L.; Basilier, E.; Hedman, S.; Helenelund, E.; Siegbahn, K. *Nucl. Instr. Methods Phys. Res.* **1984**, *B1*, 85.
2. Gurker, N.; Ebel, M. F.; Ebel, H.; Mantler, M.; Hedrich, H.; Schon, P. *Surf. Interface Anal.* **1987**, *10*, 242.
3. Binnig, G.; Quate, C. F.; Gerber, Ch. *Phys. Rev. Lett.* **1986**, *56*, 930.
4. Hansma, P. K.; Elings, V. B.; Marti, O.; Bracker, C. E. *Science* **1988**, *242*, 209.
5. Kono, S.; Goldberg, S. M.; Hall, N. F. T.; Fadley, C. S. *Phys. Rev.* **1980**, *B22*, 6085.
6. Egelhoff, W. F. *Phys. Rev.* **1984**, *B30*, 1052.
7. McLaren, J. M.; Pendry, J. B.; Rous, P. J.; Saldin, D. K.; Somorjai, G. A.; Van Hove, M. A.; Vvendensky, D. D. *Surface Crystallographic Information Service, A Handbook of Surface Structures*; Kluwer Academic: Norwell, MA, 1987.
8. Horsley, J. A. *MO Calculations by SWX $\alpha$* , a course and text given at Lehigh University, 1987.
9. Klier, K. *Langmuir* **1988**, *4*, 13.

RECEIVED April 27, 1989

## Chapter 3

# Relationship Between Catalyst Preparation and Characterization

Stephen D. Griffith

Katalistiks International, 1501 Sulgrave Avenue, Baltimore, MD 21209

Catalytic processes are used throughout the world as an integral part of an industrialized nation's economy. Commercial use of catalysts in the United States during 1987 was well over \$1.5 billion dollars and is expected to approach \$2 billion by 1992 (1). Just over one third of this is used by the petroleum industry with the remaining two-thirds shared among the chemical, automotive, and pollution control industries. Of the \$590 million dollars spent on petroleum catalysts in 1987, about \$270 million were spent on catalytic cracking, \$175 million for alkylation, \$75 million for hydrotreating and \$70 million split among hydrocracking, reforming, and isomerization. With the exception of alkylation catalysts (HF and H<sub>2</sub>SO<sub>4</sub>), all are specialty heterogenous catalysts designed specifically for use in a particular process. A recent survey (2) listed nearly 1000 different catalysts available from 31 suppliers. Ninety-four new or modified catalysts were introduced during 1987 and half of these were fluid catalytic cracking (FCC) catalysts while hydrocracking accounted for another 21 new entries.

All of this activity in the commercial marketplace is a direct result of activity at research and development organizations around the world. In the past, much of the demand for new petroleum catalysts was fueled by market conditions, price and availability of feedstocks, and price/demand of end products. For example, higher crude oil prices in the seventies, led refiners to process more residual stocks, thereby placing greater demands on FCC and HDS (hydrodesulfurization) catalysts. In the eighties, the crude oil prices have eased, however federally mandated reductions in lead content of gasoline have spurred research into improved octane catalysts. In addition, many areas of the world have imposed limits upon SO<sub>x</sub> and NO<sub>x</sub> emissions. While these pollutants can be removed from exhaust gas streams using wet gas scrubbers, a catalytic approach is desirable since it does not usually involve major capital investment and subsequent high operating costs.

Preparation and characterization of petroleum catalysts each utilize an extremely wide variety of tools, techniques, and technologies, which must be carefully combined to achieve success. Not only must the catalyst preparation personnel understand the signifi-



cance and reliability of the characterization tests, but the people performing the characterization studies must also know why and how the various catalysts were made. In this way, deficiencies in methods or strategies can be recognized at an early stage, and corrected before unnecessary tests are performed, or worse, a research program terminated prematurely due to negative results.

### CATALYST PREPARATION

Catalyst preparation will be discussed only briefly, since the details are considered most proprietary and are outside the scope of this paper. It is this art in preparing catalyst that separates a commercially viable process from a research program. In general, nearly all heterogenous petroleum catalysts consist of a support or matrix and one or more active components incorporated into/onto the support. Thus the manufacturing process may be as simple as "impregnation" of a single component onto a previously formed support or as complex as blending a variety of components, forming to desired shapes, and further processing to achieve special characteristics and performance. The simple scheme is exemplified by combustion promoters in which a platinum solution is added to a spray dried or ground alumina support, until the alumina pores are nearly filled. The complex system, on the other hand, is probably best exemplified by the FCC catalyst manufacturing process. Here, the support, usually clay mixed with either an alumina (see Secor and LIM patents, 3a, b, c) or silica binder (see Elliot and Ostermaier patents, 4a, b, c), is blended with the active component(s) and spray dried. Following spray drying steps, the material can be further improved by exchanging the zeolite component with various cations depending upon desired performance.

As might be expected, finished catalyst shapes are dictated by the process for which they are used; fixed bed, moving bed, or fluidized bed. Each process type has its own physical performance requirements of hardness, abrasion resistance, pressure drop, flow characteristics, pore size distribution, surface area, shape, etc., and these are generally supplied by the support. The active component is primarily responsible for the catalytic performance, when it is properly dispersed throughout the support.

### CATALYST CHARACTERIZATION

Characterization, as it applies to catalyst science, is usually used to describe both the performance characteristics (evaluation) and the physical attributes (analyses) of the materials under investigation. Personnel involved in catalyst evaluation utilize custom designed equipment to determine the performance of a catalyst in a particular process. The design of the equipment typically follows that of the process, but on a much smaller laboratory scale. These simulations attempt to "mimic" the process, or parts of the process, and as such the data generated are relative not only to the process but to the test equipment and conditions (see Dartzenburg). Conversion, activity, stability, abrasion resistance, crush strength, etc. are terms often encountered in evaluation. Analysis, on the other hand, describes or measures the physical quantities of size or mat-

ter. Theoretically, these measurements should be totally independent of the material being tested or the methods used in their determination; however, in practice, this is rarely the case. Elemental analysis, surface area, particle size, density, etc. are tests used in analytical characterization.

Evaluation techniques and equipment are as varied as the individual catalytic processes themselves. The long term goal of catalyst evaluation is to reduce the size of the testing equipment consistent with reliable and accurate data as it relates to the commercial process. Invariably, the farther removed in physical size the process simulation attains, the more likely that errors will be introduced which can affect data accuracy, accuracy being defined as commercial observations. In addition, smaller equipment size also places less demand on the physical integrity of a catalyst particle; therefore, additional test methods have been developed to simulate these performance characteristics. Despite these very important limitations, laboratory reactors fully eight orders of magnitude (100 million times) smaller are routinely used in research laboratories by both catalyst manufacturers and petroleum refiners.

Smaller reactor size reduces the cost, improves control, and isolates process variables, however, effects of catalyst aging/deactivation as a function of time are not similarly reduced. These effects can be accelerated in the laboratory environment by increased temperature, water partial pressure, contaminant gas partial pressure, and various contaminant metals. As with scaled down equipment, these efforts are not without problems, however, when some catalyst lifetimes are measured in years, this is the only viable solution to meaningful catalyst research and development. This type of testing, coupled with characterization, has resulted in FCC catalysts with less resistance to coking and thus longer service life.

Most catalyst manufacturers, because of their extensive data bases correlated to actual operations, possess the ability to test new catalyst formulations using several scales of evaluation equipment. These range from very small scale pulse type reactors using less than a gram of catalyst, to laboratory pilot plants using several kilograms of catalyst. Thus, it is possible to perform many catalyst screening tests in a relatively short time with small amounts of material (a necessity for most basic research programs). As the development of a catalyst continues, the scale of testing can be increased until sufficient data exist to warrant commercialization, with subsequent testing in a commercial process - the ultimate evaluation.

Analytical characterization includes measurement of absolute sizes and concentrations of species present in the catalyst. For the purpose of clarity, these techniques have been organized, starting with the bulk macroscopic properties, down to the component, microscopic features. The underlying goal of analytical characterization is to provide information about the sample which will allow research personnel to relate the properties measured to some aspect of a catalyst's performance, either in the field or in the evaluation laboratory. Macroscopic characterization includes both chemical compositions and physical properties such as particle size, density and total surface area. Chemical analysis techniques are well

known and three predominate in practical catalyst testing; atomic absorption spectroscopy (AAS), inductively coupled plasma spectroscopy (ICP) and x-ray fluorescence spectroscopy (XRF). Each has its own particular strengths and are generally considered complimentary methods, that is, where one is weak another may be particularly strong.

Physical measurements of size, shape, and density are very important to catalyst performance, however, they do not seem to be studied as often as other properties; perhaps because the instrumentation needed is usually not very complex, or the properties are highly process dependent. Size measurement techniques vary depending upon sizes and shapes of particles to be measured. Larger extrudates can be measured directly with micrometers or calibrated light microscopes. Sizes of large spherical materials are best determined by screen or sieve analysis; dry screens being suitable for sizes above 40 microns diameter and wet screens preferred for sizes below 40 microns. As sizes become smaller, commercial equipment using a variety of light scattering, sedimentation, resistance zone techniques, and image analysis, are available. The latter, particle image analysis (PIA), provides not only particle size information but information on particle morphology as well. This information is very important in understanding transport, catalyst loading, and movement within a particular unit. FCC catalysts, for example, are circulated through their respective hardware at rates as high as 2000 pounds per second!

Nitrogen physisorption methods for total surface area (BET), and more recently macropore surface area determination (t-plot) are used to quantify relationships of the amount and type (zeolite, matrix) of surface present. Nitrogen and mercury pore size distribution (NPSD & HGPSD) are used to determine sizes of pores within the catalyst. Bulk, particle, and skeletal densities can be measured with standard volumetric apparatus or more recently with sophisticated pycnometers using helium as a fill gas.

The next stage of characterization focuses upon the different phases present within the catalyst particle and their nature. Bulk, component structural information is determined principally by x-ray powder diffraction (XRD). In FCC catalysts, for example, XRD is used to determine the unit cell size of the zeolite component within the catalyst particle. The zeolite unit cell size is a function of the number of aluminum atoms in the framework and has been related to the coke selectivity and octane performance of the catalyst in commercial operations. Scanning electron microscopy (SEM) can provide information about the distribution of crystalline and chemical phases greater than 100nm within the catalyst particle. Differential thermal analysis (DTA) and thermogravimetric analysis (TGA) can be used to obtain information on crystal transformations, decomposition, or chemical reactions within the particles. Cotterman, et al describe how the generation of this information can be used to understand an FCC catalyst system.

Microanalytical methods are used to move further down in the characterization scale. X-ray photoelectron spectroscopy (XPS or ESCA), (see Barr); Auger electron spectroscopy (AES), and secondary ion mass spectroscopy (SIMS) as presented by Leta for imaging FCC catalysts, are surface analysis techniques providing chemical analy-

sis and bonding information from the upper 1 to 20 atomic layers. Transmission electron microscopy (TEM, STEM) can provide both structural and chemical analysis with resolutions to 1nm (see Targos and Bradley).

The final level is the characterization of the atomic and/or active species present. A variety of techniques exist and can be divided into two areas, noninvasive, and use of a "probe" molecule with subsequent analysis. Examples of the former are magic angle-spinning nuclear magnetic resonance (MASNMR) as discussed by Welsh and Lambert, electron spin resonance (ESR), and extended x-ray absorption edge fine structure (EXAFS) as used by Woolery. The NMR techniques analyze the nuclear environment of the target atom which can lead to location of atoms within a crystal lattice. For example, using  $^{29}\text{Si}$  MASNMR, one can estimate how alumina atoms are distributed throughout the faujasite framework. This information aids in understanding the catalyst's performance since the cracking activity and selectivity are directly related to the tetrahedral alumina site within the zeolite structure. ESR and EXAFS are directed at the electrons of a specific element and can identify coordination numbers and interatomic distances. Tests such as chemisorption, infrared spectroscopy (IR), and temperature programmed desorption (TPD) using "probe" molecules are useful in measuring acid site density and distribution. Use of chemisorption techniques such as these, can yield information about the nature of the acidic reaction; the strength and distribution of the active sites are fundamental to understanding catalyst performance now, and for designing new systems for the future. Peri, and Mieville and Reichmann describe these techniques in greater detail.

#### CATALYST TESTING PROGRAM

While catalyst testing programs at various laboratories differ in details and execution, certain fundamental tests performed are very similar. A typical fluid catalytic cracking catalyst testing laboratory must provide a method for determining the activity and selectivity of the catalyst of interest. The micro-activity test (MAT) is used for this and is described in detail in American Society for Testing and Materials (ASTM) method D-3907. The basic D-3907 test has been extended by most evaluation laboratories to include different feedstocks, operating conditions, and analyses in order to predict most commercial FCC product yields. While quantitative estimates are difficult to interpret from such small scale experiments, the general direction or trends in product yields, gasoline, coke, light gas, etc., are easily discernible.

As mentioned previously, attrition testing is performed in a variety of equipment designed to simulate the conditions existing within an operating unit. For FCC catalysts, this means high velocity transport, therefore the apparatus used consists of a high velocity air jet, at or near sonic velocity, directed into the catalyst bed. Such action generates fine particles (less than 20 microns) and these "new" fines are measured over a fixed time period. Higher numbers indicate a softer product which generally would give correspondingly higher losses in actual operation.

X-ray diffraction is used to quantify the crystalline species such as zeolite, alumina, and kaolin in raw materials and finished products. Such information is used not only by research scientists, but also by quality assurance personnel during the manufacturing process. Changes in any of these materials can affect the catalysts' performance and cost, therefore they must be precisely controlled.

Because FCC catalysis is a surface reaction, nitrogen physisorption and mercury porosimetry are widely used to measure the distribution of surface area and pore volume within the FCC catalyst. By using nitrogen adsorption techniques for example, it is possible to distinguish between micro- and macropores. Since zeolites fall within the micropore region, using this technique in conjunction with suitable standards, can quantify the amount of zeolite present. This is particularly helpful when looking at hydrothermally deactivated samples in which both the zeolite and matrix have been partially destroyed. In addition, as residual feedstocks (higher molecular weight) become more widely used, the size of the "access" pores becomes important since molecular size increases with molecular weight. Also, along with the heavier oils, the contaminant metals, notably nickel and vanadium, will desposit on the catalyst along with additional coke, further reducing the size of the pores; thereby denying access to the large oil molecules.

Other important physical measurements are bulk densities used to estimate hopper contents and circulation factors, and particle size analysis. The correct distribution of fine particles (30 - 180 microns) is essential to proper fluidization and transfer within the FCC unit. Generally, particles less than 30 microns are lost to the atmosphere or fines recovery system and are destined for a landfill. If the catalyst is too coarse, it may not circulate through the unit, necessitating a shutdown. Both problems are costly to the refiner and must be avoided. In addition, observation of particle size distribution changes at various points within the unit can pinpoint equipment malfunctions that might otherwise go undetected.

Bulk chemical analysis is used during manufacturing to determine the level of zeolite ion exchange and effectiveness of subsequent washing procedures. It is also useful to verify the correct component formulation. For example, rare earth oxides, when exchanged into the zeolite structure, generally produce a more active and gasoline selective catalyst. Increased rare earth, however, also lowers gasoline octane by promoting hydrogen transfer reactions. Thus, the amounts of rare earth elements are a delicate balance between gasoline production and octane requirements, with each refinery operating at different levels depending upon their economic requirements. In the field, various metals are deposited on the catalyst depending upon the operation. Accurate and precise analytical work can again pinpoint problems. For example, nickel and vanadium present in the oil, will desposit quantitatively on the catalyst. Simultaneous changes in the level of both metals with their ratio remaining constant is an indication that catalyst additions have changed. If on the other hand, the ratio Ni:V has changed, then a different feedstock was probably responsible. Appearance of other elements can signal problems as well; sodium

indicates a desalter may be a problem, while increases in lead means leaded gasoline is finding its way to the FCC unit.

The foregoing tests are applied to each sample returned to the catalyst vendor from a customer's unit. Since the operation of an FCC unit is very dynamic, response time is critical, and data is generally available from the manufacturer's lab two to five days following receipt of sample. Most of the analytical and some of the evaluation tests are also performed as a function of the manufacturing quality control laboratory, but response times are measured in minutes, not days. Presently, many of the characterization tests discussed in the previous section are not essential, however, they provide additional understanding in the very complex areas of catalyst research. Much of today's routine testing was thought to be either too complex, costly, or time consuming just a decade ago.

#### **SUMMARY**

As can be seen, the field of catalyst characterization makes extensive use of most available chemical testing methodologies, and requires the cooperation and collaboration of many different people to be successful. Due to the complexity of catalyst preparation and use, it is not surprising that different laboratories have developed different methods and procedures to measure the same property.

Indeed, it is entirely possible to obtain a competitive edge by possessing a method or technique that better predicts true commercial catalyst performance. As catalyst testing matures and computerized instrumentation improves, the "art" of catalyst manufacturing is slowly yielding to science.

#### **JOURNAL EXAMPLES:**

1. Winton, John M., "Catalysts '88 - Restructuring for Technical Clout", Chemical Week, (June 29, 1988).
2. Corbett, Richard A., "More Specialization Coming From Catalyst Suppliers", Oil & Gas Journal, (October 5, 1987).

#### **PATENT EXAMPLES:**

3. a. Secor, R.B., Van Nordstrand, Pegg, D.R., U.S. Patent 4,010,116 (1977).  
b. Lim, J., and Stamiros, D., U.S. Patent 4,086,187 (1978).  
c. Lim, J., Stamiros, D., Brady, M., U.S. Patent 4,206,085 (1980).
4. a. Elliott, Jr., C.H., U.S. Patent 3,867,308 (1975).  
b. Ostermaier, J.J. and Elliott, Jr., C.H., U.S. Patent 3,957,689 (1976).  
c. Elliott, Jr., C.H., U.S. Patent 4,022,714 (1977).

RECEIVED April 27, 1989

## Chapter 4

# Relationship Between Structure and Catalytic Performance of Dealuminated Y Zeolites

R. L. Cotterman, D. A. Hickson, and M. P. Shatlock

W. R. Grace and Company, Washington Research Center,  
Columbia, MD 21044

Dealuminated Y zeolites which have been prepared by hydrothermal and chemical treatments show differences in catalytic performance when tested fresh; however, these differences disappear after the zeolites have been steamed. The catalytic behavior of fresh and steamed zeolites is directly related to zeolite structural and chemical characteristics. Such characteristics determine the strength and density of acid sites for catalytic cracking. Dealuminated zeolites were characterized using X-ray diffraction, porosimetry, solid-state NMR and elemental analysis. Hexadecane cracking was used as a probe reaction to determine catalytic properties. Cracking activity was found to be proportional to total aluminum content in the zeolite. Product selectivity was dependent on unit cell size, presence of extraframework alumina and spatial distribution of active sites. The results from this study elucidate the role that zeolite structure plays in determining catalytic performance.

Dealuminated Y zeolites are widely used commercially in fluid cracking catalysts to produce high-octane gasoline-range products(1). Various methods of preparation of dealuminated zeolites can lead to materials with a range of different structural and chemical characteristics(2). These characteristics play a key role in determining activity and selectivity during catalytic cracking. Structural features such as unit cell size, presence of extraframework material, pore-size distribution, and active site spatial distribution affect zeolite acidity and diffusional properties which, in turn, influence hydrocarbon reactivity.

The objective of this work is to identify relationships between structure and catalytic performance in the specific case of hydrocarbon cracking over dealuminated Y zeolites. Dealuminated zeolites are prepared using chemical and hydrothermal methods and the effect of dealumination method on structure-performance

relationships is investigated. Zeolites are evaluated after calcination and after severe steaming to simulate the properties of fresh and equilibrium FCC catalysts.

Hydrothermal dealumination is carried out by treating an ammonium-exchanged form of the zeolite in the presence of mild steam(3). The resulting zeolites are called "ultrastable Y" (USY) zeolites due to their enhanced thermal and hydrothermal stability. During the steam treatment, aluminum is expelled from the framework into zeolite cages(4). This aluminum then relocates preferentially to the outer portions of the crystal giving rise to an aluminum-rich surface(5). Framework vacancies created by aluminum expulsion are believed to be annealed by silicon migration from other framework locations(6). This silicon migration subsequently results in collapse of portions of the zeolite framework. Hence, hydrothermal dealumination generates a secondary pore system (mesoporosity) within the zeolite and with an overall loss of crystallinity. Evidence for the presence of mesopores is provided indirectly by sorption(7) measurements and directly by electron microscopy studies(8).

Chemical dealumination involves reaction of the zeolite framework with any one of a variety of reagents(2). In this work, zeolites were reacted with ammonium hexafluorosilicate in aqueous solution(9-12) to prepare dealuminated products. Aluminum was extracted from the zeolite framework and removed from the crystal as a soluble fluoroaluminate complex; the resulting lattice vacancies are believed to be filled by silicon in solution. Composition profiles of chemically dealuminated zeolites (AFS) are homogeneous and indicate the entire crystal is accessible for dealumination(13). Sorption data indicate that AFS zeolites do not possess a secondary pore system although pore blockage may occur due to occlusion of fluoroaluminate species(13).

The structural features of dealuminated zeolite samples were characterized using X-ray powder diffraction, porosimetry and solid-state NMR measurements. Hexadecane cracking was used as a probe reaction to investigate catalytic properties of pure zeolites.

### Experimental

Two sets of chemically and hydrothermally dealuminated zeolites were prepared from separate sources of partially ammonium-exchanged Y zeolite. The first set of samples, designated USY-1 and AFS-1, were prepared from Davison ammonium-exchanged Y zeolite (Y-1). The second set of samples, designated USY-2 and AFS-2, were prepared from Linde LZ-Y62 zeolite (Y-2). Typical physical and chemical properties of the two starting materials are compared in Table I; the primary difference between these materials is the extent of soda removal by ammonium exchange.

The hydrothermally dealuminated zeolites (USY-1 and USY-2) used in this study were plant-grade materials and were used without further exchange. The chemically dealuminated zeolites (AFS-1 and AFS-2) were prepared in our laboratory following the method of Breck and Skeels(12). The AFS samples were washed thoroughly until residual fluoride was no longer detected in the filtrate; AFS-1 received additional warm-water washes to reduce further fluoride levels in the solid. AFS samples were prepared so as to have the same extent of framework dealumination as the USY samples.



Table I. Characterization of Starting Materials

	Y-1	Y-2
Composition, wt%		
Al <sub>2</sub> O <sub>3</sub>	23.63	23.93
SiO <sub>2</sub>	69.69	70.06
Na <sub>2</sub> O	3.94	2.94
Bulk SiO <sub>2</sub> /Al <sub>2</sub> O <sub>3</sub>	5.0	5.0
Degree of Na Exchange, %	73	80
XRD Unit Cell, Å	24.71	24.70
N <sub>2</sub> Surface Area, m <sup>2</sup> /g		
Total BET	947	993
Micropore (< 20 Å)	929	975
N <sub>2</sub> Pore Volume, cc/g		
Total	0.482	0.473
Micropore (< 20 Å)	0.356	0.376
Mesopore (20-200 Å)	0.033	0.025

Dealuminated zeolite samples were calcined in air at 540°C for three hours prior to catalytic testing. A portion of each sample was further modified using high-temperature steam. Zeolite samples were placed in a fixed-bed quartz tube; 95% steam was passed through the bed at 750°C and atmospheric pressure for 4 hours.

Bulk elemental analyses were determined using X-ray fluorescence (Si,Al), inductively coupled plasma (Al,Na) and ion chromatography (F) techniques. The unit cell constant was determined by X-ray diffraction with a Siemens D-500 powder diffractometer following the method outlined in ASTM D3942-80. Nitrogen sorption data were obtained using a Quantachrome Autosorb 6 porosimeter operated at liquid nitrogen temperature. Pore-size distributions were calculated using the desorption branch of the isotherm; micropore contributions were determined by T-plot analysis.

Starting materials and dealuminated products were characterized using <sup>29</sup>Si and <sup>27</sup>Al MAS-NMR. <sup>29</sup>Si spectra were obtained on a Bruker MSL-200 spectrometer at 39.7 MHz using 30° pulses and 5 second repetition rates. Spinning rates were typically 4.5 kHz and 5000-10000 scans were obtained per sample. <sup>27</sup>Al spectra were run on a Bruker AM-400 instrument at 104.3 MHz with 10° pulses and 0.1 second repetition rates. Spinning rates were typically 5.0 kHz and 2000-10000 scans were obtained per sample.

Hexadecane cracking reactions were carried out over pure zeolites in an atmospheric fixed-bed reactor at 500°C. Zeolites were sized to 40/80 mesh and mixed with glass beads prior to testing. The catalyst bed was purged with dry nitrogen at 500°C for 30 minutes prior to reaction and 10 minutes following reaction. Hexadecane feed was injected via a syringe pump at a constant rate of 27.8 g/hr. Space velocities were varied by changing catalyst loading. Separate gas and liquid products were collected over a three minute run and analyzed by gas chromatography. Approximately 350 components in the liquid product were separated and identified using a 50m x 0.2mm methyl silicone capillary column with 0.5µm film thickness. Spent catalysts were removed from the reactor and calcined in air for 3 hours at 540°C to determine coke yield. Coke amount is reported as the difference in catalyst weight before and after calcination.

Presentation of Results

Catalyst Characterization. The compositions of dealuminated products are reported in Table II on a volatile-free basis. The two USY samples have similar bulk compositions; however, both samples have higher silica-alumina ratios than the starting Y zeolites (Table I) indicating some alumina was lost during preparation. The two AFS samples have similar bulk compositions and lower aluminum contents than the USY samples. The extra wash given to AFS-1 results in a lower fluoride level than that of AFS-2. Fluorides remain after calcination but drop below 0.01% after steaming. Soda levels in the AFS materials are slightly higher than those in USY materials in spite of several exchanges and extensive washing and indicates that sodium remains bound in the dealuminated zeolite. Both sets of AFS and USY samples have similar unit cell dimensions.

Table II. Characterization of Dealuminated Zeolites

	USY-1	USY-2	AFS-1	AFS-2
Composition, wt%				
Al <sub>2</sub> O <sub>3</sub>	21.37	23.88	16.74	17.08
SiO <sub>2</sub>	77.77	76.06	81.35	80.98
Na <sub>2</sub> O	0.86	0.70	1.46	1.54
F	<0.01	<0.01	0.05	0.37
Bulk SiO <sub>2</sub> /Al <sub>2</sub> O <sub>3</sub>	6.2	5.4	8.3	8.1
XRD Unit Cell, Å	24.56	24.58	24.56	24.53

Table III shows XRD and porosimetry data for calcined USY and AFS zeolites. All samples show shrinkage of the unit cell to comparable values following calcination. As a result, calcined samples are compared at similar silica-alumina framework ratios. All calcined samples have well developed microporous structures and comparable total pore volumes. These porosimetry data confirm that the hydrothermally dealuminated materials contain a significant fraction of mesopores relative to chemically dealuminated materials. The extensive washing given to AFS-1 results in higher micropore surface area and volume compared to AFS-2 and suggest that AFS-2 contains occluded fluoroaluminate and fluorosilicate compounds within the microporous structure.

Table III. Characterization of Calcined Dealuminated Zeolites

	USY-1	USY-2	AFS-1	AFS-2
XRD Unit Cell, Å	24.49	24.50	24.49	24.48
N <sub>2</sub> Surface Area, m <sup>2</sup> /g				
Total BET	705	798	923	729
Micropore (< 20Å)	645	738	903	711
% Micropore	91.3	92.5	97.8	97.5
N <sub>2</sub> Pore Volume, cc/g				
Total	0.438	0.511	0.453	0.405
Micropore (< 20Å)	0.250	0.282	0.346	0.268
Mesopore (20-200Å)	0.089	0.095	0.036	0.052

Porosimetry and XRD data are given in Table IV for steamed USY and AFS zeolites. Following steaming, the unit cell sizes of AFS and

USY zeolites reduce to comparable values. Steam treatment decreases micropore surface area and increases mesopore volume. With the exception of AFS-1, all samples have comparable micropore volumes and surface areas. AFS-1 shows a large decrease in surface area relative to the other samples.

Table IV. Characterization of Steamed Dealuminated Zeolites

	USY-1	USY-2	AFS-1	AFS-2
XRD Unit Cell, Å	24.30	24.33	24.32	24.32
N <sub>2</sub> Surface Area, m <sup>2</sup> /g				
Total BET	559	615	545	581
Micropore (< 20Å)	513	542	492	547
% Micropore	91.0	88.1	90.3	94.1
N <sub>2</sub> Pore Volume, cc/g				
Total	0.407	0.462	0.324	0.395
Micropore (< 20Å)	0.190	0.204	0.185	0.206
Mesopore (20-200Å)	0.112	0.154	0.073	0.071

Figures 1 and 2 show spectra obtained using <sup>29</sup>Si and <sup>27</sup>Al MAS-NMR. The peaks in the <sup>29</sup>Si spectra are labeled with Si(nAl) for n=0,1,2,3 or 4 indicating the number of nearest aluminum neighbors. The <sup>27</sup>Al spectra are labelled with Al(IV), Al(V) and Al(VI), indicating aluminum coordination number. The starting material Y-1 is shown in the upper left-hand corner of each figure. Figure 1 shows the silicon in Y-1 are randomly distributed throughout the framework whereas Figure 2 verifies that all of the aluminum is tetrahedrally coordinated(IV). The corresponding NMR spectra for Y-2 (not shown) are nearly identical to those for Y-1.

The spectra of the as-synthesized materials show the AFS and USY zeolites prior to calcination. The USY-2 zeolite shows distinct differences in silicon distribution compared to the two AFS samples although both USY and AFS materials have similar framework composition (as evidenced by unit cell size). The <sup>27</sup>Al spectra show that USY-2 contains aluminum in octahedral coordination (VI) whereas the AFS materials contain only Al(IV).

Following calcination, both USY and AFS materials undergo framework changes but continue to show differences. The <sup>29</sup>Si spectra show an enhancement of the n=0 peak in both USY and AFS spectra but indicate that silicon distributions are different in AFS and USY materials. Silica-alumina framework ratios calculated from the <sup>29</sup>Si NMR spectra are in good agreement with values obtained from unit cell measurements. The <sup>27</sup>Al spectra show the presence of some Al(VI) in all samples; however, the <sup>27</sup>Al spectra were not run under quantitative conditions. Furthermore, the peak corresponding to Al(IV) may contain contributions from both framework and extraframework species(14). Therefore, a quantitative determination of framework and extraframework aluminum species is not possible with these data.

After steaming, the NMR spectra of USY and AFS materials show distinct similarities. The <sup>29</sup>Si spectra show a major peak for n=0 with only minor contributions from higher coordinations. The <sup>27</sup>Al spectra show the presence of amorphous material represented as a broad background peak in all samples and the generation of a third

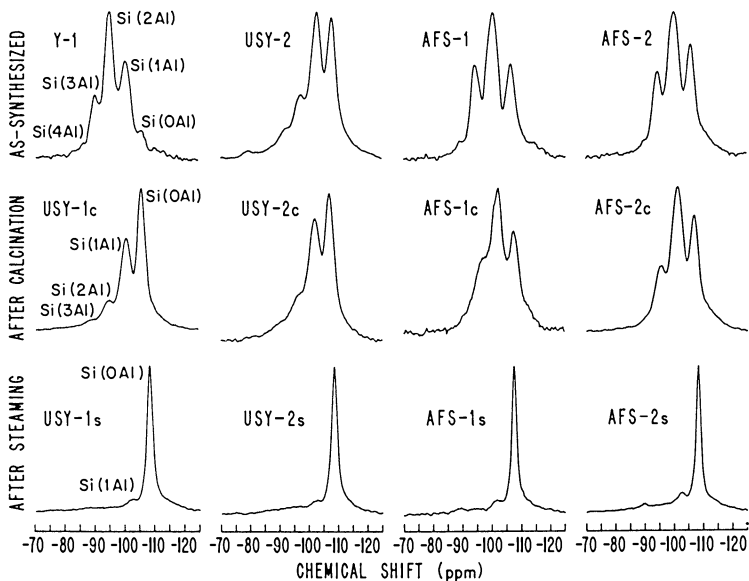


Figure 1.  $^{29}\text{Si}$  MAS-NMR of hydrothermally and chemically dealuminated Y zeolites.

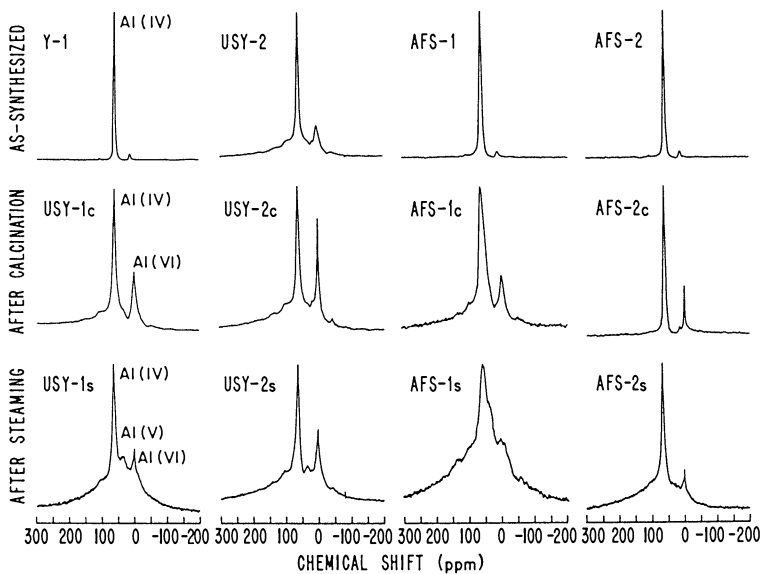


Figure 2.  $^{27}\text{Al}$  MAS-NMR of hydrothermally and chemically dealuminated Y zeolites.

peak near 30 ppm. The nature of the aluminum species giving rise to this third peak is currently the subject of controversy and has been attributed to both pentacoordinated(V)(15) and tetrahedrally-coordinated (16) extraframework aluminum. The  $^{27}\text{Al}$  spectra of AFS-1 indicate the structure has been degraded by steaming which is consistent with the loss in surface area.

Catalytic Properties. Catalytic properties were determined for both calcined and steamed zeolites using hexadecane cracking as a test reaction. Hexadecane cracking provides information on zeolite activity and selectivity which can be used to estimate octane production. Data were obtained for both calcined and steamed zeolites at hexadecane conversions from 30% to 70%; multiple runs were made for each catalyst.

Catalyst activities are expressed in Table V as apparent first-order rate constants. Results are reported in dimensionless form relative to USY-1. The initial rate constants are estimated for AFS and USY zeolites by extrapolating data to zero conversion and show USY zeolites are more active than AFS zeolites. The data indicate that steaming does not significantly alter initial activity. Observed rate constants are reported at 50% conversion and reflect effects due to catalyst deactivation. As a result, observed activities for steamed catalysts are higher than those for calcined catalysts.

Table V. Hexadecane Cracking Results for Dealuminated Zeolites. Relative First-Order Rate Constants\*

	USY-1	USY-2	AFS-1	AFS-2
Initial Rate Constant	1.00	1.50	0.34	0.37
Apparent Rate Constant at 50% Conversion				
Calcined	0.65	0.40	0.15	0.22
Steamed	0.93	1.40	0.32	0.35

\* Rate constants calculated from  $k = -\text{WHSV} \ln(1-x)$  where  $x$  is fractional conversion and WHSV is weight hourly space velocity.

Selectivity results at constant 50% conversion are reported in Tables VI and VII for calcined and steamed zeolites, respectively. Product selectivities are divided into light gas ( $\text{C}_1\text{-C}_4$ ), gasoline ( $\text{C}_5\text{-C}_{12}$ ) and coke. The gasoline fraction is further divided into paraffin, olefin, naphthene and aromatic (PONA) components. Research and motor octane numbers are calculated for the gasoline fraction using a GC-based compositional octane model.

Table VI indicates that calcined USY and AFS materials show differences in product selectivities and gasoline compositions. AFS samples show lower gasoline selectivities and higher coke yields than USY samples. In addition, products from AFS show slightly decreased olefins and increased aromatics and branched paraffins than those from USY. Calculated octanes are higher for AFS than for USY.

Figure 3 shows the molecular weight distributions of cracked products made over calcined USY-2 and AFS-2. Cracked products from AFS have a sharper distribution which is shifted towards lower molecular weights than those from USY. In addition, the distribution

for AFS-2 shows an increase in the C<sub>7</sub>-C<sub>10</sub> range which corresponds to high aromatic yields.

Table VI. Hexadecane Cracking Results for Calcined Zeolites.  
Product Slate at 50% Conversion

	USY-1	USY-2	AFS-1	AFS-2
Selectivity, wt%				
C <sub>1</sub> -C <sub>4</sub> Fraction	36.6	38.8	43.6	42.6
C <sub>5</sub> -C <sub>12</sub> Fraction	58.2	56.2	47.8	49.6
C <sub>12+</sub> Fraction	2.4	2.6	2.4	1.7
Coke	2.8	2.4	6.2	6.1
C <sub>5</sub> -C <sub>12</sub> Composition, wt%				
Paraffins	51.0	54.2	56.3	55.9
Olefins	36.0	32.9	27.2	30.5
Naphthenes	3.5	2.7	2.2	2.4
Aromatics	9.4	10.3	14.4	11.2
C <sub>5</sub> -C <sub>12</sub> Octane Number				
Research	86.5	87.1	88.2	88.0
Motor	76.0	76.8	78.4	78.1

Steamed AFS and USY zeolites give similar product selectivities as shown in Table VII (gasoline selectivity for AFS-1 is slightly lower than for the other zeolites). Consistent with the selectivity data, Figure 4 shows identical molecular weight distributions of cracked products from steamed AFS-2 and USY-2 zeolites. Steam treatment produces a shift to higher-molecular-weight products with an increase in gasoline selectivity. Gasoline olefinicity increases upon steaming and calculated octane numbers decrease.

Table VII. Hexadecane Cracking Results for Steamed Zeolites.  
Product Slate at 50% Conversion

	USY-1	USY-2	AFS-1	AFS-2
Selectivity, wt%				
C <sub>1</sub> -C <sub>4</sub> Fraction	30.9	31.3	34.3	30.6
C <sub>5</sub> -C <sub>12</sub> Fraction	64.0	64.6	61.1	64.7
C <sub>12+</sub> Fraction	3.4	2.4	2.3	2.9
Coke	1.7	1.7	1.7	1.9
C <sub>5</sub> -C <sub>12</sub> Composition, wt%				
Paraffins	47.0	48.7	48.3	49.9
Olefins	43.4	41.2	41.6	38.9
Naphthenes	4.0	4.1	4.2	3.7
Aromatics	5.6	6.0	6.0	7.5
C <sub>5</sub> -C <sub>12</sub> Octane Number				
Research	85.7	85.3	85.8	85.5
Motor	74.9	74.4	74.8	74.8

Figure 5 shows normalized PONA selectivities in the C<sub>5</sub>-C<sub>12</sub> fraction from hexadecane cracking. Data are included at conversions between 30%-70% over both AFS and USY zeolites. Calcined and steamed samples are represented by open and closed symbols, respectively. The data display general correlations which are independent of yield structure and catalyst modification. These correlations are unique to the Y zeolite structure.

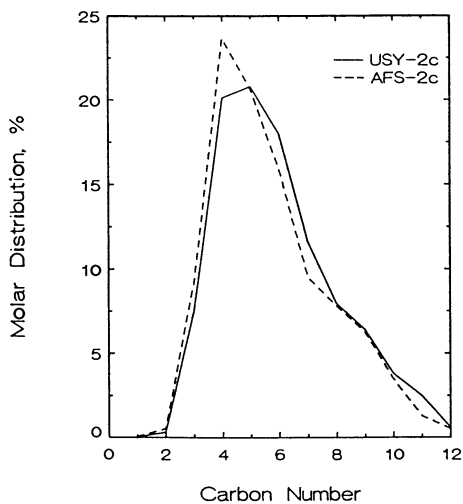


Figure 3. Molecular weight distribution from hexadecane cracking at 50% conversion over calcined USY and AFS zeolites.

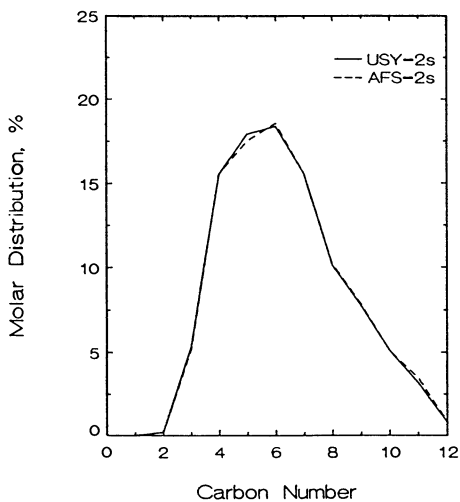


Figure 4. Molecular weight distribution from hexadecane cracking at 50% conversion over steamed USY and AFS zeolites.

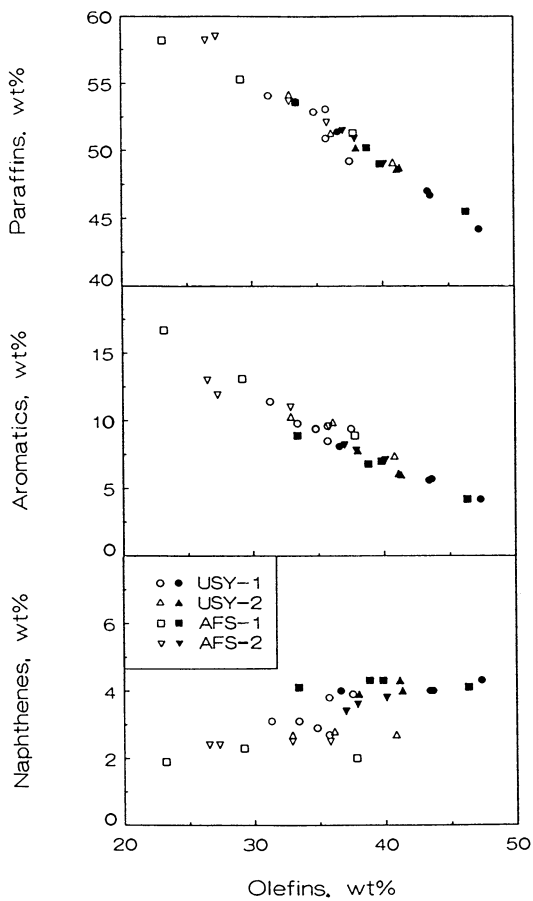


Figure 5. PONA selectivities in gasoline fraction from hexadecane cracking over USY and AFS zeolites.



Light gas compositions are shown in Table VIII for hexadecane cracking at constant 50% conversion. Results are reported as iso-to-normal and olefin-to-paraffin ratios for  $C_4$  products. Calcined AFS and USY zeolites show significant differences in both selectivity ratios whereas steamed zeolites show similar light gas selectivities. However, steamed selectivities are dramatically different from those of calcined zeolites. These results are in good qualitative agreement with results obtained for AFS and USY zeolites by gas-oil cracking (17).

Table VIII. Hexadecane Cracking Results for Dealuminated Zeolites. Light Gas Composition at 50% Conversion

	Isobutane/n-Butane Ratio			
	USY-1	USY-2	AFS-1	AFS-2
Calcined Zeolites	2.65	2.57	2.82	2.83
Steamed Zeolites	1.81	1.93	1.89	1.95
	Butenes/Butanes Ratio			
	USY-1	USY-2	AFS-1	AFS-2
Calcined Zeolites	0.83	0.78	0.54	0.57
Steamed Zeolites	1.84	1.67	1.74	1.61

### Discussion of Results

Catalyst Structural Characteristics. Structural features of AFS and USY materials have been characterized in this work in terms of unit cell size, presence of extraframework material, active-site distributions, and pore-size distributions. These features are similar for both sets of USY and AFS samples which indicates that structural characteristics are not related to the source of Y zeolite.

XRD measurements show that calcined AFS and USY zeolites have comparable unit cell sizes. Upon steaming, the unit cell sizes for both AFS and USY reduce to identical values. Hence, framework silica-alumina ratios equilibrate to comparable levels independent of the method by which the zeolites were originally dealuminated.

As synthesized, both USY and AFS materials show distinct differences by  $^{29}\text{Si}$ -NMR in the distribution of framework silicon. The framework silicon distribution depends on the mechanism of aluminum removal and silicon replacement during preparation. These differences remain after calcination but disappear upon steaming. Severe steaming results in loss of a large portion of framework aluminum such that only the strongest-bound aluminum species remain in the framework. Consequently, steamed AFS and USY zeolites have similar framework silicon distributions.

As-synthesized AFS zeolites do not contain extraframework aluminum as evidenced by  $^{27}\text{Al}$  NMR. As-synthesized USY zeolites contain appreciable amounts of extraframework material as seen by comparing framework and bulk silica-alumina ratios and by examining  $^{27}\text{Al}$  spectra. Upon calcination both AFS and USY materials contain extraframework aluminum. The amount of extraframework aluminum in both AFS and USY materials increases on steaming.

Porosimetry data confirm the presence of mesopores in calcined

USY zeolites; this mesoporosity increases on steaming. Calcined and steamed AFS zeolites show some mesoporosity; however, the amounts remain lower than those in USY zeolites.

Catalyst Performance Relationships. Hexadecane cracking activity of AFS and USY zeolites, when corrected for deactivation effects, shows little or no dependence on framework composition. Rather, as shown in Figure 6, activity appears to be a function of total aluminum content independent of the method of dealumination. This result implies that hexadecane cracking occurs over both framework and extraframework acid sites and that it is the total number of such sites which determines catalytic activity. Hence, extraframework material in the USY samples makes a significant contribution to catalyst activity as reported by others(18,19).

Coke selectivity directly influences the rate of catalyst deactivation as seen by comparing coke selectivities in Tables VI and VII with observed rate constants in Table V. Our data indicate calcined AFS zeolites show higher coke selectivities than USY zeolites when compared at similar unit cell sizes. This result suggests that distribution of framework acid sites(as reflected by the distribution of framework silicon) has a strong impact on coke selectivity. In addition, coke selectivity has been shown to correlate with the density of strong acid sites in the framework(20). Our data confirm this and show that steaming decreases the density of such sites which, in turn, leads to decreased coke selectivities.

Gasoline selectivity is influenced by both the method of dealumination and steam treatment and, hence, depends on framework acid sites and on presence of extraframework material. Both framework and extraframework sites contribute to the overall zeolite acidity. Framework Al(IV) acid sites are associated with Bronsted acidity whereas extraframework Al(VI) acid sites are associated with Lewis acidity(21). Calcined AFS samples are reported (22) to contain greater Bronsted acidity than USY samples from infrared characterization and to have stronger acidity as measured by ammonia desorption. As a result, the stronger acidity of calcined AFS samples cracks hexadecane to lower molecular weight products than USY. After steaming, the acidities of both AFS and USY are reduced to similar levels and lead to similar gasoline selectivities which are increased relative to the calcined zeolites.

Light gas selectivities from hexadecane cracking (Table VIII) confirm the Bronsted/Lewis acid character of AFS and USY zeolites. High iso-to-normal ratios and low olefin-to-paraffin ratios correlate with increased Bronsted acid character(23). Calcined AFS has more Bronsted acidity than calcined USY zeolites; after steaming, both AFS and USY have strong Lewis acid character. Differences between AFS and USY samples are subtle relative to the differences seen between steamed and calcined samples. Hence, effects due to steaming override effects due to original method of dealumination.

Gasoline composition from hexadecane cracking over calcined and steamed AFS and USY zeolites can be represented by general correlations as shown in Figure 5. As these correlations are unique to zeolite Y, they indicate that the Y zeolite framework topology plays an important role in the mechanism of product formation. The method of dealumination and subsequent steam treatment lead to various PONA compositions; however, these compositions result from a

single mechanism for hydrocarbon conversion. This result suggests that modifying Y zeolite influences the relative rate of individual steps in the overall mechanism (for example, hydrogen-transfer reactions) through modification of zeolite acidity.

Figure 7 shows calculated octane numbers from hexadecane cracking as a function of gasoline yield. Calcined and steamed zeolites are represented by open and closed symbols, respectively. The calculated octane number reflects changes in the gasoline molecular weight distribution and, to a lesser extent, composition effects. Increases in octane for calcined AFS zeolites are offset by decreased gasoline yields.

Gasoline octane number for steamed USY zeolites has been shown to correlate with unit cell size(24). This concept has been exploited to design USY catalysts for octane production(25). In this work we demonstrate that parameters other than unit cell size have an impact on octane; similar conclusions have been reported by others (26). As shown in Figure 7, calcined zeolites with similar unit cell sizes demonstrate different octane-producing behavior. Hence, structural characteristics such as extraframework aluminum and spatial distribution of acid sites are important factors affecting zeolite acidity. After steaming, the octane behaviors of AFS and USY zeolites are similar reflecting similarities in zeolite acidities.

Extraframework aluminum contributes to the observed catalytic behavior in both activity and selectivity. It is interesting to note that although steamed USY contains more extraframework aluminum than steamed AFS, both AFS and USY give similar product selectivities. Observed product selectivities from steamed zeolites are insensitive to the amount of extraframework aluminum present within the composition range investigated in this study.

Through the use of hexadecane cracking alone, we have been unable in this work to elucidate the role of mesoporosity in the catalytic behavior of calcined or steamed zeolites. Steamed AFS and USY zeolites show differences in mesoporosity but exhibit similar catalytic performance. While mesoporosity may affect diffusion in actual FCC catalysts, larger molecules than hexadecane will be required to determine mesopore effects.

### Conclusions

Characterization and catalytic data have been presented for chemically and hydrothermally dealuminated Y zeolites. These data show that zeolite structural differences lead to differences in catalytic behavior. USY and AFS zeolites show distinct structural differences when freshly prepared and after calcination, however, these differences are diminished on steam treatment. As a result, the catalytic behavior of calcined AFS and USY zeolites appears different while that of steamed zeolites is similar. No apparent effects due to source of Y zeolite were observed.

Hexadecane cracking activity correlates with total aluminum content; USY materials are more active than AFS materials before and after steaming. Extraframework aluminum contributes to catalytic cracking activity.

Gasoline selectivity and octane performance are functions of not only unit cell size but also factors such as extraframework material and spatial distribution of active sites. These factors influence

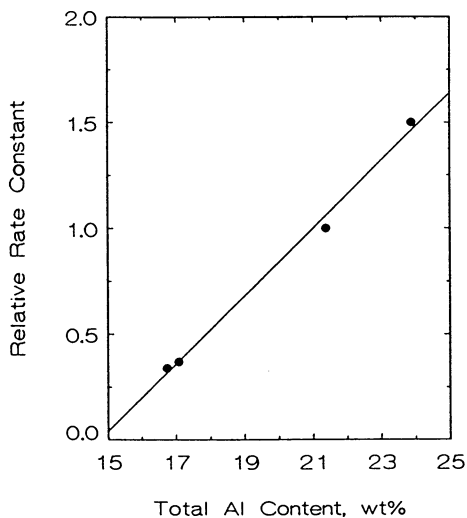


Figure 6. Cracking activity of dealuminated zeolites as a function of total aluminum content.

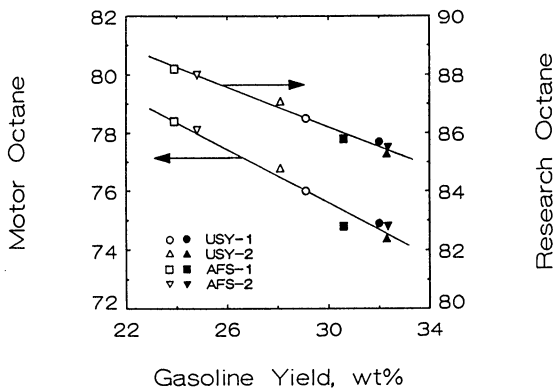


Figure 7. Octane performance of USY and AFS zeolites from hexadecane cracking at 50% conversion.

overall zeolite acidity. Strong acidity in calcined AFS zeolites leads to decreased gasoline selectivities and higher octane products than calcined USY. After steaming, however, acidity levels of USY and AFS are comparable and yield similar product distributions.

No effects due to mesoporosity were observed in hexadecane cracking.

#### Acknowledgments

The authors are grateful to W.R. Grace and Co. for permission to publish this work and to L. Peters, D.M. Roberts and C.F. Miller for assistance with experimental measurements.

#### Literature Cited

1. Catalytica Advances in Fluid Catalytic Cracking-Part 1; Study No. 4186CC: Mountain View, California, 1987.
2. Scherzer, J. ACS Symposium Series No. 248; American Chemical Society: Washington, DC, 1984, p 157.
3. Maher, P.K.; McDaniel, C.V. U.S. Patent 3 293 192 assigned to W.R. Grace and Co., 1966.
4. Kerr, G.T. J. Phys. Chem. 1968, 72, 2594.
5. Dwyer, J.; Fitch, F.R.; Qin, G.; Vickerman, J.C. J. Phys. Chem. 1982, 86, 4574.
6. Maher, P.K.; Hunter, F.D.; Scherzer, J. Advances in Chemistry Series No. 101; American Chemical Society: Washington, DC, 1981; p 266.
7. Lohse, U.; Mildebrath, M. Z. Anorg. Allg. Chem. 1981, 476, 126.
8. Lynch, J.; Raatz, F.; Dufresne, P. Zeolites 1987, 7, 333.
9. Elliot, C.H. U.S. Patent 3 594 331 assigned to W.R. Grace and Co., 1971.
10. Elliot, C.H. U.S. Patent 3 933 983 assigned to W.R. Grace and Co., 1976.
11. Skeels, G.W.; Breck, D.W. Proc. Sixth Intl. Zeolite Conf., Reno, 1984, p 87.
12. Breck, D.W.; Skeels, G.W. U.S. Patent 4 503 023 assigned to Union Carbide Corp., 1985.
13. Akporiaye, D.; Chapple, A.P.; Clark, D.M.; Dwyer, J.; Elliot, I.S.; Rawlence, D.J. Proc. 7th Intl. Conf. Zeolites, Tokyo, 1986, p 351.
14. Ray, G.J.; Meyers, B.L.; Marshall, C.L. Zeolites 1987, 7, 4.
15. Gilson, J.-P.; Edwards, G.C.; Peters, A.W.; Rajagopalan, K.; Wormsbecher, R.F.; Roberie, T.G.; Shatlock, M.P. J. Chem. Soc., Chem. Commun. 1987, 91.
16. Freude, D.; Hunger, M.; Pfeifer, H. Z. Phys. Chemie (NF) 1987, 152, 171.
17. Corma, A.; Herrero, E.; Martinez, A.; Prieto, J. ACS Preprints, Div. of Pet. Chem., Sept. 1987, p 639.
18. Beyerlein, R.A.; McVicker, G.B.; Yacullo, L.N.; Ziemiak, J.J. J. Phys. Chem. 1988, 92, 1967.
19. Corma, A.; Fornes, V.; Martinez, A.; Melo, F.; Pallota, O. Int. Symp. on Innovation in Zeolite Matl. Science, Nieuwpoort (Belgium), 1987, p 495.
20. Rajagopalan, K.; Peters, A.W. J. Cat. 1987, 106, 410.

21. Freude, D.; Frohlich, T.; Hunger, M.; Pfeifer, H.; Scheler, G. Chem. Phys. Letters 1983, **98**, 263.
22. Macedo, A.; Raatz, F.; Boulet, R.; Janin, a.; Lavalley, J.C. Int. Symp. on Innovation in Zeolite Matl. Science, Nieuwpoort (Belgium), 1987, p 375.
23. Wojciechowski, B.W.; Corma, A. Catalytic Cracking: Catalysts, Chemistry and Kinetics; Marcel-Dekker: New York, 1986.
24. Pine, L.A.; Maher, P.J.; Wachter, W.A. J. Cat. 1984, **85**, 466.
25. Ritter, R.E.; Creighton, J.E.; Chin, D.S.; Roberie, T.G. Paper AM-86-45 presented at NPRA Annual Meeting, Los Angeles, March 1986.
26. Corma, A.; Fornes, V.; Martinez, A.; Orchilles, A.V. ACS Symposium Series No. 368; American Chemical Society: Washington, DC, 1988; p 542.

RECEIVED January 26, 1989

## Chapter 5

# Tin Passivation of Vanadium Contaminants in Model Fluid Cracking Catalysts

### Spectroscopic Studies

S. L. Suib<sup>1</sup>, M. W. Anderson<sup>2</sup>, and M. L. Ocelli<sup>3</sup>

<sup>1</sup>Department of Chemistry, University of Connecticut, Storrs, CT 06268

<sup>2</sup>Department of Chemical Engineering, University of Connecticut,  
Storrs, CT 06268

<sup>3</sup>Unocal Corporation, Brea, CA 92621

Components of fluidized cracking catalysts (FCC), such as an aluminosilicate gel and a rare-earth (RE) exchanged zeolite Y, have been contaminated with vanadyl naphthenate and the V thus deposited passivated with organotin complexes. Luminescence, electron paramagnetic resonance (EPR) and Mossbauer spectroscopy have been used to monitor V-support interactions. Luminescence results have indicated that the naphthenate decomposes during calcination in air with generation of (V=O)<sup>2+</sup> ions. After steam-aging, V<sub>2</sub>O<sub>5</sub> and ReVO<sub>4</sub> formation occurred. In the presence of Sn, formation of vanadium-tin oxide species enhance the zeolite stability in the presence of V-contaminants.

Interest in studying metal effects on cracking catalysts has continued during the last ten years and is still an active area of research today (1). Recent results from studies of vanadium contaminated fluid cracking catalysts (FCC) have shown that several vanadium species can exist on FCC surfaces. In fact, luminescence measurements have been used to verify that, initially, V<sub>2</sub>O<sub>5</sub> is generated during calcination of the catalysts (2). Furthermore, transmission electron microscopy experiments with vanadium contaminated FCC's have also been reported and rare earth vanadate formation was proposed based on electron diffraction and energy dispersive x-ray analysis data (3) together with Laser Raman spectroscopy results (4).

In addition to V<sub>2</sub>O<sub>5</sub> and ReVO<sub>4</sub>, formation of vanadic acids like H<sub>3</sub>VO<sub>4</sub> have also been postulated (5); however, stability and Raman data indicate that species like H<sub>4</sub>V<sub>2</sub>O<sub>7</sub> are more likely to occur during steam-aging of the catalysts (6). Formation of rare-earth eutectic compounds with V<sub>2</sub>O<sub>5</sub> have also been mentioned in the literature (7). These aforementioned studies suggest that vanadium

(V) is the important oxidation state involved in catalyst deactivation. Identification of all the vanadium species and their relative concentrations have yet been reported.

There are several methods to passivate metal contaminants in FCC (1). Passivating agents such as Sn (8), Bi (9), P and B (10), and Al, P, Ti, Li and W (11) have been proved useful for reducing the deleterious effects of metals on FCC. These agents are believed to form inert residues on the FCC surface thus increasing metals tolerance. The use of Sb to passivate Ni is commercially accepted and practiced; antimony decreases coke and hydrogen formation and generates an overall increase in activity with respect to untreated metals contaminated catalysts. Metals impregnation methods have been described in the literature; thus the degree of metal resistance of fresh FCC can readily be compared (12). In a recent article concerning the cracking of heavy oils, the deleterious effects of Ni and V impurities have been discussed in detail (13); the need for further studies concerning the poisoning and passivation process of FCC was shown (13). MAT-evaluation in the laboratory has demonstrated that best results concerning metals tolerance are obtained with DFCC systems since these types of catalysts can retain useful cracking activity even when loaded with as much as 1.0-1.5% V (1,5,14).

This paper reviews literature data on model fluid cracking catalysts (FCC) and reports results of spectroscopic studies performed in our laboratories for catalysts in which vanadium has been passivated by tin. Mossbauer spectroscopy, luminescence, x-ray powder diffraction and electron paramagnetic methods have been used to monitor vanadium-tin interactions in all the catalysts studied.

### Experimental

Two main components were used in the model catalysts described in this paper. One component was a europium exchanged ammonium Y zeolite ( $\text{EuNH}_4\text{Y}$ ). The other component was an amorphous aluminosilicate containing about 75%  $\text{SiO}_2$  and 25%  $\text{Al}_2\text{O}_3$  (AAA-alumina). All materials were artificially V-contaminated by impregnation with vanadyl naphthenate solutions in benzene. Tetraphenyl tin (in hot toluene) was the passivating agent used. It was added either before or after loading vanadium on the zeolite ( $\text{EuNH}_4\text{Y}$ ), on the gel or on a gel-zeolite mixture.

Samples were studied after drying ( $100^\circ\text{C}$ ), after calcination in air to  $540^\circ\text{C}$ , and after hydrothermal treatment with 95% steam/5%  $\text{N}_2$  mixtures at  $730^\circ\text{C}$ . Calcination and steaming were performed in quartz reactors. For electron paramagnetic resonance studies samples were sealed off in 2 mm quartz tubes; luminescence studies were performed with the same sealed off tubes. Samples sealed in Teflon cells were used for Mossbauer studies.

X-ray powder diffraction experiments were performed on a Phillips x-ray diffractometer with a Diano interface as described earlier (15). Mossbauer spectroscopy studies were all done at 77K with a homebuilt spectrometer consisting of an Elscint transducer, a Canberra amplifier and multichannel analyzer, and a NaI Harshaw



scintillation detector. Data were transferred from the MCA to an IBM mainframe computer for data analysis. Luminescence spectra were collected at room and liquid nitrogen temperatures on a Spex 202X fluorometer operating in the right angle mode. Electron paramagnetic resonance studies were performed with a Varian E-3 spectrometer as described previously (15).

### Results and Discussion

All data are summarized in Table I. After vanadium deposition on the zeolite, on the gel, or on a gel-zeolite mixture, electron paramagnetic resonance studies indicate that vanadium is predominantly in the form of vanadyl ( $\text{VO}^{2+}$ ) ions (16). On the zeolite surface, the vanadyl ions are somewhat mobile but on the matrix (the gel) they appear to be fairly well localized. EPR data for the premixed zeolite/gel mixture show a lack of  $\text{VO}^{2+}$  mobility, suggesting that vanadyl ions are preferentially depositing on the matrix. In these systems, extra signals from iron impurities could not be observed. The calcined V-loaded EuHY gives EPR spectra showing that  $\text{VO}^{2+}$  ions are much less mobile and in an axial crystal field. In fact, EPR results are very similar to those from a  $\text{VO}^{2+}$  exchanged Y zeolite. After steaming the vanadium-containing EuHY, the relative intensity of the EPR signal decreases by a factor greater than 30, indicating that few  $\text{VO}^{2+}$  ions are left in steam aged catalysts. Vanadyl ions on the surface of the matrix, on the other hand, significantly diminish after calcination, probably because exchange sites are not abundant on this gel. The steam aged vanadium-loaded gel gives, in general, a very weak EPR signal. These results suggest that after calcination of the vanadium-contaminated matrix and after steaming the vanadium-containing zeolite, other oxidation states of vanadium (besides  $\text{V}^{5+}$ ) are present.

In agreement with EPR results, luminescence data show that after the thermal and hydrothermal treatment used to age the fresh materials,  $\text{V}_2\text{O}_5$  is formed in large amounts. The fact that steam and the presence of vanadium in the zeolite quickly lead to irreversible loss of crystallinity suggest that the breakdown of the zeolite framework by vanadium is facilitated by the presence of steam (2). Luminescence and EPR data indicate that  $\text{V}_2\text{O}_5$  is the main species that leads to structural collapse of the zeolite. The  $\text{V}_2\text{O}_5$  may interact with steam (and with the zeolite Bronsted acid sites) to form acidic species (like  $\text{H}_4\text{V}_2\text{O}_7$ ) that degrade the zeolite, may react with rare earth ions to form rare earth vanadates (4), and may react with framework aluminum causing a dealumination of the faujasite structure. Furthermore, luminescence data for the V-contaminated EuHY indicate that, on calcination,  $\text{EuVO}_4$  is formed; the quantity of orthovanadate generated is relatively small with respect to the total amount of europium present in these samples.

X-ray powder diffraction results have shown that addition of tetraphenyl tin to the vanadium contaminated zeolite or to the zeolite-gel mixture leads to significantly more retention of

Table I. Summary of Spectral and Diffraction Data for V Loaded Materials

Sample*	Experiment**	Observations	Conclusions
EuY	L	Broad bands.	Several sites.
EuY, C	L	Sharp, split bands.	Eu migration to Sodalite cage.
EuY, VC	L	Excitation, <350 nm	EuVO <sub>4</sub> , 2 Eu types
AAA, V, EuY	L	" " "	"
AAA, V, C	L	Emission, 525 nm	V <sub>2</sub> O <sub>5</sub>
AAA, V, EuY	L	" " "	"
EuY, V	E	Broad, axial	VO <sup>2+</sup> , some motion
AAA, V	E	Sharp, axial	VO <sup>2+</sup> , rigid
EuY, V, C	E	Sharp, axial	" "
EuY, V, S	E	Sharp, axial, weak	Little VO <sup>2+</sup>
AAA, V, C	E	" " "	" "
AAA, V, C, S	E	" " "	" "
EuY, V, C, S	E	" " "	" "
EuY, Sn	M	I.S. = 1.37 mm/s	Sn(C <sub>6</sub> H <sub>5</sub> ) <sub>4</sub>
EuY, Sn, C	M	I.S. = 0.06 mm/s	Sn <sup>4+</sup> -O <sup>2-</sup>
EuY, Sn, C, V, C	M	I.S. = 0.03 mm/s	Sn <sup>4+</sup> -O <sup>2-</sup>
EuY, Sn, C, V, C, S	M	I.S. = 0.15 mm/s	Sn <sup>4+</sup> -O <sup>2-</sup> -V <sup>5+</sup>
AAA, Sn	M	I.S. = -0.3 mm/s	Sn(Ph) <sub>x</sub> O <sub>4-x</sub>
AAA, Sn, C	M	I.S. = 0.04 mm/s	Sn <sup>4+</sup> -O <sup>2-</sup>
AAA, Sn, C, V, C	M	I.S. = 0.02 mm/s	"
AAA, Sn, C, V, C, S	M	I.S. = 0.06 mm/s	"
AAA/EuY, Sn, C	M	I.S. = 0.06 mm/s	"
AAA/EuY, Sn, C, S	M	I.S. = 0.06 mm/s	"

\* - C = calcined, S = steamed, see experimental section for details.

\*\* - L = luminescence, E = EPR, M = Mossbauer.

crystallinity in these model FCC even after steam-aging, suggesting that tin is preventing (limiting) vanadium-zeolite interactions. In the  $\gamma$  vanadium and tin loaded EuHY, the Eu luminescence of the  $^5D_0 - ^7F_1$  transition splits into more than one band, suggesting that after tin addition there are at least two types of europium species. One represented by Europium ions still in the zeolite and the other by  $\text{EuVO}_4$ , which forms even in the presence of tin. Addition of vanadium to the matrix and calcination followed by  $\text{EuNH}_4\text{Y}$  addition and calcination also cause (relatively small amounts of)  $\text{EuVO}_4$  formation. This suggests that vanadium initially deposited on the matrix can (after calcination in air) migrate to the zeolite and react with europium ions.

EPR data for systems containing tin indicate that most of the vanadium after calcination or steaming is in the  $\text{V}^{5+}$  state. Luminescence spectra for all tin vanadium systems show a band in the same region as  $\text{V}_2\text{O}_5$ ; however, the vibrational structure seen when tin is not present disappears after tin addition. It is thus believed that tin reacts with vanadia to form a tin vanadium complex where the vanadium is very similar to  $\text{V}_2\text{O}_5$  but probably without the V-O double bond (15). In all the vanadium-tin systems, Mossbauer spectroscopic results indicate that after calcination and after steaming, tin is in the  $\text{Sn}^{4+}$  state; Mossbauer parameters suggest that the tin species are probably oxides (15).

Thus, x-ray powder diffraction, electron paramagnetic resonance, luminescence and Mossbauer data suggest that a complex of  $\text{Sn}^{4+}$ ,  $\text{V}^{5+}$  and oxygen forms that leads to the passivation of vanadium when deposited on the zeolite, and on zeolite/gel mixtures. This complex may be a compound like  $\text{V}_2\text{SnO}_7$  or similar higher molecular weight species. Evidence of  $\text{Sn}/\text{V}$  alloy formation has not been found from Mossbauer spectroscopy.

### Conclusions

Luminescence experiments with europium exchanged Y-zeolites loaded with vanadium and tin, indicate that  $\text{EuVO}_4$  and  $\text{V}_2\text{O}_5$  are both formed. X-ray powder diffraction data suggest that the combination of vanadia and steam quickly lead to degradation of the zeolite and that tin protects the zeolite from degradation. Electron paramagnetic resonance experiments indicate that after calcination and steaming, V(IV) complexes are present but in low amounts. Mossbauer data has shown that tin is converted to a  $\text{Sn}^{4+}$  species that reacts with  $\text{V}_2\text{O}_5$  and form an oxide-like species;  $\text{Sn}/\text{V}$  alloy formation was not observed.

### Acknowledgment

The financial support of the National Science Foundation under Grant No. NSF CPE-8317876 and the Department of Energy, Office of Basic Energy Sciences, Division of Chemical Sciences are gratefully acknowledged.

Literature Cited

1. Occelli, M. L., PREPRINTS, Div. of Petrol. Chem., ACS, 32, 3-4, 616 (1987).
2. Occelli, M. L., Psaras, D., Suib, S. L., J. Catal., 96, 363 (1985).
3. Mauge, F., Courcelle, J. C., Engelhard, Ph., Gallezot, P., Grosmanin, J., 7th Int. Zeolite Conf., Tokyo, 803, (1986).
4. Occelli, M. L. and Stencel, J. M. in "Proc. Int. Symp. on Zeolites as Catalysts," Wurzburg, FDR, 1988, in press.
5. Wormsbecher, R. F., Peters, A. W., Maselli, J. M., J. Catal., 100, 130 (1986).
6. Occelli, M. L. and Stencel, J. M., PREPRINTS, Div. of Petrol. Chem., ACS, 32 (1987).
7. Murphy, J. R., Katalistiks, 3rd FCC Symposium, Amsterdam, May 1982.
8. Mitchell, B. R., Swift, H. E., U.S. Patent No. 4,401,417 (1978).
9. Readal, T. C., McKinney, J. D., Titmus, R. A., U.S. Patent No. 3,977,963 (1976).
10. Mathy, E. V., Helmers, L. J., U. S. Patent No. 2,564,268 (1951).
11. Dale, J. H., McKay, D. L., Hydrocarbon Processing, 97, Sept. 1977.
12. Chester, A. W., I. E. C. Res., 26, 863 (1987).
13. Otterstedt, J. E., Gevert, S. B., Jaeras, S. G., Menon, P. G., Appl. Catal., 22, 159 (1986).
14. Occelli, M. L. Kennedy, J. V., U.S. Patent No. 4,465,588 (1983).
15. Carrado, K. A., Suib, S. L., Skoularikis, N. D., Coughlin, R. W., Inorg. Chem., 22, 117 (1986).
16. Anderson, M. W., Occelli, M. L., Suib, S. L., in preparation.

RECEIVED July 7, 1989

## Chapter 6

# Preparation and Characterization of Magnesium Aluminate Spinel for SO<sub>x</sub> Abatement in Fluid Catalytic Cracking

Alak A. Bhattacharyya, Gerald M. Woltermann, and William E. Cormier

Katalistiks International, 4810 Seton Drive, Baltimore, MD 21215

Recent studies have demonstrated that cerium containing magnesium aluminate spinels such as MgAl<sub>2</sub>O<sub>4</sub> and Mg<sub>2</sub>Al<sub>2</sub>O<sub>5</sub> are very effective SO<sub>x</sub> reduction catalysts for FCC units. These magnesium aluminate spinels can be prepared by three different techniques: (i) thermal co-condensation (ii) co-precipitation and (iii) Co-gel formation. Some of the important physical and chemical properties of a spinel depends on the preparative route used. This paper will discuss the preparation methods and characterization techniques utilized for these spinels and how the SO<sub>x</sub> abatement activity of these spinels are related to the preparative route used.

Designing a catalyst for effective removal of SO<sub>x</sub> (SO<sub>2</sub> + SO<sub>3</sub>) in a fluid catalyst cracking unit regenerator is a challenging problem. One must come up with a particle having physical properties similar to FCC catalysts which will: 1) oxidize SO<sub>2</sub> to SO<sub>3</sub>, 2) chemisorb the SO<sub>3</sub>, and 3) be able to release it as H<sub>2</sub>S as it enters the reactor side of the unit. A cerium containing magnesium aluminate spinel was found to be very effective for this purpose (1). The preparation methods and characterization techniques utilized for this spinel catalyst and how the SO<sub>x</sub> abatement activity of this catalyst is related to the preparative route used are discussed in this paper.

### **EXPERIMENTAL**

Pseudoboehmite alumina (Condea Chemie), high surface area magnesium oxide (Basic Chemicals), magnesium

nitrate hexahydrate (Mallinckrodt), sodium aluminate (Nalco), and cerium nitrate hexahydrate (Molycorp) were used as received.

Preparation of MgAl<sub>2</sub>O<sub>4</sub> by Co-condensation Method. A pseudoboehmite alumina (95.55g, 75% Al<sub>2</sub>O<sub>3</sub>) was thoroughly mixed with high surface area magnesium oxide (30.45g, 93% MgO). This material was calcined at 1400°C for 5 h. The material was cooled, thoroughly pulverized, and calcined again at 1400°C for 2 h. This process was repeated for two more times. The surface area of the material was measured to be 2 m<sup>2</sup>/g. Anal. Calcd for MgAl<sub>2</sub>O<sub>4</sub>: MgO, 28.33%. Found: MgO, 26.4%.

Preparation of MgAl<sub>2</sub>O<sub>4</sub> by Co-Precipitation Method(5-7). A solution containing Mg(NO<sub>3</sub>)<sub>2</sub>.6H<sub>2</sub>O (128.22g, 100%) and H<sub>2</sub>O (225 mL) was added to a 2 L beaker containing 600 mL of H<sub>2</sub>O. A solution containing NaAlO<sub>2</sub> (112.87g, 45.14% Al<sub>2</sub>O<sub>3</sub>) and H<sub>2</sub>O (400 mL) was then added dropwise via a separatory funnel to the beaker. The pH was adjusted with either NaOH or HNO<sub>3</sub> to keep it within the 8.5 - 9.0 range. The precipitate was filtered and washed with 3000 mL of deionized H<sub>2</sub>O. This material was dried at 135°C for 8 h and calcined at 700°C for 2 h. The surface area of this material was 180 m<sup>2</sup>/g. Anal. Calcd for MgAl<sub>2</sub>O<sub>4</sub>: MgO, 28.33%. Found: MgO, 26.1%.

The high magnesium spinel, Mg<sub>2</sub>Al<sub>2</sub>O<sub>5</sub>, can be synthesized following the same procedure and using the required amounts of Mg(NO<sub>3</sub>)<sub>2</sub>.6H<sub>2</sub>O and NaAlO<sub>2</sub>. Anal. Calcd for Mg<sub>2</sub>Al<sub>2</sub>O<sub>5</sub>: MgO, 44.15%. Found MgO, 45.9%.

Preparation of MgAl<sub>2</sub>O<sub>4</sub> by Co-gel Formation Method (8). A gel having a pH of 9 was prepared using aqueous slurries of pseudoboehmite alumina (71.7 g Al<sub>2</sub>O<sub>3</sub>), MgO (28.3 g), and an acid. The material was dried at 110°C for 8 h and calcined at 700°C for 2 h. The surface area of this material was 169m<sup>2</sup>/g. Anal. Calcd for MgAl<sub>2</sub>O<sub>4</sub>: MgO, 28.33%. Found: MgO, 26.3%. The high magnesium spinel can be prepared using the same procedure and using the required amounts of pseudoboehmite alumina and MgO. Anal. Calcd for Mg<sub>2</sub>Al<sub>2</sub>O<sub>5</sub>: MgO, 44.15%. Found: 44.1%.

Cerium Impregnation. All of the above spinels were impregnated(1) by cerium nitrate hexahydrate. A portion (87.7 g) of the spinel prepared by any of the above methods was impregnated with a solution containing 42.9 g of 70% Ce(NO<sub>3</sub>)<sub>3</sub>.6H<sub>2</sub>O (CeO<sub>2</sub> content 28.7%) and 40 g water. This material was dried at 120°C for 3 h and calcined at 700°C for 1 h.

Thermal Studies. Thermogravimetric studies were performed for the testing of these materials. This was

accomplished by placing a small amount (5 to 25 mg) of virgin sample on a quartz pan and passing a desired gas. This experiment was divided into four zones:

- Zone A: Under  $N_2$ , the sample was heated to  $700^\circ C$ .  
Zone B: Nitrogen was replaced by a gas containing 0.32%  $SO_2$ , 2.0%  $O_2$ , and balance  $N_2$ . The flow rate was 200 mL/min. The temperature was kept constant at  $700^\circ C$ . This condition was maintained for 15 min.  
Zone C: Passage of  $SO_2$  containing gas was ceased and replaced by  $N_2$ . Temperature was reduced to  $650^\circ C$ . This is a 10 min. time zone.  
Zone D: Nitrogen was replaced by pure  $H_2$ . This condition was maintained for 10 minutes.

X-Ray powder diffraction patterns of these materials were obtained on a Philips APD 3720 Automated Powder X-Ray diffractometer using  $CuK$  alpha radiation. Surface areas were measured with a Micromeritics Flowsorb II Model 2300 Analyzer with  $P/Po = 0.3$  utilizing the BET isotherm.

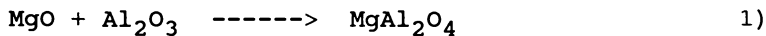
## RESULTS AND DISCUSSION

Several redox oxides such as  $PtO_2$ ,  $V_2O_5$ ,  $Fe_2O_3$ , and  $CeO_2$  can be used for the oxidation of  $SO_2$  to  $SO_3$ . Cerium dioxide is preferred over other oxides because platinum is expensive and vanadium and iron oxides are poisons for FCC catalysts. Usually an aqueous solution of a cerium salt is used to impregnate a spinel base which is then calcined to obtain the  $CeO_2$  active form. We have found that a 10 to 12%  $CeO_2$  is sufficient for effective  $SO_2$  oxidation(1).

The magnesium aluminate spinels that we have tested are  $MgAl_2O_4$  and  $Mg_2Al_2O_5$ . The latter is a solid solution (2,3) of pure spinel ( $MgAl_2O_4$ ) and  $MgO$ . The spinel structure (4) is based on a cubic close packed array of oxide ions. Typically, the crystallographic unit cell contains 32 oxygen atoms; one eighth of the tetrahedral holes are occupied by the divalent metal ions ( $Mg^{2+}$ ), and one half of the octahedral holes are occupied by the trivalent metal ions ( $Al^{3+}$ ).

Magnesium aluminate spinels can be prepared(5-8) by various methods such as i) thermal co-condensation of oxides, ii) co-precipitation of hydroxides, and iii) co-gel formation. The results obtained from each of these procedures are briefly discussed below.

Co-condensation of oxides. The stoichiometric spinel  $MgAl_2O_4$  can be prepared (4) by reacting boehmite type reactive alumina with high surface area  $MgO$  at a temperature higher than  $1200^\circ C$  (equation 1).



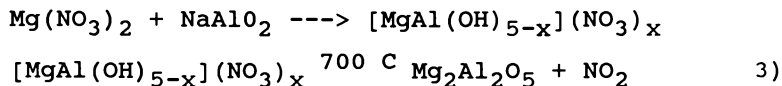
This procedure is very useful when preparing ceramic spinel. The MgO can be replaced with MgCO<sub>3</sub> if desired which eventually at 1200°C yields MgO. Repetitive pulverization and calcination steps are required to quantitatively generate high quality spinel, MgAl<sub>2</sub>O<sub>4</sub>. X-ray diffraction of this material is shown in Figure 1. At a temperature below 1200°C, the spinel formation is very poor (Figure 1). High temperature calcination which is essential for the formation of good quality spinel causes sintering. Because of sintering the spinel material becomes denser (sharper X-Ray peaks) and loses surface area and pore volume (Table I).

When impregnated with Ce(NO<sub>3</sub>)<sub>3</sub> solution and calcined this spinel produces a material that has a very poor SO<sub>x</sub> removal activity (Table I, Figure 2) because of a lack of surface area and low pore volume. The amount of SO<sub>3</sub> picked up by this catalyst is 3% of its initial weight. This, we believe, is because of a lack of surface area and low pore volume. In Zone D when the sulfated catalyst is reacted with H<sub>2</sub> the reduction is very unsatisfactory. The rate of reduction is slow and the material does not release all the absorbed sulfur even after 10 minutes of H<sub>2</sub> reduction.

The solid solution spinel, Mg<sub>2</sub>Al<sub>2</sub>O<sub>5</sub>, cannot be prepared by this method because such a higher temperature (>1200°C) causes the MgO to dissociate out of the spinel framework (equation 2)



**Co-precipitation of Hydroxides.** Some of the important factors favoring solid state reactions are high surface area and homogeneous mixing of starting materials. All these conditions would be met if the hydroxides of aluminum and magnesium could be co-precipitated in the appropriate proportions to produce spinels. Various workers (5-7) have used this co-precipitation technique to prepare spinels MgAl<sub>2</sub>O<sub>4</sub> and Mg<sub>2</sub>Al<sub>2</sub>O<sub>5</sub> using water soluble salts of aluminum and magnesium.



This method, unlike the co-condensation method, does not require a very high temperature calcination to produce spinel structure from co-precipitated double hydroxides. Usually a temperature of 700 to 800°C and 2 to 3 hours of calcination is sufficient to convert the co-precipitated double hydroxide to spinel. The characteristic X-Ray diffraction patterns of MgAl<sub>2</sub>O<sub>4</sub> and Mg<sub>2</sub>Al<sub>2</sub>O<sub>5</sub> are presented in Figure 3. It may be



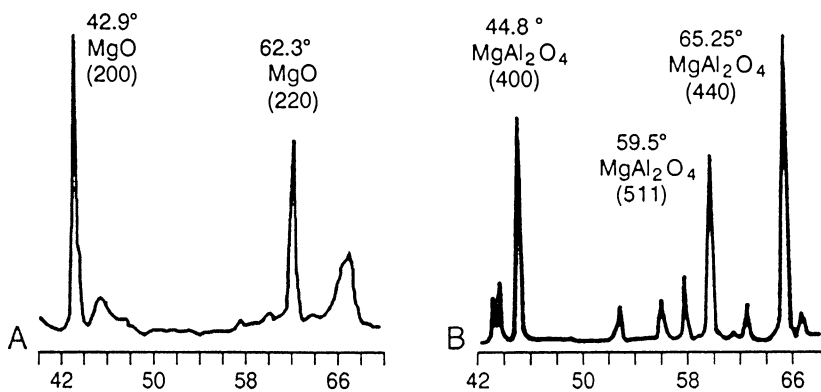


Figure 1. X-Ray Diffraction Patterns of  $\text{MgAl}_2\text{O}_4$  Prepared by Thermal Co-Condensation Method. A=Incomplete ( $1000^\circ\text{C}$ , 7h); B=Complete.

Table I. Physical and Chemical Properties of Spinel Prepared by Different Methods

Preparative Route	Spinel Type	Surface Area ( $\text{m}^2/\text{g}$ )	Pore Volume ( $\text{cc}/\text{g}$ )	% $\text{SO}_3$ Absorbed
Co-condensation	$\text{MgAl}_2\text{O}_4$	2	0.15	3.0
Co-precipitation	$\text{MgAl}_2\text{O}_4$	180	0.40	10.9
	$\text{Mg}_2\text{Al}_2\text{O}_5$	150	0.41	13.6
Co-gellation	$\text{MgAl}_2\text{O}_4$	169	0.32	8.8
	$\text{Mg}_2\text{Al}_2\text{O}_5$	165	0.36	11.4

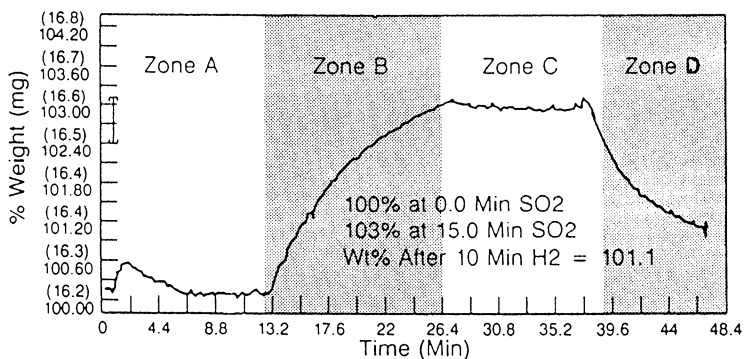


Figure 2. TGA Test of a  $\text{CeO}_2/\text{MgAl}_2\text{O}_4$  Catalyst Prepared by Co-Condensation Method.

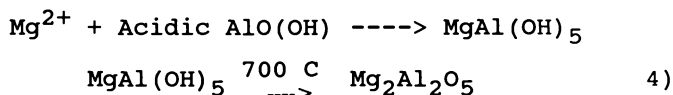
noted here that the diffraction pattern of Mg<sub>2</sub>Al<sub>2</sub>O<sub>5</sub> is very similar to MgAl<sub>2</sub>O<sub>4</sub> and does not exhibit a MgO peak. In a same plane (hkl) the reflection occurs at a slightly lower angle (2θ) in Mg<sub>2</sub>Al<sub>2</sub>O<sub>5</sub> compared to MgAl<sub>2</sub>O<sub>4</sub> (Figure 3).

The physical properties of the spinels prepared by this method (Table I) are very different from those prepared by the co-condensation method. The spinels prepared by this method have a very high surface area (~150 m<sup>2</sup>/g).

When impregnated with Ce(NO<sub>3</sub>)<sub>3</sub> solution and calcined the resulting catalysts are extremely active towards SO<sub>x</sub> abatement (Table I, Figure 4). The solid solution spinel catalyst is nearly 25% more active than the stoichiometric spinel catalyst. This can be explained by assuming that -MgO- structural fragments of the spinel are the chemisorption active sites (1). There are more active sites in Mg<sub>2</sub>Al<sub>2</sub>O<sub>5</sub> than in MgAl<sub>2</sub>O<sub>4</sub>. We also see that the catalyst prepared by co-precipitation method is 4 times more active than the catalyst prepared by the thermal co-condensation method. In Zone D we see that the sulfated catalyst is very effectively reduced by H<sub>2</sub>. Nearly 70% of the absorbed species is reduced within 2 min. of reduction.

The CeO<sub>2</sub> exists in the catalyst as a well dispersed but X-Ray identifiable microcrystalline solid. The X-Ray diffraction peaks at 2θ = 47.9° (220) and 56.7° (311) (Figures 3 and 5) are characteristic of CeO<sub>2</sub> crystallites.

**Co-gel formation.** In addition to the co-precipitation of the two hydroxides we have found that a very homogeneous mixture of Mg<sup>2+</sup> and Al<sup>3+</sup> species can be obtained by co-gel formation (8). This co-gel, usually prepared by combining aqueous slurries of pseudoboehmite alumina, high surface area MgO, and an acid, is dried and calcined at 700 to 800°C to produce both stoichiometric and high magnesium spinels (reaction 4).



The characteristic X-Ray diffraction patterns of these spinels, which are very similar to the one prepared by the co-precipitation method, are presented in Figure 5. The diffraction pattern of Mg<sub>2</sub>Al<sub>2</sub>O<sub>5</sub> is very similar to MgAl<sub>2</sub>O<sub>4</sub> and does not exhibit a MgO peak. Again, in a same plane (hkl) the reflection occurs at a slightly lower angle (2θ) in Mg<sub>2</sub>Al<sub>2</sub>O<sub>5</sub> compared to MgAl<sub>2</sub>O<sub>4</sub> (Figure 5).

The physical properties such as surface area and pore volume of these spinels are very similar to the ones prepared by co-precipitation method (Table I).

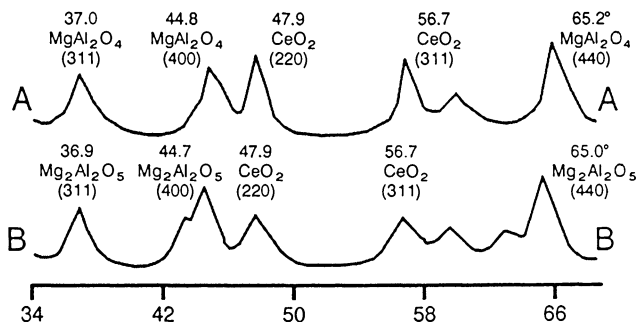


Figure 3. X-Ray Diffraction Patterns of MgAl<sub>2</sub>O<sub>4</sub> (A) and Mg<sub>2</sub>Al<sub>2</sub>O<sub>5</sub> (B) Prepared by Co-Precipitation Method.

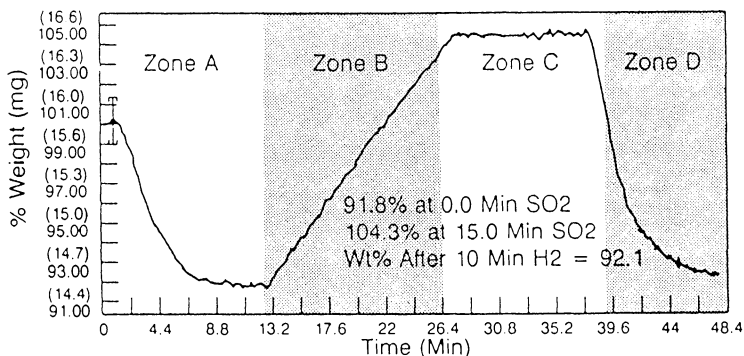


Figure 4. TGA Test of CeO<sub>2</sub>/Mg<sub>2</sub>Al<sub>2</sub>O<sub>5</sub> Catalyst Prepared by Co-Precipitation Method.

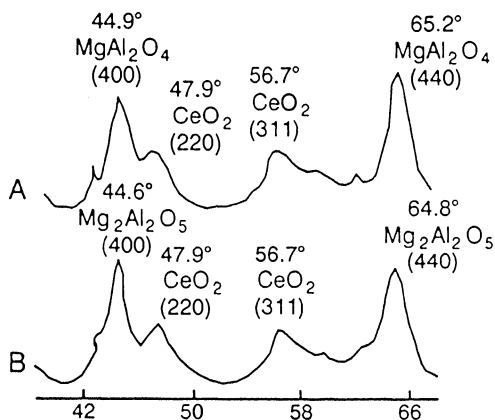


Figure 5. X-Ray Diffraction Patterns of MgAl<sub>2</sub>O<sub>4</sub> (A) and Mg<sub>2</sub>Al<sub>2</sub>O<sub>5</sub> (B) Prepared by Co-Gelation Method.

When these spinels are impregnated with  $\text{Ce}(\text{NO}_3)_3$  and calcined the resulting catalysts are nearly as active as the co-precipitated products (Table I, Figure 5). The amount of  $\text{SO}_3$  absorbed in Zone B by the high magnesium spinel catalyst is 11.4% of its initial weight in 15 min. which is about four times more than the catalyst prepared by co-condensation method (Figure 6). Once again the high magnesium spinel is about 25% more active than the stoichiometric spinel possibly because of higher absorption active site density in the former material. In zone D the  $\text{H}_2$  reduction is very effective. Similar to the catalyst prepared by the coprecipitation method this material releases 70% of the absorbed sulfur within 2 min.

### Conclusion

It is very apparent from this work that co-precipitation and co-gel formation methods for the preparation of spinels provide very active catalysts for FCC SO<sub>x</sub> reduction whereas the co-condensation method produces very dense ceramic type spinels with low activity. The high magnesium spinel catalyst is more active than the stoichiometric spinel catalyst. The co-gel formation method is more convenient and also provides a more attrition resistant product than the co-precipitation technique.

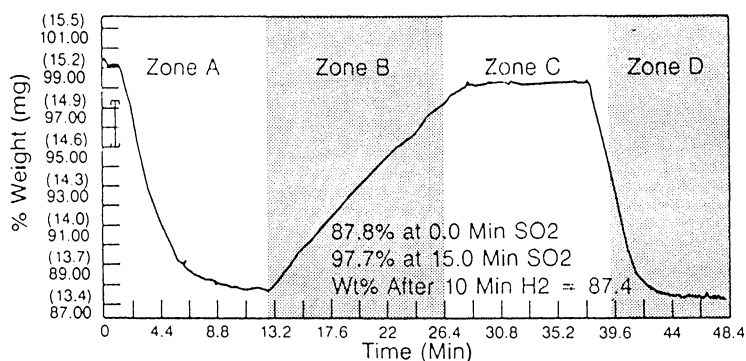


Figure 6. TGA Test of a  $\text{CeO}_2/\text{Mg}_2\text{Al}_2\text{O}_5$  Catalyst Prepared by Co-Gellation Method.

### ACKNOWLEDGMENTS

The authors wish to thank John Karch, John Magee, Joseph Powell, and Jin Yoo for valuable suggestions and Kathleen Kennedy for sample preparations.

### LITERATURE CITED

- (1) Bhattacharyya, A. A.; Woltermann, G. M.; Yoo, J.

- S.; Karch, J. A.; Cormier, W. E., Ind Eng. Chem. Res. 1988, 27, 1356.
- (2) Alper, A.M.; McNally, R.N.; Ribbe, P.H.; Doman, R.C., J. Am. Ceram. Soc. 1962, 45, 263.
  - (3) Ramkin, G.A.; Merwin, H.W., J. Am. Chem. Soc. 1916, 38, 568.
  - (4) West, A.R., In Solid State Chemistry and Its Applications John Wiley and Sons, 1987, pp. 4-14.
  - (5) Mukherjee, S. G.; Samaddar, B. N. Trans. Indian Ceram. Soc. 1966, 25, 33
  - (6) Bratton, R. J. Amer. Ceram. Soc. Bull., 1969, 48, 759.
  - (7) Yoo, J. S.; Jaecker, J. A. U.S. Patent 4,469,589, Sept. 4, 1984
  - (8) Bhattacharyya, A. A.; Cormier, W. E.; Woltermann, G. M. U.S. Patent No. 4,728,635, March 1, 1988

RECEIVED April 27, 1989

## Chapter 7

# Attrition-Resistant Porous Particles Produced by Spray Drying

Horacio E. Bergna

Chemicals and Pigments Department, Experimental Station, E. I. du Pont  
de Nemours and Company, Wilmington, DE 19880-0262

Attrition resistance can be conferred to porous grains in the micron size range by filling the pores on the periphery of the grains with sub-colloidal or very small colloidal particles capable of coalescing or sintering to form a hard egg shell. This approach requires only a fraction of the hard phase volume required to form an attrition resistant continuous framework or skeleton within the grain pores. When slurries made of mixtures of micron sized particles and discrete small nanoparticles are spray dried, the nanoparticles not strongly adsorbed on the surface of the larger particles migrate to the periphery of the spray droplets where they coalesce forming an egg shell. Special characterization techniques such as electron probe microanalysis (EPMA) combined with scanning electron microscopy, X-ray and electron diffraction, and surface area measurements played a crucial role in showing that the egg shell zone is made of the micron size particles with the inter-particle voids filled by the coalesced nanoparticles.

Industrial powders made of grains in the micron size range are often used in processes that require high attrition resistance. A good example of such powders are catalysts for fluid bed processes which are generally made of ca. 45 to ca. 150 or 200 $\mu$ m porous grains hereby referred to as "porous micrograins" or, if they are spheroidal, "porous microspheres" (PMS). A conventional approach to impart attrition resistance to a catalyst grain is to embed small particles of the active catalyst in a continuous framework or skeleton made of a hard and relatively inert material. In this case, the percentage of hard materials required to impart sufficient attrition resistance to the catalyst composite particle can be as high as 50% and there-

fore it may affect the activity and/or the selectivity of the catalyst.

Satisfactory attrition resistance can be conferred to the porous grains of the active catalyst with a much smaller amount of the hard, mostly inert material (around 10 percent weight) simply by distributing the hard phase in a thin layer around the peripheral zone of the catalyst porous grains (1). It is reported in this paper that when aqueous slurries made of a mixture of micron-size particles (for example 0.2 to 2 $\mu\text{m}$  size) and discrete sub-colloidal or very small colloidal particles (preferably less than ca. 5nm diameter) are spray dried, the sub-colloidal or small colloidal particles migrate with the evaporating water to the periphery of the droplets. As a consequence, the spray dried product is constituted by porous microspheres (PMS) made of the micron-size particles with a narrow peripheral layer made mostly of the coalesced sub-colloidal or very small colloidal particles embedding the outer zone of the micron-size particles. It is essential to retain the discreteness of the sub-colloidal or small colloidal particles in the slurry prior to spray drying so that these particles can migrate easily by diffusion or capillary flow in between the larger catalyst particles. Aggregated clusters of sub-colloidal or colloidal particles do not migrate easily around the micron sized particles to the periphery of the droplet, but tend to remain distributed at random within the residual microsphere, since they constitute a very small fraction of the volume of the solids; in this case, they are not very effective in contributing to the mechanical strength of the resultant PMS.

On the basis of these findings, by judicious selection of a system of discrete sub-colloidal or very small colloidal particles of a hard material, attrition resistant catalyst powders can be made with only a small amount of the hard phase by the spray drying method. Figure 1 (2) illustrates both the conventional approach and my novel concept of attrition resistant porous microspheres. In the conventional approach, ca. 50% colloidal silica (22 nm diameter) form a continuous supporting framework for the larger catalyst particles. In my novel approach, the polysilicic acid particles (ca. 2-3 nm diameter) are embedded with the much larger catalyst particles in a narrow peripheral range of the PMS. In both cases, silica constitutes the hard, fairly inert phase conferring attrition resistance to the PMS.

#### **MATERIALS AND METHODS**

Vanadyl phosphates (VPO) and multiple component molybdate (MCM) are good examples of catalysts, and alpha alumina, amorphous silica and alumino-silicates are good examples of catalyst supports that can be fabricated in the form of 45 to 150  $\mu\text{m}$  diameter spray dried porous spheres with attrition resistance improved by a relatively thin peripheral layer rich in amorphous silica, amorphous alumina, or phosphorus oxides. The hard phase component or precursor is selected in each case so that it will not interfere with the catalytic performance of the catalyst.

As an example, the precursor to the vanadyl phosphate catalyst was prepared following a method (1) based on reference (3). The MCM

was prepared by precipitation of cobalt and nickel nitrate aqueous solutions with ammonium molybdate, followed by additions of iron nitrate aqueous solution, bismuth nitrate in dilute nitric acid, magnesium and potassium nitrate in water, and phosphoric acid (1). The slurry was concentrated to 40% solids and centrifuged. The supernatant was discarded and the cake of MCM was used to prepare a MCM-10% SiO<sub>2</sub> aqueous slurry for spray drying.

In the case of the VPO catalyst for the butane oxidation process and the MCM catalyst for the acrylonitrile process, the preferred precursor of the peripheral hard phase is polysilicic acid (PSA). The term "polysilicic acid" is generally reserved for those "silicic acids that have been formed and partially polymerized in the pH range 1-4 and consist of ultimate silica particles generally smaller than 3-4 nm diameter" (4). Small, discrete particles of colloidal silica also migrate to the periphery of the droplet, but they do not coalesce as extensively as PSA in drying. The larger the particle size, the lower the mechanical strength of the coalesced dry product.

In our case a 6% SiO<sub>2</sub> solution of polysilicic acid was prepared by deionizing to pH 3 a dilute solution of filtered Du Pont JM grade sodium silicate with Dowex HCR-W2-H resin, a strongly acidic nuclear sulfonic acid cation exchanger supplied by Dow Chemical Company.

The preferred procedure to fabricate attrition resistant PMS consists simply in spray drying aqueous slurries made of comminuted particles of VPO or MCM around 0.5-2 $\mu$ m size and a small amount of PSA. In a typical slurry, silica is only 10% of the VPO or MCM.

We spray dried the slurries in a Bowen Engineering Co. No.1 Ceramic Type Spray Dryer. The spray dried products were screened to obtain active and selective attrition resistant powders made of 45 to 150 $\mu$ m diameter porous microspheres of the catalyst with a thin silica-rich peripheral layer.

Attrition resistance was measured on catalyst powders with and without PSA. The attrition resistance method measured attrition at a high and constant air jet velocity. The fluidized samples were subject to attrition conditions for a specified length of time. Results are given in catalyst weight loss percent per hour versus elapsed time in hours.

The distribution of the hardening phase was investigated using electron probe microanalysis techniques (EPMA) and scanning electron microscopy (SEM) before and after leaching the catalysts with acids. EPMA was done with a JEOL microprobe using a Tracor Northern X-ray system. X-ray diffraction and electron diffraction analysis were used to identify the phases of the catalysts. Microelectrophoretic measurements of the VPO aqueous slurry with and without PSA added were made at various pH values to investigate the possible change of character of the VPO surface by chemisorption. However, no significant changes were observed in the zeta potentials or the isoelectric point of the VPO after addition of PSA, suggesting that the PSA remains free in the aqueous phase without being adsorbed on the VPO surface.



## RESULTS AND DISCUSSION

Figure 2a illustrates the improvement in attrition resistance of a VPO catalyst by the addition of only 10% silica as PSA. Both samples of VPO, one with no PSA added and the other with 10% PSA, were tested as catalysts in the butane oxidation process to make maleic anhydride and showed no difference in activity or selectivity. Both fluid bed and recirculating solids reactors were used for the tests of catalytic performance (1) (2).

Figure 2b shows that MCM catalyst made with only 10% silica as PSA achieves practically the same attrition resistance as the MCM catalyst made with about 50% colloidal silica with particle diameter 22 nm.

The difference between the two approaches to develop attrition resistant PMS as described in the introduction are illustrated in Fig. 3 which includes scanning electron micrographs of the pure silica residue obtained by leaching with acids three different catalysts. The first one was originally the MCM catalyst constituted by about 50% of metal oxide active catalyst particles embedding a continuous silica framework or skeleton (3-a). In this case, after leaching out the metal oxides with acids, the silica framework retains its morphology and it is almost as attrition resistant as the original untreated MCM/silica catalyst (3-b).

Micrograph (3-d) shows what originally was the VPO catalyst made of vanadyl phosphate with only 10% of 14nm colloidal silica concentrated in the periphery of the vanadyl phosphate spheres (3-c). In this case, leaching with acids leaves the silica egg shell without support producing a collapse of the structure. The silica residue obtained by leaching with acids the VPO-10% PSA catalyst is made of fragments with the shape of the peripheral layer originally made of VPO embedded in silica (3-e,f). The small cavities seen in the fractured edge of the egg shell are sites with the size and shape of the vanadyl phosphate particles that occupied them. The nitrogen specific surface area of the silica residue obtained by acid leaching out the VPO particles is between 300 and 500 m<sup>2</sup>/g as opposed to about 20-30 m<sup>2</sup>/g for the original VPO-10% SiO<sub>2</sub> catalyst. Since the surface area of the VPO without PSA is also about 20-30 m<sup>2</sup>/g, the results suggest that the VPO and the PSA are tightly embedded in the periphery of the microsphere. The specific surface area of the silica residue (300-500 m<sup>2</sup>/g) shows how extensively the silica has coalesced from the original 1000-1200 m<sup>2</sup>/g of the PSA dispersion used for the fabrication of the catalyst.

Micrographs obtained by EPMA are shown in Figure 4. The sample in this case was VPO with 10% amorphous silica as the hard phase. This composition was prepared by spray drying an aqueous slurry with about 40% solids made of 1-2μm particles of the VPO catalyst precursor and polysilicic acid. The back-scattered image shows all elements present in the porous microsphere. The X-ray image of silicon clearly shows this element concentrated exclusively on the periphery of the microsphere. Independent X-ray diffraction and electron diffraction analysis of the peripheral layer of the microspheres showed that the silicon is present as amorphous silica.

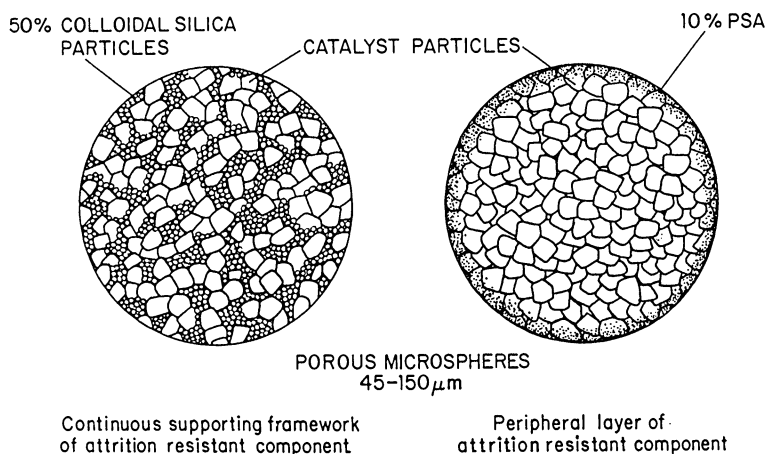


Figure 1. Diagrams illustrating two different concepts to confer attrition resistance to porous microspheres (PMS). (Reproduced with permission from Ref. 2. Copyright 1987 Elsevier.)

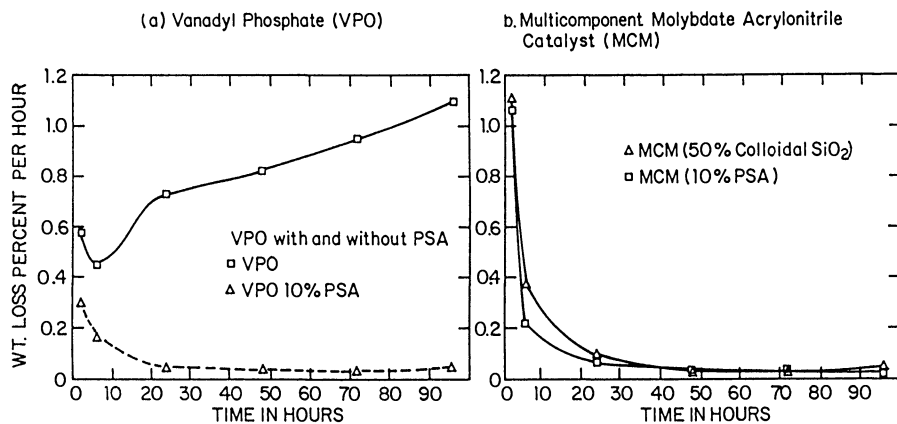


Figure 2. Attrition resistance of catalyst powders with and without polysilicic acid (PSA).

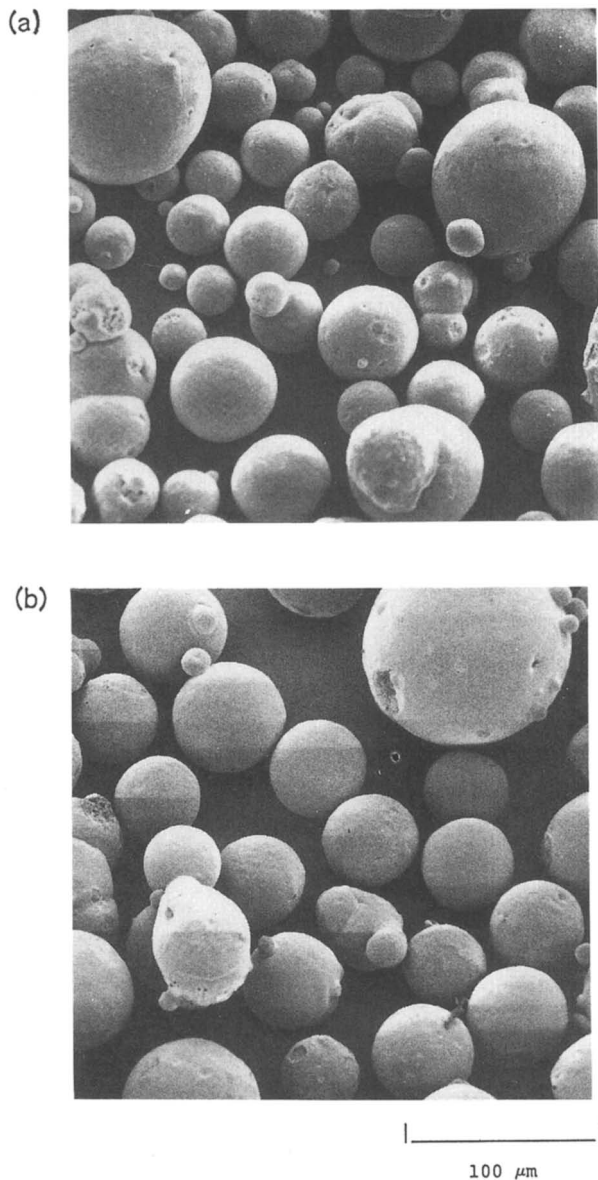


Figure 3. Scanning electron micrographs of catalyst microspheres before and after leaching with acids. (a) Commercial MCM powder made with ca. 50% colloidal silica 22 nm particle size. (b) Same powder after acid leaching the active metal oxide components. *Continued on next page.*

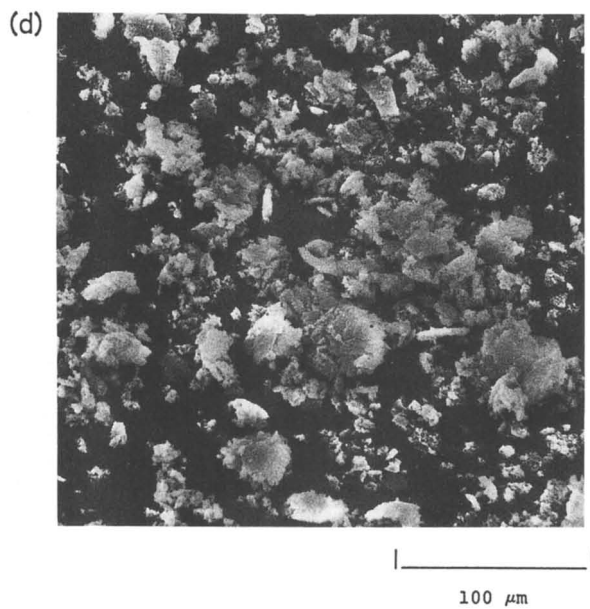
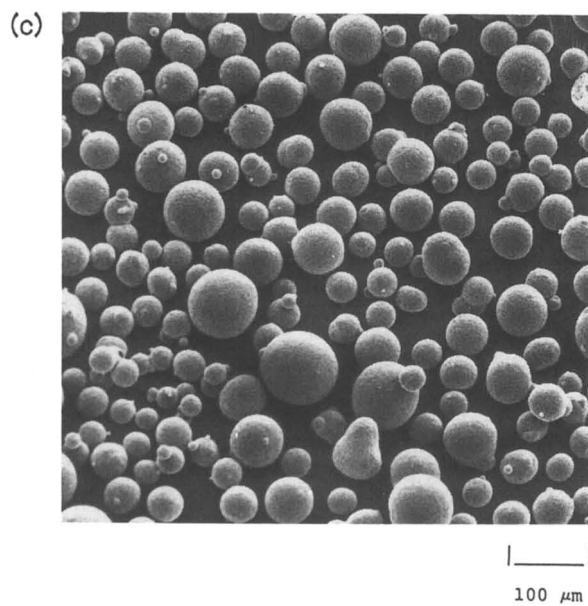
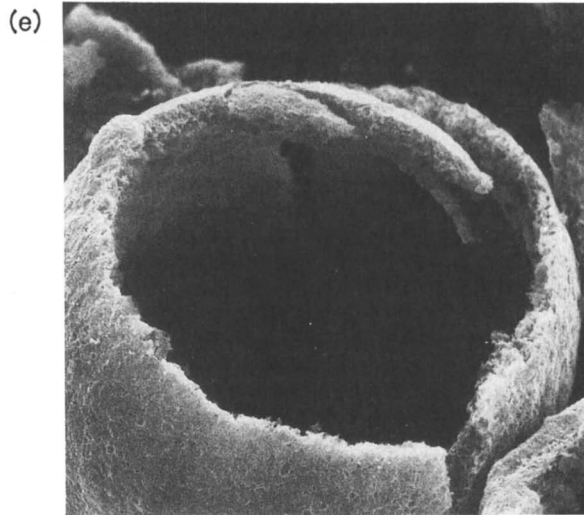
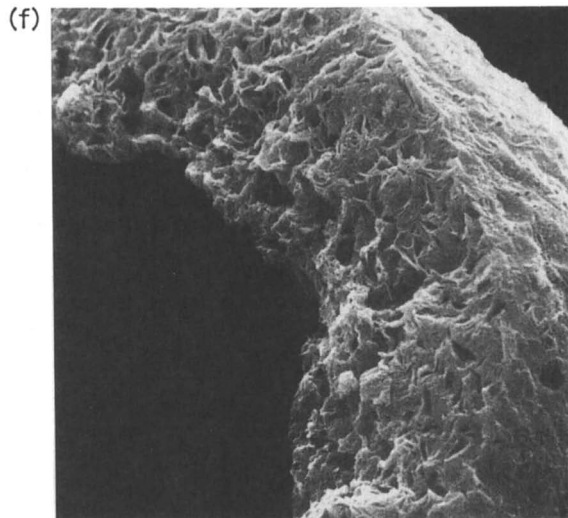


Figure 3. Continued. (c) VPO catalyst powder made with 10% colloidal silica 14 nm particle size. (d) Same powder after acid leaching the VPO. *Continued on next page.*



10  $\mu\text{m}$



10  $\mu\text{m}$

Figure 3. Continued. (e) and (f) Residual silica egg shell after acid leaching a VPO-10% PSA catalyst.

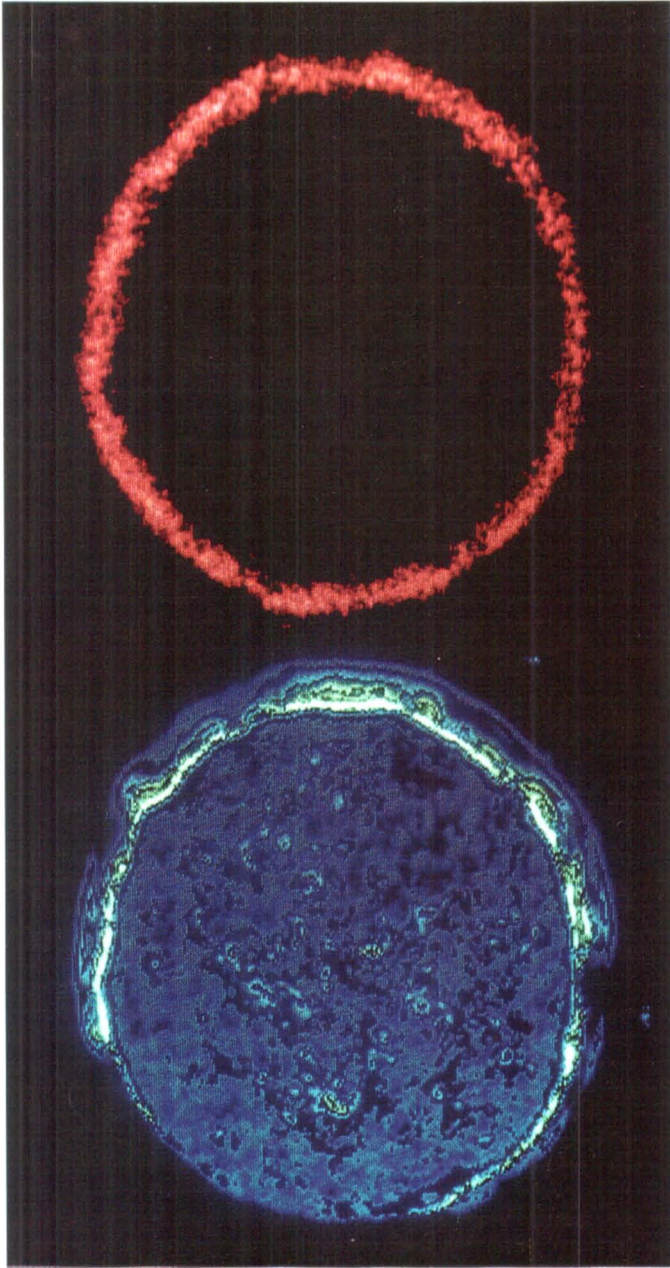


Figure 4. Micrographs of the cross section of a vanadyl phosphate porous microsphere with 10% amorphous silica obtained by electron probe microanalysis (EPMA). Left: backscattered electron image showing average atomic number across the specimen. Right: X-ray image showing silicon distribution.

**CONCLUSIONS**

Attrition resistance can be conferred to porous grains in the micron size range by filling the pores on the periphery of the grains with sub-colloidal or very small colloidal particles capable of sintering to form a hard egg shell. This approach requires only a fraction of the hard phase volume required to form an attrition resistant continuous framework or skeleton within the grain pores. When slurries made of mixtures of micron sized particles and discrete small nanoparticles not significantly adsorbed on the micron sized particle surface are spray dried, the nanoparticles migrate to the periphery of the spray droplets where they coalesce forming an egg shell. The egg shell zone is made of the micron size particles with the interparticle voids filled by the coalesced nanoparticles. For this reason, spray drying is a preferred method to make attrition resistant porous microspheres with a relatively small amount (5-10 wt. %) of particles of a hard phase.

**ACKNOWLEDGMENTS**

I am grateful to my colleagues at the Du Pont Experimental Station listed below for their help and support to apply the novel concepts described in this report to produce viable catalysts. Brian S. Malone and Rashmi M. Contractor conducted the attrition resistance and activity/selectivity measurements of the VPO-PSA catalysts in apparatuses of their own design. William J. Linn tested catalytic performance of the MCM-PSA products in the acrylonitrile process. EPMA micrographs were obtained by Joseph W. Brennan. SEM pictures were taken by Michael L. Van Kavelaar. The late Gunther Teufer conducted the X-ray diffraction and electron diffraction analysis. E. Carroll made the BET measurements of surface area and R. E. Johnson and G. Hughes the electrokinetic measurements. Oral R. Van Buskirk directed most of the spray drying experiments. H. J. McQueston, W. B. Hambleton, Jr., R. E. Polini, J. Watson, P. W. Johnston, Jr., and D. Nickerson assisted in the experimental work. I am specially grateful to Uma Chowdhry, Arthur W. Sleight, and J. Peter Jesson for intelligently suggesting and enthusiastically supporting our work in this specific area of technology.

**REFERENCES**

1. Bergna, Horacio E. U. S. Patents 4 677 084, 1987 and 4 769 477, 1988.
2. Contractor, R.M., Bergna, H.E., et al. *Catalysis Today*, 1987, **1**, 54.
3. Bither, T. U. S. Patent 4 371 703, 1987.
4. Iler, R.K. *The Chemistry of Silica*; John Wiley and Sons: New York, 1979; p 287.

RECEIVED January 26, 1989

## Chapter 8

# Hydrous Sodium Titanate Ion-Exchange Materials for Use as Catalyst Supports

B. C. Bunker<sup>1</sup>, C. H. F. Peden<sup>2</sup>, S. L. Martinez<sup>1</sup>, E. J. Braunschweig<sup>2</sup>,  
and A. K. Datye<sup>2</sup>

<sup>1</sup>Sandia National Laboratories, Albuquerque, NM 87185

<sup>2</sup>University of New Mexico, Albuquerque, NM 87131

Understanding how the activity of a catalyst is related to the concentration and dispersion of active metals on the catalyst support is critical to designing materials having the optimum catalytic properties. We have developed synthetic techniques for controlling both the concentration and dispersion of nickel on hydrous sodium titanate catalyst supports. The techniques require an understanding of the solution chemistry of both the support material and dissolved metal species (hydrolysis products). In this paper, we present the results of a study of three nickel-loaded samples of hydrous sodium titanate in which the scale of the nickel dispersion ranges from the atomic level to the scale of large (50 nm) clusters. The catalysts are characterized by transmission electron microscopy (TEM), hydrogen chemisorption, and BET surface area measurements. In addition, the activity and selectivity of the Ni catalysts for the n-butane hydrogenolysis reaction is used to monitor the surface structures of Ni in the catalysts.

A group of hydrous oxide ion exchangers of Ti, Zr, Nb, and Ta, prepared via hydrolysis of respective metal alkoxides, have shown great promise for use as catalyst substrates (1). For example, coal liquifaction catalysts prepared on hydrous sodium titanates are up to two orders of magnitude more active for the hydrogenation of model solvents such as pyrene than are catalysts prepared on traditional alumina supports on a per gram of metal basis (2). One reason for improved catalytic activity may be that active metals such as nickel can be atomically dispersed at high (> 5%) metal loadings on sodium titanate via ion exchange in aqueous solutions.



The method of preparing the titanate support powder offers the possibility of controlling the ion-exchange properties (capacity, pH dependence, etc.) of the material during the synthesis. In addition, other important material properties such as the surface area are, in principle, controllable by the solution chemical techniques used to prepare the powders.

To optimize the use of the amorphous sodium titanate powders as catalyst substrates, it is important to fully characterize the ion-exchange properties of the material. Further, the solution properties of the active metal to be loaded onto the support will be an important parameter in the control of the adsorption process. For example, exposure of sodium titanate to a nickel salt solution does not guarantee that nickel will be loaded onto the sodium titanate, or that the nickel, if loaded, will be dispersed on an atomic level. Sodium titanate only behaves as a cation exchange material under certain pH conditions. The solution pH also influences the hydrolysis and speciation of dissolved nickel ions (3), which can form large polymeric clusters or colloidal particles which are not adsorbed by the sodium titanate via a simple ion-exchange process.

This paper describes some of our initial studies of the solution properties of sodium titanate powders in order to understand and control the metal-loading process in the preparation of a heterogeneous catalyst from the materials. The purposes of this study are: 1) to define the pH and concentration regimes in which nickel is loaded onto sodium titanate as monomeric ions via ion exchange, as polymeric clusters via hydrolysis, or as discrete particles of colloidal nickel hydroxide, and 2) to characterize the catalysts with respect to the dispersion of the active metal under reaction conditions by measuring the activity and selectivity of the catalysts for a known "structure-sensitive" reaction, the hydrogenolysis of n-butane.

### Experimental

Hydrous sodium titanate was prepared by the method of Dosch and Stephens (1). Titanium isopropoxide was slowly added to a 15 wt% solution of sodium hydroxide in methanol. The resulting solution was hydrolyzed by addition to 10 vol% water in acetone. The hydrolysis product is an amorphous hydrous oxide with a Na:Ti ratio of 0.5 which contains, after vacuum drying at room temperature, approximately 13.5 wt% water and 2.5 wt% residual alcohol. The ion-exchange characteristics of the sodium titanate and the hydrolysis behavior of the nickel nitrate solutions were characterized using a combination of potentiometric titrations, inductively coupled plasma atomic emission (ICP) analysis of filtrates, and surface charge measurements obtained using a Matec electrosonic amplitude device.

Three different nickel-loaded sodium titanates were prepared by exposing 5 gm of the sodium titanate powder to aqueous solutions of nickel nitrate containing sufficient nickel to incorporate one mole of nickel for every two moles of sodium on the support (corresponding to the stoichiometry associated with complete ion exchange). Each sample was prepared using different pH conditions (and thus, different Ni(II) concentrations) to vary the mechanism of

nickel loading (see Results and Discussion). To obtain atomic dispersions of Ni(II) via ion exchange, the titanate powder was added to pH 5-6 solutions of aqueous  $\text{Ni}(\text{NO}_3)_2$ . This procedure was performed three times with intermediate filtrations. To favor the formation of small, hydrolyzed clusters, a stoichiometric nickel solution was added dropwise to a slurry of the titanate powder in deionized water at a pH of 11. Concurrent with the Ni addition, NaOH was added to maintain the pH at or near 11. To favor the formation and adsorption of colloidal nickel hydroxide, sodium hydroxide was used to adjust the pH of the nickel nitrate solution to pH 12.7 prior to the addition of the sodium titanate. The pH adjustment caused the dissolved nickel to form a colloidal suspension of nickel hydroxide which was then adsorbed on the sodium titanate support. All three samples were analyzed for Na, Ni, and Ti by redissolving the titanate powders in strong acid and analyzing the solutions using atomic adsorption and ICP spectroscopies.

Transmission electron micrographs were obtained from either a JEM 200CX instrument or a JEOL 2000FX TEM/STEM using low beam intensity to avoid beam alteration of the samples. The powders were supported on holey carbon films mounted on copper grids. Powder surface areas were measured using  $\text{N}_2$  adsorption in a Micromeritics Digisorb 2600 analyzer. The samples were outgassed at 150 °C for 4 hours in flowing He before taking the measurements. Metal surface area was determined by static volumetric chemisorption using research purity gases obtained from Matheson. The chemisorption was performed at room temperature and total uptake of  $\text{H}_2$  was used as a measure of the surface concentration of Ni. All catalysts had a nominal loading of 10-11% Ni. The catalytic activity for n-butane hydrogenolysis was measured in a quartz U-tube reactor using a feed stream containing  $\text{H}_2$  and n- $\text{C}_4\text{H}_{10}$  in the ratio 20:1 at a total pressure of 101.4 kPa. UHP (99.999%)  $\text{H}_2$  was obtained from Big Three Industries and research purity (99.99%) n- $\text{C}_4\text{H}_{10}$  from Matheson. Both gases were used without further purification. The reaction proceeded with little or no deactivation over several (10-15) hours. Rates are reported as a turnover frequency (TOF), or the number of n-butane molecules reacted per second per surface Ni atom, with the latter quantity being determined by  $\text{H}_2$  chemisorption. Chemisorption measurements were performed after reduction at 673 K followed by cooling to room temperature in vacuum.

### Results and Discussion

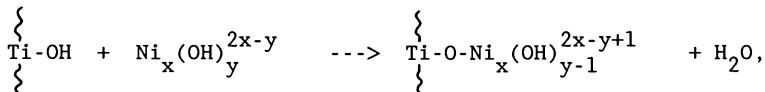
In order to control the mechanism by which nickel is loaded onto sodium titanate and to control the degree of nickel dispersion, we need to understand the ion-exchange properties of the sodium titanate support, the hydrolysis chemistry of the dissolved nickel, and how the different nickel species are expected to interact with the titanate support.

Ion-Exchange Behavior of Sodium Titanate. The ion-exchange characteristics of sodium titanate supports are summarized in Fig. 1 (2). In the figure, proton consumption is plotted by the solid line as the  $\text{Na}_{0.5}\text{Ti}$  is titrated from a basic pH ( $\approx 12$ ) with HCl.  $\text{Na}^+$  (+) loss from and  $\text{Cl}^-$  (-) adsorption onto the support are followed by

analysis of the solutions by ICP. At pH values above the isoelectric point (iep) of sodium titanate (pH 5), the surfaces of the sodium titanate particles are covered with anionic surface sites that are charge compensated by cations such as sodium. Above pH 5, the titanate support can function as a cation exchanger. For example if Ca(II) ions are added to a sodium titanate slurry, solution analyses indicate that one calcium ion is adsorbed by the support for every two sodium ions released into solution. Below pH 5, surface sites on the titanate support are primarily cationic, and the support behaves as an anion rather than a cation exchanger. In the above example, neither Ca(II) or Na(I) ions are adsorbed by the titanate powder when the solution pH is highly acidic (below pH 4). Therefore, the solution chemistry of sodium titanate suggests that if the powder is exposed to Ni(II), and if the Ni(II) is to be loaded via an ion-exchange process, little or no Ni(II) adsorption is to be expected below pH 5.

Also apparent in Fig. 1 (note the two regimes of H<sup>+</sup> consumption at nearly constant pH of about 8 and 12) and in surface charge measurements as a function of pH (not shown, see Ref. 4), is the presence of at least two anionic surface sites above pH 5. The distribution of these two sites is controllable during the synthesis of the sodium titanate powder. Using Raman and solid state <sup>170</sup>NMR spectroscopies (5) we are attempting to identify specific adsorption sites responsible for the differing solution behavior, and to characterize changes in the distribution of such sites. In this way, the tailoring of the support's ion-exchange properties can be realized. We have also found (4,5) that irreversible changes in the titanate support structure, and in the type and number of ion-exchange sites can occur during ion exchange in acidic solutions. This result demonstrates that the chemical stability of the support during metal loading needs to be considered.

Ni(II) Hydrolysis Chemistry. Although Ni(II) exists in solution as a simple aquated cation in acidic solutions, increases in the solution pH can lead to the deprotonation of bound water molecules, leading to hydrolysis and condensation of Ni(II) to form insoluble polymeric clusters. The calculated hydrolysis diagram (3) for Ni(II) (Fig. 2), shows that for a 3 x 10<sup>-2</sup> M nickel nitrate solution, hydrolysis and condensation commence at a pH of 6.5. This is evidenced by the coincidence of the calculated Ni(II) concentration and the total Ni calculated to be soluble (Fig. 2) above pH 6.5. Further increases in pH lead to the formation of larger insoluble polymeric species with nickel becoming less and less soluble as the pH is raised to pH 10. Although the solubility increases with pH above pH 10, the calculated solubility is still below 10<sup>-4</sup> M even at pH 14. The hydrolysis diagram suggests that Ni(II) can only be loaded by a simple ion-exchange process at pH values below 6.5 where hydrolysis is negligible. Above pH 6.5, polymeric nickel clusters will be present which can either condense with surface sites on the titanate support via reactions such as:



Equilibrium Titration of Na<sub>0.5</sub>Ti

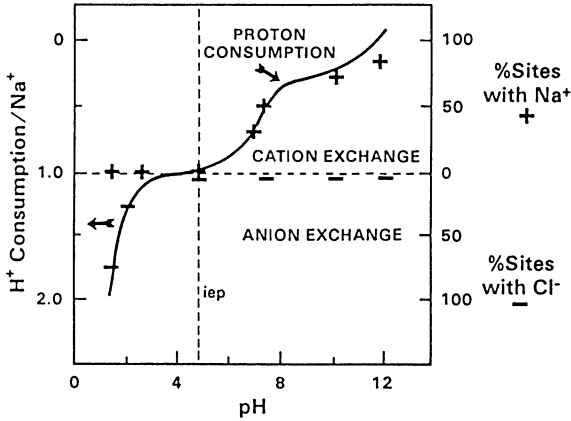


Figure 1: Plot of the H<sup>+</sup> and Cl<sup>-</sup> consumption from solution and Na<sup>+</sup> depletion from a Na<sub>0.5</sub>Ti during titration with HCl (starting pH = 12). Adapted from Reference 2.

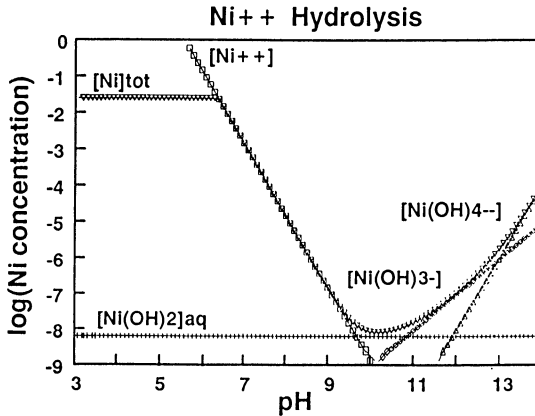


Figure 2: Calculated (3) dissolved Ni species concentrations as a function of solution pH. [Ni]Total was calculated for a 0.25M Ni(NO<sub>3</sub>)<sub>2</sub> solution, while all other species are the predicted concentrations at infinite [Ni]Total concentrations.

or can condense with each other to form larger colloidal particles of nickel hydroxide. The relative amounts of nickel which are adsorbed as small clusters and as colloidal particles should be influenced by the relative availability of reactive sites on the support vs. the other clusters present in solution. In any case, the hydrolysis diagram predicts that above pH 6.5, Ni(II) adsorption should occur via hydrolysis and condensation rather than by ion exchange.

Nickel Loading Experiments. Combining the information obtained in our studies of the ion-exchange properties of sodium titanate with what is known concerning the hydrolysis characteristics of Ni(II), we would predict that below pH 4, Ni(II) is not adsorbed by sodium titanate, between pH 4 and pH 6.5, Ni(II) is adsorbed as a monomeric cation via an ion-exchange process, and that above pH 6.5, Ni(II) should be adsorbed as polymeric clusters and colloids via hydrolysis and condensation mechanisms. To check the above hypothesis, we have titrated acidic nickel nitrate solutions with sodium hydroxide in the absence and in the presence of sodium titanate and analyzed solution aliquots for Ni(II) as a function of pH (Fig. 3). The results obtained for nickel nitrate alone show that the hydrolysis of nickel leading to the formation of insoluble nickel hydroxide occurs between pH 7.5 and 8 (slightly higher than the pH of 6.5 predicted from simple hydrolysis diagrams, Ref. 3). Results obtained in the presence of sodium titanate suggest that as predicted, little Ni(II) is adsorbed by the sodium titanate below pH 4. Between pH 4 and pH 7.5, Ni(II) is removed from solution via ion exchange, with more Ni(II) being adsorbed as the solution pH increases. Above pH 7.5, the precipitous drop in the dissolved Ni(II) concentration indicates that Ni(II) hydrolysis occurs at about the same pH in the presence of sodium titanate as in its absence. In this basic pH regime, Ni(II) adsorption should no longer occur via an ion-exchange reaction.

Nickel-Loaded Catalysts. The goal of the current study was to investigate how the degree of nickel dispersion depends on the loading conditions. In particular, we were most concerned with determining the degree of dispersion when the metal was loaded solely by ion exchange since results from earlier catalytic studies (1,2) suggest that we have good metal dispersion even at high metal loadings (> 5%) on the sodium titanates, relative to materials prepared by traditional methods. Our objective was to synthesize nickel-loaded sodium titanates with equivalent Ni(II) loadings in which the degree of dispersion would vary from individual ions to small polymeric clusters to large colloidal clusters of nickel hydroxide. Three nickel-loaded sodium titanate catalysts were prepared (see Experimental). Sample #1 was loaded by contacting the sodium titanate powder with three aqueous solutions, each containing enough Ni(II) (from Ni(NO<sub>3</sub>)<sub>2</sub>) to completely ion-exchange for Na, at a solution pH of 5-6. Sample #2 was loaded by slowly titrating a sodium titanate slurry (initial pH near 11) with a nickel nitrate solution until 0.5 moles of nickel were added per mole of Na(I) on the support. Concurrent with the addition of the Ni(NO<sub>3</sub>)<sub>2</sub> solution, we added NaOH to maintain the pH at 10-11. Under these conditions,

nickel should be hydrolyzed within the slurry, promoting the adsorption of nickel as polymeric clusters. Sample #3 was loaded by prehydrolyzing a nickel nitrate solution to form a colloidal suspension of nickel hydroxide and then adding the sodium titanate.

The nickel-loaded titanate catalysts have been characterized using solution analyses on redissolved material and transmission electron microscopy. To date, only Samples #1 and #3 have been completely characterized. Solution analyses for Sample #1 indicate that it contains 11.1 wt% Ni and 0.5 wt% Na. This composition is close to that calculated for material which has undergone complete ion exchange (11.1 wt% Ni + 0.0 wt% Na, down from 9.3 wt% Na in the starting sodium titanate powder). There is no evidence in TEM images of this sample, taken either before or after reduction in H<sub>2</sub> at 400°C, for the presence of any metallic particles (Fig. 4). However, energy dispersive X-ray analysis (EDAX) of the support from the same area where no metallic particles were observed in TEM identifies only Ni and Ti rather than the Na and Ti present in the support prior to nickel loading. Therefore, all analyses of the particles confirm that complete loading of nickel has occurred via Ni:Na ion exchange. Although the similarity in the atomic weight of Ni and Ti makes it difficult to estimate a minimum detectable particle size, the absence of distinguishable Ni particles in the TEM images suggests that the Ni has maintained a high degree of dispersion even after 400°C H<sub>2</sub> reduction.

The solution analyses for Sample #3 show that this sample has almost the same nickel content (10.2 wt%) as the ion-exchanged Sample #1 (11.1 wt%). However, the analysis suggests that none of the nickel in Sample #3 has been incorporated via ion exchange, since the sample has retained all of its sodium (10 wt%). Dark-field TEM images of the sample before reduction (Fig. 5) confirm that Ni-rich colloidal particles are observed adhering to the sodium titanate particles. TEM micrographs of the reduced Sample #3 catalyst (4) clearly show the presence of large (100-500 Å) Ni particles. EDAX analyses of the bright regions in Fig. 5 contain only Ni, while the underlying particle contains Na and Ti in the same ratios found in the starting sodium titanate. Thus, no ion exchange has taken place, and all of the nickel in the samples is present as metallic Ni particles that are derived from colloidal nickel hydroxide as predicted on the basis of our nickel-loading experiments described above.

Although we expected little or no ion exchange of Ni for Na to take place in Sample #2, solution analysis showed that roughly 25-30% of the Na content was removed during preparation. This may indicate that some Ni(II) cations can undergo ion exchange for Na since Ni is present at very low concentrations during preparation (the Ni(NO<sub>3</sub>)<sub>2</sub> solution is added slowly to the pH 11 solution containing the titanate powder). In fact, it is the low concentration of Ni that may allow control of the cluster size of nickel hydroxide when loading in this manner. Further characterizations (*e.g.*, TEM, catalytic activity) are being performed on Sample #2 at this time.

BET and H<sub>2</sub> Chemisorption Measurements. In Table 1 we list the BET surface areas and H<sub>2</sub> chemisorption uptakes for the Sample #1 and #3

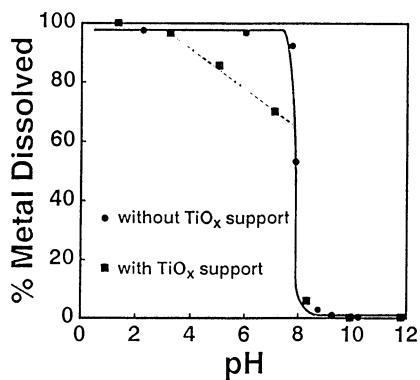


Figure 3: Plot of the amount of Ni in a 0.25M Ni(NO<sub>3</sub>)<sub>2</sub> solution as a function of pH both in the presence and absence of a Na<sub>0.5</sub>Ti powder.

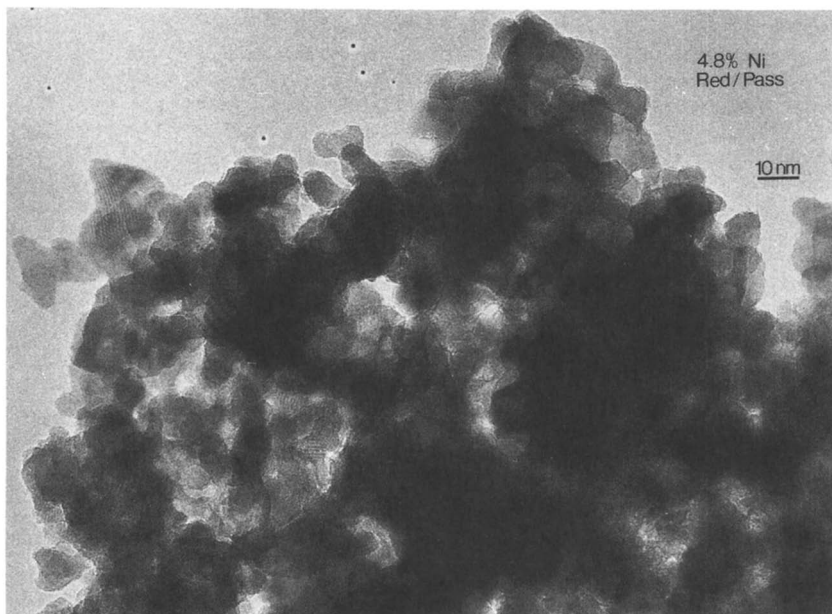


Figure 4: TEM image of Sample #1 after H<sub>2</sub> reduction at 400 °C.

catalysts described above. Also listed in the table are the calculated dispersions (or the % of exposed Ni on the surface relative to the total Ni in the catalyst) assuming 1 H/1 Ni atom.

Table 1. Surface Area (BET) and H<sub>2</sub> Chemisorption Measurements on two Ni Catalysts

	BET Surface Area (m <sup>2</sup> /gm)	H <sub>2</sub> Uptake (μmoles/gm)	%Ni Dispersion
<u>Sample #1</u>			
Before 400 °C H <sub>2</sub> Reduction	275	---	---
After	86	37	3.92
<u>Sample #3</u>	---	5	0.58

Although the ion-exchanged catalyst (Sample #1) contains more exposed Ni atoms than Sample #3, the dispersion is still considerably below expectations for Sample #1 assuming all the Ni was initially atomically dispersed on the support. However, this discrepancy can be rationalized on the basis of the BET surface area measurements made before and after H<sub>2</sub> reduction on Sample #1 (Table 1). The surface area of Sample #1 decreased from about 275 to 86 m<sup>2</sup>/gm after H<sub>2</sub> reduction at 400 °C. This dramatic reduction in surface area is accompanied by the crystallization of the titanate support which is evident in TEM, X-ray diffraction (XRD) and differential thermal analysis (DTA) measurements (4). During this structural change, a considerable fraction of the nickel could become encapsulated within densified TiO<sub>2</sub> particles and, thus, the accessibility of the adsorbed Ni for H<sub>2</sub> chemisorption (and for reactants in a catalytic reaction) can be lost. However, the metal still accessible might remain highly dispersed. Evidence for this was described above in that metallic Ni particles were absent in the TEM images while Ni could be detected by EDAX from the same area of the sample. Assuming spherical particles, one can calculate an average particle size of 100 Å for a dispersion of 3.92%. Such large Ni particles would be readily visible in the TEM images based on the results shown in Fig. 4. Further support for highly dispersed Ni was obtained from XRD measurements (4), and in the catalytic activity measurements described below.

Catalytic Activity of Nickel-Loaded Titanates. A good test of the dispersion of the active metal is the activity and selectivity for the hydrogenolysis of n-butane. For example, it is well known (6) that the hydrogenolysis of saturated hydrocarbons, or the rupture of carbon-carbon bonds by hydrogen, are structure sensitive; that is, their rates per surface metal atom (TOF's) vary with the percentage of metal exposed on the catalyst (*i.e.*, the dispersion). Typically,



the turnover frequencies are found to decrease with decreasing dispersion (increasing metal particle size). For example, Carter, et al. (7) found the rate of ethane hydrogenolysis to decrease by two orders of magnitude in going from Ni particles of less than 40 Å to particle sizes of greater than 80 Å. It has also been reported that highly dispersed Ir catalysts are particularly selective for ethane by preferential scission of the central C-C bond in n-butane (8).

In Fig. 6, we plot the turnover frequency for n-butane hydrogenolysis over Sample #1 and Sample #3. Dramatic differences in both the rate and activation energy were observed. The catalyst prepared by ion exchange of monomeric Ni<sup>2+</sup> cations (Sample #1) is up to two orders of magnitude more active than the precipitated Ni catalysts. These results will be discussed in more detail in a forthcoming publication (4). For the purposes of this paper, at least part of this difference in activity can be ascribed to a particle size effect; notably, that the higher activity obtained on the ion-exchanged Ni catalyst is due to its higher dispersion which correspondingly gives rise to a smaller amount of less active, close-packed Ni surfaces in the catalyst (9).

Fig. 7 displays the results obtained for the selectivity for C<sub>1</sub>, C<sub>2</sub> and C<sub>3</sub> paraffin hydrocarbons as a function of temperature on Sample #1 (ion-exchanged) and Sample #3 Ni catalysts. It can be seen that the catalyst prepared by ion exchange is very selective for C<sub>2</sub> hydrocarbons (ethane) at temperatures below 540 K. At higher temperatures (> 550 K), methane is the predominant product. In the case of the catalyst prepared by pre-hydrolysis (Sample #3), methane is the primary product for all temperatures studied. These results confirm our earlier conclusions concerning the dispersion of nickel in the two catalysts based on the TEM and chemisorption data. That is, reactivity on Sample #3 is characteristic of large metal particles while the selectivity observed on Sample #1 clearly indicates that at most very small, highly dispersed Ni particles are formed even at these high metal loadings (10 %).

### Summary and Conclusions

We have prepared and studied the properties of a sodium hydrous titanium ion-exchange material which shows great promise for use as a heterogeneous catalyst support. In these studies we have identified the solution conditions (e.g., pH) in which the sodium titanates contain sites for the adsorption of either metal cations or anions. For the exchange of Na for Ni(II) cations, solutions with a pH of 5 or more are required. However, Ni(II) undergoes extensive hydrolysis and condensation reactions above a pH of about 7-8 which competes with ion-exchange onto the support when both are present in solution. We have prepared three Ni-loaded hydrous titanates under different solution conditions to compare their material and catalytic properties. The catalysts were characterized by solution analyses, TEM, hydrogen chemisorption, BET surface area measurements, and the activity and selectivity of the n-butane hydrogenolysis reaction. The catalyst prepared via ion exchange displayed a high degree of selectivity for ethane from scission of the central C-C bond in n-butane indicative of highly dispersed

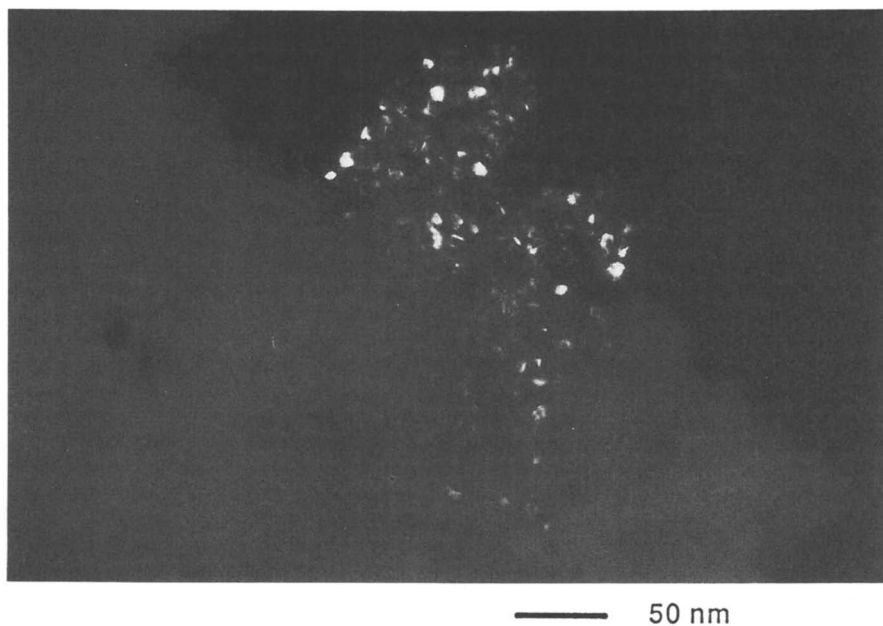


Figure 5: Dark-field TEM micrograph of Sample #3 as prepared.

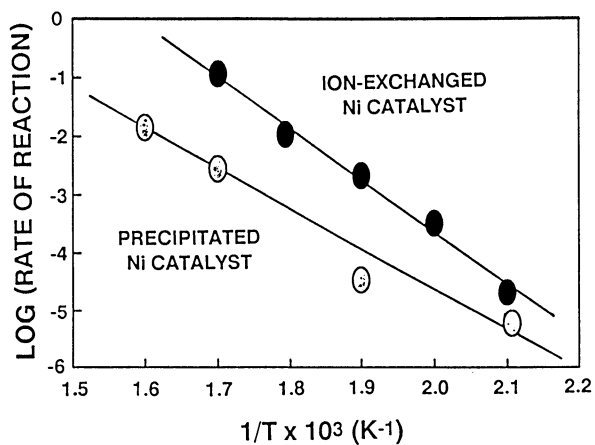


Figure 6: Arrhenius plot of the rate of n-butane hydrogenolysis over Sample #1 (ion-exchanged Ni catalyst) and Sample #3 (precipitated Ni catalyst).

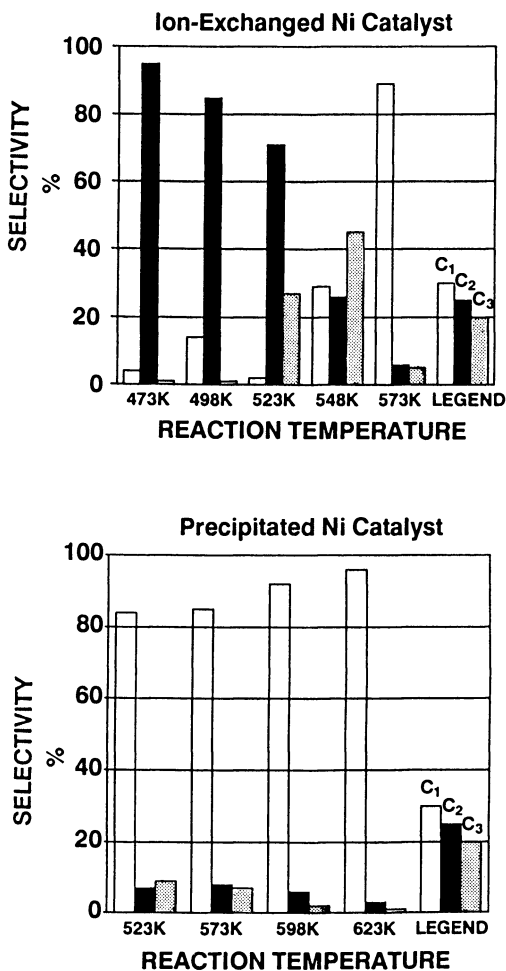


Figure 7: Selectivity for C<sub>1</sub> (CH<sub>4</sub>), C<sub>2</sub> (C<sub>2</sub>H<sub>6</sub>), and C<sub>3</sub> (C<sub>3</sub>H<sub>8</sub>) hydrocarbon formation from the hydrogenolysis of n-butane over Sample #1 and Sample #3.

metal even at the loading of 10% used in this study. The absence of metallic Ni in TEM images of this catalyst is further support for such a morphology. This is good evidence that atomic level dispersions of Ni are present in the as prepared catalyst and that high metal dispersions are maintained upon hydrogen reduction at 400 °C. However, H<sub>2</sub> chemisorption indicates that only a small portion of the Ni is accessible on the surface of the catalyst. We believe that the crystallization of the titanate support that accompanies the reduction of Ni at 400 °C in H<sub>2</sub>, encapsulates most of the metal within the densified titanate particles making it inaccessible to gas-phase species.

The high dispersion of the metal in catalysts prepared by ion exchange onto the hydrous titanate supports may well explain the high activity (on a per gram of metal basis) of these catalysts relative to catalysts prepared by more conventional methods (1,2). In these latter studies, the metal is reduced in-situ during reaction at much lower temperatures than used here to reduce Ni. Thus, the accessibility of the metal may not be compromised by the restructuring of the catalyst support material. In the future, we will investigate more moderate metal reduction methods, more easily reducible metals, and modifications of the synthesis of the sodium titanate powders. In this way, we hope to maintain the accessibility of the metal while still achieving the good dispersion at high metal loadings afforded by the use of ion exchange to prepare a catalyst on the hydrous titanates.

#### Acknowledgments

The authors would like to thank K. M. Kimball for preparing the three Ni-loaded catalysts, T. J. Headley for a portion of the TEM work, and D. H. Doughty for carrying out the nickel solubility computations. This work was supported by the Advanced Research and Technology Development Program, Office of Fossil Energy of the U. S. Department of Energy. A portion of the electron microscopy was performed at the Electron Microbeam Analysis Facility supported by the Department of Geology at the University of New Mexico. Sandia National Laboratory is supported by U.S. Dept. of Energy contract No. DE-AC04-76DP00789.

#### Literature Cited

1. a) Stephens, H. P.; Dosch, R. G.; Stohl, F. V. *I&EC Prod. Res. Dev.* 1985, **24**, 15. b) Dosch, R. G.; Stephens, H. P. U.S. Patent 4 511 455, 1985.
2. Stephens, H. P.; Dosch, R. G. In *Preparation of Catalysts IV*; Delmon, B.; Grange, P.; Jacobs, P. A.; Poncelet, G., Eds.; Studies in Surface Science and Catalysis Series; Elsevier: Amsterdam, 1987; Vol. 31, p. 271.
3. Baes, C. F., Jr.; Mesmer, R. E. *The Hydrolysis of Cations*; John Wiley & Sons: New York, 1976; pp. 241-247.
4. Braunschweig, E. J.; Datye, A. K.; Peden, C. H. F.; Bunker, B. C.; Martinez, S. L. In preparation.
5. Bunker, B. C.; Peden, C. H. F.; Martinez, S. L.; Tallant, D. R.; Turner, G. L. In *Better Ceramics Through Chemistry III*; Brinker, C. J.; Clark, D. E.; Ulrich, D. R., Eds.; Materials Research Society: New York, 1988; p. 105.

6. Boudart, M. Adv. Catal. 1969, 20, 153.
7. Carter, J. T.; Cusumano, J. A.; Sinfelt, J. H. J. Phys. Chem. 1966, 70, 2257.
8. Foger, K.; Anderson, J. R. J. Catal. 1979, 59, 325.
9. Engstrom, J. R.; Goodman, D. W.; Weinberg, W. H. J. Am. Chem. Soc. 1986, 108, 4653; and references therein.

RECEIVED January 10, 1989

## Chapter 9

# Decoking and Regeneration of a Hydrotreating Catalyst by Supercritical Extraction

M. Seapan and Z. Guohui

School of Chemical Engineering, Oklahoma State University,  
Stillwater, OK 74078

An industrially spent hydrotreating catalyst from naphtha service was extracted with tetrahydrofuran, carbon dioxide, pyridine and sulfur dioxide under subcritical and supercritical conditions. After extraction, the catalyst activity, coke content, and pore characteristics were measured. Tetrahydrofuran was not effective in the removal of coke from catalyst, but the other three solvents could remove from 18% to 54% of the coke from catalyst. The coke was removed predominantly from pores in the range of 4-12 nm, resulting in a bimodal pore size distribution and an increase in the pore volume and surface area. The amount of coke removed depended on the extraction temperature, pressure and duration. In the most severe extraction conditions, the silica foulant of the catalyst could also be removed as fine particles. Pyridine poisoned the catalyst during extraction, however its removal by acetone wash could restore the catalyst activity.

Hydrotreating catalysts are extensively used in petroleum processing, coal liquefaction, and generally in upgrading of liquid fossil fuels. These catalysts deactivate by coverage of their active sites with poisoning compounds and by blockage of their pores by deposition of carbonaceous solids and metallic foulants. Depending on the type of feedstock, the catalyst life may vary from a few months for heavy oils to a few years for naphthas. At the end of their active lives, the spent catalysts are removed from the reactor and replaced by fresh catalysts. Most of the spent catalysts are disposed of as solid wastes in landfills or used for metals reclamation. Only a small fraction of these catalysts is regenerated by controlled oxidation and reused as low activity catalyst in guard chambers. At present, no in-situ regeneration technique is available for these catalysts. This work discusses the merits of in-situ catalyst regeneration and investigates the

potential of supercritical fluid extraction as an in-situ catalyst decoking and regeneration technique.

Advantages of In-situ Catalyst Regeneration. Replacement of hydrotreating catalysts is an expensive operation in refineries. In addition to the purchase price of catalysts, the refining operation has to be shut down for several days to replace the catalyst, which represents a lost revenue. Refiners always try to schedule catalyst replacements at the time of routine maintenance shutdowns. However, the need for catalyst replacement sometimes necessitates costly unscheduled shutdowns. An in-situ catalyst regeneration process not only can increase the life of the catalyst but also can alleviate the unscheduled shutdowns.

Hydrotreating catalysts are usually alumina supported molybdenum based catalysts with cobalt or nickel promoters. By 1990, the demand for hydrotreating catalysts is expected to reach 80,000,000 pounds annually (1). The increased demand for these catalysts and the limitations on the availability and supply of the active metals increase the urgency to develop effective catalyst regeneration techniques.

Recent developments in oxidative regeneration have resulted in carefully controlled combustion techniques which can remove the coke and cause the gain of a significant portion of the catalyst activity without sintering. However, these processes are useful only when the metals laydown on the catalyst is minimal. Furthermore, they require the catalyst to be removed from the reactor and sent to catalyst regeneration companies. In-situ catalyst decoking and regeneration can be an attractive alternative to an off-site catalyst regeneration process.

Supercritical fluid extraction is a novel technique, which can potentially regenerate the catalysts in-situ in the hydrotreating reactor. Most solvents that are suitable for decoking have critical points lower than the operating conditions of hydrotreating processes, as shown in Table I. Therefore, the supercritical catalyst decoking and regeneration can be conducted inside the existing hydrotreating reactors. The regeneration process would only require the reactor to be depressurized and cooled to the conditions of extraction. After the extraction is completed, the reactor conditions can be easily changed to those of hydrotreating and the refinery operation resumed. Thus the time lost will be mainly the time required for extraction, which can be only a few hours under proper conditions, as shown in this work. Supercritical fluid regeneration can also be done periodically during refinery operations without allowing the catalyst to become completely deactivated. This periodic regeneration will allow the catalyst to be operated at lower temperatures by maintaining the catalyst at its peak activity for a longer period of time, thus reducing the operating costs of refining.

Principles of Extractive De-Coking. Hydrotreating catalysts deactivate by three major mechanisms:

1. Poisoning occurs by strong adsorption of stable molecules on the active sites of catalysts. Basic heterocyclic nitrogen compounds can usually poison the acidic sites. Adsorption of

Table I. Critical Properties of Solvents and Typical Hydrotreating Conditions

Compound	T <sub>c</sub> , K	P <sub>c</sub> , atm
Tetrahydrofuran (THF)	535.6	41
Pyridine	620	55.6
CO <sub>2</sub>	304.2	72.8
SO <sub>2</sub>	430.8	77.8
Typical Hydrotreating Conditions	590-680	70-170

basic compounds on catalysts is usually fast, reaching an equilibrium level immediately after the oil contacts the catalyst. The only long-term significance of poisoning in catalyst deactivation is the potential of nitrogen compounds to act as coke precursors.

2. Coking or formation of solid carbonaceous deposits in the catalyst pores occurs by decomposition and polymerization of hydrocarbons on the catalyst surface. Carbonaceous material continuously forms on the catalyst, causing active site coverage and pore plugging. Coking is a long-term deactivation phenomenon. After an initial rapid coking, the coke continuously builds up on the catalyst, while its composition and structure change. Accumulation of coke causes a slow deactivation of the catalyst. In industrial practice, the operating temperature is gradually raised to compensate for the activity loss. The increased temperature, in turn, increases the rate of coking and the rate of change of coke composition, accelerating the catalyst deactivation until the maximum allowable temperature is reached.
3. Fouling occurs by decomposition of organometallic compounds of the oil and deposition of the generated metals in the porous structure of the catalyst, blocking the active sites and plugging the pores. Long-term accumulation of these metals in the catalyst pores can result in permanent deactivation of the catalyst.

Very little is known about the chemical structure of coke. The chemical analyses of different coked catalysts have indicated that coke is not pure carbon, but is composed of 90-95% carbon, 5-7% hydrogen, 0-2% nitrogen, and traces of other elements found in the processed oil. The existence of different organic bonds indicates that coke has a macromolecular structure. This macromolecular structure can be broken down by certain reactive and strong solvents.

Fluids around their critical point show unusual physical property changes. Under supercritical conditions, fluids have lower viscosities and surface tensions and higher diffusivities



than those under normal conditions. High solubility of supercritical fluids can be used to solubilize hard to dissolve solids. This has resulted in the development of supercritical fluid extraction technology in food processing, pharmaceutical and other industries.

Supercritical fluid extraction can be used to remove carbonaceous material from spent catalysts. De Filippi and Robey (2) used supercritical carbon dioxide extraction to regenerate adsorbents. Abel (3) tried supercritical carbon dioxide extraction to regenerate a certain catalyst. Tiltscher et al. (4,5) studied the isomerization of 1-hexene on an alumina catalyst and showed that under supercritical conditions, 1-hexene was able to remove the oligomeric compounds ( $C_{12}$ - $C_{30}$ ) from the catalyst surface and prevent coking.

Solubilities of heavy hydrocarbons in supercritical fluids depend on the type of solvent (6). Moradinia and Teja (7) showed that the solubilities of solid n-alkanes ( $n$ - $C_{28}$ ,  $n$ - $C_{30}$ ,  $n$ - $C_{32}$ ) are about ten times higher in supercritical ethane than in carbon dioxide. Therefore, it is reasonable to search and find an appropriate solvent which can disintegrate and dissolve the carbonaceous deposits from hydrotreating catalysts, resulting in their decoking and regeneration.

In this project, the feasibility of catalyst regeneration by supercritical fluid extraction was studied. A spent catalyst from an industrial naphtha hydrotreater was extracted with tetrahydrofuran, pyridine, carbon dioxide, and sulfur dioxide under subcritical and supercritical conditions. The coke reduction and changes in the catalyst pore characteristics were measured and to a limited extent the catalyst activity was evaluated. It is shown that by supercritical extraction, the coke content of spent hydrotreating catalysts can be reduced and the catalyst pore volume and surface area can be increased.

### Experimental Work

Experimental apparatus used in this study consisted of a 12.5 mm internal diameter stainless steel tubular reactor with a length of 864 mm (34 in). It was originally constructed and used as a trickle bed downflow reactor. With proper modification of the plumbing it was used to regenerate the catalyst in either an upflow or downflow mode.

An industrially spent nickel-molybdenum catalyst from a naphtha hydrotreatment service was loaded in the reactor. Approximately 80 g of the spent catalyst was packed between two layers of glass beads in the reactor. The initial catalyst activity was tested by hydrogenation of a mixture of 10% quinoline in Tetralin in the temperature range of 355-380°C and 10.3 MPa (1500 psia). After stopping the flow of the reactants, the operating conditions were adjusted to those required for extraction experiments. The extraction was conducted by pumping the solvent into the reactor. After completion of the extraction process, the catalyst activity was measured again. The catalyst hydrogenation activity was calculated as the percentage of Tetralin converted to trans- and cis-decalins. The hydrodenitrogenation (HDN) activity was calculated as the percentage of quinoline converted to

propylbenzene and propylcyclohexane, the major hydrocarbons formed from quinoline. Neither of these reactants were suitable to measure the potential activity gain associated with the coke removal. Coke removal occurred mainly from large pores ( $\sim 10$  nm) which are not expected to affect the reaction rates of such small molecules as Tetralin and quinoline. However, these activity tests were useful in identification of the potential poisoning effects of the solvents.

The catalyst was removed and analyzed for its coke content, pore size distribution, pore volume, and surface area. All the catalyst samples were analyzed after a Soxhlet extraction with tetrahydrofuran for 24 h and drying in oven at 100 C. The catalyst weight loss due to combustion at 550 C was considered as the coke on catalyst. The catalyst pore characteristics were measured by a Quantachrome Autoscan Porosimeter.

The spent catalyst contained an average of about 17.5% coke. It had a monomodal pore distribution in the range of 4.4 to 12 nm pore diameter, with a most probable pore size of 5.4 nm. The pore volume and surface area of the catalyst were  $0.17 \text{ cm}^3/\text{g}$  and  $106 \text{ m}^2/\text{g}$  respectively. The spent catalyst also contained significant amounts of silica fouling, which had deposited on the catalyst from de-foaming agents added to the oil during the industrial use of the catalyst.

### Results and Discussion

The effectiveness of tetrahydrofuran, pyridine, carbon dioxide, and sulfur dioxide as solvents to remove the coke from catalyst under supercritical and subcritical conditions was studied. The critical properties of these solvents are listed in Table I and the extraction conditions are shown in Table II.

Two extraction runs, runs #1 and #2, were conducted with tetrahydrofuran at a reduced pressure of 1.05 and a reduced temperature of about 1.35 for 5 and 11 h respectively. The reduction of the coke content of catalyst was insignificant. The catalyst activities before and after extraction were measured at 355 C. The hydrogenation activity of the catalyst did not change, whereas, the quinoline HDN activity of the catalyst was decreased from 50% to about 20% when the catalyst was extracted for only 5 h. This initial low activity gradually increased to 50% in about 4 h. However, the catalyst that was extracted for 11 h, after stabilization showed an HDN activity of about 80%. These changes in the catalyst activity are not related to the coke. They are rather attributed to the interaction of tetrahydrofuran with the adsorbed species on the catalytic sites responsible for HDN reactions.

Three extraction experiments, runs #11-13, were conducted with carbon dioxide. Run #12 was conducted at a reduced pressure of 0.93 and a reduced temperature of 1.05 for 13 h. The catalyst coke content was reduced from 17.5% to 11%, where the coke was primarily removed from pores of 9.6 nm diameter. This represented a 37% removal of coke from the catalyst and resulted in a bimodal pore size distribution with a pore volume of  $0.22 \text{ m}^3/\text{g}$  and a surface area of  $137 \text{ m}^2/\text{g}$ . The changes in the pore size distribution are shown in Fig. 1. The other two extractions with carbon dioxide

Table II. Experimental Conditions of Catalyst Extraction

RUN #	SOLVENT	$P_r$	$T_r$	TIME, h	COMMENTS
1	THF*	1.05	1.35	5	
2	THF	1.03	1.38	11	
3	Pyridine	1.1 - 1.6	1.07	9	
4B	Pyridine	Atmospheric	--	24	
4A	Pyridine	1.02 1.36 1.85	0.99 1.03 1.07	5 3 3	Run 4A is the continuation of Run 4B
7	Pyridine	Atmospheric		24	Presulfided after extraction
8	Pyridine	0.63 1.00 1.36	0.92 1.00 1.06	5 17 7.5	After extraction, catalyst was removed, washed with acetone, dried, reloaded and sulfided
9	--	--	--	--	Presulfided only (No Extraction)
10	Pyridine	Atmospheric		12	Extracted, dried in oven loaded and sulfided
11	CO <sub>2</sub>	1.14	1.06	22	Batch
12	CO <sub>2</sub>	0.93	1.05	13	Semi-Batch
13	CO <sub>2</sub>	0.95	1.06	8	Flow extraction followed by sulfidation
14	SO <sub>2</sub>	0.05	1.05	8	Batch extractions
15	SO <sub>2</sub> + Pyridine	2.22 0.05	1.04 1.75	4 4	Pyridine extraction followed by SO <sub>2</sub> extraction

\* Tetrahydrofuran

were conducted at similar pressures and temperatures, but for 8 and 22 h periods. The catalyst from 8 h extraction was further sulfided with a 5% H<sub>2</sub>S in H<sub>2</sub> gas to study the effect of catalyst sulfidation. Tetralin hydrogenation activity was not changed measurably in any of these cases. Quinoline HDN activity was slightly reduced in the plain carbon dioxide extractions and slightly improved when the catalyst was sulfided after extraction. This indicated that carbon dioxide has no poisoning effect on the catalyst.

Several catalyst regeneration experiments were conducted with pyridine as the solvent using different extraction conditions and the catalyst activities were measured. The conditions of catalyst extractions are listed in Table II and the stabilized activities of the catalysts after 5-6 h of activity tests are shown in Figures 2 and 3. The catalyst characteristics were examined only in one run, which are shown in Table III.

Table III. Effect of Extraction on Catalyst Characteristics

Run #	Solvent	Coke Content Wt%	Pore Volume cm <sup>3</sup> /g	Surface Area cm <sup>2</sup> /g
	Catalyst as Received	17.5	0.17	106
4	Pyridine	14.3	0.22	119
12	CO <sub>2</sub>	11.0	0.22	137
14	SO <sub>2</sub>	10.3	0.23	129
15	Pyridine + SO <sub>2</sub>	8.1	0.22	132

In run 4A, the catalyst after Soxhlet extraction with pyridine for 24 h was loaded in the reactor and further extracted under a reduced temperature of about 1.0 and at successively increasing reduced pressures of 1.02, 1.36, and 1.85 for 5, 3, and 3 h respectively. The color of the extract was monitored during this process. The first extract had a moderately dark brown color, which turned into yellow after 5 h. When the pressure was increased, the color of the extract became brown again which gradually changed to light brown in 3 h. The last increase of pressure caused a major darkening of the color of the extract, followed by a lightening of color in 3h. Supercritical extraction removed more coke than subcritical extraction and the extent of coke removal depended on the duration and severity of conditions of extraction. This process reduced the coke content of the catalyst from 17.5% to 14.3%, a reduction of about 18% in the coke content of the catalyst. The coke was primarily removed from pores of 8 to

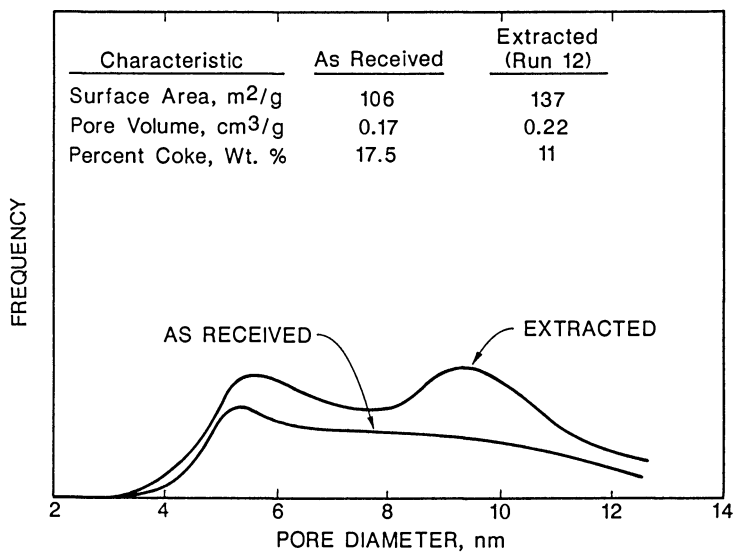


Figure 1. Effects of CO<sub>2</sub> Extraction on Catalyst Characteristics.

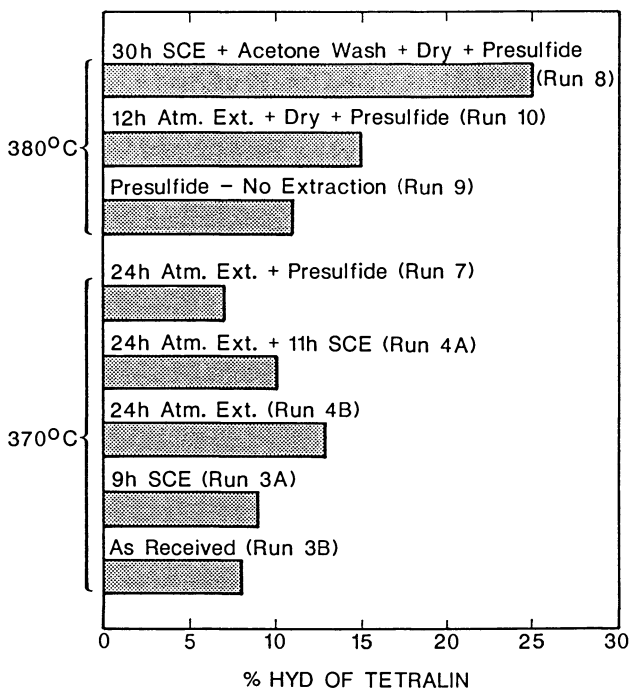


Figure 2. Effects of Pyridine Extraction on Hydrogenation Activity of Catalyst.

12 nm, resulting in a bimodal pore size distribution for the extracted catalyst. Consequently, the pore volume and surface area increased to  $0.22 \text{ cm}^3/\text{g}$  and  $119 \text{ m}^2/\text{g}$  respectively. As Figures 2 and 3 show the change in the hydrogenation activity of the catalyst was insignificant, while the catalyst lost its HDN activity from approximately 90% to 50%. This showed the strong poisoning effect of pyridine extraction.

As Figure 2 shows, neither extraction with pyridine (runs #3 and #4) nor sulfidation (runs #7 and #9) had any significant effect on the hydrogenation activity of the catalyst. Only in run #8 where the pyridine extracted catalyst was washed with acetone, dried, and presulfided, the gain in hydrogenation activity became significant. Similar phenomena were observed for the catalyst HDN activity, as shown in Figure 3. Extraction with pyridine reduced the HDN activity of the catalyst by poisoning of the HDN sites. A comparison of runs 3B, 3A, 4B and 4A of Figure 3 shows that the catalyst HDN activity decreased with an increase in the total catalyst-pyridine contact time. However, removal of the adsorbed pyridine by sulfidation (run #7) or by washing with acetone and subsequent sulfidation of catalyst (run #8) increased the catalyst HDN activity to about 90%. In summary, these activity tests showed that even though pyridine can remove some of the coke from catalyst, it can poison the denitrogenation sites of the catalyst. Therefore any catalyst decoking by pyridine should be followed by a pyridine removal process.

Extraction of catalyst with sulfur dioxide at a reduced pressure of 0.05 and a reduced temperature of 1.05 resulted in a reduction in coke content of catalyst from 17.5% to 10.3%, which increased the pore volume and surface area to  $0.23 \text{ cm}^3/\text{g}$  and  $129 \text{ m}^2/\text{g}$  respectively (run #14). When the catalyst was first extracted with pyridine then with sulfur dioxide, the coke content was reduced to 8.1%, which represents a 54% reduction in the coke content of the catalyst (run #15). The coke was again primarily removed from the pores of about 10 nm, resulting in a bimodal distribution of pores in the regenerated catalyst, as shown in Figure 4. The catalyst activities did not stabilize in the 6 h experiments conducted after these extractions, however the general trend showed an increase in the HDN activity and insignificant gains in the hydrogenation activity of the catalyst.

In summary, extraction with carbon dioxide, pyridine and sulfur dioxide can remove the coke from catalyst. The amount of coke removed depends on the extraction temperature, pressure and duration. Consecutive extractions with two solvents appear to remove more coke than the individual solvents do. Adsorption of certain solvents on the catalyst during extraction can poison the catalyst. Therefore, if poisoning solvents are used for decoking, their remains must be removed from the extracted catalyst to restore the catalyst activity.

In two of these extraction experiments (runs #8 and #15), in addition to coke reduction the silica foulant of the catalyst was also removed as glassy white fine powder. In these cases, the catalyst, after extraction with pyridine, was either washed with acetone or extracted with sulfur dioxide. Obviously, when the extraction is severe the structure of coke disintegrates, allowing the loosened foulant particles to be separated from the catalyst.

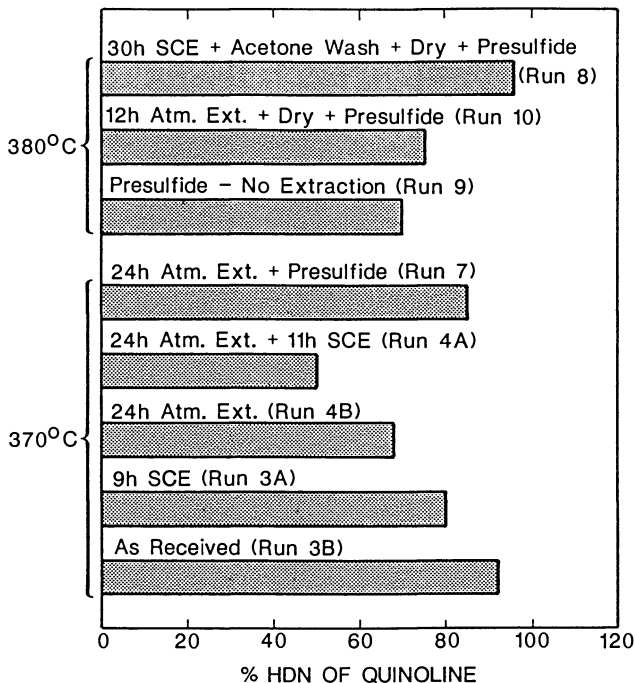


Figure 3. Effects of Pyridine Extraction on HDN Activity of Catalyst.

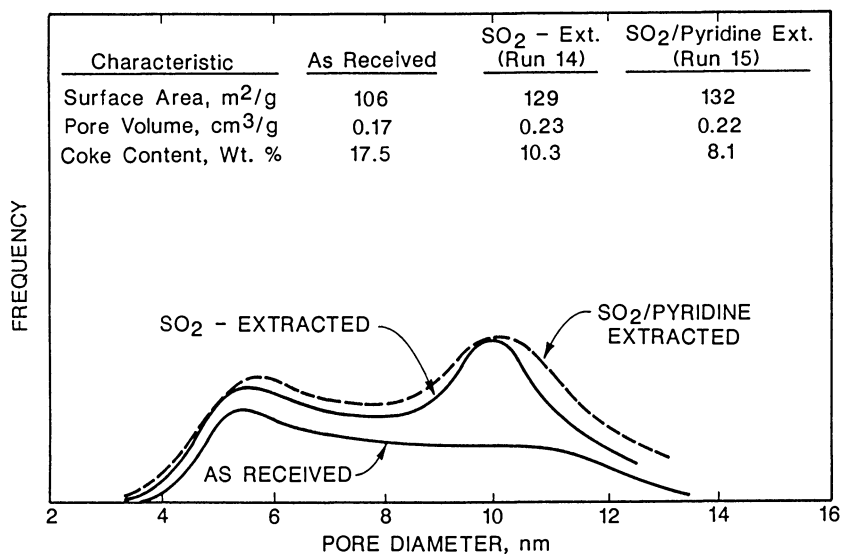


Figure 4. Effects of SO<sub>2</sub>/Pyridine Extraction on Catalyst Characteristics.

### Conclusions

1. Supercritical fluid extraction is a potentially viable technique in removing carbonaceous coke deposits from hydrotreating catalysts.
2. Tetrahydrofuran is not a good solvent for coke removal, but pyridine, carbon dioxide, and sulfur dioxide, can remove significant amounts of coke from the catalysts. The extent of coke removal depends on duration and severity of extraction. In the best case, 54% of the catalyst coke was removed from a spent hydrotreating catalyst. This was achieved by a supercritical pyridine extraction followed by a subcritical sulfur dioxide extraction.
3. In addition to coke removal, in two severely extracted cases, the silica foulant of the catalyst could also be removed from the catalyst.
4. Pyridine extraction poisons the catalyst, reducing its HDN activity. Removal of the adsorbed pyridine by acetone or acidic gases such as sulfur dioxide can regenerate the HDN activity.

### Acknowledgments

This project was supported by the University Center for Energy Research of Oklahoma State University.

### Literature Cited

1. Stinson, S. C. Chem. Eng. News, Feb. 1986, 64(7), 27.
2. De Filippi, R. P.; Robey, R. J. Supercritical Fluid Regeneration of Adsorbents; Environmental Protection Agency EPA-600/52-83-038, 1983.
3. Abel, H. West German Patent 28-53-065, 1978.
4. Tiltscher, H.; Wolf, H.; Schelchshorn, J. Angew. Chem. Int. Ed. Engl., 1981, 20, 892.
5. Tiltscher, H.; Wolf, H.; Schelchshorn, J. Ber. Bunsenges. Phy. Chem., 1984, 88, 897.
6. Schmitt, W. J.; Reid, R. C. In Supercritical Fluid Technology; Penninger, J. M. L.; Radosz, M.; McHugh, M. A.; Krukonis, V. J. Ed., Elsevier Science Publishers, Amsterdam, 1985.
7. Moradnia, I.; Teja, A. S. Fluid Phase Equil. 1986, 28, 199.

RECEIVED April 27, 1989



## Chapter 10

# A Philosophy for Testing

W. H. Flank<sup>1</sup>

Molecular Sieve Technology Department, UOP, Tarrytown, NY 10591

What do we usually do when we want to test or evaluate something? All too often, we attempt to compare some selected data of interest for a given material or process with other presumably comparable or similar data. These data can be for materials or processes about which we think we know something, or in which we are also interested. A minimal degree of structuring is commonly employed, and there are numerous pitfalls that must be avoided if the conclusions drawn are to be worth very much.

Is there a better way? Of course there is, and I shall try to describe some guidelines to use. Much of what should be done takes place before "going into the lab"; each step along the way should be planned in advance, and should be part of a coherent overall strategy. The process comprises a hypothesis, a testing protocol that has been constructed to meet perceived needs, collecting of meaningful responses, analysis of those responses in a number of ways, and extracting significant conclusions.

### The Hypothesis

A formal hypothesis can be constructed, as is often taught in graduate research or statistics courses. This usually takes the form of a null hypothesis, for arcane reasons. A question of some sort needs to be posed, so that the objective of the testing program is clear. The question can have a yes-or-no answer, or a quantitative one. The terms under which the question will be answered should be set before, and not after, the results are seen, to avoid compromising the unbiased nature and reliability of the conclusions. It is often the case that the criteria for proving or disproving the hypothesis are changed after the fact to accommodate poor data or a pre-conceived conclusion, and this should be avoided by setting specific criteria in advance.

The question or questions that are posed need to be amenable to empirical testing, preferably by a designed experiment. A carefully designed small set of experiments will almost always be

<sup>1</sup>Current address: Quantachrome Corporation, Syosset, NY 11791

more reliable and tell you more than endless reams of historical data that are not where you want them and were not carefully obtained under the conditions you wanted or even know about. One should also seek to define the effects of truly independent and uncoupled variables. It is all too easy to define inappropriate variables that are convenient to measure, or to pick ones that cannot readily be controlled and are defined in an after-the-fact manner. Careful attention to the concept of causality is needed.

### The Testing Protocol

If the relevant variables are well-established, or the hypothesis to be tested is very narrowly drawn, then only the ranges of interest need be chosen. The number of levels to be tested within that range is a function of the degree of confidence that is to be required for the conclusions, the anticipated sensitivity of a response to a given variable, the expected degree of linearity of the response, and the variability of the measurement process or processes employed as distinguished from the degree of control of the variables themselves.

If the relevant variables are not well-established, or if one is not willing to just assume that they are, an initial screening design can be employed. These usually involve a saturated factorial design in the simplest cases, with the size of the set of experiments depending on the number of variables to be screened for significance. Since in theory  $(n-1)$  variables can be tested for main effects (but not interaction effects) in  $(n)$  experiments, a large number of possibly significant factors can be examined to cover almost all the possibilities. Once the significant main effects have been identified, blocks of experiments can be devised to more fully define the responses of the system of interest to the key variables and their interactions.

In all of the steps in the testing process, it is important to set the levels of confidence that are to be used. The degree of risk that the wrong conclusion will be reached needs to be weighed carefully, and a choice needs to be made in advance. That choice will often determine the number of experiments to be performed, the way in which the responses will be measured, and the way the data are analyzed and conclusions drawn from them.

There are two types of risk that must be considered in choosing a confidence level by which results are assessed. There is the risk of rejecting the formal null hypothesis when it should be accepted, commonly referred to as the alpha or seller's risk. If we reduce this by specifying a very high confidence level requirement, then we increase the risk of failing to detect a real change or difference. There is also the risk of accepting the null hypothesis when it should be rejected, commonly called the beta or buyer's risk. Setting a significance level for the beta risk requires a specification of the magnitude of the difference that we desire to detect. This risk is usually reduced by increasing the size of the test set.

It should be obvious that, for a given set size, decreasing the likelihood of one of these risks necessarily involves an increase in the likelihood for the other risk. The only way both

risks can be reduced is to increase the size of the data set to be evaluated. If, however, one type of risk is deemed more serious than the other, then either an increase in required confidence level or a reduction in the sensitivity for difference detection can accordingly be chosen.

In sum, a block or set of experiments should be designed to answer defined and structured questions, in the form of hypotheses, at a given cost in time and money, and with a given degree of reliability. Testing protocols can range from the disarmingly simple to the bizarrely complex, but they all have these features in common, either explicitly or implicitly, and they are all constructed before "going into the lab." They can also vary considerably in degree of formality, and they can be linked in both serial and parallel configurations, but they should not merely investigate single points in experimental space or fixed sets of conditions that are resolutely applied no matter where the optima lie. These last sins are all too commonly found.

### Responses

Cause-and-effect relationships should be chosen for investigation, rather than proxy ones or, as is so common, effect-and-effect ones. Levels should be selected for truly independent and uncoupled variables that will avoid either a vanishingly small or a swamping or overwhelming response that would mask or even obliterate some other response of importance or interest. This will sometimes necessitate the use of unconventionally designed or even unbalanced blocks of experiments.

Responses should be relevant to the questions being asked, as well as being fairly easy to obtain. They should provide both necessary and sufficient answers to the questions being posed. An ambiguous response is a poorly designed one, from which it is often hard to salvage meaning, especially after the fact and after the deadline for decision.

The evaluation methodology must be capable of providing statistically reliable results at the levels in which we are interested. The measurement processes that are used to obtain responses need to be robust in the sense that they are resistant to both determinate accidental and random perturbations. This requirement for robustness applies to the processes for producing, representatively sampling, and evaluating products, be they materials, processes or otherwise.

### Analysis of Responses

One of the most important things to define is the sensitivity of a result to a given variable. If an inappropriate level is chosen at which to define a response, the conclusions can easily be misleading at best. It is also necessary to define sensitivities with respect to different levels for relevant co-variables as well. A comprehensive analysis will examine interaction effects and identify regions in experimental space where strong curvature exists. The possibility of strong two-factor and, rarely, three-factor interactions cannot be ignored.

Where the range covered for a given variable is large and the number of levels chosen for investigation is small, it is easy to miss maxima or minima. Even more severe than the problems of interpolation between large gaps in data are the pitfalls of extrapolation. The linearity of a dependence, or, if not linear, its monotonic behavior, may hold for only a limited region, or be strongly affected at different levels for other variables. The high risks in "going beyond the data" should be self-evident, even if frequently ignored.

What is very often neglected in analyses of data is the significance of the results in both the practical and statistical senses. Has the right question been answered in a meaningful way? What is the statistical significance associated with that answer? In almost all cases, a number by itself is relatively meaningless unless some estimate is available for the uncertainty in that number. Even a yes-or-no answer is generally derived from a numerical result, and that result has a certain amount of uncertainty associated with it. The significance of the difference between two or more test results is what is invariably missing in most data comparisons.

There are three components in the uncertainty surrounding a given numerical result. One is due to variation in the process by which the test sample was produced, another is due to sampling variability, and the third is due to the measurement process by which the result was obtained. Due attention must be paid to all of these, for maximum reliability in the conclusions based on that result. It should be obvious that good data don't cost so much as they pay!

### Drawing Conclusions

The reliability or degree of confidence that can be associated with the conclusions that are drawn should be determined and reported, preferably in unambiguous statistical terms. Not much can be gleaned from such statements as "the results are good to plus or minus 1%", "the difference is known within 5%", or "the average value is 30." "The product failed" is even worse, because almost everything is left to the imagination. Defined terms like 2S% repeatability, or least significant difference, or level of significance should be employed, together with information on sample or set sizes and confidence levels used. Whether the reliability changes or is constant with magnitude of the result needs to be determined. In cases where there are linked conclusions, the overall confidence level is generally reduced to the product of the individual confidence levels.

Conclusions should always be tempered by the possible importance of untested or uncontrolled variables, and by the risks assumed in the testing protocol. The problem of outlying values and their effects needs to be considered also. Retrospective correlations of historical data are frequently employed with no consideration of weighting for unbalanced distributions, with the result that one often ends up with merely a mathematical description of random error. Finally, as noted above, there is the danger of comparisons at fixed points, or at fixed sets of

conditions that are either inappropriate or sub-optimal for one or more of the members of the comparison set, or at conditions that are not really comparable.

If all of the cautions and constraints described above are addressed, the final results would comprise part of a very small minority of studies whose conclusions are well nigh unassailable.

Several examples can be described to illustrate some of the points that have been discussed.

Example 1. The surface area of a pair of zeolite samples was compared, and Sample A was higher than Sample B by 685 to 663  $\text{m}^2/\text{g}$ . Questioning uncovered the fact that the measurements were made at an inappropriate relative pressure of 0.30, and when the measurements were re-done at  $p/p_o = 0.03$ , the results were 862  $\text{m}^2/\text{g}$  for Sample A and 874  $\text{m}^2/\text{g}$  for Sample B. This caused a reversal in the conclusion reached concerning which was the better sample, until it was recognized that the results were statistically indistinguishable. Since the least significant difference between pairs of results from this test, at the 95% confidence level, was about three times the measured difference, it was clear that the only way to definitively determine which was the better sample was to perform a series of replicate determinations, rather than relying on a comparison of single values.

Example 2. Deactivation curves for two catalyst samples equivalent in most every other way were measured as a function of severity of temperature treatment. Catalyst A showed very little deactivation at lower temperatures, but performance dropped off sharply beyond a critical temperature. Catalyst B, whose initial activity was lower, declined gradually with increasing treatment temperature out to very high temperatures, and the curve crossed over that of Catalyst A before the rate of deactivation began to accelerate. If one assumes that higher treatment temperature is a proxy for longer time in the unit, then one is led to a different conclusion than if one assumes that higher activity at treatment temperatures more closely approximating those actually found in a reactor unit is the key measure.

Another way to assess these catalysts is to evaluate deactivation as a function of time at different levels of treatment temperature, according to a simple design. If one employs a very high temperature, Catalyst B is invariably more active than Catalyst A while, at a low temperature, Catalyst A is invariably more active than Catalyst B. If a treatment temperature is selected such that it is only somewhat higher than the intended reactor temperature, and the catalyst activity shows a measurable decline with time, corresponding to an accelerated aging test, then it can be observed in a reasonable testing time whether the deactivation curves will cross or not. Integration of the areas under the two curves between specified limits will show which catalyst is the better choice in a given situation.

Example 3. In attempting to make meaningful selectivity comparisons between FCC catalysts using pilot unit test data, the testing program must be carefully designed. Several specific criteria must be met:

- a. Selectivity comparisons must be conducted at identical operating conditions, with these conditions providing

equivalent conversion levels for each catalyst. It is not sufficient merely to achieve equivalent conversion levels, because the conditions employed to do this may not be as easily achievable in a commercial unit, which generally has a restricted range of operating conditions.

- b. The required equivalent conversions at constant operating conditions are achieved by a combination of steam deactivation conditions and zeolite content that is unique for each zeolite material and must be empirically defined.
- c. The deactivation conditions chosen must simulate as closely as possible the condition of equilibrium catalyst in a commercial unit for which the product is intended. Appropriate conditions must be determined for each formulation used.
- d. The conditions that are optimum for each test unit - feedstock combination must be defined. These conditions are found by varying the evaluation severity and generating yield-selectivity data. Optimum conditions are then used for the selectivity comparisons at constant conversion.

If these criteria are not met, artificial differences may be created that will be misleading, and real differences may be compressed into insignificance. This can easily happen if activity levels are matched in ways that do not reflect the limited range of operating conditions available in a heat-balanced commercial cat cracker. This point can't be emphasized too strongly.

Intrinsically low-activity catalysts can be made to appear artificially attractive, and high-activity catalysts can be made to appear relatively non-selective, with real differences being made small enough to be lost in the data scatter. If a catalyst is too severely deactivated, it will appear overly selective, and if it is insufficiently deactivated, over-cracking and poor selectivity may result. Low-activity catalysts can artificially be made to achieve higher conversion levels by a change in catalyst-to-oil ratio that is outside the operating capabilities of a commercial heat-balanced unit. It is thus possible to make a low-activity catalyst appear more attractive than higher-activity catalysts. Proper testing control is therefore essential for meaningful comparisons between catalysts.

Example 4. In comparing rare earth exchanged FCC formulations derived from ultrastable Y zeolite and ammonium fluorosilicate-treated Y zeolite, it is necessary to look at comparison curves rather than fixed-value or single-point comparisons. If the conversion activity in a standard micro-activity test is compared for these two zeolite materials exchanged with very low levels of rare earth cations and given equivalent steam deactivation treatments, the ultrastable Y form appears to be slightly more active. This difference can be shown to be statistically significant, even if not that significant in a practical sense. If, however, the comparison is made after exchange with high levels of rare earth cations, the AFS-treated Y form shows considerably better activity.

But just making comparisons at low and high values for the rare earth exchange variable does not provide the complete

picture. The iso:normal paraffin ratio, indicative of gasoline product quality, is almost the same for these two materials at high rare earth levels, and favors the AFS-treated zeolite at low rare earth levels. Superficially, then, the conclusion echoes a familiar story: You can trade off activity for selectivity, and vice versa, but you can't get both at the same time. However, if an intermediate level of rare earth exchange for these two materials is investigated, a window of opportunity is defined within which it is possible to achieve both higher conversions and higher iso:normal paraffin ratios with the AFS-treated zeolite. It turns out, then, that with careful attention to the way in which you go about the catalyst testing process, you can indeed "both have your cake and eat it too."

RECEIVED April 27, 1989

## Chapter 11

# Ten Guidelines for Catalyst Testing

Frits M. Dautzenberg

Catalytica, 430 Ferguson Drive, Mountain View, CA 94043

This paper presents ten guidelines for an effective catalyst research program. The guidelines were devised specifically for scientists investigating catalysts in laboratory-scale equipment. These guidelines include identifying the objectives, planning an effective strategy, selecting the appropriate reactor, establishing an ideal flow pattern, ensuring isothermal conditions, diagnosing and minimizing transport disguises, gathering meaningful data, assessing catalyst stability, following good experimental practice, and providing perspective on results. The guidelines represent years of experience rather than a review of the literature. They will help newcomers to the field operate effectively and will give experienced researchers new insights to current and future situations.

An abundance of literature describes how experimental rate data and insights into catalytic chemistry help us understand reaction mechanisms, formulate improved catalysts, and generate kinetic models. However, this literature typically is oriented toward engineering and is beyond the needs of most scientists investigating catalysts in laboratory-scale equipment.

This paper provides valuable advice on catalyst testing in a research setting. It focuses on two key requirements for an effective catalyst research program: (1) how to obtain reliable data and (2) how to do this with a well-conceived strategy. This paper also promotes an awareness of the impediments to reliable measurements of catalytic activity, the appropriate steps to overcome these interferences, and the special situations in which assistance of a reactor engineering specialist is needed. The overall emphasis is on catalyst testing rather than on reactor engineering. With these objectives in mind, the following “ten commandments” were formulated.

### I. Specify Objective

It is important to define the objective of the envisioned catalyst testing program before starting the experiments. During preliminary screening, many catalysts are



rated in relatively simple reactors, and easily determined performance parameters are measured. Few candidate catalysts go beyond this stage. This preliminary catalyst screening is generally followed by determining the key parameters that influence the reaction. Subsequently, the candidate catalysts are compared in more detail.

When a catalyst with practical potential is identified, further experimentation usually includes characterization of the reaction mechanism and kinetic measurements. More careful experimentation and higher accuracy are increasingly important. Subsequently, catalyst life tests may be required, preferably in a simulated industrial environment, to determine the long-term catalyst behavior. This may necessitate optimization of reaction conditions and further catalyst improvements.

Knowing how the catalyst will react in an industrial environment is required to assess how scale up will affect the catalyst performance. This information also will optimize the industrial reactor design. Many times pilot plants are the only source for this information.

These stages of a catalyst research and development program are usually sequential and are obviously subject to iteration. Because time and resource allocation usually increase with each iteration, it is beneficial to identify the specific objective, which will influence equipment selection, experimental strategy, and required accuracy.

## II. Use Effective Strategy

Well-designed, appropriate experimental strategies will greatly enhance the effectiveness of a laboratory testing program. Statistically derived experimental strategies developed over recent decades provide the following benefits:

- More information per experiment
- Key variables isolated early
- Valid conclusions despite experimental uncertainty
- Built in procedures to check the validity of conclusions
- Interactions among variables detected
- Significant time savings
- Organized collection and presentation of results
- Up front estimate of required number of experiments

The recommended strategy depends on the available information and the objective of the catalyst testing program. In exploratory programs it is important to establish which of the many variables (e.g., temperature, pressure, pretreatment conditions, catalyst preparation method) will have the greatest influence on catalyst performance. Factorial designs are recommended for such situations (1). Beyond simply identifying the key variables, one usually wants to know quantitatively how the variables affect catalyst performance. The required mathematical relationships can be generated by regression methods (2). In other situations one may want to know what combination of values of the key variables leads to optimum performance. Optimization strategies can quickly lead to this result (3).

Table I compares results achieved when seven variables that may affect the performance of a particular catalyst were tested *one-at-a-time* with results from a statistical design (fractional factorial) approach. In this comparison, a shift in measured performance is assumed to be *real* if it represents at least twice the uncertainty of the measuring technique. The one-at-a-time strategy, still prevalent among many catalyst researchers, requires 48 experiments to determine with 95% confidence which variables significantly impact catalyst performance. Whereas, with the fractional factorial approach, this same information was obtained in only 16 experiments with a 98.5% confidence level. The fractional factorial approach also shows possible interactions among the variables; the classical one-at-a-time approach does not.

Table I. Statistical Design versus One-Variable-at-a-Time Approach

	One-at-a-time strategy	Fractional factorial design
Number of variables	7	7
Experiments required	48	16
Confidence level	95%	98.5%
Information about interactions	No	Yes

Note: Real effect is 2X experimental uncertainty

Many catalyst researchers are unaware of the potential benefits of statistical design of experiments. Others have had unfortunate experiences with so-called *designed* experiments because they underestimated the influence of experimental uncertainties on the reliability of the conclusions. In both cases familiarity with the fundamentals of statistical inference in the experimentation strategy is beneficial (4). Statistically derived strategies can certainly offer many important benefits, although they obviously cannot replace creativity or sound technical judgment.

### III. Select Appropriate Reactor

Selection of the laboratory reactor requires considerable attention. There is no such thing as a *universal* laboratory reactor. Nor should the laboratory reactor necessarily be a reduced replica of the envisioned industrial reactor. Figure 1 illustrates this point for ammonia synthesis. The industrial reactor (5) makes effective use of the heat of reaction, considering the non-isothermal behavior of the reaction. The reactor internals allow heat to exchange between reactants and products. The radial flow of reactants and products through the various catalyst beds minimizes the pressure drop. In the laboratory, intrinsic catalyst characterization is done with an isothermally operated plug flow microreactor (6).

Generating the desired information in a reliable and reproducible manner is a leading criterion in selecting a laboratory reactor. This is not a straightforward exercise, and many factors must be considered such as the purpose of the

experiment, the physical nature of the reaction system, the ease of construction and operation, cost efficiency, and the integrity and evaluation of the resulting data. Often the laboratory reactor must be capable of continuous, steady-state operation under conditions of isobaricity, isothermality, ideal flow, and without concentration gradients. These elements will be discussed in more detail later in this paper.

For the reasons outlined above, continuously stirred tank reactors (CSTR) and plug flow reactors (PFRs) are usually preferred over batch, fluidized-bed, bubble column, and trickle-bed reactors. Batch reactors, although still popular in many laboratories, are not well suited for kinetic investigations. It is impossible to uncouple the main reaction kinetics from deactivation, and it is difficult to determine the actual reaction time. The complex hydrodynamics in fluidized-bed and bubble column reactors do not permit accurate assessment of intrinsic catalyst behavior. Expert assistance is required to interpret process conditions. Laboratory-scale trickle-bed reactors can be designed to compare catalysts. They are also suitable for life testing of catalyst samples. However, laboratory-scale trickle-bed reactors are generally not good tools for determining reaction kinetics or for characterizing highly active catalysts.

A CSTR is preferred for laboratory catalyst testing. Operated properly, a CSTR offers the following attractive features:

- Gradientless operation
- Simple mathematical treatment of the data
- Separation of reaction kinetics and deactivation parameters
- Uniform catalyst deactivation

The PFR is efficient for screening solid catalyst in a single fluid phase. It can also be used in later research stages to assess commercial criteria. Consider the evaluation of the ultimate commercial performance of a newly developed fixed-bed catalyst. The theory of similarity teaches that for the laboratory and the industrial reactor, the Damköhler number ( $N_{Da}$ ), the Sherwood number ( $N_{Sh}$ ), and the Thiele modulus ( $\phi$ ) need to be kept constant (Figure 2). As a result, the laboratory reactor must have the same length as the envisioned commercial reactor (7). In this case, scale up is done by increasing the diameter of the reactor. This example further illustrates that laboratory reactors are not necessarily small in size.

#### IV. Establish Ideal Flow Pattern

Continuous reactors ( $\delta n/\delta t = 0$ ) are characterized by the nature of their flow pattern, which lies between the ideal extremes of the plug flow and completely mixed patterns (Figure 3). These two patterns are called *ideal* because they enable reliable and straightforward treatment of data avoiding the radial and axial dispersion terms in the continuity equation (8). Analyzing data from other than an ideal flow pattern requires complicated mathematical treatment, if possible at all, and should therefore not be used for laboratory testing (9).

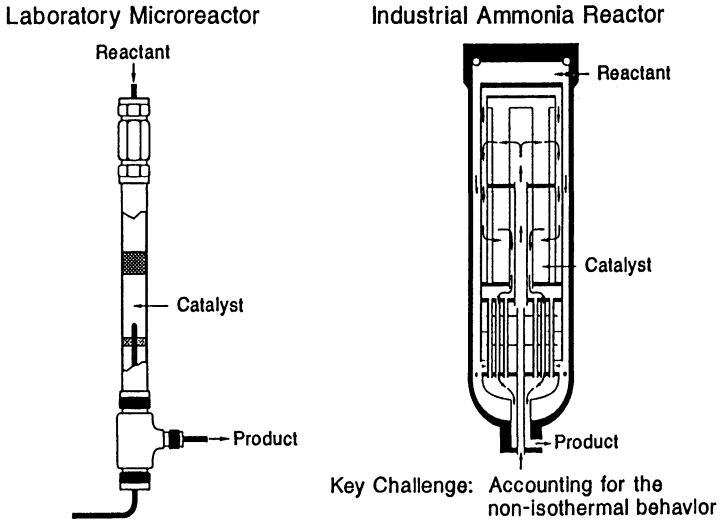


Figure 1. Comparison of a laboratory microreactor and envisioned industrial reactor for ammonia synthesis.

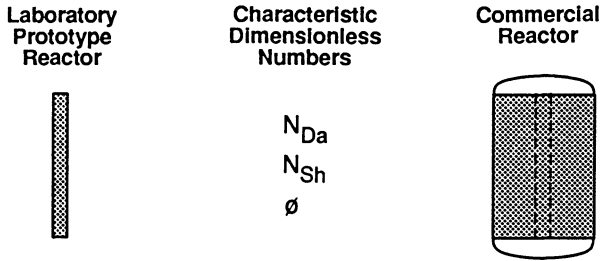
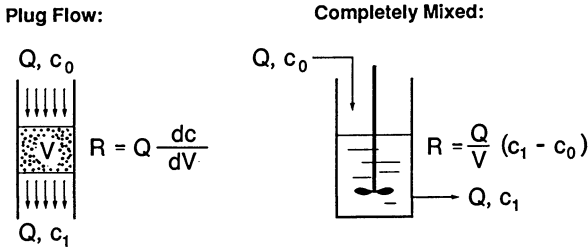


Figure 2. Schematic of prototype tube.



Any Other Flow Pattern:

$$R = \frac{1}{V} \frac{\partial n}{\partial t} + \frac{\partial Qc}{\partial V} - D_z \frac{\partial^2 c}{\partial z^2} - \frac{D_r}{r} \frac{\partial}{\partial r} \left( r \frac{\partial c}{\partial r} \right)$$

Figure 3. Effect of flow pattern on rate analysis.

Even when plug flow or complete mixing is believed to prevail, great care must be exercised to ensure that the flow pattern is ideal. The diameter of the PFR must be at least 10 times the catalyst particle diameter. This eliminates the influence of the reactor walls on the flow pattern. Furthermore, axial gradients may exist by virtue of conversion. These effects are minimized by selecting the correct ratio of bed length to particle diameter ( $L/d_p$ ) (10,11). Table II gives the steps for calculating the required  $L/d_p$  for laboratory fixed-bed reactors.

According to Table II, much higher  $L/d_p$  ratios are required in laboratory experiments than are expected from the established rule-of-thumb that  $L/d_p > 50$  is usually acceptable. For fixed-bed reactors,  $L/d_p > 50$  is indeed a sufficient requirement, provided a particle Reynolds number ( $NR_e$ ) is 10 or above. In laboratory experiments the particle Reynolds numbers, however, are usually much smaller, and  $Re < 0.1$  is more the rule than the exception. The literature does not stress this point sufficiently, which has led to confusion and many misconceptions.

## V. Ensure Isothermal Conditions

In many laboratory situations, intrinsic kinetic parameters are obtained under isothermal conditions. This is extremely important because relatively small changes in temperature can affect reaction rates significantly. Figure 4 shows how much the reaction rate will change for a 3 °C deviation as function of the activation energy and the assumed operating temperature.

Macrogradients in the reactor temperature may cause *intrareactor* gradients, which can cause deviations from isothermality (12). In addition to temperature gradients at the reactor level, temperature gradients (*interphase* gradients) can also occur at the boundary between the catalyst and the reactor fluid. With solid catalyzed reactions, such gradients may also occur within the catalyst particles. These gradients are called *intraparticle* gradients (Figure 5).

Axial and radial gradients can be distinguished with respect to intrareactor temperature gradients. In fixed-bed reactors, axial temperature gradients always exist because of conversion. These gradients can be minimized by increasing the ratio of bed length to catalyst particle diameter,  $L/d_p$  (see Table II). Radial temperature gradients probably cause unreliable data in plug flow reactors, which are attributable to the low effective thermal conductivity (13) of the catalyst bed. These intrareactor temperature gradients are nearly always more severe than interphase temperature gradients, which are generally more severe than intraparticle temperature gradients. The intraparticle temperature gradients are inconsequential because the effective thermal conductivity of the catalyst is usually larger than that of the surrounding fluid. In the catalyst particle, heat transfer occurs mostly by conduction through the solid phase.

The extent to which catalyst activity measurements are disturbed by intrareactor, interphase, and intraparticle effects of heat transport is assessed by evaluating experimental catalyst performance using the mathematical criteria in Table III (12).

Table II. Steps for Ensuring Plug Flow Operation in Laboratory Reactors

1. Determine the viscosity of the fluid medium at reactor conditions.
2. Calculate the superficial fluid velocity ( $u$ ):
3. Calculate the particle Reynolds number:

$$N_{Re_p} = \frac{u d_p \rho}{\mu}$$

4. Calculate the Peclet number:

$$N_{Pe} = (0.034) N_{Re_p}^{0.53} \left( \frac{L}{d_p} \right) \quad (\text{for liquid-phase operation})$$

$$N_{Pe} = (0.087) N_{Re_p}^{0.23} \left( \frac{L}{d_p} \right) \quad (\text{for gas-phase operation})$$

5. Calculate  $N_{Pe_{min}}$  :

$$N_{Pe_{min}} = 8n \ln \frac{1}{1-x}$$

6. Acceptable deviation from plug flow can be assumed if:

$$N_{Pe} > N_{Pe_{min}}$$

7. The minimum  $L/d_p$  follows from:

$$\frac{L}{d_p} > (235.3) N_{Re_p}^{-0.53} n \ln \frac{1}{1-x} \quad (\text{for liquid-phase operation})$$

and

$$\frac{L}{d_p} > (92.0) N_{Re_p}^{-0.23} n \ln \frac{1}{1-x} \quad (\text{for gas-phase operation})$$

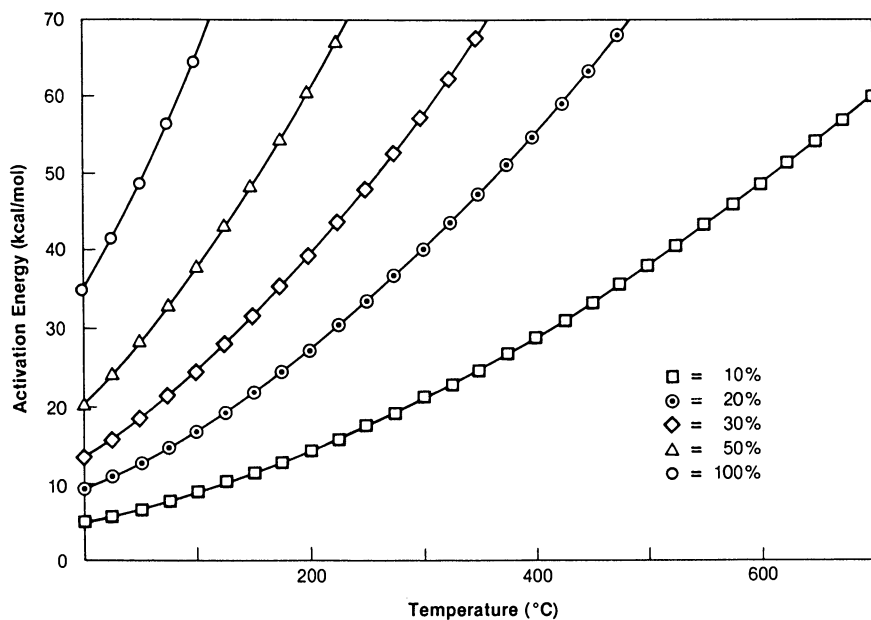


Figure 4. Deviation in reaction rate for a 3 °C deviation at a given activation energy and temperature.

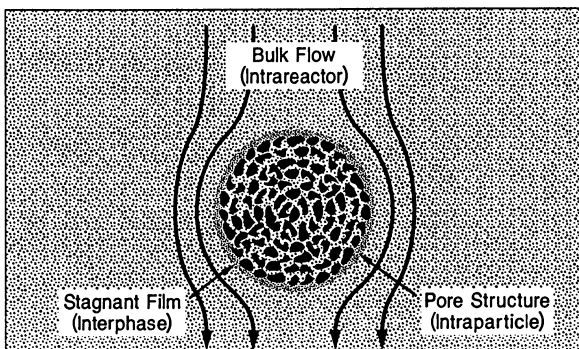


Figure 5. Reactor and catalyst gradients application to a heterogeneous catalyst.

The mathematical criteria compare functions A and B of observable or measurable parameters. If  $A < B$ , it can be assumed that the relevant temperature gradient may cause a <5% deviation of the reaction rate. One should, however, not accept a marginal satisfaction of the requirements, but rather look for an order of magnitude difference (e.g.,  $B/A > 10\%$ ).

Mathematical criteria aid in understanding what reactor system features can be manipulated to achieve better isothermal control. Based on this, the following recommendations can help establish isothermal catalyst testing:

- Use CSTR if possible
- Work at low conversion levels
- Use small catalyst particles
- Decrease bed voidage
- Select catalyst support with high thermal conductivity
- Add feed diluent with high thermal conductivity ( $H_2$  and He above 500 K)
- Apply high flow rates

#### VI. Diagnose and Minimize Transport Disguises

In investigating heterogeneously catalyzed reactions, an important, early objective is to determine whether intrinsic catalyst properties have been measured. Heat or mass transfer effects, caused by intrareactor, interphase, or intraparticle gradients (see Figure 5), can *disguise* the results and lead to misinterpretations. Before accurate and intrinsic catalyst kinetic data can be established, these disguises must be eliminated by adjusting the experimental conditions.

In a well-stirred CSTR, intrareactor gradients will be absent, but interphase and intraparticle gradients may be present. Conversely, in a fixed-bed PFR with small catalyst particles, intraparticle gradients may be eliminated, although intrareactor gradients still occur.

The following experimental tests can be performed to determine whether a certain gradient is important (5). The tests are relatively simple and require no a priori assumptions or estimates of numerical values.

- In a flow system, the flow rate can be varied while the space velocity is kept constant (Figure 6). If the conversion remains constant, the influence of interphase and intrareactor effects may be assumed to be negligible. A similar test can be done in a CSTR. In that case the absence of interphase and intrareactor effects can be assumed if the reaction rate is independent of the rate of agitation.
- Changing catalyst particle sizes can be used to test intraparticle effects (Figure 7). If there is no change of catalyst activity with change in particle size (assuming the exposed surface area of active catalyst is constant), the catalyst is considered to be free of intraparticle gradients.
- Koros and Nowak (14) proposed an alternative but more complex test. The test is based on the proportionality of the reaction rate to the number



Table III. Criteria for Isothermal Operation

Intrareactor
$\frac{ \Delta H  R_v r_t^2}{k_b T_w} < 0.2 \frac{RT_w}{E}$
Interphase
$\frac{ \Delta H  R' \rho_p r_p}{h T_b} < 0.15 \frac{RT_b}{E}$
Intraparticle
$\frac{ \Delta H  R' \rho_p r_p^2}{k_p T_s} < 0.75 \frac{RT_s}{E}$

Source: Reproduced with permission from ref. 12. Copyright 1971 Academic.

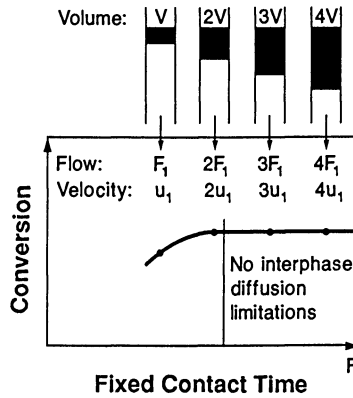


Figure 6. Diagnostic tests for interphase (external) transport limitation.

of catalyst sites only in the kinetic regime (Figure 8). Koros and Nowak suggested that catalysts with a different number of active sites but similar diffusional properties be prepared either by pelletizing mixtures of catalyst particles with inert powder or by impregnating the catalyst with different amounts of the active component. Because some reactions are structure sensitive, their intrinsic activity depends on the crystallite sizes. Thus a failure to satisfy this test does not necessarily imply the presence of diffusional limitations. Madon and Boudart (15) presented a detailed discussion of this test.

This paper does not discuss all the mathematical criteria for assessing the influence of various gradients (16,17,18). However, it is important to recognize that some parameters used in these mathematical criteria (i.e., activation energy, reaction order, and reaction rate) are not available until the initial experimental results are processed. Therefore, small catalyst particles, moderate temperature, and low conversion should be used in preliminary stages of each investigation. This will enhance the chance that the early estimates of the activation energy and reaction order are free from serious errors caused by heat or mass transport disguises. A disguise-free regime can be established through an iterative approach.

According to extensive literature on mass and heat transfer effects in laboratory systems, the importance of the various heat and mass transfer gradients decreases as follows:

- Intrareactor (radial) temperature gradient
- Interphase temperature gradient
- Intraparticle concentration gradient
- Interphase concentration gradient
- Intraparticle temperature gradient

The following guidelines will minimize the effects of these gradients:

- Intrareactor radial temperature gradients are minimized or eliminated by decreasing the reactor diameter or diluting the catalyst bed with inert particles.
- In gas-solid systems, interphase temperature gradients are avoided by using the smallest feasible particles and/or high linear flow velocities.
- Small catalyst particles are also effective in avoiding intraparticle concentration gradients.
- If the conversion at any particular space velocity is independent of the linear velocity through the bed, interphase concentration gradients are absent.
- If conversion levels are not too high, intraparticle temperature gradients are usually no problem.

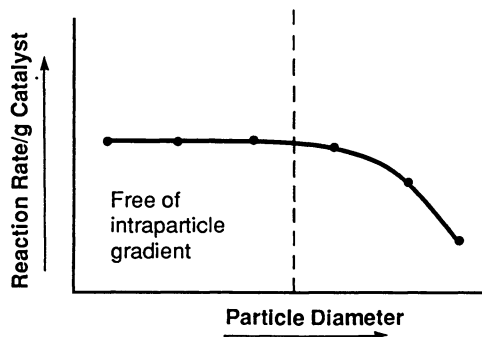


Figure 7. Diagnostic tests for intraparticle (internal) transport disguises.

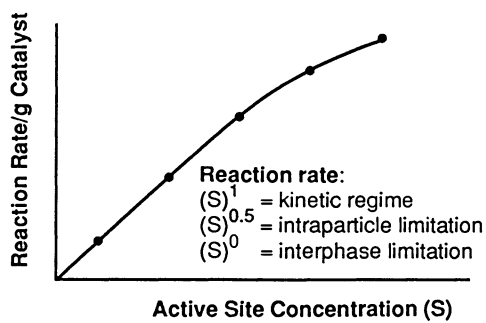


Figure 8. Koros-Nowak tests for transport disguises.

### VII. Gather Meaningful Catalyst Performance Data

Activity, selectivity, and yield are key catalyst performance characteristics. The recommended measure of catalyst activity is turnover frequency. Turnover frequency (or rate) is defined as the number of molecules that react per active site per unit time. Activity can also be defined as (1) the reaction rate per unit mass or volume of the catalyst, (2) the space velocity at which a given conversion is achieved at a specified temperature, (3) the temperature required to achieve a given conversion level, or (4) the conversion achieved under specified reaction conditions. Alternative 2 is practical for catalyst ranking. Alternatives 3 and 4 are rather uninformative. For rapid catalyst screening the latter two criteria are acceptable, but no catalyst should be eliminated from further consideration if it is only marginally inferior based on these criteria.

The relative activities of two catalysts can be determined using Equation 1:

$$\frac{a}{\text{WHSV}} = \int_0^{X_B} \frac{dX_B}{R_B M_B / X_{B_0}} = f(X_B, C_{B_0}, T) \quad (1)$$

The right side of Equation 1 is some function  $f$  of the achieved conversion of reactant B ( $X_B$ ), feed concentration of B ( $C_{B_0}$ ), and reactor temperature ( $T$ ). The underlying assumption is that all catalysts under consideration perform according to the same rate law described by the (often unknown) function  $f$ . If experiments with the various catalysts are run at fixed feed composition, at fixed temperature, and up to the same final conversion, function  $f$  is fixed and the activity ratio of two catalysts is a function only of the ratio of space velocities (Equation 2):

$$\frac{a_2}{a_1} = \frac{\text{WHSV}_2}{\text{WHSV}_1} \quad (2)$$

In comparing catalyst activities, alternative 2 gives a measurable, quantitative result without the need to know the function  $f$ . This is not the same for alternatives 3 and 4. If the catalyst comparisons are done at fixed weight hourly space velocity (WHSV), and if the temperature is varied to achieve the desired conversion, applying alternative 3 and Equation 1 gives (Equation 3):

$$\frac{a_2}{a_1} = \frac{f(X_B, C_{B_0}, T_2)}{f(X_B, C_{B_0}, T_1)} \quad (3)$$

A more active catalyst ( $a_2 > a_1$ ) will achieve the desired conversion at lower temperature ( $T_2 < T_1$ ). Equation 3, however, cannot provide any quantitative assessment without a knowledge of the functional dependence of  $f$  on all the variables. The same reasoning can be applied to alternative 4, which yields (Equation 4):

$$\frac{a_2}{a_1} = \frac{f(X_{B_2}, C_{B_0}, T)}{f(X_{B_1}, C_{B_0}, T)} \quad (4)$$

Thus for similar materials that are likely to have similar kinetic dependencies, catalytic activities are most readily compared by fixing the temperature and varying the space velocity to obtain a chosen degree of conversion.

Selectivity is another catalyst attribute that is often considered when ranking catalysts. Selectivity may be defined as the ratio of the molar amount of key reactant converted to the desired product to the total molar amount of the key reactant *converted*. As such, selectivity is a measure of the efficiency of the catalyst in promoting the formation of the desired product as compared to other products. Since selectivity is a function of the relative rates of reaction with a given reaction system, selectivity will be a function of reaction temperature, space velocity, feed composition, reactor geometry, and degree of conversion. Comparing selectivities of different catalysts is therefore only meaningful when all the latter parameters are constant.

Selectivity is sometimes called *efficiency*. As a result, selectivity can be confused with product *yield*. Yield is usually best defined as the ratio of molar amount of key reactant converted to the desired product to the total molar amount of the key reactant *fed* into the reactor system. Consequently, it follows that

$$(\text{Selectivity}) \times (\text{Conversion}) = \text{Yield}.$$

A catalytic process is commercially viable if the catalyst transformation is achieved within definite, practical limits of space and time. To quantify this aspect, one can determine the so-called *space-time yield*. This measure of activity is simply the amount of product obtained per unit time and per unit reaction space (where *reaction space* is usually the reactor volume). Weisz (19) pointed out that in industry the useful space-time yield is rarely less than  $10^{-6}$  g/mol of reactant per cubic centimeter of volume of reactor space per second. This has been called the Weisz window on reality. Figure 9 (19) shows the Weisz window and other windows of chemical activity that apply to biochemistry and petroleum geochemistry (19).

Economic necessities determine the lower limit for industrial catalysis. The reactor residence time cannot be too long because one cannot wait forever. The reactor could be enlarged, but this would require a higher investment. The upper limit is imposed by the achievable rates of mass and heat transfer, both of which are controlled by properties such as viscosity, density, diffusion coefficients, and thermal conductivity. Thus the upper limit is basically set by nature.

If natural limits are ignored, control is lost; the reactor may blow up; the catalyst may be destroyed; products may be inferior; or part of the reaction heat may be lost.

Useful chemical transformations are thus confined to the Weisz window on reality. The Weisz window is an important concept from various standpoints. For scale up, it is helpful in determining the limiting reactor sizing to be considered for a given intrinsic catalyst activity, as determined by laboratory experiments. During catalyst development, it provides guidance in assessing whether further catalyst development is necessary. It also indicates the directions for further research; e.g., in the case of certain zeolites that were found to be too active

(20). Perhaps several catalyst preparation steps will be necessary to tame the catalyst activity until it performs within the Weisz window. This can include diluting the active catalyst in an inert matrix to provide a reduction of 10 to 20 per-unit volume activity.

### VIII. Assess Catalyst Stability Early

Catalyst life is an important attribute in comparing and evaluating catalysts. Catalyst life can be defined in time units, in number of turnovers, in length of time between regenerations, in terms of maximum temperature increase a catalyst can tolerate to maintain productivity, or in terms of fresh catalyst addition rate.

Whatever definition is used, a decrease in catalyst activity with time may be extremely fast (as in fluidized catalytic cracking), or it can occur over a much longer time scale (as in residue desulfurization (Figure 10) (20)). The causes of deactivation are not always easy to identify. Any good experimental program should, however, attempt to assess the long-term performance of the catalyst to a sufficient level of confidence. It is recommended to do this during the early stages of the program.

Figure 10 shows that the most suitable catalyst is not necessarily the one that exhibits the highest initial activity (A). In this case, catalyst B maintains the highest average activity over its lifetime. The example illustrates the importance of frequent sampling and continuous reactor operation over considerable time. The overall catalyst deactivation pattern could not have been established if the experiments had been shorter than approximately 1,500 h.

The S-shape deactivation pattern in Figure 10 is determined by the process of metal deposition in the outer core of the catalyst particles; desulfurization and hydrocracking occur mainly in the inner core of the catalyst particle (21). This understanding led to development of various effective demetallation catalysts as shown in Figure 11 (22, 23, 24, 25). Furthermore, this has opened the path to industrial solutions (26) for the treatment of high metal feedstocks. Figure 12 shows catalysts with different hydrodesulfurization-hydrodemetallation (HDM-HDS) characteristics combined in a series of reactors. The front-end catalyst (A) has a high selectivity of HDM; whereas the back-end catalyst (C) has excellent HDS characteristics. The example also illustrates the need to address catalyst stability during the early phases of a catalyst program, not only to avoid pursuing the wrong avenue, but also because it can lead to new discoveries and the recognition of new opportunities.

### IX. Follow Good Experimental Practice

Catalyst evaluation is a complex procedure; it is easy to forget the relatively obvious in favor of the recondite. The following golden rules seem obvious but are important requirements for reliable experimental results:

- Always compare performance of different catalysts under identical experimental conditions (reactor design; flow rates; catalyst size, shape, and quantity; type and degree of agitation; and temperature and pressure regimes).

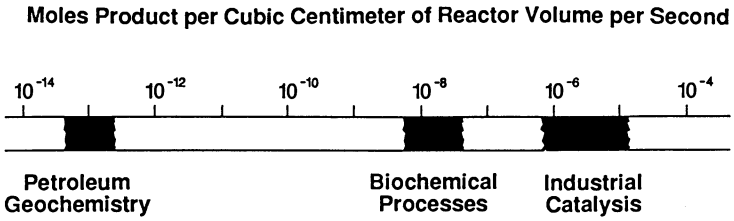


Figure 9. The Weisz window and other windows of activity.

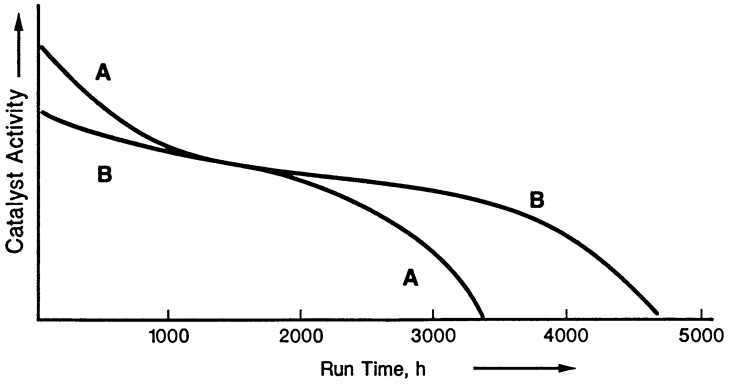


Figure 10. Long-term deactivation during residue desulfurization.

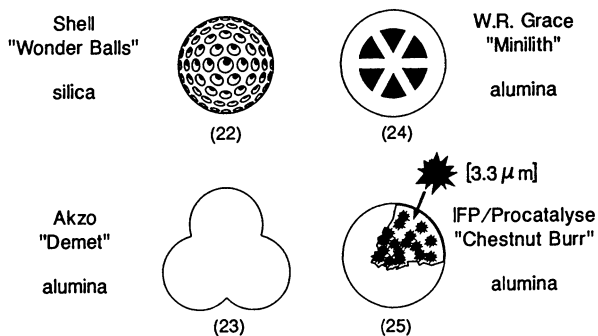


Figure 11. Commercially available hydrodemetallation catalysts.

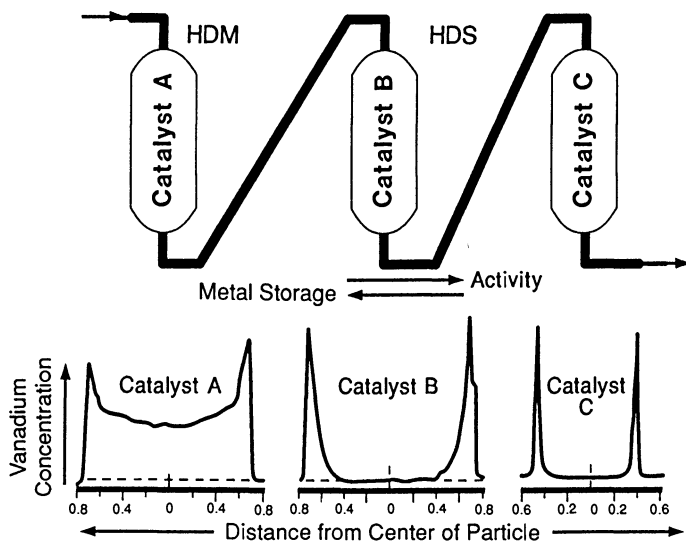


Figure 12. Catalyst tailoring.



- Always check the reproducibility of results on a regular basis.
- Determine whether the reaction thermodynamics are favorable. In particular, be aware of any limitation on conversion because of equilibrium.
- Always observe and record in full the conditions under which the experiments are carried out and the results that are obtained. Clearly define such things as rate, selectivity, and quantity of catalyst.
- Maintain high standards regarding the quality of analysis. Catalysts can be very sensitive to traces of impurities. Monitor sample reproducibility and overall material balances carefully; avoid overlapping gas chromatographic (GC) peaks; watch for unexpected condensation in effluent lines; check response factors on a regular basis; and be aware of the molecular selectivity of the GC detector.
- Always keep possible homogeneous contributions in mind with heterogeneous catalysts and vice versa. Check this mutual interference by changing surface to volume ratios in the heterogeneous or homogeneous reactor. Conducting experiments in the absence of the catalyst is not a conclusive proof of the absence of heterogeneously initiated homogeneous reactions. Nevertheless, blank experiments should be used to check the possible reactivity of reactor walls and other internals or *inert* dilution materials.

#### X. Provide Perspective on Results

The value of catalyst testing is enhanced by reporting the results in a professional way. It is important to describe the following procedures: Was a batch mode of operation or continuous, steady-state operation used? What was the reactor configuration? How were the catalysts prepared? Was activation or pretreatment required?

Unambiguous definitions of activity, selectivity, and conversion are needed to interpret the results correctly. It is also important to know the quality of the results. What is the reproducibility and the statistical validity of the conclusions? Were heat and mass transfer disguises eliminated? What tests were done to confirm ideal flow pattern, isobaricity, and isothermality? Often it is necessary to know whether catalyst performance is adequate. For that reason the space time yield and catalyst life characterization need to be addressed.

#### Conclusions

Many conclusion can be drawn from a review of the stated ten commandments. Some of them merit specific mention.

1. A catalyst research and development program proceeds through several well-defined stages, each of which focuses on different information needs. This is vital for the selection of effective equipment and experiments.
2. Many catalytic testing situations benefit from statistical methods of planning efficient sequences of experiments.

3. Laboratory reactors usually are not small replicas of commercial reactors. Selecting the best laboratory reactor is rarely straightforward.
4. Disguises due to heat and mass transfer limitations are the primary impediments to reliable data.
5. The two most important criteria are an ideal flow pattern and isothermal operation. An ideal flow pattern, either plug flow or perfectly mixed, is essential for a straightforward interpretation of reaction data. Isothermal operation is critical of generally reliable quantitative laboratory catalyst data.

### Acknowledgments

This paper includes many suggestions and ideas provided by Dr. J.C. Schlatter and Dr. J. C. De Deken. The author thanks Dr. J. Naworski, General Manager, Catalytica Studies Division, for permission to publish this paper based on *A Practical Guide to Catalyst Testing* (27).

### List of Symbols and Abbreviations

a	Catalyst activity multiplier (dimensionless)
c	Concentration (moles/volume)
$c_0$	Inlet concentration (moles length <sup>-3</sup> )
$C_i$	Concentration of species i (moles length <sup>-3</sup> )
$D_r$	Radial diffusion coefficient (length <sup>2</sup> time <sup>-1</sup> )
$D_z$	Axial diffusion coefficient (length <sup>2</sup> time <sup>-1</sup> )
$d_p$	Solid particle diameter (length)
E	Activation energy (energy mole <sup>-1</sup> )
F	Molar flow rates (moles time <sup>-1</sup> )
$\Delta H$	Heat of reaction (energy mole <sup>-1</sup> )
h	Heat transfer coefficient (energy length <sup>-2</sup> time <sup>-1</sup> temp. <sup>-1</sup> )
$k_b$	Effective thermal conductivity of catalyst bed (energy length <sup>-1</sup> time <sup>-1</sup> temp. <sup>-1</sup> )
$k_p$	Thermal conductivity of catalyst particle (energy length <sup>-1</sup> time <sup>-1</sup> temp. <sup>-1</sup> )
L	Catalyst bed length (length)
$M_B$	Molecular weight of species B (mass mole <sup>-1</sup> )
$N_{Pe}$	Peclet number (dimensionless)
$N_{Rep}$	Reynolds number based on particle diameter (dimensionless)
$N_{Sh}$	Sherwood number (dimensionless)
$N_{Da}$	Damkohler number (dimensionless)
n	Number of moles (moles)
Q	Volumetric flow rate (volume time <sup>-1</sup> )
R	Gas constant (energy mole <sup>-1</sup> temperature <sup>-1</sup> )
$R_B$	Kinetic expression for dependence of reaction rate on temperature and concentration (determined by applicable rate units)
$R'$	Rate of reaction per unit mass of catalyst (moles time <sup>-1</sup> mass <sup>-1</sup> )
$R_v$	Rate of reaction per unit volume of catalyst (moles time <sup>-1</sup> length <sup>-3</sup> )

r	Radial distance (length)
$r_p$	Radius of catalyst particle (length)
$r_t$	Radius of reactor (length)
T	Absolute temperature (temperature)
$T_b$	Temperature of bulk fluid (temperature)
$T_s$	Temperature of catalyst surface (temperature)
$T_w$	Temperature of reactor wall (temperature)
t	Time (time)
u	Superficial fluid velocity
V	Reactor volume (length <sup>3</sup> )
WHSV	Weight hourly space velocity (hour <sup>-1</sup> )
x	Fraction of reactant consumed via chemical reaction (dimensionless)
$x_B$	Fractional conversion of B (dimensionless)
Z	Distance along reactor axis (length)
$\mu$	Fluid viscosity (mass length <sup>-1</sup> time <sup>-1</sup> )
$\rho$	Fluid density (mass length <sup>-3</sup> )
$\rho_p$	Catalyst particle density (mass length <sup>-3</sup> )
$\phi$	Thiele modules (dimensionless)

### Literature Cited

- Hendrix, C.D. *Chemtechnol.* 1979, 9(3), 167.
- Draper, N.R.; Smith, H. *Applied Regression Analysis*; John Wiley & Sons: New York, 1981.
- Hendrix, C.D. *Chemtechnol.* 1980, 10(8), 488.
- Box, G.E.P.; Hunter, W.G.; Hunter, J.S. *Statistics for Experimenters*; John Wiley & Sons: New York, 1978.
- Le Page, J.-F. *Catalyse de Contact*; Editions Technip: Paris, 1978.
- Pratt, K.C. *Catalysis: Science and Technology*; Anderson, J.R., and Boudart, M., Eds.; Springer-Verlag: New York, 1987; Vol. 8, Chapter 4.
- Trambouze, P.; Van Landeghem, H.; Wanquier, J.-P. *Les Reacteurs Chimiques*; Editions Technip: Paris, 1984; p 360.
- Levenspiel, O. *Chemical Reaction Engineering*; John Wiley & Sons: New York, 1972.
- Carberry, J.J. *Chemical and Catalytic Reaction Engineering*; McGraw-Hill: New York, 1976 .
- Mears, D.E. *Chem. Eng. Sci.* 1971, 26, 1361.
- Lange, R.; Busch, A. *Chem. Technol.* 1979, 31, 232.
- Mears, D.E. *J. Catal.* 1971, 20, 127.
- Kulkarni, B.D.; Doraiswamy, L.K. *Catal. Rev.-Sci. Eng.* 1980, 22, 431.
- Koros, R.M.; Nowak, E.J. *Chem. Eng. Sci.* 1967, 22, 470.
- Madon, R.J.; Boudart, M. *Ind. Eng. Chem. Fund.* 1982, 21(4), 438.
- Satterfield, C.N.; Sherwood, T.K. *The Role of Diffusion in Catalysis*; Addison-Wesley: Reading, MA, 1963.
- Wheeler, A. In *Catalysis*; Emmett, P.H., Ed.; Reinhold: New York, 1955; Vol. II, p 105.

18. Weisz, P.B. *Z. Phys. Chem.* 1957, 11, 1.
19. Weisz, P.B. *Chem. Technol.* 1982, 424.
20. Weisz, P.B.; Miale, J.N. *J. Catal.* 1965, 4m, 527.
21. Dautzenberg, F.M.; van Klinken, J.; Pronk, K.M.A.; Sie, S.T.; Wijffels, J.-B. *Catalyst Deactivation through Pore Mouth Plugging during Residue Desulfurization*; presented at the 5th International Symposium on Chemical Reaction Engineering; Houston, March 13-15, 1978.
22. *Shell Silica Spheres*, Shell International Chemical Company, Ltd.: London, 1982.
23. Plantenga, F. L.; Sonnemans, J. W. M.; Desai, P. H.; Suzuki, T. *1984 Proc. American Petroleum Institute Refining Department, 49th Midyear Meeting*, 1984.
24. Pereira, C.J.; Hegedus, L.L. U.S. Patent 4 510 263; assigned to W. R. Grace, 1985
25. Bousquet, J.; Devanneaux, J.; Peries, J.P. *ASVAHL Hydrocatalytic Process for Heavy Oil Upgrading*; presented at 3rd International Conference on Heavy Crude and Tarsands; Long Beach, California; July 22-31, 1985
26. Dautzenberg, F.M.; George, S.E.; Ouwerkerk, C.; and Sie, S.T. *Advances in the Catalytic Upgrading of Heavy Oils and Residues*; presented at the Advances in Catalytic Chemistry Symposium; Salt Lake City, Utah, May, 1982.
27. *Catalytica A Practical Guide to Catalyst Testing*; Catalytica Studies Division: Mountain View, CA, 1987.

RECEIVED July 7, 1989

## Chapter 12

# Evaluation of Fluid Cracking Catalysts

### A Comparative Study of Testing Philosophies

E. L. Moorehead, M. J. Margolis, and J. B. McLean

Engelhard Corporation, Edison, NJ 08818

Fluid catalytic cracking (FCC) is one of the major refining processes within today's petroleum industry. For the majority of refineries this process represents the primary conversion unit for producing gasoline directly from gas oil. While discussions about FCC tend to group all units into one, average type, there are in fact many differences among FCC units. These differences include configuration, operation, and feedstock. For each refiner there is usually some limiting parameter in the unit that controls the overall operation. This may be catalyst circulation, attrition, coke selectivity (either too much or too little), or gas selectivity (compressor - either wet (LPG) or dry gas limits).

Depending upon the needs of the refiner he may be limited by any one of these at various times as he moves from a maximum octane operation to a maximum gasoline operation or switches from a light gas oil to a heavier gas oil feed. The selection of the proper catalyst provides flexibility to address these requirements in a manner otherwise unavailable.

In order to provide the refiner with as much flexibility as possible, catalyst vendors have developed a variety of FCC catalysts to meet specific demands. While all catalysts incorporate zeolites as the core, the type and amount vary widely. At present there are probably 100 catalyst variations that are available depending upon the specific application. Differences in catalysts can be significant; for example, zero versus 3 weight % REO, or 15 versus 40 % zeolite or surface areas ranging from 100 to 400 M<sup>2</sup>/G. Alternatively, differences can be very subtle. While this provides the refiner with a variety of choices, it also presents a problem in how to best evaluate various catalysts.

In an effort to understand how the petroleum industry addresses the problem of fresh FCC catalyst evaluation, a survey of testing philosophies from 15 companies was conducted. The objective was to identify the merits of various steaming procedures as well as catalyst testing. The results of the survey show that each laboratory has a unique testing program, with wide differences being practiced in both steam deactivation and Micro Activity (MAT)

testing. Steaming severities range from 1350°F for 17 hours to 1600°F for 4 hours. Some prefer slow heating of the catalyst while others practice "shock" treatment. Some treat all catalysts the same independent of application, while others steam deactivate to a constant conversion or other measurable physical property. For catalyst testing the same wide range of approaches exist. While an ASTM MAT test does exist, no laboratory was found to practice it in total. MAT temperatures vary from 900 to 1000°F, with catalyst/oil ratios of 3 to 6 and WHSV's of 10 to 40. Some laboratories test all catalysts at constant conversion by either adjusting steaming severity or maintaining steaming severity while varying C/O in the MAT unit.

To understand the benefits of various testing procedures a comparative study of testing approaches was conducted using three different Engelhard FCC catalysts. The catalysts selected represent a range from a full octane catalyst containing USY to a gasoline catalyst containing REY. The objective was to identify a preferred testing procedure that gave catalyst properties and product selectivity results that agree with commercial performance. The conclusions from this comparative study as well as a discussion of the approaches of testing used in the industry will be discussed in this paper.

### Experimental

Three Engelhard FCC catalysts, identified as catalysts A, B, and C representing typical gasoline, partial octane and octane catalysts were prepared for comparing various test methods. Chemical and physical properties are presented in Table 1.

The laboratory steamings were performed at the conditions listed in the appropriate tables using a shock steaming method. This method calls for the near instantaneous steaming of 100 grams of a catalyst by introducing the catalyst to a pre-heated steam environment. Catalyst addition is conducted in less than or equal to 15 minutes such that the temperature drop within the steaming reactor does not exceed 30°F. Catalysts are unloaded hot, giving near instantaneous cooling.

Evaluations of steamed catalysts were performed with a MAT unit using a standard mid-continent gas oil. The MAT conditions varied and are identified in the tables. Selectivities were determined from gas chromatographic analysis of liquid and gaseous products by Hewlett-Packard, simulated distillation hardware and Carle., Refinery Gas Analyzer Systems, respectively. Carbon on catalyst analyses were performed by IECO.

Surface area measurements were conducted using ASTM method D-4365-85 for both fresh and steamed samples. All other physical and chemical analysis were performed by standard techniques.

### Results and Discussion

Laboratory evaluation of the catalytic performance of fresh FCC catalysts involves steaming and activity testing. The latter is most often performed using a microactivity test (MAT). While there are other parameters that are important in comparing total performance of catalysts like attrition and fluidization, this paper

focuses only on steaming and MAT testing. A recent paper by Rawlence et. al. (1) provides a general overview for all the parameters involved in the laboratory evaluation of FCC catalysts.

While ASTM procedures for both steaming and MAT testing have been established (ASTM D-4463 and D-3907, respectively), a general survey of the petroleum industry indicates that neither of these methods are specifically practiced. Instead, each laboratory has developed individualized steaming and MAT testing procedures that best suit their needs. While many laboratories perform complete chemical and physical analyses on fresh FCC catalysts, the vast majority do not perform such analyses on the steamed catalysts. The latter actually represent the catalysts evaluated while the former are in essence a "precursor". While it may be argued that fresh properties can be used as an indicator of steamed properties, a thorough evaluation of catalysts should include an examination of the steamed chemical and physical properties.

### Steaming

Steam deactivation of fresh FCC catalysts is required to reduce the activity to a level appropriate for MAT testing. The choice of steaming conditions determines the physical and chemical characteristics of the catalyst. Therefore, under constant MAT conditions, steaming conditions are responsible for the observed activity and selectivity. Laboratory steaming of fresh FCC catalysts is generally done in the presence of 100 percent steam in a fluidized bed configuration. Catalysts are usually loaded at ambient temperature and in the presence of fluidizing nitrogen, the temperature is increased to the desired target. Steam, obtained by vaporization of injected water, is then introduced and the nitrogen flow is stopped. After a specified period of time, the water injection is stopped and the nitrogen is introduced again and the temperature is set back to an ambient or low level. Having reached the desired temperature the catalyst is unloaded and may be screened to remove fines. Alternatively, the catalyst can be introduced into a hot steam environment as opposed to the more gentle temperature ramp identified. The rapid addition of the catalyst to a hot reactor is referred to as a shock steaming.

A summary of steaming procedures that are generally employed is presented in Table 2. From this list it can be observed that a wide range of steaming severities are used. In general, the minimum temperature is 1300°F, with a maximum of 1600°F. While steaming is used to artificially deactivate a fresh sample, such that it represents a typical "equilibrium" sample, the approaches used to achieve this are varied. A number of laboratories use a fixed time and vary temperature to achieve a range of deactivated samples that when evaluated in a MAT unit will have a range of conversions so that they can make an assessment of catalyst stability and selectivity.

An alternative approach for steaming uses a fixed temperature but the time is varied to generate a hydrothermal stability curve. Temperatures in the range of 1400-1500°F are generally used with times ranging from 5-60 hours. Preferred times however, tend to be 4-24 hours. The times employed can be tied to either a target

Table 1  
FRESH CATALYST PROPERTIES  
ENGELHARD DYNAMICS CATALYSTS

Catalyst	A	B	C
	<u>REY</u>	<u>REY/USY</u>	<u>USY</u>
Wt% REO	2.7	1.5	0.0
Zeolite Index	6	17	32
UCS, $\bar{R}$	24.76	24.74	24.64
Surface Area: m <sup>2</sup> /g			
Zeolite	108	158	237
Matrix	33	63	106
<u>Total</u>	<u>141</u>	<u>221</u>	<u>343</u>

Table 2  
SUMMARY OF STEAMING CONDITIONS

	<u>PRECALCINATION</u>	<u>STEAMING TEMPERATURE OF</u>	<u>STEAMING TIME, HRS.</u>
ASTM	None	1292-1562	5
ENGELHARD	None	1300-1600*	4
	1100/1 hr	1350-1454	17
	1100/1 hr	1350-1550*	4
		1360-1430 metals	
	1100/4 hrs	1375	4.75
	None	1382-1490	17
	1200/3 hrs	1400 @ 15 psig	5 & 10
	None	1400 & 1500*	5
	1112/4 hrs	1400 & 1500	5
	1112/3 hrs	1418	15
	1300/1 hr	1425*	4
	1000/1 hr	1430-1525	5-80/20% s/a
	None	1475*	5
	1000/1 hr	1475	6 & 6
	None	1500	4

\*Shock Addition Method



conversion or some physical property. The deactivated samples are then evaluated in a MAT unit under a standard set of conditions. A third approach involves one steaming severity in conjunction with varying MAT conditions (usually cat/oil) to achieve equivalent conversions (2). While this method provides for equivalent steaming of all catalysts it provides very little information on the relative stability of the catalysts to be evaluated.

A fourth approach involves a variation from variable temperature/constant time by blending different ratio's of deactivated samples to represent the inhomogeneity of commercially deactivated samples (3). This method is not used to any extent at this time.

For all of these alternatives the goal is to produce a sample that has chemical and physical properties that are indicative of commercially deactivated catalyst (1). For example, if the goal of steaming is to target only the unit cell size, then it might be concluded that one steaming severity is needed. As suggested by McElhiney (2), this would be 1500°F for 5 hours. What this approach overlooks is that it does not account for expected changes in MAT activity, zeolite content or total surface area. Figure 1 shows that an equilibrated Unit Cell Size (UCS) for a zero rare earth catalyst (catalyst C) can be obtained at relatively mild steaming conditions; but as presented in Figure 2, the MAT activity and surface areas will continue to change with steaming. As the differences between catalysts become greater, the need to be aware of these other parameters becomes more important. This is particularly true when comparisons between gasoline and octane catalysts are to be made. While this comparison may not be performed by a particular laboratory it appears that the currently employed steaming procedures were developed for gasoline catalysts and their application to octane catalysts has to be investigated.

By way of example, Figure 3 shows the effect of steaming severity on zeolitic surface area (ZSA) for catalyst A and C. Also identified are typical values for equilibrium catalysts. What is seen is that the conditions needed to deactivate A to typical equilibrium ZSA are different than for C. If C is deactivated using the preferred conditions for A, then activity and surface areas are not in line with commercial experience. If the reverse is true, then A is deactivated too severely.

The need to have more than one steaming procedure for extremely different catalysts has been proposed by Magee et. al. (8) is consistent with commercial observations in that a zero rare earth catalyst will generally have a lower equilibrium MAT activity than a gasoline catalyst. The difficulty, of course, is that it is not practical to have a unique steaming procedure for every catalyst. However, it is practical to target steaming severity such that the steamed properties for groups of catalysts are representative of what will be observed commercially. An obvious question becomes does it matter which steaming philosophy is practiced? As will be discussed later the ranking of catalysts can be effected by the manner in which they are steamed. As such, it is important that whatever approach is selected, the time or temperature be severe enough to reach a reasonable degree of deactivation as measured by UCS, surface area and MAT activity.

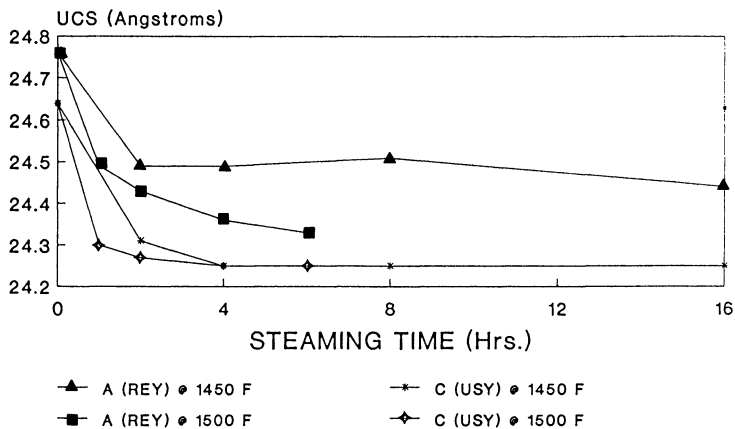


Figure 1. Unit Cell Size Equilibration is Dependent on Steaming Conditions.

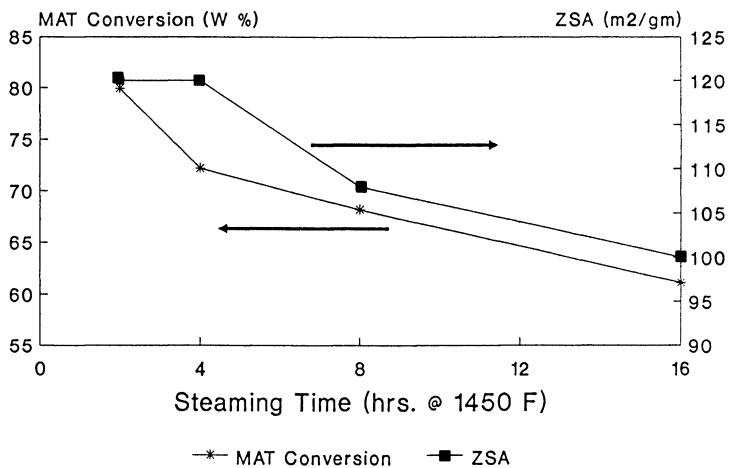


Figure 2. MAT Conversion and ZSA Continue to Decline for USY Catalyst.

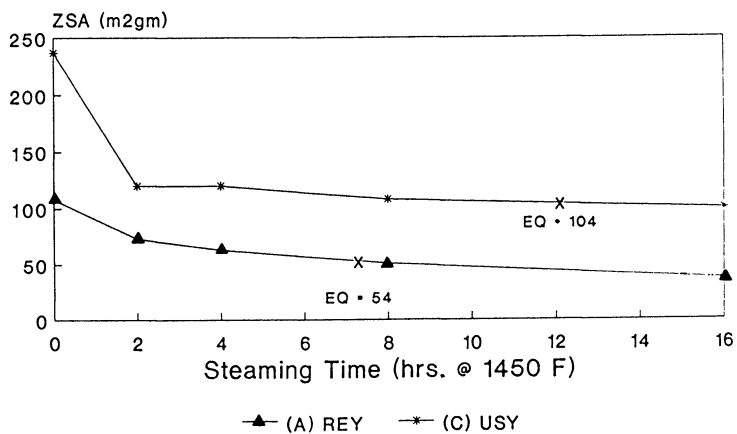


Figure 3. STEAMED CATALYST PROPERTIES Zeolite Surface Area Reduction to EQ Level is Catalyst Dependent.

### MAT TESTING

The microactivity test (MAT) was developed as a means of measuring the relative activities or conversion of FCC catalysts. As illustrated in Figure 4, the MAT unit itself uses small amount of catalyst (less than 10 grams), and small amounts of oil (less than 5 grams) in a heated, fixed bed configuration. The rate of oil injection or delivery time is controlled by the use of a syringe pump. The catalyst/oil (C/O) ratio is defined by the weight of catalyst/weight of oil. The weight hourly space velocity (WHSV) is defined as  $3600/(C/O) \cdot \text{Oil injection time (seconds)}$ . For the ASTM MAT test procedure the conditions are 900°F, 3 C/O, 75 second injection time and 16 WHSV.

Product oil or syncrude is collected in a chilled receiver with light gas collected in a glass receiver usually by the displacement of water. The syncrude and gas are analyzed chromatographically and the percent carbon on the spent catalyst is determined instrumentally. Conversion (weight percent) is defined as 100 minus (weight percent light cycle oil plus heavy cycle oil) on a weight % of feed basis. A kinetic term called activity is expressed as a simple second order rate expression defined as  $\text{conversion}/(100 - \text{conversion})$ .

Like the case for steaming, there are a variety of procedures used for MAT evaluations, none of which follow the current ASTM protocol in all respects. A summary of procedures used within the industry is presented in Table 3. One unique observation for MAT testing is that testing philosophies in Europe tend to be different than the US. In Europe, MAT testing is characterized by short injection times, less than 25 seconds, giving rise to higher space velocities, usually greater than 30 Hr-1.

Like steaming, where we identified various approaches there are an equal number for MAT testing; constant temperature and cat/oil, constant temperature and vary cat/oil. The latter is usually performed by varying the oil weight as opposed to catalyst weight, and may involve either constant or variable space velocity depending upon what injection time is used. If the C/O ratio is varied but the the injection time is fixed, then the space velocity is changed. Alternatively, the injection time can be varied to maintain a constant space velocity. The former approach is probably the most common. Using a severity relationship described by Wollaston, et. al. (4) that relates severity to cat/oil and WHSV, the greatest change in reactor severity is obtained with this methodology.

### Comparison of Steaming/MAT Procedures

The objective of MAT testing in many labs is to compare both activity and selectivity differences between catalysts. Given that a variety of testing approaches are in practice, what effects do these methods have on ranking of catalysts? To answer this question the three catalysts summarized in Table 1 were evaluated using seven different steaming/MAT approaches. Table 4 summarizes the seven methods evaluated. The definitions for cut points in this study are C5-421°F (gasoline), 421-602°F (LCO) and 602°F-plus (bottoms). Dry gas includes H<sub>2</sub>, H<sub>2</sub>S and C1-C<sub>2</sub> hydrocarbons. LPG are the C<sub>3</sub>-C<sub>4</sub>

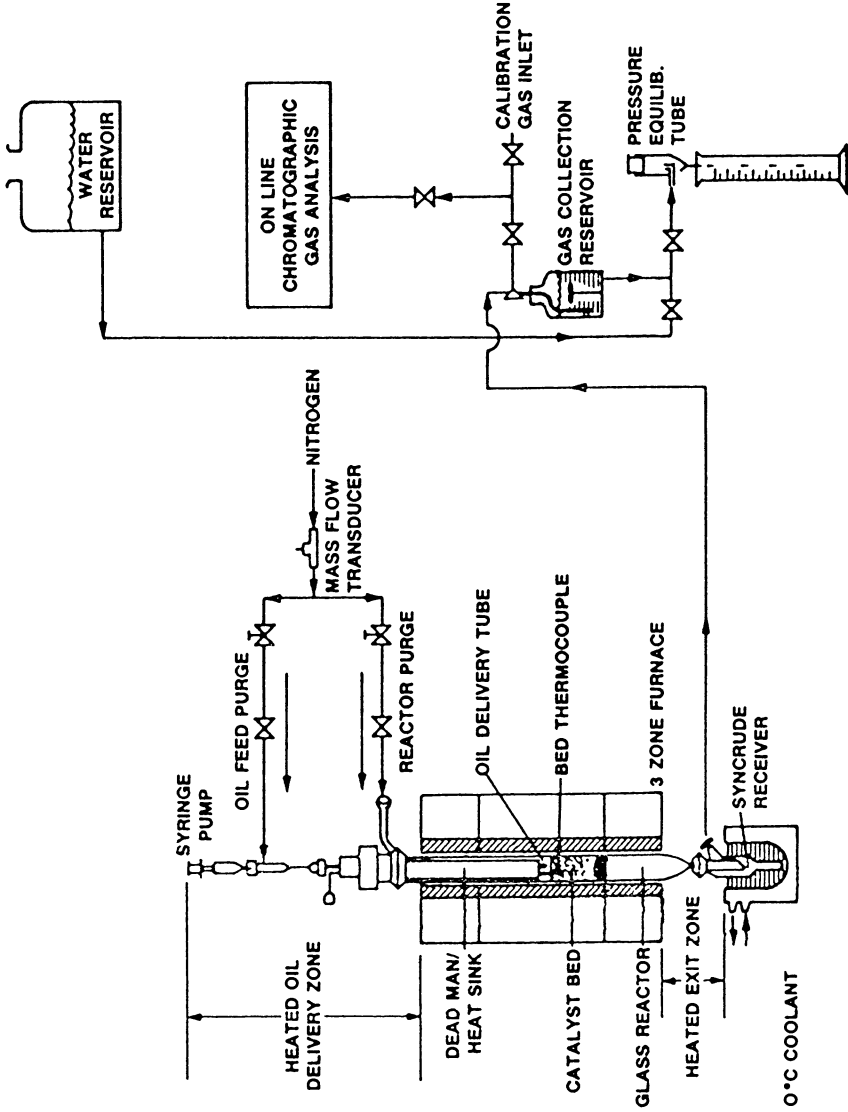


Figure 4. Englehard's MAT Process Flow Scheme.

Table 3  
SUMMARY OF MAT PROCEDURES

	<u>MAT</u> <u>Temperature °F</u>	<u>Cat/Oil Ratio</u>	<u>Delivery</u> <u>Time, Sec.</u>	<u>WHSV Hr-1</u>
ASTIM	850	2	300	6
	900	3.0	75	16
	900	Vary	75	Vary
ENGELHARD	900	2.79	94	13.7
	910	5	48	15
	915	3.0	N/A	17
	925	1.875	75	25
	950	5-9	35	11 to 21
	950	2.5 - 5.5	45 - 75	13.5 - 15.5
	950	4.0	18	50
	950	4.5	40	20
	950 - 1022	4.5	<20	>40 <100
	975	1.5 - 4.5	60	12.8 - 38.5
	985	3.3	75	14.5
	986	6.0	20	30

Table 4  
ALTERNATE STEAMING/MAT APPROACHES

<u>Approach</u>	<u>Steaming °F</u>	<u>MAT °F</u>
1. Engelhard Standard	4 hrs, 1350-1550	910, 15 SV, 5 C/O
2. Low Temp Steaming	1450, 2-16 hrs	"
3. High Temp Steaming	1500, 1-6 hrs	"
4a. Low Actvty High C/O	1500, 4 hrs	910, 15 SV, 5-10 C/O
4b. High Actvty Low C/O	1400, 4 hrs	910, 15 SV, 2-5 C/O
5a. Alternate MAT		
Typical USA	4 hrs, 1350-1500	970, 16 SV, 3 C/O
5b. Alternate MAT		
Typical Europe	4 hrs, 1350-1500	950, 50 SV, 4 C/O

All MATs Used Mid-Continent Gas Oil Feed

hydrocarbons. Comparisons of the various approaches are presented at equivalent conversions of 70 percent.

The results of this study can be presented in a number of different ways but in general we observed the following trends. The observed rankings with respect to gasoline, LPG, and dry gas yields, when compared at 70 percent conversion, were fairly consistent and tracked reasonably well with commercial experience showing that gasoline yield is a function of rare earth content ( $A > B > C$ ) and that LPG and dry gas are inversely related ( $A < B < C$ ). While the absolute yields varied as a function of method, the absolute delta's between catalysts were similar. Figures 5 to 9 summarize the relative yields (70 % conversion) obtained from this study.

Although the rankings are fairly independent of method, it is true that some approaches provide better comparisons than others. For example, the gasoline, LPG and dry gas selectivities obtained with 4B do not differentiate between the REY (catalyst A) and the USY/REY (catalyst B) as well as the other methods. The reason for this is not fully understood but may be related to the relatively mild steaming (1400°F, 4 hours) which does not severely deactivate the catalysts.

The largest variation in catalyst ranking occurred when comparing these catalysts on the basis of coke selectivity (Figure 9). For clarity a high coke selective catalyst is taken to be one that produces a high level of coke per unit of activity. The reciprocal of this is referred to as the dynamic activity (5).

The coke selectivity for catalyst C could be less than or greater than A depending upon the method selected. Based on commercial experience, a USY catalyst like C is expected to produce less coke (higher dynamic activity) than the rare earth catalyst (5,6). This is further supported by the work of Rajagopalan and Peters (7) which related coke selectivity to the unit cell size of the zeolite. Perhaps not surprising is the fact that the test approach that gave the greatest difference in coke selectivity is that which used the lowest C/O's and mildest steaming (4B). This results in the greatest difference in unit cell size and the minimum impact of entrained or C/O coke. The measured UCS for these catalysts were 24.55 A and 24.30 A for catalysts A and C respectively. As seen in Figure 1, the UCS for a USY catalyst equilibrates to a low level under mild conditions but the REY catalyst is more dependent upon steaming severity.

The exact opposite ranking of coke selectivity were obtained by steaming at 1500°F for 4 hours and adjusting C/O to vary conversion (method 4A). Here the UCS for catalysts A and C were 24.36 A and 24.25 A respectively. Based on Rajagopalan (7), the greatest effects of UCS on coke selectivity are observed within the range of 24.33 and 24.57. Given the small difference in UCS for this method evaluation, it is probably not surprising that the coke selectivities are influenced by not only UCS, but perhaps surface area and C/O in the MAT which were increased to achieve the targeted 70 % conversion. Given that the steamed total surface area of catalyst C is two times that of A (162 vs 67 M<sup>2</sup>/G) the observed coke selectivity may be controlled more by the C/O coke as opposed to the catalytic coke.

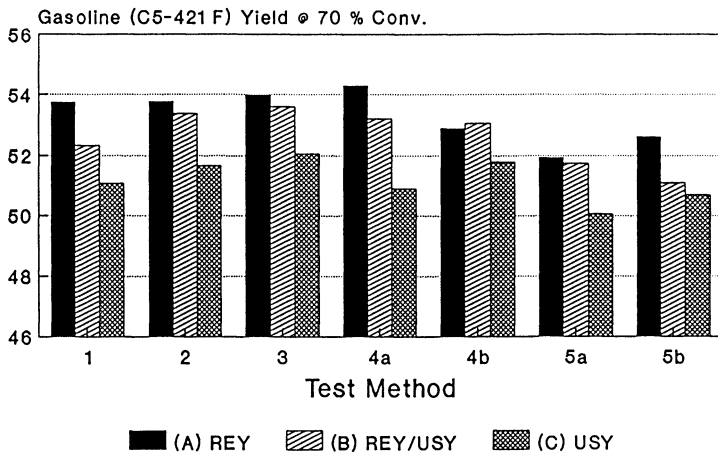


Figure 5. GASOLINE SELECTIVES Consistent Rankings for Most Methods.

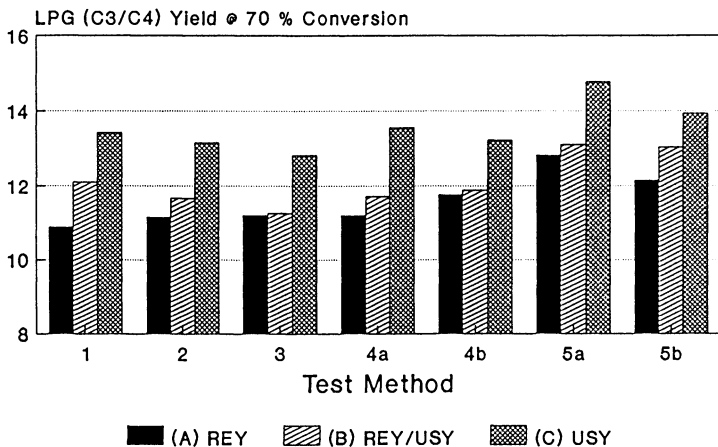


Figure 6. LPG SELECTIVES Consistent Rankings for All Methods.



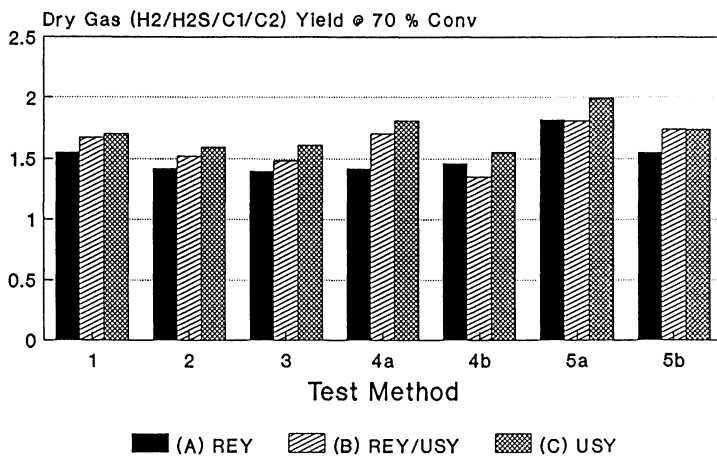


Figure 7. DRY GAS SELECTIVITIES High Cat/Oil (4a) Maximizes Differences.

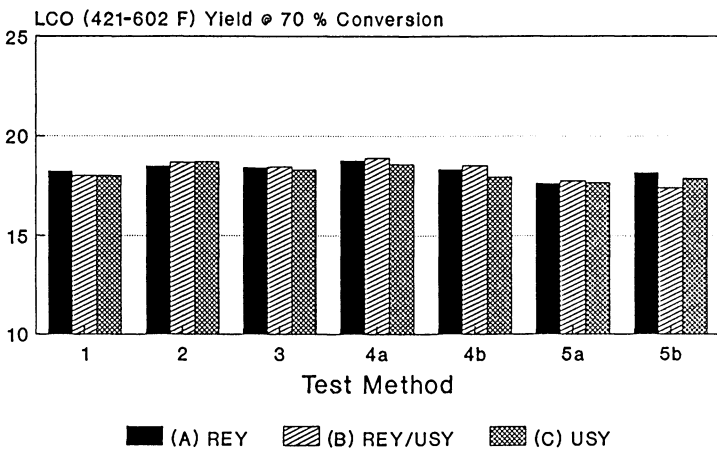


Figure 8. LCO SELECTIVES No Consistent Differences Observed.

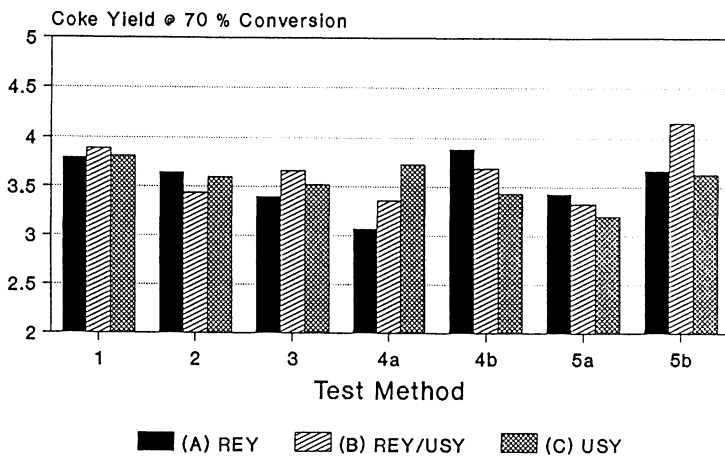


Figure 9. COKE SELECTIVES Rankings are Method Dependent.

Commercial experience shows that the equilibrium activity of a REY catalyst is generally higher than a USY catalyst by up to 10 MAT numbers (6). Table 5 presents comparative selectivity data for catalyst A and C for the case where the activity of A is greater than C. Using this approach, the coke selectivity for C is slightly less than A, as expected from commercial experience. The selectivities for dry gas to bottoms are also in good agreement with commercial experience.

Table 5  
TYPICAL EQUILIBRIUM COMPARISON  
High Activity REY vs. Low Activity USY

<u>Yields @ 70% Conv.</u>	<u>REY</u>	<u>USY</u>
Dry Gas	1.46	1.81
LPG	11.77	13.56
Gasoline	52.89	50.89
LCO	18.34	18.62
Bottoms	11.66	11.38
Coke	3.89	3.73
Catalyst Activity		
Standard MAT	76.9	63.1
Cat/Oil	2.9	7.1

### Conclusions

The results from this study show that the choice of steaming/MAT procedures selected for evaluation of fresh FCC catalyst can effect the observed ranking of catalyst performance. The most method dependent selectivity was found to be the coke yield. In making assessments of the catalytic performance of FCC catalysts it is important that consideration of the steamed catalyst properties as they relate to commercial experience be given high priority.

### Literature Cited

1. Rawlence, D. J.; Gosling, K. Symposium On Catalyst Performance Testing., 1988, p 3.
2. McElhiney, G. Oil and Gas Journal 1988 86, February 8, 35-38.
3. Keyworth, D. A.; Turner, W. J.; Reid, T. A. Oil and Gas Journal 1988 86, March 14, 65-68.
4. Wollaston, E. G.; Halfin, W. J.; Ford, W. D.; D'Souza, G. J. Hydrocarbon Processing, 1975 54 (19), 93.
5. Mott, R. W. Oil and Gas Journal 1987 85, January 26, 73-77.
6. Mauleon, J. L.; Courcelle, J. C. Oil and Gas Journal 1985 83, October 21, 64-70.
7. Rajagopalan, K., Peters, A. W. J. Catalysis 1987 106, 410.
8. Magee, J. S.; Blazek, J. J. Zeolite Chemistry and Catalysis, Rabo J. A. Ed.; ACS Monograph 171 615 1976.

RECEIVED January 26, 1989

## Chapter 13

# A Microscale Simulation Test for Fluid Catalytic Cracking

P. O'Connor and M. B. Hartkamp

Akzo, Chemical Division, Research Centre Amsterdam, P.O. Box 15,  
1000 AA Amsterdam, Netherlands

A microscale Fluid Catalytic Cracking (FCC) simulation test is presented, which results in yields and product properties which correspond very well with commercial FCC results.

Critical parameters to simulate are the ratio of Catalytic to Thermal cracking and the related chemical composition of the gasoline fraction. Obviously, these parameters are particularly important for the research into FCC product properties and, for instance, for the evaluation of potential octane catalysts.

The test conditions for this Microscale Simulation Test (MST) correspond to the low vapor contact times as applied in today's FCC riser technology. An effective feed preheat and feed dispersion is ensured, while the isothermal reactor bed is set to the dominating kinetic temperature in the riser, being approximately the feed catalyst mix temperature. The MST conditions enable the testing of high Conradson Carbon residue feedstocks.

Substantially better FCC forecasts can be made with the MST simulation conditions, making this test a very useful tool for catalyst and feedstock evaluations.

A great need exists for reliable Fluid Catalytic Cracking performance tests which can be used for the evaluation of feedstocks and catalysts.

Notwithstanding the possibility of doing detailed simulations with bench or pilot scale riser reactors, the traditional Micro Activity Test (MAT) remains the main tool for basic FCC research and catalyst and feedstock evaluation and monitoring.

The shortcomings of the existing ASTM-MAT test and possible adaptations to this relatively simple test have been discussed by J.L. Mauleon et. al. (1).

The ASTM-MAT test is in fact only intended to determine and compare the activity of cracking catalysts (2), and is not suitable for simulating the real FCC operation, using the conditions (Table 1) as defined by the ASTM (3).

Several FCC Research groups have made changes to the standard method, resulting in many different test methods (4). For instance, at Akzo Research we introduced the Ketjen-MAT test for the evaluation of production and development samples (5).

The Ketjen MAT test includes a fast preheat, a shorter contact time and a heavier feedstock than the ASTM feed.

Although this test clearly had its advantages, the deviation from actual FCC riser reactor operating conditions still remained too large as illustrated in figure 1;

The Ketjen-MAT conditions seem to simulate a FCC bed reactor, but not a riser reactor.

Especially in view of the need to obtain not only representative FCC yields, but also more detailed information on the product properties (RON, MON, Cetane), an improved simulation of the FCC process is indispensable.

### Testing Strategy

Basically we may distinguish two main lines of FCC testing:

1. Screening,  
whereby the main objective is to discriminate;
2. Forecasting,  
where the priority is to forecast the actual FCC performance.

In the latter case, the need for a correct FCC simulation is evident, however, also for screening purposes it is attractive to start from a firm base of simulation conditions, and then to adapt either the catalyst pretreatment or feedstock in order to enhance the differences in performance.

Using variations in testing conditions for screening remains a viable option; the present ASTM-MAT conditions for instance are such that "Hydrogen Transfer" (De Jong (6)) is strongly amplified.

However, there are a few drawbacks: first of all the link with commercial FCC operation becomes weak, and secondly the frequent switching of test conditions can be detrimental for the availability and the reproducibility of the test.

From the foregoing it becomes clear that the next two points are essential in order to improve microscale FCC testing:

1. Establishing a good FCC simulation.  
In general we are trying to simulate an "average" or a "representative" FCC unit. The test results need to be confronted with commercial data.
2. Adapting catalyst pretreatment or feedstock for screening purposes, while maintaining the link to commercial FCC performance.

In the next section highlights of our work leading to a new FCC Microscale Simulation Test (MST) are presented.

### Establishing a good FCC simulation

The question "What do we want to simulate?" is so complex that we are sure that also our answer is far from complete. The criteria we use for judging the simulations are:

TABLE 1. MAT TEST VS COMMERCIAL OPERATING CONDITIONS

	ASTM	MAT Ketjen	MAT Total *	Commercial FCC
Feed dispersion	no	N2	N2	> 2% St
Preheat	no	fast	fast	fast
Contact time, s				
Catalyst	75	50	5-15	2-10
Vapour	14	4	2-4	0.5-5
WHSV	16	12	40-100	60-200
Catalyst temp, C				
Initial	483	483	510-550	650-750
Mix	?	?	?	540-580
Exit	470-480	470-480	490-530	500-540

Source: Reproduced with permission from ref. 1.  
Copyright 1985 Oil and Gas Journal.

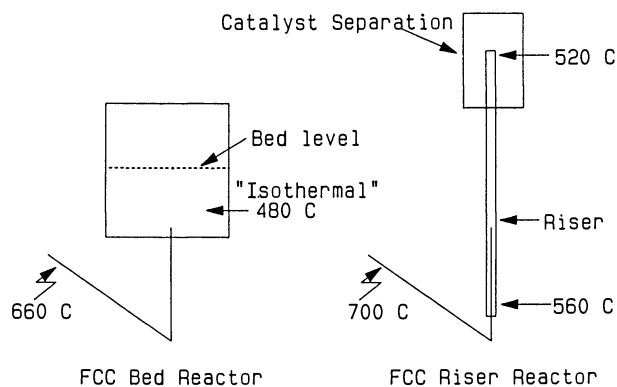


Figure 1. Ketjen MAT simulates FCC bed reactor.

1. Conversion level (C/O selection).
2. Bottoms Conversion.
3. LPG Olefinicity (C=3/C3, C4=C4).
4. Fuel gas-make and the ratio thermal/catalytic cracking (C2-minus/iC4).
5. Gasoline yield.
6. Gasoline composition.
7. Coke make and Delta Coke level.

Using equilibrium catalyst from commercial FCC units, we modified the MAT reactor conditions in order to meet the simulation criteria. This work was complemented with ARCO pilot riser plant tests, exploring the influence of the main process parameters such as residence time, mixing, reactor temperature and temperature profile.

Critical parameters to simulate are the ratio of Catalytic to Thermal cracking and the related chemical composition of the gasoline fraction. These parameters are particularly important for the evaluation of the octane potential of catalysts and feedstocks (7).

Also for the ARCO Pilot Riser this is the case, but by drastically adapting the operating conditions (Table 2) it is possible to achieve the correct FCC gasoline composition.

For microscale testing, accepting the fact that the MAT is nearly an isothermal test, we chose to take the catalyst mix temperature as the operating temperature of our new test.

This follows the approach of J.L. Mauleon et. al. (1), stressing the importance of the mix temperature above that of the riser exit. The ARCO Pilot riser tends to confirm the importance of the mix temperature. In general the mix temperature is 25 to 45 degrees Celsius higher than the riser exit temperature.

Also for a good simulation the contact time of the test has to be reduced. A 15 seconds runtime (2-4 seconds vapor contact time) gives yield breakdowns and trends which correspond very well with the actual FCC data (see example Table 3).

Using the MST test we have been able to simulate various Commercial FCC operations with a test mass balance of 96 to 100%.

An interesting point to note is that the gasoline compositions obtained from the ASTM and Ketjen-MAT deviate significantly from the commercial FCC results.

A too low gasoline olefinicity and a too high degree of branching of the paraffin and olefin compounds is found. The MAT gasoline can be analysed with the "Anderson" GC-method (see (8),(9)). In our case we applied a modified extended method. The commercial and Pilot Riser gasoline were analysed with a detailed GC-PIANO method developed by Akzo Research.

As a simple measure for the Degree of Branching (DOB) of gasoline we make use of the iC6/nC6 ratio. From our GC data base we find that this ratio correlates reasonably well with the overall gasoline branching of the paraffins (iP/P),

$$\text{DOB} = \text{iC6/nC6} \quad (1)$$

The Branching of gasoline olefins, however, does not vary much, notwithstanding the large variations in branching of the gasoline paraffins (Fig. 2).

TABLE 2. ARCO PILOT RISER TEST CONDITIONS

	Standard Riser	Modified (PRT)	Commercial FCC unit
Contact time, s			
Catalyst	25	10	2-10
Regenerator Temp, C	650	700	650-750
Catalyst temp, C			
Initial	520	700	650-750
Mix	520	545	540-580
Exit	520	520	500-540

TABLE 3.  
MST SIMULATION OF FCC UNIT

	FCC	MST
	TRX= 528 C	
CTO	6.9	6
YIELDS, %WT		
FUELGAS	3.5	3.3
LP6	17.3	19.4
GASOLINE	46.4	45.0
LCO	17.6	18.0
BOTTOMS	10.5	10.1
COKE	4.7	4.2
CONVERSION, %wt	71.9	71.9
DELTA COKE	0.68	0.69
C3=/C3	0.79	0.80
C4=/C4	0.60	0.62
RON (GC)	93.4	93.3



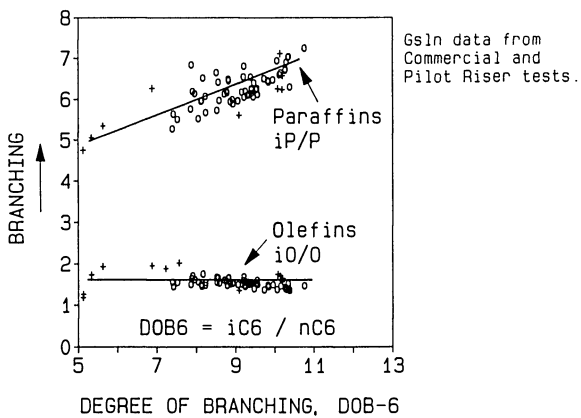


Figure 2. Gasoline Branching and DOB factor.

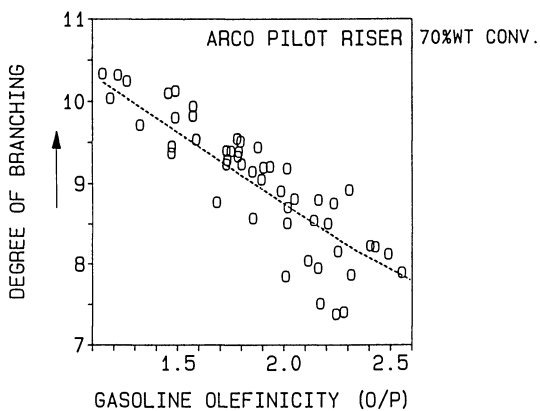


Figure 3. Degree of Branching vs Olefinicity.

Figure 3 shows the strong relation between the DOB and the olefinicity (O/P) of gasoline, which we find based on the GC-PIANO analysis of about 200 Pilot Riser and Commercial FCC gasoline samples in our gasoline database. The difference between RON and MON gains obtained with low hydrogen transfer USY catalysts, as illustrated in figure 4, can be explained with this phenomenon (7).

Figure 5 demonstrates how the correct gasoline composition can be obtained by setting the MST temperature at the level of the reactor riser feed catalyst mix temperature.

Based on the foregoing we introduced the new Micro Simulation Test (MST) in our catalyst research, in early 1987. Standardized test conditions aiming at an "average" FCC unit are given in Table 4. Obviously for an optimized simulation the MST temperature profiles deviate very significantly from the "average" FCC.

One of the prime advantages of the new test is that it enables us to make substantially better forecasts in terms of product properties, because of the congruent link of MST, ARCO Pilot riser (PRT) and the commercial FCC riser operation; i.e. octane predictions see figure 6.

Also because of the high temperature it is possible to process high Conradson Carbon containing residue feedstocks. At present we have gone up about 8% wt CCR in the total feedstock.

#### Some remarks on FCC kinetics

The results obtained in our search for optimal simulation conditions can also be interpreted in terms of the effect of reactor conditions on the cracking kinetics.

For instance the formation of aromatics in the gasoline fraction increases significantly with the reactor temperature, while the rate of aromatics formation remains relatively constant, see figure 7.

This seems to indicate that mono-aromatics shifting from the feed to the gasoline range due to shattering of large molecules can be enhanced by higher reactor bottom temperatures.

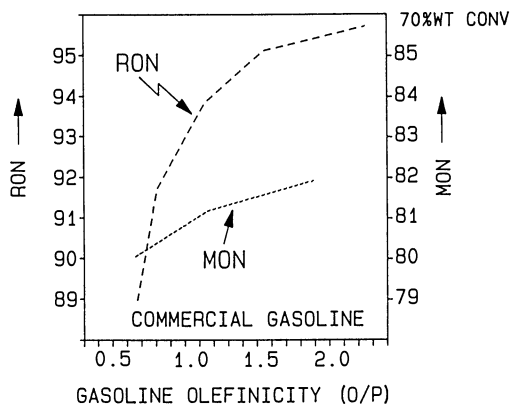


Figure 4. Gasoline vs Olefinicity.

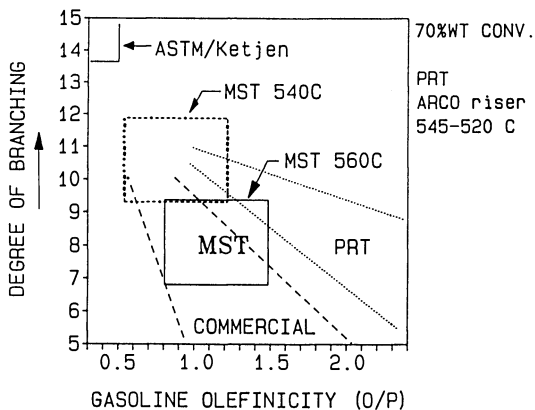


Figure 5. MST Gasoline Composition.

TABLE 4. MST - Microscale Simulation Test Conditions

	PRT Riser	MST	Commercial FCC
Feed dispersion	N2	N2	> 2% St
Preheat	fast	fast	fast
Contact time, s			
Catalyst	10	15	2-10
Vapour	1-5	1-4	0.5-5
Catalyst temp, C			
Initial	700	560	650-750
Mix	545	550-560	540-580
Exit	520	550-560	500-540

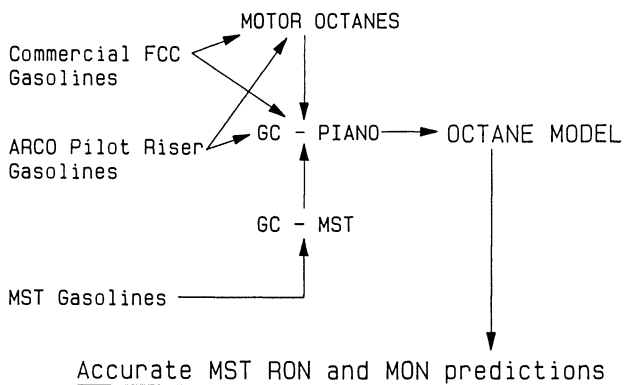


Figure 6. MST RON and MON predictions.

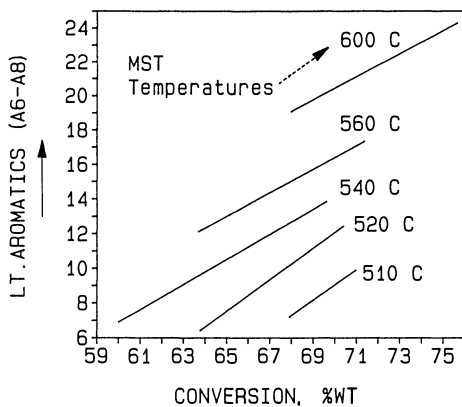


Figure 7. Aromatics in FCC gasoline.

Demar et.al. (10) stress the need for such a thermal shock in order to convert the asphaltenes present in the feed.

On the other hand, the above may also mean that the initial thermal dehydrogenation of naphthenic compounds in FCC feed is a step which determines the quantity of hydrocarbons which can be converted to aromatics by hydrogen transfer.

#### Literature cited

1. Mauleon, J.L. and Courcelle, J.C.; OGJ , Oct. 21, 1985, p 64-70.
2. Shankland, R.V. and Schmitkons; Proc. API 27 (III), 1947.
3. ASTM D-3907-86; Method for testing FCC catalysts by micro-activity test.
4. Parker, G.A. Ashton, A.G. van Catrer, G.D.L.; Katalistiks' FCC Symposium 1987, June 1987.
5. Ketjen Test Method - MAT.
6. De Jong, J.I.; Ketjen Catalyst Symposium '86, May 1986.
7. O'Connor, P; 2nd Ketjen South American Catalyst Seminar, October 1987.
8. Anderson, P.C.; Sharkey, J.M.; Walsh, R.P.; J. Inst. of Petrol. 58, (1972), p 83-93.
9. Conkright, W.A.M.; Butler, M.M. and Harter, D.A.; Ketjen Catalyst Symposium '86, May 1986.
10. Demar, M.; Triki, A; van Franck, J.P.; OGJ, Sept. 15, 1988, p 95-99.

#### APPENDIX

##### Description of the MST test

By means of a syringe pump 1 gram of feedstock is charged over the catalyst which is placed in the reactor in the furnace. The catalyst is placed in the reactor in an annular bed with an internal diameter of 9 mm and an outer diameter of 14 mm. The center of the bed is filled with a stainless steel preheater. The shape of the bed prevents a temperature drop over the catalyst bed diameter. It also increases the surface of catalyst contacting the wall, which helps to prevent the catalyst from dropping out of the reactor.

After 15 seconds feeding time the catalyst is stripped with nitrogen for 15 minutes. The liquid product is collected in a glass product receiver that is cooled with a mixture of dry-ice and acetone for the first 50 seconds. After that the mixture is replaced by ice and water. The gaseous product flows through the receiver to the gas collection bottle where it is collected over water together with the stripping nitrogen.

A gas sample is taken by refilling the gas collection bottle with water and leading the gas that is displaced by the water through the gas sample tube.

Analysis of gases, liquid product and coke on catalysts permit the calculation of conversion and product selectivity.

Process flow schemes of the MST and Pilot Riser Tests are given in figures 8 and 9.

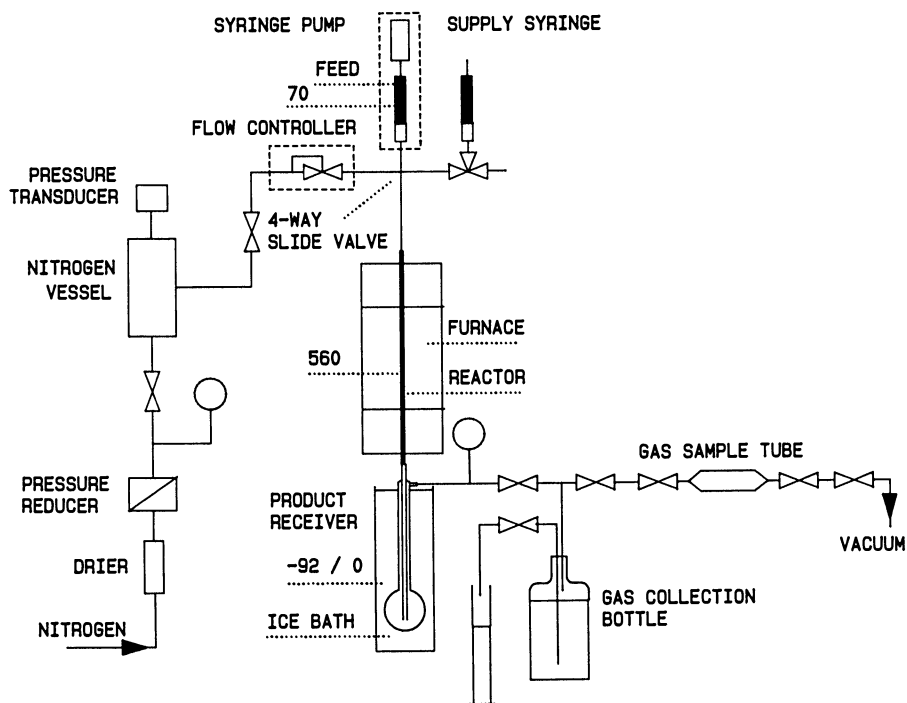


Figure 8. Flowscheme for MST.

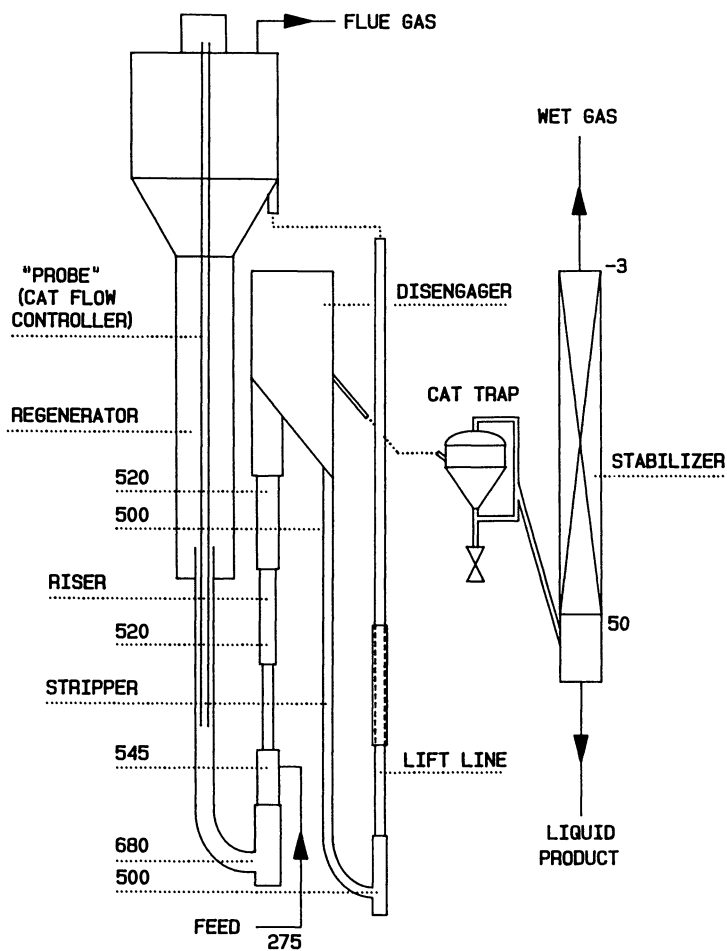


Figure 9. Flowscheme for pilot riser.

Test conditions

Reactor temperature	: 560°C
Feeding time	: 15 seconds
Prepumping time	: 10 seconds (needed for a constant oil flow)
Feedrate	: 0.0667 gram/sec.
Catalyst weight	: 3-7 grams
c/o	: 3-7
Feedstock	: Kuwait VGO
Analyticals:	
Sulphur, % wt	: 2.93
Total Nitrogen ppm wt	: 908
Viscosity, CST, 50°C	: 45.1
Density (19°C), kg/m <sup>3</sup>	: 930-935
Conradson Carbon, wt%	: 0.6-0.7
Boiling range D-1160:	
IBP, °C	: 370
10 vol %	: 391
30 vol %	: 421
50 vol %	: 451
70 vol %	: 486
90 vol %	: 527
FBP vol %	: 562

RECEIVED January 26, 1989



## Chapter 14

# Improved Regeneration Quality with Length and Density Grading

J. D. Seamans, J. G. Welch, and C. A. Vuitel

Catalyst Recovery, Inc., Baltimore, MD 21215

Primarily used as a post-regeneration treatment, the physical separation of reusable hydropressing catalysts from spent commercial material has been demonstrated using proprietary length and density grading (LDG) techniques developed by Catalyst Recovery, Inc. Length grading of catalyst extrudates provided a substantial improvement in the average length of recovered catalyst when compared to conventional screening. Density grading of spent catalysts has been shown to segregate catalyst particles based on their relative particle densities. Since the level of contaminants (e.g. V, Si, or C) can vary considerably through a catalyst bed, density grading has been used to recover the lighter (and more active) fraction for reuse. In cases where different catalysts become mixed, density differences have been used to recover the individual catalysts for reuse.

In the management of spent catalyst, the refiner must decide if recovery and reuse is a viable option to consider. Oxyregeneration to remove carbon and sulfur deposits and restore activity is commonly practiced for a wide range of hydropressing catalysts. A considerable amount of spent material has not been considered for regeneration and reuse, because it contained high levels of broken or metals contaminated particles, or, because of commingling of two or more different types of catalyst. Until recently, no physical separation techniques were commercially available to the refiner for the recovery of good quality catalyst which has been intermixed with poorer quality material.

### LDG

LDG, which stands for LENGTH AND DENSITY GRADING, is a new development in the management of spent catalysts. The objective of this new technology developed by Catalyst Recovery, Inc. is to pick out reusable catalyst particles from undesirable catalyst particles. The ability to efficiently segregate individual catalyst particles

in this manner has been shown to dramatically reduce the amount of catalyst relegated to disposal or reclamation.

Every month millions of pounds of catalyst are removed from reactors and designated as not suitable for regeneration and reuse because on an average they are too short or too highly contaminated for reuse to be practical or economical. The key phrase is on an average. In most cases the spent catalyst contains a distribution of lengths and/or a range of contaminant level. Consequently, it is common to find that a sizable portion of the spent material would be attractive for reuse if it could be gleaned from the mixture. The following data illustrate a few of the extraordinary results obtained from applying LDG to commercial situations.

### Length Grading

LDG is actually two separate techniques. As it's name indicates, Length Grading is a method of separating longer particles from shorter ones. Conventional screening can only remove fines and pellets with a length less than the catalyst diameter. Oftentimes the remaining material still does not meet length specifications. Length grading can selectively reject short catalyst particles with lengths two or three times the diameter and recover only the best catalyst particles for reuse. This is particularly beneficial for reactors which are pressure drop sensitive.

The ability of this technology to segregate catalyst at any desired length was demonstrated in a test performed on 1/32 inch diameter extruded catalyst. The spent catalyst was stripped of oil and then length graded into three fractions: a short fraction of less than 1.5 mm in length, a mid-range fraction between 1.5 mm and 3.5 mm, and the longest material in the greater than 3.5 mm fraction. Table 1 and Figures 1 through 4 illustrate the effectiveness of this process in separating catalyst by its length regardless of its diameter. The spread in average lengths for the three fractions (1.2 mm for the short, 2.3 for the mid-range, and 3.6 mm for the long) emphasizes the superiority of length grading over screening. The separation at 3.5 mm represents a length fraction which is more than four times the diameter of this catalyst.

Although Length Grading is capable of segregating catalyst at lengths of three or four times the particle diameter, it is generally not necessary to do so. Usually the objective of length grading is to remove particles with lengths that are less than two times the particle diameter and to raise the average length of the material being considered for reuse. Table 2 summarizes the results from length grading a regenerated 1/10 inch catalyst. About 22% of the catalyst was rejected as short pieces and the average length was increased from 3.3 mm to 4.3 mm on the recovered catalyst.

A simple example of how this technology can be applied was provided by a refiner who overloaded a hydrotreating unit with fresh Co/Mo catalyst. The excess was vacuumed out of the unit and, in doing so, was very badly broken. The refiner was very reluctant to use the catalyst in any of its hydrotreaters because of the high risk of pressure drop and plugging problems. The material remained in storage for over two years until CRI offered the service of length grading. Conventional screening followed by length grading

Table 1. Length grading

Stripped Catalyst (1/32 in.) (0.8mm)		
Catalyst	Yield	Average Length
	%w	mm
Feed	—	2.3
<1.5mm	16	1.2
1.5-3.5mm	71	2.3
> 3.5mm	13	3.6

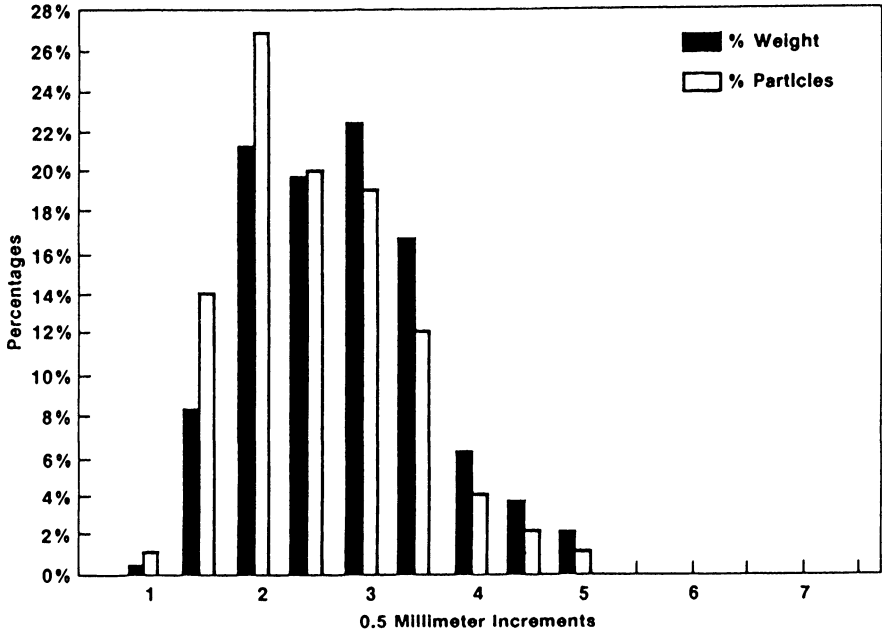


Figure 1. Stripped catalyst--ungraded.

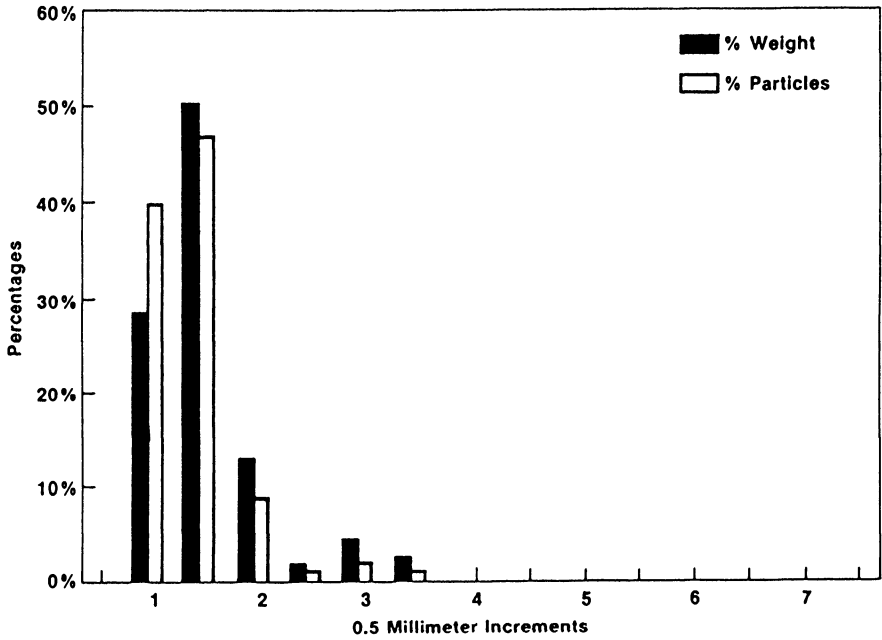


Figure 2. Stripped catalyst; <1.5 mm fraction--15.9% vol.

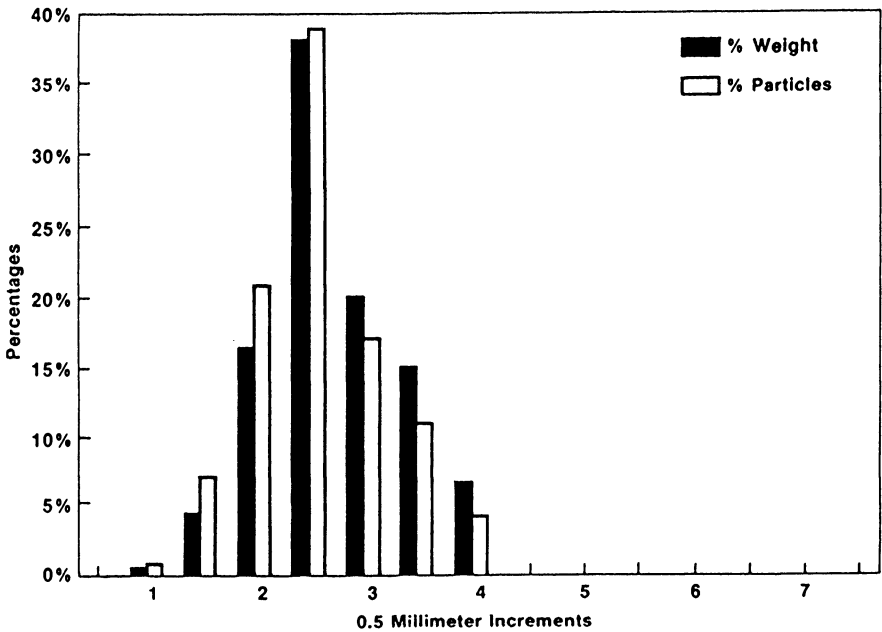


Figure 3. Stripped catalyst; 1.5-3.5 mm fraction--71.2% vol.

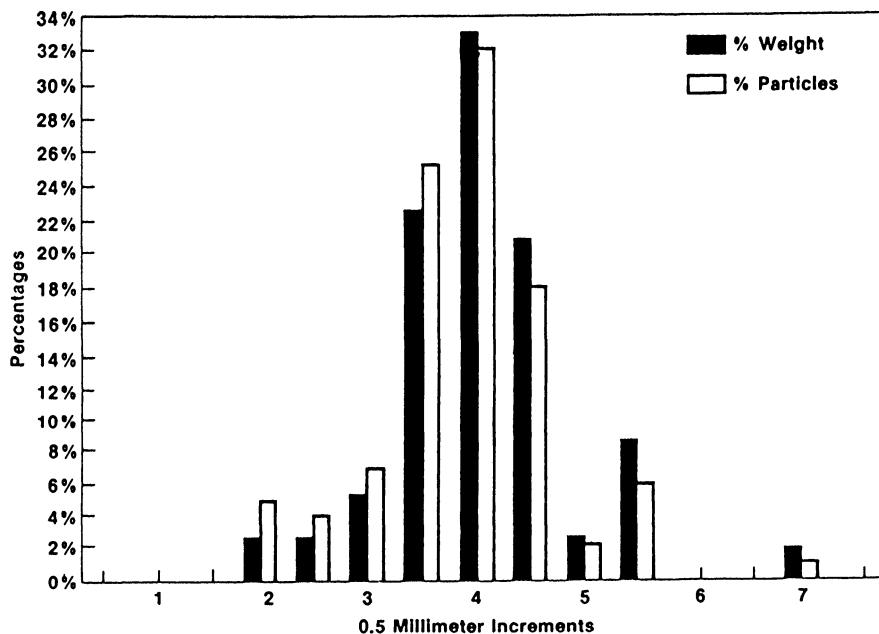


Figure 4. Stripped catalyst; >3.5 mm fraction--12.9% vol.

Table 2. Length grading

Regenerated Catalyst (1/10 in.) (2.5mm)			
Catalyst	Yield %w	Avg Length mm	<3.0mm %w
Feed	—	3.3	35
Longs	78	4.3	9
Shorts	22	2.4	90

resulted in the three products listed in Table 3. The fines and short particles were sent to reclamation. The long particles, which now had a much higher average length, were returned to the refiner for use in the hydrotreater.

Without length grading, the refiner was planning to ship all of the material to reclamation. Application of LDG provided an economical way to recover a high quality product as well as reduce the amount of waste catalyst.

Length grading is also gaining interest in reactor turnarounds. This may be performed in combination with off-site regeneration of as an alternative to screening in the typical dump, screen and reload procedure. Length grading can be applied to fresh, regenerated or ever spent catalysts as long as the material is free flowing.

#### Density Grading

Density grading is a technique by which catalyst particles are segregated based on their individual densities. This process is most often performed following length grading since the effectiveness of density grading is enhanced if the particles are of fairly uniform size.

Density grading is flexible in that it can be applied to any size or shape catalyst particle. The number of fractions produced and the weight percent of each can be adjusted to meet the refiners' needs. A typical commercial separation produces three fractions. These are a heavy (or high particle density) cut, a light (or low particle density) cut, and a medium or mixed fraction which may be recycled to the density grader for resplitting.

A wide range of opportunities for regeneration and/or recovering reusable catalysts have been identified. These include the following sources of contaminated catalyst:

- \*Fixed bed heavy oil processing units which have a gradient of vanadium and nickel contamination from top to bottom in the reactor.
- \*Ebullated bed resid units with broad distribution of catalyst age and contaminant level.
- \*Regeneration of Catalytic reforming units which includes some catalyst with high levels of residual graphitic carbon levels and high density "collapsed" particles.
- \*Coker naphtha hydrotreating units with a range of silica contamination.

In addition, density grading has been shown to be very effective in separation of catalyst mixtures to enhance regeneration quality and possibility.

- \*Hydrocracking and Hydrotreating catalyst mixtures from hydrocracker post treat beds.
- \*Mixtures of Ni/Mo and Co/Mo or Ni/W catalysts from stacked bed hydrotreaters.
- \*Active and inert bed support mixtures.

LDG segregation of catalyst by vanadium level has been studied extensively. A test performed on a nickel-molybdenum catalyst is summarized in Table 4. In this test case the vanadium level on the lightest fraction was less than a third of that on the heaviest fraction. Surface area and compacted bulk density correlated with the level of vanadium contamination. Most importantly, it was shown

Table 3. Length graded

Fresh 1/16 Inch Cobalt/Moly				
Product	Yield	Particle Size Range	Average Length	Disposition
	w%	mm	mm	
Fines	36	<1.4		Reclamation
Short Particles	23	1.2 to 2.2	1.8	Reclamation
Long Particles	41	2.0 to 4.5	2.9	Reuse

\*Catalyst Was Damaged When Excess Material Was Vacuumed From Overloaded Reactor.

Table 4. Density grading

1/25 Inch Nickel/Moly					
Catalyst	Yield	CBD	S.A.	V	RVA*
	%v	Lbs/Cu Ft	m <sup>2</sup> /g	%w	%
Fresh	—	36	330	0	100
Composite	—	53	232	9.0	74
Light	28	44	293	4.7	84
Med-Light	36	48	269	7.2	76
Med-Heavy	16	52	233	10.0	69
Heavy	20	66	125	14.7	51

\*Relative Volume HDS Activity As Compared to the Fresh Nickel/Molybdenum Catalyst.

that the light and medium-light fractions had acceptable hydrodesulfurization activity once the medium-heavy and heavy fractions were removed.

Consultation with the refiner led to the conclusion that between 1/3 and 2/3 of the spent material generated from this source could be reused before being sent to reclamation.

A second example of the potential of LDG for recovering reusable catalyst from low-grade mixtures is presented in Table 5. In this case, the primary contaminant was silica. A test application of LDG to this spent catalyst generated three product fractions with very different silica levels and desulfurization activity. Test results were then used to determine the optimum cut point to recover the most valuable catalyst and reject only the most heavily contaminated material.

Exceptional results were obtained in a test on naphtha reformer catalyst which utilized a continuous catalyst regeneration section. In this type of service, it is possible for a graphitic carbon deposit to build up over a period of time. This form of carbon does not regenerate easily. When it does burn, the localized high temperatures generated can collapse the catalyst structure resulting in a low surface area inactive pellet.

As presented in Table 6, LDG recovered 85% of the material as high quality material with a carbon level of only 0.1%. The heavy fraction contained the collapsed pellets plus the difficult-to-regenerate particles with an average residual carbon of 11%.

As mentioned earlier, LDG can also be used to segregate mixtures of different types of catalyst. Table 7 summarizes an LDG separation performed on a mixture of 1/16" spent Ni/W hydrocracking

Table 5. Density grading  
1/16 Inch Cobalt/Moly (1.6mm)

<b>As Received</b>				
Carbon, w%	3.6			
Sulfur, w%	5.5			
<b>Regenerated/Density Graded</b>				
	<u>Composite</u>	<u>Heavy</u>	<u>Medium</u>	<u>Light</u>
w% of Composite		18.4	53.6	28.0
CBD, g/cc	0.87	0.94	0.87	0.82
C, w%	0.07	0.06	0.07	0.09
S, w%	1.3	1.1	1.3	1.4
SA, m <sup>2</sup> /g	155	140	156	162
PV, cc/g	0.41	0.33	0.42	0.43
Co, w%	2.2	2.1	2.2	2.1
Mo	9	9	9	9
Contaminant Si	3.2	5.8	3.4	1.0
RVA, %*	75	67	77	85

\*Relative Volume HDS Activity As Compared to the Fresh Cobalt/Molybdenum Catalyst.



Table 6. Regenerated naphtha reforming catalyst

<u>Fraction</u>	<u>LDG Products</u>		
	<u>Yield</u> w%	<u>Carbon</u> w%	<u>Sulfur</u> w%
Light	85	0.1	0.2
Heavy* (>1.4mm)	12	11	0.2
Heavy* (<1.4mm)	3	0.04	0.02

\*The Heavy Product Was Screened at 1.4mm to Separate the Collapsed High Density Catalyst From the Carbon-Contaminated Catalyst.

Table 7. Hydrocracking/hydrotreating catalyst mixture

<u>Fraction</u>	<u>LDG Products</u>		
	<u>Yield</u> w%	<u>Surface</u> <u>Area</u> m <sup>2</sup> /g	<u>Description</u>
Light	20	165	85% HT Catalyst for Reclamation
Medium	25	200	Mix of HT and HC for LDG Recycling
Heavy	55	240	98% HC Catalyst for Reuse

and Co/Mo hydrotreating catalysts. The source of the material was a mild hydrocracker. The refiner considered the high value hydrocracking catalysts as having excellent reuse potential. The presence of the deactivated hydrotreating catalyst, however, thwarted its reuse. Reclamation of the spent Co Mo hydrotreating catalyst was also hindered by the presence of the nickel-tungsten hydrocracking catalyst since metal reclaimers have low tolerance limits for tungsten in their recovery processes.

This type of separation is very economically attractive to the refiner since it enables regeneration and reuse of the high value material and facilitates reclamation of the spent catalyst.

Clearly the preferred choice in the management of spent catalyst is to recover all of the catalyst which is still active enough for reuse. Several examples have been described in this paper in which spent material was considered unsuitable for reuse because, on an average, the mixture was too short or too highly contaminated. The LDG technology developed by Catalyst Recovery, Inc. has been shown to be a powerful tool for recovering high quality catalyst from poorer material and thereby increasing the yield of reusable catalyst and minimizing catalyst waste.

Reference:

1. Welch, J. G. and Ellingham, R. E., 1988 U. S. Patent No. 4,720,473, Production of Improved Catalyst-Type Particles Using Length and Density Grading.

RECEIVED June 20, 1989

## Chapter 15

# Statistical Models of Transport and Reaction in Porous Media and Their Applications in Catalysis

Muhammad Sahimi and Theodore T. Tsotsis

Department of Chemical Engineering, University of Southern California,  
Los Angeles, CA 90089-1211

Most industrial catalysts have a complex, tortuous porous structure. In the past, transport and reaction in such catalysts were described by continuum-type diffusion-reaction models utilizing effective transport and reaction constants and ad hoc parameters such as the tortuosity factor. In recent years it has become clear that such modeling approaches are often inadequate and in many instances lead to qualitatively wrong conclusions. This has prompted the development of a new class of models based on a statistical description of the catalyst's pore structure and on microscopic modeling of the transport and reaction processes at the single pore level. Only one class of such statistical models are discussed here, namely, those describing transport and reaction in reactive porous media, which are simultaneously undergoing morphological changes due to the reaction processes themselves. The best known such models are these which describe catalyst deactivation due to active site coverage and pore blockage. Many other phenomena and processes in catalysis are also amenable to such a theoretical description. These include the impregnation of porous supports by catalytically active metals and loss of

catalytic activity due to sintering, attrition and break-up of catalyst particles due to thermal and mechanical factors and irreversible sorption of organic macromolecules in catalysts with restricted porous structures (i.e., zeolites and pillared clays). A close relationship and analogy also exists between statistical models of transport and reaction in porous catalysts and the more general models describing fluid-solid reactive systems. The similarities and differences between these models are discussed in this paper.

Many phenomena and operations of engineering interest involve physicochemical interaction of a fluid with the solid surface of a porous medium. A number of such processes are furthermore characterized by a continuous alteration of the pore structure by virtue of physical and/or chemical changes brought upon the solid and its pore structure by the contacting fluid (1). In catalysis such processes include (the list is by no means exhaustive) catalyst deactivation due to active site coverage by poisons and pore blockage due to deposition of coke (2,3), irreversible chemisorption of organic macromolecules in catalysts with pore sizes of dimensions comparable with the adsorbing molecules (the best known example being sorption of hydrocarbons in zeolites and pillared clays (4)), porous support impregnation by metals and loss in activity due to sintering (5), and attrition and catalyst fragmentation due to thermal and mechanical causes. Best known examples from other scientific and engineering disciplines include particle deposition in deep-bed filtration (6) and fines migration in porous reservoirs (7-9), noncatalytic gas-solid reactions (10-15) and acid rock dissolution (16-18).

In catalytic systems morphological changes of the pore structure, brought upon by the reaction and sorption processes, typically result in a reduction of the available pore volume. In some instances the internal pore structure is eventually blocked and becomes completely inaccessible to transport and/or reaction. In the field of noncatalytic fluid-solid reactions and acid rock dissolution, on the other hand, the chemical reaction consumes the solid matrix of the porous medium leading eventually to fragmentation and

in some instances to total consumption of the reactive solid. Individual examples exist, however, in both fields, which do not necessarily fit the above general description. The pore plugging phenomenon, for example, also occurs in noncatalytic gas-solid reactions, when the molal volume of the solid product is larger than that of the solid reactant, as in the case of calcined limestone sulphation (19,20). In catalysis many reactions involving corrosive reactants such as HCl, HF, Cl<sub>2</sub> and O<sub>2</sub> are often accompanied by chemical dissolution of the porous solid support, which also results in pore volume enlargement, attrition and fragmentation of the porous catalyst. Models of noncatalytic fluid-solid reaction systems are of direct relevance in this case.

Catalysts like zeolites and pillared clays are generally characterized by very regular and well-defined porous structures. On the other hand, the great majority of industrial catalytic supports have very complex, tortuous and interconnected porous structures and clearly belong to the more general class of disordered porous media. Such porous media are typically characterized by several length scales and the associated inhomogeneities. Experimentally measured properties, such as effective transport coefficients of catalyst pellets are typically pellet-volume averages of local (point) transport coefficients. Unfortunately, for disordered porous media the definition of a local or point transport coefficient (or a reaction rate for that matter) is not always very clear. Such local quantities are in general, also themselves volume averages (over a local volume V) of the corresponding microscopic properties. Such a local volume V must, of course, be much smaller than the particle volume itself for the transport property to qualify as local but large enough for the transport equations to hold, when applied to that volume. Excellent discussions about volume averaging techniques as they apply to problems of transport and reaction in catalytic and noncatalytic porous media can be found in the papers by Whitaker (21,22). An alternative approach to the volume averaging technique is afforded by statistical methods.

Two different approaches have emerged in the statistical modeling of catalytic and noncatalytic reactive porous media. In the first approach, which is an integrated macroscopic-microscopic method, one uses

continuum transport and reaction field equations to describe the behavior of catalyst particles. One utilizes a microscopic statistical description of the porous structure, however, in order to develop formulas which predict the local effective (local volume averaged) transport and reaction coefficients. In the second approach, one utilizes a complete microscopic statistical description of both the catalyst's pore structure as well as the transport and catalytic reaction events occurring. The former approach is by far the most commonly utilized in the field of catalysis and in the modeling of noncatalytic fluid-solid reaction systems. The reasons for this should, of course, be obvious since the integrated macroscopic-microscopic statistical modeling approach does not represent as drastic of a philosophical departure (as are the completely microscopic statistical models) from the old macroscopic models using ad hoc effective transport properties. This modeling approach suffers from a major weakness, however, which is the result of the fundamental assumption of the model that the macroscopic continuous field equations do apply in the description of transport and reaction in disordered porous media. This is not always true for all problems. Catalyst deactivation due to site coverage and pore blockage, an example with which we deal more extensively in this paper, is one of those cases for which the applicability of macroscopic continuum equations of transport and reaction is questionable (1), especially near the point of complete macroscopic blockage of the porous structure (percolation threshold). Further discussion of these issues can be found elsewhere (1).

In what follows we review a number of technical questions and issues involved in the statistical modeling of catalytically-reactive porous media. We use catalyst deactivation as an example, in order to address some of these issues, because catalyst deactivation has received the greatest attention so far in the field of statistical modeling of chemically reactive porous media. Work is currently in progress in several laboratories on modeling, by statistical techniques, of a number of other catalytic processes such as sorption and transport in zeolites and pillared clays (4), catalyst impregnation, sintering and mechanical and thermal degradation and attrition of porous catalytic supports (5). Due to space

limitations we will not discuss any of these processes here. We would like to direct our readers, however, to one of our recent papers (1) in which the general subject of statistical modeling of reactive porous media is reviewed in great detail.

### STATISTICAL MODELING OF CATALYST DEACTIVATION

As mentioned above, an area in which the concepts and techniques of statistical physics of disordered media have found useful application is the phenomenon of catalyst deactivation. Deactivation is typically caused by a chemical species, which adsorbs on and poisons the catalyst's surface and frequently blocks its porous structure. One finds that often reactants, products and reaction intermediates, as well as various reactant stream impurities, also serve as poisons and/or poison precursors. In addition to the above mode of deactivation, usually called chemical deactivation (23), catalyst particles also deactivate due to thermal and mechanical causes. Thermal deactivation (sintering), in particular, and particle attrition and break-up due to thermal and mechanical causes, are amenable to modeling using the concepts of statistical physics of disordered media, but as already mentioned above the subject will not be dealt with in this paper.

In modeling catalyst deactivation, one has to deal with a catalyst particle which often has a tortuous porous structure. Moreover, the pore space of the catalyst changes during the deactivation process, and the pore volume always decreases with process time (24,25). It is, of course, such morphological changes that have made modeling of fluid-solid reactions and catalyst deactivation a difficult task, one that up to recently defied meaningful modeling. Because of its industrial significance, numerous theoretical and experimental investigations have so far been devoted to the study of catalyst deactivation and a comprehensive review exceeds the scope of this paper. A number of excellent general review papers exist for in an in-depth study of the subject (24-28).

Early efforts to model catalyst deactivation either utilized simplified models of the catalyst's porous structure, such as a bundle of nonintersecting parallel pores, or pseudo-homogeneous descriptions in terms of effective diffusivities and tortuosity

factors. Both modeling approaches have a number of serious shortcomings. The bundle of pores models account for the geometry (pore size distribution) of a porous medium, but fail to describe its topology (connectedness). Failure to account for the catalyst's topology often results in serious errors and wrong conclusions, as is discussed below. On the other hand, the pseudo-homogeneous models using macroscopic continuum diffusion-reaction equations appear to bypass the need for a description of the catalyst's pore structure and have, through the years, been favored by most working in the area. They require, however, a prior knowledge of diffusivity, tortuosity factor and surface area, parameters which depend on the history of the porespace. The best one can hope for is empirical formulas. The tortuosity factor, in particular, is an ad hoc parameter, the sole purpose of which is to make the predictions of the empirical formulas agree with data. As such it not only depends on the porespace and its history, but also on the molecular size of reactants and products and on conversion. As mentioned in the introduction, a number of other problems are associated with the use of macroscopic continuum differential equations to describe transport and reaction in disordered porous media and, in particular, catalyst deactivation. Near the percolation threshold, i.e., the point at which the catalyst particle loses its global connectivity, the correlation length  $\xi$ , (the length scale over which the pore space of the catalyst is macroscopically homogeneous) is large, and the system is not homogeneous on any length scale  $L$  smaller than  $\xi$ . Then, catalyst deactivation does not admit a continuum-type description for  $L < \xi$ . Even away from the percolation threshold, however, one should exercise care in the proper formulation and use of differential equations. The common practice of separating transport and reaction steps is wrong, when one deals with surface reactions characterized by fast and slow steps and mobile bulk and surface reactants, products and intermediates, and results in diffusivities and reaction constants which are concentration (conversion) dependent (for further discussion see (29)).

Some of the earliest statistical models of catalyst deactivation were developed by Froment and co-workers (30-35). Their models represent a distinct improvement over the bundle of tubes and pseudo-



homogeneous models, and have since stimulated additional interest in statistical modeling of catalyst deactivation. These models were developed to describe catalyst deactivation due to coking, but are also general enough to describe catalyst deactivation by site coverage and pore blockage due to deposits other than coke, such as metals, typical of catalyst deactivation during hydrodemetallation. We will review here some of the most important aspects of these models that have played an important role in the thinking and development of subsequent statistical models of catalyst deactivation.

For a reaction of the form  $A \rightarrow B$  one defines the rate of the reaction as

$$r_A = r_A^0 \phi_A, \quad 0 \leq \phi_A \leq 1 \quad (1)$$

where  $r_A$  is the rate at  $t=0$  (before deactivation has commenced) and  $\phi_A$  accounts for the decline in activity due to deactivation.  $r_A^0$  is typically expressed as

$$r_A^0 = k_A C_t^{n_A} f(C_A, C_B, K_A, K_B) \quad (2)$$

with  $k_A$  the reaction constant,  $C_t$  the total concentration of active sites,  $n_A$  the number of adjacent surface sites participating in the reaction and  $f$  the reaction rate expression, which includes various rate and thermodynamic equilibrium constants. The poisoning of active sites also deactivates the deactivating reaction rate  $r_c$  and one writes an expression similar to (1) for the deactivation rate  $r_c$ , i.e.,

$$r_c = r_c^0 \phi_C \quad (3)$$

and an expression similar to (2) for  $r_c^0$ . For the discussion here  $n_A = n_C = 1$  (for a more general treatment see (35)). In cases with no pore blockage (deactivation due only to poisoning) one concludes that

$$\phi_A = \phi_C = \frac{C_t - C_{ce}}{C_t} \quad (4)$$

$C_{ce}$  being the concentration of poisoned active sites. When no pore blockage occurs in general

$$\phi_A = \phi_C \neq \frac{C_t - C_{ce}}{C_t} \quad (5)$$

The exact functional form of  $\phi_A$  or  $\phi_C$  has been the subject of considerable debate in the field of catalyst deactivation (36-39). To develop this functional form on first principles, Froment *et al.* defined a local  $\phi(t)$ , which is the coverage of active sites at time  $t$ , i.e., the sites that are not poisoned and/or have not become inaccessible due to blockage in the pores. In probabilistic terms  $\phi(t)$  is expressed as (for further details see (30-35))

$$\phi(t) = P(t)S(t) \quad (6)$$

where  $P(t)$  is the probability that a site is accessible at time  $t$ , and  $S(t)$  the conditional probability that the site is not covered provided that it is accessible at time  $t$ . In the absence of intraparticle concentration and temperature gradients  $S$  is described by the following equation

$$\frac{dS}{dt} = -\frac{r_C^0}{M_c C_{ta}} S = -r_S^0 S \quad (7)$$

with  $M_c$  being the molecular weight of coke, i.e., the deposit that poisons the catalyst and blocks the pores. Integrating equation (7) (note that  $S = 1$  at  $t = 0$ ), one obtains

$$S(t) = \exp(-r_S^0 t) \quad (8)$$

For a single pore at the pore mouth one expects that  $P(t) = 1$ . Beyond the pore mouth  $P(t)$  decreases.  $\phi(t)$  as defined by equation (6) depends therefore on the location in the pore, even in the absence of any intraparticle concentration and temperature gradients. By integrating  $\phi$  over the pore length one derives a pore-averaged  $\hat{\phi}$ , and by integrating over the entire catalyst (described by a given pore network), one obtains a particle averaged  $\Phi$ .

To complete the model one needs to define a probability  $\omega(t)$  that a given site is covered with coke at time  $t$ . In mathematical terms this probability is

defined as

$$\omega(t + dt) = \omega(t) + \phi r_S^0 dt \quad (9)$$

which is equivalent to saying that the probability that a site is covered at time  $t + dt$  equals the probability that the site is covered at time  $t$  plus the probability that the site is covered during the time interval  $dt$ , provided that the site was not covered or blocked at time  $t$ . From equation (9) by integration

$$\omega(t) = \int_0^t r_S^0 \phi dt \quad (10)$$

$\omega(t)$  is again a local value, but in analogy with  $\phi(t)$  one can define a pore average value  $\hat{\omega}$  and a particle average coverage  $\Omega$ , which is directly related to the coke content of a particle

$$C_C = C_t M_C \Omega \quad (11)$$

The desired relationship between  $\Phi$  (the particle averaged activity) and  $C_c$  (particle coke content) follows directly from the relationship between  $\Phi$  and  $\Omega$ . To proceed further at this point one has to specify a pore model for the catalyst, and a model for the active site distribution. Froment and co-workers have examined a variety of cases such as single pore models (single-ended pores and pores open on both sides) with both deterministic and stochastic active site distributions, the bundle of parallel pores model and various tree-like models of the porous structure, which were earlier used by Pismen (40) to describe transport and reaction in porous systems. Such tree-like models contain interconnected pores but lack any closed loops and are usually called Bethe networks or lattices. They are completely characterized by their coordination number  $Z$ , which is the number of pores connected to the same site of the network.

Froment and co-workers were among the first to realize that the catalytic activity of a given catalyst undergoing deactivation will vanish much earlier than expected from calculations based on the surface area of the fresh catalyst. They did not

realize, however, that this was due to a percolation type phenomenon, similar to those observed with other classes of problems which are also characterized by structural phase transitions and abrupt changes in behavior, which are typical of percolation processes.

The blame for this should be placed on the use of tree-like models. These tree-like, Bethe networks of pores are characterized by a finite ratio of surface pores to those in the bulk (equal to  $(Z - 2) / (Z - 1)$ ). For the catalyst particle modeled by the network this ratio corresponds to the ratio of the geometric area to overall surface area, which for most catalysts is essentially zero as is also the case for three-dimensional networks. Accounting for the activity of the surface pores in Bethe networks tends to smooth out all the abrupt changes in the activity that would be otherwise observed at the percolation threshold.

#### PERCOLATION MODELS OF CATALYST DEACTIVATION

Catalyst deactivation was first identified as a percolation-type process by Sahimi and Tsotsis (2,3,41). The process studied by these authors was relatively simple. A porous catalyst, inside a differential isothermal reactor (with the catalytic active material uniformly distributed in its pores at an initial concentration  $C_0$ ) is reacting while simultaneously undergoing slow deactivation. The overall reaction rate  $r$  in a single pore of radius  $R$  and length  $L$  is given by

$$r = 2\pi RL r_0 (C_0 - C_s)^m \quad (12)$$

where  $(C_0 - C_s)$  is the active site concentration at time  $t$  and  $r_0$  the reaction rate per unit area. The deactivation-reaction occurring in parallel results in the deposition of a contaminant, which poisons the active sites, while simultaneously blocking part of the pore volume (the deposit is assumed to have an average volume  $b$  per mole of sites (2)).

The concentration of poisoned sites,  $C_s$ , is given as (for further details, see (2))

$$\frac{dC_s}{dt} = r_d (C_0 - C_s)^n \quad (13)$$

where  $r_d$  is the deactivation-reaction rate per unit surface area. The chemistry of the reaction processes is imbedded in  $r_0$  and  $r_d$  which, as the function  $f$  in Froment's model, depend on the reactants' concentrations and various thermodynamic and reaction constants. At any given process time (after deactivation has commenced) only part of the pore space is available for transport and reaction. At the single pore level one can conveniently describe the remaining open pore (accessible) volume by an effective radius  $R_e$ . This is defined by Sahimi and Tsotsis (2) to be the radius of a cylindrical pore (of the same length) and with volume equal to the remaining pore volume of a pore of radius  $R$ , which has undergone deactivation for a time (and which, as a result, is no further cylindrical). Sahimi and Tsotsis have shown that  $R_e$  is given as (2)

$$R_e = R \left[ 1 - \frac{\alpha}{R} g(\theta) \right]^{1/2} ; \quad \alpha = 2C_0 b \quad (14)$$

where  $g(\theta)$  is a function of dimensionless time  $\theta$  (defined as  $r_d C_0 \frac{n-1}{t}$ ) the exact functional form of which can be found in the original paper (2). When  $R_e = 0$ , the pore is considered completely blocked by deposits (plugged). Equation (14) can then be used to determine the time  $\theta_p$  at which the pore of initial radius  $R$  is completely plugged. Note, of course, that if  $R > \alpha$  (i.e., when the pore is either large, or the deactivating deposit's volume  $b$  is small - for only poisoning, for example,  $b$  is zero) the pore will never be blocked completely. As with Froment's model, to proceed further at this point one must specify a pore model for the catalyst. To realize how important the choice of a correct pore model is, one needs only to apply the so called bundle-of-pores or single-pore models to the above analysis. Both pore models predict that the catalyst's porous structure will never lose its global connectivity as long as the average pore radius  $R$  (for the single-pore or pseudo-homogeneous models) or the largest pore radius  $R_{max}$  (for the bundle of pores model) exceeds  $\alpha$ . For this case (if one assumes the process to be under kinetic control) blocking of individual pores has no additional

detrimental effect on catalyst activity beyond that caused by the poisoning of active site. The catalyst (if so allowed) will deactivate completely, when all active sites are poisoned. On the other hand, when  $R$  (or  $R_{\max}$ )  $< \alpha$ , there will be a time  $\theta_p$  at which activity will vanish due to pore blockage.

It should be intuitively clear from this discussion that both pore models offer a simplified description of the deactivation process for catalysts, which are characterized by complex interconnected porous structures. In reality, the internal pore structure of a catalyst becomes inaccessible to reaction and transport much earlier than the time predicted by these models. This discrepancy is due to the fact that in real catalysts some of the larger pores, that are only partially blocked, become inaccessible to reactant molecules because they get surrounded by pores, of smaller initial radius, which are themselves completely blocked. As the deactivation process proceeds, larger and larger isolated islands of partially blocked pores appear, which no longer contribute to transport and reaction. Intuitively, one expects that at some critical value of the fraction of completely blocked pores, the porespace will consist of isolated islands of open pores, no sample-spanning cluster of unplugged pores will exist, and the macroscopic connectivity of the porespace will be lost. This picture of catalyst deactivation just described is based on physical intuition. The same ideas, however, constitute the basis for the theory of percolation of disordered porous media. A detailed account of percolation theory and its engineering applications goes beyond the scope of this brief proceedings paper. Excellent treatments of the subject can be found in a series of papers and monographs (42-44). More detailed discussion on the application of percolation theory to catalyst deactivation and other chemical engineering problem can be found in papers by Sahimi and Tsotsis (1-4,14,15). Catalyst deactivation is only one of several processes and phenomena of relevance to catalysis for which percolation theory has found significant applications. Other examples include the interpretation of mercury porosimetry and BET data (45), modeling of sorption phenomena in pillared clays and zeolites (4), surface diffusion (46,47) etc.

We are not going to deal with all these examples of application of percolation theory to catalysis in this paper. Although the physics of these problems are different the basic numerical and mathematical techniques are very similar. For the deactivation problem discussed here, for example, one starts with a three-dimensional network representation of the catalyst porous structure. Systematic procedures of how to map any disordered porous medium onto an equivalent random network of pore bodies and throats have been developed and detailed accounts can be found in a number of publications (48). For the purposes of this discussion it suffices to say that the success of the mapping techniques strongly depends on the availability of quality structural data, such as mercury porosimetry, BET and direct microscopic observations. Of equal importance, however, is the correct interpretation of this data. It serves no purpose to perform careful mercury porosimetry and BET experiments and then use the wrong model (like the bundle of pores) for data analysis and interpretation.

Once the disordered porous medium has been mapped onto an equivalent three-dimensional network of pores and pore throats one must then model the physical and/or chemical processes occurring. Monte Carlo and Molecular Dynamics methods can be utilized. The choice depends on the complexity of the process and the desired accuracy in calculations. For the deactivation problem under kinetic control, discussed here, one can utilize Monte Carlo simulation techniques. At any given simulation time one calculates the effective radii of all pores by equation (14). One then identifies the completely plugged pores ( $R_e=0$ ), the partially-plugged pores that can be reached from the external surface of the catalyst, and the partially-plugged pores that are surrounded by completely-plugged pores. In the subsequent steps of simulation, the plugged pores and the partially blocked pores surrounded by completely blocked pores are not checked anymore, since they are not accessible to the reactant molecules. The simulations continue until a sample-spanning cluster of open pores no longer exists, i.e. the percolation threshold has been reached. All quantities of interest can be calculated by this Monte Carlo method, and further details of the numerical techniques can be found in the original publication (2).

The assumption of global kinetic control is probably valid for only a handful of catalytic reaction processes. Nevertheless, some typical simulation results of the model of catalyst deactivation under kinetic control are presented here in order to emphasize some of the unique percolation-type aspects of the problem. The overall plugging time  $\theta_p$ , i.e., the time at which the catalyst becomes completely deactivated is shown in Figure 1, where it is plotted versus  $Z$ , the average coordination number of the network of pores, (in industrial applications, of course, the useful lifetime of the catalyst is significantly smaller than  $\theta_p$ ). Note that as  $Z$  increases, (higher values of  $Z$  mean a more interconnected catalyst pore structure)  $\theta_p$  increases, i.e., the catalyst becomes more resistant to deactivation. The dependence of normalized catalytic activity ( $r/r_0$ ) ( $\phi$  in the language of Froment's models) on  $\theta$  is shown in Figure 2. It is interesting to note that all three qualitatively different types of catalytic behavior shown in this figure have also been observed experimentally.

More realistic percolation models of catalyst deactivation in which diffusional limitations are present are also now available (1, 3, 34, 49, 50). Most of these models have utilized the integrated macroscopic-microscopic modelling approach discussed above (33, 49, 50). Completely microscopic models are also available (1, 3), in which diffusion is modeled by a random walk process.

We would like to conclude this section by noting that statistical models of fluid-solid reactive systems are today finding widespread use in many diverse areas of engineering. One area, probably of interest to those working in the field of catalysis, in which these models have found particularly successful application, especially in helping to understand particle fragmentation phenomena, is coal gasification and coal and char and combustion. Particle fragmentation (51-54) is a particularly important phenomenon in this area, since it is believed to be responsible for decreased burnout times, enhanced production of fly ash, weight loss in coal combustors, and increased emission of submicron unburnt carbon and  $\text{NO}_x$  from



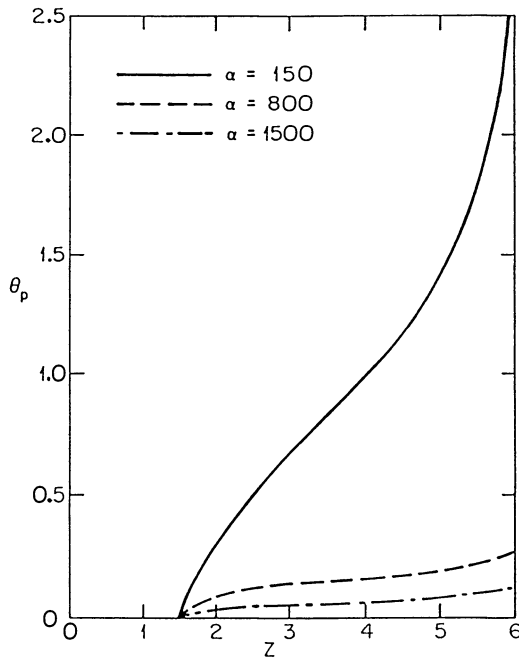


Figure 1. Plugging time  $\theta_p$  as a function of the average coordination number  $Z$  of a simple cubic network for various values of the deposit parameter  $\alpha$ .

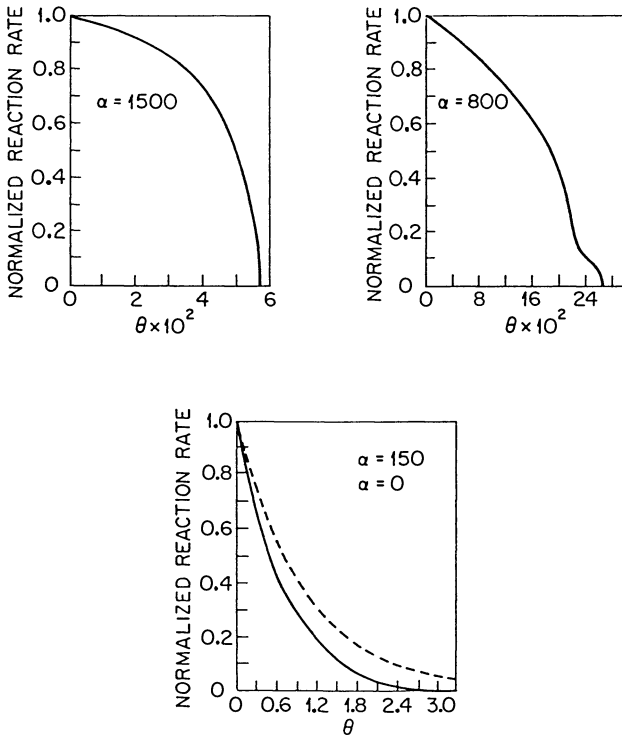


Figure 2. Normalized reaction rate as a function of time  $\theta$ .

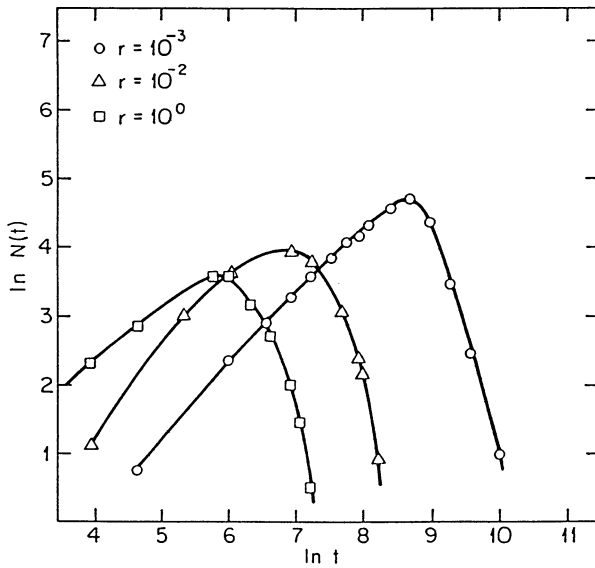


Figure 3. Variations of the total number of fragments  $N(t)$  with the time  $t$  for various values of the reactivity  $r$ .

pulverized coal combustion systems. Several statistical models of varying degree of complexity and elegance have been developed dealing with various aspects of the problem (12-15,54). Figure 3 for example, (from a recent work of Sahimi and Tsotsis (14,15)) shows the number of fragments, resulting from a single char particle (combusted in an oxygen atmosphere) as a function of reaction time. Note the existence of a maximum in the curves, which has significant implications for the optimal design and operation of these combustors.

### CONCLUSIONS

We have presented here a brief overview of the area of statistical modeling of fluid-solid reaction systems involving disordered porous media, which are themselves undergoing morphological and structural changes as a result of the reaction processes. We have dealt with the various technical aspects and questions involved in the implementation of these models by focusing our attention on a particular example from the field of catalysis, namely, catalyst deactivation, for which such models have found a particular successful application. Several other examples from the field of catalysis in which statistical modeling techniques have in the past or are currently finding significant applications are also mentioned. Today, with the advent of supercomputers and the widespread availability of powerful minicomputers it makes no good technical sense to invest resources and effort in the careful design and performance of experiments and then utilize outdated and semiempirical techniques for data analysis and interpretation. One of the best known examples of this problem is from the area of catalyst characterization by mercury porosimetry and BET, where one finds frequent use of outdated data analysis techniques, based, for example, on the bundle of parallel pores model, while meaningful statistical models are currently available for data analysis and interpretation (1,47).

### ACKNOWLEDGMENTS

One of the authors (M.S.) wishes to acknowledge the support of the University of Southern California through their Faculty Research and Innovation Fund, as

well as the donors of the Petroleum Research Fund administered by the American Chemical Society. The authors are also grateful to the U.S. Department of Energy for partial support of this work.

#### LITERATURE CITED

1. Sahimi, M., Tsotsis, T. T. and Gavalas, G. R., Chem. Eng. Sci. 1989, to be published.
2. Sahimi, M. and Tsotsis, T. T., J. Catal., 1985, 96, 552.
3. Sahimi, M. and Tsotsis, T. T., submitted for publication.
4. Sahimi, M., Occelli, M. L. and Tsotsis, T. T., Microstructure and Properties of Catalysts, Mat. Res. Soc. Symp. Ser., 1988, 111, 271.
5. Ruckenstein, E. and Dadyburjor, D. B., Rev. Chem. Eng., 1985, 3, 1.
6. Tien, C. and Payatakes, A. C., AIChE J. 1979, 25, 737.
7. Sharma, M. M. and Yortsos, Y. C., AIChE J., 1987, 33, 1654.
8. Guesbeck, C. and Collins, R. E., Soc. Pet. Eng. J., 1982, 22, 847.
9. Imdakm, A. O. and Sahimi, M., Phys. Rev. A, 1987, 36, 5304.
10. Szekely, J. and Evans, J. W., Chem. Eng. Sci., 1971, 26, 1901.
11. Hashimoto, K. and Silveston, P. L., AIChE J., 1973, 19, 259.
12. Gavalas, G. R., AIChE J., 1980, 26, 557.
13. Bhatia, S. K. and Perlmutter, D. D., AIChE J., 1981, 27, 247.
14. Sahimi, M. and Tsotsis, T. T., Phys. Rev. Lett., 1987, 59, 888.
15. Sahimi, M. and Tsotsis, T. T., Chem. Eng. Sci., 1988, 43, 113.
16. Williams, B. B., Gidley, J. L. and Schechter, R. S., Acidizing Fundamentals; Society of Petroleum Engineers of AIME: New York, 1979.
17. Daccord, G., Phys. Rev. Lett., 1987, 58, 479.
18. Hoefner, M. L. and Fogler, H. S., AIChE J., 1988, 34, 45.
19. Reyes, S. and Jensen, K. F., Chem. Eng. Sci., 1987, 42, 565.

20. Bhatia, S. K. and Perlmutter, D. D., AICHE J., 1983, 29, 76; 1983, 29, 281.
21. Whitaker, S., AICHE J., 1967, 13, 420.
22. Whitaker, S., Lat. Am. J. Chem. Eng. Appl. Chem., 1983, 13, 143.
23. Hegedus, L. L. and McCabe, R. W., In Catalyst Deactivation; Delmont, B. and Froment, G. F., Eds.; Elsevier: Amsterdam, 1980.
24. Butt, J. B., In Catalyst Deactivation; Delmont, B. and Froment, G. F., Eds.; Elsevier, Amsterdam, 1980.
25. Froment, G., F., In Catalyst Deactivation, Delmont, B. and Froment, G. F., Eds.; Elsevier, Amsterdam, 1980.
26. Bartholomew, C. H., Chem. Eng., 1984, 91, 96.
27. Hughes, R., Deactivation of Catalysts, Academic Press, New York, 1984.
28. Figueirado, J. L., ed., "Progress in Catalyst Deactivation", NATO Adv. Study Inst. Series E, 54, M. Nijhoff Pub., Boston, 1982.
29. Tsotsis, T. T., Sane, R. C., Webster, I. A., and Goddard, J. D., J. Catal., 1986, 101, 416.
30. Beeckman, J. W., Froment, G. F., and Pismen, L. M., Chem. Eng. Tech., 1978, 50, 960.
31. Beeckman, J. W. and Froment, G. F., Ind. Eng. Chem. Fundam., 1979, 18, 425.
32. Beeckman, J. W. and Froment, G. F., Chem. Eng. Sci., 1980, 35, 805.
33. Beeckman, J. W. and Froment, G. F., Ind. Eng. Chem. Fundam., 1982, 21, 243.
34. Beeckman, J. W., Nam, I. S. and Froment, G. F., Stud. Suf. Sci. Catal., 1987, 34, 365.
35. Nam, I. S. and Froment, G. F., J. Catal., 1987, 108, 271.
36. Szepe, S. and Levenspiel, O., Proc. 4th Eur. Symp. Chem. Research Eng., 1971, Pergamon Press: London, 1971, p. 265.
37. Froment, G. F., Proc. 6th Int. Congr. Catal., 1976, p. 10.
38. DePauw, R. and Froment, G. F., Chem. Eng. Sci., 1975, 30, 789.
39. Dumez, F. and Froment, G. F., Ind. Eng. Chem. Process Des. Dev., 1976, 15, 291.

40. Pismen, L. M., Chem. Eng. Sci., 1974, 29, 1227.
41. Sahimi, M. and Tsotsis, T. T., paper presented at the Ninth North American Meeting of the Catalysis Society, Houston, TX, March 1984.
42. Broadbent, S. R. and Hammersley, J. M., Proc. Camb. Phil. Soc., 1957, [224z, 81.
43. Stauffer, D., Introduction to Percolation Theory, Taylor and Francis, London, 1985.
44. Stauffer, D., Phys. Rep., 1979, 54, 1.
45. Lane, A., Shah, M. and Conner, W. C., J. Colloid Inter. Sci., 1986, 109, 235.
46. Zgrablich, G., Pereyra, V., Ponzi, M. and Marchese, J., AIChE J., 1986, 32, 1158.
47. Pereyra, V. and Zgrablich, G., Surface Sci., 1989, 209, 512.
48. Lin, S. and Cohen, M. H., J. Appl. Phys., 1982, 53, 4152.
49. Shah, N. and Ottino, J. M., Chem. Eng. Sci., 1987, 42, 73.
50. Mann, R., Sharratt, P. N. and Thomson, G., Chem. Eng. Sci., 1986, 41, 711.
51. Sundback, C. A., Beer, J. M. and Sarofim, A. F., Twentieth Symposium (International) on Combustion, The Combustion Institute: Pittsburgh, 1984, p. 1495.
52. Kerstein, A. R. and Niksa, S., Twentieth Symposium (International) on Combustion, The Combustion Institute: Pittsburgh, 1984, p. 941.
53. Gavalas, G. R., Combust. Sci. Tech., 1981, 24, 197.
54. Dutta, S., Wen, C. Y. and Belt, R. T., Ind. Eng. Chem. Process Des. Dev., 1977, 16, 20.

RECEIVED June 20, 1989

## Chapter 16

# Characterization of Catalytic Systems Using Nuclear Magnetic Resonance and Vibrational and Electron Spectroscopies

Tery L. Barr

Department of Materials and Laboratory for Surface Studies,  
University of Wisconsin—Milwaukee, Milwaukee, WI 53201

Until recently it was a common practice in catalytic science to infer information about the states and changes experienced by the components of a catalyst through knowledge gained of the reactants and products of the catalytic reaction and certain suppositions regarding the types of processes involved. This approach was generally employed because the complex physical states of the catalysts and the sparse concentrations of any metal dopants made it very difficult to directly map and follow the behavior of the catalytic components.

Recently, however, the implementation of several forms of modern, high resolution spectroscopy has made it possible to characterize, in relatively detailed fashion, the evolving chemistry of heterogeneous catalytic-type systems. In some cases, in fact, it has been possible to map the behavior of actual commercial catalysts, even following use. For example, much of our present understanding of the functionality of hydrodesulfurization catalysis has been a direct result of investigations of commercial systems with modern surface spectroscopies, as is also the case in the development of the basis reference for metals-support interactions (1).

A feature that still often impedes the latter form of analysis, however, is the common need to make many of these relatively sophisticated spectroscopic measurements in controlled, often unrealistic environments, perhaps following periodic extractions of the catalytic materials from process flow lines. As a result, numerous ingenious "minimal disturbance" procedures have been developed to circumvent possible problems (2). Generally, however, all of these schemes are based upon some degree of reliance on a "stop action" or "fix" concept (1). In the latter, we assume that the materials in question are usually altered by the previously mentioned catalytic process, but are unchanged ("fixed") following removal from that process. This concept has been shown to have some merit, but detailed analysis has demonstrated that mere exposure to ambient air can often prove deleterious to the chemical status of the surface of some catalytic ingredients (3). Thus, in



some cases it may be necessary to utilize vacuum transport and analysis to maintain the type of integrity needed to study these systems.

With all this in mind, it should also be remembered that one of the principal goals of these investigations is increased scientific understanding. Thus, it is vital to have some catalytic investigative groups purposefully employing the tack of sacrificing most of the direct semblance to commercial processes in favor of enhanced knowledge. In this manner, these groups have often been able to assure control over all the many diverse physical parameters that may influence the eventual outcome. Thus, for example, studies have been made of the effects on select catalytic processes of only the microstructural features of a metal crystal, such as platinum. Perhaps the most detailed versions of this approach to catalytic science are those practiced at the University of California--Berkeley by groups associated with Professor G. Somorjai (4). This type of controlled investigation has been labeled as "molecular catalysis" by the latter groups (4). Also described herein is a study by Bell (in conjunction with Somorjai and others) of the (molecular) catalytic effects of a relatively complex oxide (titania) on a layered metal (Rh) system. A combination of Ion Scattering Spectroscopy (ISS), Auger Electron Spectroscopy (AES) and X-ray Photoelectron Spectroscopy (XPS) was employed in this study to show that both CO hydrogenation and ethane hydrogenolysis were rate enhanced by the presence of the titania on the Rh.

The primary spectroscopies described in this session were Nuclear Magnetic Resonance (NMR), Infra-red Spectroscopies (IR and Raman) and XPS. All of these techniques permit some form of direct observation of the chemical behavior of certain catalytic components. For example, Barr and Yin employed XPS to provide the first detailed map of the chemical changes experienced by Pt in a Pt/Al<sub>2</sub>O<sub>3</sub> catalytic system with typical commercial loadings of platinum. The states of the platinum in oxidized and reduced forms were documented, as was a peculiar, unique effect of the XPS charging shift that seems to be induced when a reduced metal (e.g., Pt) is "mistreated" and forced to grow into finite sized crystallites. Hicks also investigated certain problems arising in XPS when it is employed to examine catalytic materials. He noted that the catalytic supports employed are generally insulators and pointed out that the conventional (Siegbahn) method of fixing XPS binding energies through the coupling of the Fermi edges of the sample with that of the spectrometer will not work for these types of insulating systems. Further Hicks noted that doping the support with conductive metal clusters also provides a further complication, since the latter will have both the "floating" Fermi edge (described above by Barr) and variable binding energies that seem to be a direct function of the size of the crystallites involved (5). In conclusion Hicks pointed out that all of these difficulties must be properly addressed before one will be able to determine absolute binding energies for metal supported catalysts.

The surface sensitivity of XPS generally requires an unrealistic UHV environment for analysis. This problem may sometimes be circumvented by employing IR or Raman spectroscopies. Peri

presented a fairly detailed, practical review of the assets (and defects) of these vibrational spectroscopies. He pointed out how, through adroit choice of the energy region analysed, one may avoid the overwhelming size of the support absorptions, and still generate useful information about the metals dopents. Similarly, he cautioned against the view that the more modern (FTIR and computerized) approaches are necessary panaceas to be employed in place of the more conventional dispersive forms of IR spectroscopy. In particular, he noted that, whereas the generation of very rapid FTIR results may be quite useful in studying kinetics questions, it may actually lead to problems in the more conventional characterization measurements. Adroit, expert based performance seems to be Peri's answer to many of these potential problems.

Solid state NMR is another form of spectroscopy that has experienced a virtual renaissance in catalyst characterization, particularly in studies of zeolites and support materials. In the present case, Smith et al. have demonstrated that NMR may provide a useful alternative to the common porosimetry and adsorption approaches to determine the pore sizes of supports. Certain limitations of the latter methods were described and select NMR results shown to alleviate most of these limitations. Welsh and Lambert have utilized the versatility of magic angle spinning (MAS) - NMR to explore questions related to the location of select cations in zeolites. The MAS-NMR approach has already proven invaluable in studies of structure and degradation of zeolites (6). In the present case, Welsh and Lambert were able to map the positions of sodium in mixed cation, hydrated and dehydrated zeolites. The selective presence of sodium in the supercage, as opposed to the smaller sodalite cages, was detected, and selective cation placement during exchange was described.

Although these techniques provide a great deal of insight into catalytic performance, and are often used to relate structure to activity and selectivity, they generally must be utilized in conjunction with other tools, such as TPD, microscopy, TRD and EXAFS, in order to make a major impact on catalyst development.

#### Literature Cited

1. Barr, T. L., in Practical Surface Analysis, Ed. D. Briggs and M. P. Seah, John Wiley and Sons, New York, 1983; Ch. 8.
2. Fleisch, T., private communication.
3. Barr, T. L., *J. Phys. Chem.*, 82, 1801 (1978).
4. Somorjai, G.; Zarea, F., *J. Phys. Chem.*, 86, 3070 (1982).
5. See for example, F. Parmigiani, E. Kay, P. S. Bagus and C. J. Nelin, *J. Electron Spectrosc. Rel. Phenomena*, 36, 257 (1985).
6. Klinowski, J., "NMR Studies of Zeolites," in *Progress in NMR Spectroscopy*, 16, 237-309 (1984).

RECEIVED July 27, 1989

# Chapter 17

## Surface Characterization of Metal Oxide Overlayers

K. J. Williams<sup>1,2</sup>, M. E. Levin<sup>1,2</sup>, M. Salmeron<sup>1,2</sup>, A. T. Bell<sup>1,2</sup>,  
and G. A. Somorjai<sup>1,3</sup>

<sup>1</sup>Center for Advanced Materials, Lawrence Berkeley Laboratory,  
Berkeley, CA 94720

<sup>2</sup>Department of Chemical Engineering, University of California,  
Berkeley, CA 94720

<sup>3</sup>Department of Chemistry, University of California, Berkeley, CA 94720

The structure and composition of titania deposited on the surface of a Rh foil or single crystal were investigated using ISS, AES, and XPS. The effects of the overlayer on the hydrogenation of carbon monoxide and the hydrogenolysis of ethane were examined. With increasing titania coverage, the activity of Rh for carbon monoxide hydrogenation passes through a maximum, whereas the activity for ethane hydrogenolysis decreases monotonically.

Interest in the composition and structure of submonolayer metal oxide deposits on metals has developed as a consequence of growing evidence that such deposits influence the adsorptive and catalytic properties of the substrate metal [see for example ref. (1)]. In particular, it has been shown that titania deposited on a Ni(111) (2) surface and on the surface of Pt and Rh foils (3,4) will enhance the activity of the metal for CO hydrogenation. Similar results have also been reported for niobia deposited on a Pt foil (5). The present paper discusses the characterization of titania overlayers deposited on the surface of a polycrystalline Rh foil and a Rh(111) surface.

**Experimental.** Samples were prepared by evaporation of titanium onto a Rh foil or a Rh(111) single crystal. Subsequent oxidation with oxygen at 623 K then produced a titania overlayer on the Rh substrate. Oxygen bound to the Rh was removed as carbon dioxide by repeated exposure of the oxidized sample to 4 L of carbon monoxide followed by flashing to 773 K. The freshly deposited overlayer was then characterized by ISS, AES, and XPS. The effects of the overlayer on the substrate were probed by temperature-programmed desorption of carbon monoxide, by the hydrogenation of carbon monoxide, and by the hydrogenolysis of ethane. All of these experiments were carried out in one of two ultra high vacuum chambers, one of which was equipped with a high pressure cell for carrying out catalytic reactions.

**Results and Discussion.** Coverage of the Rh surface by titania was followed by means of ISS and AES. Figures 1 and 2 show the ISS and AES signals for Rh as a function of the deposition times for metallic titanium. The ISS signal exhibits a linear decline with the deposition time, and at a time of 150-175 s, the Rh signal goes to zero. The Rh AES signal also follows a linear decrease in intensity for deposition times of less than 175 s. For longer deposition times, the AES signal decreases more slowly. Similar results were obtained with both single crystal and polycrystalline samples.

The linear decline in both the Rh ISS and AES signals for deposition times of less than 175 s, indicates that the first monolayer of titania is deposited as a

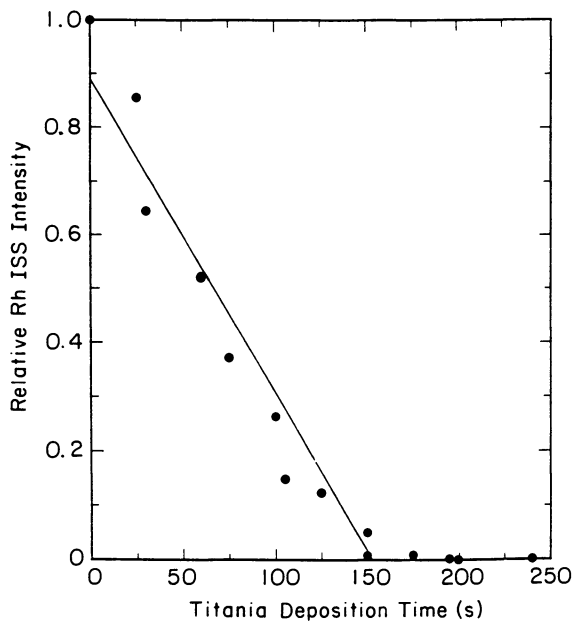


Fig. 1 Rh ISS intensity versus titania evaporation time. The substrate is a Rh(111) surface.

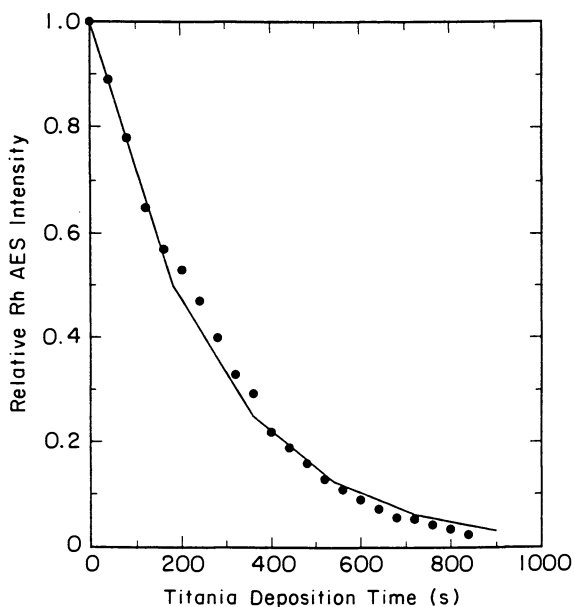


Fig. 2 Rh AES intensity versus titania evaporation time. The substrate is a Rh(111) surface.

two-dimensional overlayer. If layer-by-layer growth were sustained beyond the completion of the first monolayer, then the AES signal would be expected to follow solid line shown in Fig. 2. The deviation of the data from the curve for layer-by-layer growth in the time period of 175 to 400 s is indicative of some three-dimensional growth in the second layer. For longer deposition times, however, the data return to the curve predicted for layer-by-layer growth.

Temperature-programmed desorption (TPD) spectra of adsorbed carbon monoxide exhibit a single peak for carbon monoxide and no evidence of carbon dioxide formation. Neither the position nor the shape of the carbon monoxide peak is a function of titania coverage. A plot of carbon monoxide chemisorption capacity versus titania coverage is shown in Fig. 3. The CO coverage is observed to decrease linearly with increasing titania coverage. A similar trend has been observed previously for titania deposited on a Pt foil (6) and on a Ru(0001) single crystal surface (7). The linear relationship between CO chemisorption capacity and titania coverage seen in Fig. 3 contrasts with that reported earlier by Levin et al. (8) for titania deposited on a Rh foil. As discussed by Williams et al. (9), this discrepancy is attributable to an incorrect determination of titania coverage by Levin et al. (8). When correctly interpreted, the data of Levin et al. (8) also show a linear dependence of CO chemisorption capacity on titania coverage. A further consequence of the reanalysis is that the titania coverages reported by Levin et al. (8) should be multiplied by a factor of 3.3 (9).

An XPS spectrum of the Ti(2p) core levels for Rh foil covered with 0.3 ML of titania is shown in Fig. 4 (10). Spectrum (1) obtained after oxidation, exhibits two peaks centered at 463.6 and 458.5 eV that can be assigned to the  $2p_{1/2}$  and  $2p_{3/2}$  core levels of  $Ti^{4+}$  (11). A slight asymmetry is observed in the  $2p_{3/2}$  peak on the low energy side, indicating the presence of a small percentage of  $Ti^{3+}$ . CO titration causes an attenuation of the  $Ti^{4+}$  peaks and the appearance of a peak at 455.7 eV that is assigned to  $Ti^{3+}$  species (11). A peak at 461.4 eV is assigned to the corresponding  $Ti^{3+}$  ( $2p_{1/2}$ ) level.  $H_2$  reduction causes a further decrease of the  $Ti^{4+}$  peak intensity and a corresponding increase in the  $Ti^{3+}$  peak intensity. Small shifts to higher binding energies of the  $2p_{3/2}$  peak of  $Ti^{4+}$  are also observed as the degree of reduction increases. In spectrum (3) of Fig. 4, for example, the  $Ti^{4+}$ ( $2p_{3/2}$ ) binding energy is 459.0 eV. Reoxidation of the sample returns the titanium to the  $Ti^{4+}$  state. Similar changes in the XPS spectrum were observed for all titania coverages studied. The principal difference noted was an increase in the proportion of  $Ti^{3+}$  as the coverage of titania decreased. This trend suggests a preferential concentration of  $Ti^{3+}$  species at the periphery of the two-dimensional  $TiO_x$  islands.

Displayed in Fig. 5 is the methane production rate from CO and  $H_2$  for varying  $TiO_x$  coverages (12). Reaction rates were measured at a temperature of 553 K, and at  $H_2$  and CO partial pressures of 0.67 and 0.33 atm, respectively. With the addition of small amounts of  $TiO_x$  to the clean Rh surface, a sharp rise in reaction rate is noted. At the maximum corresponding to 0.15 ML [0.50 ML on the corrected scale (9)], a threefold increase in the rate is observed. Beyond this coverage, the rate decreases monotonically.

Titania promotion also alters the selectivity of Rh, as may be seen in Fig. 6. The methane content of the hydrocarbon product falls from a value of 94% when no titania is present to nearly 60% for a titania coverage of 0.20 ML [0.66 ML on the corrected scale (9)]. Ethylene and propylene are the predominant higher hydrocarbon species, comprising roughly 34 mol% of the total hydrocarbon product. At higher titania coverages, the selectivities return to values more characteristic of clean Rh.

XPS characterization of  $TiO_x/Rh$  samples after their exposure to synthesis gas under reaction conditions showed that a significant fraction of the titanium ions were still in the  $Ti^{3+}$  state. A summary of these observations is given in Table 1. It is evident that

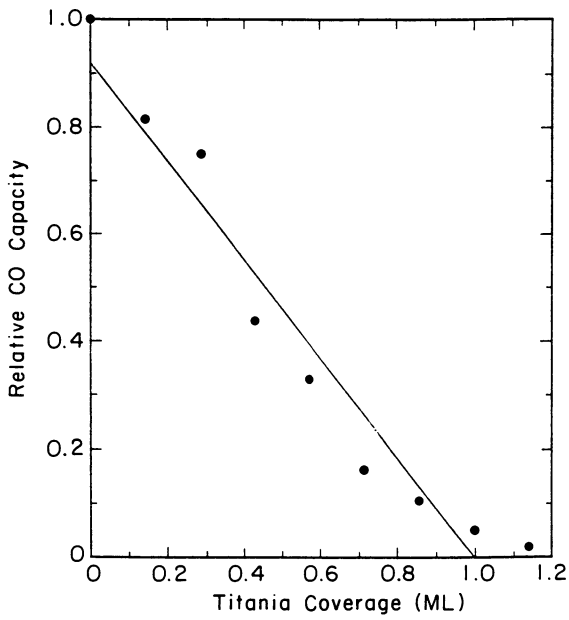


Fig. 3 CO chemisorption capacity versus titania coverage. The substrate is a Rh(111) surface.

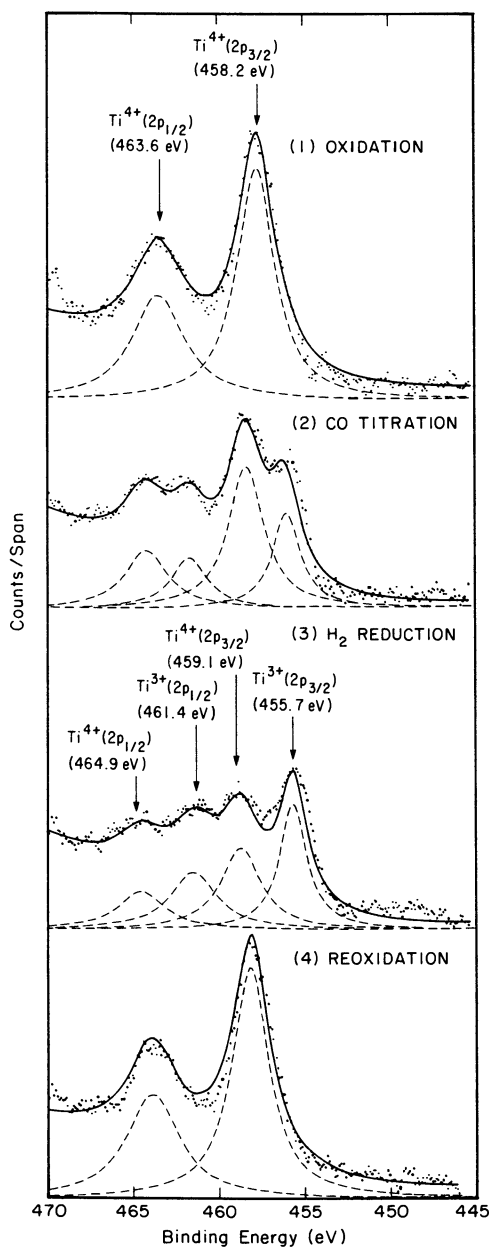


Fig. 4 XPS spectra of the Ti(2p) region for 0.50 ML of  $TiO_x$  on a Rh foil. Spectra 1, 2, 3, and 4 were observed after oxidation, CO titration,  $H_2$  reduction, and reoxidation, respectively.

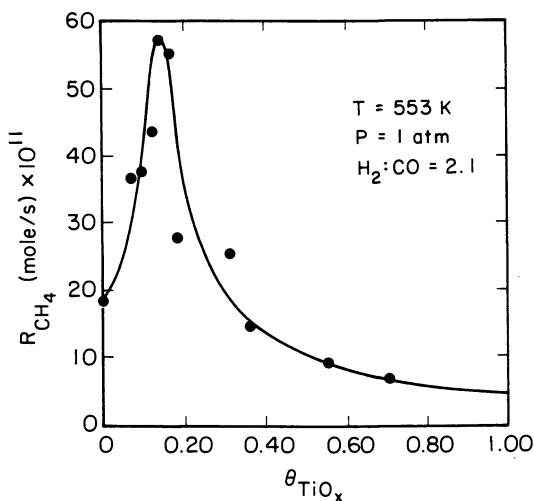


Fig. 5 Methanation rate on  $\text{TiO}_x/\text{Rh}$  foil as a function of  $\text{TiO}_x$  coverage. Reaction conditions were 553 K, 1 atm total pressure, and a  $\text{H}_2:\text{CO}$  ratio of 2:1 (12). The indicated  $\text{TiO}_x$  coverages should be multiplied by a factor of 3.3 to account for the corrections recently reported by Williams et al. (9).

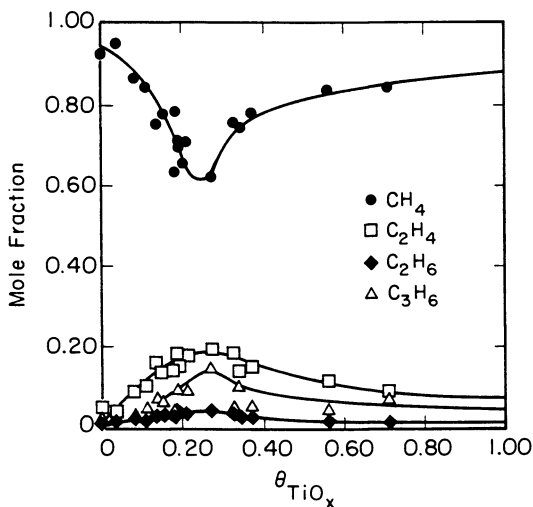


Fig. 6 Hydrocarbon product selectivity as a function of  $\text{TiO}_x$  coverage on a Rh foil (12). The indicated  $\text{TiO}_x$  coverages should be multiplied by a factor of 3.3 to account for the corrections recently reported by Williams et al. (9).



Table 1  
 Percentage of  $Ti^{3+}$  Following CO Hydrogenation

$\theta_{TiO_x}$	After CO Titration	After $H_2$ Reduction	After CO Hydrogenation
0.50	0.22	---	0.15
0.50	---	0.62	0.26

sample pretreatment has only a moderate effect on the oxidation state of Ti in the  $TiO_x$  overlayer. It would thus appear that during reaction the oxidation state of Ti adjusts to reflect the composition of the gaseous environment. This conclusion concurs with the observation that prereduction of  $TiO_2$ -supported and  $TiO_2$ -promoted metal catalysts does not significantly change the activity of these catalysts for CO hydrogenation (13-16).

The enhancement in CO hydrogenation activity of Rh is ascribed to the presence of  $Ti^{3+}$  sites at the perimeter of  $TiO_x$  islands. It is proposed that these sites interact with the oxygen in CO chemisorbed on nearby Rh atoms and assist in the dissociation of CO. Since the dissociation of CO is believed to be the rate-limiting step in this reaction, the participation of  $Ti^{3+}$  in this step leads to a higher activity. The dependence of the methanation rate on  $TiO_x$  coverage, seen in Fig. 5, is attributable to the variation in the concentration of  $Ti^{3+}$  centers with  $TiO_x$  coverage.

The effects of titania deposits on the hydrogenolysis of ethane are quite different from those for the hydrogenation of CO. Ethane hydrogenolysis was carried out at 450 K with 25 torr ethane and 25 torr hydrogen. The rate of hydrogenolysis was found to decrease monotonically with increasing titania coverage, the curve exhibiting a shape nearly identical to that observed for CO chemisorption. The presence of titania on the Rh surface was found to have no effect on the activation energy for the reaction. Taken together, these results suggest that hydrogenolysis can occur only on those Rh sites not affected by titania islands.

**Conclusions.** Submonolayer deposits of titania grow on the surface of Rh in the form of two-dimensional islands until a coverage of nearly a monolayer is achieved, at which point some three-dimensional growth of the islands is observed. The titania islands exclude CO chemisorption on Rh sites covered by the titania. The  $Ti^{4+}$  ions in the overlayer are readily reduced to  $Ti^{3+}$ . This process begins at the perimeter of the islands and extends inwards as reduction proceeds. Titania promotion of Rh enhances the rate of CO hydrogenation by up to a factor of three and increases the selectivity to  $C_{2+}$  hydrocarbons. By contrast, the activity of Rh for the hydrogenolysis of ethane decreases monotonically with increasing titania promotion.

**Acknowledgment.** This work was supported by the Division of Materials Sciences, Office of Basic Energy Sciences, U. S. Department of Energy, under Contract No. DE-AC03-76SF00098.

Literature Cited.

1. Bell, A. T. In Catalyst Design - Progress and Perspectives; Hegedus, L. L., Ed.; Wiley: New York, 1987.
2. Chung, Y. W.; Xiong, G.; Kao, C. C. J. Catal. 1984, **85**, 237.
3. Demmin, R. A.; Ko, C. S.; Gorte, R. J. J. Phys. Chem. 1985, **89**, 1151.
4. Levin, M. E.; Salmeron, M.; Bell, A. T.; Somorjai, G. A. J. Chem. Soc., Faraday Trans. 1 1987, **83**, 2061.
5. Demmin, R. A.; Gorte, R. J. J. Catal. 1986, **98**, 577.
6. Dwyer, D. J.; Cameron, S. D.; Gland, J. Surf. Sci. 1985, **159**, 430.
7. Bodyal, J. P. S.; Gellman, A. J.; Judd, R. W.; Lambert, R. M. Catal. Lett. 1988, **1**, 41.
8. Levin, M. E.; Salmeron, M.; Bell, A. T.; Somorjai, G. A. Surf. Sci. 1986, **169**, 123.
9. Williams, K. J.; Salmeron, M.; Bell, A. T.; and Somorjai, G. A.; Surf. Sci., in press.
10. Levin, M. E.; Salmeron, M.; Bell, A. T.; Somorjai, G. A. Surf. Sci., in press.
11. Handbook of X-Ray Photoelectron Spectroscopy; Perkin Elmer Corp.: Eden Prairie, MN, 1979.
12. Levin, M. E.; Salmeron, M.; Bell, A. T.; Somorjai, G. A. J. Catal. 1987, **106**, 401.
13. Vannice, M. A.; Twu, C. C.; Moon, S. H. J. Catal. 1983, **82**, 213.
14. Solymosi, F.; Tombacz, I.; Kocsis, M. J. Catal. 1982, **75**, 78.
15. Morris, S. R.; Moyes, R. B.; Wells, P. B. In Studies in Surface Science and Catalysis; Imelik, B. et al., Eds.; Vol. 11, p. 247, Elsevier, Amsterdam, 1982; Vol. 11, p. 247.

RECEIVED April 27, 1989

## Chapter 18

# Surface Properties of Mixed-Metal Catalysts

D. W. Goodman

Department of Chemistry, Texas A&M University, College Station, TX 77843

The chemical behavior of monolayer coverages of one metal on the surface of another, i.e., Cu/Ru, Ni/Ru, Ni/W, Fe/W, Pd/W, has recently been shown to be dramatically different from that seen for either of the metallic components separately. These chemical alterations, which modify the chemisorption and catalytic properties of the overlayers, have been correlated with changes in the structural and electronic properties of the bimetallic system. The films are found to grow in a manner which causes them to be strained with respect to their bulk lattice configuration. In addition, unique electronic interface states have been identified with these overlayers. These studies, which include the adsorption of CO and H<sub>2</sub> on these overlayers as well as the measurement of the elevated pressure kinetics of the methanation, ethane hydrogenolysis, cyclohexane dehydrogenation reactions, are reviewed.

In addition to modification of surfaces by non-metals, the catalytic properties of metals can also be altered greatly by the addition of a second transition metal (1). Interest in bimetallic catalysts has risen steadily over the years because of the commercial success of these systems. This success results from an enhanced ability to control the catalytic activity and selectivity by tailoring the catalyst composition (2-3). A long-standing question regarding such bimetallic systems is the nature of the properties of the mixed metal system which give rise to its enhanced catalytic performance relative to either of its individual metal components. These enhanced properties (improved stability, selectivity and/or activity) can be accounted for by one or more of several possibilities. First, the addition of one metal to a second may lead to an electronic modification of either or both of the metal constituents. This electronic perturbation can result from direct bonding (charge transfer) or from a structural

modification induced by one metal upon the other. Secondly, a metal additive can promote a particular step in the reaction sequence and, thus, act in parallel with the host metal. Thirdly, the additive metal can serve to block the availability of certain active sites, or ensembles, prerequisite for a particular reaction step. If this "poisoned" reaction step involves an undesirable reaction product, then the net effect is an enhanced overall selectivity. Further, the attenuation by this mechanism of a reaction step leading to undesirable surface contamination will promote catalyst activity and durability.

The studies reviewed here are part of a continuing effort (4-10) to identify those properties of bimetallic systems which can be related to their superior catalytic properties. A pivotal question to be addressed of bimetallic systems (and of surface impurities in general) is the relative importance of ensemble (steric or local) versus electronic (nonlocal or extended) effects in the modification of catalytic properties. In gathering information to address this question it has been advantageous to simplify the problem by utilizing models of a bimetallic catalyst such as the deposition of metals on single-crystal substrates in the clean environment familiar to surface science.

These studies were carried out utilizing the specialized apparatus described in references (11-12). This device consists of two distinct regions, a surface analysis chamber and a microcatalytic reactor. The custom built reactor, contiguous to the surface analysis chamber, employs a retraction bellows that supports the metal single crystal and allows translation of the catalyst in vacuo from the reactor to the surface analysis region. Both regions are of ultrahigh vacuum construction, bakeable, and capable of ultimate pressures of less than  $2 \times 10^{-10}$  Torr. Auger spectroscopy (AES) is used to characterize the sample before and after reaction. A second chamber was equipped with Auger spectroscopy, low energy electron diffraction (LEED) and a mass spectrometer for temperature programmed desorption (TPD).

Many such model systems have been studied but a particularly appealing combination is that of Cu on Ru. Cu is immiscible in Ru which facilitates coverage determinations by TPD (4) and circumvents the complication of determining the 3-d composition. The adsorption and growth of Cu films on the Ru(0001) surface have been studied (4-10,13-20) by work function measurements, LEED, AES, and TPD. The results from recent studies (4-10) indicate that for submonolayer depositions at 100K the Cu grows in a highly dispersed mode, subsequently forming 2-d islands pseudomorphic to the Ru(0001) substrate upon annealing to 300K. Pseudomorphic growth of the copper indicates that the copper-copper bond distances are strained approximately 6% beyond the equilibrium bond distances found for bulk copper.

A comparison of CO desorption from Ru (7) from multilayer Cu (10ML) on Ru and 1ML Cu on Ru is shown in Fig. 1. The TPD features of the 1ML Cu (peaks at 160 and 210K) on Ru are at temperatures intermediate between Ru and bulk Cu. This suggests that the monolayer Cu is electronically perturbed and that this perturbation manifests itself in the bonding of CO. An increase in the desorption temperature relative to bulk Cu indicates a

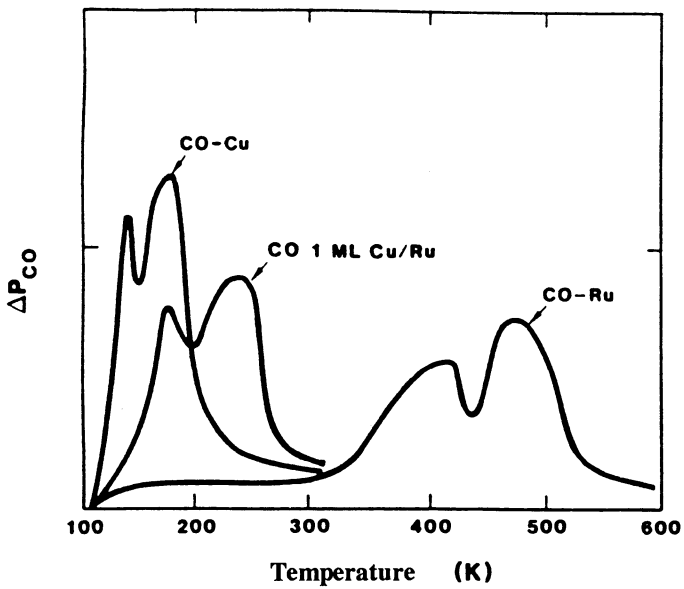


Figure 1. TPD results for CO adsorbed to saturation levels on clean Ru(0001), on multilayer Cu, and on a 1ML Cu covered Ru(0001). (Reproduced with permission from ref. 7. Copyright 1986 Academic.)

stabilization of the CO on the monolayer Cu suggesting a coupling of the CO through the Cu to the Ru. The magnitude of the CO stabilization implies that the electronic modification of the Cu by the Ru is significant and should be observable with a band structure probe. Recent angular resolved photoemission studies (7) indeed show a unique interface state which is likely related to the altered CO bonding on Cu films intimate to Ru.

Figure 2 shows the results (7) of CO chemisorption on the Cu/Ru(0001) system as a function of the Cu coverage. In each case the exposure corresponds to a saturation coverage of CO. Most apparent in Figure 2 is a monotonic decrease upon addition of Cu of the CO structure identified with Ru (peaks at 400 and 480K) and an increase of the CO structure corresponding to Cu (peaks at 160 and 210K). The buildup of a third feature at ~300K (indicated by the dashed line) is assigned to correspond to CO desorbing from the edges of Cu islands. Integration of the 200, 275, and 300K peaks provides information regarding island sizes, that is, perimeter-to-island area ratios, at various Cu coverages. For example, at  $\theta_{Cu} = 0.66$  the average island size is estimated to be approximately 50Å in diameter. This island size is consistent with an estimate of the 2-d island size corresponding to this coverage of 40-60Å derived from the width of the LEED beam profiles (7).

Model studies of the Cu/Ru(0001) catalyst have been carried out (10) for methanation and hydrogenolysis reactions. These data suggest that copper merely serves as an inactive diluent, blocking sites on a one-to-one basis. Similar results have been found in analogous studies (21) introducing silver onto a Rh(111) methanation catalyst.

Sinfelt (22) has shown that copper in a Cu/Ru catalyst is confined to the surface of ruthenium. Results from the model catalysts discussed here then should be relevant to those on the corresponding supported, bimetallic catalysts. Several such studies have been carried out investigating the addition of copper or other Group 1B metals on the rates of CO hydrogenation (23-25) and ethane hydrogenolysis (25) catalyzed by ruthenium. In general, these studies show a marked reduction in activity with addition of the Group 1B metal suggesting a more profound effect of the Group 1B metal on ruthenium than implied from the model studies. A critical parameter in the supported studies is the measurement of the active ruthenium surface using hydrogen chemisorption techniques. Haller and coworkers (26-27) have recently suggested that hydrogen spillover during chemisorption may occur from ruthenium to copper complicating the assessment of surface Ru atoms. Recent studies in our laboratory (5-6) have shown directly that spillover from Ru to Cu can take place and must be considered in the hydrogen chemisorption measurements. H<sub>2</sub> spillover would lead to a significant overestimation of the number of active ruthenium metal sites and thus to significant error in calculating ruthenium specific activity. If this is indeed the case, the results obtained on the supported catalysts, corrected for the overestimation of surface ruthenium, could become more comparable with the model data reported here. Finally, the activation energies observed on supported catalysts in various laboratories

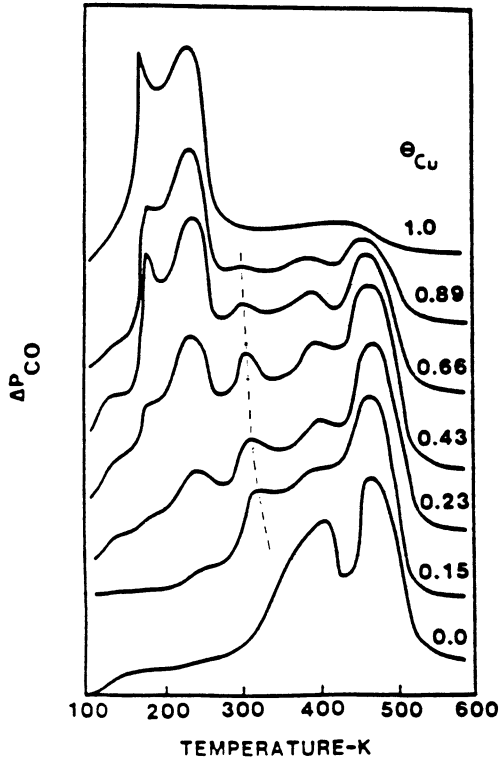


Figure 2. TPD results corresponding to CO adsorbed to saturation levels on the clean Ru(0001) surface, and from this same surface containing various coverages of Cu. (Reproduced with permission from ref. 7. Copyright 1986 Academic.)

are generally unchanged by the addition of Group 1B metal (26-28) in agreement with the model studies.

These arguments suggest that Ru specific rates for methanation and ethane hydrogenolysis on supported Cu/Ru catalysts approximate those values found for pure Ru. As a consequence, the rates for cyclohexane dehydrogenation reaction on supported Cu/Ru, similarly corrected, must exceed those specific rates found for pure Ru. The uncorrected specific rates for cyclohexane dehydrogenation on the supported Cu/Ru system remain essentially unchanged upon addition of Cu to Ru (10). An activity enhancement for cyclohexane dehydrogenation in the mixed Cu/Ru system relative to pure Ru is most surprising given that Cu is less active for this reaction than Ru.

Figure 3 shows the effect of the addition of Cu to Ru on the rate of cyclohexane dehydrogenation to benzene. The overall rate of this reaction is seen to increase by approximately an order of magnitude at a copper coverage of 3/4 of a monolayer. This translates to a Ru specific rate enhancement of ~40. Above this coverage, the rate falls to an activity approximately equal to that of Cu-free Ru. The observation of non-zero rates at the higher Cu coverages is believed to be caused by three dimensional clustering of the Cu overlayers (10). Similar data have been obtained for this reaction on epitaxial and alloyed Au/Pt(111) surfaces (29).

The rate enhancement observed for submonolayer Cu deposits may relate to an enhanced activity of the strained Cu film for this reaction due to its altered geometric (7) and electronic (9) properties. Alternatively, a mechanism whereby the two metals cooperatively catalyze different steps of the reaction may account for the activity promotion. For example, dissociative H<sub>2</sub> adsorption on bulk Cu is unfavorable due to an activation barrier of approximately 5 kcal/mol (30). In the combined Cu/Ru system, Ru may function as an atomic hydrogen source/sink via spillover to/from neighboring Cu. A kinetically controlled spillover of H<sub>2</sub> from Ru to Cu, discussed above, is consistent with an observed optimum reaction rate at an intermediate Cu coverage.

Finally, we note the differences between a Ru(0001) catalyst with or without added Cu with respect to attaining steady-state reaction rates. On the Cu-free surface, an induction time of approximately 10 minutes is required to achieve steady state activity. During this time, production of benzene is quite low while the hydrogenolysis to lower alkanes, primarily methane, is significantly higher than at steady-state. During this induction time the carbon level (as determined by Auger spectroscopy) rises to a saturation value coincidental with the onset of steady state reaction. This behavior suggests that a carbonaceous layer on the metal surface effectively suppresses carbon-carbon bond scission, or hydrogenolysis, on the Ru surface.

Cu addition leads to an enhanced rate of benzene production with little or no induction time. That is, the initial rate of cyclohexane hydrogenolysis, relative to the Cu-free surface, is suppressed. Further, Cu reduces the relative carbon buildup on the surface during reaction. Thus, Cu may play a similar role as the carbonaceous layer in suppressing cyclohexane hydrogenolysis while concurrently stabilizing those intermediates leading to the product



benzene. In addition, copper may serve to weaken the chemisorption bond of benzene and thus limit self-poisoning by adsorbed product. This latter possibility has been proposed by Sachtler and Somorjai (29) to explain the role of Au in Au/Pt(111) catalysts for this reaction. A weakening of benzene chemisorption satisfactorily accounts for our observation that the reaction changes from zero order in cyclohexane on Ru(0001) to approximately first order upon the addition of Cu.

A second bimetallic system which has been thoroughly studied is nickel adsorbed onto tungsten (31-33). On both W(110) and W(100), Ni is adsorbed layer-by-layer. Annealing Ni layers with coverages less than 1.3 ML to 1200K produces little change in the Ni(848eV)/W(179eV) AES ratio. However, for Ni coverages above 1.3ML, a 1200K anneal results in a very slow increase in this AES ratio with coverage, indicating either alloy or 3-dimensional island formation.

CO adsorption (32) as a function of Ni coverage on W(110) has been investigated. As the Ni coverage is increased from 0.3 to 1.0ML, adsorption on the W(110) substrate decreases, as evidenced by a reduction in the CO features between 225 and 350K, while a feature at 380K becomes more prominent. The 380K CO TPD peak maximum for 1ML Ni compares with 430K for the CO TPD peak maximum for Ni(111) (35). Increasing the Ni coverage above 1.0ML results in a broadening of the 380K CO TPD peak and in the development of a shoulder feature, suggestive of bulk Ni CO desorption, at ~430K.

CO chemisorption on the Ni/W(100) surface as a function of Ni coverage is similar to CO adsorption on Ni/W(110). As the Ni coverage is increased from 0.3 to 1.0ML, decreasing intensity in the TPD features associated with W(100) is evident near 300K. At a Ni coverage of 1ML, the CO TPD peak maximum is reduced by approximately 50K from the corresponding peak maximum on Ni(100) (35). For coverages greater than 1ML, a clear shoulder at 420-450K is observed, indicating that second and successive Ni layers have chemisorptive properties very similar to bulk Ni. Thus the W substrates clearly alter the chemisorptive properties of the first Ni layer, but have only slight effects on the second and subsequent layers.

That CO chemisorption is perturbed on strained-layer Ni is not surprising in view of CO chemisorption behavior on other metal overlayer systems. For example, on Cu/Ru it has been proposed that charge transfer from Cu to Ru results in decreased occupancy of the Cu 4s level. This electronic modification makes Cu more "nickel-like," and results in an increase in the binding energy for CO. Similarly Cu/W (36) also exhibits charge transfer to the substrate and an increase in CO binding strength to Cu. In another case where the CO binding energy increases, Ni/Ru (37), an increase in the density of states is observed close to the Fermi level. The increased electron density may result in increased metal-CO backbonding, which in turn would increase the binding energy of CO.

In contrast to the above examples, CO on Ni/W is less strongly bound to the Ni monolayer than to bulk Ni. One explanation for this effect is that the charge transfer observed from Ni to W results in a shift of the Ni d levels, relevant to CO bonding, to higher binding energies (i.e. farther from the Fermi

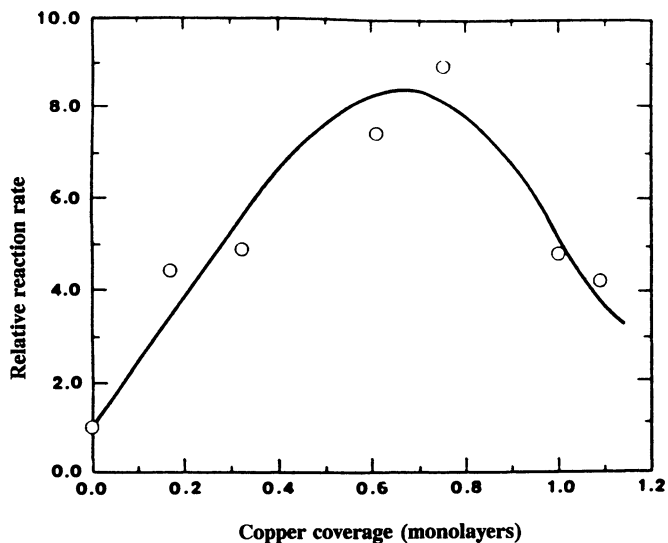


Figure 3. Relative rate of reaction versus surface Cu coverage on Ru(0001) for cyclohexane dehydrogenation to benzene.  $P_T = 101$  Torr.  $H_2/\text{cyclohexane} = 100$ .  $T = 650\text{K}$ . (Reproduced with permission from ref. 10. Copyright 1987 Elsevier.)

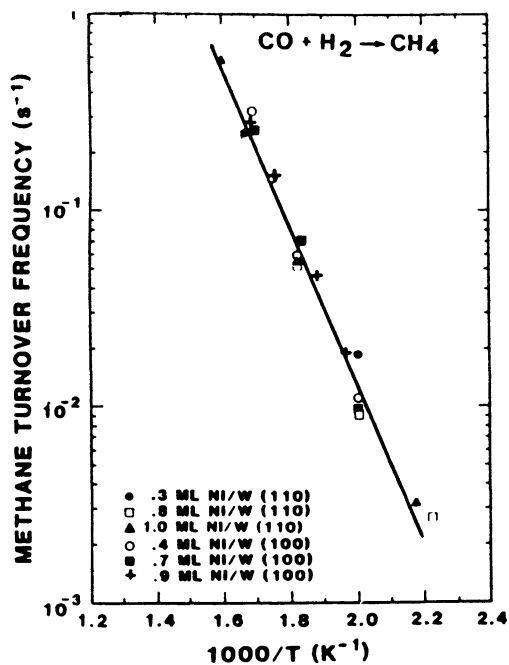


Figure 4. Arrhenius plot for  $CH_4$  synthesis over several different Ni coverages on W(110) and W(100) at a total reactant pressure of 120 Torr,  $H_2/CO = 4/1$ . (Reproduced from ref. 41. Copyright 1987 American Chemical Society.)

level). Indeed, such an effect has been observed in the case of Ni/Nb(110) and Pd/Ta(110) (38). Similarly, results on other group VIII metal - W systems (39-40) have shown a decrease in the CO binding strength.

The catalytic activity of strained layer Ni on W(110) for methanation and ethane hydrogenolysis has been studied as a function of Ni coverage (41). The activity per Ni atom site for methanation, a structure insensitive reaction, is independent of the Ni coverage (Fig. 4) and similar to the activity found for bulk Ni. The activation energy for this reaction is lower on the strained metal overlayer, however, very likely reflecting the lower binding strength of CO on the bimetallic system.

In contrast, ethane hydrogenolysis, which is a structure sensitive reaction over bulk Ni, displayed marked structural effects on the Ni/W system (41). We have observed, as shown in Figure 5, that the specific rate, or rate per surface metal atom, but not the activation energy, is a strong function of metal coverage on the Ni/W(110) surface, suggesting that the critical

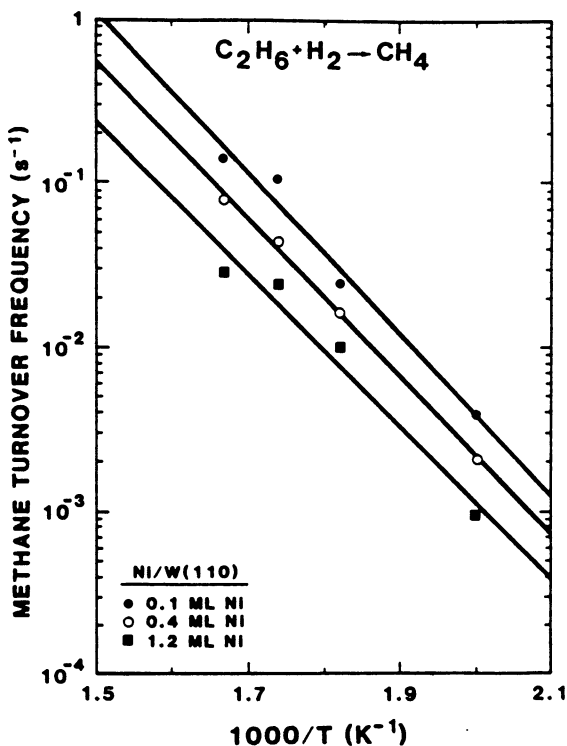


Figure 5. Arrhenius plots of the rates of ethane hydrogenolysis versus Ni coverage on W(110) at a total pressure of 100 Torr,  $H_2/C_2H_6 = 100$ . (Reproduced from ref. 41. Copyright 1987 American Chemical Society.)

reaction step involves the need for a single, sterically unhindered Ni atom. On the Ni/W(100) surface the specific reaction rate was independent of Ni coverage. In addition, the rate on bulk Ni(100), Ni/W(110) in the limit of zero coverage, and Ni/W(100) were all equal, as were the activation energies. This implies that on Ni/W(100) the Ni atom geometry is sufficiently open to allow unhindered access to each Ni atom. Apparently on the Ni/W(110) surface only island edges and individual atoms display activity similar to the Ni(100) surface; the island interiors, in contrast, exhibit behavior similar to Ni(111) which has a much lower specific rate and higher activation energy. As the Ni coverage is reduced, the number of active, Ni(100)-like atoms increases, leading to an increase in the specific rate. The activation energy, however, remains unchanged.

We have studied several other metal overlayers on W(110), W(100), and Ru(0001) substrates (42). Table 1 lists properties of the metal overlayers, and the effect of the substrate on CO chemisorption. In general only the first monolayer grows pseudomorphically, though more than one monolayer may be stable before three dimensional islands are formed (e. g. Cu/Ru grows two stable layers). The binding strength of CO is always altered from the bulk metal, though the magnitude of the effect is seemingly more dependent on the metal overlayer, than on the degree of strain induced by the substrate (represented as the atom density mismatch). As with Ni/W and Cu/Ru, the effect on CO binding energy extends primarily to only the first monolayer; subsequent layers exhibit behavior close to the bulk metal.

Table 1. Comparison of Strained-Metal Overlayer Systems

Adsorbate	Substrate	Atom Density Mismatch/ML	Pseudomorphic/ Epitaxial Layers	Change in CO Desorption T
Cu	Ru(0001)	6%	1/2	50K
Cu	W(110)	20	1/1	80
Ni	W(110)	21	1/1	-50
Ni	W(100)	42	1/1	-50
Ni	Ru(0001)	15	1/1	50
Pd	W(110)	10	1/1	-200
Pd	W(100)	35	2/2	-170
Pd	Ta(110)	18	1/1	-230
Fe	W(110)	9	1/2	-50
Fe	W(100)	35	2/2	-60

#### ACKNOWLEDGMENT

We acknowledge with pleasure the partial support of this work by the Department of Energy, Office of Basic Energy Sciences, Division of Chemical Sciences.

LITERATURE CITED

1. Grimley, T. B.; Torrini, M., J. Phys. Chem. 1973, 87, 4378.
2. Sinfelt, J. H. Bimetallic Catalysts: Discoveries, Concepts, and Applications; John Wiley & Sons: NY, NY, 1983.
3. Schwab, G. M., Disc. Faraday Soc. 1950, 8, 166.
4. Yates, J. T., Jr.; Peden, C. H. F.; Goodman, D. W., J. Catal. 1985, 94, 576.
5. Goodman, D. W.; Yates, J. T., Jr.; Peden, C. H. F., Surf. Sci. 1985, 164, 417.
6. Goodman, D. W.; Peden, C. H. F., J. Catal. 1985, 95, 321.
7. Houston, J. E.; Peden, C. H. F.; Blair, D. S.; Goodman, D. W., Surf. Sci. 1986, 167, 427.
8. Houston, J. E.; Peden, C. H. F.; Feibelman, P. J.; Goodman, D. W., I&EC Fundamentals 1986, 25, 58.
9. Houston, J. E.; Peden, C. H. F.; Feibelman, P. J.; Hamann, D. R., Phys. Rev. Lett. 1986, 56, 375.
10. Peden, C. H. F.; Goodman, D. W., J. Catal. 1986, 100, 520; ibid. 1987, 104, 347.
11. Goodman, D. W.; Kelley, R. D.; Madey, T. E.; Yates, J. T., Jr., J. Catal. 1980, 64, 479.
12. Goodman, D. W. Ann. Rev. Phys. Chem. 1986, 37, 425; Accts. Chem. Res. 1984, 17, 194; J. Vac. Sci. Tech. 1982, 20, 522.
13. Shimizu, H.; Christmann, K.; Ertl, G., J. Catal. 1980, 61, 412.
14. Vickerman, J. C.; Christmann, K.; Ertl, G., J. Catal. 1981, 71, 175.
15. Shi, S. K.; Lee, H. I.; White, J. M., Surf. Sci. 1981, 102, 56.
16. Richter, L.; Bader, S. D.; Brodsky, M. B., J. Vac. Sci. Techn. 1981, 18, 578.
17. Vickerman, J. C.; Christmann, K., Surf. Sci. 1982, 120, 1.
18. Vickerman, J. C.; Christmann, K.; Ertl, G.; Heiman, P.; Himpfel, F. J.; Eastman, D. E., Surf. Sci. 1983, 134, 367.
19. Bader, S. D.; Richter, L., J. Vac. Sci. Technol. 1983, A1, 1185.
20. Park, C.; Bauer, E.; Poppa, H., Surf. Sci., submitted for publication.
21. Goodman, D. W.; Heterogeneous Catalysis (Proceedings of IUCCP Conference), Texas A&M University, 1984.
22. Sinfelt, J. H.; Via, G. H.; Lytle, F. W., Catal. Rev.-Sci. Eng. 1984, 26, 81.
23. Datye, A. K.; Schwank, J., J. Catal. 1985, 93, 256.
24. Bond, G. C.; Turnham, B. D., J. Catal. 1976, 45, 128.
25. Luyten, L. J. M.; Eck, M. V.; Grondelle, J. V.; Hooff, J. H. C. V., Phys. Chem. 1978, 82, 2000.
26. Rouco, A. J.; Haller, G. L.; Oliver, J. A.; Kemball, C., J. Catal. 1983, 84, 297.
27. Haller, G. L.; Resasco, D. E.; Wang, J., J. Catal. 1983, 84, 477.
28. Sinfelt, J. H. J. Catal. 1973, 29, 308.
29. Sachtler, J.W.A.; Somorjai, G.A., J. Catal. 1984, 89, 35.
30. Balooch, M.; Cardillo, M. J.; Miller, D. R.; Stickney, R. E., Surf. Sci. 1975, 50, 263.

31. Berlowitz, P. J.; Goodman, D. W, Surf. Sci. 1987, 187, 463.
32. Balooch, M.; Cardillo, M. J.; Miller, D. R.; Stickney, R. E., Surf. Sci. 1975, 50, 263.
33. Kolaczkiwicz, J.; Bauer, E., Surf. Sci. 1984, 144, 495.
34. Christmann, K.; Schober, O.; Ertl, G., Chem. Phys. 1974, 60.
35. Goodman, D. W.; Yates, J. T.; Madey, T. E., Surf. Sci. 1980, 93, 135.
36. Hamedeh, I.; Gomer, R., Surf. Sci. 1985, 154, 168.
37. Houston, J. E.; White, J. M.; Berlowitz, P. J., Goodman, D. W., Surf. Sci., 1988, 205, 7.
38. Ruckman, M. W.; Strongin, M.; Pan, X., *ibid.*
39. Prigge, D.; Schlenk, W.; Bauer, E., Surf. Sci. 1982, 123, 698.
40. Judd, R. W.; Reichelt, M. A.; Lambert, R. M., to be submitted for publication.
41. Greenlief, C. M.; Berkowitz, P. J.; Goodman, D. W., *J. Phys. Chem.* 1987, 91, 6669.
42. Berlowitz, P. J.; Peden, C. H. F.; Goodman, D. W., Mat. Res. Soc. Symp. Proc. 1987, 83, 161.

RECEIVED July 17, 1989

## Chapter 19

# Studies of Pt Metal Catalysis by High-Resolution Electron Spectroscopy for Chemical Analysis

Tery L. Barr and M. P. Yin

Department of Materials and Laboratory for Surface Studies,  
University of Wisconsin—Milwaukee, Milwaukee, WI 53201

In the present study we report the use of high resolution/acute sensitivity ESCA to examine high surface area alumina matrices after they have been doped with various platinum metals and other ingredients in a manner designed to simulate different preparative and use stages of Pt metal catalysis. Initially described are the electronic properties of the alumina itself. Valence band spectra are used to demonstrate the relatively large ionicity of the Al-O bond and its corresponding effect on acidity. The implanting and the subsequent oxidation of platinum are shown to produce a surface dominated by Pt(+2), rather than Pt(+4), species. Reduction of this system yields Pt<sup>0</sup>, as indicated by the Pt(4d) ESCA spectra. The latter were reported, for the first time, for systems doped in the conventional catalytic range. Certain forms of catalytic abuse and alkali cation addition are also shown to produce a unique, substantial shift in the resulting Pt and/or Pd ESCA spectra. These shifts are found to result from a little known anomaly that sometimes occurs in high resolution ESCA due to the charging and Fermi edge coupling problem.

In the present case we report ESCA examinations of composite systems realized when varying amounts of platinum metals (i.e., Pt or Pd) and other species are doped by some conventional means onto a standard  $\gamma$ -alumina support in a manner designed to simulate systems often employed in Pt metals catalysis (1,2). A unique feature of the present study is that the doping compositions are typical of those of real catalysts, e.g.,  $0.2 < \text{Pt wt\%} < 0.75$ . Generally the Pt metals can be assumed to be the principal active metal species added, although the function of that dopant has been suspected to depend significantly on the other species present (3).

Examples of the latter are demonstrated along with the clarification of certain other questions for bimetallic systems (3,4). It is not our intention to describe a catalytic process, but rather the materials alterations that seem to occur during common set up procedures, such as oxidation and reduction. We will also report on a unique ESCA based method that seems to determine the important feature of metals dispersion in the alumina matrix, a feature that may be disturbed as a result of the "abuse" experienced by a catalyst (1).

### Experimental

As indicated, the range of metals doping employed herein is common to "real" reforming catalysts as reported in the published and patent literature (2). It should be noted that these values are quite different from those generally reported in previous publications dealing with ESCA studies of Pt metal systems simulating the reforming process. In general, those studies examined materials with either unrealistically large compositions (5), or inappropriate (but interesting) supports (6), or ignored altogether the Pt in their analyses (7). This was done because these analyses were plagued by the problem of the blockage of the major ESCA signal for platinum, the Pt(4f) peaks, by the Al(2p). We have succeeded in circumventing this problem by employing extremely long scans of the much weaker (in cross section) Pt(4d) lines (compared to the aforementioned Pt(4f)) and exploiting the relatively high resolution, acute sensitivity and long-time stability of the HP-5950 ESCA located at the Allied Signal Engineered Materials Research Center. This system was equipped with all of the conventional peripheral equipment, plus certain sample handling and treatment chambers and devices, that markedly facilitated this type of study. Of particular importance among the tools was an electron flood gun that was often employed to assist in the ESCA analysis of insulating systems (1).

### Results

Analysis of the Alumina Support. Any analysis of the alumina supported metals catalyst should begin with the alumina itself. Numerous ESCA researchers have examined various aluminas, but they have almost exclusively studied the prominent core level peaks, particularly the Al(2p) lines (1). We have done so as well, and find for all cases (including the former) nothing unusual, except that the Al(2p) binding energies detected in studies of conventional alumina powders (73.8 eV) are generally significantly smaller than many of the binding energies reported for Al<sub>2</sub>O<sub>3</sub> grown as a film on Al<sup>o</sup> (8). Generally, for example, little, if any, difference is detected between the ESCA core level results for different alumina phases (e.g.,  $\gamma$  vs.  $\alpha$ ), and very little can be said about the nature of alumina (compared to other possible support matrices) from these core level results (1).

Recently we have extended analyses of oxides such as alumina to include high resolution, XPS generated, valence band spectra (9,10). These long neglected spectroscopic structures are



relatively weak in size and require very high resolution to yield sufficient reproducibility for useful analysis. Employing the previously mentioned spectrometer we have achieved these conditions and found the resulting spectra to be more revealing than core peaks with respect to studies of chemical features, such as ionicity and acidity (7,8). For example, careful analysis of the valence band spectra for  $\alpha$ -SiO<sub>2</sub> and  $\gamma$ -Al<sub>2</sub>O<sub>3</sub> suggests that the M-O bond (M=Si or Al) of the former is much more covalent than the latter (7,11), see Figure 1. This has led us to conclude that the Si-O-H system may exhibit greater Bronsted acidity than the Al-O-H system, but that the Lewis acidity should be reversed. The degree of these different effects may be directly related to the magnitude of the covalent shift,  $E_c$ , revealed in Figure 1.

Oxidized Material. Most of the systems utilized for the purposes mentioned above are initially formed from oxidized versions of the platinum often placed into the alumina matrix by a quasi ion exchange of a particular platinum complex (1). One of the most popular procedures involves the use of the platinum (+4) acid, H<sub>2</sub>PtCl<sub>6</sub>. Generally this system is then subjected to further oxidation, to ensure a consistency of materials states before subsequent reduction.

We have employed ESCA to examine a number of systems formed in this manner following oxidation, and have always detected essentially the same, somewhat surprising distribution of products. In all cases the principal platinum species found by the ESCA is not Pt(+4), but rather Pt(+2). A representative case is displayed in Figure 2. It should be noted that we are not alone in detecting this "anomaly." Czaran et al. (12) have also determined that hexachloroplatinic acid yields a surface dominated by Pt(+2) species, with the Pt(+4) state retained at the surface only when the hexamine complex is employed. It should also be noted that the enumeration of the Pt(+2) state was achieved by determining the peak binding energies, and comparing those to the values found for other platinum species in various oxidation states (1). This procedure and detailed analysis further suggests that modest amounts of the surface platinum in the oxidized system may be in the Pt(+4) and Pt<sup>0</sup> states, see Figure 2. The latter may, in fact, be distributed subsurface to the Pt(+2), and treatment of the resulting system with ion etching to remove the outer surface seems to suggest that some degree of this Pt(+2) "coating" is occurring.

Metals Reduction and Dispersion. A major question in metals catalysis, and many other fields of materials science, concerns the reduction of the metal(s), perhaps to their zero valent form, e.g., Pt<sup>0</sup>, and the distribution (or dispersion) of the metal throughout the oxide support matrix, e.g., Al<sub>2</sub>O<sub>3</sub> (1,2).

Since the Al<sub>2</sub>O<sub>3</sub>, in question, is a surface insulator, the ESCA examination of these systems must consider the aforementioned charging problem. In addition, since there is some question herein as to the distribution of a conductive metal in this insulator, one must also be cognizant of the more difficult feature generally labeled as differential charging (13).

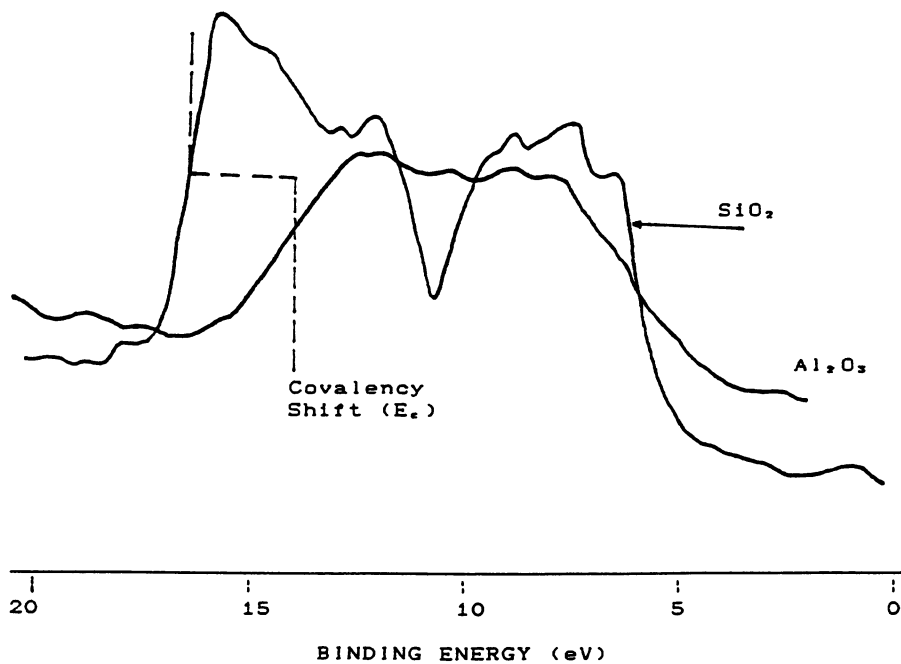


Fig. 1. Overlay of  $\text{SiO}_2$  and  $\text{Al}_2\text{O}_3$  valence bands with leading edges forced to align (at half maximum). Enlarged width of  $\text{SiO}_2$ , primarily due to its enhanced covalency.

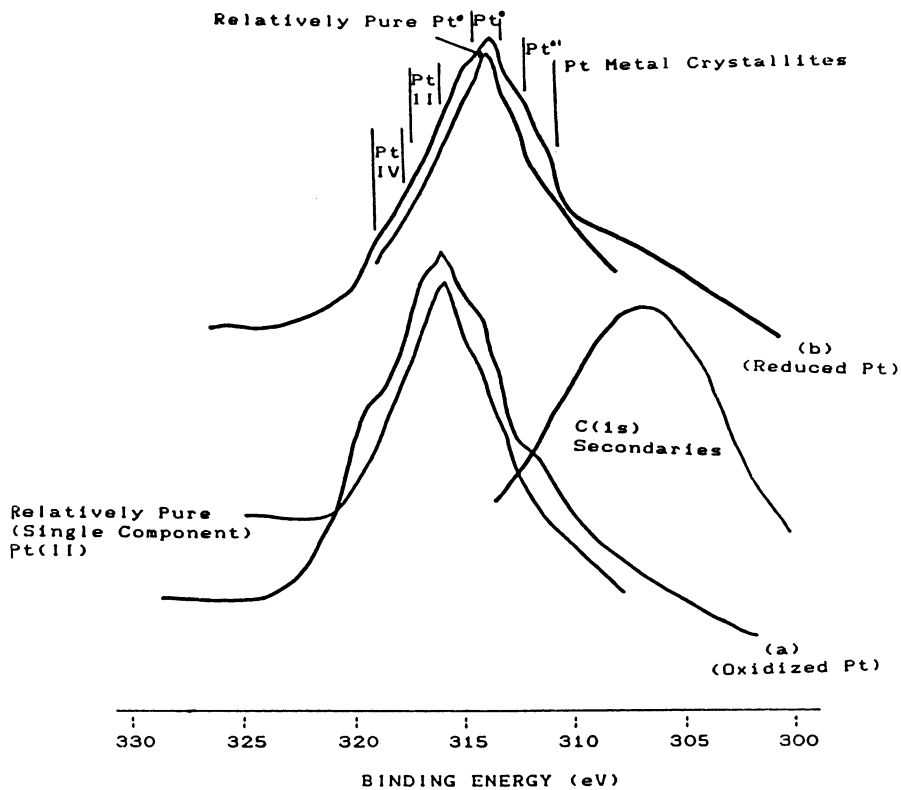


Fig. 2. Pt(4d<sub>5/2</sub>) spectra for select Pt on Al<sub>2</sub>O<sub>3</sub> catalysts.

A detailed description of the charging shift must be reserved for a more appropriate source (1,10,13). Herein we note that charging occurs during the photoelectron process because the negatively charged emissions leave behind positive centers that must be compensated, or they will build into a macroscopic, positive charge. If the emitting surface is a conductor, conduction band electrons will provide the compensation and no shift will occur. If not, however, a positive charging shift will develop. In the latter case, the attributes of the conduction electrons may be simulated by a low energy, electron flood gun, such as the one referred to in the previous section. If properly applied, this device often facilitates the removal of charging, but it should be noted that the standard process does nothing to bring about a coupling of the Fermi edge of the insulating sample and that of the spectrometer (1,9,13). Thus, during standard measurements the Fermi edge of the former may be floating, and the realized binding energy values may be inappropriate.

The latter is obviously the case during ESCA measurements of a doped alumina system. Interjection of conductive metal particles into this insulating matrix may produce the differential charging feature, (13). Thus, if two species, A and B, have distinctly different conductivities, the degree of charging (and Fermi edge coupling) observed will depend upon the relative concentrations and extent of mixing (13). Thus, for a (near) solid solution, if  $[A] \approx [B]$ , a composite value (dominated by the most conductive species) will be realized, whereas, if  $[A]$  or  $[B]$  substantially exceeds the other, the conductive behavior of the major species will predominate.

In our case there is 0.2-0.7 wt% Pt[A], generally well dispersed (essentially dissolved) in a matrix of  $Al_2O_3[B]$ , and the previous argument would suggest a system that exhibits the charging properties of [B], the alumina. Thus, despite the excellent conductivity of  $Pt^0$  when it is a macroscopic continuum, in the present case it will, for all measurable purposes, charge along with the  $Al_2O_3$  matrix, particularly if the  $Pt^0$  is, as suggested, a contiguous (near solid solution) part of the mixture. This has been observed on numerous occasions during ESCA studies of platinum doped alumina systems, where the  $Pt^0$  has been confirmed to be well dispersed by those who (bulk) analyze, and use, these systems (3,14).

If we attempt to compensate for the charging with the use of the electron flood gun, we find that we are able to essentially accomplish this for both the  $Al_2O_3$  and  $Pt^0$ . However, this observation does not readily facilitate ESCA detection of this system, since, as noted above, the relatively strong Pt(4f) lines remain hidden under the dominant Al(2p) peak. Fortunately, in the present case, one may exploit the high resolution and acute sensitivity of the HP ESCA to realize the weak Pt(4d<sub>5/2</sub>) peak, as displayed in Figure 2b for a representative case. This is the first presentation of a Pt ESCA spectrum with this wt% Pt in  $Al_2O_3$ , and several chemical states appear to be present. However, although the spectrum is seemingly not singular, it is dominated by one line that seems to peak at ~ 314.0 eV. This

value is almost identical to that ( $4d_{5/2}$ ) produced by the  $Pt^0$  in a continuous (sheet) of platinum metal (15).

Returning now to our system containing  $\sim 0.5$  wt% Pt doped into  $Al_2O_3$ , we have previously noted that the contiguous dispersion of the platinum may be extensively disturbed by submitting the system to certain forms of physical (and/or chemical) abuse. Such treatment has been recognized often to effect extensive crystallite growth (1-3,13,14). When we have examined such (nondispersed) systems with ESCA, a very peculiar result is observed. We find that the systems seem to charge in a manner that is similar to the contiguous mixture; but, following attempts to use the electron flood gun to remove charging, the components of the alumina behave as expected, but the metals peaks are all significantly shifted, usually to extremely low, seemingly unrealistic binding energies. A typical example for Pt doped  $Al_2O_3$  is displayed in Figure 3.

No certain explanation exists for this effect, but a reasonable rationale (13) seems to be: As the systems are abused, the Pt atoms are induced to cluster into small crystallites that should exhibit the initial vestiges of the behavior of a true metal (valence electron delocalization and formation of a Fermi edge, etc.). These newly formed "clumps" of metal are, seemingly, "awash" in a sea of the  $Al_2O_3$  insulator. (If one were to examine the crystallites microscopically, one would find that the size of these clusters, P, is still very small relative to their separation in the matrix, Q, i.e.,  $P/Q \ll 1$ .) Thus, each unit of platinum metal in this system should have a Fermi edge that is isolated (by the  $Al_2O_3$ ) from the Fermi edge of the spectrometer, and each other, i.e., thermal equilibrium between the Pt clusters and the spectrometer is not established. Since ESCA measurements are still made against the latter's Fermi edge, and the Fermi edge of the former may be floating anywhere relative to that position, the resulting measured binding energies are, therefore, not real. But it should be observed that we primarily find this effect when the metals in question have cloistered into the crystallites, thus imparting to the  $Pt^0$  a metallic character. Further, we have found evidence that suggests that the relative position of this new  $Pt^0$ ' binding energy is not entirely independent, but seems to depend upon the size, shape and positions of the metal crystallites. For reasons that are not entirely understood, this differential charging shift, for most metals, is in a negative binding energy direction. Thus, we find for a thermally abused Pt metal catalyst that it exhibits a substantially negative shift, as for example, seen in Figure 3.

Bimetallic Cases. In addition, we have discovered that a result, perhaps related to this differential charging effect, may, in some cases, be chemically induced. In this regard, we have examined a series of Pd doped-alumina systems that are also infused with different alkali cations. Even without physical abuses, these systems produce the aforementioned negative shift (with respect to "normal"  $Pd^0$ ), and one also finds that the size of the shift seems to depend, in a regular fashion, on which alkali cation is employed (i.e., the relative ionicity of the latter?), see Figure 4. This result seems to suggest two possible explanations. Either the

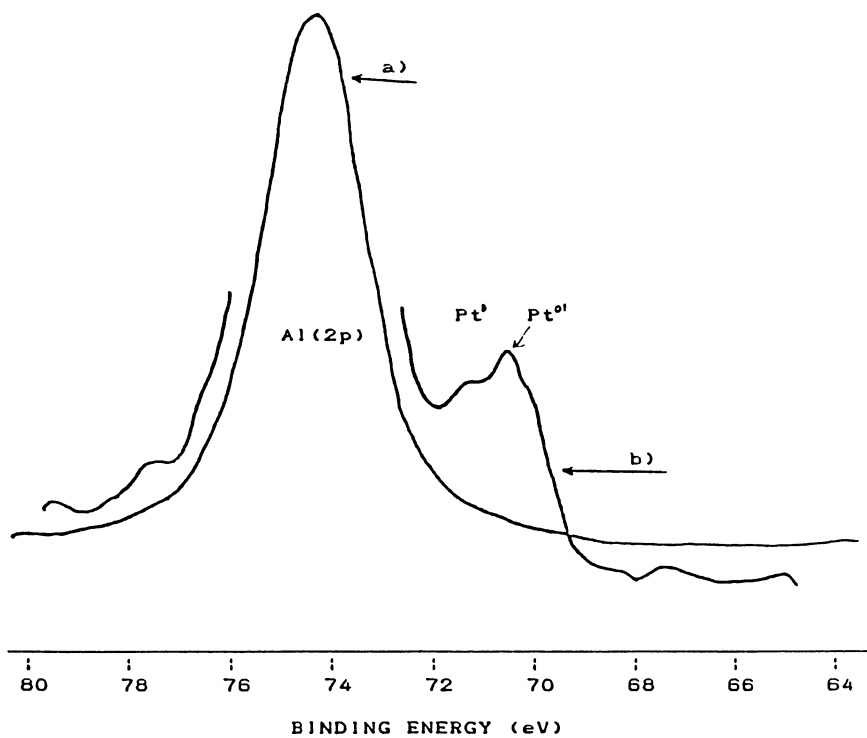


Fig. 3. Example of Pt crystallite ( $Pt^0$ ) growth in  $Pt/Al_2O_3$  catalyst. a) Reduced pre-abuse case (note no visible Pt (4f)). b) Extensively abused.

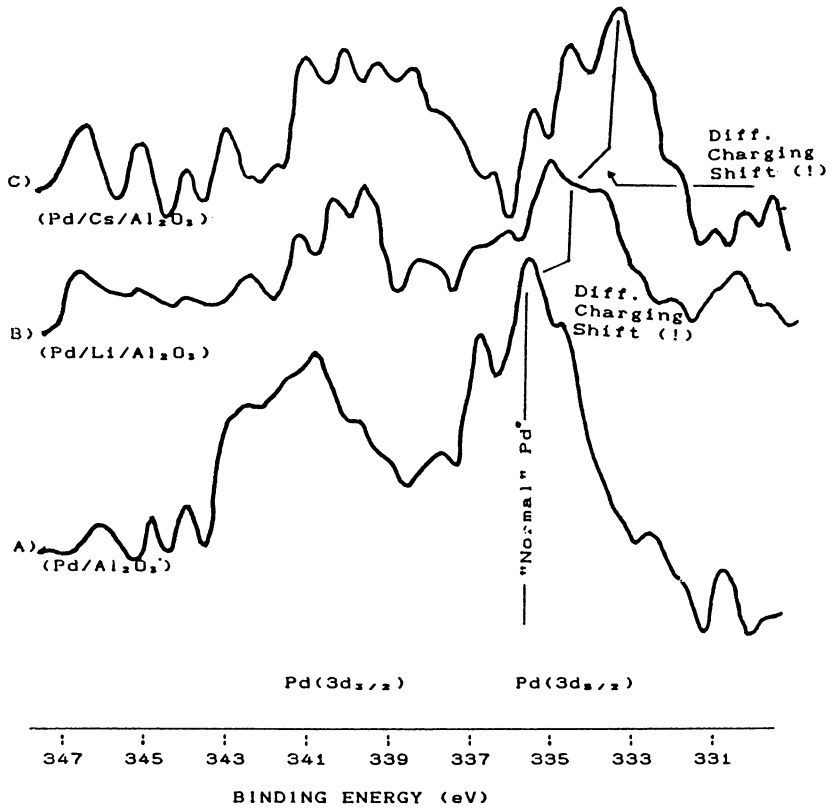


Fig. 4. Example of increase in Pd<sup>0'</sup> (differentially charged Pd) with increased basicity of alkaline dopent.

different cations induce the presence of different sized and shaped Pd clusters, and the effect is as previously explained, or these alkali cations are able to force differing amounts of excess electrons into the partially vacant Pd d bands. At this time we are uncertain of the origins of this effect, but based upon additional, as yet unreported work, we suspect a mixture of both explanations.

Numerous other bimetallic situations may occur in catalysis, perhaps related to the addition of alkali cations. For example, Burch (3) has examined cases where Group 4A species such as Sn are added to the Pt/Cl/Al<sub>2</sub>O<sub>3</sub> reforming combination in order to enhance the stability, and also favorably affect related features. Sexton et al. (7) have examined similar systems with ESCA, and, as noted above, have found that in the common catalytic doping range, e.g., Pt(0.25-0.75 wt%) and Sn(0.4-0.75 wt%), they were able to monitor the behavior of the tin and found that in the oxidized version Sn(+4) species were present, whereas, following reduction, surface Sn(+2) entities persisted (7). We have also examined simulated Pt/Sn catalysts of similar composition and found that reduction yields Sn(II). This was consistent with the arguments of Burch (3), and seemed to be contrary to the alloy formation concept of Sachtler et al. (4b) and Clarke (4a).

### Conclusion

In this report, we have demonstrated how ESCA may be employed to produce detailed (primarily chemical) information about the states of all the components in systems that closely replicate those commonly used in various types of Pt metals catalysts. Beginning with the support matrix (e.g.,  $\gamma$ -Al<sub>2</sub>O<sub>3</sub>), we have demonstrated how XPS valence band studies may be employed in the description of certain bonding features (e.g., covalency/ionicity and, perhaps, types and degrees of acidity) that have been shown to be critical to the choice of these components. We have subsequently demonstrated how high resolution/acute sensitivity ESCA may be employed to circumvent the problem of the blockage of the Pt(4f) lines by the Al(2p) for realistically doped systems. Long time scans of the Pt(4d) have revealed that the surface platinum (introduced as PtCl<sub>6</sub>) in the prerduced system favors the Pt(+2) state even following a traditional oxidation step. ESCA examination of a reduced system containing less than 0.75 wt% Pt and 1.0 wt% Cl on  $\gamma$ -Al<sub>2</sub>O<sub>3</sub> reveals "normal" Pt<sup>0</sup>, when the latter is apparently well dispersed into the alumina. When the platinum is not well dispersed (for example, as a result of extensive abuse) the Pt ESCA signals produce unusual, reproducible, negative shifts after being exposed to the flood gun current, suggesting differential charging behavior. Similar progressive, negative shifts seem to arise in selected Pd catalysts when doped with various alkali metals.

It also should be noted that we have herein, in effect, turned the charging problem around and made it an auxiliary morphological tool. In order to demonstrate the versatility of this tool, we have employed the aforementioned negative shift with cluster formation not only to study metals dispersions, but also to assist in the study of the integrity of thin film interfaces (16), and metals segregation during alloying corrosion (17).



Literature Cited

1. Barr, T. L., in Practical Surface Analysis, Ed. by D. Briggs and M. P. Seah, John Wiley and Sons, Inc., New York, 1983; Chapter 8.
2. See for example, H. Heinemann, in Catalysis: Science and Technology, Eds. J. R. Anderson and M. Boudart, Springer-Verlag, Berlin, 1981; pp. 1-41.
3. Burch, R., *J. Catal.* 1980, 71, 348, 360.
- 4a. Sachtler, W. M. H.; Van Santen, R. A., *Adv. in Catal.* 1977, 26, 69.
- 4b. Clarke, J. K. A.; Creamer, A. C. M., *Ind. Eng. Chem. Prod. and Dev.* 1981, 20, 575.
5. Bouwman, R.; Biloen, P., *J. Catal.* 1977, 48, 209.
6. Biloen, P.; Helle, T. N.; Verbeek, H.; Dautzenberg, F. M.; Sachtler, W. M. H., *J. Catal.* 1980, 63, 112.
7. Sexton, B. A.; Hughes, A. E.; Foger, R., *J. Catal.* 1984, 88, 466.
8. Cocke, D. L.; Johnson, E. Q.; Merrill, R. P., *Catal. Rev.* 1984, 26.
9. Barr, T. L.; Chen, L. M.; Mohsenian, M.; Lishka, M. A., *J. Amer. Chem. Soc.*, in press.
10. Barr, T. L.; Chen, L. M., submitted to *J. Phys. Chem.*
11. Barr, T. L.; Bagus, P. S., submitted to *Phys. Rev. B*.
12. Czarán, E.; Finster, J.; Schnabel, K. H., *Z. Anorg. Abg. Chem.* 1978, 443, 175.
13. Barr, T. L., to be presented National AVS Meeting, Atlanta, Ga., Oct. 1988, to be published.
14. Dautzenberg, F. M.; Walters, H. B. M., *J. Catal.* 1984, 51, 267 (1984).
15. Barr, T. L., *J. Phys. Chem.* 1978, 82, 1801.
16. Barr, T. L., *Applications of Surface Science*, 1983, 15, 1.
17. Barr, T. L.; Hackenberg, J. J., *J. Amer. Chem. Soc.* 1982, 104, 5390.

RECEIVED July 27, 1989

## Chapter 20

# Characterization of Supported Metal Catalysts by X-ray Photoelectron Spectroscopy

### The Problem of the Binding Energy Reference

Robert F. Hicks

Department of Chemical Engineering, University of California,  
Los Angeles, CA 90024-1592

The energy levels for x-ray photoemission from metal particles on insulating supports are described. Metal particles on insulators are not grounded to the spectrometer. The vacuum levels of the metal particle and the insulator align at some unknown potential relative to the vacuum level of the spectrometer. Referencing the binding energy to an internal standard, as is usually done for catalysts, introduces two unknowns in the binding energy equation: the work function of the metal and the work function of the internal standard. If the support is a semiconductor or semimetal, or the metal particles are small (<25 angstroms), additional unknowns are introduced. These observations are confirmed by recent experiments. X-ray photoemission studies of metal-support interactions are reinterpreted in light of these results.

In the early seventies, x-ray photoelectron spectroscopy (XPS) emerged as an important tool for characterization of catalysts (1-3). The principle advantages of XPS are that it identifies the elemental composition of the sample surface, and it gives some indication of the chemical state of these elements. The latter capability has been exploited most often in catalysis research.

The goal of catalyst development is to understand how the chemical and physical properties of the catalyst affect its activity and selectivity for a desired reaction. For a supported metal, the variables affecting its function are the metal composition, the metal particle size, the particle shape, the structure of the metal surface, the oxidation state of the metal, the composition of the support, and the presence of promoters or poisons. These variables influence catalytic activity by altering both the structure and electronic state of the metal. The relative importance of the structure effect versus the electronic effect has been a question that catalyst researchers have long sought to answer.

Many years ago Schwab proposed that the reactivity of a metal could be modified through an electronic interaction with the support (4,5). Boudart and other researchers have presented a strong case for such an effect occurring in the Pt/Y zeolite system (6). Electronic interactions have been postulated for other systems exhibiting metal-support interactions: group VIII metal/TiO<sub>2</sub> (Strong-Metal-Support-Interaction) (7,8); Pd/La<sub>2</sub>O<sub>3</sub> (9); and Pt/WO<sub>3</sub>/SiO<sub>2</sub> (10). Much evidence has been accumulated to show that these metal-support interactions result in partial covering of the metal crystallites by the oxide support (10-19). To what extent the oxide patches interact electronically with the surrounding exposed metal surface remains unclear.

X-ray photoelectron spectroscopy has been used to investigate metal-support interactions (9,10,18,20–25). In these studies, it was assumed that a shift in the binding energy of the metal particles is indicative of electron transfer with the support. However, this interpretation hinges on an absolute calibration of the binding energy scale for the series of samples (or supports) being tested. The zero point on the binding energy scale is an unresolved issue for supported metal catalysts. The purpose of this paper is to delineate those factors affecting the position of the metal binding energy in the photoelectron spectrum of the catalyst. We will show that this position cannot be established with any degree of confidence.

### Photoemission From Insulators

In handbooks and review articles on XPS, there are very nice, accurate descriptions of the energy transitions which occur during photoemission from metals (1,26–29). Unfortunately, a metallic catalyst is comprised of 95% or more support, and this support is usually insulating. Photoemission from an insulator is fundamentally different from the process for a metal (30,31). A metal grounds itself to the sample holder, so that the Fermi levels of the sample and spectrometer are equilibrated. The Fermi level provides an unambiguous zero for the energy scale. A schematic of the energy levels for photoemission from a metal is shown in Figure 1. Shifts in the core levels of a metal sample are recognizable as changes in chemical composition (an initial state effect). Thus, the formation of an oxide layer on the surface of aluminum can be observed by a 2.5 eV increase in the Al 2p binding energy (30).

An insulator, on the other hand, has an ill-defined Fermi level which does not equilibrate with the spectrometer. Instead, the vacuum level of the insulator ( $E_V^I$ ) aligns with the local electrostatic potential surrounding its surface. An insulator more than a micron thick (which is the case for most catalyst samples analyzed by XPS) will not be within the local potential of the metal sample holder. The insulator will be separated from the spectrometer vacuum level ( $E_V^S$ ) by some voltage ( $V_p$ ) (30). This voltage will depend on the geometry of the sample holder and on the energy and flux of electrons from the x-ray source, the flood gun, the sample itself, and all other sources within the chamber. The potential  $V_p$  cannot be reliably measured.

A metal particle placed on top of an insulator will also align itself with the insulator vacuum level. A schematic of the energy levels for photoemission from a metal on an insulator are shown in Figure 2. The diagram assumes that the electrostatic field is uniform across the sample surface. Since the spectrometer is grounded, the kinetic energy of the photoelectron is measured relative to the spectrometer vacuum level, which is separated by an unknown  $V_p$  from the sample vacuum level. If the metal particle is placed on a semiconductor or a semimetal, the Fermi levels of the spectrometer, substrate and metal particle will attempt to align themselves with varying degrees of success. In this case, the Fermi level of the metal particle will float relative to the Fermi level of the spectrometer. Another alternative is for the electrostatic field to vary across the sample surface. This will give rise to multiple peaks for photoemission from a single energy level.

An energy balance of the photoemission process can be constructed for the two limiting cases shown in Figures 1 and 2:

Metal

$$E_B^M = h\nu - E_{kin}^M - \phi_s \quad (1)$$

Metal on Insulator

$$E_B^M = h\nu - E_{kin}^M - \phi_M + V_p \quad (2)$$

where  $E_B^M$  is the metal binding energy,  $E_{kin}^M$  is the metal photoelectron kinetic energy,  $\phi_s$  is the spectrometer work function, and  $\phi_M$  is the metal particle work function.

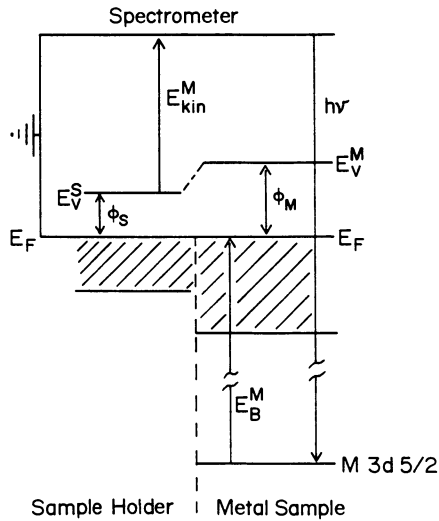


Figure 1. A schematic of the energy levels for photoemission from a metal sample.

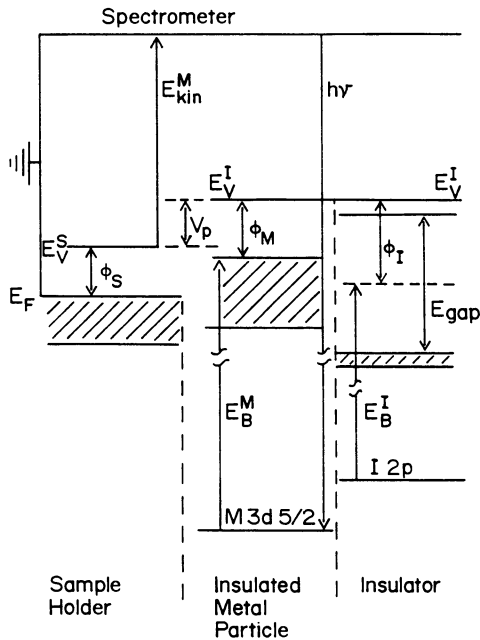


Figure 2. A schematic of the energy levels for photoemission from a large metal particle on an insulator.

If one is confident that the catalyst support is an insulator, then equation (2) can be used to estimate the binding energy of the metal. However, some independent measurement is needed to obtain values of  $\phi_M$  and  $V_p$ . A value for the metal work function cannot be assumed a priori. The work function can vary  $\pm 0.5$  eV depending on the structure of the surface and the coverage of adsorbed molecules (32). As stated earlier,  $V_p$  depends on a number of variables which are difficult to measure.

It has been suggested that these problems can be overcome by using an internal standard, such as the C 1s peak of the carbon impurity, or the Au 4f 7/2 peak of vapor deposited gold (31,33). If equation (2) holds for the internal standard as well, the unknown  $V_p$  can be eliminated by subtraction:

$$E_B^M - E_B^{Au} = E_{kin}^{Au} - E_{kin}^M + \phi_{Au} - \phi_M \quad (3)$$

However, equation (3) still contains two unknowns: the work function of the metal and the work function of the gold deposit. A multilaboratory study has shown that neither carbon nor gold provide a suitable internal standard for catalyst supports (34). Alternatively, the binding energy scale has been referenced to a core level of the support metal cation, for example, the Si 2p peak of silica. This is no improvement. The work function of a high surface area, amorphous catalyst support has never been measured.

#### Photoemission from Small Metal Clusters on Insulators

So far the discussion has focused on large metal particles on insulators. These particles exhibit "bulk-like" electronic properties: their valence band is similar to the valence band of a  $1 \text{ cm}^2$  metal foil. Ultraviolet photoemission studies have shown that the "bulk-like" band structure is attained for particles larger than 25-50 angstroms in diameter (35). X-ray photoemission from metal clusters smaller than 25 angstroms in diameter is even more problematic than for large particles. When clusters are deposited on insulating substrates, positive shifts in the metal binding energies are observed with decreasing cluster size. These shifts result from a number of competing phenomena (35-41): the charge on the cluster during the lifetime of the core hole, the reduced screening of the core hole, the decomposition of the valence band, and the rehybridization of the valence orbitals. The first two are final state effects, while the latter two are initial state effects. The final state cluster charge can dominate the binding energy shift, and extends over a range of sizes where the cluster exhibits metallic behavior, i.e., 10 to 25 angstroms (40,41). The insulating support will reduce the magnitude of the cluster charge by forming an opposite image charge. The image charge will depend on the cluster-substrate geometry and the polarizability of the substrate (40).

Recent experiments by Citrin and coworkers (41) have clarified the role of the support in photoemission from small metal clusters. They condensed several monolayers of krypton onto either platinum or sodium metal substrates. By varying the thickness of the krypton from one to ten monolayers, the surface could be converted from metal to semimetal to insulator. The krypton peak position provides a direct measure of the sample vacuum level (32). The krypton layers are thin, less than 10 monolayers, so that the vacuum level is determined by the metal substrate. Onto the krypton layers, sodium clusters were deposited at varying coverages. Shifts in the Kr 4s and Na 2p binding energies were recorded relative to the Fermi level of the grounded substrate.

The results obtained by Citrin and coworkers are shown in Figure 3. For sodium clusters on a metal support (wig1 ML Kr/Pt, filled circles), the Kr 4s binding energy decreases with cluster coverage. This shows that the Fermi levels of the sodium and platinum equilibrate. As the sodium is added, the work function decreases from the value for platinum to the value for a sodium film. Conversely, the Na 2p peak position does not shift with cluster coverage. The rapid electron transfer between the sodium and platinum prevents any accumulation of charge on the cluster in the photoemission final state (41).

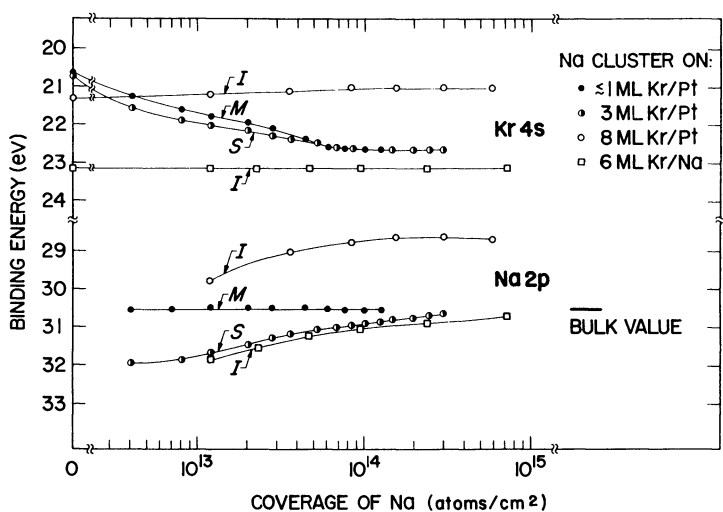


Figure 3. The dependence of the Kr 4s and Na 2p binding energies on the coverage of sodium, the thickness of krypton, and the substrate. (Reproduced with permission from Ref. 41. Copyright 1987 The American Physical Society.)

For sodium deposited on insulating supports (8 ML Kr/Pt, open circles; 6 ML Kr/Na, open squares), the Kr 4s peak position does not change with sodium cluster coverage. Here, the krypton keeps the clusters from transferring charge with the underlying metal. Proof that the metal substrate determines the vacuum level is demonstrated by the shift in the Kr 4s peak when platinum (open circles) is substituted for sodium (open squares). The 2 eV shift is approximately equal to the work function difference between platinum and sodium metal. Since the sodium clusters on the insulating krypton are aligned with the vacuum level, the Na 2p lines also maintain a constant 2 eV separation for the two different substrates used. In this particular experiment, the vacuum level is known and we can "correct" the position of the Na 2p line. The increasing Na 2p binding energy with decreasing cluster size can be attributed to the positive charge left on the cluster in the core ionized final state.

Semimetal or semiconductor supports were also simulated by depositing 3 monolayers of krypton on platinum (half filled circles in Figure 3). In this case the results are intermediate between metal and insulator. The Kr 4s peak shifts with cluster coverage, indicating a decrease in the substrate work function. This occurs because the sodium clusters are able to transfer charge with the platinum and are grounded to it as in the case of a metal support. At the same time, the Na 2p peak shifts to higher binding energy with decreasing cluster size. This indicates that the clusters are charged in the photoemission final state as in the case of an insulating support. An explanation of why the clusters can be grounded to the semimetal substrate, but still accumulate a final state cluster charge is given in reference 41.

The significance of these results for catalysts comprised of small metal clusters is twofold: (1) The clusters will exhibit large positive binding energy shifts that are simply an artifact of the photoemission process, i.e., the charge resulting from the ionized core. This final state charge is sensitive to the support composition through its image charge. (2) On semiconductor or semimetal supports, the cluster Fermi level may drift towards that of the support and spectrometer, creating a partially charged condition for the initial state of the system.

#### Implications for Metal-Support Interactions

The results of XPS studies of metal-support interactions (9,10,18,20-25) can be re-examined in light of the analysis presented above. All of the binding energy measurements made in these studies were referenced to an internal standard. For large metal particles, the core level shifts may be explained by any combination of the following:

- a. the binding energy of the metal is affected by a metal-support interaction.
- b. the work function of the metal is affected by a metal-support interaction, or a change in the structure of the metal surface.
- c. the work function of the reference material changes.
- d. the conductivity of the support changes.

For small metal clusters, the core level shifts may be explained by all of the above plus a final state effect, i.e., the charge on the ionized cluster. In an XPS experiment, it is impossible to distinguish between these different phenomena. Therefore, binding energy shifts, or a lack thereof, cannot be taken as evidence for or against an electronic interaction with the metal.

In spite of this drawback, there is still much to be gained from XPS characterization of supported metal catalysts. Among these are the interconversion of metal salts into oxide and metal during catalyst pretreatment, the identification of poisons, and the distribution of metal within a zeolite or a porous pellet.

### Acknowledgments

The author wishes to thank T. H. Fleisch for his strong support of this work, J. Z. Shyu, J. Schreiner, and Amoco Corporation for many revealing XPS experiments, and P. H. Citrin for helpful discussions and for the use of his data.

### Literature Cited

1. Delgass, N. W.; Hughes, T. R.; Fadley, C. S. Catal. Rev. 1970, **4**, 179.
2. Hercules, D. M. Anal. Chem. 1970, **42**, 20A.
3. Brinen, J. S. Accts. Chem. Res. 1976, **9**, 86.
4. Schwab, G. M. Trans. Faraday Soc. 1946, **42**, 689.
5. Schwab, G. M. Discuss. Faraday Soc. 1950, **8**, 166.
6. Boudart, M.; Djega-Mariadassou, G. Kinetics of Heterogeneous Catalytic Reactions; Princeton University Press: Princeton, NJ, 1984.
7. Tauster, S. J.; Fung, S. C.; Baker, R. T. K.; Horsley, J. A. Science 1981, **211**, 1121.
8. Horsley, J. A. J. Amer. Chem. Soc. 1979, **101**, 2870.
9. Fleisch, T. H.; Hicks, R. F.; Bell, A. T. J. Catal. 1984, **87**, 398.
10. Fleisch, T. H.; Bell, A. T.; Regalbuto, J. R.; Thomson, R. T.; Lane, G. S.; Wolf, E. E.; Hicks, R. F. Stud. Surf. Sci. Catal. 1988, **38**, 791.
11. Santos, J.; Phillips, J.; Dumesic, J. A. J. Catal. 1983, **81**, 147.
12. Dumesic, J. A.; Stevenson, S. A.; Sherwood, R. D.; Baker, R. T. K. J. Catal. 1986, **99**, 79.
13. Belton, D. N.; Sun, Y. M.; White, J. M. J. Phys. Chem. 1984, **88**, 5172.
14. Resasco, D. E.; Haller, G. L. J. Catal. 1983, **82**, 279.
15. Hicks, R. F.; Yen, Q. J.; Bell, A. T. J. Catal. 1984, **89**, 498.
16. Rieck, J. S.; Bell, A. T. J. Catal. 1986, **99**, 262.
17. Rieck, J. S.; Bell, A. T. J. Catal. 1986, **99**, 278.
18. Regalbuto, J. R.; Fleisch, T. H.; Wolf, E. E. J. Catal. 1987, **107**, 114.
19. Regalbuto, J. R.; Allen, C. W.; Wolf, E. E. J. Catal. 1987, **108**, 304.
20. Vedrine, J. C.; Dufaux, M.; Naccache, C.; Imelik, B. J. Chem. Soc. Faraday Trans. I 1978, **74**, 440.
21. Foger, K.; Anderson, J. R. J. Catal. 1978, **54**, 318.
22. Kao, C. C.; Tsai, S. C.; Bahl, M. K.; Chung, Y. W.; Lo, W. J. Surf. Sci. 1980, **95**, 1.
23. Sexton, B. A.; Hughes, A. E.; Foger, K. J. Catal. 1982, **77**, 85.
24. Chien, S. H.; Shelimov, B. N.; Resasco, D. E.; Lee, E. H.; Haller, G. L. J. Catal. 1982, **77**, 301.
25. Huizinga, T.; Van T. Blik, H. F. J.; Vis, J. C.; Prins, R. Surf. Sci. 1983, **135**, 580.
26. Seigbalm, K.; Nordling, C.; Fahlman, A.; Nordberg, R.; Hamrin, K.; Hedman, J.; Johansson, G.; Bergmark, T.; Karlsson, S. E.; Lindgren, I.; Lindberg, B. Nova Acta Regiae Societatis Scientiarum Upsaliensis Ser. IV 1967, Vol. 20. p. 1.
27. Fadley, C. S. In Electron Spectroscopy: Theory, Techniques, and Applications; Brundle, C. R.; Baker, A. D., Eds.; Academic Press: New York, 1978.
28. Delgass, W. N.; Haller, G. L.; Kellerman, R.; Lunsford, J. H. Spectroscopy in Heterogeneous Catalysis; Academic Press: New York, 1979.
29. Feldman, L. C.; Mayer, J. W. Fundamentals of Surface and Thin Film Analysis; Elsevier Science Publishing: New York, 1986.



30. Lewis, R. T.; Kelley, M. A. *J. Electron Spectrosc. Rel. Phenom.* 1980, **30**, 105.
31. Edgell, M. J.; Baer, D R.; Castle, J. E. *Appl. Surf. Sci.* 1986, **26**, 129.
32. Wandelt, K. *Stud. Surf. Sci. Catal.* 1987, **32**, 280.
33. Evans, S. In *Handbook of X-ray and Ultraviolet Photoelectron Spectroscopy*; Briggs, D., Ed.; Heyden: Philadelphia, PA, 1977.
34. Madey, T. E.; Wagner, C. D.; Joshi, A. *J. Electron Spectrosc. Rel. Phenom.* 1977, **10**, 359.
35. Takasu, Y.; Unwin, R.; Tesche, B.; Bradshaw, A. M.; Grunze, M. *Surf. Sci.* 1978, **77**, 219.
36. Mason, M. G. *Phys. Rev. B* 1983, **27**, 748.
37. Citrin, P. H.; Wertheim, G. K. *Phys. Rev. B* 1983, **27**, 3176.
38. Cheung, T. T. P. *Surf. Sci.* 1984, **140**, 151.
39. Parmigiani, F.; Kay, E.; Bagus, P. S.; Nelin, C. J. *J. Electron. Spectrosc. Rel. Phenom.* 1985, **36**, 257.
40. Wertheim, G. K.; DiCenzo, S. B.; Buchanan, D. N. E. *Phys. Rev. B* 1986, **33**, 5384.
41. Qiu, S. L.; Pan, X.; Strongin, M.; Citrin, P. H. *Phys. Rev. B* 1987, **36**, 1292.

RECEIVED April 27, 1989

## Chapter 21

# Catalyst Characterization by Infrared Spectroscopic Methods

J. B. Peri

Department of Chemical Engineering, Northeastern University,  
Boston, MA 02115

Infrared spectroscopic methods are highly effective for characterization of catalyst surfaces. Improved understanding resulting from infrared studies has contributed significantly to catalyst development in the past and has the potential for even greater future contributions. Improvements in spectrometers and techniques have heightened interest in infrared characterization of catalysts, but possible problems, both experimental and theoretical, should be recognized. Simplest subjects for routine characterization are surface groups, acid sites, and "strained" bonds. Supported metals, although highly important, are usually more difficult to characterize.

Although infrared spectroscopy has been widely used for characterization of catalyst surfaces for over thirty years, many reviews (1-4), books (5-7) and articles attest to its continued popularity. Past applications of this technique in studies of commercially important catalysts have in some instances (e.g. refs. 7,16) led to improved understanding of these catalysts which has aided catalyst development or led to better pretreatment procedures. The prospects for important contributions to catalyst development from future infrared studies are very bright. Understanding remains imperfect, however, and factors other than surface chemistry are often vitally important in practical catalysts. Improvements in spectrometers and computer treatment of spectral data have in recent years greatly increased the convenience and sensitivity of infrared characterization and enhanced interest in the use of infrared for routine analytical characterization of catalysts. Infrared can, of course, give the same information on bulk composition of solid catalysts as that obtainable for other solids. It can also be a highly sensitive and gentle, non-destructive technique for surface

characterization, occasionally under reaction conditions. Owing to strong absorption of infrared by the support, however, typical transmission infrared studies of oxide-supported catalysts are usually limited to the region above  $1000\text{ cm}^{-1}$ , and conducting supports, such as carbon, may make infrared study impractical. Raman spectroscopy can provide additional information in favorable cases. Diffuse-reflectance, emission, photoacoustic, and other related spectroscopic methods also offer potential advantages, particularly in ease of sample preparation, but transmission methods are preferred when they can be used and quantitative comparisons are sought (2.4).

#### Experimental Considerations

Use of transmission infrared (either Fourier transform or dispersive) in surface studies usually imposes special requirements on sample preparation. Infrared is inherently a bulk technique, and the surface species of interest usually represent only a small fraction of the material in the infrared beam. Samples must normally be fairly thick, to provide sufficient surface, uniform thickness, and adequate mechanical strength. High scattering losses with typical commercial catalysts result in low signal-to-noise ratios in spectra. KBr disks or oil mull techniques cannot be used to reduce scattering losses without modifying the surface and rendering it inaccessible for further adsorption studies. Signal averaging, or other techniques, can largely offset energy losses caused by scattering, but improved methods of preparing thin samples are still needed. At present, samples are commonly prepared by the "pressed disk" method, in which a powder is pressed in a stainless steel die, without a binder, to produce a self-supporting disk. Typical "thicknesses" range between 5 and  $20\text{ mg/cm}^2$ . Thinner disks would usually be preferable. Adhesion of samples to the die can be troublesome, but use of gold-plated dies can minimize this problem. Pressing samples between sheets of paper or precalcining before pressing can sometimes also prove helpful. Other procedures can be used. Spraying a slurry, or depositing a thin powder layer, on a infrared-transparent window can provide thinner samples and better temperature control than the pressed disk method (8), but potential problems include interaction of the catalyst with the supporting window during high-temperature treatments and non-uniform, irreproducible thickness. Samples have also been successfully prepared by pressing powders into metal screens and in other ways.

A suitable infrared cell must be used for study of catalyst surfaces under controlled conditions. Many cell designs have been published, but no cell design is ideal. Cells made of Pyrex and fused quartz are usual. A cell for high-pressure infrared study must be made of metal, which entails possible problems with metal contamination. Even when a cell does not produce contaminants, metals from catalyst samples can be deposited on cooler portions of the cell via formation of volatile oxides, carbonyls, etc.. These metals may again form carbonyls or other volatile compounds during

subsequent experiments and contaminate later samples. Blanks must be run, and cells must be cleaned or replaced if metal contamination is likely. Sample movement out of the infrared beam is important for obtaining spectra of the gas phase or material on cell windows, but reproducible sample positioning is vital, particularly in Fourier transform infrared (FTIR) studies. Combination of infrared with gravimetric or other techniques is desirable, but the added complexity of cells permitting gravimetric measurements has limited their use. A major need exists for better gasketing materials and cements bakeable to at least 500 C for attaching cell windows. Cells can permit characterization under high-vacuum or high pressure and under static or flow conditions. Ultrahigh vacuum is seldom needed in studies of high-area catalysts, but trace impurities in gases used in flow experiments can lead to problems.

Either FTIR or computerized dispersive spectrometers can be effective for infrared surface characterization. (Even noncomputerized dispersive spectrometers are often still useful.) Their relative merits depend heavily on the particular application and, of course, on practical difficulties in obtaining economical service on "obsolete" instruments. FTIR is not a panacea. FTIR spectrometers give more-accurate frequencies and, in principle, major advantages in energy throughput, permitting faster recording of a spectrum, of major importance in kinetic studies (3,9). Fast recording of a complete spectrum is seldom needed in surface characterization, however. Other factors can be more important (4). FTIR is a single beam technique, and an ability to accurately subtract (or "ratio") a background can be extremely important in catalyst studies. Problems with "stray light", once thought to be non-existent with FTIR, have in some instances been quite serious, causing actual inversion of absorption bands in the OH-stretching region. Other problems can be caused by a changing background. This can be particularly troublesome in in-situ infrared studies of catalytic reactions. A quickly-obtained spectrum may not be useful if a changing background must be subtracted before useful information is obtained. The problem becomes worse if many scans must be averaged to produce good spectra. The noise level of FTIR spectrometers is much worse at the ends of the spectrum (including the important O-H and C-H stretching regions) than in the center, and the use of MCT (mercury-cadmium-telluride) liquid-nitrogen-cooled detectors or cutoff filters is often essential for studies above 2500  $\text{cm}^{-1}$ . Computer treatment of spectra has simplified quantitative analyses, but pitfalls exist for the unwary in subtraction of backgrounds and when dealing with broadened or shifted bands.

Adsorbed molecules have long been used as "probes" to provide information on surface sites in adsorption studies, but potential problems exist in the use of such "probes". Pure reagents are obviously essential, but it is easy to underestimate possible effects of trace contaminants in probe gases or vapors. A typical experiment can expose a catalyst sample to a large excess of a probe. After appreciable contact time, trace impurities can adsorb to a highly observable extent. Such impurities include metal

carbonyls, commonly found in "pure" CO, and water, often present in pyridine and other nitrogen bases. Problems with trace impurities have become more serious as the sensitivity of infrared characterization has increased.

Pretreatment is extremely important in determining surface chemistry. Samples must be carefully prepared, dried, oxidized, reduced, and kept in the desired final state until admission of probe molecules and recording of spectra. Seemingly minor differences in preparation or pretreatment can produce major differences in the surface chemistry of many catalysts. Adsorbable impurities in conventional high vacuum systems do not usually seriously contaminate typical high-area catalyst samples. If, however, samples stand for many hours significant changes can often be observed, particularly with reduced supported metals.

### Typical Important Applications

#### Characterization of Surface Groups on Supports and Catalysts.

Surface groups, such as -OH,  $-\text{NH}_2$ ,  $\text{CO}_3^{2-}$ , etc., which give bands in an accessible spectral region are usually readily detectable and identifiable. Pretreatment may merely consist of evacuation at desired temperatures (using a liquid-nitrogen-cooled trap to remove desorbed water). Deconvolution and detailed interpretation of spectra can present major problems, however.

As illustrated in Figure 1, many bands can appear in hydroxyl spectra of zeolites and other catalysts. Deconvolution can be aided by progressive drying and selective exchange of hydroxyl groups with deuterated compounds. Broad underlying bands can complicate deconvolution and lead to erroneous conclusions as to relative rates of disappearance of different types of hydroxyl groups. Even after satisfactory deconvolution, determining the nature and origin of the different types of hydroxyl groups responsible for the bands usually still poses problems.

Characterization of Surface Acid Sites. Characterization of surface acidity was one of the first successful applications of infrared in catalyst studies (1). Catalyst acidity is typically a function of surface hydration, and water is relatively easy to remove.

Desorption of water often converts Bronsted to Lewis acids, and readsorption of water can restore Bronsted acidity. Probe molecules, such as ammonia, pyridine, etc., are used to evaluate Bronsted and Lewis acidity. These compounds may contain water as an impurity, however. Water produced by reduction of metal oxides can also be readsorbed on acid sites. Probe molecules can in some cases react on surface acid sites, giving misleading information on the nature of the original site. Acidity, and accessibility, of hydroxyl groups or adsorbed water on zeolites and acidic oxides can vary widely. Study of adsorbed nitrogen bases is very useful in characterization of surface acid sites, but potential problems in the use of these probes should be kept in mind.

Figure 2A shows hydroxyl spectra (after background subtraction) typical of highly-dried ZSM-5 zeolite. The acidities of the

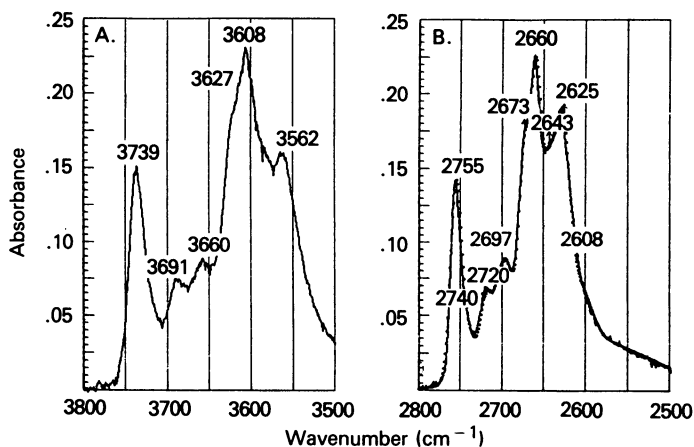


Figure 1. Hydroxyl and Deuteriohydroxyl bands for a "US-Y" zeolite. A. US Sieve steamed 65 hr at 500 C and dried in vacuum at 500 C. B.- A. after exchange with D<sub>2</sub>O and redrying at 500 C.

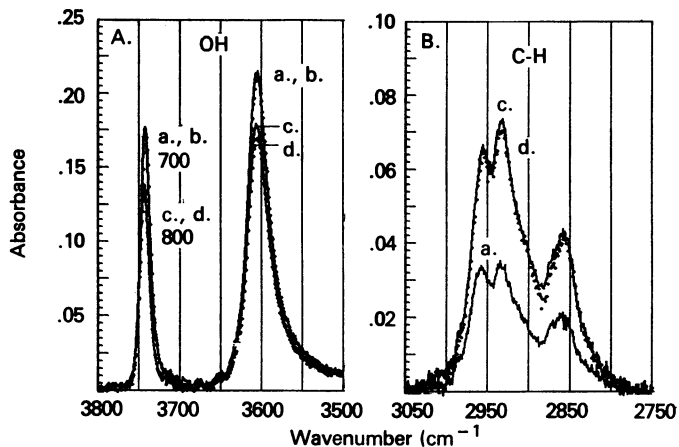


Figure 2. A. Hydroxyl bands on a ZSM-5 zeolite (1.35% Al<sub>2</sub>O<sub>3</sub>). Predried: a. 700 C, 1 hr.; b. 700 C, 2 hr.; c. 800 C, 1.5 hr.; d. 800 C, 3 hr. B. C-H bands produced after 1 hr. contact with ethylene (2 Torr) following spectra of A.

hydroxyl groups responsible for the two bands seen have been shown to be quite different by adsorption of ammonia, pyridine, or other bases. Changes in the relative numbers of these groups on further dehydration can also be evaluated rather easily. As described elsewhere (1, 4-7), formation of ammonium or pyridinium ions gives bands in the 1400-1600  $\text{cm}^{-1}$  region which permit assessment of Bronsted acidity. The production of such bands is usually accompanied by disappearance of a band or bands in the hydroxyl-stretching region. Although not shown in Figure 2, adsorption of ammonia would selectively eliminate the band near 3605  $\text{cm}^{-1}$  and produce a band near 1470  $\text{cm}^{-1}$  arising from ammonium ions. The 3605  $\text{cm}^{-1}$  band evidently arises from hydroxyl groups which are strong Bronsted acids.

Figure 2B shows C-H stretching bands representing oligomer produced on the same catalyst, dried as in Figure 2A, after 1 hour contact with ethylene at 50 C. The amount of oligomer produced increased as the acidic hydroxyl band decreased, suggesting that oligomerization required Lewis rather than Bronsted acids. Adsorption of ammonia or pyridine also provides information on Lewis acids, but these probes tend to adsorb unselectively on far more sites than appear catalytically important. Adsorption of CO or CO<sub>2</sub> is often more useful in identifying important Lewis acid sites.

Figure 3 shows FTIR spectra obtained for CO<sub>2</sub> adsorbed on Na-Y and Na-H Y zeolites. The band near 2355  $\text{cm}^{-1}$  apparently results from adsorption on Na<sup>+</sup> ions, while that at 2370 shows adsorption on exposed Al ion -oxide ion sites where both cation and anion are coordinatively unsaturated. Similar sites can be seen on many other zeolites and on highly dried amorphous silica-alumina.

Figure 4 shows that similar Al ion sites can be produced on a ZSM-5 zeolite by high-temperature drying and that activity for ethylene oligomerization accompanies formation of such sites. These sites are evidently created on zeolites by removal of Al from the crystalline framework at high temperatures, leading to the exposure of Al ions, possibly as AlO<sup>+</sup>, outside the framework.

Although no oligomerization was seen on the original Bronsted acidic ZSM-5, and oligomerization activity increased as the catalyst was progressively dried, subsequent readdition of water, which entirely removed the sites which held CO<sub>2</sub>, did not eliminate, but instead somewhat increased this activity.

Figure 5 shows (on ZSM-5 completely exchanged with deuterium oxide and dried at 800 C) that readdition of water (D<sub>2</sub>O) gave two new bands, possibly arising from hydration of AlO<sup>+</sup> ions to form Al(OD)<sub>2</sub><sup>+</sup> ions. This suggests that either hydrated or anhydrous complex Al cations, held outside the zeolitic framework can be active for ethylene oligomerization.

Strained Bonds on Oxides and Zeolites. Many dry oxides and silicates, including zeolites, contain oxide linkages which are highly "strained". Such strain can be relieved by chemisorption of water, ammonia, methanol, etc., which opens strained linkages by

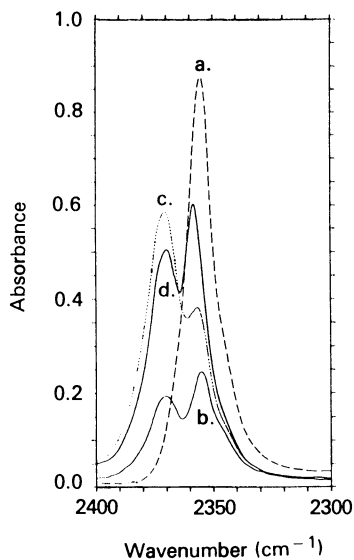


Figure 3. Spectra of  $\text{CO}_2$  on Na-Y and H-Na Y zeolites. a. Na-Y dried at 500 C; b. H-Na Y dried at 300 C; c. H-Na Y dried at 500 C; d. H-Na Y dried at 700 C.

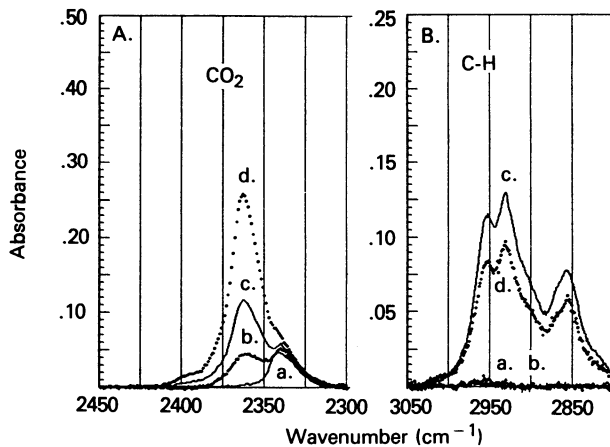


Figure 4. Spectra of  $\text{CO}_2$  and of oligomer subsequently formed on ZSM-5 (1.35%  $\text{Al}_2\text{O}_3$ ) after 1 hr contact with ethylene (2 Torr). Dried: a. 500 C; b. 600 C; c. 800 C; d. 800 C, 3 hr.



hydrolysis, ammonolysis, methanolysis, etc.. Spectra obtained before and after adsorption of methanol on high-silica molecular sieves predried at 500 C show, with computer subtraction, that although some methoxy groups are attached by replacement of OH groups, many others are attached by methanolysis of strained siloxane linkages. Similar chemisorption of other molecules can also be demonstrated.

Figure 6 presents spectra of methanol adsorbed on silicalite (13 ppm Al) predried at 500 and 700 C. The background has in all cases been subtracted. Although on 500 C-predried silicalite some methanol was attached by replacement of existing OH groups with methoxy groups (as shown by the negative OH bands), more methanol was apparently attached by methanolysis of strained siloxane bonds, forming methoxy (bands between 2800 and 3000  $\text{cm}^{-1}$ ) and new hydroxyl (3400  $\text{cm}^{-1}$ ) groups. On 700 C-predried Silicalite nearly all the methanol was chemisorbed by methanolysis of siloxane bonds.

#### Characterization of Metal Sites on Supported Metal Catalysts.

Characterization of supported metals is usually more difficult. Considerable variation can frequently be found in the state of the reduced metal as a result of apparently minor differences in pretreatment, impurities in the support, or residual water or other contaminants. The problem is most severe with readily oxidizable metals. Ni (10), Mo (11), Re (12) and other metals can all show major variations depending on sample pretreatment and reduction procedures. Even in the case of platinum group metals many complications exist. The frequencies of bands observed when CO is adsorbed in a given manner (e.g. "linear" or "bridged") can shift by up to 100  $\text{cm}^{-1}$  with coverage by CO or between different samples. This results in large part from dipole-dipole interactions between neighboring adsorbed CO molecules (13-14), but changes in the types of sites available for CO adsorption on one or more exposed crystal faces or electronic modification of the sites remaining as a result of initial adsorption of a partial monolayer may also lead to frequency shifts. Supported metals can be influenced by neighboring cations or anions, which cause changes in the electronic nature of exposed metal atoms and in the frequencies of CO or other molecules adsorbed on these atoms. Such electronic support effects should only become significant for very highly dispersed metals, however. Even very small crystals of clean supported metals probably differ little from large crystals in their electronic properties except insofar as size influences face exposure and edge and corner atom abundance. Spectra apparently showing effects of Pt crystal size on the frequency of adsorbed NO have been published (15). Despite much work, doubt still exists on the proper interpretation of shifts seen in the frequencies of adsorbed CO and NO on supported metals. This situation arises partly because different investigators have looked at samples differing in metal loading, preparation, pretreatment, and cleanliness. Use of the most effective techniques available cannot lead to agreement when different investigators look at different surfaces.

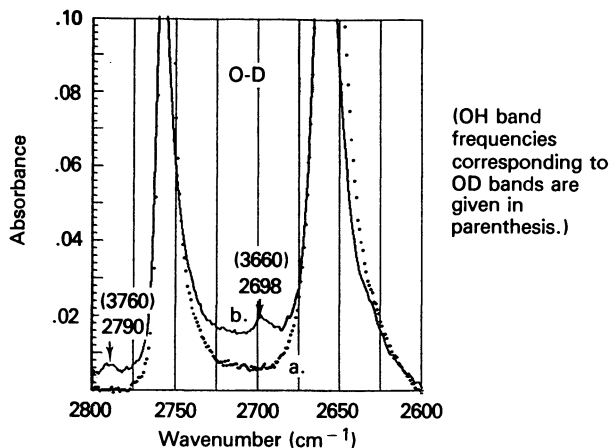


Figure 5. Effects of rehydration (with deuterium oxide) on deuteroyxl bands of ZSM-5 (1.35%  $\text{Al}_2\text{O}_3$ ). Pretreatment: a. Dried at 800 C; b. Rehydrated with  $\text{D}_2\text{O}$  and dried at 300 C following a.

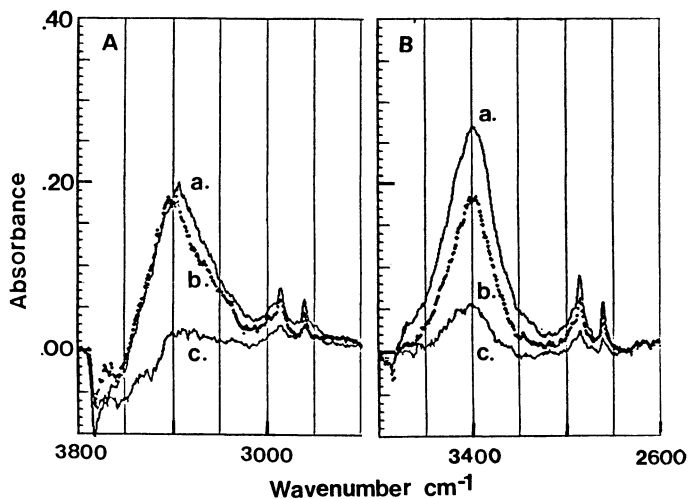


Figure 6. Spectra of methanol chemisorbed on Silicalite (after subtraction of original background). Silicalite predried at A: 500C.; B: 700 C. Spectra shown are after adsorption of excess methanol and desorption at a., 150 C; b., 300 C; c., 400 C.

Figure 7 illustrates the marked variations observed in spectra of NO adsorbed on 1% Ir/pure gamma-alumina reduced by three different methods. Reduction in static hydrogen evidently left more unreduced Ir (as indicated by the band at  $1895\text{ cm}^{-1}$ ) than did reduction in flowing hydrogen, although reduction at 700 C was fairly effective even in static hydrogen. The reduction at 300-500 C in flowing hydrogen may have produced a more-crystalline iridium, however, because the NO band frequency (1805) is substantially lower than that seen on the catalyst reduced at 700 C.

In the case of alumina supported rhenium (12), the nature of the supported metal also seems highly dependent on pretreatment of the catalyst. Increasing the precalcination temperature from 500 to 700 C, evidently increased the amount of exposed, fully reduced Re shown subsequently (after reduction in hydrogen at 500 C) by adsorption of CO. Additional types of reduced Re adsorption sites were also apparently present on the sample precalcined at 700 C.

As shown in Figure 8, pretreatment of Re/alumina with dimethyl sulfide prior to reduction can eliminate at least one of the two characteristic bands typically seen for NO adsorbed on unsulfided samples. The elimination of the sites responsible for this band appears to correlate with the elimination of the excessive hydrogenolysis activity shown by unsulfided fresh Pt-Re/alumina catalysts. The probable nature of the sites responsible for the two NO bands has been discussed elsewhere (16). It is likely that the band at the higher frequency arises from NO on exposed Re ions. Regardless of the origin of the two bands, however, some of the exposed Re atoms have clearly been rather permanently altered by sulfiding, with important catalytic consequences.

A wealth of detailed evidence on the nature of supported metals can readily be obtained from infrared characterization studies, but correct interpretation of much of this evidence is still far from clear. The surface chemistry of supported metals is generally very complex, and assertions as to the origins of various band shifts and the exact nature of adsorption sites should be taken with some caution at present. Clearly, however, better understanding of the complex nature of supported metal catalysts should contribute greatly to the development of more efficient catalysts for many important industrial processes and to more efficient pretreatment and regeneration procedures.

### Conclusions and Future Prospects

The role of infrared spectroscopic characterization of catalysts should become increasingly important in catalyst development, but present problems, both experimental and theoretical must be recognized and overcome before reliable information can be routinely obtained using infrared methods. Techniques and understanding will improve as more information becomes available, but detailed interpretation of spectra will continue to present problems for some time. Partial interpretation and "fingerprinting" can still be

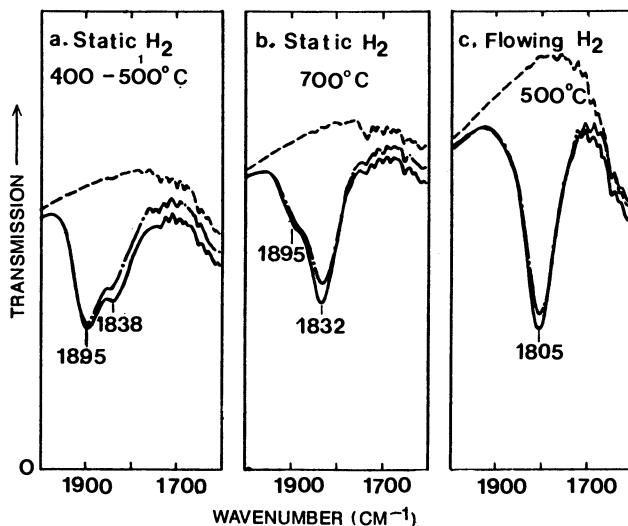


Figure 7. Spectra of NO adsorbed on 1% Ir/pure gamma-alumina prereduced using three different procedures. Dashed spectra -- background after reduction; solid -- after addition of NO; dot-dash -- after 5 min. evacuation.

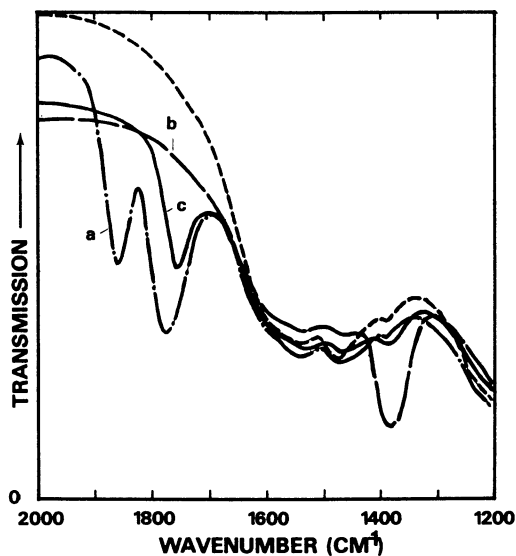


Figure 8. Effect of sulfide treatment on infrared bands of NO adsorbed on reduced 0.6% Re/alumina. a., NO added after prereduction at 500 C; b., NO added after exposure to dimethyl sulfide, heating in oxygen, and reduction at 500 C; c. NO readded after reduction at 600 C following the above.

highly useful at present in catalyst development, quality control or patent matters, however.

#### Acknowledgments

The examples given of applications of infrared to catalyst characterization have been taken from my past work in the Amoco Oil Company Research and Development Department. Amoco Oil Company's consistent support for nearly thirty years, the assistance of a series of able technicians, and the advice and encouragement of many other colleagues are gratefully acknowledged.

#### Literature Cited

1. Eischens, R. P.; Pliskin, W. A. Advances in Catalysis 1958, 10, 1.
2. Haller, G. L. In Spectroscopy in Heterogeneous Catalysis; Delgass, W. N.; Haller, G. L.; Kellerman, R.; Lunsford, J. H., Eds.; Academic Press: New York, 1979; pp 19-57.
3. Bell, A. T. In Vibrational Spectroscopies for Adsorbed Species; Bell, A. T.; Hair, M. L., Eds.; American Chemical Society: Washington, DC, 1980; pp 13-35.
4. Peri, J. B. In Catalysis; Anderson, J. R.; Boudart, M., Eds.; Springer-Verlag: Berlin-New York, 1984; Vol. 5, pp 172-219.
5. Little, L. H. Infrared Spectra of Adsorbed Species; Academic Press: New York, 1966.
6. Hair, M. L. Infrared Spectroscopy in Surface Chemistry; Marcel Dekker: New York, 1967.
7. Kiselev, A. V.; Lygin, V. I. Infrared Spectra of Surface Compounds; John Wiley & Sons: New York-Toronto, 1975.
8. Yates, J. T., Jr.; Gelin, P.; Beebe, T. In Catalyst Characterization Science; Deviney, M. L.; Gland, J. L., Eds.; ACS Symposium Series No. 288; American Chemical Society: Washington, DC, 1985; pp 404-421.
9. Perkins, W. D. J. Chemical Education 1987, 64, A269-271.
10. Peri, J. B. J. Catal. 1984, 86, 84.
11. Peri, J. B. J. Phys. Chem. 1982, 86, 1615.
12. Peri, J. B.; Mieville, R. L. PREPRINTS, Div. of Petrol. Chem., ACS 1987, 32, 3, 737.
13. Hammaker, R. M.; Francis, S. A.; Eischens, R. P. Spectrochim. Acta 1965, 21, 1295.
14. Hendrickx, H. A. C. M.; Des Bouvrie, C.; Ponec, V. J. Catal. 1988, 109, 120.
15. Primet, M.; Basset, J. M.; Garbowski, E.; Mathieu, M. V. J. Am. Chem. Soc. 1975, 97, 3655.
16. Peri, J. B. J. Catal. 1978, 52, 144.

RECEIVED January 26, 1989

## Chapter 22

# Light-Off Temperature Determination of Oxidation Catalyst Using Fourier Transform IR Technique

Chen C. Hsu

U.S. Army Chemical Research, Development, and Engineering Center,  
Aberdeen Proving Ground, MD 21010-5423

Light-off temperatures of oxidation catalysts are considered as one of the important parameters for catalyst performance evaluation. In this study, the in-situ FTIR technique was developed and used to determine the light-off temperatures and reaction products of three three-way automotive catalysts with 20 torr monomethylamine in air at 0.5 l/min flow rate. Light-off temperatures were found to be 140, 143, and 170°C for Davison, Allied-Signal, and Degussa oxidation catalysts, respectively. CO, CO<sub>2</sub>, H<sub>2</sub>O, and nitric acid were found to be the major oxidation products. The activation energies of formation of CO and CO<sub>2</sub> on the catalysts were also determined.

There are various techniques to evaluate the performance of oxidation catalysts. Measurements of surface composition, surface structure, surface area, porosity, acidity, and dispersion of active metals of oxidation catalysts, etc., can be related to the catalyst performance (1). Other methods such as the decoloration of the indigo carmine solution to correlate the catalytic activity with the flash point (2) and the recorder-equipped calorimeter technique to determine the ignition time, maximum temperature and maximum combustion temperature (3) were used. For an oxidation catalyst, however, one direct measurement of its performance is to determine its light-off temperature, the temperature at which significant oxidation reactions occur. In general, it is true that the lower the light-off temperature, the more effective will be the catalyst performance (4-5). Indeed, this correlation was used in the past to select the optimum reduction temperature and the duration of reduction for the preparation of the best Ni-containing catalyst (6). We have developed an in-situ FTIR technique for simultaneously determining the light-off temperatures and identifying catalytic oxidation products of oxidation catalysts. Using this newly developed technique, three three-way automotive catalysts were evaluated. The details of the subject technique and the results of catalyst performance evaluation are described below.

### Experimental

Anhydrous monomethylamine (MMA) used in this study was supplied by Matheson Gas Products with a purity of 99.99%. MMA was used as received without further purification. Three three-way automotive oxidation catalysts were provided by Allied-Signal (UOP# 4576-136), Davison (alumina catalysts code 701), and Degussa (TWC-1, MS-599). Bead-type catalyst samples were dried inside an oven at 110°C overnight before use. The schematic diagram of the in-situ FTIR catalyst light-off temperature measurement system is shown in Figure 1. The measurement system consists of a flow IR cell, a K-type thermocouple with a chart recorder and digital thermometer display, a mass flow controller, a lecture bottle of MMA, an MKS pressure gauge, and Nicolet FTIR Model 60SX. The details of the flow IR cell are illustrated in Figure 2. This flow IR cell has 10 cm optical pathlength and 25x4 mm NaCl window, the heating element and sample holder, the gas inlet and outlet, and the thermocouple. The thermocouple is positioned in the proximity of the sample to measure the temperature of an oxidation reaction. For accurate determination of the light-off temperature of a catalyst, a chart recorder was used along with a digital thermometer display. Initially, a correlation between the temperature setting on the heater controller and the temperature reading on the digital thermocouple display was obtained. It was found that the temperature reading on the digital thermometer was about 30 to 40% of the temperature setting on the heater controller. To run an experiment, the IR background spectra were taken at various temperatures with the flow IR cell purged with dried air at 0.5 l/min flow rate which was automatically controlled by an Matheson mass flow controller. It is to be noted that the dried air was not preheated before purging the IR cell. Background spectra were taken in the mixture of dried air and 20 torr MMA in the absence of catalyst. The background spectra essentially remain the same in the temperature range of 25-363°C, indicative of no catalytic activity due to the heating element. For catalyst evaluation, three catalyst beads were placed on the sample holder (the heating element with a V-shape) and the thermocouple was positioned in the proximity of catalyst beads. After the light-off temperature measurement system was assembled, the flow IR cell was evacuated with a vacuum pump and MMA was injected and maintained at 20 torr. The system was disconnected with the vacuum pump and the IR cell was brought to ambient pressure with compressed air at 0.5 l/min flow rate. The heater controller was set at around 200°C (equivalent to the thermocouple reading of 80°C) and the setting was increased at ten degrees increment every 15-20 minutes. During this period of time, an IR spectrum was taken in the range between 4000 and 400  $\text{cm}^{-1}$  with 4  $\text{cm}^{-1}$  resolution. Normally, 32 scans were taken for each IR spectrum at every temperature setting. Significant oxidation reaction was detected around 140°C thermocouple reading on the digital thermometer display. The determination of light-off temperature was carried out using the chart of the temperature recorder. The light-off temperatures were found reproducible with repeated on and off cycles of MMA. These procedures described above were used for three three-way automotive oxidation catalysts provided by Davison, Allied-Signal, and Degussa.

### Results and Discussion

Typical IR spectra at various temperatures are illustrated in Figures 3-5 with Davison three-way catalyst samples. At 94°C, the IR features are

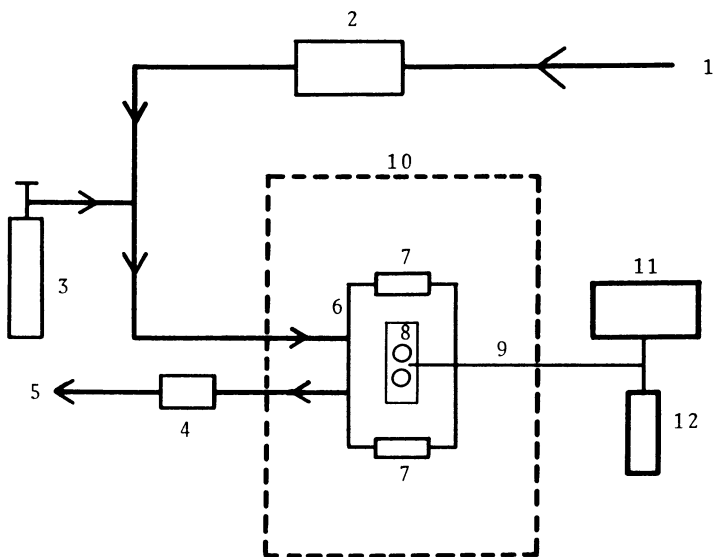


Figure 1. In-situ FTIR catalyst light-off temperature measurement system. 1. compressed air; 2. mass flow controller; 3. gas lecture bottle; 4. MKS pressure gauge; 5. exhaust; 6. IR cell; 7. IR window; 8. catalyst sample; 9. thermocouple; 10. sample compartment of Nicolet FTIR Model 60SX; 11. chart recorder; 12. digital thermometer display.

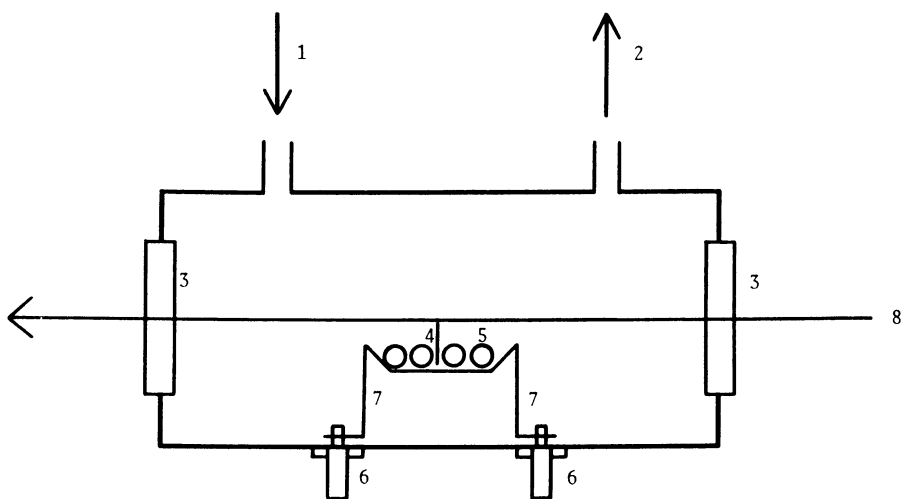


Figure 2. Schematic diagram of the flow IR cell. 1. gas inlet; 2. gas outlet; 3. IR window; 4. thermocouple; 5. catalyst sample; 6. electrical leads for heating; 7. heating element and sample holder; 8. IR beam.



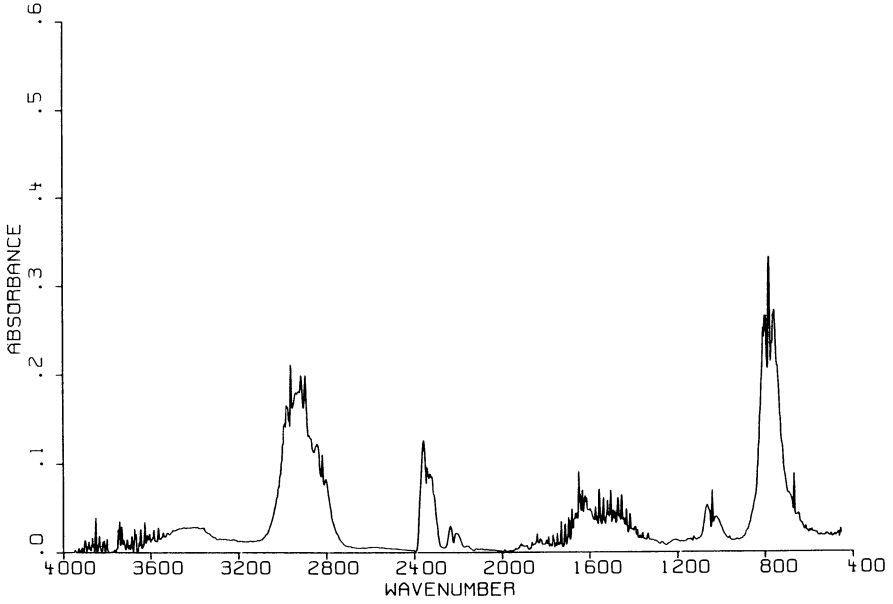


Figure 3. IR spectrum of MMA with Davison catalyst at 94°C.

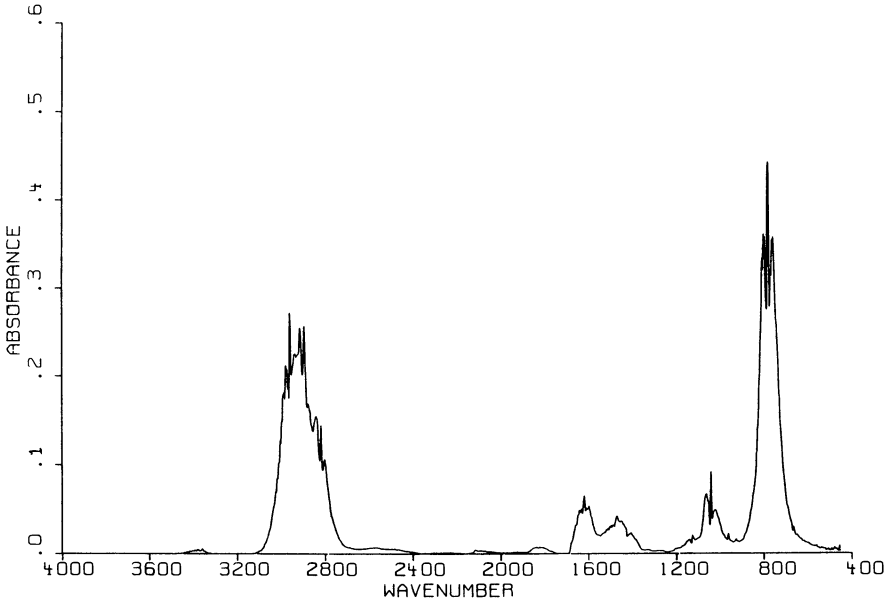


Figure 4. IR spectrum of MMA with Davison catalyst at 190°C.

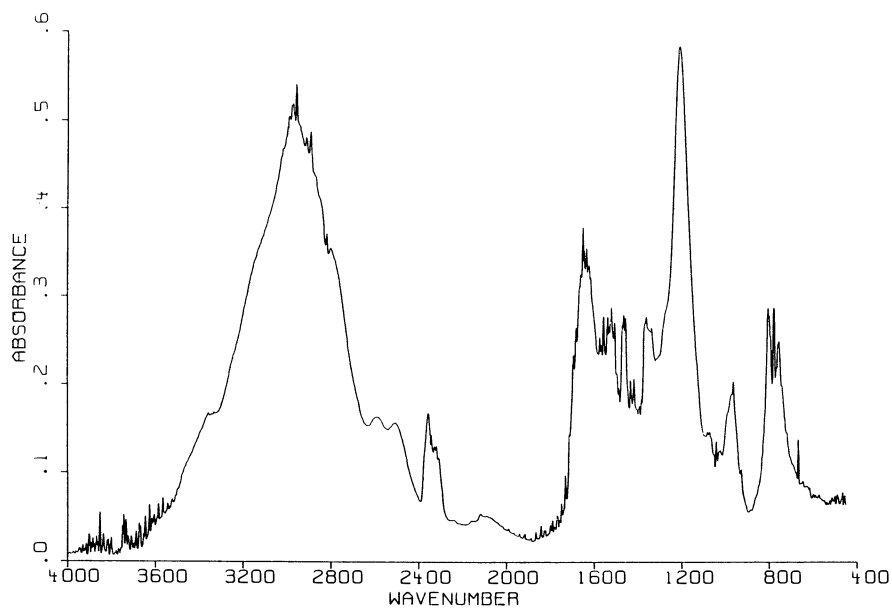


Figure 5. IR spectrum of MMA with Davison catalyst at 261°C.

very much the same as MMA as shown in Figure 3. When the temperature was increased to 190°C as shown in Figure 4, peaks around 2154 and 2351  $\text{cm}^{-1}$  respectively corresponding to CO and  $\text{CO}_2$ , and peaks around 1540 and 3770  $\text{cm}^{-1}$  corresponding to  $\text{H}_2\text{O}$  grow substantially. As the temperature reaches to 261°C, the formation of  $\text{HNO}_3$  and the effect of water on nitric acid (7-9) corresponding to the bands centered around 2964, 1700, 1320, 760  $\text{cm}^{-1}$  appear to be the major reaction products, Figure 5. For each sample, at least three experiments were conducted and the light-off temperatures were determined using the charts from the temperature recorder. The average light-off temperatures for three three-way automotive catalysts are shown in Table 1. In the increasing light-off temperature, the order is Davison, Allied-Signal, and Degussa catalysts. For Davison and Allied-Signal

Table 1. Light-Off Temperatures of Three-Way Automotive Catalysts

Davison	140°C $\pm$ 5%
Allied-Signal	143°C $\pm$ 3.5%
Degussa	170°C $\pm$ 2.3%

samples, the light-off temperatures are very close to each other. However, for Degussa sample, the light-off temperature is about 30°C higher than that of Davison and Allied-Signal. The absorbance of CO and  $\text{CO}_2$  were taken from the IR spectra at various temperatures from which Arrhenius plots were obtained as shown in Figures 6-7. The activation energies of formation of CO and  $\text{CO}_2$  were found using the relation of slope =  $-E_a/R$ , where  $E_a$  is the activation energy and R is the ideal gas constant which is equal to 1.987 cal/mol/K. Table 2 shows the activation energies of formation of CO and  $\text{CO}_2$  for three three-way automotive catalysts. In general, the acti-

Table 2. Activation Energy of Formation, Kcal/mol

	$\text{CO}_2$	CO
Davison	2.29	6.41
Allied-Signal	2.68	12.07
Degussa	5.76	21.60

vation energy of formation of  $\text{CO}_2$  is lower than that of CO consistent with the fact that the free energy of formation of  $\text{CO}_2$  is lower than that of CO. It is to be noted that the lower the light-off temperature, the lower will be the activation energy of formation for both CO and  $\text{CO}_2$  from the three-way automotive catalysts investigated. It was also observed that the condensation of water and nitric acid inside the IR cell during the catalytic oxidation of MMA may be attributed to the scattering of the data points in Figures 6-7.

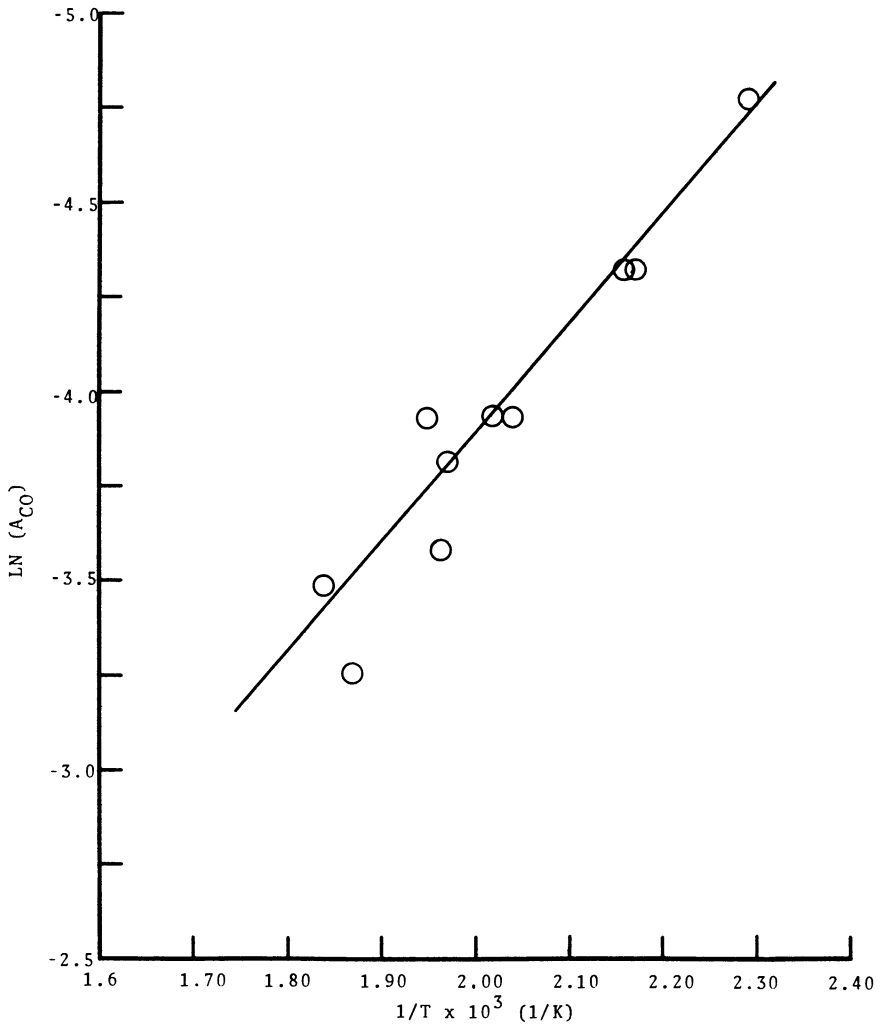


Figure 6. Arrhenius plot of CO on Davison oxidation catalyst.

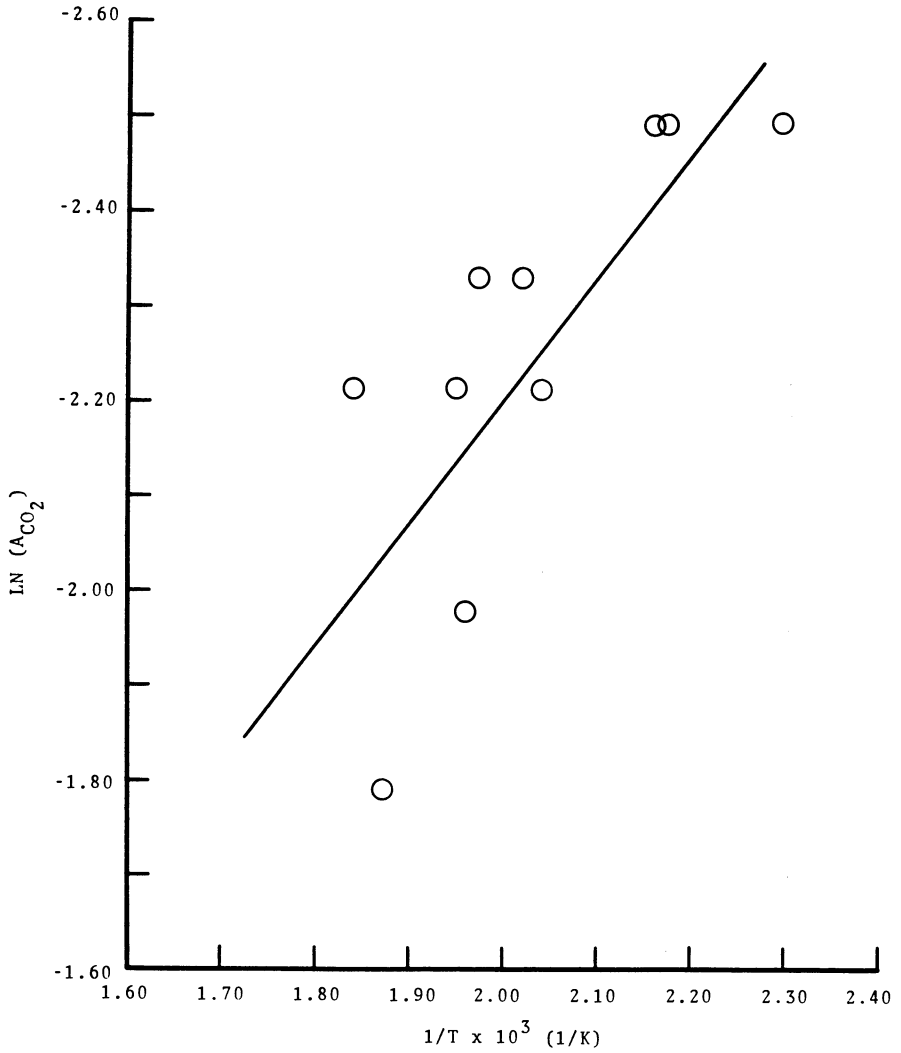


Figure 7. Arrhenius plot of  $CO_2$  on Davison oxidation catalyst.

### Summary

The results can be summarized as follows.

1. In-situ FTIR technique was developed and demonstrated for the light-off temperature determination and the identification of reaction products of oxidation catalysts.
2. Light-off temperatures with 20 torr MMA for Davison, Allied-Signal, and Degussa three-way automotive catalysts were determined to be 140, 143, and 170°C in air with 0.5 l/min flow rate, respectively.
3. The reaction products were identified to be CO, CO<sub>2</sub>, H<sub>2</sub>O, and HNO<sub>3</sub> for three three-way automotive catalysts.
4. The activation energies of formation for CO and CO<sub>2</sub> on three three-way catalysts were determined. For CO, they are 6.41, 12.07, and 21.60 Kcal/mol; and for CO<sub>2</sub>, they are 2.29, 2.68, and 5.76 Kcal/mol, for Davison, Allied-Signal, and Degussa three-way automotive catalysts, respectively.

### Acknowledgments

Sincere appreciation is due to Marie A. Yeh of C. Milton High School, MD, who performed the experiments during her tenure as a DoD Science Apprentice in the summer of 1987. Special thanks are due to Dr. G. R. Lester of Allied-Signal, Dr. R. F. Freese of Degussa, and Dr. P. A. Smith of Davison who provided the three-way automotive catalysts used in this study.

### Literature Cited

1. Delannay, F.; Delmon, B. in Characterization of Heterogeneous Catalysts, F. Delannay, Ed.; Marcel Dekker, Inc., New York and Basel, 1984.
2. Krause, A.; Nowakowski, E. Chem.-Zig. Chem. App. 1968, 92, 774-5.
3. Guveev, A. A.; Dovlator, I. A.; Kazaryan, S. A.; Naftulin, I. S. Determination of the Octane Number of Gasoline from Catalytic Reforming According to the Characteristics of Low-Temperature Gas-Phase Oxidation, Neftepererab. Neftekhim., Moscow, 1987, Vol. 9, pp 5-8.
4. Pfefferle, L. D.; Pfefferle, W. C. Catal. Rev.-Sci. Eng. 1987, 29, 219-267.
5. Prasad, R.; Kennedy, L. A.; Ruckenstein, E. Catal. Rev.-Sci. Eng. 1984, 26, 1-58.
6. Anderlohr, A.; Hedden, K. Chem.-Ing.-Tech. 1979, 51, 811.
7. McGraw, G. E.; Bernitt, D. L.; Hisatsune, I. C. J. Chem. Phys. 1965, 42, 237-244.
8. Ingold, C. K.; Millen, D. J. J. Chem. Soc. 1950, 2612.
9. Stern, S. A.; Mullhaupt, J. T.; Kay, W. B. Chem. Revs. 1960, 60, 185.

RECEIVED July 27, 1989

## Chapter 23

# Temperature-Programmed Desorption Study of CO on Pt-Reforming Catalysts

R. L. Mieville and M. G. Reichmann<sup>1</sup>

Amoco Oil Company, Amoco Research Center, Naperville, IL 60566

The characterization technique of CO Temperature-Programmed Desorption has been studied with Pt reforming catalysts. Critical factors in the experimental procedure and the catalyst pretreatment conditions were examined. The CO desorption spectrum consists mainly of two peaks which are probably combinations of other peaks and the result of various binding energy states of CO to Pt. These in turn could be due either to the interaction between Pt and the alumina support or the results of high and low coordination sites on the Pt crystallites. No significant relationship between the character of the CO desorption profile and the activity of commercial catalysts was observed.

The routine characterization of Pt reforming catalysts has depended mainly on the techniques of X-ray diffraction and CO and H<sub>2</sub> chemisorption for the state of the Pt, and N<sub>2</sub> BET surface area measurements for the support. Although these techniques can signal gross changes in the performance of the catalyst, instances occur when decreases in activity and selectivity are not reflected in measurements made by the above methods. Evidently a more detailed analysis of Pt is required. In theory this could be provided by a CO TPD method, but as yet no relationship between catalyst performance and the CO desorption spectrum has been established. In fact, the literature is surprisingly sparse on CO TPD studies of supported Pt. Partly this may be due to the realization that the desorption process from porous catalysts occurs primarily under equilibrium conditions (1). Also the variety of CO profiles reported suggest that experimental procedures may be difficult to reproduce (2-7). In order to overcome some potential experimental problems, special care was taken to eliminate contamination. The results of this and other investigations are presented in this paper.

<sup>1</sup>Current address: Amoco Chemicals, Naperville, IL 60566

### Experimental

The TPD apparatus consisted of a stainless steel flow system connected to a thermal conductivity cell. Catalyst samples of 0.1 g were placed in one arm of an L-shaped, 6 mm Vycor tube. A dual adsorption bed containing alumina and Oxy-Trap (Alltech) was placed in the other arm to prevent contamination by water and O<sub>2</sub>, respectively. Frequent regeneration in H<sub>2</sub> and He was required. This in-situ adsorption bed was found necessary despite purification traps on all gas lines coming into the flow system. Pulses of 0.25 cc of a 10% mixture of CO in He were injected into the He carrier gas and passed over the pretreated catalyst at room temperature. All runs were programmed heated at a rate of 20 K min<sup>-1</sup>. The Pt catalysts, either commercial or laboratory produced, were prepared by the impregnation of chloroplatinic acid on Cyanamid's Aero 1000 alumina, except for two catalysts which were prepared by platinum diamino dinitrite impregnation.

### Results and Discussion

Some preliminary runs were made on the Al<sub>2</sub>O<sub>3</sub> support in the absence of Pt. Heating this alumina without CO pulsing showed a small peak appearing near 100°C. This was identified as N<sub>2</sub> adsorbed as an impurity from the carrier gas. CO completely displaces the N<sub>2</sub> on pulsing at room temperature and, as previously reported, probably results from the presence of Lewis acid-base sites on the alumina (8). The amount of this peak was approximately 10<sup>-6</sup> moles per g of Al<sub>2</sub>O<sub>3</sub> which represents less than 5% of the CO desorbing from a well dispersed Pt catalyst of 0.4 wt% loading. Runs without the in-situ H<sub>2</sub>O and O<sub>2</sub> trap had shown that CO<sub>2</sub> desorbed with the CO. However, with the in-situ trap minimal CO<sub>2</sub> was observed. This was confirmed by a pair of runs shown in Figure 1 with and without Al<sub>2</sub>O<sub>3</sub> (CO<sub>2</sub> trap) placed at the exit of the desorption tube.

One of the most important variables in the TPD of CO from a supported Pt catalyst is the sample pretreatment. Calcination at 500°C for one hour followed by reduction is the conventional method to obtain the maximum exposed Pt and this follows closely to refinery practice for start-up and regeneration of commercial catalysts. The final step in our case was a 600°C He sweep for 30 minutes to ensure a fully dehydrated catalyst up to this temperature so that no water evolved during the subsequent TPD. We had previously observed that a high temperature He sweep could reduce the Pt catalyst without a prior H<sub>2</sub> reduction presumably by the decomposition of the Pt oxide.

Figure 2 shows the effectiveness of this procedure as a function of the preoxidation temperature. At 500°C preoxidation no difference is observed between either a He or H<sub>2</sub> reduction. After a 600°C calcination the He reduction was less effective, especially for higher temperature peaks, and this difference was more pronounced after a 700°C calcination temperature. It is important to note that more than oxidation occurs at high temperatures, sintering of the Pt and dehydration of alumina also occur. However, it is not surprising that hard to reduce Pt occurs at the highest temperature of preoxidation. All these factors contribute to the change in the



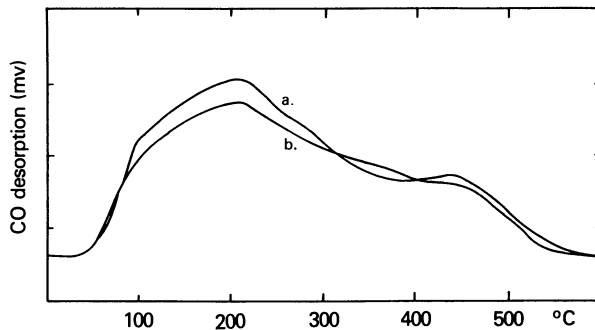


Figure 1. TPD Spectra of CO from 0.6 wt% Pt/Al<sub>2</sub>O<sub>3</sub>  
 a) Without CO<sub>2</sub> trap b) With CO<sub>2</sub> trap.

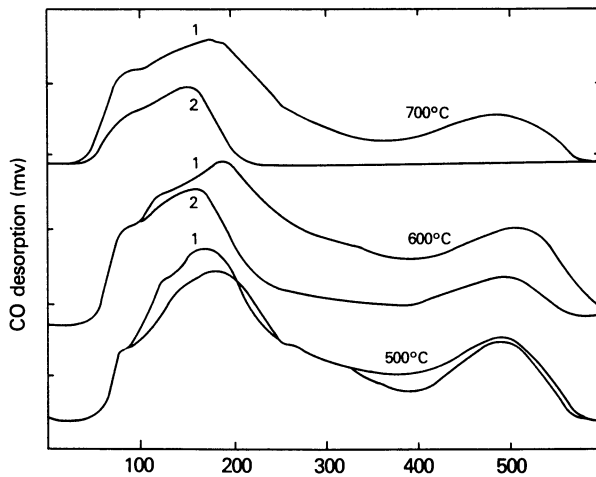


Figure 2. Effect of Calcination Temperature With Different Reductions

CO TPD from 0.4 wt% Pt/Al<sub>2</sub>O<sub>3</sub>

1) 1 Hr H<sub>2</sub> at 500°C than He at 600°C (30 min.)

2) 1 Hr He at 600°C.

amount of CO desorbed and the character of the desorption profile with the calcination temperature.

Figure 3 shows three TPD spectra ranging from 0.1 to 0.3 g of catalyst sample. Besides the amount of CO desorbed, no major change in the spectra was observed. However, a small discernible shift to increasing temperatures is seen on increasing sample amount which suggests a small interparticle readsorption effect.

Pore diffusion effects on the CO TPD spectra were investigated by varying the particle size of the catalyst. Figure 4 shows three spectra ranging in particle size from 60-80 mesh to 14-20 mesh, and essentially no difference in the spectra was observed.

The effect of titrating the Pt with small pulses of CO below the total saturation coverage was examined. Figure 5 shows the results of the desorptions of previously adsorbed integral amounts of 0.036cc of CO on a 0.3 g sample of 0.6 wt% Pt/Al<sub>2</sub>O<sub>3</sub>. CO desorbs stepwise from the high to the low temperature range which probable results not from selective adsorption but from movement of CO to higher binding sites on desorption indicating that readsorption is occurring freely.

Figure 6 compares three TPD spectra, ranging from 0.3 to 2.0 wt% Pt, and shows that there is an overall increase in the size of the high, relative to the low temperature peak as the Pt loading increases. At the same time, there is an upward shift in temperature for this low temperature peak. It might be expected that the larger crystallites formed at higher Pt loadings would have more terrace sites, while smaller crystallites have more steps and kinks which are associated with the higher binding states (9-12). However, this is contrary to the observed peak shift. One possible explanation which is consistent with the observed peak shift involves the platinum-support interaction. In this explanation, there is a limit to the Al<sub>2</sub>O<sub>3</sub> sites which can interact strongly with Pt (low temperature peak) and on further addition, Pt moves to less interacting sites.

However, this theory is only partially consistent with the spectra in Figure 7 where two samples of the same Pt loading (0.2 wt%) but of different dispersion (H<sub>2</sub>/Pt of 0.40 and 1.07) are shown. Although the sample with the higher dispersion did show a larger low temperature peak, it also appears to contain higher binding states which are completely absent in the low dispersion case. On the basis of the platinum support interaction theory, we would expect a smaller high temperature peak for the less highly dispersed sample (13). It should be noted that decrease in dispersion cannot always be explained by crystallite formation. Evidentially further study and development is needed.

The main goal of this work was to define that part of the TPD spectrum which contributes most to the activity of the catalyst. Four used reforming catalysts with relative activities ranging from 0.49 to 1.00 (on the basis of performance in a pilot plant) were examined. The results of these runs are shown in Figure 8 and no obvious correlation seems to exist between the spectra and the corresponding activities.

An attempt was made to learn whether increased interaction of platinum with exposed Al ions could be seen on more highly dried alumina. The population of such ions increases with temperature of dehydration of the alumina (8). A Pt/Al<sub>2</sub>O<sub>3</sub> catalyst was predried at various temperatures in He. The results in Figure 9 show a

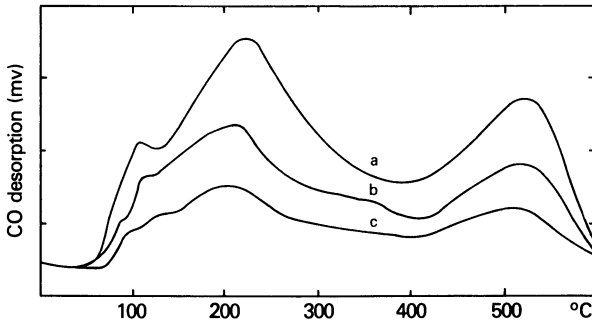


Figure 3. Effect of Sample Amount  
0.4 wt% Pt a) 0.3 g b) 0.2 g c) 0.1 g.

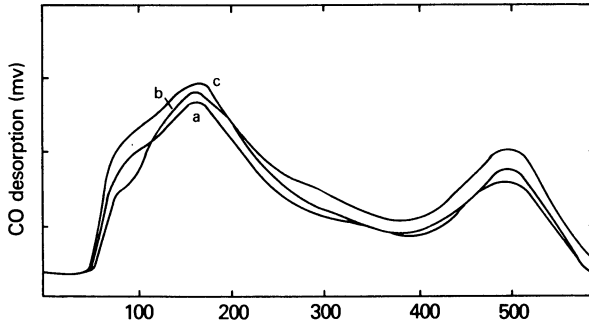


Figure 4. Effect of Particle Size  
0.4 wt% Pt a) 60-80 mesh b) 20-60 mesh c) 14-20 mesh.

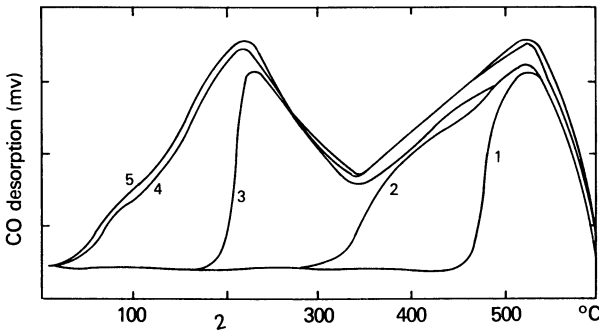


Figure 5. Coverage Variation  
CO added in 0.036cc pulses.  
Number of pulses as indicated (0.3 g, 0.5 wt% Pt/Al<sub>2</sub>O<sub>3</sub>).

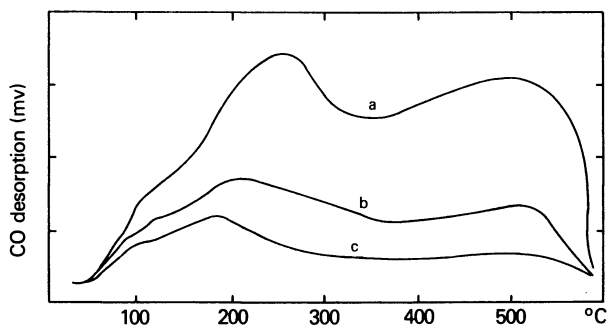


Figure 6. Effect of Pt Loading  
Pt wt% a) 2.00 b) 0.70 c) 0.30.

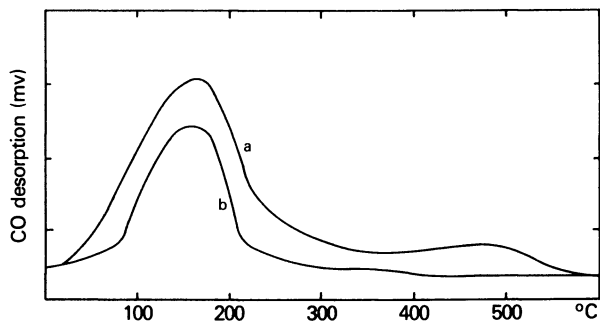


Figure 7. Effect of Pt Dispersion  
0.2 wt% Pt/Al<sub>2</sub>O<sub>3</sub> (diamino-dinitrite impregnation)  
Dispersion a) 107% b) 40%.

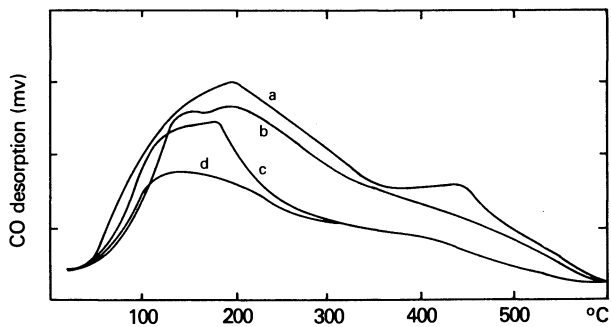


Figure 8. CO TPD Spectra of Pt/Al<sub>2</sub>O<sub>3</sub> Catalyst With Different Activities  
Relative Activities a) 1.0 b) 0.83 c) 0.49 d) 0.56.

progressive increase in the relative size of the low temperature peak as the predrying temperature is increased but the decrease in high temperature peak, as might be expected, is not consistently seen here.

Similar experiments were performed in an IR spectrometer. In these experiments the same Pt catalyst was predried by evacuation at 500° and 700°C after initial calcination at 500°C, but in this case before reduction in H<sub>2</sub> at 500°C. CO was added at room temperature and then progressively removed at higher temperatures. This results, as seen in Figure 10, in a series of decreasing size bands with a frequency shift to lower wave numbers. Such shifts in the IR frequency with CO coverage could possibly occur by changes in

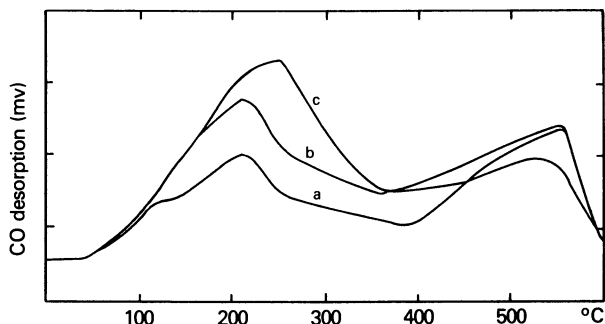


Figure 9. Effect of Predrying Temperature  
0.74 wt% Pt/Al<sub>2</sub>O<sub>3</sub> a) 500°C b) 600°C c) 700°C.

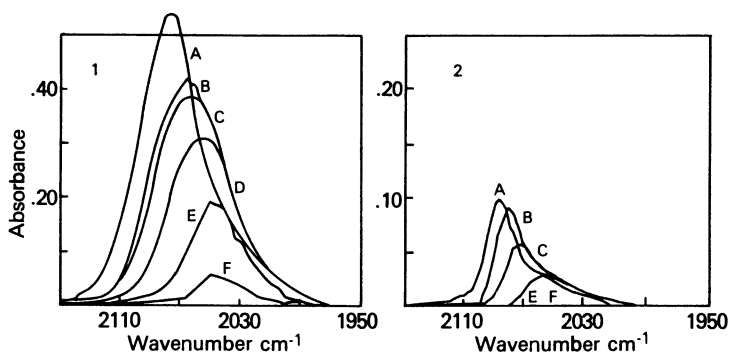


Figure 10. Effects of Predrying and Partial Desorption on the IR Spectra of Absorbed CO

1. Calcined at 500°C      2. Calcined at 700°C

Desorption Temperature A) After CO added B) 60°C C) 150°C  
D) 250°C E) 350°C F) 400°C.

dipole-dipole coupling. However, it has been previously observed that no changes in frequency occur during the titration of a 0.6% Pt/Al<sub>2</sub>O<sub>3</sub> sample with small known amounts of CO up to a coverage of 0.7 CO molecules/Pt atom (pressure  $\sim 7 \times 10^{-3}$  Torr).<sup>-1</sup> At higher pressures, the band shifted from 2060 to 2070 cm<sup>-1</sup> (14). This equivalent shift is seen in Figure 10 between spectra A and B. All further shifts are then likely caused by the removal of weaker held CO by thermal desorption which results in the subsequent increase in the strength the CO to Pt bond while decreasing the bond strength of the C to O. The major loss of Pt surface area seen after the 700°C pretreatment was expected on the basis of previous work showing that heating preoxidized Pt/alumina in vacuum gave essentially the same loss in area as heating in oxygen (14).

Figure 10 also shows that the spectra obtained from the more strongly dried catalyst (the 700°C treatment) shifts in the band maxima to frequencies higher than seen on the less strongly dried catalyst (the 500°C treatment). This peak shift indicates that the Pt interacts more with the more highly dried alumina surface and therefore confirms the TPD results.

In conclusion, the TPD spectra can be characterized by two broad peaks, one at 100° and the other at 450°. However, these could be made up of a combination of several different peaks. Assignments of these individual peaks to specific Pt states are hardly possible, but the broad TPD profile arises out of two possible causes: either to structural changes in the Pt crystallite forms or to variation of Pt-alumina interactions due to the heterogeneity of the alumina surface.

We would like to acknowledge the two 0.2 wt% Pt catalyst samples given to us by Professor R. L. Burwell and the I.R. spectra obtained from Dr. J. B. Peri. We should also like to thank them both for many helpful discussions.

#### LITERATURE CITED

1. Herz, R. K., Kiela, J. B. and Marin, S. P., *J. Catal.* 1982, 73, 66.
2. Darling, T. A., and Moss, R. L., *J. Catal.* 1967, 7, 378.
3. Hoang-Van, C., Ghorbel, A., Pommier, B., and Teichner, S. J. *Bull. Soc. Chim.* 1976, 355.
4. Bain, F. T., Jackson, S. D., Thomson, S. J., Webb, G., and Willocks, E., *J. Chem. Soc. (Faraday)*. 1976, 72, 2516.
5. Foger, K., Anderson, J. R., *Appl. Surface Sci.* 1979, 2, 335.
6. Zhang, X. Q., Xue, H. and Xiexian, G., *Cuihua Xueba.* 1981, 2, 100.
7. Saveleva, G. A., Galeev, T. K., Popova, N. M., Vozdvizhenskii, V. F., and Mishchenko, V. M., *Kinet. Katal.* 1981, 22, 1253.
8. Mieville, R. L., *J. Catal.* 105, 1987, 536.
9. Morgan, A. E., and Somorjai, G. A., *Surface Sci.* 1968, 12, 405.
10. McCabe, R. W., and Schmidt, L. D., *Surface Sci.* 1977, 66, 101.
11. Altman, E. I., and Gorte, R. J., *Surface Sci.* 1986, 172, 71.
12. Gdowski, G. E., and Madix, R. J., *Surface Sci.* 1982, 115, 524.
13. Herz, R. K., and McCready, D. F., *J. Catal.* 1983, 81, 358.
14. Peri, J. B., *J. Phys Chem.* 1978, 52, 144.

RECEIVED January 10, 1989

## Chapter 24

# Pore Structure Characterization of Catalyst Supports via Low-Field NMR Spectroscopy

D. M. Smith<sup>1</sup>, C. L. Graves<sup>1</sup>, D. P. Gallegos<sup>1</sup>, and C. J. Brinker<sup>2</sup>

<sup>1</sup>Center for Micro-Engineered Ceramics, University of New Mexico, Albuquerque, NM 87131

<sup>2</sup>Division 1846, Sandia National Laboratories, Albuquerque, NM 87185

Two characterization techniques (mercury porosimetry and nitrogen adsorption/condensation) are widely employed for pore structure analysis of catalyst supports. Pore structure analysis is an important component of catalysis at several levels ranging from quality control for catalyst support production to the understanding of mass transfer resistance in laboratory experiments. Although porosimetry and adsorption/condensation are widely used, they suffer from several disadvantages. In an effort to avoid these disadvantages and to extract more detailed pore structure information, techniques such as small-angle x-ray/neutron scattering (SAXS/SANS), phase-change porosimetry, and low-field NMR spin-lattice relaxation measurements have been recently employed. In this paper, the application of low-field NMR to both surface area and pore structure analysis of catalyst supports will be presented. Low-field (20 MHz) spin-lattice relaxation ( $T_1$ ) experiments are performed on fluids contained in alumina and silica catalyst supports. Pore size distributions (PSD) calculated from these NMR experiments are compared to those obtained from mercury porosimetry and nitrogen condensation.

### BACKGROUND - Conventional Pore Structure Characterization

Mercury porosimetry employs the measurement of mercury volume intruded (or retracted) into a sample as a function of pressure. The applied pressure is related to the desired pore size via the Washburn Equation [1] which implies a cylindrical pore shape assumption. Mercury porosimetry is widely applied for catalyst characterization in both QC and research applications for several reasons including rapid reproducible analysis, a wide pore size range ( $\approx 2$  nm to  $>100 \mu\text{m}$ , depending on the pressure range of the instrument), and the ability to obtain specific surface area and pore size distribution information from the same measurement. Accuracy of the method suffers from several factors including contact angle and surface tension uncertainty, pore shape effects, and sample compression. However, the largest discrepancy between a mercury porosimetry-derived pore size distribution (PSD) and the actual PSD usually

arises as a result of network/percolation effects. An implicit assumption in porosimetry analysis is that every individual pore is in direct contact with the pellet surface. In fact, a particular pore in a catalyst support will be connected to the surface via a network of various size/shape pores. Mercury will intrude into the pore not at the pressure associated with the size of that specific pore but at a pressure corresponding to the smallest constriction in the largest branch of the network connecting the pore to the surface. This effect will result in the apparent PSD being skewed to smaller pore sizes. When the pressure is lowered, (i.e., retraction), a different pressure will be observed for the same pore as the retraction will occur through the path with the largest constrictions.

Investigators have attempted to model this network problem using percolation theory in an attempt to extract additional pore structure information from the intrusion curve. Using a pore model based on the pore space surrounding random packing of solid monodisperse spheres (a reasonable model for a catalyst support with a monodisperse pore structure or with macropores surrounding a packing of porous microspheres), Mason [2] concluded that only 16% of the pores could be observed as a result of network/percolation effects. Recently, Smith, et. al. [3] refined Mason's work and demonstrated that actually 27% of the pores could be observed with porosimetry but these would primarily be the smaller pores. In an attempt to extract further pore size information, some investigators also employ the depressurization (retraction) curve. For example, Conner, et. al. [4] indicate that pore morphology information may be obtained by comparing the intrusion and extraction curves. This approach seems to work reasonably well for materials with narrow, unimodal pore size distributions. However, Ciftcioglu, et. al. [5] have recently demonstrated that the retraction curve may be dominated by the size of only a few large internal pores and that negligible information concerning the majority of the pores is obtained if the material has a broad distribution with a "well-connected" pore network. In principle, further pore structure information may be obtained by performing repeated scanning curves in the hysteresis region but the additional effort is rarely justified in terms of the additional information obtained.

Nitrogen adsorption/condensation is used for the determination of specific surface areas (relative pressure  $< 0.3$ ) and pore size distributions in the pore size range of 1 to 100 nm (relative pressure  $> 0.3$ ). As with mercury porosimetry, surface area and PSD information are obtained from the same instrument. Typically, the desorption branch of the isotherm is used (which corresponds to the porosimetry intrusion curve). However, if the isotherm does not plateau at high relative pressure, the calculated PSD will be in error. For PSD's, nitrogen condensation suffers from many of the same disadvantages as porosimetry such as network/percolation effects and pore shape effects. In addition, adsorption/condensation analysis can be quite time consuming with analysis times greater than 1 day for PSD's with reasonable resolution.

Despite the shortcomings of these methods, they serve as the principle analytical tools for catalyst support characterization. If one is interested in quality control applications and solely looking for qualitative differences between different batches of the same or similar supports, the errors associated with these methods



are minor. However, if one requires detailed structural information, the use of additional and/or more sophisticated techniques is required.

#### BACKGROUND - Characterization via NMR

The attractiveness of surface/pore characterization via NMR spin-lattice relaxation measurements of pore fluid lies in the potential advantages this technique has as compared to the conventional approaches. These include: rapid analysis, lower operating costs, analysis of wet materials, no pore shape assumption, a wide range of pore sizes can be evaluated (0.5 nm to  $>1 \mu\text{m}$ ), no network/percolation effects and the technique is non-destructive. When determining specific surface areas, NMR analysis does not require out-gassing and has the potential for on-line analysis of slurries.

Early studies involving NMR include the work by Hanus and Gillis [6] in which spin-lattice relaxation decay constants were studied as a function of available surface area of colloidal silica suspended in water. Senturia and Robinson [7] and Loren and Robinson [8] used NMR to qualitatively correlate mean pore sizes and observed spin-lattice relaxation times. Schmidt, et. al. [9] have qualitatively measured pore size distributions in sandstones by assuming the value of the surface relaxation time. Brown, et. al. [10] obtained pore size distributions for silica, alumina, and sandstone samples by shifting the  $T_1$  distribution until the best match was obtained between distributions obtained from porosimetry and NMR. More recently, low field (20 MHz) NMR spin-lattice relaxation measurements were successfully demonstrated by Gallegos and co-workers [11] as a method for quantitatively determining pore size distributions using porous media for which the "actual" pore size distribution is known a priori. Davis and co-workers have modified this approach to rapidly determine specific surface areas [12] of powders and porous solids.

#### THEORY - NMR

The technique is based on the observed decrease in the spin-lattice relaxation decay constant,  $T_1$ , of a fluid in contact with a solid surface as compared with the  $T_1$  for the fluid alone. Within this fluid there are assumed to exist two discrete regions: a surface affected region, in which relaxation is fast, and a region which acts as bulk fluid. If diffusion between the regions is much faster than relaxation, then for a given pore size, a single  $T_1$  will exist and can be described by the "two-fraction, fast-exchange" model [13]. In terms of the hydraulic pore radius,  $r_p$ , this governing equation for a saturated porous medium is given as [11]:

$$1/T_1 = \alpha + \beta/r_p \quad (1)$$

where  $\alpha$  is the reciprocal bulk fluid  $T_1$  and  $\beta$  is a surface relaxation parameter inversely proportional to the surface phase  $T_1$ , and incorporating the surface layer thickness.  $\alpha$  may be determined by performing a relaxation experiment on the fluid and is a function of temperature and the fluid. For water at ambient temperature,  $\alpha$  is on the order of  $0.3-0.5 \text{ s}^{-1}$ .  $\beta$  will be a function of fluid, temperature, proton frequency and surface chemistry. For decreasing proton frequency (field strength),  $\beta$  will increase resulting in increased pore sizing sensitivity. Also with decreasing frequency, the signal to noise ratio of the  $T_1$  measurements will decrease

implying a decrease in sensitivity. Therefore, the optimum frequency will depend upon both the pore size and pore volume of the sample. For most applications, frequencies in the range of 10 to 60 MHz are satisfactory.

The measured data for a single pore size or a bulk fluid is an exponentially decaying fluid magnetization vector versus time in which  $T_1$  is the decay constant. For a  $180^\circ$ - $\tau$ - $90^\circ$  pulse sequence, the return to equilibrium of the magnetization vector is described by:

$$M(\tau) = M_0 [1 - 2 \exp(-\tau/T_1)] \quad (2)$$

where  $M_0$  is the magnetization at equilibrium. However, a typical porous media will have a distribution of pore sizes, resulting in a magnetization curve which receives contributions from each pore size in the form of different  $T_1$ 's. This implies that the observed magnetization is described by:

$$M(\tau) = M_0 \int_{T_{1\min}}^{T_{1\max}} [1 - 2 \exp(-\tau/T_1)] f(T_1) dT_1 \quad (3)$$

$T_{1\max}$  is the maximum expected value of  $T_1$  and is usually taken to be the  $T_1$  for the bulk fluid.  $T_{1\min}$  is the minimum  $T_1$  value and is usually taken to be equal to the shortest  $T_1$  which can be measured with the particular instrument used. Deconvolution of Equation 3 to yield the desired  $T_1$  distribution has been accomplished via non-negative least squares (NNLS) [14] (discrete distributions) and regularization [15] (continuous distributions) algorithms. The desired pore size distribution can then be determined from the  $T_1$  distribution via the application of Equation 1.

Equation 1 is applicable (i.e., no pore shape assumption) for pores with radius greater than about 5 nm. However, the model has been extended to pores as small as 0.5 nm [16] by assuming a pore shape. In addition, the fraction of pore volume with pore sizes less than 0.5 nm may be obtained (assuming that the concept of pore size in this size range has physical significance) although distribution information in that region can not be determined.

The value for  $\alpha$  can be determined independently but the magnitude of the surface interaction parameter,  $\beta$ , must be found for the particular frequency/fluid/temperature/solid system being studied. Schmidt and co-workers [9] simply assumed a  $\beta$  value. Other workers [10,11] matched the NMR and mercury porosimetry derived pore size distributions to estimate  $\beta$ . More recently, Davis and co-workers [12] have shown that  $\beta$  can be found via a series of  $T_1$  experiments, varying the quantity of fluid sorbed on the solid surface. In that work it was shown that a plot of inverse average  $T_1$  versus the surface area (as determined via conventional methods) times solid concentration (SA\*C) will give a line with slope  $(\beta/2)$  and intercept  $\alpha$ . This value of  $\beta$  can then be applied to find unknown surface areas and pore size distributions using experimentally determined  $T_1$ 's for similar material at the same fluid, frequency and temperature.

## EXPERIMENTAL

The pore structure of two types of catalyst support material were studied:  $\gamma$ -alumina and silica aerogel. The alumina samples were commercial catalyst supports made in 1/8 inch diameter pellet form by Harshaw Chemical. Silica aerogels were prepared from silica gels synthesized by a two step acid/base catalyzed procedure employing TEOS with a water to silicon ratio equal to 3.7 [17] and ammonium hydroxide concentration of 0.005 M (sample A) or 0.01 M

(sample B). Following gelation, the samples were aged in their respective liquor at 323 K for 3 weeks (sample A) or 2 weeks (sample B). The aged samples were solvent exchanged with CO<sub>2</sub> (at 298 K and 54 atm) and critical point dried at 313 K and 81.7 atm to produce aerogels. As we will show, the aerogel pore structure is sensitive to the ammonium hydroxide concentration employed in the aging procedure. The pore size distribution of the alumina material was determined via NMR and compared to results obtained by mercury intrusion and nitrogen adsorption/condensation techniques. The pore size distributions of the two aerogel samples were measured via NMR and nitrogen adsorption/condensation only; the material being too compressible for porosimetry (the small pores of the aerogel imply that that very high pressures are required).

NMR spin-lattice relaxation inversion recovery ( $180^\circ\text{-}\tau\text{-}90^\circ$ ) experiments were conducted on the samples using distilled water as the fluid probe. Additional NMR experiments using cyclohexane were performed on the alumina material. NMR experiments were performed using a Spin Lock Ltd. CPS-2 pulse NMR at a frequency of 20 MHz and temperature of 303 K. Relaxation curves were obtained by measuring the free induction decay (FID) at approximately 30 different  $\tau$  values between 10  $\mu\text{s}$  and 9 s. Samples for NMR experiments were saturated via a number of techniques. For full saturation, the alumina samples were immersed in the fluid of interest, whereas the aerogel samples were allowed to equilibrate with vapor introduced after evacuating the samples to approximately 5 Pa. Partial saturation was accomplished by evacuating the samples and then allowing them to equilibrate with vapor over salt solutions. Fluid uptake was determined gravimetrically.

Nitrogen adsorption/condensation measurements were performed using an Autosorb-1 analyzer to calculate sample surface area and pore size distribution. BET analysis at 77 K was applied for extracting the monolayer capacity from the adsorption isotherm and a N<sub>2</sub> molecular cross-sectional area of 0.162 nm<sup>2</sup> was used to relate the monolayer capacity to surface area. PSD's were calculated from the desorption branches of the isotherms using a modified form of the BJH method [18]. Mercury intrusion measurements were performed using an Autoscan-33 continuous scanning mercury porosimeter (12-33000 psia) and a contact angle of 140°.

## RESULTS AND DISCUSSION

Sample pore volumes and surface areas via nitrogen adsorption/condensation and mercury intrusion are given in Table I. For the alumina sample, the total pore volumes obtained from condensation and mercury intrusion are in reasonable agreement. The larger value from mercury may be the result of sample compression and/or the presence of pores  $\approx 70$  nm (i.e., corresponding to the largest relative pressure used). For the silica aerogels, pore volumes could not be obtained by porosimetry because sample compression effects dominated the observed intrusion (based on the observation that no mercury was extracted from the samples on the depressurization curve and visual inspection of the sample before and after analysis). For the sample B aerogel, nitrogen adsorption indicated the presence of a small amount of microporosity.

Table I. Pore Volume and Surface Area

Sample	Pore Volume (cc/g)		Surface Area (m <sup>2</sup> /g)
	Hg	N <sub>2</sub>	N <sub>2</sub>
Alumina	0.76	0.74	235
Aerogel A	--	4.34	427
Aerogel B	--	4.20	751

Magnetic relaxation data from the NMR spin-lattice relaxation experiments on fully saturated samples were deconvoluted into continuous  $T_1$  distributions via the regularization algorithm. NMR experiments at different saturation levels were used to obtain the  $\alpha$  and  $\beta$  parameters which relate the  $T_1$  distributions to pore size distributions (eq 1.) Figure 1 is a plot showing the result of these partial saturation experiments for water, with the inverse average  $T_1$  (obtained from NNLS) plotted vs. the surface area multiplied by the solid concentration. The partial saturation experiments for water exhibited single  $T_1$  decay. The slope and intercept of the lines in Figure 1 were used to calculate  $\beta$  and  $\alpha$  respectively.

Cyclohexane was also used as a fluid for the alumina pellets. When partial saturation NMR experiments were performed using cyclohexane, the resulting  $T_1$  distributions were very broad, making a plot similar to those in Figure 1 impossible to construct.  $\alpha$  and  $\beta$  were instead calculated for the alumina/cyclohexane system via a one-point method, i.e. taking  $\alpha$  to be the inverse of the  $T_1$  for bulk cyclohexane and calculating  $\beta$  from the average  $T_1$  of the fully saturated sample (a single  $T_1$  decay) using:

$$1/T_1 = \alpha + \beta/2 SA + C \quad (4)$$

$C$  was determined gravimetrically and  $SA$  was taken as the  $N_2$  surface area.  $\alpha$  and  $\beta$  values calculated for the various samples are given in Table II. Also included are values of  $\alpha$  for water and cyclohexane obtained from experiments on bulk fluid. Differences between  $\alpha$  values for the same fluid are the result of uncertainty arising from extrapolation and/or the presence of dissolved impurities from the pore wall. Regardless, because of the small pore sizes of the materials studied, the calculated pore size is only a very weak function of  $\alpha$ . Partial saturation experiments for the aerogel material were conducted only on sample A. The  $\alpha$  and  $\beta$  values obtained were assumed to be the same for sample B which was of similar composition, differing in pore structure only. The validity of this assumption has been demonstrated in other work [12] wherein samples of similar material but different pore structure fit the same straight line on plots of the type shown in Figure 1.

Table II.  $\alpha$  and  $\beta$  Values

Material	Fluid	$\alpha$ (s <sup>-1</sup> )	$\beta$ (nm/s)
Alumina	Water	1.19	105.5
Alumina	Cyclohexane	0.481	8.28
Aerogel	Water	0.566	8.64
Bulk fluid	Water	0.381	
Bulk fluid	Cyclohexane	0.480	

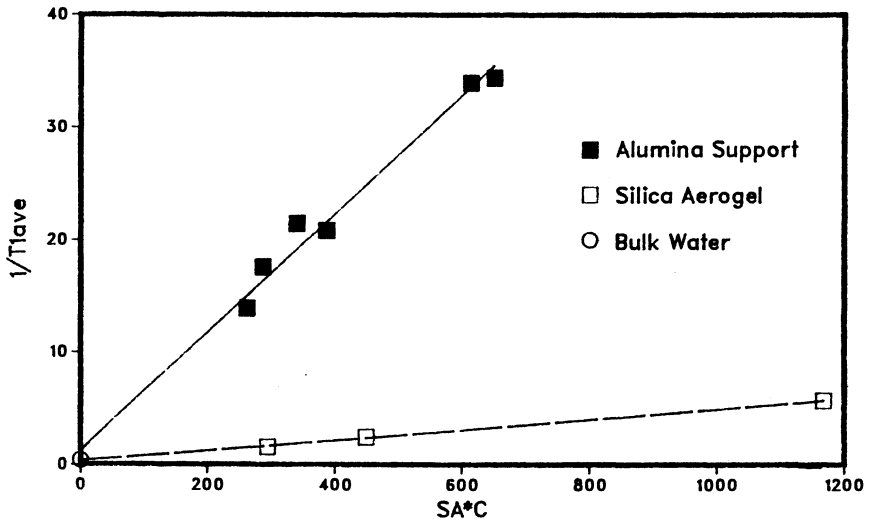


Figure 1.  $SA^*C$  plots for determination of  $\alpha$  and  $\beta$ .

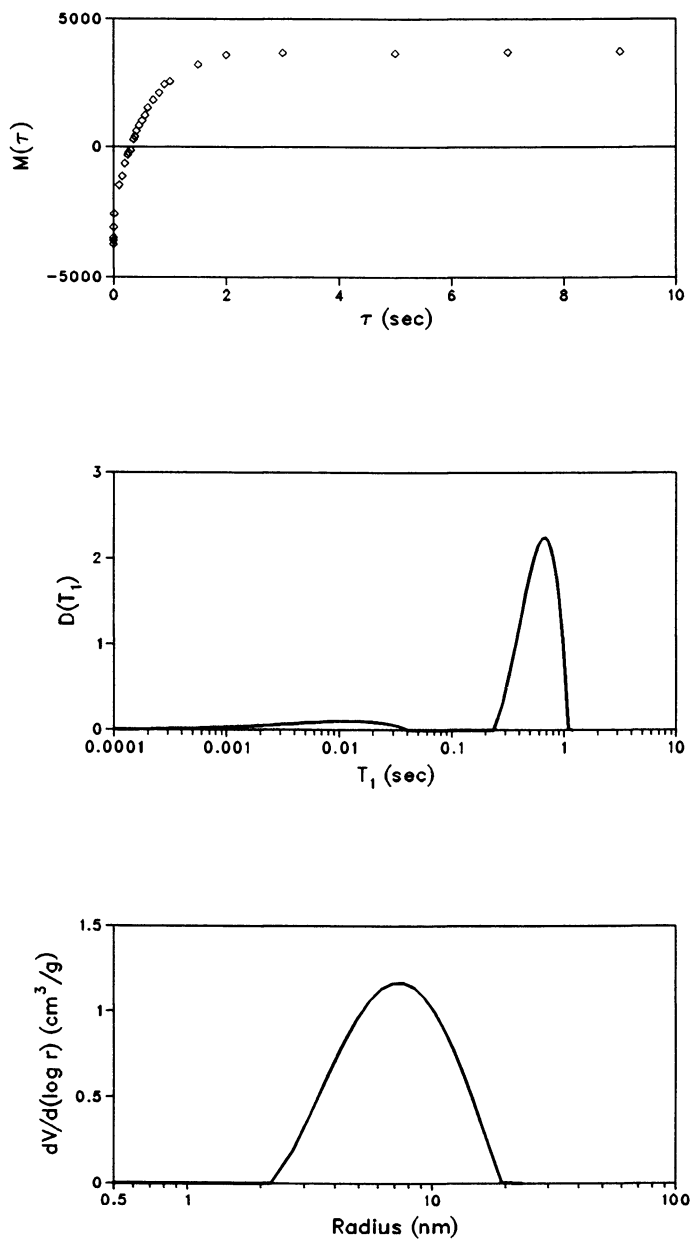


Figure 2.  $M(\tau)$ ,  $D(T_1)$  and PSD plots for cyclohexane in alumina.

The calculation of NMR pore size distributions is a three step process once the values of  $\alpha$  and  $\beta$  are known. First a spin-lattice relaxation experiment is undertaken on a saturated sample and a data set of magnetization-delay time,  $M(r)$ , is obtained. The magnetization data is subsequently deconvoluted using regularization to obtain a distribution of pore volume with  $T_1$  [in this work, the distribution of volume with the log of  $T_1$  is calculated,  $dV/d\log(T_1)$ ]. Finally, Equation 1 is applied to convert from  $T_1$  to pore size and obtain the desired pore size distribution. Since the pore shape which best describes the actual pore shape in these solids is unknown, we simply use Equation 1. For 1 nm pores, errors of up to 10% could arise from this assumption depending on the actual pore shape [16]. This calculation process is illustrated in Figure 2 for the alumina sample saturated with cyclohexane.

The  $T_1$  distributions of fully saturated samples were combined with the  $\alpha_1$  and  $\beta$  values of Table II to produce pore size distributions for each material. The NMR pore size distributions were compared for each type of material to pore size distributions obtained via nitrogen adsorption/condensation (all materials) and mercury porosimetry (alumina samples). The results are shown in Figure 3 for alumina and in Figure 4 for the aerogels. In each case the NMR agrees fairly well with the other techniques, but is seen to result in slightly larger pore sizes. This is consistent with the limitations of the other techniques which generally result in smaller than actual pore size measurements due to constricted pores and network/percolation effects. The difference between the two aerogels is the result of the longer aging conditions for Aerogel A. The NMR results for water and cyclohexane in alumina should agree closely. The difference noted is probably due to inaccuracies in the cyclohexane  $\alpha$  and  $\beta$  which had been calculated using a one-point method.

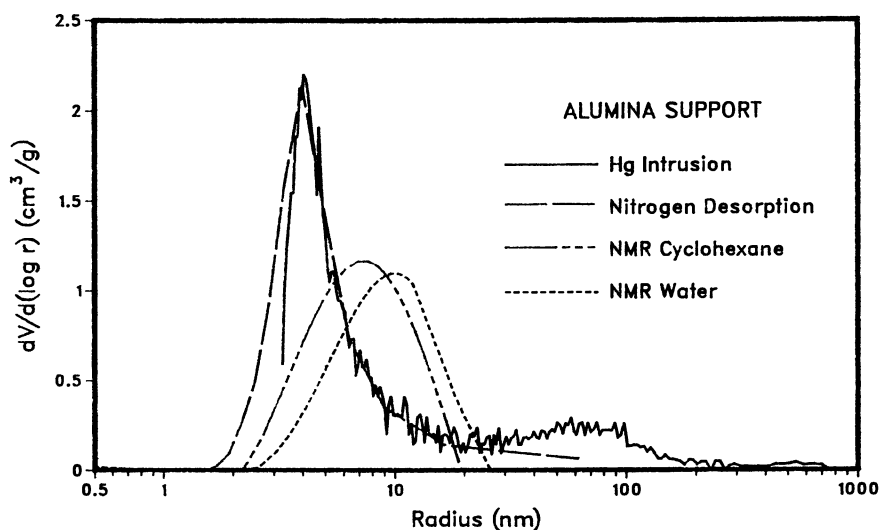


Figure 3. NMR, nitrogen condensation and porosimetry PSD's for alumina.

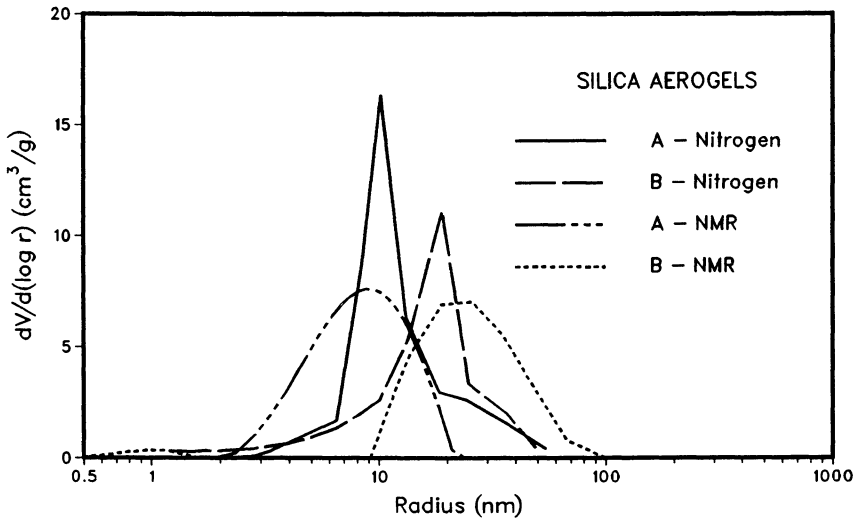


Figure 4. NMR and nitrogen condensation PSD's for silica aerogels.

#### ACKNOWLEDGMENTS

This work has been supported by Sandia National Laboratories (#55-6778) and the ALCOA Foundation. Nitrogen adsorption and mercury porosimetry measurements were performed by S.B. Ross. Aerogels were prepared by Carol S. Ashley of SNL.

#### REFERENCES

- [1] Washburn, E.W.; Phys. Rev., 1921, 17, 273.
- [2] Mason, G.; J. Colloid Interface Sci., 1972, 41, 208.
- [3] Smith, D.M., Gallegos, D.P., Stermer, D.L.; Powder Tech., 1987, 53, 11.
- [4] Conner, W.C., Weist, E.L., Pedersen, L.A.; PREPARATION OF CATALYSTS IV: Delmon, Grange, Jacobs, and Poncelet Editors, Elsevier, Amsterdam, 1987.
- [5] Ciftcioglu, M., Smith, D.M., Ross, S.B.; Powder Tech., 1988, 55, 193.
- [6] Hanus, F., Gillis, P.; J. Mag. Resonance, 1984, 59, 437.



- [7] Senturia, S.D., Robinson, J.D.; Soc. Pet. Eng. J., 1970, 10, 237.
- [8] Loren, J.D., Robinson, J.D.; Soc. Pet. Eng. J., 1970, 10, 268.
- [9] Schmidt, E.J., Velasco, K.K., Nur, A.M.; J.Appl.Phys., 1986, 59, 2788.
- [10] Brown, J.A., Brown, L.F., Jackson, J.A., Milewski, J.V., Travis, J.V.; Proceedings of the SPE/DOE Unconventional Gas Recovery Symposium, 1982, 201.
- [11] Gallegos, D.P., Munn, K., Smith, D.M., Stermer, D.L.; J. Colloid Interface Sci., 1987, 19, 127.
- [12] Davis, P.J., Gallegos, D.P., Smith, D.M.; Powder Tech., 1987, 53, 39.
- [13] Brownstein, K.R., Tarr, C.E.; J. Mag. Resonance, 1980, 39, 297.
- [14] Munn, K., Smith, D.M.; J. Colloid Interface Sci., 1987, 119, 117.
- [15] Gallegos, D.P., Smith, D.M.; J. Colloid Interface Sci., 1988, 122, 143.
- [16] Gallegos, D.P., Smith, D.M., Brinker, C.J.; J. Colloid Interface Sci., 1988, 124, 186.
- [17] Brinker, C.J., Keefer, K.D., Schaefer, D.W., Ashley, C.S.; J. Non-Crystalline Solids, 1982, 48, 47.
- [18] S. Lowell and J. Shields, Powder Surface Area and Porosity; Chapman & Hall: London, 1984.

RECEIVED January 10, 1988

## Chapter 25

# Characterization of Y Zeolites by $^{23}\text{Na}$ Magic-Angle-Spinning NMR Spectroscopy

L. B. Welsh and S. L. Lambert

UOP Research Center, Des Plaines, IL 60017

Sodium-23 MASNMR results have been obtained on Na-Y zeolites and a series of partially exchanged  $(\text{NH}_4,\text{Na})$ -Y,  $(\text{Ca},\text{Na})$ -Y and  $(\text{La},\text{Na})$ -Y zeolites which demonstrate that the sodium cations in the supercages can be distinguished from those in the smaller sodalite cages and hexagonal prisms for both hydrated and dehydrated Y zeolites. For the hydrated Y zeolites, spectral simulation with symmetric lines allows the cation distributions to be determined quantitatively. The sodium-23 MASNMR results are consistent with the selective removal of sodium cations from the Y zeolite supercages by the partial cation exchange. The results demonstrate that this technique can be used to monitor how cation distributions in Y zeolites change with various sample treatments.

Considerable characterization of the silica-alumina framework of Y and other large pore zeolites has been reported in recent years (1-2). For example, the dealumination of Y zeolite has been extensively studied using various techniques including silicon-29 NMR, aluminum-27 NMR and STEM/EDX analysis (3-4). On the other hand, the characterization of the state and location of cations in zeolites has been less well studied. The locations of the cations can play an important role in the intrazeolite diffusion of molecules and in the shape selectivity exhibited by the zeolite. For example, potassium A zeolite can adsorb only very small molecules such as hydrogen or water, while a sodium exchanged A zeolite adsorbs molecules as large as ethane; however, if A zeolite is exchanged with calcium, halving the number of cations required for charge compensation, it is capable of exchanging larger n-paraffins (5). In any zeolite containing more than one

type of nonequivalent cation site, the relative populations of those sites may be very important in determining how the material performs in a particular application. In Y zeolite there are at least three inequivalent cation sites (6,7) which are believed to have different accessibilities based on cation exchange studies (7). For this reason, and because Y zeolite is of considerable commercial interest, it was chosen for this study of cation distributions by sodium-23 NMR.

At this time, the locations of cations in zeolites have been determined primarily by X-ray diffraction (XRD) techniques. Unfortunately, this method has the drawback of being able to locate only the most stationary cations in zeolites. In some studies of hydrated zeolites, less than 50% of the total cation population can be accounted for. A higher percentage of the cations can be located in dehydrated samples, but the effect of the dehydration step on the location of the cations is generally not well known. NMR measurements, on the other hand, are most sensitive to mobile cations and cations in high symmetry sites. The XRD data collected on dehydrated Na-Y zeolites indicate that the detectable sodium cations reside in three sites (6). Site I is located in the hexagonal prism and has a low occupancy, about 10% of the total cations. Site I' is located in the sodalite cage and about 30% of the cations occupy these sites. The remaining cations, approximately 60%, are found in Site II, which is located in the supercage of the Y zeolite (6). The ammonium/sodium exchange isotherm for Y zeolite (7) shows that with one exchange at room temperature a maximum of 60 to 65% of the sodium ions can be replaced by ammonium ions. In light of the above X-ray diffraction data, these ion exchange data indicate that only those cations in the supercage sites of Y zeolite are readily exchanged at room temperature. A similar isotherm is observed for the exchange of sodium by calcium in Y zeolite (7), and for the exchange of sodium by lanthanum in Y zeolite (7,8).

The ability to distinguish at least two types of sodium cations in hydrated Y zeolites, using high field sodium-23 magic angle spinning NMR (MASNMR), has recently been demonstrated by the authors (9). Spectra of hydrated Na-Y and series of partially exchanged (NH<sub>4</sub>,Na)-Y and (Ca,Na)-Y zeolites were obtained which allowed the specific sodium-23 MASNMR lines to be associated with sodium cations in either the supercage or the smaller cage sites. At least two, and possibly three, lines were identified. A resonance near -2 ppm, which is initially the most intense line, loses intensity rapidly as the sodium is exchanged out of the Y zeolite. This resonance has been assigned to the sodium cations in the supercage. The second major resonance is located near -7 ppm and its intensity decreases only very slowly, even after the majority of the sodium has been exchanged out of the zeolite. This second line is assigned to sodium cations in the sodalite cages and possibly the hexagonal prism sites. There is also the possibility of a third, poorly resolved line of low intensity. This line is broad, making its NMR properties difficult to determine. The origin of this third line may include

contributions from sodium cations in Type I sites, nonmobile cations in the supercages, and residual sodium which is not associated with the cation sites.

The work discussed here compares the relative site occupancies for three series of hydrated Y zeolites: ammonium, calcium and lanthanum exchanged. The data for these same three series of samples in the dehydrated forms are also presented and the assignment of the observed resonances is discussed.

## EXPERIMENTAL

### Sample Preparation

Three series of partially exchanged Y zeolites were used for this NMR study: ammonium, calcium and lanthanum exchanged. These samples were prepared using a single, 72 hour, room temperature exchange of LZV-52, a sodium Y zeolite. Ten grams, volatile-free, of LZV-52 were used per 100 cc of exchange solution. To achieve the varying degrees of exchange, the molarities of the exchange solutions were varied as indicated in Table I. Each sample was washed with 250 cc deionized water and then dried at 40°C. The analyses obtained on each sample, as well as the calculated percent exchange, are given in Table I. The hydrated samples were prepared by equilibrating the samples for 24 hours in a chamber maintained at 50% relative humidity. The dehydrated samples were prepared by drying the materials at 150°C for 24 hours. The dehydrated samples were sealed immediately upon removal from the oven and were transferred to the NMR rotor under a dry nitrogen atmosphere.

### Acquisition, Processing and Simulation of Sodium-23 NMR Spectra.

Sodium-23 MASNMR spectra were obtained on 6.3, 8.45, and 11.7 Tesla multinuclear solids NMR spectrometers at Spectral Data Services and the University of Illinois in Champaign, Illinois. For the hydrated Y zeolites, sample spinning rates of 3 to 5 KHz were used in most cases. A typical spectrum was acquired using 1000 scans, a recycle time of 0.5 sec. and an rf excitation pulse width of 2.0 microsec, which is less than 1/4 of a 90° pulse width of sodium in solution. Under these conditions, the integrated intensity of the different sodium NMR lines in the spectrum closely approximates the concentration of different sodium species giving rise to the NMR lines. For the dehydrated Y zeolites, samples, spinning rates of 6 to 9 KHz were used. A typical spectrum was acquired using 5000 scans, a 2 sec. recycle time and a pulse width less than that of a solids 45° pulse (about 2.5 microsec).

## RESULTS

To determine the origin of the sodium-23 lines observed in Na-Y zeolites, they were partially exchanged with either  $\text{NH}_4$  or Ca

TABLE I  
CATION EXCHANGED SAMPLES OF Y ZEOLITE

Sample Type	% Exchange (of Sites)	% Na <sub>2</sub> O (VF)	% SiO <sub>2</sub> (VF)	% Al <sub>2</sub> O <sub>3</sub> (VF)	Molarity of Exchange Solution
LZY-52	0	14.02	61.17	20.67	-----
(Ca, Na) -Y	11	11.11	---	---	0.028 M
(Ca, Na) -Y	21	9.95	---	---	0.050 M
(Ca, Na) -Y	35	8.20	---	---	0.082 M
(Ca, Na) -Y	45	6.92	---	---	0.123 M
(Ca, Na) -Y	50	6.32	---	---	0.163 M
(Ca, Na) -Y	52	5.99	---	---	0.245 M
(Ca, Na) -Y	56	5.51	---	---	0.299 M
(Ca, Na) -y	58	5.19	---	---	0.367 M
(Ca, Na) -Y	62	4.81	---	---	0.463 M
(NH <sub>4</sub> , Na) -Y	9	11.40	---	---	0.080 M
(NH <sub>4</sub> , Na) -Y	26	9.32	---	---	0.161 M
(NH <sub>4</sub> , Na) -Y	32	8.56	---	---	0.241 M
(NH <sub>4</sub> , Na) -Y	41	7.37	---	---	0.361 M
(NH <sub>4</sub> , Na) -Y	47	6.59	---	---	0.482 M
(NH <sub>4</sub> , Na) -Y	53	5.95	---	---	0.723 M
(NH <sub>4</sub> , Na) -Y	55	5.64	---	---	0.883 N
(NH <sub>4</sub> , Na) -Y	56	5.48	---	---	1.084 M
(La, Na) -Y	2	12.31	---	---	0.014 M
(La, Na) -Y	9	11.43	---	---	0.027 M
(La, Na) -Y	22	9.81	---	---	0.041 M
(La, Na) -Y	41	7.45	---	---	0.054 M
(La, Na) -Y	52	6.03	---	---	0.068 M
(La, Na) -Y	60	5.01	---	---	0.095 M
(La, Na) -Y	68	4.08	---	---	0.122 M
(La, Na) -Y	66	4.32	---	---	0.149 M

cations (9). Since neither of these cations is small enough to enter the sodalite cages or hexagonal prisms in the hydrated form, the spectral changes observed for the partially exchanged zeolites can be identified with the replacement of the Na cations in the supercages by the  $\text{NH}_4$  or Ca cations. Simulations of such spectra with symmetric lines of mixed Gaussian/Lorentzian character quantitatively establish the amount of Na cations removed from the supercage sites by the cation exchange (9).

This type of analysis was extended to the (La,Na)-Y zeolite system for two reasons. First, to establish if the behavior of a triply charged cation can be analyzed by sodium-23 NMR in a fashion similar to that of the singly charged  $\text{NH}_4$  cations and the doubly charged Ca cations. Second, ion exchange experiments have established that hydrated La cations can not penetrate the smaller cages, but that low temperature calcination of the zeolite (<200°C) dehydrates the La cation and results in substantial La occupation of the cation sites in the smaller cages (8). Thus, the calcination temperatures needed to ensure La penetration to the smaller cages and a consequent Na migration to the supercages are known and can be used to verify the interpretation of the sodium-23 MASNMR spectra.

For the hydrated (La,Na)-Y zeolite series, the La cations are believed to replace only those Na cations in the supercages (8). The sodium-23 MASNMR spectra of the series of hydrated (La,Na)-Y zeolites obtained at 96 MHz, are presented in Figure 1. The spectra are shown from top to bottom, in order of increasing La cation concentration. As in the cases of the ( $\text{NH}_4$ ,Na) and (Ca,Na) series of exchanged Y zeolites (9), the integrated intensity of the sodium-23 MASNMR spectra of the (La,Na)-Y zeolites decreases linearly with increasing cation exchange. This indicates that all of the Na in the zeolite is contributing to the observed NMR signal. Inspection of Figure 1 clearly shows that the peak near -2 to -3 ppm loses intensity relative to the peak near -7 ppm. At the highest exchange levels, there is little evidence of the line near -2 to -3 ppm. These changes are virtually the same as those observed for the ( $\text{NH}_4$ ,Na)-Y and (Ca,Na)-Y zeolite systems (9). Simulations of the  $^{23}\text{Na}$  MASNMR spectra of the (La,Na)-Y zeolites have been made in the same manner as for the other zeolite series, using symmetric lines of mixed Gaussian/Lorentzian character. These simulations can be used to establish that virtually all of the Na cations in the supercages have been replaced by the La cations for the most highly exchanged zeolites.

The similarities in the Na cation distributions between the ( $\text{NH}_4$ ,Na), (Ca,Na) and (La,Na) mixed cation systems in hydrated Y zeolites can be best demonstrated by comparing the sodium-23 MASNMR spectra at cation exchange levels where the NMR lines from the Na cations in the supercages and smaller cages are best resolved. For the ( $\text{NH}_4$ ,Na), (Ca,Na) and (La,Na) cation systems these occur at exchange levels of 41, 45, and 52%, respectively.

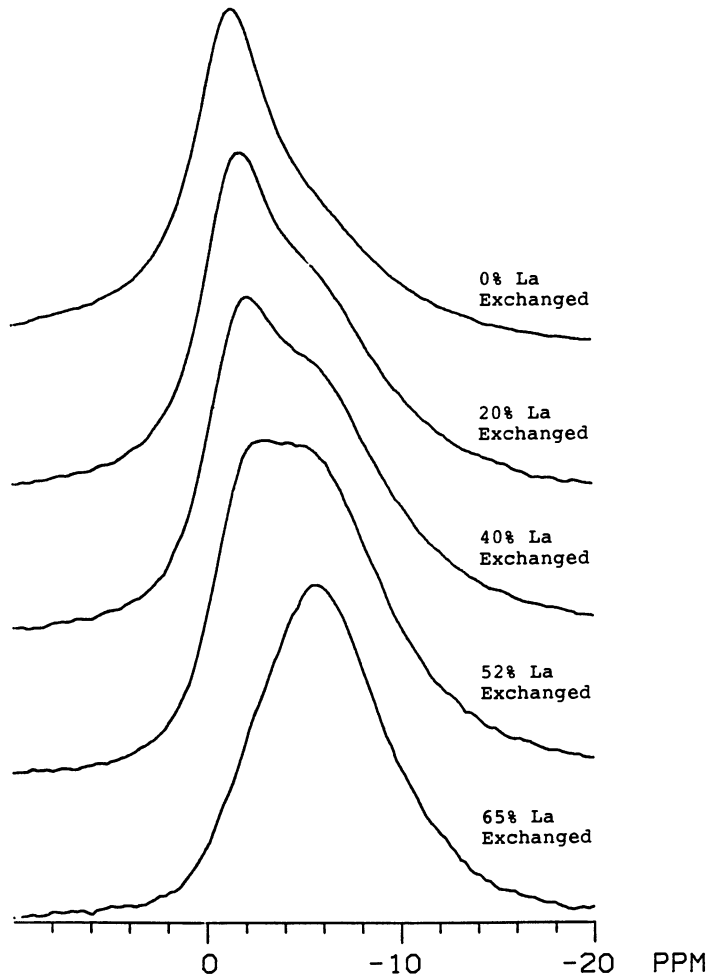


Figure 1. Sodium-23 MASNMR spectra of a series of hydrated, partially lanthanum exchanged Na-Y zeolites at 96 MHz. The level of lanthanum exchange is as indicated.

The sodium-23 MASNMR spectra of the Y zeolite samples with these particular levels of cation exchange are shown in Figure 2, along with the spectrum of the Na-Y zeolite. Simulations of these spectra indicate that about 25, 10, and 20% of the integrated NMR intensity of the respective exchanged zeolites arises from residual Na cations in the supercages. The different Na NMR lines are best resolved in the case of the  $(\text{NH}_4, \text{Na})$ -Y zeolites.

Sodium-23 MASNMR spectra of the three mixed cation systems have also been obtained in the dehydrated form, where the residual water content is less than 10 molecules per unit cell. Removal of the water from the zeolite results in the cations being more highly localized in the cation sites. In the case of Na-Y zeolites, X-ray diffraction measurements have established that the Na cations are located primarily in the Type II sites in the supercages and the Type I' sites in the Sodalite cages (6). For the samples used in this particular study, only about 10% or less of the Na cations were identified as occupying the Type I sites in the hexagonal prisms. Dehydration also results in the Na cations generally having increased quadrupolar interactions which broaden and shift the sodium-23 MASNMR lines, possibly to the point of unobservability. Previously, it has been reported that the sodium-23 NMR line in dehydrated Y zeolites is unobservable (10).

In this study we report that the sodium-23 MASNMR spectra of Na cations in dehydrated Na-Y and mixed cation Y zeolites can be observed at 96 MHz. Using MAS rates in excess of 5 KHz reveals structure to the spectrum which can be associated with lines arising from cations sites in the different Y zeolites cages. However, it is estimated that only about 70 to 80% of the Na atoms present in the zeolite may be observable by NMR under these conditions. As an example of the sodium-23 MASNMR spectra obtainable from the dehydrated Y zeolites, the spectra of a Na-Y and the three mixed cation Y zeolites are presented in Figure 3. For the  $(\text{NH}_4, \text{Na})$ ,  $(\text{Ca}, \text{Na})$  and  $(\text{La}, \text{Na})$ -Y zeolites, the degrees of cation exchange were 56, 58, and 65%, respectively. In contrast to the NMR spectra of the hydrated Y zeolites presented in Figure 2, the spectra of the dehydrated mixed cation Y zeolites show substantial differences from each other as well as from that of the Na-Y zeolite. The spectrum of the Na-Y zeolite consists of a line with a peak between about -7 and -12 ppm, with a substantial shoulder to the high field (more negative ppm) side. As  $\text{NH}_4$  cations are exchanged into the supercage sites and Na cations are removed, the high field shoulder decreases in strength and eventually disappears. This is clearly demonstrated by the spectrum of the 56%  $\text{NH}_4$  exchanged Y zeolite displayed in Figure 3. Such changes suggest that this shoulder is arising from Na cations in the supercage Type II sites, since the  $\text{NH}_4$  cations are too large to penetrate to the smaller cages and exchange with the Na cations in those cages.

A different behaviour is observed for the dehydrated  $(\text{Ca}, \text{Na})$  and  $(\text{La}, \text{Na})$  cation systems. For these cation systems, dehydration of the Y zeolite is known to result in Ca or La penetration into



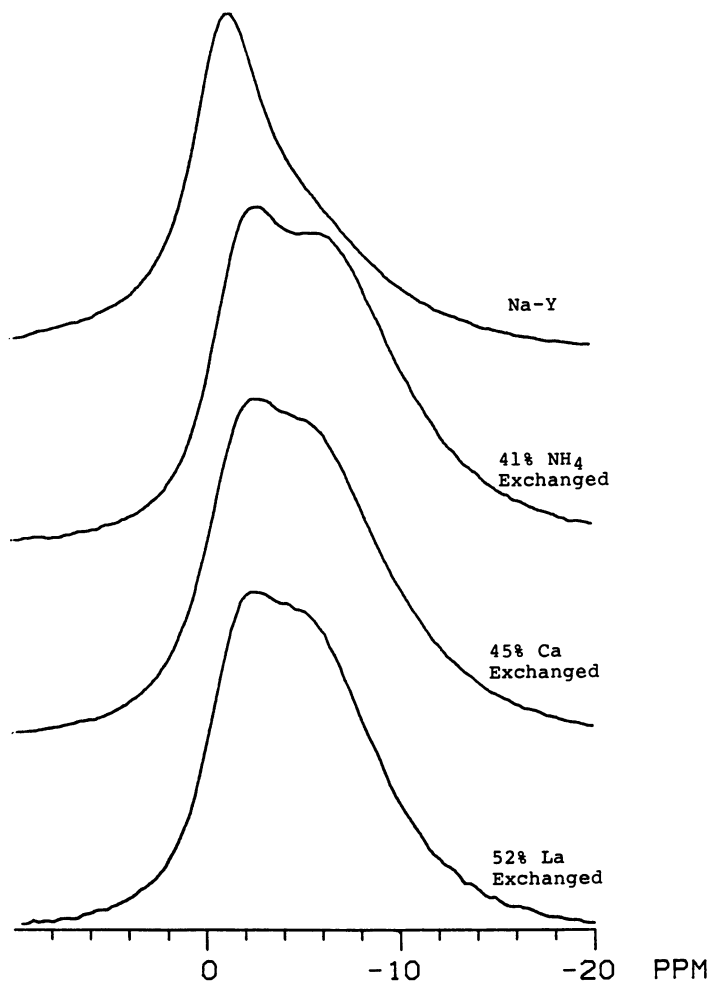


Figure 2. Comparison of sodium-23 MASNMR spectra of hydrated Na-Y and partially ammonium, calcium, or lanthanum exchanged Na-Y zeolites at 96 MHz.

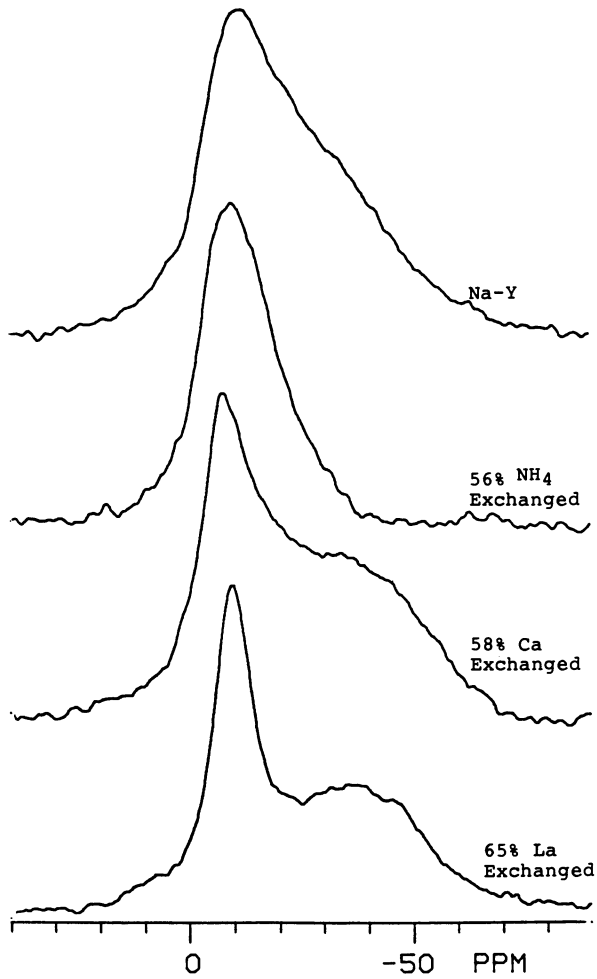


Figure 3. Comparison of sodium-23 MASNMR spectra of dehydrated Na-Y and partially ammonium, calcium, or lanthanum exchanged Na-Y zeolites at 96 MHz.

the sodalite cages and hexagonal prisms, with a consequent displacement of the Na cations to the supercages. As shown in Figure 3 for both cation systems, the relative intensity of the sodium-23 MASNMR line near about -7 to -12 ppm has decreased substantially relative to the line structure at higher field for high cation exchange levels. The broad high field line now appears as a separate line, which can be associated with the Na cation occupation of Type II sites in the Y zeolite supercages. Although the features of the broad line are not clearly those of a quadrupole interaction dominated lineshape, spectra obtained at 76 and 132 MHz establish that the line position and width change with magnetic field are consistent with quadrupole interactions causing line broadening, particularly at the lower magnetic field. The lack of structure for this line may arise from the supercage Na cations having a distribution of environments and hence quadrupole interactions in the Type II sites. With the association of the broad line near -40 ppm as arising from Na cations in the supercages, the narrower line at -7 to -12 ppm can presumably be associated with Na cations located in the Types I and I' sites of the smaller cages. Given the X-ray diffraction result that the occupancy of Type I' sites is much larger than that of Type I sites for dehydrated Na-Y zeolites (6), we believe that this line arises primarily from Na cations located in the Sodalite cages.

#### SUMMARY

Sodium-23 MASNMR measurements have been used to examine the extent to which this method can be used to determine the cation distribution in hydrated and dehydrated Y-zeolites. Results have been obtained on Na-Y and series of partially exchanged (NH<sub>4</sub>,Na)-Y, (Ca,Na)-Y and (La,Na)-Y zeolites which demonstrate that the sodium cations in the supercages can be distinguished from those in the smaller sodalite cages and hexagonal prisms. For the hydrated Y zeolites, spectral simulation with symmetric lines allows the cation distribution to be determined quantitatively. The sodium-23 MASNMR results are consistent with the selective removal of sodium cations from the Y zeolite supercages by the partial cation exchange. This demonstrates that this technique can be used to monitor how cation distributions in Y zeolites change with various sample treatments.

#### REFERENCES

1. Engelhardt, G. and Michel, D., "High Resolution Solids State NMR of Silicates and Zeolites", John Wiley and Sons, 1987.
2. Klinowski, J., "Nuclear Magnetic Resonance Studies of Zeolites", in *Progress in NMR Spectroscopy*, Vol. 16, p237-309, 1984.
3. Ray, G. J., Meyers, B. L., and Marshall, C. L., *Zeolites* 1987, 7, 307.
4. Kubelkova, L., Seidl, V., Novakova, J., Bednarova, S., and Jiru, P., *J. Chem. Soc. Faraday Trans. 1*, 1984, 80, 1367.

5. Ruthven, D. M., Chem. Eng. Prog. Feb 1988, p 42.
6. Mortier, W. J., Van den Bossche, E. and Uytterhoeven, J. B., Zeolites, 1984, 4, 41.
7. Breck, D. W., "Zeolite Molecular Sieves: Structure, Chemistry and Use," Wiley Interscience, New York, 1974.
8. Lee, E. F. T. and Rees, L. V. C., Zeolites, 1987, 7, 143.
9. Welsh, L. B. and Lambert, S. L., in "Perspectives in Molecular Sieve Science", ACS Symposium series #368, 1988, W. H. Flank and T. E. Whyte Editors, pp 33-47.
10. W. D. Basler, Colloids and Surfaces, 1984, 12, 59.

RECEIVED January 26, 1989

## Chapter 26

# X-ray and Electron Microscopic Analyses of Catalysts

Heinz J. Robota<sup>1</sup> and Steven A. Bradley<sup>2</sup>

<sup>1</sup>Allied-Signal Engineered Materials Research Center, Des Plaines, IL 60017

<sup>2</sup>UOP Research Center, Des Plaines, IL 60017

X-ray and electron microscopic analyses are widely used techniques for characterizing catalysts. The papers that follow this introductory chapter will describe the application and utility of these techniques in understanding and developing new and improved catalysts.

X-ray analysis methods play an important analytical role in the characterization and subsequent development of catalysts. For example, the development of shape selective zeolites such as ZSM-5 made extensive use of x-ray methods for structural characterization. Among the most widely utilized analytical methods are powder x-ray diffraction (XRD) techniques. Powder XRD methods find utility for determining crystallinity in zeolite preparations, determining Si/Al ratios through changes in zeolite lattice parameters, identifying crystalline phases in new catalyst preparations as well as identifying contaminant phases in spent catalysts of many varieties, determining metal crystallite sizes in supported metal catalysts, identifying alloying of different supported metallic components, as well as a wide variety of other determinations. Many examples are provided by Rohrbaugh and collaborators. Both explicit and implicit application of these methods can be found in the papers comprising this volume. Davis et al. have found intermetallic phases of the Pt-Sn alloy system in supported Pt, Sn catalysts following a variety of treatments. Bergna has utilized diffraction to determine the crystallinity of the silica material formed on the surfaces of spray dried particles. While not explicitly discussed, powder XRD methods are routinely applied to the characterization of the zeolitic materials for the development of FCC catalysts.

In addition to identifying and characterizing known crystalline phases, single crystal, and more recently, powder diffraction methods can be used to determine the atomic positions within the crystal structures of new and uncharacterized materials. An excellent demonstration of how XRD structure determination methods can be applied in concert with other characterization techniques for

identifying unknown structures is given by Vaughn et al in the determination of a structure for a new zeolitic material.

A more recent addition to the diverse array of x-ray based methods is x-ray absorption spectroscopy. In contrast to x-ray diffraction methods which derive their utility from the properties of well defined crystallites, x-ray absorption methods are atomic probes, capable of obtaining both electronic and structural information about a specific type of atom. The growing use of x-ray absorption methods is a result of the greater availability of synchrotron radiation sources which provide the intense broad band x-radiation required. In some instances laboratory based spectrometers utilizing either sealed tubes or rotating anode x-ray generators can also be used.

The electronic transitions probed by x-ray absorption spectroscopy involve the excitation of a core electron into either unoccupied bound electron states near the Fermi level of the material or at higher energies into the continuum of states producing a photoelectron. These electronic excitations must obey spectroscopic selection rules and thus can provide information about the symmetry of an atom's environment, its oxidation state, and sometimes, with the assistance of comprehensive theoretical calculations, details about the geometry of ligands and other nearby atoms. This information is derived from excitations into bound states and low lying resonances above the Fermi level and is referred to as the x-ray absorption near edge structure (XANES). Some examples of using XANES to obtain information about the immediate local environment of the atom being probed are Woolery et al's study of the vanadium species found in used FCC catalysts. Bouwens et al have used the variation of the intensity of pre-edge XANES features in Co containing catalysts to identify the symmetry of ligands bound to Co in Co-Mo-S hydrodesulfurization (HDS) catalysts.

Structural studies using XAS more typically rely on the modulations of the absorption coefficient at x-ray energies well beyond the absorption threshold. These modulations are known as the extended fine structure and the technique is commonly known as EXAFS analysis. Structural and chemical information is contained in the frequency and amplitude of superimposed oscillatory modulations of the x-ray absorption coefficient. As with XANES, the structural information is centered at the atom probed with the information content decreasing as one moves beyond the probed atoms nearest neighbors. However, for catalytic purposes, this information represents the chemical identity of the microscopic atomic arrangements which constitute catalytic sites and thus should yield very valuable information about the active catalytic arrangements. Information of this type is also particularly valuable when other structural characterization methods fail due to the extremely small size of the active aggregates as is often the case in supported noble metal catalysts. One such case pertains to the interaction of Pt with other elements in petroleum reforming catalysts. For example, the nature of Pt-Sn interactions is explored by Davis et al in a study of model Sn modified Pt based catalysts. It is anticipated that a more complete understanding of such interactions will result in the development of significantly improved reforming

catalysts. Bouwens et al demonstrate how XANES and EXAFS can be used together to obtain a consistent description of interacting catalyst components in specially prepared Co-Mo-S HDS catalysts. Similarly, Woolery et al. have probed the local environment of Ni in steamed FCC catalysts to determine the nature of the Ni species formed.

Application of x-ray methods, either diffraction or absorption, to the development of commercial catalysts still relies predominantly on two approaches. In one approach, a real commercial material is treated under real test conditions and then characterized following transfer of the used material to the appropriate instrument. A second approach attempts to recreate some critical aspect of the catalyst's reaction environment in an in situ reactor attached to the appropriate instrument, but uses a model catalyst. Considerable opportunity exists in the careful melding of these two approaches so that real catalysts are treated under real conditions and are measured without intervening exposure to ambient. Only under such well controlled conditions can we hope to extract the maximum amount of information from x-ray based measurements. This area calls for creative method development and research should be geared along these lines in the future.

In the development of catalyst systems the electron microscope is becoming a highly utilized interactive tool. Many reviews have been written on the use of electron microscopy in characterizing catalysts. Targos and Bradley describe the utility of scanning transmission and analytical electron microscopy to characterize commercial catalysts. As catalysts become more complex with two or more metals impregnated onto a support or mixed oxide or zeolitic systems being employed, relating structure with properties becomes critical in the optimization of the catalyst. Targos and Bradley also demonstrate how this information can be obtained by microscopy and related to performance.

One of the heavy uses of electron microscopy is for the evaluation of metals distribution. The reason that metals distribution analysis is so important is that (a) the chemist has a variety of methods for impregnation and (b) catalytic activity and selectivity have been related to metals location (1). This type of information can be easily obtained with an energy dispersive x-ray or wavelength dispersive x-ray spectrometer attached to a scanning electron microscope. With this method metals concentration as a function of position can be developed. The selection of whether to use the energy or wavelength dispersive spectrometer is related to metals concentration and the number of elements that require analysis. For a Be window energy dispersive spectrometer, elements with an atomic number greater than Na can be simultaneously detected. With a wavelength dispersive microprobe only a single element can be detected at a time. However, detectability is greater with a dedicated wavelength dispersive x-ray microprobe. Sample preparation requires a smooth surface, typically polished, followed by a carbon coating for electrical conductivity. Puls describes in a later section how metals distribution analysis was used to qualify a catalyst for a specific petrochemical process. Other techniques that can be used for metals distribution include Auger electron spectroscopy, scanning ion microprobe, and scanning transmission electron microscopy.

Identifying micron-sized components or impurities on catalysts in the scanning electron microscope is complicated by electron beam broadening. Ultramicrotomy of the catalyst coupled with transmission electron microscopy is one technique that can be used to identify such constituents. Csencsits and Gronsky combined high resolution and analytical electron microscopy to study FeZSM-5 and show the spatial distribution of the Fe-rich second phase particles. Auger electron spectroscopy is another approach that can be used to investigate surface contaminants but the insulating nature of most catalyst supports causes sample charging problems. Special sample preparation (pressed powder into indium foil), operating conditions (low accelerating voltage) or conductive samples (heavy carbon deposits) are often required. One technique that seems to avoid the beam broadening and charging problems is secondary ion spectroscopy.

Imaging individual elements with secondary ion mass spectroscopy as shown by Leta appears to be a very good way to study and demonstrate metals interaction in a FCC catalyst. This should facilitate the development of more metals tolerant catalysts.

Support morphology can be altered by varying the processing conditions. Both scanning electron and transmission electron microscopy can assist in relating morphology to activity. Csencsits and Gronsky describe such a characterization of Fe ZSM-5 zeolite. Similar studies have helped commercialize new zeolite preparations (2).

In some systems the presence or absence of metal crystallites determines catalytic activity. Both x-ray diffraction and electron microscopy are complementary techniques in evaluating these catalysts. The advantages of the scanning transmission electron microscope for these studies is described by Targos and Bradley. Masel (3) has related catalytic activity with specific exposed crystallite surfaces for nitric oxide reduction. Performing such studies on a high surface area support becomes extremely exhaustive but may have to be performed to optimize certain reactions. The interactive approach of utilizing a combination of characterization tools including electron microscopy was well documented in the development of a Fischer-Tropsch catalyst (4). Automotive catalysts are quite complex and their further development will require an understanding of the interrelationships of each component (5). Determining whether 1 nm crystallites are on the outside or inside of the pores of a zeolite (6) is necessary for the development of some catalysts.

For many heterogeneous catalysts the presence of 2 nm crystallites may be deleterious to performance. Unfortunately the positive identification of 1 nm Pt crystallites on a high surface area  $\gamma$ -Al<sub>2</sub>O<sub>3</sub> support is extremely difficult. Although EXAFS has been used, it is not a routine technique. High resolution electron microscopy has not been successful with low metals loading. Improved annular dark field detectors for the scanning transmission electron microscopes may assist in detecting 1nm crystallites. For tailoring a catalyst to a specific reaction, one must be able to relate the structure of the site to catalytic activity and selectivity. Possibly future developments in high resolution electron microscopy will address this problem.



In most microscopy studies the catalyst is examined under vacuum. To understand the system, the catalyst should be examined under reactor conditions. Environmental chambers that do not reduce instrument resolution are presently not available. Similarly, pretreatment systems attached to the instrument would extend characterization insight. At the very least, sample delivery systems that minimize air exposure are necessary. For example, air exposure during sample transfer as might occur with a reduced Pd catalyst can alter the crystallite morphology. Such studies would be expected to enhance catalyst development.

### References

1. Roth, J.F.; Richard, T.E.; *J. Res. Inst. Catalysis, Hokkaido University* 1972 20 85.
2. Lynch, H.; Raatz, F.; Dufresne, P.; *Zeolites* 1987 7 333.
3. Masel, S.I.; *Catal. Rev. - Sci. Eng.* 1986 28 335.
4. Abrevaya, H.; Targos, W.; Robota, H.; Cohn, M.; *Proceedings of the Tenth North American Catalysis Society Meeting, Ward, J., Ed.; San Diego, May 1987.*
5. Kim, S.; *Proceedings of the 46th Annual Meeting of the Electron Microscopy Society of America, Bailey, G.W., Ed.; San Francisco 1988.*
6. Rice, S.B.; Treacy, M.M.J.; *Proceedings of the 46th Annual Meeting of the Electron Microscopy Society of America, Bailey, G.W., Ed.; San Francisco 1988.*

RECEIVED June 20, 1989

## Chapter 27

# Factors Affecting X-ray Diffraction Characteristics of Catalyst Materials

Wayne J. Rohrbaugh and Ellen L. Wu

Mobil Research and Development Corporation, Paulsboro Research Laboratory, Paulsboro, NJ 08066-0480

X-ray diffraction (XRD) is a major tool employed to identify and characterize catalytic materials. A brief review of the diffraction phenomenon and the effect of crystallite size is presented. Applications of XRD to catalyst characterization are illustrated, including correlation of XRD powder patterns to molecular structural features, determination of Pt crystallite size and others. Factors that affect the appearance of XRD powder patterns, such as framework structure perturbations, extra-framework material, crystal morphology, impurities, sample preparation, instrument configurations, and x-ray sources, are discussed.

X-ray diffraction (XRD), in particular x-ray powder diffraction, has been used extensively to identify and characterize materials used as catalysts in the petroleum refining and petrochemical industries. This is not surprising, since many of the materials are crystalline; i.e., the atoms can be arranged in three-dimensional periodic arrays. Every atom in a crystalline solid contributes to the observed XRD pattern, thus making the pattern characteristic of the material- a virtual fingerprint. The diffraction data obtained for catalytic materials can tell us many things about these materials, ranging from the structural nature of the crystalline components to the average Pt crystallite size on a supported-metal catalyst. It can be used to monitor and correlate molecular structural features to catalytic process and reaction variables, or to specify composition for patent definition. In short, XRD is an invaluable technique in catalyst research and development. This discussion will illustrate some of the applications of XRD to catalyst characterization and point out some of the factors that affect the appearance of x-ray powder diffraction patterns of these materials.

XRD Fundamentals

X-rays have both electric field and magnetic field components associated with them. Classically, the oscillating electric field can accelerate electrons, and these electrons, in turn, can emit new x-rays usually of the same energy (elastic scattering), but in arbitrary directions in space. Since the dimension of an atom's electron cloud is approximately the same as an x-ray wavelength, interference occurs. Diffraction is an interference phenomenon that produces scattered x-ray intensity maxima and minima dependent upon the arrangement of the scatterers (1,2).

If the scatterers are somewhat randomly oriented, diffraction maxima are diffuse and ill-defined, e.g., as seen in XRD powder patterns of clays and zeolites with disordered structures or stacking faults. If the scatterers are well ordered and periodic in real space, then so are the diffraction maxima in "diffraction" space. Ideally, by measuring the position (scattering angle) and the amplitude (containing the sign or phase information) of elastically diffracted x-rays, it is possible to determine the position in space of all the atoms which comprise the material and, therefore, unambiguously characterize it. The calculation is straightforward in terms of an electron density distribution function,

$$\rho(x,y,z) \propto \sum_{hkl} F_{hkl} e^{2\pi i(hx+ky+lz)}$$

where the electron density,  $\rho$ , at any position in real space  $(x,y,z)$  is related to the summation over diffraction space  $(h,k,l)$  of the Fourier transform of the diffracted wave amplitude and phase,  $F_{hkl}$ , known as a "structure factor". Each structure factor, for a particular reciprocal lattice vector  $(h,k,l)$ , is a summation of the scattering density over all atoms. However, there are several properties of both the materials and the diffraction experiment which make the calculations somewhat more complicated.

First, although the diffraction angle can be measured quite accurately, the phase and magnitude of the diffracted x-rays cannot. The measurement of diffracted-wave intensity provides a quantity that is related to the square of the amplitude, cf. Figure 1, which consequently lacks the phase information necessary for the calculation of the electron density distribution. In addition, spectral, instrumental and sample factors can contribute to line broadening, thus making it more difficult to resolve individual diffraction peaks at nearly equal scattering angles. Indeed, crystallite size broadening can have a profound effect on the quantity of information that can be obtained using x-ray diffraction.

$$I_{hkl} = \left\{ \left[ I_0 S \left( \frac{e^2}{mc^2} \right)^2 \left( \frac{\lambda^3}{32R} \right) \right] \left[ \frac{1}{2\mu V^2} \right] \right. \\ \left. \left[ p \left( \frac{1 + \cos^2 2\theta}{\sin^2 \theta \cos \theta} \right) |F_{hkl}|^2 e^{-2B \sin^2 \theta / \lambda^2} A'(\theta) g \right] \right\}$$

where

$$F_{hkl} = \sum_j f_j e^{-2\pi i (hx_j + ky_j + lz_j)}$$

- $I_0$  - incident beam intensity per unit area
- $S$  - cross-sectional area of the beam
- $e$  - electron charge
- $m$  - electron mass
- $c$  - speed of light
- $\lambda$  - x-ray wavelength
- $R$  - distance to the detector slit
- $\mu$  - linear absorption coefficient
- $V$  - unit cell volume
- $p$  - multiplicity factor
- $\theta$  - Bragg angle
- $B$  - isotropic or anisotropic thermal parameter
- $A'(\theta)$  - angularly dependent absorption factor
- $g$  - experimental condition function
- $F_{hkl}$  - structure factor
- $f_j$  - atomic scattering factor for atom  $j$
- $x_j, y_j, z_j$  - spatial coordinates of atom  $j$
- $h, k, l$  - crystallographic indices

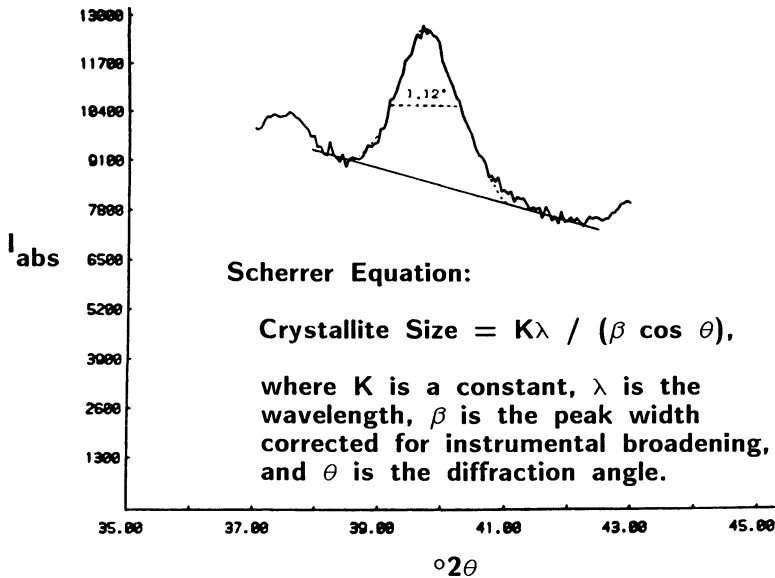
Figure 1. Expression for the diffracted x-ray intensity from each crystallographic plane ( $h, k, l$ ). [Note the role of the structure factor, which includes the scattering contributions from all atoms in the unit cell.]

For example, if a crystal has dimensions of  $100\mu\text{m}$  on a side, then the number of diffracted x-rays at any given orientation of that crystal satisfying the Laue condition can be statistically significant (using a conventional sealed-tube source). In practice, a large volume of diffraction space will be sampled, and the Fourier-transformed information can ultimately provide three-dimensional atomic coordinates. Such single-crystal analyses have been used to determine zeolite framework structures and to locate cations and other extra-framework material (3-7). In fact, single-crystal data can make it possible to differentiate between aluminum and silicon atom sites in zeolites. Smaller crystals, however, require more incident x-ray flux, perhaps synchrotron sources, but eventually the diffraction from small single crystals (e.g., less than 10 or so microns) will have intensity difficult to measure above background. Generally, materials of commercial interest contain crystalline components with crystal sizes too small for a conventional single-crystal analysis. Many crystals may be needed to produce sufficient diffracted beam intensity to be measured; thus, the remainder of this paper will discuss x-ray diffraction by powders.

Of course, looking at the diffraction from a powder limits us to some degree in the ability to properly resolve and correlate diffraction maxima to specific crystal "planes". For any given structure, there may be several sets of planes identified by different crystallographic indices separated by nearly equal "d-spacings" (and consequently observed at nearly equal scattering angles), thus making the proper assignment of intensities to each plane difficult. In addition, as the average crystallite size of the powder decreases, the physical characteristics of each crystal become important and a larger distribution of intensity about each scattering angle occurs, thus resulting in larger peak widths and poorer resolution of peaks in the XRD powder pattern.

### Line Broadening

This XRD line broadening versus crystallite size effect can be exploited to determine the average sizes of zeolite crystals in a catalyst or metal crystallites on various supports, e.g., Pt crystallite sizes in reforming catalysts. Figure 2 demonstrates the use of peak areas for the determination of % Pt and the Scherrer equation (1) for average Pt crystallite size. Here the use of the Pt(111) peak is illustrated as a general purpose technique, but particularly for alumina-supported catalysts, the Pt(311) peak may be preferred (8). The primary reason for using the Pt(311) is to minimize interference of the alumina support in measuring the Pt line width. However, for Cu  $K\alpha$  radiation, the magnitude of x-ray scattering decreases and the peak widths increase as functions of  $\sin \theta$ . Thus, the use of the Pt(311) at higher scattering angle can increase the uncertainty in the measured peak width and thereby limit the ability to determine average Pt crystallite sizes at very low concentration levels or



**For Example :**

$$\text{Wt. \% Pt} = \frac{(A_{\text{sample}} - A_{\text{alumina}}) \times C_{\text{standard}}}{A_{\text{standard}} - A_{\text{alumina}}} = \frac{(3770 - 612) \times 0.54}{5760 - 612} = 0.33\%$$

$$\beta = (\text{FWHM} - \text{intrinsic width}) \times (\pi/180) = (1.12 - 0.02) \times (\pi/180)$$

$$\text{Crystallite Size} = (1 \times 1.5418) / ((1.10 \times (\pi/180)) \times 0.9403) = 85 \text{ \AA}$$

Figure 2. Use of diffraction peak widths and areas to determine average Pt crystallite size and weight percent Pt in a supported metal catalyst.

very small crystallite sizes. In such cases, the alumina support can be removed via dissolution techniques (9), and measurement of the Pt(111) peak width is then used for maximum sensitivity.

In utilizing the Scherrer equation, care must be exercised to properly account for instrumental factors which contribute to the measured peak width at half maximum. This "intrinsic" width must be subtracted from the measured width to yield a value representative of the sample broadening. When the experimental conditions have been properly accounted for, reasonably accurate values for the average crystallite size can be determined. Peak shapes and widths, however, can also provide other information about the catalyst materials being studied. For example, combinations of broad and sharp peaks or asymmetric peak shapes in a pattern can be manifestations of structural disorder, morphology, compositional variations, or impurities.

#### Factors Affecting Zeolite XRD Powder Patterns

In fact, peak broadening is just one of several effects observed in XRD powder patterns that can be used to gain characterization information about various catalyst systems. Particularly in zeolite systems, factors such as framework structure perturbations and modifications, extra-framework material, crystal morphology, impurities, and instrument configurations can produce observable differences in the XRD patterns, which require close scrutiny, in some cases, to understand and utilize.

Framework Structure. Framework-related factors include symmetry changes, for example, orthorhombic vs. monoclinic ZSM-5 (10), cf. Figure 3. Subtle symmetry differences are manifested in this case as the appearance of additional diffraction lines in the XRD patterns of the monoclinic versus the orthorhombic symmetry form. A reversible minor displacive transformation of tetrahedral atoms can reduce the symmetry of the ZSM-5 framework to monoclinic, and thus make the appearance of the additional lines in the powder pattern possible. The observation of this type of line splitting in XRD patterns of ZSM-5 thus provides insights into subtle framework motions.

In addition, structural similarities can often be determined from careful interpretation of XRD powder patterns. The powder patterns of offretite and erionite look quite different, but are easily understood in terms of the crystallographic consequences of a change in the ordered layer stacking sequence (11), cf. Figure 4. In offretite, the layers are stacked in an AAB sequence, while in erionite, they are ordered in an AABAAC arrangement that doubles one of the crystallographic unit cell parameters. The doubled c-parameter is readily deduced from an analysis of the XRD powder pattern of erionite. Another framework structure effect, isomorphous substitution, can result in changing unit cell sizes, observed as shifts in XRD line positions for such systems as X and

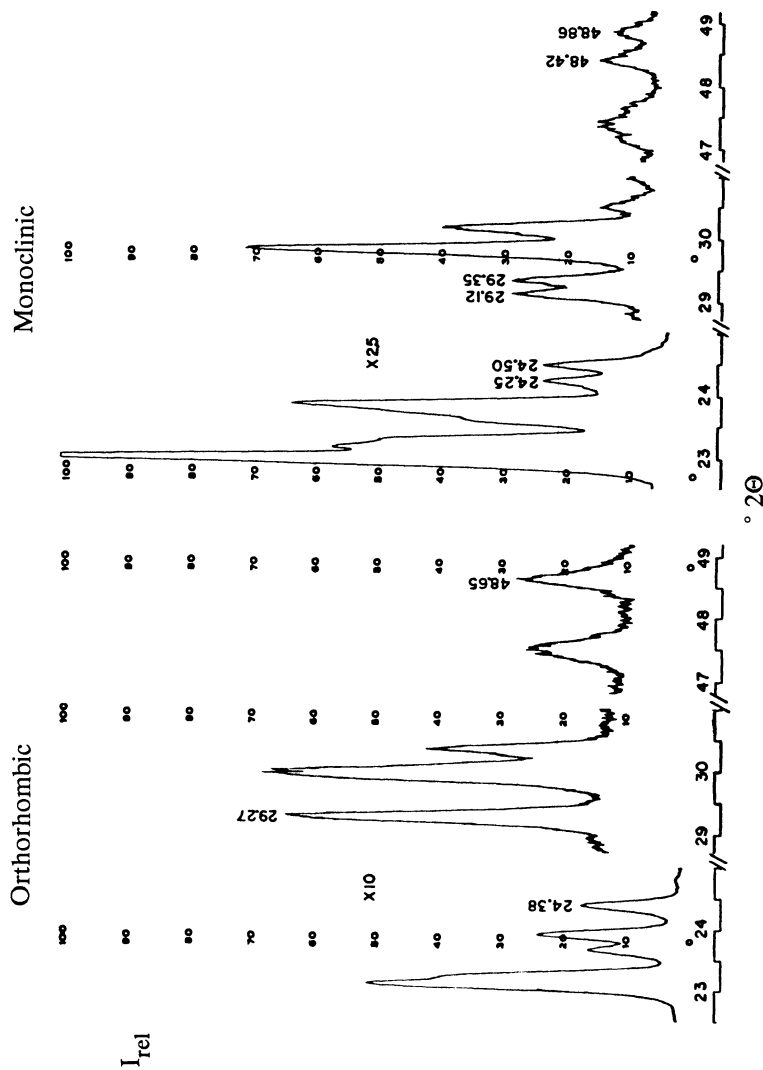


Figure 3. Structural symmetry changes can affect XRD powder patterns. Additional peaks observed in a ZSM-5 XRD pattern indicate a symmetry reduction from orthorhombic (as-made) to monoclinic (calcined/ammonium-exchanged). Reproduced from ref. 10. Copyright 1979 American Chemical Society.)



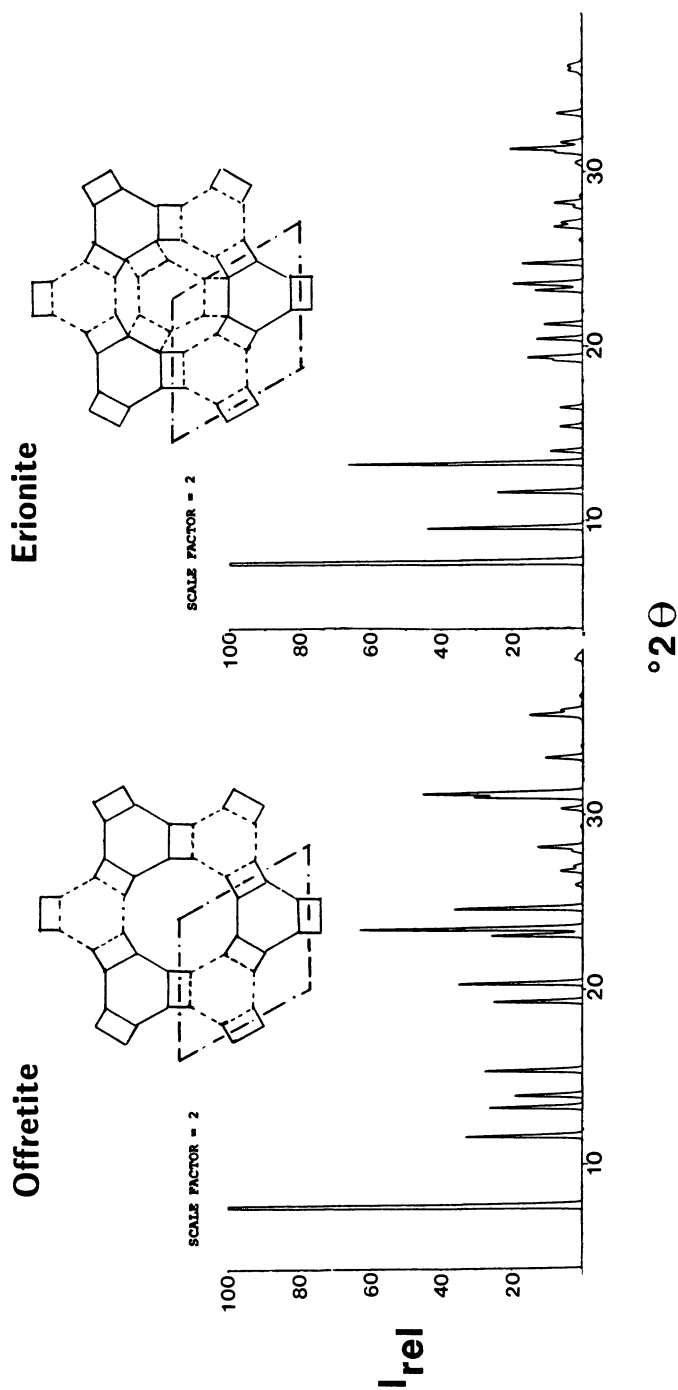


Figure 4. XRD differences caused by changes in an ordered stacking sequence. Calculated XRD patterns of offretite and erionite based on framework atomic coordinates.

Y zeolites (12), in which Si atoms are substituted for Al atoms in the framework. Thus, this effect has been used to monitor  $\text{SiO}_2/\text{Al}_2\text{O}_3$  ratios, for example.

Stacking faults and structural disorder can produce selective line broadening and non-zero intensity for "extinct" reflections as in ZSM-3 (13) and ZSM-34 (14). Figure 5 shows the appearance of the "odd *l*-lines" in a ZSM-34 XRD pattern which are "forbidden" by the ideal framework topological symmetry and unit cell parameters of offretite. If the lines were stronger and sharper, the XRD pattern could correspond to that of erionite. If they were still weak but sharp, it could suggest a mixture of offretite and erionite. Since these lines are weak and broad, however, they suggest the presence of very small domains of erionite intergrown with larger offretite domains. The XRD pattern of ZSM-34 excludes from consideration a mixture of small crystallites of erionite with large crystallites of offretite, since that would require all of the offretite peaks present in the XRD pattern to have broad bases with sharp apices.

Extra-framework Material. Extra-framework material, such as organic agents and disordered species like water and coke can also affect the intensities and positions of XRD lines. Organic directing agents, such as tetrapropylammonium (TPA) ions in some ZSM-5 preparations, can occupy specific positions in the zeolite channels (15). If the arrangement of this organic matter is ordered and periodic, then the atoms comprising the TPA moiety can contribute to the intensities of the x-ray diffraction lines as described in our earlier discussion. For smaller organic agents, steric hindrance within the zeolite channels could be significantly less than for TPA, and thus we could think of their placement as being somewhat random. Therefore, we might expect the XRD powder patterns of ZSM-5 synthesized with various organic agents to differ slightly in appearance from that of the hydrogen form. Indeed, minor changes are predicted from calculated XRD powder patterns (16) based on single-crystal structure coordinates for TPA-ZSM-5 versus the framework only, cf. Figure 6, and are, in fact, observed, cf. Figure 7 (17). Of course, calcination in air of the ZSM-5 preparations effectively removes all contributions to the XRD pattern due to organic material.

Zeolite loading, e.g., with water, ammonia, or sorbed organics, is often observed in the XRD powder pattern as a suppression of the intensities of the low-angle (high *d*-value) lines relative to the "dry" form (cf. Figure 7). Coke formation can introduce strain on the zeolite framework resulting in minor shifts of diffraction line positions as well as intensity suppressions. In addition, the presence of inorganic cations in zeolites can have significant effects on the characteristics of the XRD powder patterns. Harmotome (Ba) and phillipsite (K) are examples of isostructural zeolites, but with different cations (18,19). The differences in the XRD patterns, however, can be substantial as indicated in Figure 8.

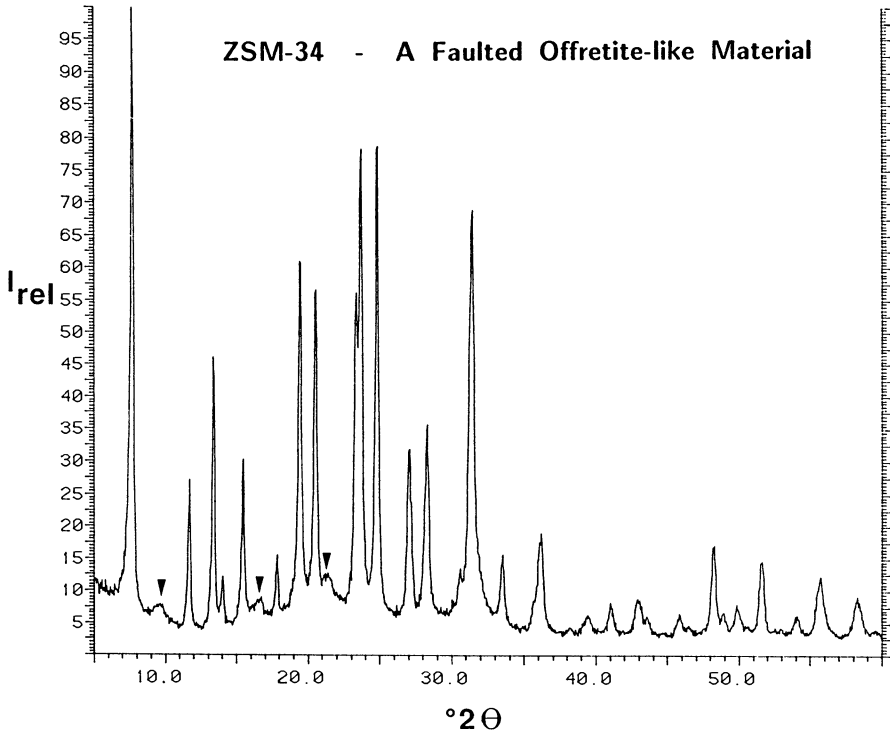


Figure 5. An example of disordered stacking faults. The diffraction lines denoted by ( $\blacktriangledown$ ) are forbidden by the offretite framework, allowed for erionite, and also allowed for ZSM-34 due to stacking faults between offretite layers.

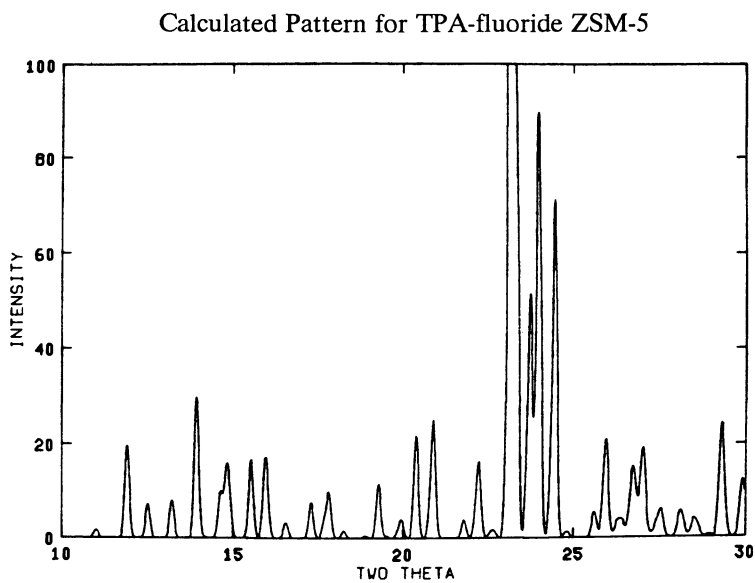
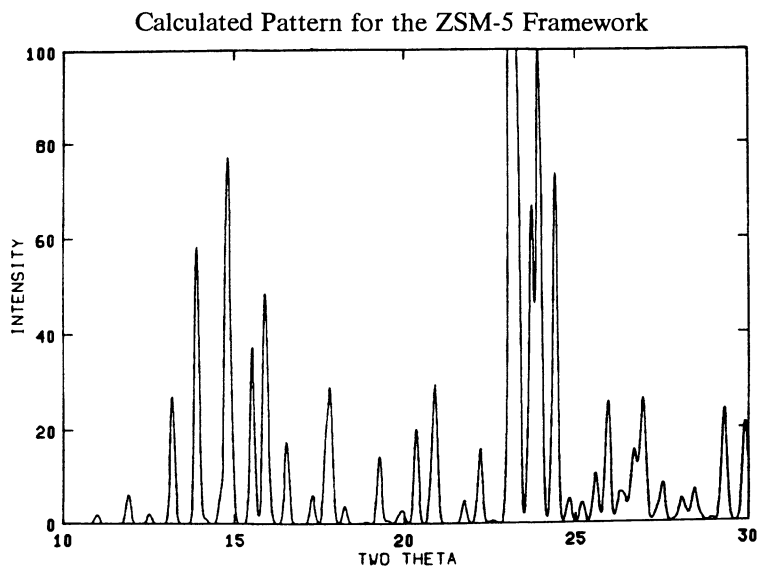


Figure 6. Effect of extra-framework material on XRD powder patterns. Calculated XRD patterns for ZSM-5 with and without ordered tetrapropylammonium and fluoride ions in the unit cell.

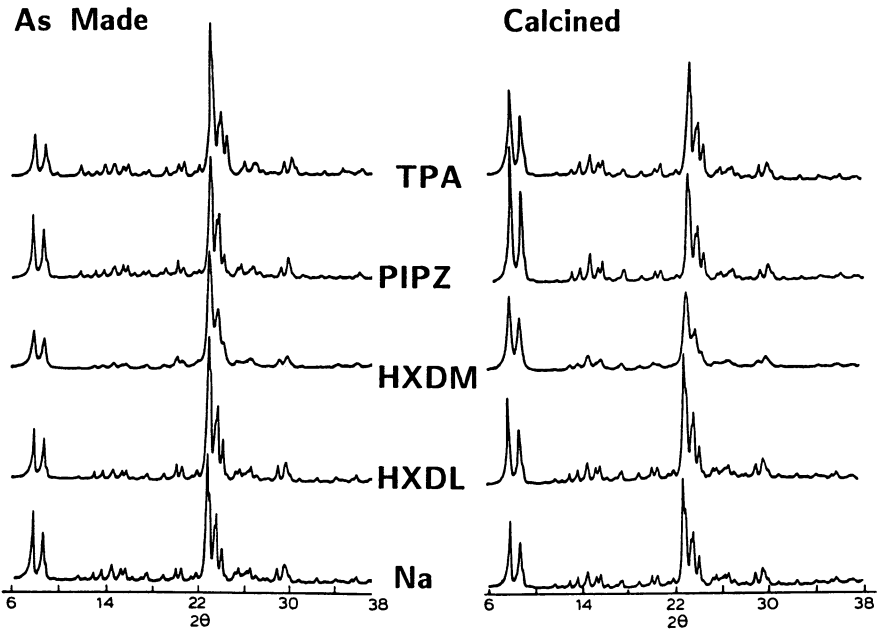


Figure 7. Comparison of observed XRD patterns of ZSM-5 synthesized with different directing agents. [TPA- tetra-propylammonium bromide, PIPZ- piperazine, HXDM- hexane-1, 6-diamine, HXDL- hexane-1,6-diol, and Na- organic free.] (Reproduced with permission from ref. 17. Copyright 1986 Butterworth.)

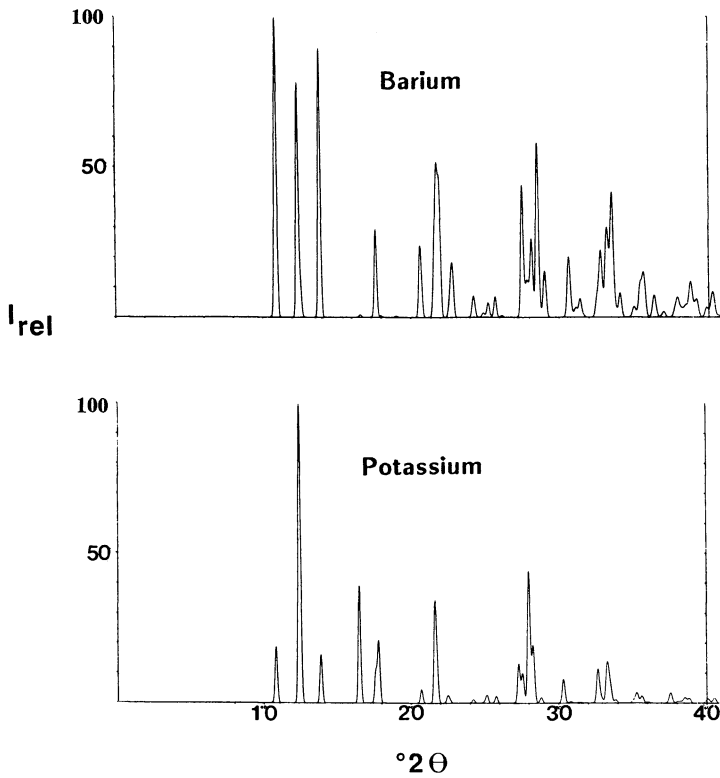


Figure 8. Cation effect on XRD powder patterns. Calculated XRD patterns for isostructural zeolites with different inorganic cations- harmotome (Ba) and phillipsite (K).

Morphology. Crystal morphology, size and shape, can be an important factor affecting zeolite XRD powder patterns. Previous discussion has described some of the consequences of crystallite size, but crystal shape merits no less attention, particularly for the cases of large rod-like or plate-like habits. When a powder of crystallites with these shapes is prepared for the XRD experiment, it becomes extremely difficult to pack a sample so that the crystallites are randomly oriented. Indeed, preferred orientation of the crystallites is quite likely, thus statistically biasing the numbers of specific crystal planes in proper orientation for diffraction at any given scattering angle. The result is enhanced intensity for certain classes of reflections, thus producing an XRD powder pattern which appears different from others of the same material with a different crystal size or shape, e.g., the patterns of ZSM-5 comprised of nearly isometric crystals ( $15 \times 15 \mu\text{m}$ ) versus a preparation comprised of crystals  $140 \times 20 \mu\text{m}$  shown in Figure 9 (20). This comparison clearly demonstrates a profound difference in the appearance of the XRD powder patterns induced by preferred orientation effects.

In cases where preferred orientation is suspected, the effect can be further enhanced by packing the sample very tightly in the XRD sample holder prior to data collection. Figure 10 displays the differences in XRD powder patterns for the same ZSM-5 sample resulting from loose and tight packing in the XRD sample holder. Emphasizing the preferred orientation effect can be valuable in powder pattern indexing to determine unit cell parameters and for providing other information useful to crystallographers in structure determinations. However, when specifying XRD characteristics of new materials, one must endeavor to recognize the possibility of preferred orientation, e.g., with electron microscopy, and to account for the possible intensity alterations caused by it.

Impurities. Of course, the presence of impurities in a sample will have a dramatic effect on the XRD characteristics. Zeolite preparations, as synthesized, can contain both organic and inorganic impurities. After washing and calcination, many impurities become amorphous, and the resulting XRD powder pattern will clearly show changes from the as-synthesized material. Some impurities, however, are stable to calcination and can make identification and characterization of the material (especially a new material) rather difficult. This is particularly true for cases where only a small number of samples, prepared in a narrow synthesis regime, are available for XRD examination. Common impurities found in zeolite preparations are the stable silicates, quartz and cristobalite.

In a characterization study of Nu-13 (21), cf. Figures 11 and 12, electron microscopy was used to verify the presence of three stable crystalline materials. Figure 11 shows the electron

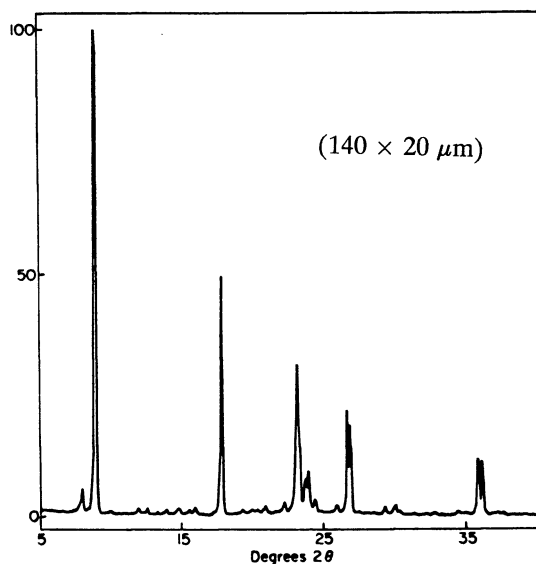
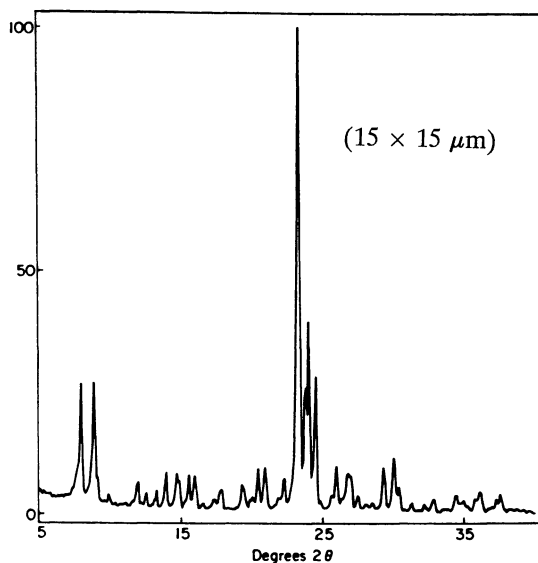


Figure 9. Preferred orientation- crystal morphology can affect ZSM-5 XRD powder patterns. Here, crystals with very dissimilar length and width (140 x 20 μm) produce XRD intensities that differ greatly from those of nearly isometric crystals (15 x 15 μm). (Reproduced with permission from ref. 20. Copyright 1983 Butterworth.)



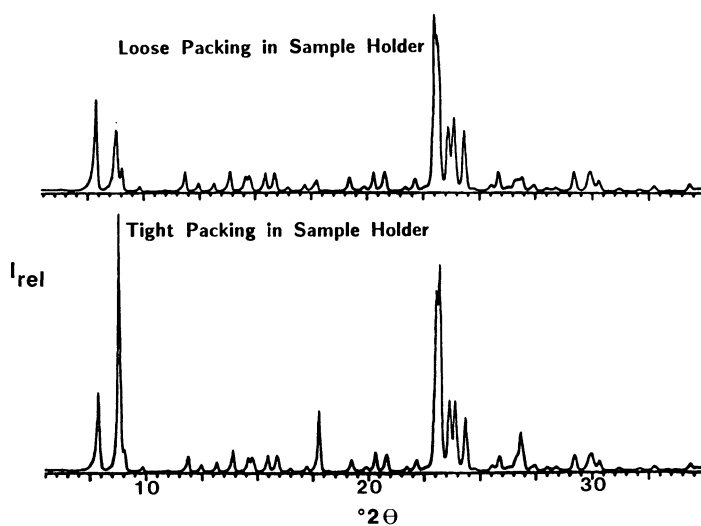


Figure 10. Effect of the physical preparation of a ZSM-5 sample for XRD measurement.

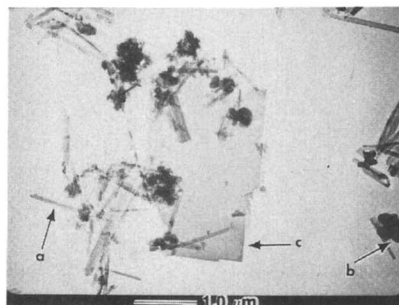
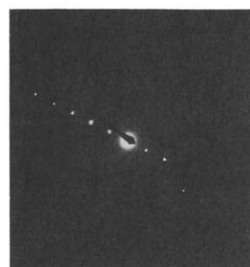
**Transmission Electron Micrograph****Electron Diffraction Patterns****Crystal Type (a)****Crystal Type (b)****Crystal Type (c)**

Figure 11. Electron microscopy data for Nu-13. A transmission electron micrograph demonstrates the presence of three crystal morphologies. Lattice parameters derived from electron diffraction patterns for each crystal type confirm the composition of Nu-13 as a mixture of (a) ZSM-12, (b) cristobalite, and (c) ferrierite.

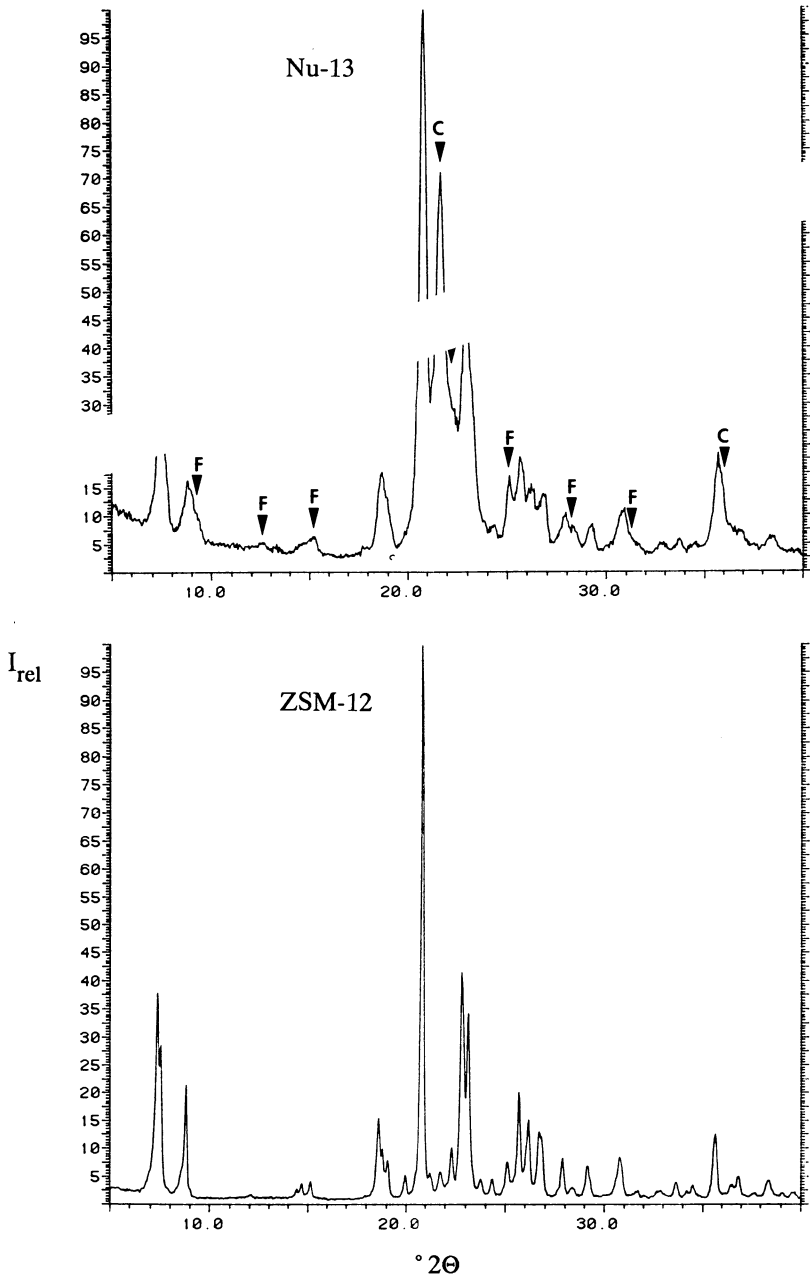


Figure 12. Deconvolution of the XRD powder pattern of Nu-13. The pattern is a superposition of the ZSM-12 pattern with additional lines due to the presence of cristobalite (C) and ferrierite (F).

micrograph of three distinct crystal types and the corresponding electron diffraction patterns. Analysis of tilt-rotate electron diffraction data (22) revealed distinct sets of lattice parameters, which were consistent with the composition of ZSM-12, ferrierite, and cristobalite suggested by a deconvolution of the XRD powder pattern of Nu-13. Thus, electron microscopy confirmed that the observed XRD pattern for Nu-13 is actually a superposition of the patterns of ZSM-12, ferrierite, and cristobalite, cf. Figure 12.

Instrumental Factors. Instrumental factors can produce marked differences in XRD patterns of identical materials and, in some cases, be used effectively to learn more about the structural nature of them. Different x-ray wavelengths can alter absorption characteristics and change the observed scattering angles ( $2\theta$ 's). Of course, the crystal interplanar d-spacings remain constant (Bragg's law) and appropriate absorption corrections can be applied to observed intensities. Monochromators can help eliminate fluorescence background and remove sometimes confusing multiple-wavelength diffraction patterns, e.g., for Ni-filtered Cu radiation-  $K\alpha_1\alpha_2$  plus  $K\beta$  lines are observed. Theta-compensating slit systems can produce patterns for the same material with different relative intensities compared to XRD instruments equipped with fixed-slit systems, and a direct correlation of intensities between the two systems is not generally possible. Finally, care must be exercised in the use of divergence slit systems (fixed or variable), to insure that the beam is fully subtended by the sample at all measured diffraction angles.

Diffraction geometry can be extremely important, especially for materials whose morphologies suggest preferred orientation problems for the XRD experiment. With the higher x-ray fluxes now available at synchrotron sources and focussed incident x-rays provided by some diffractometer systems using conventional sources, transmission and Debye-Scherrer geometries become feasible. Figure 13 shows the effect geometry has on the information obtained in an XRD powder pattern for  $\text{MoO}_3$ , a material with a thin plate morphology. Here we compare the diffraction patterns in reflection, transmission, and Debye-Scherrer geometries (23). It is clear that characterization of a material of this type, using only conventional reflection geometry, could be misleading.

#### XRD - Present and Future

Finally, we must consider the recent availability of synchrotron x-ray sources for industrial use. The high resolution now made possible by these sources produces zeolite XRD powder patterns with features perhaps calculated, but never observed before. Figure 14 shows the enhanced resolution from a synchrotron experiment versus that obtained from a conventional one. Here the XRD patterns of ZSM-5 clearly demonstrate the enhanced resolution and wealth of diffraction information that can be obtained at such sources as the

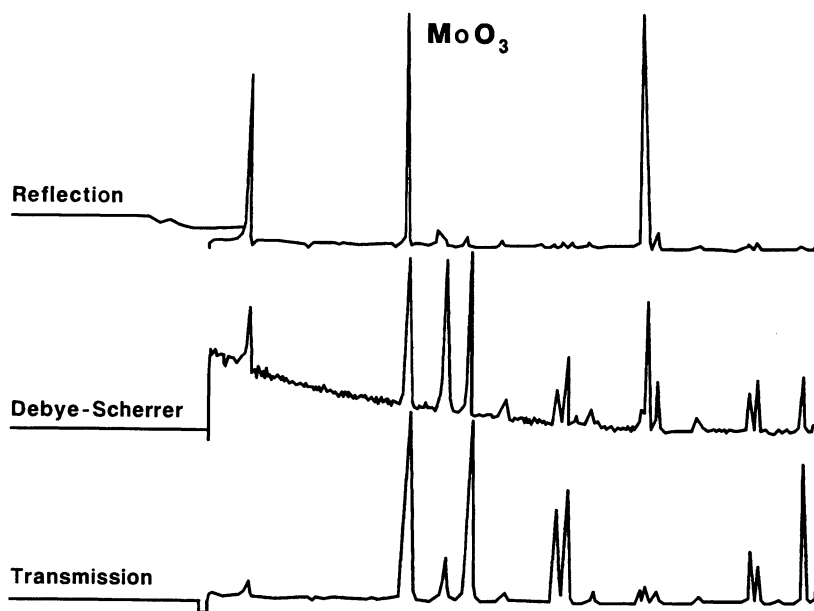


Figure 13. Effect of diffraction geometry on XRD powder patterns.

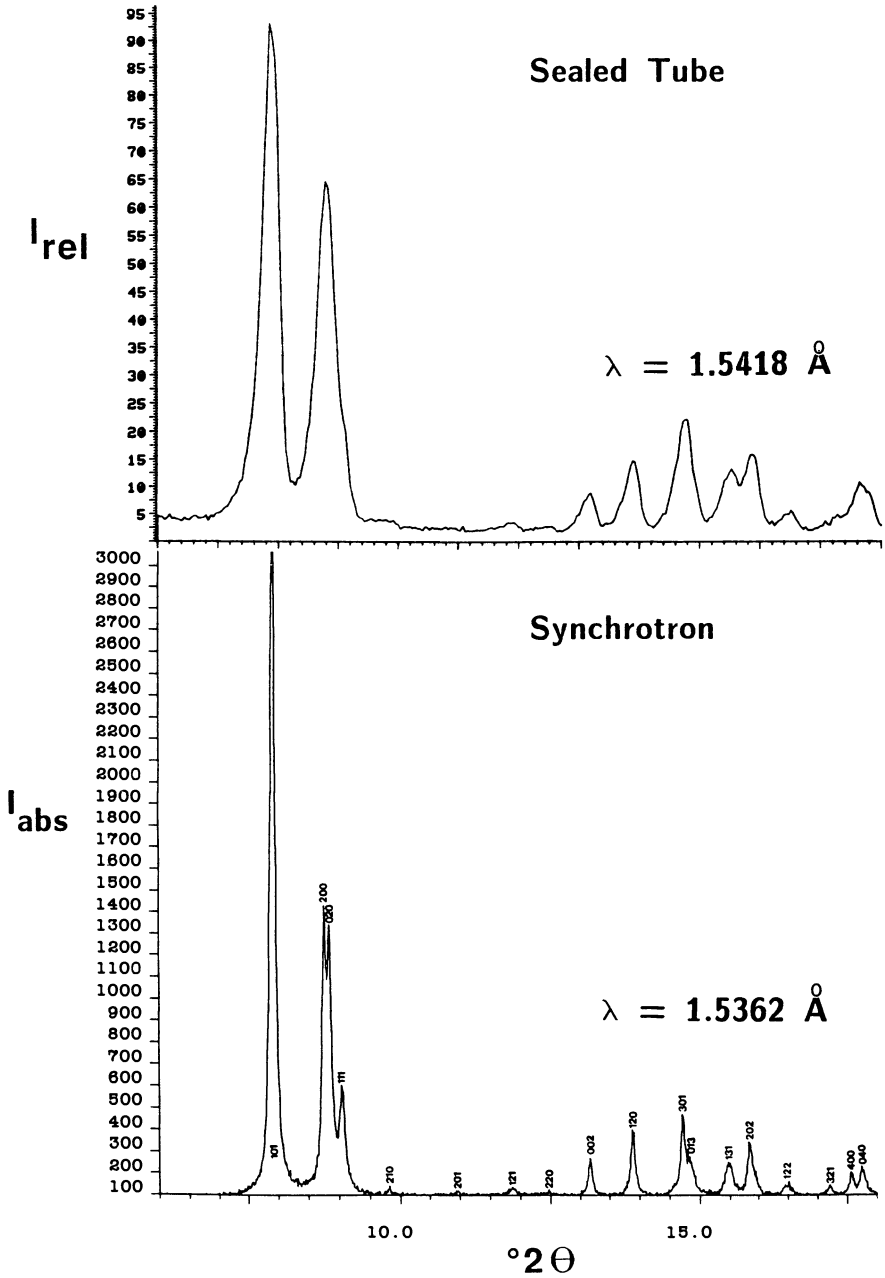


Figure 14. Comparison of conventional (sealed tube) and synchrotron x-ray diffraction patterns for ZSM-5. Enhanced resolution from the synchrotron apparatus permits the assignment of crystallographic indices to individual diffraction maxima.

National Synchrotron Light Source at Brookhaven National Laboratory. With data such as these, structural research efforts are bolstered significantly and, as was mentioned at the beginning of this discussion, knowledge of the atomic positions in space is of immense value in the characterization of a material.

X-ray powder diffraction has been the primary tool used in zeolite structure research. With new high-flux sources, the size requirement of useful single-crystals for structure determination studies has decreased significantly. In addition, refinements of atomic coordinates of known structures using Rietveld powder techniques have become common (24). The solution of a dozen or more new zeolite structure types within the last several years has added to our knowledge base for looking at unknowns (for examples, see references 25-31), and has made us better able to characterize catalyst materials and to correlate synthesis, sorptive, catalytic, and process parameters to their structures (32,33).

### Summary

The identification and characterization of new catalyst materials are important and often very complex tasks. When the catalysts are crystalline solids, diffraction techniques have clear advantages over most other characterization tools. Since, as discussed, every atom in a crystal contributes to every observed diffraction peak, XRD powder patterns are truly representative of the material being studied. The arrangement of atoms dictates the "d-spacings" and intensities observed in the XRD powder pattern. As that arrangement of atoms is characteristic of the material, then too is the XRD powder pattern.

It has been shown how various factors can affect the appearance of XRD patterns and how the subtle differences in those patterns can be used to gain valuable structural and characterization information. It is clear that in order to understand a material and define it properly, all of these factors must be examined carefully. Techniques in addition to XRD, particularly electron microscopy, but also sorption and spectroscopy, should be utilized when attempting to understand the nature of a new catalyst material. Finally, it must be recognized that published XRD powder data for a given material can tell much about its structural nature; but, to interpret the XRD data properly, it is also necessary to be aware of sample history, data collection parameters, morphology, etc. In short, one must know as much as possible about the various factors that affect the x-ray diffraction characteristics of catalyst materials.

### Acknowledgments

The authors are indebted to many individuals at Mobil Research and Development Corporation who have contributed to the catalyst characterization knowledge for many years. For the preparation of

this paper, in particular, we thank S. L. Lawton for the calculated XRD patterns from his in-house atlas (1972 and 1975), and J. L. Schlenker and J. B. Higgins for the synchrotron XRD data.

#### Literature Cited

1. Klug, H. P. and Alexander, L. E., X-ray Diffraction Procedures for Polycrystalline and Amorphous Materials, John Wiley & Sons, New York, 1974.
2. Stout, G. H. and Jensen, L. H., X-ray Structure Determination, The Macmillan Company, New York, 1968.
3. Meier, W. M., "The Crystal Structure of Mordenite", Z. Kristallogr. 1961, **115**, 439.
4. Olson, D. H., Kokotailo, G. T., Lawton, S. L., and Meier, W. M., "Crystal Structure and Structure-Related Properties of ZSM-5", J. Phys. Chem. 1981, **85**, 2238.
5. Rohrbaugh, W. J., Rubin, M. K., and Wood, J. D., "Crystal Structure of ZSM-50", Mobil R&D Corporation, unpublished data, 1983.
6. Rohrbaugh, W. J. and Rubin, M. K., "Crystal Structure of ZSM-51", Mobil R&D Corporation, unpublished data, 1983.
7. Olson, D. H., Kokotailo, G. T., and Charnell, J. F., "The Crystal Chemistry of Rare Earth Faujasite-Type Zeolites", J. Coll. Inter. Sci. 1968, **28**, 305.
8. Van Nordstrand, R. A., Lincoln, A. J., and Carnevale, A., "Determination of Metallic Platinum in Platinum-Alumina Catalysts by X-ray Diffraction", Anal. Chem. 1964, **36**, 819.
9. Plank, C. J., Kokotailo, G. T., and Drake, L. C., paper presented at the 140th Meeting, ACS, Chicago, 1961.
10. Wu, E. L., Lawton, S. L., Olson, D. H., Rohrman, A. C., Jr., and Kokotailo, G. T., "ZSM-5-Type Materials. Factors Affecting Crystal Symmetry", J. Phys. Chem. 1979, **83**, 2777.
11. Bennett, J. M. and Gard, J. A., "Non-identity of the Zeolite Erionite and Offretite", Nature 1967, **214**, 1005.
12. Dempsey, E., Kuehl, G. H., and Olson, D. H., "Variation of the Lattice Parameter with Aluminum Content in Synthetic Sodium Faujasites. Evidence for Ordering of the Framework Ions", J. Phys. Chem. 1969, **73**, 387.
13. Kokotailo, G. T. and Ciric, J., "Synthesis and Structural Features of Zeolite ZSM-3", Adv. Chem. Ser. 1971, **101**, 109.
14. Rubin, M. K., Rosinski, E. J., and Plank, C. J., U. S. Patent 4,086,186, 1978.
15. Price, G. D., Pluth, J. J. Smith, J. V., Araki, T., and Bennett, J. M., "Crystal Structure of Tetrapropylammonium Fluoride-Silicalite", Nature 1981, **292**, 818.
16. Smith, D. K., A Revised Program for Calculating X-ray Powder Diffraction Patterns, UCRL-502.64, Lawrence Radiation Laboratories, 1967.
17. Araya, A. and Lowe, B. M., "Effect of Organic Species on the Synthesis and Properties of ZSM-5", Zeolites 1986, **6**, 111.



18. Sadanaga R., Marumo F., and Takeuchi Y., "The Crystal Structure of Harmotome", Acta Crystallogr. 1961, 14, 1153.
19. Steinfink, H. S., "The Crystal Structure of the Zeolite Phillipsite", Acta Crystallogr. 1962, 15, 644.
20. Nastro, A. and Sand, L. B., "Growth of Larger Crystals of ZSM-5 in the System  $4(\text{TPA})_2\text{O}-38(\text{NH}_4)_2\text{O}-x(\text{Li,Na,K})_2\text{O}-\text{Al}_2\text{O}_3-59\text{SiO}_2-750\text{H}_2\text{O}$ ", Zeolites 1983, 3, 57.
21. Whittam, T. V., European Patent Specification 0059059, 1984.
22. Leonowicz, M. E., Mobil R&D Corporation, personal communication, 1988.
23. Christensen, A. T., CSS-Nicolet-XRD, personal communication, 1981.
24. Baerlocher, Ch., "Zeolite Structure Refinements Using Powder Data", Zeolites 1986, 6, 325.
25. Schlenker, J. L., Dwyer, F. G., Jenkins, E. E., Rohrbaugh, W. J., Kokotailo, G. T., and Meier, W. M., "Crystal Structure of a Synthetic High Silica Zeolite - ZSM-39", Nature 1981, 294, 340.
26. LaPierre, R. B., Rohrman, A. C., Jr., Schlenker, J. L., Wood, J. D., Rubin, M. K., and Rohrbaugh, W. J., "The Framework Topology of ZSM-12: A High Silica Zeolite", Zeolites 1985, 5, 346.
27. Kokotailo, G. T., Schlenker, J. L., Dwyer, F. G., and Valyocsik, E. W., "The Framework Topology of ZSM-22: A High Silica Zeolite", Zeolites 1985, 5, 349.
28. Rohrman, A. C., Jr., LaPierre, R. B., Schlenker, J. L., Wood, J. D., Valyocsik, E. W., Rubin, M. K., Higgins, J. B., and Rohrbaugh, W. J., "The Framework Topology of ZSM-23: A High Silica Zeolite", Zeolites 1985, 5, 352.
29. Schlenker, J. L., Rohrbaugh, W. J., Chu, P., Valyocsik, E. W., and Kokotailo, G. T., "The Framework Topology of ZSM-48: A High Silica Zeolite", Zeolites 1985, 5, 355.
30. Meier, W. M. and Olson, D. H., Atlas of Zeolite Structure Types, International Zeolite Association, Butterworth, 1988.
31. Higgins, J. B., LaPierre, R. B., Schlenker, J. L., Rohrman, A. C., Wood, J. D., Kerr, G. T., and Rohrbaugh, W. J., "The Framework Topology of Zeolite Beta", Zeolites 1988, 8, 446.
32. Wu, E. L., Landolt, G. R., and Chester, A. W., "Hydrocarbon Adsorption Characterization of Some High Silica Zeolites", New Developments in Zeolite Science Technology; Murakami, Y. et al., Ed.; Kodansha: Tokyo, 1986; p 547.
33. Bendoraitis, J. G., Chester, A. W., Dwyer, F. G., and Garwood, W. E., "Pore Size and Shape Effects in Zeolite Catalysis", New Developments in Zeolite Science Technology; Murakami, Y. et al., Ed.; Kodansha: Tokyo, 1986; p 669.

RECEIVED January 10, 1989

## Chapter 28

# Characterization of the New Zeolite ECR-1

D. E. W. Vaughan, M. E. Leonowicz<sup>1</sup>, and K. G. Strohmaier

Exxon Research and Engineering Company, Annandale, NJ 08801

Results from diverse experimental methods were combined to arrive at structure proposals for ECR-1, a typical example of a micro-crystalline zeolite. The zeolite features a 12-ring single channel, formed by a regular alternation of connected sheets of mordenite and mazzite. Crucial clues to the structure came from the HREM observation of a mazzite epitaxial overgrowth on an ECR-1 crystal. Electron and x-ray diffraction, infra-red spectroscopy and synthesis phase relationships were essential additional data sources.

Knowing the structural topology of a new zeolite allows one, by analogy with the properties of other established and well researched zeolites, to readily assess potential applications for the new material. However, rarely do new synthetic zeolites grow as crystals large enough to be rapidly analyzed by single crystal diffraction methods. Although single micro-crystal analyses ( $<10^3 \mu\text{m}^3$ ) using synchrotron radiation have been demonstrated(1), such methods still await routine application. Similarly, new developments in the application of direct methods to zeolite powder samples(2), although beginning to be successful(3), have yet to meet wider testing. They may have particular problems in application to either high symmetry materials, or those having pseudo-symmetry, which have many overlapping diffraction peaks. A new zeolite structure solution therefore largely remains a detective exercise, where one accumulates indirect and circumstantial evidence until a point is reached where it

<sup>1</sup>Current address: Mobil Research and Development Corporation, Paulsboro, NJ 08066

is possible to propose and test a model structure. This general approach has been recently described by Thomas and Vaughan (4).

In recent years the publication of many theoretical structures provides a coarse screen against which one can compare readily available diffraction patterns or unit cell values. The recent syntheses of two such structures - TAMU-1(5) and VPI-5(6) - are witness to the utility of these theoretical tabulations, not only for the conventional aluminosilicate zeolites, but also the increasing number of substituted zeolites and phosphates. However, the ECR-1 structure proposal (7) was not in any of the presently known structure tabulations.

The proposed structure for ECR-1 was solved by accumulating evidence from many "traditional" sources, such as the synthesis phase relationships, powder x-ray diffraction (PXD) and electron diffraction (ED), molecular probe sorption, infra-red analysis (IR) and electron microscopy (EM). Initial unsuccessful models were based on extended merlinoite frameworks, followed by modifications based on mordenite. The observation of crystal overgrowths of mazzite in high resolution lattice images was the key to recognizing the compatibility of mordenite and mazzite structural layers, and that intimate intergrowth of the two structures was possible.

### Synthesis and Chemical Properties

ECR-1 crystallizes from a bis(2-hydroxyethyl)-dimethyl ammonium (DHEDM) templated gel at temperatures above about 100°C (8), and seems to be very template specific, in the sense that a particular cation stereo-chemistry is necessary both to initiate and propagate the structure. Below 100°C faujasite is the primary product, occluding this alkylammonium cation in the supercage. When the template is tetramethyl ammonium (TMA), mazzite cocrystallizes with faujasite, and is the only product at long crystallization times. Syntheses with templates contaminated with only small amounts of TMA caused the nucleation and crystallization of mazzite at temperatures over 100°C, and increasing Si/Al ratios in the synthesis gel move the crystalline products into the mordenite phase stability field. Other details of the synthesis of ECR-1 are presented in a companion paper at this conference (9). Suffice it to say that ECR-1 is a specific template directed boundary phase, crystallizing in a restricted region between the major crystallization fields of mazzite and mordenite, the former seemingly favored by TMA (as an impurity in, or degradation product of DHEDM) and the latter by higher Si/Al gel ratios.

The chemical analyses of several ECR-1 samples were similar to mazzite (Si/Al=2.6 for the mineral (10) and 3.2 for

synthetic products), with Si/Al= 3.4, rather than mordenite (Si/Al > 5), indicating a possible close relationship between ECR-1 and mazzite. However, the new zeolite forms long lath-like crystals - a morphology very similar to mordenite in natural and synthetic occurrences.

### Sorption Properties

Experiments to optimize the ECR-1 crystallization resulted in apparently pure ECR-1 on the basis of PXD and scanning EM analyses, but some samples had variable hexane sorption properties reminiscent of large and small port mordenite, offretite or gmelinite. Variations in hydrocarbon sorption capacities usually indicate blockage of the channels in these structures by faulting, intergrowths of secondary coexistent structures (such as chabazite in gmelinite, or erionite in offretite), detrital gel components or residual coke from the template burn off procedure. In optimum material, sorption isotherms for linear hydrocarbons were similar to those for offretite or L (FIGURE 1), having a maximum n-hexane capacity of 8wt.%, and similar but slower sorption of cyclo-hexane, indicating a possible 10- or 12-ring channel system.

Thermogravimetric analyses (FIGURE 2) showed that the dimethyl diethyl ammonium template was removed from ECR-1 at about 450°C and from the ECR-4 faujasite(11) supercage at about 350°C. In contrast, TMA is removed from from the mazzite 8-ring gmelinite cages at about 560°C, and TEA(12) from the Linde L 12-ring channels at 460°C, indicating that ECR-1 probably had a 10- or 12-ring pore opening. After purging of the template from optimum ECR-1 samples, the zeolite sorbed between 14 and 15% wt. of water.

### Spectroscopic Analyses

$^{29}\text{Si}$ -MASNMR spectra of ECR-1 are complex, and attempts to dealuminate ECR-1 were unsuccessful, making such information difficult to interpret ( the ECR-1 models turn out to have ten different T atoms). A typical ECR-1 IR spectrum is compared with spectra for mazzite and mordenite in FIGURE 3, and contains two sharp peaks at 1210 and 1240  $\text{cm}^{-1}$ , a region previously assigned to 5-ring elements(13). Mordenite shows a peak at 1220  $\text{cm}^{-1}$  but mazzite shows no absorption in this region, even though the structure contains 5-rings. ECR-1 also has a 6-ring peak at 615  $\text{cm}^{-1}$ , in the identical position to mazzite, and mordenite has strong absorptions at 580 and 625  $\text{cm}^{-1}$ . These analyses strengthened our orientation towards 5-ring structures of the mordenite type. However, many proposed theoretical possibilities in this system(14,15) failed to give the required unit cell values.

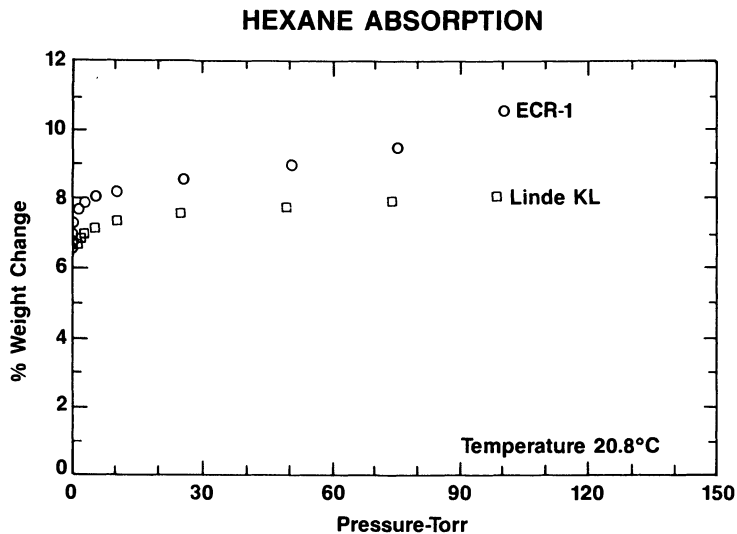


FIGURE 1: Hexane isotherms (21°C) for Linde KL and Na,H ECR-1 (after burning out the template).

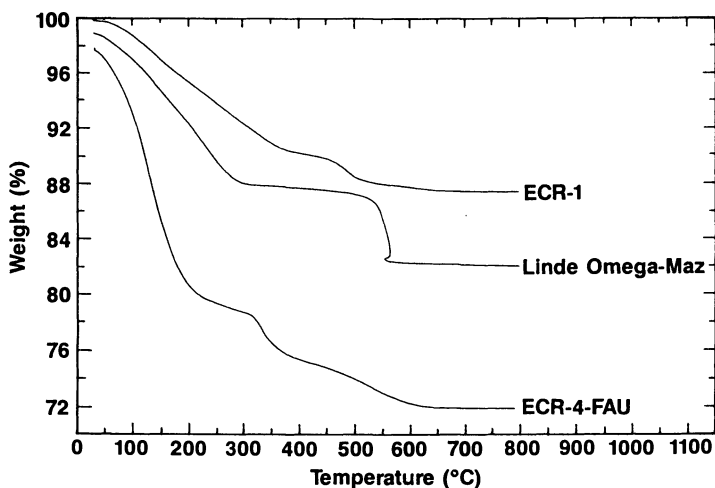


FIGURE 2: Thermogravimetric analyses for ECR-1, Linde Omega (mazzite) and ECR-4 (faujasite), run at 10°C/min. in air, using a DuPont 951/1090 TGA. The distinctive high temperature weight losses represent the decomposition and desorption of the organic "templates".

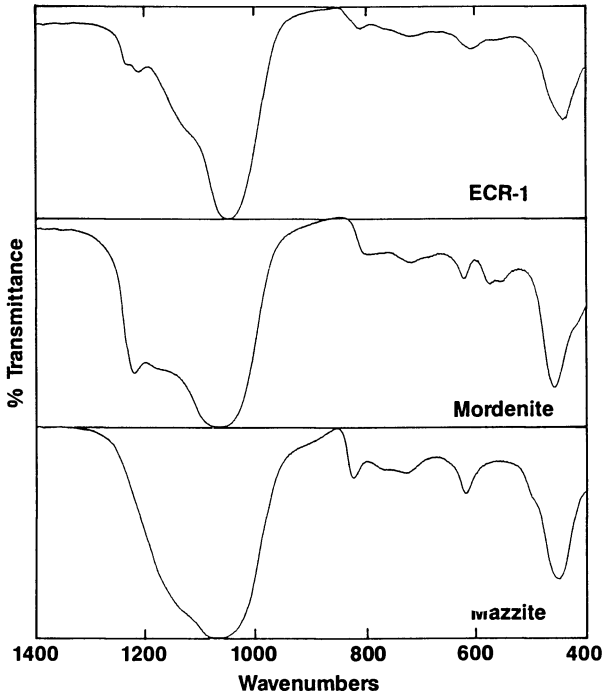


FIGURE 3: IR spectra for ECR-1, mordenite and Linde Omega (mazzite), showing common framework vibrations, and a distinctive 5-ring doublet at 1210 and 1240cm.<sup>-1</sup> for ECR-1.

### X-ray and Electron Diffraction Analysis

Most initial syntheses of ECR-1 were contaminated with analcime, and a cursory evaluation of PXD patterns showed a similarity to those of mordenite and mazzite (FIGURE 4), but with distinctive differences. Scanning EM clearly showed only one phase in addition to analcime, and later samples were clearly monophasic. In both cases the data resisted indexing by conventional computer techniques, probably due to the combined effect of disparate cell lengths and systematic absences in the patterns (*vide infra*). The unit cell geometry was elucidated with selected area electron diffraction experiments, although a complete description of the lattice from patterns tilted about a common reciprocal lattice vector could not be obtained because of instrumental constraints. Approximate cell constants obtained from electron diffraction patterns of the three principal reciprocal lattice projections, shown in FIGURE 5 were used to index the PXD pattern with a primitive orthorhombic unit cell having least-squares refined values of  $a=7.310(4)\text{\AA}$ ;  $b=18.144(6)\text{\AA}$ ;  $c=26.31(1)\text{\AA}$ . Furthermore, the  $hk0$  projection displayed a systematic extinction condition  $h+k=2n+1$ , implying an  $n$ -glide plane normal to the  $26\text{\AA}$  axis.  $Pm\bar{m}n$  is the only centro-symmetric space group consistent with these diffraction data.

Unit cell constants play a critical role in zeolite structure determination with model building techniques. Different three dimensional frameworks often contain common structural subunits, the presence of which are indicated by "magic number" lattice constants, such as  $5\text{\AA}$ ,  $7.5\text{\AA}$  and  $10\text{\AA}$ . Such diverse structure types as offretite, mazzite, Linde L, mordenite and the hypothetical omega structure all contain corrugated three tetrahedra chains, repeating every  $7.5\text{\AA}$ , and interconnected to form 8-ring pores normal to the chain. Thus, the presence of a  $7.5\text{\AA}$  unit cell constant in an unknown structure suggests this candidate connectivity. The last four structures listed above also have an  $18\text{\AA}$  cell constant, but long repeat distances allow so many permutations in tetrahedral connectivity that similarities are tenuous. However, some assumptions must be made about the topology of complex, unknown structures to reduce the degrees of freedom to manageable proportions in model building. Similarities in unit cell values and symmetries between known and unknown structures may indicate a starting point. For ECR-1 the combined data described in the previous sections indicated that mordenite, a structure with a centered orthorhombic lattice of dimensions  $18\text{\AA} \times 20\text{\AA} \times 7.5\text{\AA}$ , would be a good candidate structure. Unfortunately, efforts to interconnect  $7.5\text{\AA} \times 18\text{\AA}$  mordenite sheets within the constraints of  $Pm\bar{m}n$ , whilst stretching the repeat distance from  $20\text{\AA}$  to  $26\text{\AA}$  were unsuccessful. Models based on modifications of other related frameworks were equally disappointing.

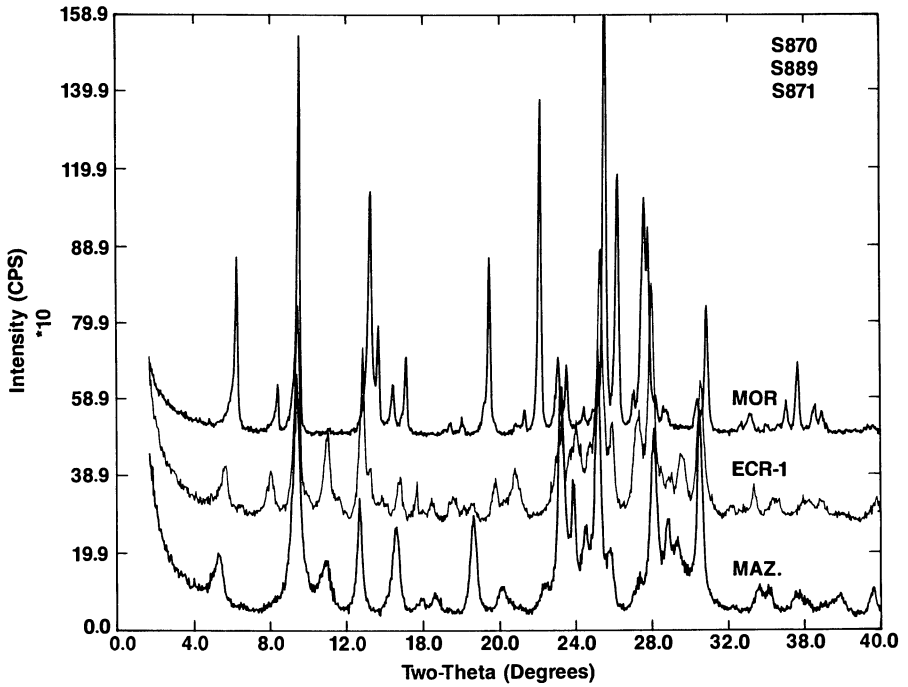


FIGURE 4: A comparison of PXD patterns for mordenite, ECR-1 and Linde Omega (mazzite).



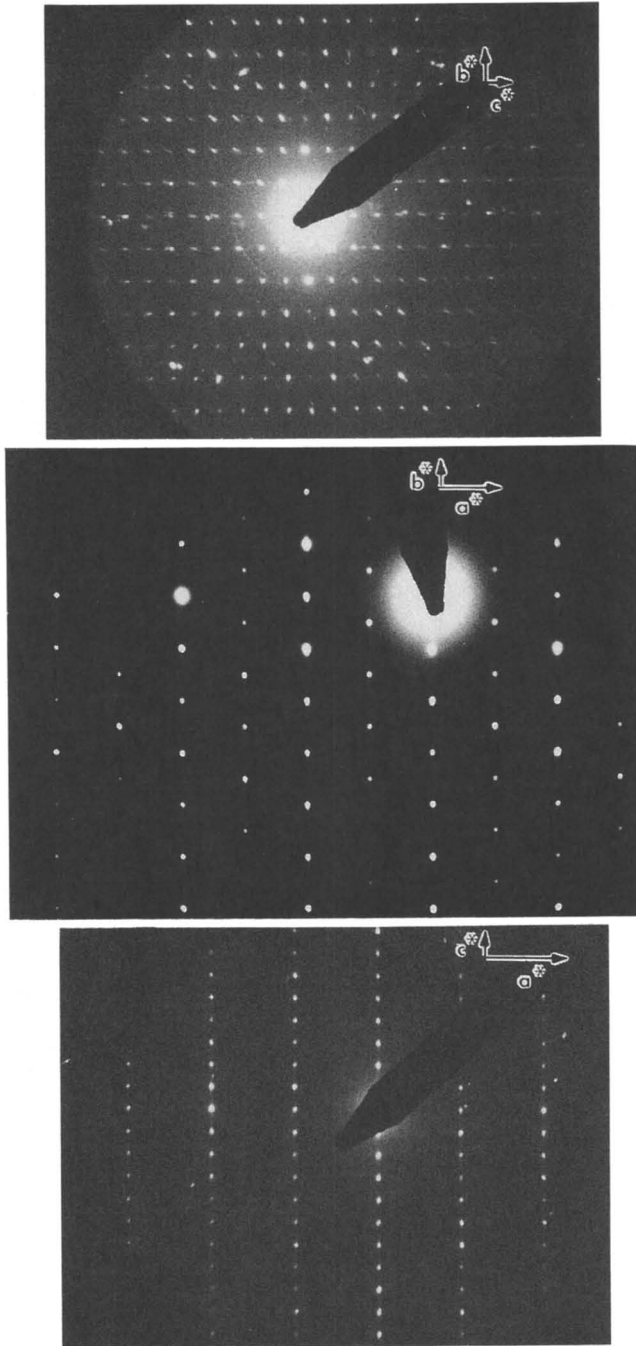


FIGURE 5: ED patterns of different projection planes in ECR-1: ac, ab and cb.

### High Resolution Lattice Imaging

High resolution transmission electron microscopy (HRTEM) lattice imaging has recently been demonstrated as one of the most powerful methods of solving unknown zeolite structures(16). The failure to solve the ECR-1 structure by alternate methods clearly indicated that HRTEM was the preferred approach, particularly as the sorption data indicated the presence of large channels and the possibility of structural faulting. Unfortunately, samples thin enough for imaging along the lath axis, the direction of any 10- or 12-ring channels in the material, required ultramicrotomy of embedded crystallites. Microscopy efforts were also hampered by the sensitivity of the zeolites to damage by the 120KV beam of the Philips 420ST TEM that was available for the imaging experiments; low dose techniques were employed to obtain lattice images of ECR-1 with this instrument.

Lattice images taken normal to the lath axis were structurally uninformative, but regularity in the fringe patterns suggested that faulting was not an important mechanism in channel blockage ( FIGURE 6 ). The deficiencies in sorption properties therefore probably result from a combination of the high aspect ratio of the lath crystals (ie. very long channels) and detrital material occluded in the channels. Images along the lath axis were much more revealing, showing a regular array of circular channels. One such image showed a twin mode of ECR-1 that provided key structural information. In the micrograph shown in FIGURE 7 a hexagonal phase is observed to syntactically overgrow on an ECR-1 lath, sharing a twin plane defined by the  $7.5\text{\AA} \times 18\text{\AA}$  directions. Detailed examination of the contrast patterns in this region of the micrograph reveals that the layer used to construct the hexagonal phase is also present in the ECR-1 region of the crystallite, but with a different layer interposed to extend the periodicity to  $26\text{\AA}$ . This suggests that ECR-1 and its hexagonal overgrowth phase share a common structural layer. Although naive interpretation of lattice images can be misleading because contrast levels are strongly affected by sample thickness and orientation and by microscope defocus (well illustrated by the examples in (17)); such affects should be minimal in the short distances over which this overgrowth extends.

Three well known zeolite structure types - Linde L(18), mazzite(19) and the hypothetical omega-structure(20) - have essentially identical hexagonal lattice constants with  $a=18\text{\AA}$  and  $c=7.5\text{\AA}$ , but only mazzite has a  $7.5\text{\AA} \times 18\text{\AA}$  layer that contains an  $n$ -glide plane operator; the thickness of this layer is  $\sim 15.5\text{\AA}$ . If the hexagonal overgrowth is mazzite, the electron micrograph interpretation implies that ECR-1 comprises mazzite sheets interconnected with some other subunit to form the observed  $26\text{\AA}$  repeat distance. The

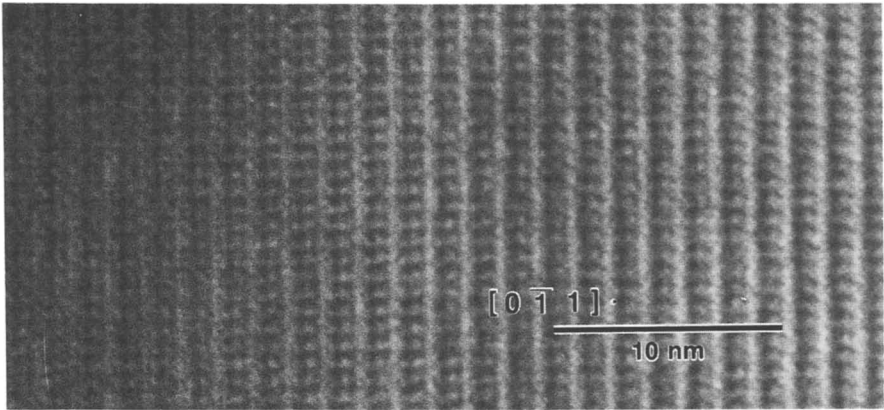


FIGURE 6: Lattice image of the crystal side view along the ECR-1 laths (011), showing a high degree of regularity, and no evidence of defects associated with channel blockage.

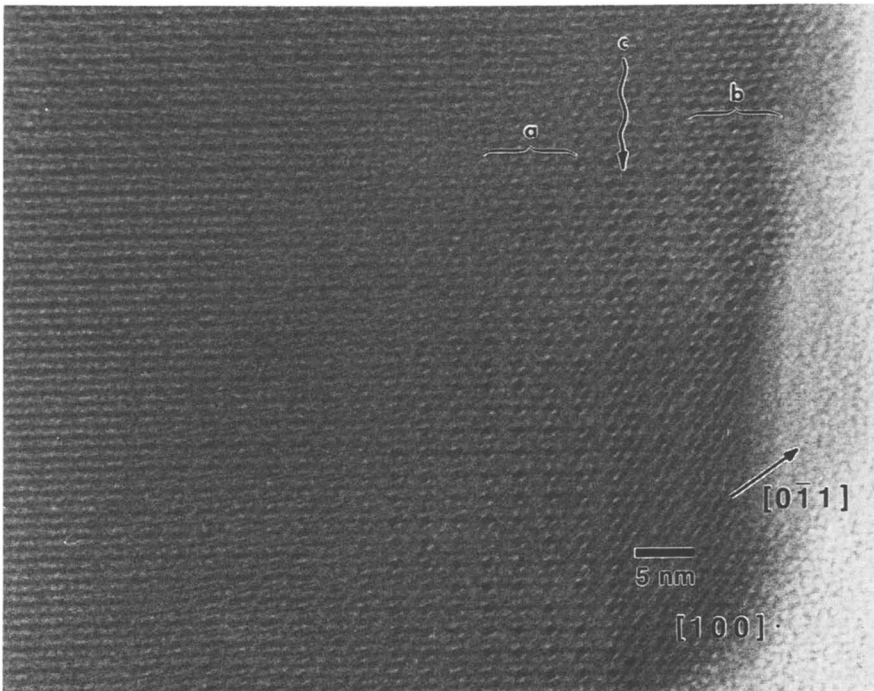


FIGURE 7: Lattice image of the section normal to the lath length, showing circular features equated with 12-ring channels in ECR-1(a), a transition zone corresponding to a mazzite twin plane(c), and a surface overgrowth of mazzite(b) showing the characteristic hexagonal arrangements of channels.

structure model materialized with the recognition that mordenite has a  $\sim 10.5\text{\AA}$  thick (  $26\text{\AA} - 15.5\text{\AA}$  ),  $7.5\text{\AA} \times 18\text{\AA}$  sheet containing an  $n$ -glide plane, and that it can be interposed with the mazzite sheet while simultaneously fulfilling the symmetry requirements of Pmmn and the constraints of three dimensional tetrahedral network bonding; the interconnection of mazzite and mordenite sheets is illustrated in FIGURE 8.

Even within the unit cell and symmetry constraints of this system, there are two ways to interconnect mazzite and mordenite sheets in three dimensions - one related to the other by a shift of  $a/2$ . Differentiation of the two models will be best resolved by full Rietveld refinement of the observed data. This situation of several related structures having the same two dimensional projections but different three dimensional connectivity is common in zeolite structural chemistry ( eg. mazzite - omega; several members of the ABC-6 family of structures ).

### Structural Modelling

The objective of structure modelling is the invention of a zeolite structure having a theoretical x-ray diffraction pattern (21) that matches the PXD spectrum for the unknown experimental material. A short-cut is to use a previously generated source of PXD patterns for the many theoretical structures already described in the literature (eg. see 22). Although such a valuable data bank has been proposed by Smith(23), it is not yet funded or available, except in partial form within a few individual companies and university departments.

To substantiate a proposed model structure, the experimental PXD pattern must compare favorably with the computer generated pattern for the model. Regardless of the source of the model, accurate atom positions are required in order to calculate accurate unit cell values, which are the starting point for generating the PXD pattern. In the case of zeolite framework atoms, such data can be obtained from distance least squares (DLS) refinement of the model structure(24). The compatibility of the unit cell values of the proposed framework with the observed experimental values, is a good indicator of model validity. Weighted mean residual values less than 2% are considered indications of good agreements with unit cell and symmetry constraints (25)- a minimum requirement for a valid structure model. Figure-of-merit for ECR-1 models are lower than this threshold.

Once the refined atom coordinates are available, calculation of the powder pattern is straight-forward using POW-10 (21). However, a pattern so calculated only contains contributions from framework atoms - usually the  $\text{SiO}_2$  form - and does not include contributions from cations and water

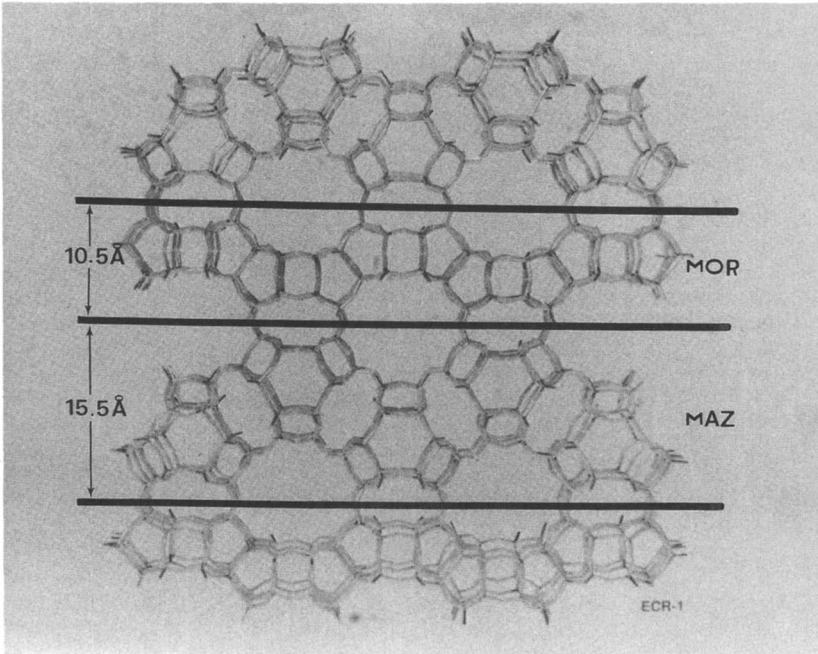


FIGURE 8: Model showing the ECR-1 connectivity between 10.5Å sheets of mordenite (MOR) and 15.5Å sheets of maz-zite (MAZ). The two possible structures are related by a shift of  $a/2$  in the marked planes normal to the page.

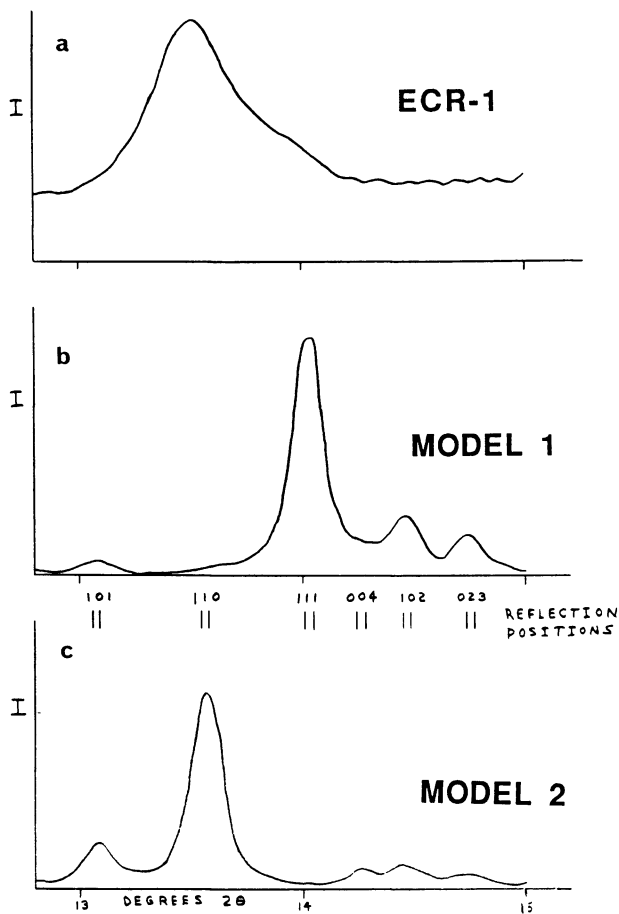


FIGURE 9: A comparison of the experimental x-ray diffraction pattern for calcined ammonium ECR-1(a), with the calculated patterns for Model 1 (b) (5-ring connectivity) and Model 2 (c) (4&6-ring connectivity) in the range  $12^{\circ}$  to  $14^{\circ}$   $2\theta$ .

molecules (in any case the positions of these would not be known at this stage of the modelling). The affect of these latter components may substantially alter the relative intensity values of the peaks in the spectrum. Ideally, the agreement between model and experimental PXD patterns can be optimized by using highly dealuminated zeolite samples that are largely cation and water free. Unfortunately, attempts to highly dealuminate ECR-1 using conventional techniques were not successful and the best available materials were hydrogen exchanged samples. (In fact few low Si/Al ratio zeolites can be as effectively dealuminated as can the open faujasite structure.) A comparison of PXD patterns for hydrated and dehydrated ECR-1 show major intensity differences, reflecting the pronounced effect of water on the peak intensities. In view of this, one does not expect good matching of peak intensities, but the peak positions do match in the ECR-1 system. Despite these problems we have sought to differentiate the two possible ECR-1 models. DLS refined coordinates were used to calculate X-ray powder patterns for the two ECR-1 models. These are very similar, but a difference in the peak intensities in the region  $12^{\circ}$ - $14^{\circ}$   $2\theta$  is a basis for differentiating the two structure models. As shown in FIGURE 9, the experimental pattern for a calcined ammonium exchanged ECR-1 in this region matches the 4-6-ring sheet interconnectivity model pattern (Model 2) better than the 5-ring connectivity model pattern (Model 1) and is the basis for favoring Model 2 at this time (a mixture of both structures would probably give an optimum match). Only a full refinement of the structure, including contributions from framework and non-framework atoms, would be expected to give good agreement in both line position and intensity data, and definitively resolve the specific ECR-1 model.

### Conclusions

Despite many advances in analytical methods in recent years, the structural characterization of materials that only occur as microcrystals less than about  $30\mu$  in diameter remains difficult and laborious. High resolution electron microscopy in the lattice imaging mode is by far the most powerful tool in giving the direct evidence of structural details essential for modelling clues, as has been demonstrated in the cases of recent zeolite structure solutions of theta-1/ZSM-23 (26) and beta (27), in addition to ECR-1. X-ray diffraction methods provide the essential confirmatory data, and sorption molecular probing and various well established spectroscopic methods are useful ancillary tools.

### LITERATURE CITED

1. Eisenberger, P.M., Newsam, J.M., Leonowicz, M.E. and Vaughan, D.E.W., *Nature*, (1984), 309, 45-47.
2. Baerlocher, Ch., *Zeolites*, (1986), 6, 325-333.



3. McCusker, L.B., *Jour. Applied Crystallogr.*, (1988), **21**, 305.
4. Thomas, J.M. and Vaughan, D.E.W., *J. Phys. Chem. Solids*, *in press*.
5. Rudolf, P.R., Saldarriaga-Molina, C. and Clearfield, A., *J. Phys. Chem.*, (1986), **90**, 6122-6125.
6. Davis, M.E., Saldarriaga, C., Montes, C., Garces, J. and Crowder, C., *Nature*, (1988), **331**, 698-9.
7. Leonowicz, M.E. and Vaughan, D.E.W., *Nature*, (1987), **329**, 819- 821.
8. Vaughan, D.E.W. and Strohmaier, K.G., *Proc. 7th. Intl. Zeolite Conf. (Tokyo)*, Ed. Murakami, Y. et al, Kodansha/Elsevier Press (Tokyo), (1986), 207-214.
9. Vaughan, D.E.W. and Strohmaier, K.G., *Amer. Chem. Soc. Symp. Ser.*, Ed. Ocelli, M. and Robson, H.E., (1988), *in press*.
10. Gottardi, G. and Galli, E., "Natural Zeolites", Springer- Verlag (Berlin), (1985), 163.
11. Vaughan, D.E.W., US Patent 4,714,601, (1987).
12. Vaughan, D.E.W., US Patent 4,554,146, (1985).
13. Jacobs, P.A., Beyer, H.K. and Valyon, J., *Zeolites*, (1981), **1**, 161-168.
14. Kerr, I.S., *Nature*, (1963), **197**, 1194-5.
15. Sherman, J.D. and Bennett, J.M., *Proc. 3rd. Intl. Zeolite Conf.*, *Adv. Chem. Ser.* **121**, Ed. W.M. Maier and J.B. Uytterhoeven, (1973), 52-65.
16. Thomas, J.M., Millward, G.R., Ramdas, S. and Audier, M., *Amer. Chem. Soc. Symp. Ser.* #**218**, Ed. G. Stuckey, (1983), 181-198.
17. Millward, R.M., Ramdas, S. and Thomas, J.M., *Proc. Roy. Soc.*, (1985), **A399**, 57-71.
18. Barrer, R.M. and Villiger, H., *Zeit. Kristallogr.*, (1969), **128**, 352-370.
19. Galli, E., *Cryst. Struct. Comm.*, (1974), **3**, 339-344.
20. Barrer, R.M. and Villiger, H., *J. Chem. Soc. Chem. Comm.*, (1969), 659-660.
21. Smith, D.K., Nichols, M.C. and Zolensky, M.E., "POWD 10...", Dept. Geosciences, Pennsylvania State Univ., Pa., USA, (1983).
22. Smith, J.V., *Chem. Rev.*, (1988), **88**, 149-182 .
23. Smith, J.V., personal communication.
24. Baerlocher, Ch., Hepp, A. and Meier, W.M., *Monogr. "DLS-76..."*, Dept. Kristallogr. & Petrogr., ETH, Zurich, Switzerland.
25. Meier, W.M., *Proc. 3rd. Intl. Zeolite Conf.*, *Amer. Chem. Soc. Adv. Chem. Ser.* **121**, Ed. W.M. Maier and J.B. Uytterhoeven, (1973), 39-51.
26. Barri, S.A.I., Smith, G.W., White, D. and Young, D., *Nature*, (1984), **312**, 533.
27. Treacy, M.M.J. and Newsam, J.M., *Nature*, (1988), **332**, 249-251.

## Chapter 29

# Structure of Cobalt Sulfide Phase in Carbon-Supported Co and Co-Mo Sulfide Catalysts

### Studies by Extended X-ray Absorption Fine Structure (EXAFS) and X-ray Absorption Near Edge Structure (XANES)

S. M. A. M. Bouwens, D. C. Koningsberger, V. H. J. de Beer, and R. Prins<sup>1</sup>

Laboratory for Inorganic Chemistry and Catalysis, Eindhoven, University  
of Technology, P.O. Box 513, 5600 MB Eindhoven, Netherlands

An X-Ray absorption spectroscopy study has been carried out on a carbon-supported Co and Co-Mo sulfide catalyst, the latter consisting of a fully sulfided Co-Mo-S (type II) phase. Detailed information on the structure of the cobalt sulfide phase is obtained by comparing the EXAFS and XANES spectra of the catalysts with those of  $\text{Co}_9\text{S}_8$  and  $\text{CoS}_2$  reference compounds. It is shown that the cobalt atoms in the Co-Mo-S phase have an octahedral-like sulfur coordination while the cobalt atoms in the sulfided Co/C catalyst have a larger fraction of octahedral cobalt than  $\text{Co}_9\text{S}_8$ . On the basis of these results, the high HDS activity of a sulfided Co/C catalyst can be understood since it appears that the structure of the cobalt sulfide phase in Co/C is in agreement with that in Co-Mo/C. In the Co-Mo-S phase, approximately one cobalt atom is in contact with one molybdenum atom at a distance of 2.85 Å.

The EXAFS (Extended X-Ray Absorption Fine Structure) technique is nowadays a valuable tool in the characterization of catalysts. The strength of EXAFS is that it can provide structural information on highly dispersed systems that are difficult to study with other conventional techniques. With respect to hydrotreating catalysts (e.g., sulfided Co-Mo/ $\text{Al}_2\text{O}_3$  or Ni-Mo/ $\text{Al}_2\text{O}_3$ ) EXAFS has been able to provide direct information regarding the local structure of the phases present in a working catalyst (1-3). Although the study of hydrotreating catalysts in general has received much attention during the last decade, several important questions regarding the structural characteristics are still unanswered. One of these concerns the role of the promoter Co and Ni ions in sulfided Co(Ni)-Mo catalysts.

<sup>1</sup>Current address: Technisch-Chemisches Laboratorium, ETH-Zentrum, 8092 Zürich, Switzerland

Topsøe and coworkers showed that the cobalt atoms are situated at  $\text{MoS}_2$  crystallite edges in a so-called "Co-Mo-S" structure, which structure governs almost completely the hydrodesulfurization (HDS) activity (4,5). Nevertheless, the exact structure of this phase or more precisely the location of the cobalt promoter is still unknown. Furthermore, the high specific activity of the Co-Mo-S structure is not understood. Recently, Ledoux et al. (6) showed with the use of  $^{59}\text{Co}$  NMR that the promotion effect of cobalt was correlated with the concentration of cobalt sites having a distorted tetrahedral symmetry. These cobalt sites were stabilized by so-called "rapid octahedral" cobalt atoms acting as a glue between the tetrahedral cobalt sites and the  $\text{MoS}_2$  phase. Although the "rapid octahedral" cobalt atoms could not be related to the HDS activity, Ledoux et al. lately proposed that they could be the origin of very active sites (7). Their explanation, based upon the theory of Harris and Chianelli (8), was that an electron transfer takes place between the "rapid octahedral" cobalt to the molybdenum ion resulting in a strong activation of the three sulfur ions sandwiched between them.

A different model was postulated by Duchet et al. (9) and by Vissers et al. (10) who observed a high activity for pure cobalt sulfide supported on activated carbon and hence explained the activity of a sulfided Co-Mo/C catalyst completely by the very high activity of the cobalt sites. In their theory the authors implicitly assumed that a cobalt site in sulfided Co/C has the same activity as a cobalt site in sulfided Co-Mo/C. However, this does not have to be the case since the structure of cobalt sulfide in Co/C can be very different from that in Co-Mo/C. In order to elucidate the structure of the cobalt sulfide phase in a sulfided Co/C and a Co-Mo/C catalyst we applied in this study the EXAFS and XANES (X-Ray Absorption Near Edge Structure) techniques at the Co K-edge.

### Experimental

The carbon support used was a Norit activated carbon (RX3 extra) having a surface area of  $1190 \text{ m}^2 \cdot \text{g}^{-1}$  and a pore volume of  $1.0 \text{ cm}^3 \cdot \text{g}^{-1}$ . The Co/C catalyst (4.1 wt% Co) was prepared by pore volume impregnation with an aqueous solution of cobalt nitrate (Merck p.a.) followed by drying in air at 383 K (16 h). The promoted catalyst (1.5 wt% Co, 7.7 wt% Mo) was prepared in a special way to ensure a maximum amount of the Co-Mo-S phase (11). Mössbauer spectroscopy of this promoted catalyst clearly showed that only the Co-Mo-S phase was present after sulfiding (11) and furthermore that this Co-Mo-S is probably a Co-Mo-S type II phase, meaning a minor influence of active phase-support interaction (11,12). The catalytic activity of the sulfided catalysts was determined by a thiophene HDS measurement at 673 K and atmospheric pressure, as described elsewhere (10). The thiophene HDS reaction rate constant  $k_{\text{HDS}}$  per mol Co present (approximated as a first order reaction) was found to be  $17 \cdot 10^{-3} \text{ s}^{-1}$  for Co/C and  $61 \cdot 10^{-3} \text{ s}^{-1}$  for Co-Mo/C.

The X-Ray absorption measurements were carried out on freshly in situ sulfided catalysts at liquid nitrogen temperature at the SRS in Daresbury (EXAFS station 9.2). The sulfidation was carried out in a

10% H<sub>2</sub>S in H<sub>2</sub> flow, flow rate 60 ml.min<sup>-1</sup> under atmospheric pressure, the temperature was increased linearly from 293 to 673 K (8.5 K.min<sup>-1</sup> for Co/C, 2 K.min<sup>-1</sup> for Co-Mo/C) and kept constant at 673 K for 2 h (Co/C) or 1 h (Co-Mo/C). The preparation of the model compounds Co<sub>9</sub>S<sub>8</sub> and CoS<sub>2</sub> has been described in (13) and (14), respectively. The purity of these compounds was checked by X-Ray diffraction. Phase shifts and backscattering amplitudes from reference compounds were used to calculate the EXAFS contributions. For the Co-S EXAFS signals CoS<sub>2</sub> was used, for the Co-Co contributions the Ni-Ni coordination in NiO (Merck p.a.) was chosen, and for the Co-Mo contribution in the Co-Mo/C catalyst we took ((C<sub>6</sub>H<sub>5</sub>)<sub>4</sub>P)<sub>2</sub>Ni(MoS<sub>4</sub>)<sub>2</sub> as a model compound. The use of a Ni absorber and backscatterer instead of Co is justified since calculations of Teo and Lee (15) showed that phases and backscattering amplitudes of nearest and next-nearest neighbours in the periodic table hardly differ.

## Results

In Figure 1 (a,b) the Fourier-Transformed (FT) EXAFS spectra of the Co/C and the Co-Mo/C catalyst together with the Co<sub>9</sub>S<sub>8</sub> reference compound are plotted. The absolute FT spectrum of Co<sub>9</sub>S<sub>8</sub> (Fig. 1 (a)) exhibits two peaks. The first peak is attributed to combined Co-S and Co-Co coordinations, the second one only to a Co-Co coordination (denoted Co-Co(2), to differentiate it from the Co-Co(1) coordination in the first peak). In bulk Co<sub>9</sub>S<sub>8</sub> 8/9 of the cobalt atoms are tetrahedrally coordinated and 1/9 are octahedrally coordinated by sulfurs. The Co-S coordination distances are in the range 2.13-2.39 Å. The Co-Co coordination distance of Co-Co(1) is 2.50 Å, for Co-Co(2) the distance is 3.51 Å. From Figure 1 (a) it is apparent that in the catalyst spectra the first peak is shifted to lower *r*-values compared to that in Co<sub>9</sub>S<sub>8</sub>. This shift is larger for Co-Mo/C than for Co/C. It is furthermore clear that a Co-Co(2) coordination is also present in the Co/C catalyst, but not in the promoted catalyst. On the other hand, the latter catalyst shows an additional peak which is not present in Co<sub>9</sub>S<sub>8</sub> and Co/C and, consequently, might be ascribed to Mo backscatterers.

The imaginary FT spectra in Figure 1 (b) show the separate Co-S and Co-Co(1) coordinations which cannot be discerned in the absolute FT spectra. It appears that the Co-S peak amplitude increases in the order Co<sub>9</sub>S<sub>8</sub> Co/C Co-Mo/C, whereas the Co-Co(1) peak amplitude decreases in the same order. Data analysis was carried out by isolating the first and second peak in the absolute FT spectra and fitting the resulting EXAFS functions using Co-S and Co-Co EXAFS contributions. For a detailed description of the data analysis procedure we refer to (16). The structural parameters (*N*, *R* and  $\Delta\sigma^2$ ) obtained in this way are collected in Table I.

Supplementary information on the cobalt coordination can be derived from the XANES region. The near-edge structure of the samples is shown in Figure 2. The spectra all show a weak absorption peak near threshold which has been identified as a 1s → 3d transition (17,18). This transition has been observed to be more intense in te-

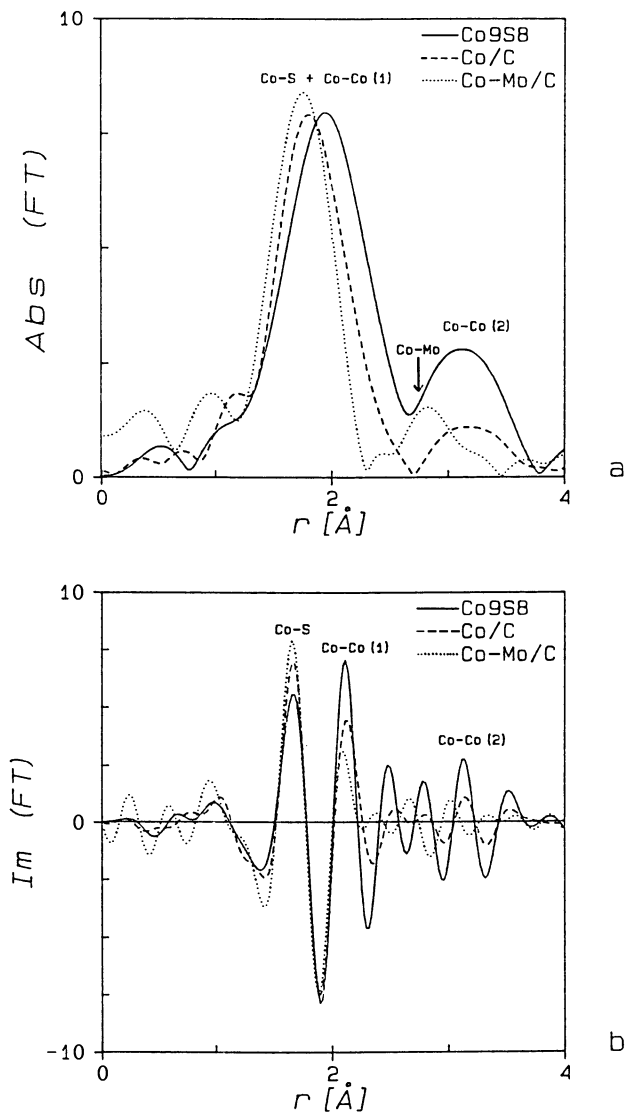


Figure 1: Imaginary  $k^3$ -weighted Fourier-Transforms ( $\Delta k=3.0 - 10.9 \text{ \AA}^{-1}$ ) of the EXAFS data of  $\text{Co}_9\text{S}_8$ , Co/C and Co-Mo/C: (a) absolute part, (b) imaginary part.

Table I. Structural parameters for the Co-S, Co-Co(1), Co-Co(2) and Co-Mo coordinations

	Co-S			Co-Co(1)			Co-Co(2)			Co-Mo		
	N <sup>a</sup>	R(Å) <sup>b</sup>	$\Delta\sigma^2(\text{Å}^2)$ <sup>c</sup>	N	R(Å)	$\Delta\sigma^2(\text{Å}^2)$	N	R(Å)	$\Delta\sigma^2(\text{Å}^2)$	N	R(Å)	$\Delta\sigma^2(\text{Å}^2)$
Co <sub>9</sub> S <sub>8</sub>	4.3	2.22	0.0038	2.4	2.51	0.0015	2.8	3.54	-0.0011			
Co/C	5.2	2.22	0.0029	1.6	2.55	0.0017	1.5	3.54	0.0018			
Co-Mo/C	6.7	2.21	0.0045	0.6	2.55	0.0076				0.8	2.85	0.0050

<sup>a</sup> Coordination number  
<sup>b</sup> Coordination distance  
<sup>c</sup> Debye-Waller factor

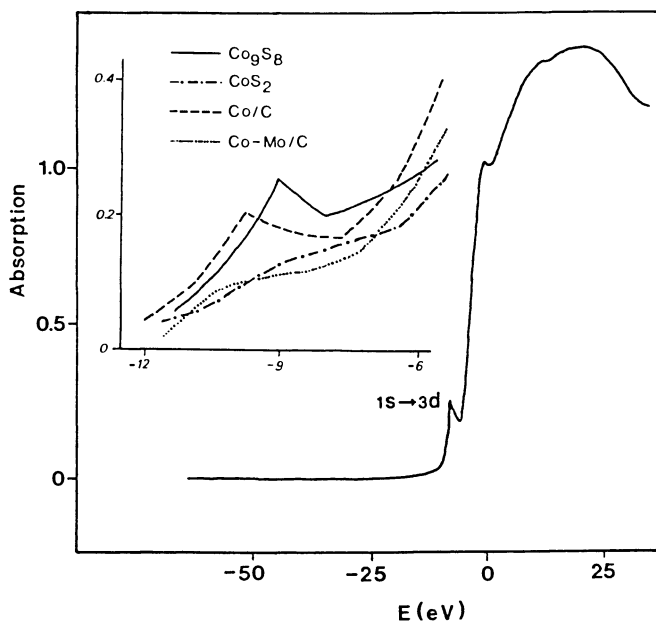


Figure 2: XANES spectrum of  $\text{Co}_9\text{S}_8$ . The expanded inset shows the  $1s \rightarrow 3d$  transition of  $\text{Co}_9\text{S}_8$ ,  $\text{CoS}_2$ ,  $\text{Co/C}$  and  $\text{Co-Mo/C}$ .

tetrahedral than in octahedral coordination of the absorbing atom (17), hence, it can be used as a measure of the coordination of the cobalt atoms. In Figure 2 the XANES spectra of both catalysts are compared with that of  $\text{Co}_9\text{S}_8$ , consisting of 89% tetrahedral and 11% octahedral cobalt, and with  $\text{CoS}_2$ , consisting of 100% octahedral cobalt. It is clear in this Figure that the  $1s \rightarrow 3d$  transition is most intense for  $\text{Co}_9\text{S}_8$  whereas in  $\text{CoS}_2$  its intensity is very small. The sulfided Co/C catalyst shows a somewhat smaller intensity than that of  $\text{Co}_9\text{S}_8$  while the Co-Mo/C catalyst shows a very small intensity, comparable to the  $\text{CoS}_2$  compound.

### Discussion

The data analysis reveals that the Co-S coordination number increases in the order  $\text{Co}_9\text{S}_8 < \text{Co/C} < \text{Co-Mo/C}$ . This means that the cobalt atoms in the catalysts have a higher sulfur coordination than those in  $\text{Co}_9\text{S}_8$  and furthermore, that this phenomenon is more pronounced when cobalt is present in a Co-Mo-S structure. The EXAFS results are substantiated by the XANES spectra. The  $1s \rightarrow 3d$  transition of the Co/C catalyst suggests a somewhat higher percentage of octahedral cobalt as present in  $\text{Co}_9\text{S}_8$  whereas for the Co-Mo/C catalyst it indicates an octahedral-like sulfur coordination.

Our results stress the importance of studying the imaginary FT spectra in combination with the absolute ones. By doing so, the observed shift of the first peak in the absolute FT spectra to lower  $r$ -values in the order  $\text{Co}_9\text{S}_8 > \text{Co/C} > \text{Co-Mo/C}$  can be fully explained by the increase in the corresponding Co-S peak amplitude and the simultaneous decrease in the Co-Co(1) peak amplitude. In fact, the Co-S coordination distance in the three samples is similar (2.22 Å). From these observations it might be clear that conclusions based only upon absolute FT spectra can turn out to be erroneous.

The EXAFS parameters for the Co/C catalyst show a Co-Co(1) coordination distance of 2.55 Å, which is slightly larger than that in  $\text{Co}_9\text{S}_8$  (2.51 Å). On the other hand, the Co-Co(2) coordination distances of both samples are equal. These results suggest that the cobalt sulfide phase in the sulfided Co/C catalysts essentially has a  $\text{Co}_9\text{S}_8$ -like structure, the only difference being its higher sulfur coordination. In case of the Co-Mo/C catalyst, the presence of a small Co-Co(1) contribution is evident. From the large Debye-Waller factor it can be inferred that this coordination has a high degree of disorder. Surprisingly, however, its coordination distance (2.55 Å) corresponds exactly to that in Co/C. The expected Co-Mo peak could be fitted well using the Ni-Mo EXAFS functions from the  $((\text{C}_6\text{H}_5)_4\text{P})_2\text{Ni}(\text{MoS}_4)_2$  reference compound, which confirms the presence of molybdenum neighbouring atoms. The Co-Mo coordination distance is calculated to be 2.85 Å, which is in good agreement with our EXAFS study of a sulfided Co-Mo/C catalyst at the Mo K-edge (19), in which we reported a Mo-Co coordination distance of 2.8 Å. The calculated Co-Mo coordination number of 0.8 (Table I) suggests that in the Co-Mo-S (II) structure approximately one cobalt atom is in contact with one molybdenum atom.

According to our EXAFS and XANES results, the structure of the cobalt phase in sulfided Co/C is in agreement with that in the



Co-Mo/C catalyst: in both catalysts a high sulfur coordination of the cobalt atoms is present. This is an interesting observation with regard to the activity per cobalt atom in both catalyst systems. Viissers et al. (10) stated that the intrinsic activity of a cobalt site in sulfided Co/C can be close to that in sulfided Co-Mo/C. Hence, our results of the structural resemblance between sulfided Co/C and Co-Mo/C, support the theory of Viissers et al. (10) that the cobalt phase in sulfided Co-Mo catalysts can be the actual active phase. Moreover, on the basis of these results the high HDS activity of a sulfided Co/C catalyst can be understood.

Our findings also coincide with the proposal of Ledoux et al. (7) that the "rapid octahedral" cobalt atoms might be the origin of very active sites, since we observe an octahedral-like coordination in the promoted catalyst. However, the earlier proposal of Ledoux et al. of tetrahedral cobalt sites being responsible for the high HDS activity of cobalt-molybdenum sulfide catalysts (6) must be rejected. Finally, our observation that the cobalt sulfide phase in the Co/C catalyst contains a higher sulfur coordination than that in  $\text{Co}_9\text{S}_8$ , which is expected from thermodynamical considerations, might point to a modification of the active cobalt sites through the carbon carrier. Support for the latter idea can be found in the work of Burch and Collins (20) who discussed a possible interaction between the nickel sulfide phase and an alumina, silica and carbon carrier. These authors proposed that a metal sulfide-support interaction may alter the morphology or composition of the nickel sulfide phase.

### Conclusions

Detailed information on the structure of the supported cobalt sulfide phase could be obtained by studying the imaginary Fourier Transformed EXAFS spectra as well as the cobalt  $1s \rightarrow 3d$  transition in the XANES spectra. It is shown that the cobalt atoms in the Co-Mo-S (II) phase have an octahedral-like sulfur coordination while the sulfided Co/C catalyst has a larger fraction of octahedral cobalt than  $\text{Co}_9\text{S}_8$ . On the basis of these results, the high HDS activity of a sulfided Co/C catalyst can be understood since it appears that the structure of the cobalt sulfide phase in Co/C is in agreement with that in Co-Mo/C. In the Co-Mo-S (II) phase approximately one cobalt atom is in contact with one molybdenum atom at a distance of 2.85 Å.

### Acknowledgments

The authors would like to thank Dr. J.A.R. van Veen of the Koninklijke/Shell-laboratory (KSLA) in Amsterdam for providing a sample of a specially prepared Co-Mo/C catalyst. Thanks are also expressed to Dr. F. Bauman of the University of Bielefeld (West Germany) for supplying us with the model compound  $((\text{C}_6\text{H}_5)_4\text{P})_2\text{Ni}(\text{MoS}_4)_2$ . The information in this paper is partly derived from a contract (EN3V-0009/NL) concluded with the European Economic Community.

Literature cited

1. Clausen, B.S., Topsøe, H., Candia, R., Villadsen, J., Lengeler, B., Als-Nielsen, J., and Christensen, F., J. Phys. Chem. 1981, 85, 3868.
2. Parham, T.G., and Merrill, R.P., J. Catal. 1984, 85, 295.
3. Sankar, G., Vasudevan, S., and Rao, C.N.R., J. Phys. Chem. 1987, 91, 2011.
4. Topsøe, H., Clausen, B.S., Candia, R., Wivel, C., and Mørup, S., J. Catal. 1981, 68, 433.
5. Wivel, C., Candia, R., Clausen, B.S., Mørup, S. and Topsøe, H., J. Catal. 1981, 68, 453.
6. Ledoux, M.J., Michaux, O., Agostini, G., and Panissod, P., J. Catal. 1985, 96, 189.
7. Ledoux, M.J., J.C.S. Faraday Trans. I 1987, 83, 2172.
8. Harris, S., and Chianelli, R.R., J. Catal. 1986, 98, 17.
9. Duchet, J.C., van Oers, E.M., de Beer, V.H.J., and Prins, R., J. Catal. 1983, 80, 386.
10. Vissers, J.P.R., de Beer, V.H.J., and Prins, R., J.C.S. Faraday Trans. I 1987, 83, 2145.
11. van Veen, J.A.R., Gerkema, E., van der Kraan, A.M., and Knoester, A., J.C.S. Chem. Commun. 1987, 1684.
12. Candia, R., Sørensen, O., Villadsen, J., Topsøe, N.-Y., Clausen, B.S., and Topsøe, H., Bull. Soc. Chim. Belg. 1984, 93, 763.
13. Bouwens, S.M.A.M., Koningsberger, D.C., de Beer, V.H.J., and Prins, R., Catal. Letters 1988, 1, 55.
14. Morris, B., Johnson, V., and Wold, A., J. Phys. Chem. Solids 1967, 28, 1565.
15. Teo, B.K., and Lee, P.A., J. Am. Chem. Soc. 1979, 101, 2815.
16. van Zon, J.B.A.D., Koningsberger, D.C., van 't Blik, H.F.J., and Sayers, D.E., J. Chem. Phys. 1985, 12, 5742.
17. Shulman, R.G., Yafet, Y., Eisenberger, P., and Blumberg, W.E., Proc. Natl. Acad. Sci. U.S.A. 1976, 73, 1384.
18. Gregor, R.B., Lytle, F.W., Chin, R.L., and Hercules, D.M., J. Phys. Chem. 1981, 85, 1332.
19. Bouwens, S.M.A.M., Koningsberger, D.C., de Beer, V.H.J., and Prins, R., Bull. Soc. Chim. Belg. 1987, 96, 951.
20. Burch, R., and Collins, A., J. Catal. 1986, 97, 385.

RECEIVED January 10, 1989

## Chapter 30

# X-ray Absorption Near Edge Structure (XANES) and Extended X-ray Absorption Fine Structure (EXAFS) Spectra of Pt–Sn–Alumina Catalysts

Yong-Xi Li<sup>1</sup>, N.-S. Chiu<sup>1</sup>, W.-H. Lee<sup>1</sup>, S. H. Bauer<sup>1</sup>, and B. H. Davis<sup>2</sup>

<sup>1</sup>Baker Laboratory of Chemistry, Cornell University, Ithaca, NY 14853–1301

<sup>2</sup>Center for Applied Energy Research, 3572 Iron Works Pike, Lexington, KY 40511

This report concerns one of four groups of Pt/Sn loaded catalysts, prepared according to selected protocols, which incorporated a range of Sn loadings (0.4 to 3.4%), with Pt maintained at 1%. The X-ray fluorescence and absorption spectra of these preparations were recorded, for both the calcined and reduced states, at the CHESS facility. The near-edge and extended-edge spectra, at the Pt *L*<sub>III</sub> and Sn K-edges, were analyzed to ascertain the states of the metallic constituents. Spectra of the pure metals, of alloys (Pt/Sn 1:1 and 3:1), of their oxides and chlorides were used for calibration. Both the near and extended edge spectra show that reduction with H<sub>2</sub> at 773K (one atm) for 5 hours leaves major fractions of oxides and chlorides unreduced, but enhances dispersion. Differences due to tin loading are discernible. A radial distribution peak may be assigned to (Sn-Pt) scattering, but by itself is not sufficient to demonstrate the development of alloy clusters upon reduction.

Supported Pt/Sn bimetallic catalysts are assuming increasingly significant roles in the processing of petroleum, operating as reforming catalysts. They provide high selectivity for aromatics, they are stable, and permit operation at high reaction temperatures (~780K) at relatively low pressures of hydrogen (10–15 psig). The many current studies of these materials (1–12) are a measure of their practical importance. Nonetheless, the atomic configurations about the metallic constituents and their structural coordination have not yet been clarified. Indeed, different diagnostic techniques lead to incompatible conclusions regarding the formal oxidation states, extents of dispersion, Pt/Sn

association, etc. It appears that the critical molecular parameters may be highly sensitive to details of the preparative procedures, and to the nature of the support. Therefore we have undertaken a comparative study of four groups of Pt/Sn catalysts prepared according to selected protocols. These incorporate a range of Sn loadings (0.4 to 3.4%) with Pt maintained at about 1%. As a diagnostic of bulk structure we measured both the near and extended X-ray fluorescence and absorptions at the Pt  $L_{III}$  and Sn K-edges, and correlated these with available Mössbauer, XPS and XRD data. Here we report on one group of catalysts, prepared according to the acetone-complexation method, on low and high area alumina.

### Experimental

Twenty grams of support [low area alumina:  $110 \text{ m}^2/\text{g}$ ; high area alumina:  $250 \text{ m}^2/\text{g}$ ] were wetted with 20 ml of acetone, followed by slow addition (with stirring) of 20 ml of an acetone solution containing the desired amounts of  $\text{H}_2\text{PtCl}_6$  and  $\text{SnCl}_2 \cdot 2\text{H}_2\text{O}$ . The impregnated material was dried in air at room temperature, then at 393K for 6 hours, and finally calcined in air at approximately 770K for four hours. Portions of the dried and calcined preparations were reserved for NEXAFS and EXAFS spectral scans.

The catalysts were then reduced in flowing  $\text{H}_2$  at atmospheric pressure, at approximately 770K for a total of five hours (including heating to the operating temperature); cooled in hydrogen, then swept with high purity argon, and maintained sealed in the reducing tube until opened for mounting in the sample holder in an argon filled glove box. Under the argon atmosphere, the powdered sample was tightly packed into a wafer of appropriate thickness, and tightly sealed with Mylar windows prior to removal from the glove box. Tests were made to ascertain the retention of the reduced state during X-ray exposure at room temperature by successive scanning of samples, as initially sealed; then after exposure to air for ten minutes; two hours; 24 hours. No change in the X-ray spectra could be detected after 10 minutes (windows retained) of exposure indicating that even if slight oxidation had taken place on the surface of the tightly pressed powder sample, diffusion in the bulk material was negligible. In the near edge spectra slight shifts were discernible only after two hours of exposure to the atmosphere. No detectable changes were noted between the XRD pattern obtained in-situ and one recorded following exposure to air for one hour at room temperature. Table I is a listing of the metallic content of the six catalysts.

X-ray spectra were recorded at the CHESS Facility in the fluorescence mode for both Pt and Sn edges and

TABLE I  
The Catalyst Compositions

Catalyst	Support	Content, wt. %		
		Pt	Sn	Cl
A	alumina	1.0	0.45	1.2
B	(250 m <sup>2</sup> /g)	1.0	1.50	1.2
C		1.0	3.50	1.2
D	alumina	1.0	0.55	1.2
E	(110 m <sup>2</sup> /g)	1.0	1.60	1.2
F		1.0	3.15	1.2
Ref	alumina (250 m <sup>2</sup> /g)	1.0	0	1.2

absorption mode for Sn edge. One to three scans were recorded for each sample. Reference materials were: Pt and Sn as metal foils;  $H_2PtCl_6$ ;  $PtCl_2$ ;  $PtO_2$  [run at the  $L_{III}$  edges at 11.59 keV]. Also,  $SnCl_4 \cdot 5H_2O$ ;  $SnCl_2 \cdot 2H_2O$ ;  $SnO$  and  $SnO_2$  [run at the K-edge at 29.19 keV]. Scans were made of alloys with nominal composition  $PtSn$  and  $Pt_3Sn$ . Spectra were recorded for both calcined and reduced  $Pt/Al_2O_3$  and  $Sn/Al_2O_3$ , prepared by the  $H_2PtCl_6$  impregnation and  $SnCl_2$  co-precipitation methods, respectively. All the spectra were reduced using computer codes developed at Cornell, which provide for successive refinement of the radial distribution curves [background correction; termination correction; phase shift (13-15)]. While "split" side bands appeared in the major radial distribution peak of metallic platinum, for other scattering pairs they were of low amplitude, not significantly larger than the noise. Many variants in the data reduction procedures were tested; ultimately all correlations of radial distribution curves (of a catalyst and the reference compounds) were made on the basis of strictly comparable procedures. Initially the entire spectrum was reduced even where there was much noise at high  $k$ , in order to achieve the best resolution in the radial distribution curves. Then the spectra was terminated at  $k \sim 11 \text{ \AA}^{-1}$  to minimize the effect of noise and thus derive quantitative peak areas for comparisons of the various preparations. It is worth noting that the area under an RDF peak is not proportional to the amount of the element present in the sample. Given the computed area under a peak at  $R_{ij}$  for an atom pair (ij), where  $j$  designates the central atom and  $i$  any one of the surrounding atom types in that coordination shell, then after multiplying the area by  $r_{ij}^2$ , the result is roughly proportional to  $Z_j \sum Z_i$  (in the coordination shell). However, experience indicates that structural distortions reduce the effective contributions of coordinating atoms within selected shells.

In the following the results of our analyses are presented in sequence: NEXAFS for Pt and Sn; EXAFS for Pt and Sn, for the reference compounds and catalysts on low and high area alumina. Our general conclusions are then compared with those derived from other diagnostics.

**NEXAFS.** The near-edge profiles, both for Pt  $L_{III}$  and Sn K, show no distinctive features for any of the reference substances or the various catalysts preparations. However, the steep increases in absorption appear at different locations, and the initial maxima rise to characteristic amplitudes. These may be compared when the patterns are normalized to unit level, established by extrapolating the EXAFS background to  $E_0$ . The corresponding absorptions have been assigned to

$2P_{3/2} \rightarrow 5d[\text{Pt } L_{III}]$  (16-18) and to  $1s \rightarrow 5p[\text{SnK}]$  transitions. All edge positions are determined from the energy derivative curve ( $\mu/E$ ) and are measured relative to those of the corresponding metal foils, assigned zero.

Within  $\pm 0.5$  eV, the  $L_{III}$  edges of the alloys,  $\text{Pt}_3\text{Sn}$  and  $\text{PtSn}$ , appear at the same energy as that of the metal; the initial rise of absorption coefficients attains a level of 1.2, relative to the background. In  $\text{Pt}^{+2}\text{Cl}_2 \cdot 2\text{H}_2\text{O}$ , the edge appears 1.0 eV above the metal and the peak height is  $\sim 1.38$ . For  $\text{Pt}^{+4}\text{O}_2$  and  $\text{H}_2\text{Pt}^{+4}\text{Cl}_6$  the rise in absorption is 3 eV higher than that of the metal and attains 1.95. For an analogous series of compounds, for a given central element, the peak height is a measure of its ionicity, i.e. the number of 5d electrons partially removed by chemical bond formation (19). For the catalyst preparations, we found that in the dried condition (prior to calcining) the edge position is 1 eV above the metal, and the peak height is close to that of  $\text{Pt}^{+2}\text{Cl}_2$ . In the calcined state, the initial rise appears at 2.6 - 2.7 eV above the metal and peaks sharply at 2.4 level relative to the background, indicative of fully oxidized Pt, possibly with a lower 5d occupancy than in crystalline  $\text{PtO}_2$ .

For all the reduced catalysts, regardless of Sn metal loading or support area, the edge is at 1 eV above the metal; all have closely similar peak heights that are a little lower than in  $\text{Pt}^{+2}\text{Cl}_2$ . No unique assignment of a unique oxidation number is thus provided, except that such profiles are not incompatible with that for a mixture of  $\text{Pt}^0$ ;  $\text{Pt}^{+2}$ ;  $\text{Pt}^{+4}$ , as suggested by the EXAFS spectra; see below.

At the Sn K-edge, the near edge profiles are also featureless. Unexpectedly the alloys appear at  $\sim -0.1$  eV; the initial rise for  $\text{Sn}^{+2}\text{Cl}_2$  is not shifted relative to that of the metal, while  $\text{Sn}^{+2}\text{O}$  is at + 0.5 eV. Their peak height are 1.09 and 1.28, respectively, relative to the background. The edge for  $\text{Sn}^{+4}\text{Cl}_4 \cdot 5\text{H}_2\text{O}$  appears at 4 eV, and for  $\text{Sn}^{+4}\text{O}_2$  at 5 eV above the metal; their peak heights are 1.17 and 1.46, respectively. Upon reduction of the high area support preparations the edge locations revert close to zero, with peak heights of 1.16, consistent with mixtures of  $\text{Sn}^{+2}\text{O}$  and the reduced metal. Exposure to air for about two hours brings the edge back to higher values but somewhat smaller than that of  $\text{Sn}_4^{+4}\text{O}_2$ . Again, no definitive conclusion regarding the oxidation state of the Sn follows from the near edge data other than suggestion of the presence of mixed oxidation states.

EXAFS. The peaks in the radial distribution functions for the reference compounds, after background and termination error corrections, provide the basis for

assignments of the catalyst RDF's. The major peak in Pt (metal) appears at 2.62 Å (add phase shift correction; 0.15 Å). The (Pt-O) distance in PtO<sub>2</sub> (unfortunately the structure of which is not well defined) is 1.66 Å with 0.38 Å phase shift correction, while (Pt-Pt) appears at 3.28 Å. In PtCl<sub>2</sub>, the major peak is (Pt-Cl) = 1.94 Å (add phase shift correction; 0.42 Å), with a small peak at 3.1 Å assigned to (Pt-Pt). In H<sub>2</sub>PtCl<sub>6</sub>, (Pt-Cl) = 1.93 Å (add phase shift correction; 0.39 Å). As expected it has a larger area. There are no other peaks above noise in this radial distribution function. In calcined Pt/Al<sub>2</sub>O<sub>3</sub>, prepared by adding an H<sub>2</sub>PtCl<sub>6</sub> solution to the support, the (Pt-O) peak is prominent with a shoulder that can be assigned to a small fraction of (Pt-Cl).

Catalysts prepared on high and low area alumina have closely similar RDF's. In all cases, whether calcined or reduced, the major peak is a superposition of (Pt-O) and (Pt-Cl) contributions but with varying proportions depending on the treatment and the tin content. For the calcined, low area preparation the peak at 1.64 Å has a larger area than that for PtO<sub>2</sub>, due to (Pt-Cl) contributions (1.64 Å and 2.02 Å were found if entire data set was used). There is a peak at 2.68 Å which may be assigned to (Pt-Sn) scattering. The (Pt-Pt) peak at 3.34 Å is small. In these preparations reduction moves the peak to 1.89 Å (0.44% Sn) or 1.84 Å (1.47 and 3.4% Sn) but decreases its area (Table II). Clearly Sn loading increases the Pt-Cl fraction as indicated by displacement of the peak to higher R values, with a corresponding reduction in peak area, which suggests increased distorted configuration in the first coordination shell. The sequence of changes in the RDF's for preparations on the low area support is illustrated in Figure 1. This, we believe, may be a consequence of incomplete reduction in flowing hydrogen at 770°K. Preliminary results from XRD studies support this view, with respect to the formation of some alloy crystals large enough to be detected by XRD.

For preparations on high area support reduction does not show a significant shift in peak position, consistent with the expected enhanced difficulty to reduce the oxide, which is tightly bonded to the substrate. Indeed, increased Sn loading tends to shift the first peak to lower R values. The second peak in the reduced preparations may be assigned to an overlap of (Pt-Pt) and (Pt-Sn) interactions. Unfortunately, these critical distances are too close to be resolved. The phase shift corrected distance for Pt-Pt in metal is 2.77 Å, whereas Pt-Sn are 2.62 Å and 2.83 Å in PtSn and Pt<sub>3</sub>Sn, respectively. By itself the presence of this peak does not prove the existence of an alloy because dried and calcined samples (at the Sn K edge) also show a strong peak at 2.5 Å. A variety of solid solutions of the



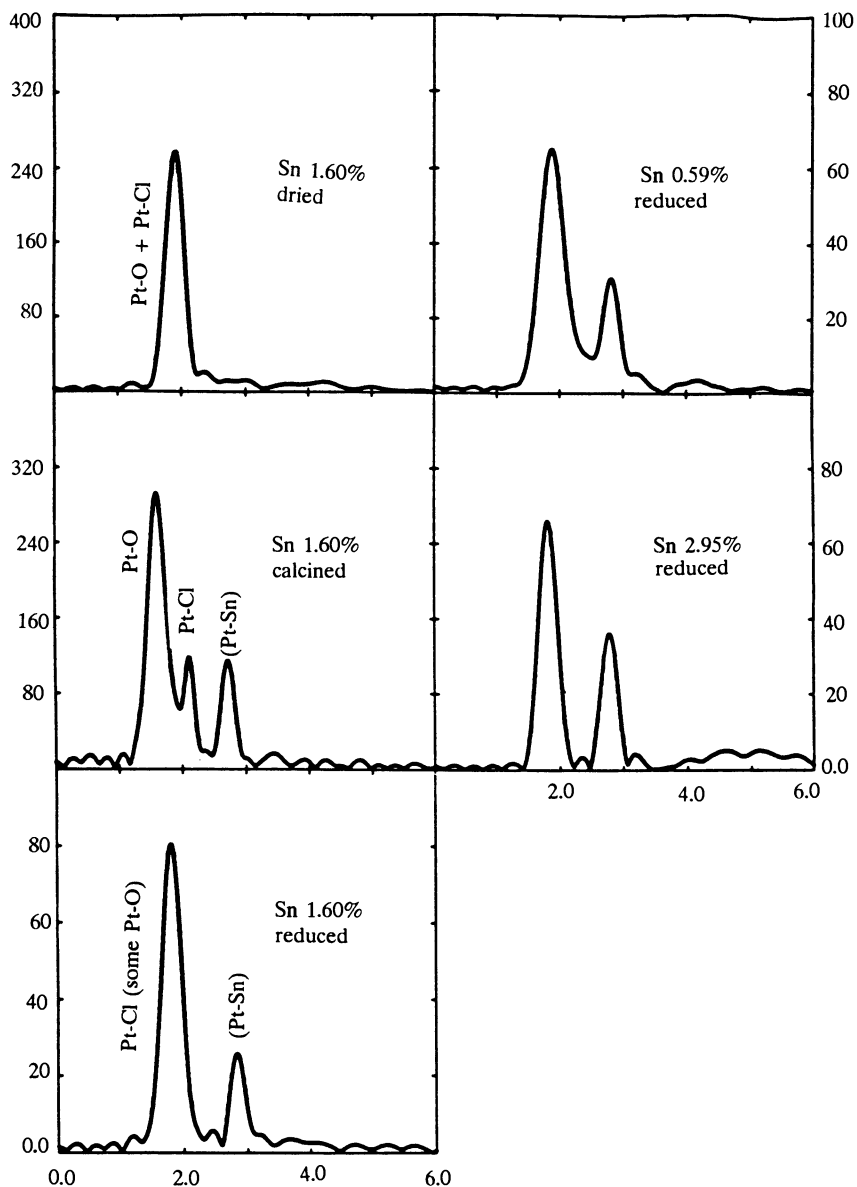
TABLE II

Reduced Radial Distribution Peaks at Pt L<sub>III</sub> Edge [Pt at 1%]  
(converted, phase shifted, with area multiplied by R<sup>2</sup>)

Reference Materials	1st Peak		2nd Peak		3rd Peak		4th Peak		5th Peak	
	Position	Area	Position	Area	Position	Area	Position	Area	Position	Area
PtO <sub>2</sub>	2.05 Å	400			3.50 Å	300				
PtCl <sub>2</sub> ·2H <sub>2</sub> O	2.36	658			3.32	---				
H <sub>2</sub> PtCl <sub>6</sub>	2.32	1070								
Pt <sub>3</sub> Sn			2.83Å	510	3.97	90	4.79Å	94		
Pt foil			2.77	881	3.96	176	4.72	267	5.34 Å	284
<u>Low Area Catalysts</u>										
Sn 1.60% (Dry)	2.30	489								
Sn 1.60% (Calcined)	1.99 <sup>a</sup>	536	2.80 <sup>c</sup>	240 <sup>c</sup>	3.47	78				
Sn 1.60% (Calcined)*	2.00	416	{ 2.42	{ 156						
			{ 2.81 <sup>c</sup>	{ 236	3.52	78				
Sn 0.59% (Reduced)	2.32 <sup>b</sup>	169	3.02 <sup>c</sup>	93						
Sn 1.60% (Reduced)	2.26 <sup>b</sup>	150	3.00 <sup>c</sup>	76						
Sn 2.95% (Reduced)	2.24 <sup>b</sup>	120	2.98 <sup>c</sup>	100						
<u>High Area Catalysts</u>										
Sn 1.47% (Dry)	2.26 <sup>b</sup>	270	2.58 <sup>c</sup>	150						
Sn 1.47% (Calcined)	2.00 <sup>a</sup>	498	2.78 <sup>c</sup>	216	3.42	67				
Sn 0.44% (Reduced)	2.26 <sup>b</sup>	168	2.98 <sup>c</sup>	105						
Sn 1.47% (Reduced)	2.20 <sup>b</sup>	137	3.03 <sup>c</sup>	28						
Sn 3.40% (Reduced)	2.24 <sup>b</sup>	118	2.57 <sup>c</sup>	54						

\* Long data

a. (Pt-O) phase shift was used. b. (Pt-Cl) phase shift was used. c. (Pt-Pt) phase shift was used.



R in Angstroms (phase shift uncorrected)

Figure 1. Radial distribution functions from fluorescence intensities at the Pt  $L_{III}$  edge for a sequence of preparations on low area alumina. Note change of vertical intensity scale.

oxides, moderated by the presence of an interactive support, could be present. Note that the radial distribution functions clearly show that reduction is always incomplete. The variations in peak areas indicate that dispersion is high, and the first coordination shell is highly distorted.

Parallel conclusions follow from the RDF's derived from EXAFS spectra at the Sn K-edge. The RDF peaks in the reference compounds were readily assigned. In  $\text{SnO}_2$ , the major peak at 1.66 Å [phase corrected to 2.05 Å (20)] is due to Sn-O scattering; peaks at 2.96 Å and 3.52 Å are superpositions of (Sn-Sn) and various (Sn-O) contributions [phase corrected to 3.19 Å and 3.79 Å, respectively]. In  $\text{SnCl}_4 \cdot 5\text{H}_2\text{O}$  the (Sn-O) peak appears at 1.66 Å (21)]. In SnO, due to the lower positive charge on a metal atom, the (Sn-O) peak appears at 1.76 Å, and (Sn-Sn) shifts to 3.26 Å.  $\text{SnCl}_2 \cdot 2\text{H}_2\text{O}$  has four peaks: (Sn-O) at 1.81 Å [phase shifted to 2.16 Å]; (Sn-Cl) at 2.29 Å [phase shifted to 2.59 Å (22)]; another (Sn-Cl) at 3.02 Å and (Sn-Sn) at 4.30 Å [phase shifted to 3.33 Å and 4.50 Å, respectively].

The dried and calcined preparations on high area alumina have very similar RDF's, which strongly resemble that of  $\text{SnCl}_4 \cdot 5\text{H}_2\text{O}$  (Table III). However, the (Sn-O) and (Sn-Cl) split is larger in the catalysts, wherein the (Sn-O) distance is ~ 0.1 Å smaller than in the tetrachloride. This suggests that in the calcined state the tin atom carries a high positive charge. The area under the (Sn-O) peak increase significantly upon calcination (from 130 to 200 for 1.47% Sn of high area support sample). These preparations also show prominent peaks at ~ 2.50 Å (phase shifted uncorrected), tentatively assigned to (Sn-Pt) scattering. Small peaks at 3.14 - 3.26 Å are due to (Sn-Sn), as in Sn-O.

Upon reduction (on the high area alumina) the small (Sn-Sn) peak disappears. There remains a strong (Sn-O) peak at 1.58 - 1.64 Å, reverting to that present in  $\text{SnCl}_4 \cdot 5\text{H}_2\text{O}$ . The areas decrease with Sn loading (224 for 0.44%; 133 for 1.47%; 100 for 3.4%). There is an insignificant (Sn-Cl) peak for the lowest tin sample, but it is clearly present at the higher loadings. The small (Sn-Pt) peak at ~2.5 Å remains but its area shrinks with increasing Sn content (Figure 2). These results suggest that increased dispersion is mediated by larger levels of tin, and clearly underscores that treatment with hydrogen, as carried out under operating conditions, leaves a major fraction of the metal in the oxide form. The amount of chlorine that remains correlates directly with the amount of tin present.

The preparation on the low area alumina do not show the small (Sn-Sn) peak at 3.3 Å, otherwise, their RDF's are similar to those on the high area support. The trends with Sn loading, relative to peak positions and

TABLE III

Reduced Radial Distribution Peaks at Sn K-edge [Pt at 1.8 Å]  
(converted, phase shifted, with area multiplied by R<sup>2</sup>)

Reference Materials	1st Peak		2nd Peak		3rd Peak		4th Peak		5th Peak	
	Position	Area	Position	Area	Position	Area	Position	Area	Position	Area
SnCl <sub>4</sub> ·5H <sub>2</sub> O*	2.10 Å	118	2.39 Å	248						
SnCl <sub>4</sub> ·5H <sub>2</sub> O	2.26	295								
SnCl <sub>2</sub> ·2H <sub>2</sub> O*	2.16	40			2.59Å	101	3.33 Å	45	4.50 Å	63
SnO <sub>2</sub>	2.05	276					3.19	277		
							3.71	665		
SnO	2.18	114			2.82	88	3.48	373		
Metal foil					2.83	220	3.96	90		
Pt <sub>3</sub> Sn										
<b>Low Area Catalysts</b>										
Sn 1.60% (Dry)	1.97 <sup>a</sup>	240	2.45 <sup>b</sup>	109	2.68 <sup>c</sup>	44				
Sn 0.69% (Reduced)	1.96 <sup>a</sup>	260	2.44 <sup>b</sup>	49	2.69 <sup>c</sup>	67				
Sn 1.60% (Reduced)	1.98 <sup>a</sup>	146	3.43 <sup>b</sup>	44	2.69 <sup>c</sup>	25				
Sn 2.95% (Reduced)	1.97 <sup>a</sup>	122	2.42 <sup>b</sup>	44	2.64 <sup>c</sup>	30				
<b>High Area Catalysts</b>										
Sn 1.47% (Dry)	1.95 <sup>a</sup>	130	2.41 <sup>b</sup>	140	2.69 <sup>c</sup>	81	3.49 <sup>c</sup>	43		
Sn 1.47% (Calcined)	1.96 <sup>a</sup>	200	2.42 <sup>b</sup>	70	2.69 <sup>c</sup>	81	3.34 <sup>c</sup>	50		
Sn 0.44% (Reduced)	1.98 <sup>a</sup>	224			2.69 <sup>c</sup>	66				
Sn 1.47% (Reduced)	1.98 <sup>a</sup>	133	2.46 <sup>b</sup>	78	2.69 <sup>c</sup>	41				
Sn 3.40% (Reduced)	2.04 <sup>a</sup>	100	2.48 <sup>b</sup>	30	2.68 <sup>c</sup>	20				

\* Long data

a. (Sn-O) phase shift of SnCl<sub>4</sub>·5H<sub>2</sub>O was used. b. (Sn-Cl) phase shift of SnCl<sub>4</sub>·5H<sub>2</sub>O was used.c. (Sn-Sn) phase shift of SnO<sub>2</sub> was used (Sn-Sn); phase shift (~ 0.1 Å) of metal is smaller than that in SnO<sub>2</sub> (~ 0.22 Å).

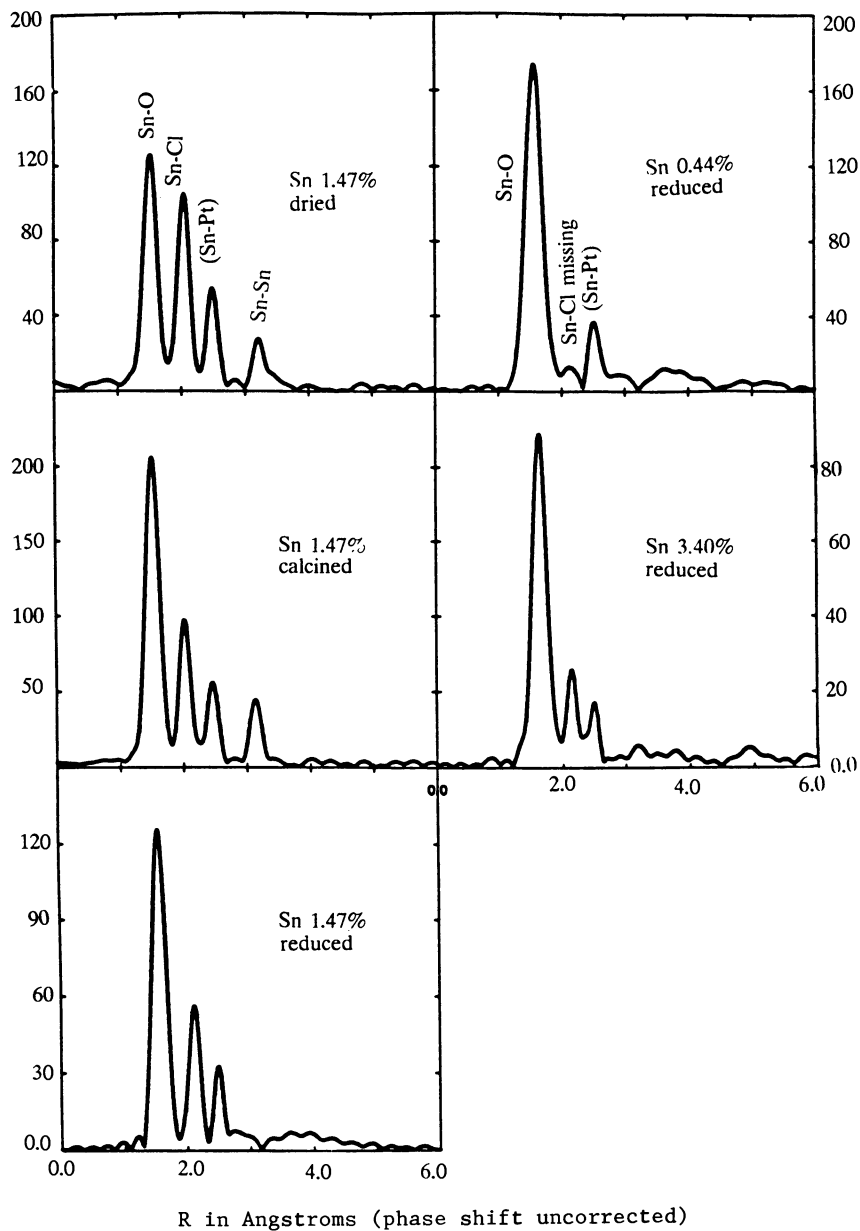


Figure 2. Radial distribution functions from fluorescence at the Sn K-edge for a sequence of preparations on high area of alumina. Note change of vertical intensity scale.

areas appear to be independent of the support area. The assignment of the small peak at 2.5 Å (unshifted) to (Sn-Pt) scattering remains somewhat ambiguous. It indicates either a solid solution of the oxides or possibly a Pt/Sn alloy, for which at least four different phases have been reported (24).

Review of Reported Structures. A theoretical analysis of XANES profiles at the  $L_{III}$  edge of platinum in  $PtCl_4^{-2}$  and  $PtCl_6^{-2}$  was presented by Nemarova, et al. (24). However, in assigning transitions from the 2p states to vacant bound orbitals, these authors postulated highly symmetric structures [octahedral and square configurations]. It is doubtful that the corresponding orbital designations correctly apply to the distorted fields that exist on the surfaces of these supported catalysts.

The state of tin in Pt/Sn/alumina catalysts was investigated by Li and Shia (25) via Mössbauer spectroscopy ( $^{119}Sn$  enriched isotopes) and XPS. The former technique indicated the presence of  $Sn^{+4}$ ,  $Sn^{+2}$  and  $Sn^0$ , in proportions that depended on the method of preparation, but in all cases the  $Sn^{+4}$  component dominated. These conclusions were confirmed by the XPS experiments. Additional TPR tests on the reduced catalyst and on samples exposed to air showed that reoxidation of Pt/Sn/alumina reduced preparations was rather slow, confirming our EXAFS observations. The presence of zero valent tin in similar preparations, using the acetone complexation procedure, was recently confirmed by Li, Stencel and Davis (12) in an extended XPS investigation. For reduced samples, with a Pt:Sn ratio 1:5, these authors estimated that approximately 68% of the tin was in the metallic state. However, they observed that exposure of the sample to air for 10 minutes entirely eliminated the XPS detectable  $Sn^0$ . Their data also indicated that upon reduction, chlorine migrated from the surface to the alumina. Thus, XPS which measures surface composition indicates a higher sensitivity to oxidation than was demonstrated by our EXAFS experiments, which is a bulk diagnostic.

The most direct evidence for the development of metallic platinum and PtSn alloy, by reduction of a catalyst prepared by the incipient wetness technique on low area Degussa alumina (110  $m^2/g$ ), was presented by Davis, et al. (11). Their conclusions were based on detailed XRD patterns, recorded *in situ* at elevated temperatures under flowing hydrogen. With 0.68% platinum samples containing tin, only Pt/Sn alloy diffraction lines were observed.

In the most recent report on the structures of these catalysts investigated via EXAFS, Meitzner, et al. (10) reached conclusions in essential agreement with ours

although they followed a different data reduction procedure. They state that the tin atoms are extensively coordinated to oxygen atoms and only to a small degree to other tin or platinum atoms. They also cite XRD data that suggest the development of bimetallic clusters, but for their preparations the phase was  $Pt_3Sn$ .

In a subsequent report we shall present NEXAFS and EXAFS structural data for bimetallic supported catalysts prepared via the SMAD procedure and other techniques.

#### Acknowledgment

The EXAFS spectra were recorded at the Cornell High Energy Synchrotron Source, supported by NSF Grant DMR-78/267. Thanks are due to the donors of the Petroleum Research Fund for partial support of this research.

#### Literature Cited

1. McNicol, B. D. J. Catal. 1977, 46, 438.
2. Bacaud, R.; Bussiere, P.; Figueras, F. J. Catal. 1981, 69, 399.
3. Kuznetsov, V. I.; Yurchenlca, E. N.; Belyi, A. S.; Zalolokina, E. V.; Smolikov, M. A.; Duplyakin, V. K. React. Kinet. Catal. Lett. 1982, 21, 419.
4. Li, Y-X.; Shia, Y-F. "Proceedings of International Conference on the Applications of the Mössbauer Effect", (Jaipur) 1982, 438.
5. Burch, R. Platinum Metal Rev. 1978, 22, 57.
6. Short, D. R.; Khalid, S. M.; Katzer, J. R.; Kelley, M. J. J. Catal. 1981, 72, 288.
7. Adkins, S. R.; Davis, B. H. J. Catal. 1984, 89, 371.
8. Sexton, B. A.; Hughes, A. E.; Fogger, K. J. Catal. 1984, 88, 466.
9. Li, Y-X.; Shia, Y-F. Hyperfine Interactions 1986, 28, 875 and 879.
10. Meitzner, G.; Via, G. H.; Lytle, F. W.; Fung, S. C.; Sinfelt, J. H. J. Phys. Chem. 1988, 92, 2925.
11. Srinivasan, R.; DeAngelis, R. J.; Davis, B. H. J. Catal. 1987, 106, 449.
12. Li, Y-X.; Stencel, J. M.; Davis, B. H. submitted to React. Kin. Catal. Lett.
13. Chiu, N.-S.; Bauer, S. H.; Johnson, M. F. L. J. Mol. Struct. 1984, 125, 33.
14. Chiu, N.-S.; Bauer, S. H.; Johnson, M. F. L. J. Catal., 1984, 89, 226.
15. Chiu, N.-S.; Bauer, S. H.; Johnson, M. F. L. J. Catal., 1986, 98, 32.
16. Brown, M.; Peierls, R. E.; Stern, E. A. Phys. Rev. 1977, B15, 738.
17. Short, D. R.; Mansour, A. N.; Cook, J. W., Jr.; Sayers, D. E.; Katzer, J. R. J. Catal. 1983, 82, 299.
18. Sham, T. K. Chem. Phys. 1986, 84, 7054.

19. Lytle, F. W.; Wei, P. S. P.; Greigor, R. B.; Via, G. H.; Sinfelt, J. H. J. Chem. Phys. 1979, 70, 4849.
20. Baur, Von Wermer H. Acta Cryst. 1956, 9, 515-20.
21. Barnes, J. C.; Sampson, H. A.; Weakley, T. J. R.; J. C. S. Dalton 1980, 949-53.
22. Kamenar, B.; Grdenic, D. J. Chem. Soc. 1961, 3954 (Our radial distribution is compatible with the K and g value for Sn-O, given as  $2.16 \pm 0.04\text{\AA}$  in reference 22, but not with that reported by Kiriyaama, H., Kitaham, K., Nakamura, O., and Kiriyaama, R., (Bull. Chem. Soc. Japan, (1973) 46, 1389) at 2.325\AA. The latter value not only would require that we assume a very large phase shift correction (0.515\AA) but it is also inconsistent with Sn-O bond distances reported for SnO, SnO<sub>2</sub> and SnCl<sub>4</sub>·5H<sub>2</sub>O).
23. Larchav, V. I.; Popva, S. V. Inorg. Materials 1984, 20, 804.
24. Nemanova, V. I.; Kondratenko, A. V.; Ruzankin, S. F.; Bausk, N. V.; Zhidomirov, G. M.; Mazalov, L. N. Chem. Phys. 1987, 116, 61.
25. Li, Y-X.; Shia, Y-F. Hyperfine Interactions 1986, 28, 875.

RECEIVED July 27, 1989



## Chapter 31

# Characterization of Catalysts by Scanning Transmission Electron Microscopy

William M. Targos and Steven A. Bradley

UOP Research Center, Des Plaines, IL 60017

The dedicated scanning transmission electron microscope (STEM) is an integral tool for characterizing catalysts because of its unique ability to image and analyze nano-sized volumes. This information is valuable in optimizing catalyst formulations and determining causes for reduced catalyst performance. For many commercial catalysts direct correlations between structural features of metal crystallites and catalytic performance are not attainable. When these instances occur, determination of elemental distribution may be the only information available. In this paper we will discuss some of the techniques employed and limitations associated with characterizing commercial catalysts.

The electron microscope offers a unique approach for measuring individual nano-sized volumes which may be catalytically active as opposed to the averaging method employed by spectroscopic techniques. It is just this ability of being able to observe and measure directly small crystallites or nano-volumes of a catalyst support that sets the microscope apart from other analyses. There have been many studies reported in the literature over the past fifteen years which emphasize the use of analytical and transmission electron microscopy in the characterization of catalysts. Reviews (1-5) of these studies emphasize the relationship between the structure of the site and catalytic activity and selectivity. Most commercial catalysts do not readily permit such clear distinction of physical properties with performance. The importance of establishing the proximity of elements, elemental distribution and component particle size is often overlooked as vital information in the design and evaluation of catalysts. For example, this interactive approach was successfully used in the development of a Fischer-Tropsch catalyst (6). Although some measurements on commercial catalysts can be made routinely with a STEM, there are complex catalysts which require

tedious analytical approaches. The methodology and limitations as they apply to commercial catalysts will be discussed in this paper.

Most of the studies reported in the literature use transmission electron microscopes, TEM or a modified TEM with scanning features called a scanning transmission electron microscope, STEM. These modified microscopes are referred to as TEM/STEM. There is also another type of microscope, a dedicated scanning transmission electron microscope (STEM), which offers unique advantages with regard to the analytical aspects of the measurements made in characterizing catalysts. The primary advantage the STEM has over a conventional TEM is that a more intense electron beam can be routinely focused into an 1.0nm beam size. The reason for this advantage is that a field emission electron source is used to generate the electron beam. Thus nano-sized crystallites can be easily identified and characterized. In general, the two instruments complement each other and should be used together when characterizing catalysts. Most of the comments made in this paper will be from the point of view of using the dedicated STEM. Finally, as with most problems encountered in industry, a multiple technique approach should be implemented when possible to achieve a better understanding of the problem.

### Experimental

The microscope used in obtaining the results presented in this paper was a Vacuum Generators HB-5 STEM. A Kevex energy dispersive x-ray spectrometer, EDS, with 10mm<sup>2</sup> Be window was used for the elemental microanalysis.

Specimen preparation for catalysts is not as severe a problem as is commonly found for metallurgical or ceramic samples. For example, reasonably good specimens can be prepared by simply grinding a catalyst into a fine powder, suspending the powder in isopropanol, and depositing the suspension on a carbon coated nylon or copper grid. This approach results in a wide range of particle sizes from which to observe unique morphological features and determine the composition and structural properties of the catalyst.

Ultramicrotoming a catalyst can also provide unique information to the analyst. Since the thickness is uniform throughout the specimen, elemental particle information, metals distribution and structural information not obtained by the grinding method can be obtained (7-8). The limitations are that it is more time consuming and costly than the grinding or scraping method. Also specimens may not necessarily be obtained from the exact region of interest.

In both preparative methods the integrity of the catalyst is compromised. Exposure to ambient conditions, exterior chemical environments, and exposure to high vacuum in the microscope may alter the catalyst properties. Employment of special chambers for redox pretreatments and/or environmental microscopes provides some assistance in overcoming these problems (9). It appears that regardless of the approach taken, compromises in specimen preparation or instrumental performance must be made. These factors must be kept in mind when interpreting results obtained from electron microscopic measurements.

### Commercial and Experimental Catalysts

Many of the TEM studies of catalysts reported in the literature use model catalysts with visible metal crystallites supported on a metal oxide support, which usually is selected because it offers minimal electron scattering interference. These model catalysts are studied because direct measurements regarding crystallite size and structure can be made. Extrapolation of this information to smaller metal cluster sizes usually present in commercial catalysts is anticipated to provide insight into the relationship between structure and chemical reactivity (10).

Commercial fresh, spent, and regenerated catalysts exhibit a wide range of metal distributions and dispersions. Ideally, the catalytic chemist would like to know in detail the structure, quantity, and distribution of the catalytic sites. There are a number of experimental limitations which inhibit such a complete survey of the properties of the catalyst. Often commercial catalysts will not have readily identifiable sites, i.e., crystallites which can be observed and analyzed for structural and compositional properties. This is usually the case encountered for fresh catalysts which have metal loadings below 0.5 wt.% and on supports which offer a high degree of interference from electron scatter. On a catalyst of this type, often only information on the uniformity of the elemental distribution can be determined. In general, the dedicated STEM will allow the microscopist to determine compositional analyses on volumes of approximately 40 nm<sup>3</sup>. An example of two supports synthesized by similar procedures and analyzed for uniformity is shown in Table I. It is obvious from the standard deviation that support A was not made as well as B. This problem was resolved by altering mixing variables. Subtle variations of this type often have a dramatic influence on catalyst performance. Catalytically active metals on supports can also be monitored in this manner (11).

Many commercial catalysts employ mixtures of several metal oxides. The advantages of these mixed oxide systems varies from thermal stability to enhanced acidic properties and/or support metal interactions. The dedicated STEM does an excellent job of identifying the individual mixed oxide components and determining location of the catalytic metals.

Being able to obtain information on the metals distribution and dispersion as a function of preparative, operational, and regeneration conditions is vitally important in helping direct the optimization of new catalyst formulations. After a catalyst has been exposed to operating and/or carbon burn conditions, metals agglomeration may occur. Also there may be circumstances wherein the fresh catalyst might have specified size metal crystallites. In these cases, the characterization by STEM becomes more complex. Thorough characterization requires compositional and structural information of the different size crystallites, and to what extent all of the crystallites comprise the total amount of metal present. This is a difficult if not impossible task to carry out in some cases because of the interference the support lends to the analysis problem. In Figure 1, a micrograph of 2-3 nm platinum-crystallites on  $\gamma$ -Al<sub>2</sub>O<sub>3</sub> is shown. Although there are many contrasting features, only those indicated by arrows were platinum. This information

Table I Comparison of Two Differently Prepared Silica-Alumina Supports

<u>Support A</u>		<u>Support B</u>	
<u>Weight %</u>		<u>Weight %</u>	
Al	Si	Al	Si
47.0	53.0	35.1	64.9
33.0	67.0	30.5	69.5
21.1	78.9	36.6	63.4
40.9	59.1	34.1	65.9
20.1	79.9	34.9	65.1
26.2	73.8	33.8	66.2
50.2	49.8	34.0	66.0
59.3	40.8	32.3	67.7
60.0	40.0	36.7	63.3
<u>30.4</u>	<u>68.6</u>	28.6	71.4
38.8±14.9	61.2±14.9	33.9	66.1
		<u>37.0</u>	<u>63.0</u>
		34.0±2.5	66.0±2.5

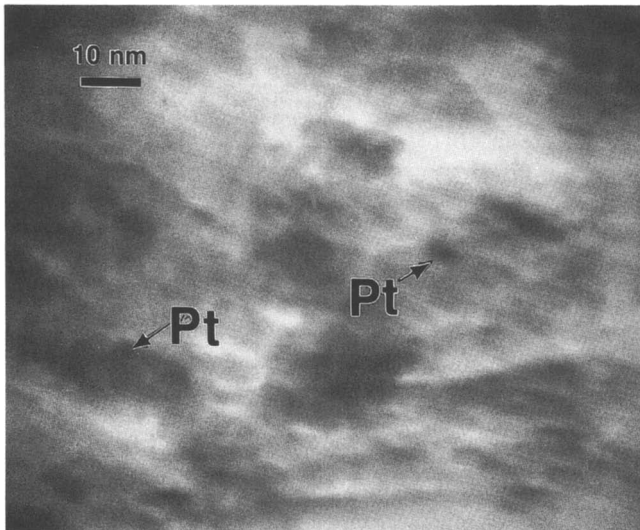


Figure 1. Platinum crystallites on  $\gamma$ -alumina.

could only be verified by a point by point microanalysis using EDS. X-ray mapping usually does not provide sufficient signal to noise for distinguishing 2-3nm crystallites from the support(12). Increased sweep times with state of the art EDS detectors may in some cases provide sufficient sensitivity to make this measurement. Consequently, the electron beam must be directed to a very small volume of catalyst by operating at high magnifications, i.e., 20 million times in a raster or spotted beam mode. Often count times of up to 100 seconds or more are required to determine if an area of high contrast contains a catalytic metal. This experiment is tedious, but in many instances is the only practical approach.

There are situations in which crystallites are readily visible, especially on supports which do not offer excessive electron scatter. In these cases, metal content can be quantitatively determined for areas which have highly dispersed metal and agglomerated metal. This information in conjunction with the crystallite size distribution provides the microscopist with the information required to make an estimate of metal dispersion (13). These estimates are valuable especially in situations where conventional gas adsorption measurements cannot be made on the metal, i.e., when the crystallites are contaminated, have multiple oxidation states, or are poisoned.

One of the difficulties in directly analyzing structures of crystallites with a 1-3 nm size range is their beam sensitivity. Some crystallites will dissociate in the beam while others tend to agglomerate (14). The mass of the crystallite, support-metal interaction, chemical environment, oxidation state of the metal, etc., all have an influence on how the crystallite and electron beam interact. In order to formulate a correlation of these variables with crystallite reactivity with the beam, the crystallite site chemistry is required. This is difficult if not impossible to do because the site chemistry is altered during microscopic examination. With parallel EELS detection the time may be sufficiently reduced that useful chemical information can be obtained and correlations of the type previously described can be made.

The sensitivity of these small crystallites to the electron beam makes obtaining microdiffraction patterns very difficult. Usually apparatus which involves specialized optics and electronic monitoring devices such as those developed by Cowley (15) can reduce beam exposure time and thus provide some meaningful data which might be useful in studying the support-metal interaction or structure-reactivity relationship.

There are two approaches which enhance observation of 1-2 nm supported metal crystallites. One is annular dark field or Z-contrast detection (16) and the other is called axial dark field (17). These techniques can be easily utilized for simple catalyst compositions. The annular dark field detection method analyzes elastically scattered electrons at wide angles from the central beam. The scattering angle is a function of atomic number. Consequently, elements such as platinum are effectively observed in low atomic number supports such as  $\text{Al}_2\text{O}_3$  or  $\text{SiO}_2$  (18). The method is also effective in detecting larger crystallites in support particles

usually too thick for electron beam transmission. Such an example for 10-60 nm platinum crystallites on alumina is shown in Figure 2. Varying the black level of the photomultiplier can enhance imaging of the crystallites by making them look lighter or darker with respect to the support. The axial dark field imaging is achieved by obtaining a micro-diffraction pattern of a crystallite, tilting the electron beam so as to move one of the diffraction spots to the optic axis, and then imaging with this diffracted beam. If the crystallites present have sufficiently different lattice spacings from the support, the crystallites will be highlighted on the dark field image. For example, in Figure 3, crystallites on carbon are shown using this technique. Cowley and Garcia (19) demonstrated this technique on the more complicated Rh/CeO<sub>2</sub> system. Attempts to use this approach for platinum on  $\gamma$ -Al<sub>2</sub>O<sub>3</sub> will not work, because the major diffraction spots for Pt and  $\gamma$ -Al<sub>2</sub>O<sub>3</sub> cannot be differentiated.

The ease of analysis depends on how well some of these techniques are integrated with one another to establish how the catalyst is designed. For monometallic supported catalysts previously described, more of these techniques are applicable because of the reduced interference from the support. The options are reduced as the support composition becomes more complex. There are some commercial catalysts which contain multimetallic sites on complex metal oxide supports. Direct microanalysis of areas by EDS is sometimes the only approach that can be taken, especially if the metals are highly dispersed. If crystallites are present, x-ray mapping (20) might be a feasible approach for quickly establishing the extent of bimetallic formation. Sometimes bimetallic crystallites have specific morphological characteristics which enable the microscopist to identify the bimetallic crystallites. In Figures 4a and b, a catalyst comprised of Ru/Ir on  $\gamma$ -Al<sub>2</sub>O<sub>3</sub> and Ru on  $\gamma$ -Al<sub>2</sub>O<sub>3</sub>, respectively are shown. The Ru/Ir crystallites are elongated whereas the Ru crystallites are symmetrical. EDS shows these Ru/Ir crystallites to have a composition of 80 wt.% Ru and 20 wt.% Ir. Thus by visual observation a rapid evaluation of the extent of bimetallic formation can be made for this catalyst. However, most of the time the data are not easily obtained and individual analyses of areas of interest must be made.

There are also catalyst formulations which have highly dispersed metals which are deliberately heterogeneously distributed on a support. If the microscopist is aware of the situation, he can take precautions in the sample preparation. This type of sample is the worst possible case to analyze because not only does the analyst have a complex mixture of components to sort out, but the analysis statistics are very poor. Consequently, additional time is usually required to survey the catalyst particles in order to establish a consensus of how it was constructed. Specialized specimen preparation such as ultramicrotoming and scraping the exterior of a sphere or extrudate may alleviate some of the interpretation problems. Additional aid may be solicited from a scanning electron microscope wherein an elemental distribution of a polished cross section of the catalyst sphere or extrudate can be made.

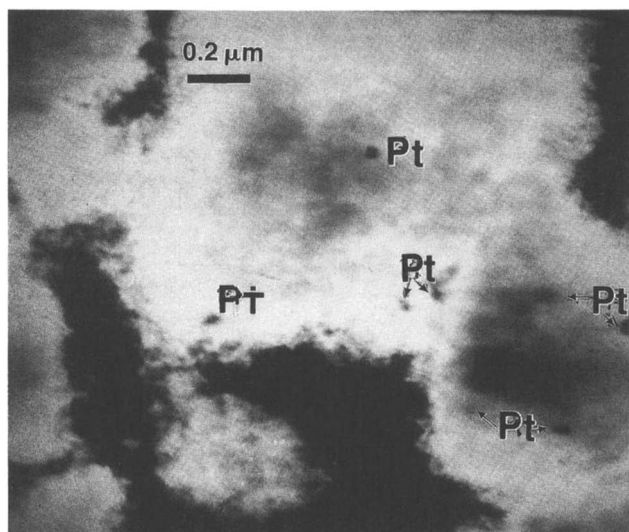


Figure 2. Platinum crystallites on thick particles of  $\gamma$ -alumina using annular dark field.



Figure 3. Platinum crystallites on a carbon film using axial dark field.

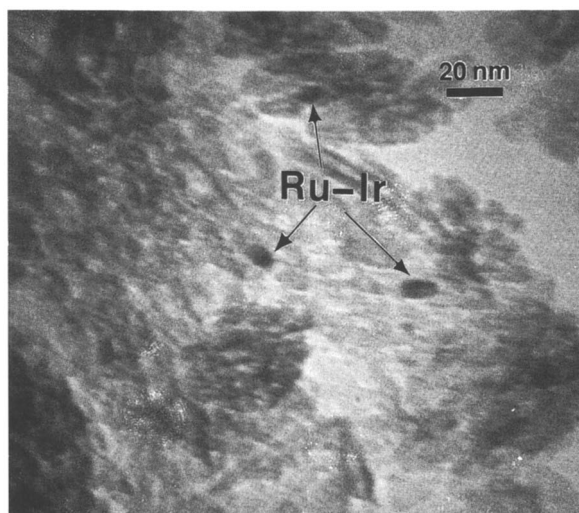


Figure 4a. Ruthenium - iridium elongated crystallites on  $\gamma$ -alumina.

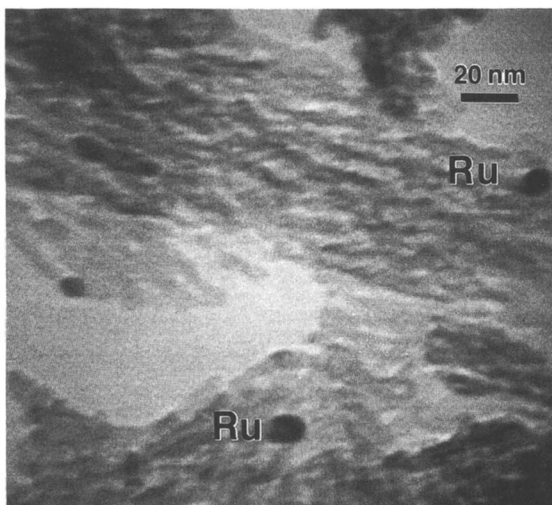


Figure 4b. Ruthenium on  $\gamma$ -alumina.



### Catalyst Poisons

Any catalyst exposed to reaction conditions may have been subjected to poisons. In some cases, analysis by STEM of individual crystallites will detect the poison (12). This is primarily because the active catalyst site may selectively scavenge the poison thus concentrating it to a level of detectability. In many cases, however, the poisons are at low concentrations and may remain undetected by STEM.

### Catalyst Stability Under Beam Exposure

It may be taken for granted that analysis for all elements on a catalyst support work equally well. We have performed experiments on many different catalysts and have found that elements such as Cl, K, Na, and S are very sensitive to the electron beam. Cl and S appear to volatilize in the vacuum while K and Na move away from the incident beam. This is especially true when the beam is spotted directly onto the particle versus using the less damaging raster mode. Examples of how elemental analyses of a  $\text{BaSO}_4$ , zeolite, and NaCl particles vary as a function of time are shown in Figure 5.

Often catalyst materials are viewed as being extremely stable because they are exposed to severe oxidation and reduction conditions at very high temperature and are consequently stabilized by such treatments. In analyzing a catalyst with an electron beam many interesting chemical reactions may occur which render the support metastable. Many examples have been sighted in the literature (21) which show supports such as zeolites, alumina, and silica degrade under an electron beam. It is of interest to note that although beam damage may occur in all cases, the extent of degradation appears to be highly variable. We have observed instances in which zeolites and/or alumina have shown variable reactivity in an electron beam. Sometimes particles obtained from the same catalyst may exhibit different beam sensitivity. It is possible that the catalyst was not completely transformed to a stable condition during preparation.

Atomic rearrangement and/or further reduction of crystallites with mixed oxidation states (22) as a function of electron beam exposure have been observed. We have noted that metal crystallites less than 4 nm in size are particularly susceptible to beam irradiation damage.

Another phenomenon commonly observed in the analysis of catalysts is the deposition of carbon in the area of beam concentration (23). In many instances this can be associated with residual organic material left on the carbon coated grids. We have also found that the catalyst particles themselves may have organic debris on them which subsequently react in the electron beam creating carbonaceous material. Unfortunately, this may disrupt observation of small crystallites and/or the quantitative analysis of the particle. For example, STEM examination of a Fischer-Tropsch catalyst which had wax deposited on the alumina particles containing Ru crystallites was made. Due to the reactivity of the wax in the electron beam the particles turned progressively darker as a function of exposure time, until finally the Ru crystallites were not

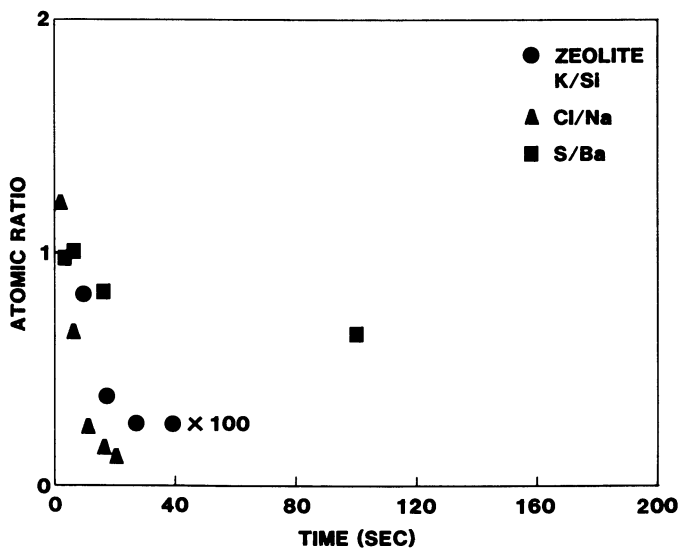


Figure 5. Effect of the electron beam on the K/Si ratio for a zeolite, Cl/Na ratio for NaCl, and S/Ba ratio for BaSO<sub>4</sub>.

observable. Catalysts which contain carbon from other reactions in which the carbon is highly unsaturated show little beam interaction.

Sometimes the origin of the carbon deposition and/or other contamination effects may not be readily identifiable. Additional preparation may be required to obtain a specimen which can be analyzed. For example, placing the catalyst particles on different carbon coated grids, using a different method for depositing the catalyst particles, or using a different grid film such as silica may offer alternative approaches for obtaining useful electron micrographs.

#### Analysis of Light Elements

A means of probing carbon and the light elements may be more effectively achieved with electron energy loss spectroscopy, EELS. With the implementation of the parallel EELS detector (24), the sensitivity of this technique has increased dramatically, maybe 1000 fold. Small clusters of atoms may be detectable, <1 nm in size, and/or analysis of areas with low concentration of elements can be performed which were beyond previously detectable limits. Consequently, very low levels of carbon, oxygen, nitrogen, magnesium, and lithium should be theoretically detectable. Obviously, a serious problem with obtaining analysis of these elements is their susceptibility to radiation damage. The parallel EELS detector will reduce counting times dramatically, maybe to less than 1 sec. This may or may not be satisfactory in minimizing radiation damage at the area of interest, especially if quantitative information is desired.

Other types of information which can be obtained using EELS are oxidation state, coordination number, and cluster size of heavier atomic number elements (25). Applicability and feasibility is just starting to be demonstrated. There are many problems associated with trying to obtain useful quantitative information on small volumes of catalyst. The major concern is radiation damage. Others include, contamination, sample preparation, beam reactivity (especially crucial for redox information), cluster migration and redispersion, support reactivity with the catalyst metals, and desorption of some elements under high vacuum.

#### Summary

The dedicated STEM offers unique instrumental capabilities for directly observing and determining the composition of small crystallite and nano-volumes of catalyst supports. This provides a distinct advantage to the catalytic chemist in characterizing complex supported metal systems. The statistics in microscopic analysis are poor thus impairing decisive interpretation of data. The availability of an extensive data base and corresponding catalyst background may aid the microscopist in the decision making process. The limitation of specimen preparation and beam sensitivity must be recognized and considered in the evaluation process. Finally, use of a multiple technique approach should be implemented whenever possible to ensure that correct interpretation of the chemical and structural properties of the catalyst are made.

Literature Cited

1. Delaney, F.; Catal. Rev. Sci. Eng. 1980, 22(1), 141-170.
2. Burton, J.J.; Catal. Rev. Sci. Eng. 1974, 9(2), 209-222.
3. Matyi, R.J., Schwartz, L.H.; and Butt, J.B.; Cat. Rev. Sci. Eng. 1987, 29(1), 41-99.
4. Freund, E., Lynch, J., and Szymanski, R.; Ultramicroscopy 1986, 20, 107-118.
5. Sanders, J.V.; Catalysis Science and Technology; Vol. 7, Chapt. 2, New York, 1985.
6. Abrevaya, H., Targos, W., Robota, H., Cohn, M.; Proceedings of the Tenth North American Catalysis Soc. Meeting, Ward, J., Ed.; San Diego, May 1987.
7. Hall, J.B., and Hruskoci, P.P.; Proceedings of the 41st Annual Meeting of the EMSA, San Francisco Press, 1983, 342-343.
8. Treacy, M.M.J., and Rice, S.B.; MRS Symposium Proceedings, Brauman, J.C., Anderson, R.M., and McDonald, M.L., Eds.; 115, 1987, 15-27.
9. Baker, R.T.K.; Catal. Rev. Sci. Eng. 1979, 19, (2), 161-209.
10. Robota, H., Broach, R.W., Sachtler, J.W.A., and Bradley, S.A.; Ultramicroscopy 1987, 22, 149-158.
11. Targos, W.M., and Abrevaya, H.; Microbeam Analysis; Romig Jr, A.D., and Chambers, W.F.; Ed., San Francisco Press, 1986, 605-608.
12. Lyman, C.E., Stenger, Jr., H.G., and Michael, J.R.; Ultramicroscopy 1987, 22, 129-134.
13. Targos, W.M.; Catalyst Characterization Science; ACS Symposium Series 288, 1984, 376.
14. Dayte, A.K., and Logan, D.A.; Proceedings of the 46th Annual Meeting of EMSA, Baily, G.W., Ed.; San Francisco Press, 1988, 704.
15. Cowley, J.M.; Catalyst Characterization Science; ACS Symposium Series No. 288; 1984, 329.
16. Treacy, M.M.J., Howie, A., and Pennycook, S.J.; Electron Microscopy and Analysis; Mulvey, T., Ed.; Institute of Physics, Bristol, England; 1980, 261.
17. Cowley, J.M.; Ultramicroscopy 1984, 14, 27.
18. Wall, S.; Introduction to Analytical Electron Microscopy; Hren, J.J., Goldstein, J.I., and Joy, D.C., Eds.; Plenum Press, New York, 1979, 347.
19. Cowley, J.M., and Garcia, R.; Micron and Microscopics Acta, 1987, 18, No. 3, 168-169.
20. Lyman, C.E.; Ultramicroscopy 1986, 20, 119-124.
21. Treacy, M.M.J. and Newsam, J.M.; Ultramicroscopy 1987, 23, 411-420.
22. Smith, D.J., McCartney, M.R., and Bursill, L.A.; Ultramicroscopy 1987, 23, 299-304.
23. Hren, J.J.; Introduction to Analytical Electron Microscopy; Hren, J.J., Goldstein, J.L., and Joy, D.C., Eds.; Plenum Press, New York, 1978, 484-505.
24. Krivanek, O.L., Ahn, C.C. and Keenney, R.B.; Ultramicroscopy 1987, 22, 103-116.
25. Egerton, R.F.; Electron Energy Loss Spectroscopy in the Electro Microscope; Plenum Press, New York, 1986, 129-350.

## Chapter 32

# Characterization of Fluid Cracking Catalysts by Imaging Secondary-Ion Mass Spectrometry

D. P. Leta and E. L. Kugler

Exxon Research and Engineering Company, Annandale, NJ 08801

In the field of catalysis SIMS has primarily been used in the static mode to monitor the presence of surface species and contaminants. In 1981 Jaras(1) showed the use of SIMS images to detect laboratory doped metallic poisons in petroleum cracking catalysts. We have done extensive imaging SIMS of commercial catalyst systems for the purpose of trace metal characterization, particularly for fluidized catalytic cracking (FCC) catalysts. FCC catalysts are used to convert high boiling petroleum fractions into lighter fuels, especially gasoline and home heating oils.

FCC catalyst particles, with diameters in the 40-150 micrometer range, are composed of mixtures of zeolite and clay particles, additives, binders, and contaminants. The characterization of the different submicron phases within each particle, with elemental concentrations of interest from the ppm to tens of percent range, presents a formidable analytical challenge. Metals in hydrocarbon feedstocks can deposit on processing catalysts and change catalyst performance with time. In FCC, nickel and vanadium often present at several ppm concentration in the feed accumulate quantitatively on the catalyst and severely affect operations. Both metals increase hydrogen and coke, and decrease gasoline yields at concentrations in the hundreds to thousands of ppm range. The necessity or desirability of processing high metal feeds in an FCC unit has generated much research on how metals affect catalyst particles and how metal effects can be controlled.

Imaging SIMS studies of such systems can overcome many of the limitations of electron microprobe measurements commonly used. Imaging analyses of cracking catalysts by electron probe are limited by the several micron excitation volume of the electrons in a light oxide matrix. The resultant resolution is normally insufficient to cleanly define the sub-micron phases of the cracking catalyst. Additionally, elemental sensitivities are often surpassed by factors of thousands by the SIMS technique, particularly when applying direct imaging SIMS, in which a multiplex advantage is obtained by collecting signal for an entire elemental image simultaneously. The

very high sensitivity of imaging SIMS allows real-time elemental viewing of the cracking catalyst particles making it possible, and even convenient, to carefully inspect tens to hundreds of particles before drawing conclusions about elemental distributions. The ability to view light elements, submicron lateral resolution, and far superior sensitivity makes new types of experiments and characterizations possible with SIMS. In addition to being able to view the homogeneity and distribution of each of the component phases within each catalyst particle, imaging SIMS can follow the movement and interaction of the nickel and vanadium catalyst poisons. Although nickel seems to be relatively immobile following its deposition, we have found that vanadium is partially free to move from particle to particle as well as within an individual particle. The attack of vanadium on the active zeolite phase of the catalyst can be seen directly, and the modifying effects of catalyst composition on this attack can be observed. Imaging SIMS also has the unique utility of identifying and analyzing individual catalyst particles in mixtures of catalyst types from actual five hundred ton catalyst load refinery units, making tracer studies possible.

#### EXPERIMENTAL

Prior to analysis, the FCC catalyst samples were embedded in copper doped thermosetting epoxy to provide increased electrical conductivity. They were dry polished with silicon carbide to approximate cross-sections.

The SIMS analyses were performed using a CAMECA IMS-3F ion microprobe/microscope, equipped with an ion image collection system described in detail elsewhere(2). The heart of the system is an ultra-high gain video camera (Zeiss TV-2M) which incorporates two multichannel plate intensifiers prior to its video tube, which together with the multichannel plate integral to the IMS-3F's ion to light conversion system, provides sufficient gain to view individual ions while retaining high spacial resolution. The second stage of the image collection system, a 512x512 video digitizer (MCI's CRYSTAL), performs integration, recursive addition and image subtraction at video rates. In this way ion images arising from very low count rates which may look much like noise because of the slow ion arrival rate may be formed into viewable high resolution images. The processor may also perform programmable kernel deconvolutions on frozen images to improve the apparent spacial resolution, as well as adjusting the ion image's contrast and brightness for viewability. Once the ion image collection is complete the video signal is passed to an Optical Laser Disk Recorder (Panasonic) for permanent storage with very high fidelity. Post-analysis multiple element processing is accomplished by transferring the ion images to a Gould/VAX based image processing computer which has extensive image math capabilities. This type of video based image collection and manipulation system surpasses other methods in its ease of use, speed, dynamic range, storage capacity and resolution.

Oxygen as  $O_2^+$  was used as the primary ion bombardment species, at an impact energy of 10.5 keV, with primary currents in the several microampere range. In order to eliminate the effects of polishing damage and contamination on the surfaces of the samples, they were pre-sputtered to a depth of several microns before elemental images were collected. This presputtering is an essential step possible with this type of high primary ion current SIMS analysis in that the mixing of the crystallites of the cracking catalyst particles which occurs during polishing, particularly in dry polishing, obscures the true positions of the phases and the trace elements. The atomic mixing which this type of heavy sputtering causes, on the size scale of tens to hundreds of angstroms only, does not change the 5000 angstrom resolution microelemental analysis results but instead incredibly gently removes from consideration the catalyst layer disturbed by sample preparation.

### RESULTS AND DISCUSSION

Most types of FCC catalyst are manufactured by mixing submicron sized zeolite crystals, usually rare earth exchanged to improve activity and hydrothermal stability, with a clay such as kaolin, and a silica and/or alumina binder, followed by spray drying to obtain the desired particle size range. Due to this method of manufacture, the individual particles are internally heterogeneous. Imaging SIMS allows the rapid identification of the individual phases, an extremely difficult task by electron microscopy. Figure 1 shows the positive ion images of Al, Si, La, V and Ni taken from an equilibrium catalyst particle withdrawn from a petroleum refinery FCC unit. This particle is typical of a simple zeolite/kaoline/binder type of FCC catalyst that is normally used to crack vacuum gas oil feeds. This catalyst grade contains about 20% rare earth exchanged Y-zeolite, while this specific equilibrium sample has average metal contaminant concentrations of 1500 ppm Ni and 3300 ppm V. The cross-sectioned particle's diameter is approximately 150 microns from top-to-bottom. The image shows two different concentration levels, with the brighter areas arising from clumps of kaolin which has a higher Al/Si ratio than does the rare earth exchanged Y-zeolite, which show as the darker areas. The black areas within the particle have no aluminum ion concentration and are probably holes within the catalyst that were filled with epoxy during mounting.

The Si ion image shows the full size of the particle as did the image, but the brightness within the sample is reversed, now disclosing greater Si/Al ratios as brighter areas. The edge of the particle is also highlighted since the silica sol binder that cements the particulates together concentrates at the edge of the particle to make a hard external surface. The La image clearly identifies the locations of the rare earth exchanged zeolite phases, which are the high activity component of FCC catalysts. The zeolites are actually submicron crystallites that are present as aggregates in the 5 micron size range. The V distribution shown

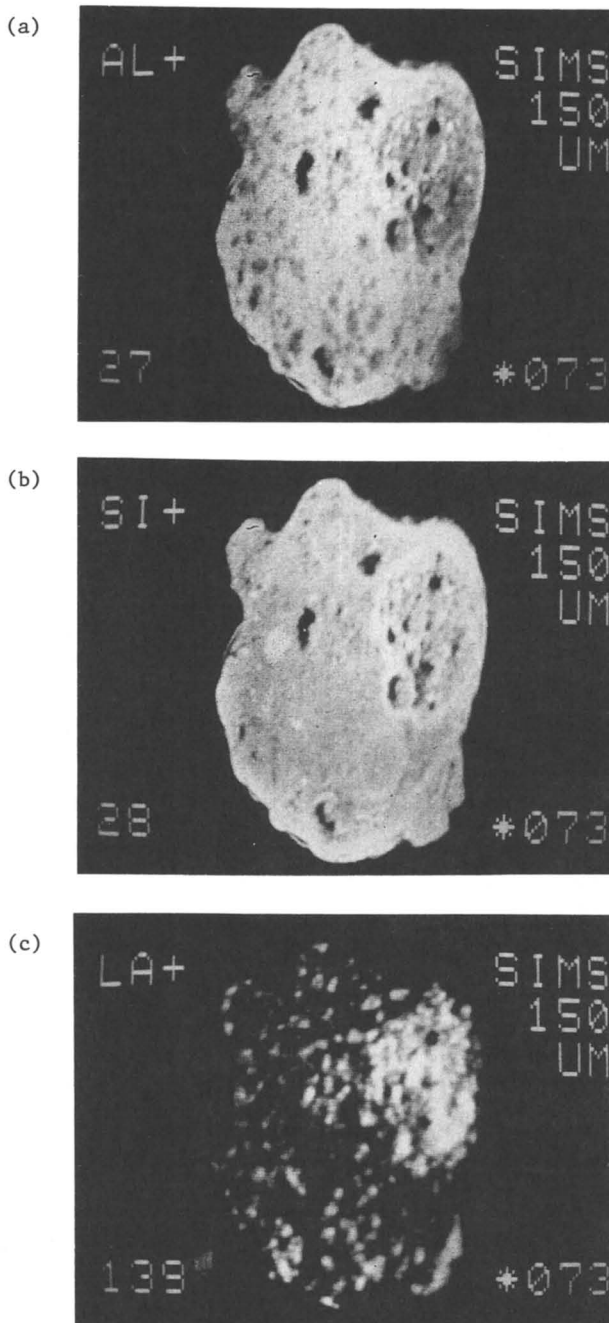
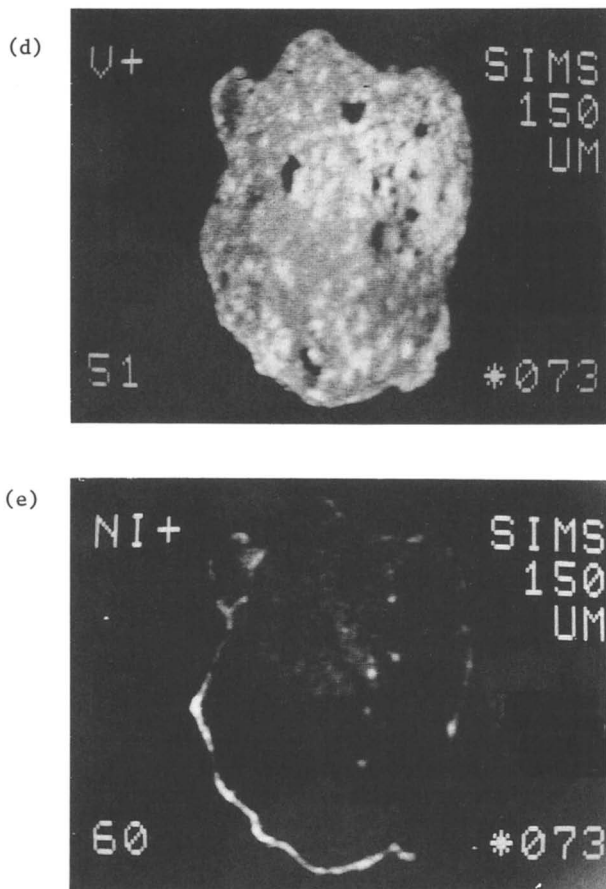


Figure 1. Cross section of typical gas oil conversion catalyst; (a) aluminum, (b) silicon, (c) lanthanum. *Continued on next page.*





arises from vanadium impurities in the feedstock being cracked in the FCC unit. It may be seen by comparing the V ion image with the La image that in this type of catalyst vanadium has accumulated preferentially on the zeolite phase where it poisons the catalyst by destroying the zeolite's crystal structure(3). The Ni image shows that the nickel impurity in the feedstock has deposited only at the external surface of the particle. Nickel concentrated at the particle edge in contradistinction to vanadium being spread throughout the sample. This observation agrees with prior reports that vanadium has high mobility in FCC operations(4-8).

Cracking catalysts containing only zeolite, clay and binder are commonly used for vacuum gas oil conversion, but are atypical of catalysts used to convert heavier feeds. Resid cracking catalysts usually have some high surface area, large pore size component for large molecule cracking. The equilibrium catalyst particle shown in Figure 2 contains a pure alumina phase to provide bottoms conversion. The Al distribution may now be seen to contain three "grey levels" with the brightest being the alumina phases. Kaolin and zeolite are darker due to their lower aluminum concentrations. The Si distribution again shows just the opposite ordering in brightness. The alumina particles appear as darker areas within the Si image of the catalyst particle, with kaolin and zeolite being increasingly brighter. This particle like the one in the previous example is made with a silica sol binder, so that the exterior surface has the greatest silicon ion density. Again, the La distribution reveals the location of the zeolite aggregates but in this example, the vanadium and lanthanum images do not overlay. The vanadium impurities on this catalyst particle are concentrated on the alumina phase rather than on the zeolite. Comparing the alumina and vanadium distributions shows nearly a one-to-one correspondence between the bright areas in the two pictures.

The nickel concentration on this particle is extremely low with traces of the nickel impurity at the external surface. This low nickel concentration means that the particle in Figure 2 was in the refinery unit only a short time, otherwise more nickel would be present for the average particle (by bulk chemical analysis) contains 900ppm Ni and 4700 ppm V. The particle in this image contains a disproportionate amount of vanadium relative to nickel. If the nickel on the external skin of the catalyst accumulates by nickel porphyrin cracking at the first surface contacted, then vanadium must arrive not only by cracking vanadyl porphyrins but also by some other means like transfer from older catalyst particles in the FCC unit. The high vanadium concentration relative to nickel on new catalyst particles provides evidence that vanadium has interparticle mobility as well as intraparticle mobility.

A second cracking catalyst manufacturing method involves spray drying kaolin particles with a silica binder, calcining at high temperature to produce very hard particles composed of meta-kaolin and mullite, followed by chemical treatment to synthesize zeolites from meta-kaolin within the preformed spheres. Figure 3 shows images from two catalyst particles prepared by this method. Both the Al and Si images have only small variations in brightness within these particles. This suggests that individual crystallites in the

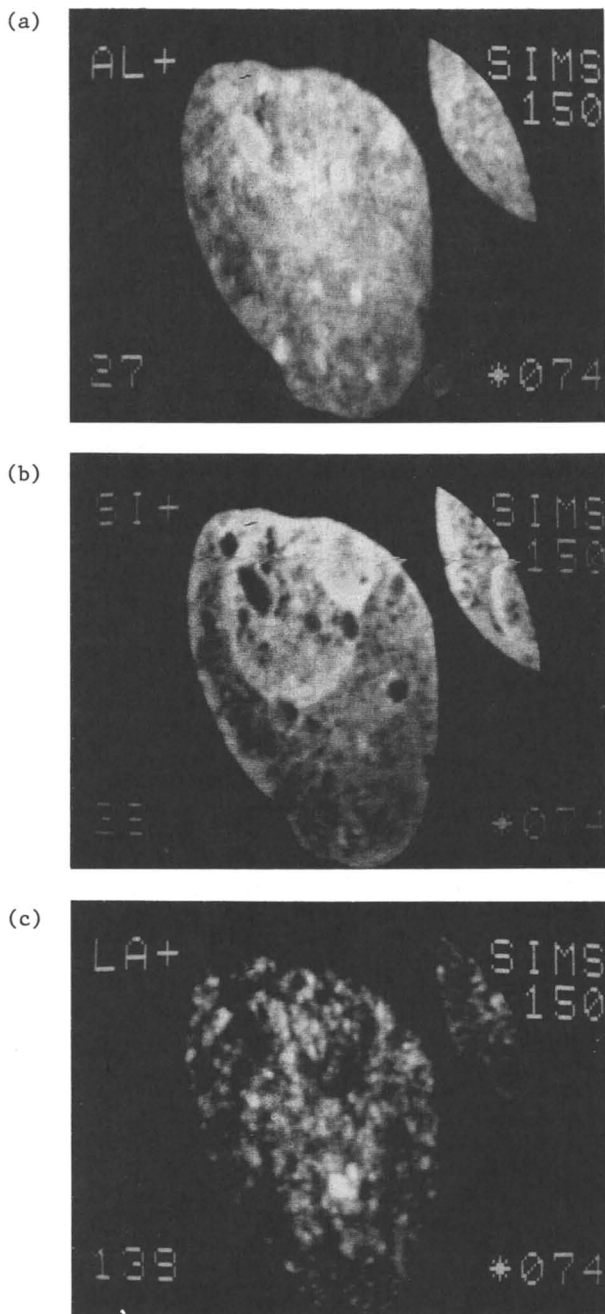


Figure 2. Cross section of bottoms conversion FCC catalyst; (a) aluminum, (b) silicon, (c) lanthanum. *Continued on next page.*

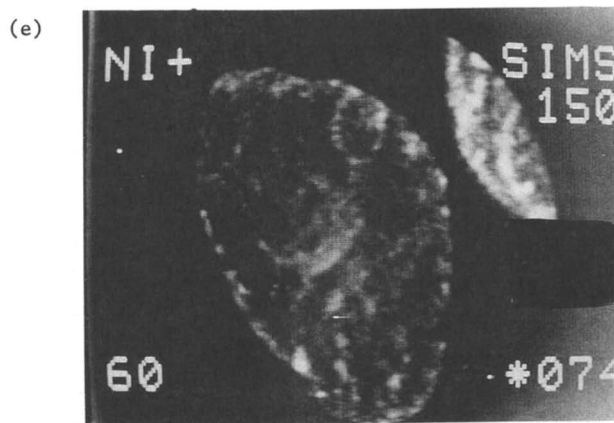
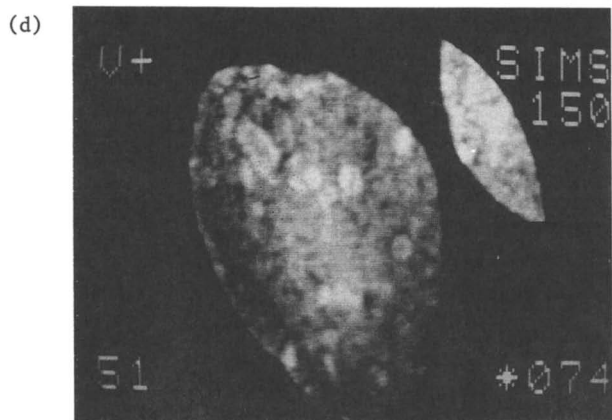


Figure 2. Continued. (d) Vanadium, (e) nickel.

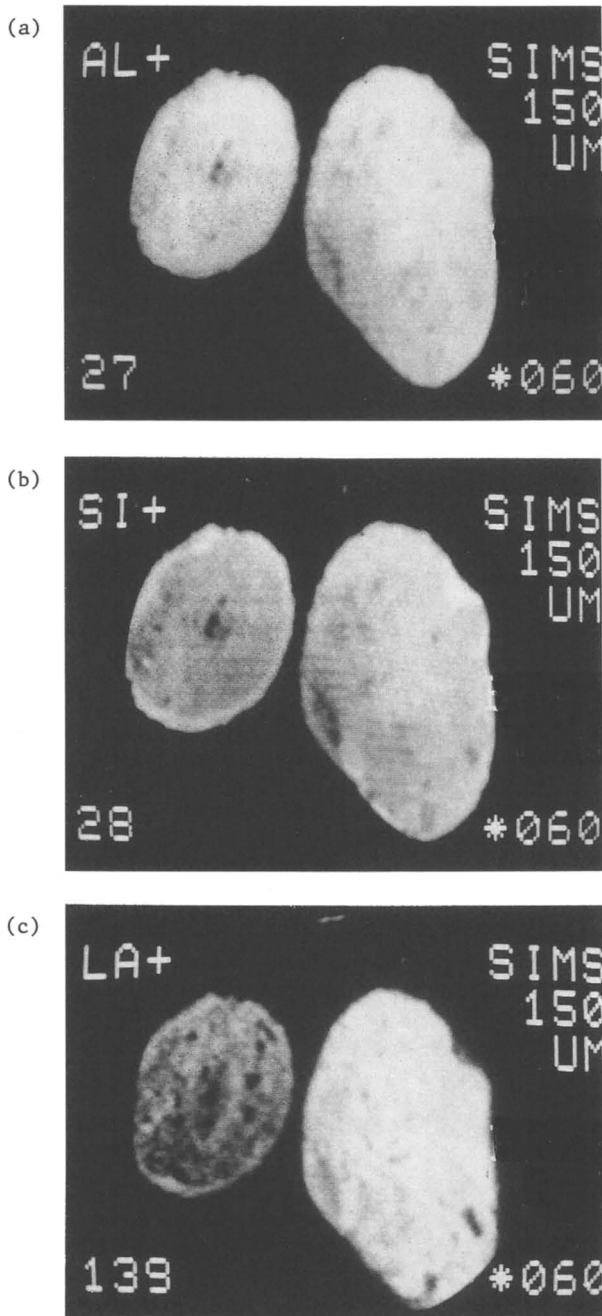


Figure 3. Cross sections of old and new catalyst particles; (a) aluminum, (b) silicon, (c) lanthanum. *Continued on next page.*



Figure 3. Continued. (d) Vanadium, (e) nickel.

composites are well dispersed and in a size range comparable to the instrument resolution of 0.5 microns. As in the prior two examples, the Si image is brightest at the external skin of the catalyst. The La distributions reveal the first major variations in particle texture. The particle on the left contains much less rare earth than the one on the right. Full mass spectral analyses of these two particles and many others from fresh catalyst samples revealed that this particular commercial catalyst contained a blend of three different particle types. The two particles in the image were manufactured in different batches and contain different zeolite concentrations. The left particle is from a batch estimated to contain about 20% zeolite while the one on the right is from another batch estimated to have about 40% zeolite.

The V and Ni images show that the left particle has been in the unit for a long time while the right particle is very new. In the older particle, the vanadium distribution is nearly homogeneous while the new particle shows vanadium diffusing from the external surface. This observation shows that vanadyl as well as nickel porphyrins must crack on the external catalyst skin. Vanadium migration then occurs after the metal deposit is on the catalyst surface. The Ni distribution confirms the age of the pair, but also reveals that edge enhancement persists on very old particles. This confirms that the deposited nickel has very little or no mobility in the FCC unit.

We hope to have indicated in this brief report the excellent match possible between the capabilities of current imaging SIMS technology and some of the characterization needs of the catalysis community. In cases where heterogeneity, poisoning, and diffusion limitations are present, imaging SIMS offers a way to gain a novel view of catalyst composition, performance, and reaction pathways.

#### LITERATURE CITED

1. Jaras, S. Appl. Catal. 1982, 2, 207.
2. Leta, D. P., "Springer Series in Chemical Physics 44" A. Benninghoven, R. J. Colton, D. S. Simons and H. W. Werner, Eds.), p 232, Springer-Verlag, Berlin 1986.
3. Ritter, R. E.; Rheume, L.; Welsh, W. A.; Magee, J. S. Oil & Gas J., July 6, 1981, p 103.
4. Masuda, T.; Ogata, M.; Ida, T.; Takakura, K.; Nishimura, Y. J. Japan Pet. Inst. 1983, 26, 344.
5. Nishimura, Y.; Masuda, T.; Sato, G.; Egashira, S. PREPRINTS, Div. of Petrol. Chem. ACS 1983, 28, 707.
6. Maselli, J. A.; Peters, A. W. Catal. Rev. Sci. Eng. 1984, 26, 525.
7. Wormsbacher, R. F.; Peters, A. W.; Maselli, J. M. J. Catal. 1986, 100, 130.
8. Kugler, E. L. and Leta, D. P., J. Catal. 1988 109, 387.

RECEIVED January 10, 1989

## Chapter 33

# Microstructural Study of an Iron Silicate Catalyst by Electron Microscopy

Roseann Csencsits<sup>1,3</sup> and Ronald Gronsky<sup>2</sup>

<sup>1</sup>Center for Advanced Materials, Materials and Chemical Sciences Division, Lawrence Berkeley Laboratory, and Materials Science and Mineral Engineering Department, University of California, Berkeley, CA 94720

<sup>2</sup>National Center for Electron Microscopy, Materials and Chemical Sciences Division, Lawrence Berkeley Laboratory, and Materials Science and Mineral Engineering Department, University of California, Berkeley, CA 94720

The effects of various synthesis conditions on the structure of iron silicate analogs of zeolite ZSM-5 were considered. Scanning electron microscopy (SEM) was used to determine the particle size distributions and morphologies. Particle sizes vary from tenths of a micron to several microns, depending on degree of agitation during crystal growth, while morphology is additionally dependent on the concentration of iron in the gel during crystallization. Transmission electron microscopy (TEM) was used to determine the size and spatial distributions of iron-rich (as compared to the FeZSM-5 matrix) second phase particles within the ZSM-5 framework as a function of  $\text{SiO}_2/\text{Fe}_2\text{O}_3$ -ratio, thermal and hydrothermal treatments.

Iron silicate analogs of the zeolite ZSM-5 may be directly synthesized from iron silicate gels in a manner which differs slightly from the aluminosilicate ZSM-5 (1). The resultant white, crystalline iron silicate is referred to as FeZSM-5 in the as-synthesized form. Thermal treatment removes the organic crystal-directing agent and moves some of the framework iron into non-framework sites producing the calcined form of the molecular sieve FeZSM-5 (2-4). Subsequent hydrothermal treatment removes more of the iron from the molecular sieve framework (2-4). This iron-rich second phase and the ZSM-5 pore structure can be used to convert synthesis gas (CO and  $\text{H}_2$ ) to "gasoline range" hydrocarbons and water (Fischer-Tropsch synthesis). To optimize the Fischer-Tropsch catalyst, homogeneity is desired in the particle size distribution and in the distribution of catalytic iron throughout the particles.

Electron microscopy, with its high spatial resolution, plays an important role in the physical characterization of these catalysts. Scanning electron microscopy (SEM) is used to characterize the molecular sieve particle sizes and morphologies as a function of preparation conditions. Transmission electron microscopy (TEM) is used to follow the changes in the microstructure of the iron silicates caused by different growth conditions and subsequent thermal and hydrothermal treatments.

<sup>3</sup>Current address: Digital Equipment Corporation, 30 Forbes Road, NRO5, Northboro, MA 01532



### Scanning Electron Microscopy

The particle sizes and morphologies as a function of various preparatory conditions, thermal and hydrothermal treatments were studied using SEM. Samples of FeZSM-5 in the as-synthesized form showed marked differences in particle size as well as morphology depending on whether or not the gel was stirred during crystallization. When the gel was stirred the particles were generally less than  $1\mu\text{m}$  diameter and appeared to be spherical and "cauliflower-shaped" aggregates of smaller crystallites (5). Particles grown from unstirred gels varied in size as well as morphology, shown in Figure 1a. Most particles appeared to be  $2\text{--}5\mu\text{m}$  diameter aggregates of smaller elementary crystallites; however, some single, twinned and inter-grown crystals were observed.

Decreasing the iron concentration in the gel from  $\text{SiO}_2/\text{Fe}_2\text{O}_3 \simeq 50$  to  $\text{SiO}_2/\text{Fe}_2\text{O}_3 \simeq 200$  resulted in more spherical particle aggregates in the stirred samples and larger particle aggregates in the unstirred samples; in the unstirred batch some of the spherical particles were greater than  $5\mu\text{m}$  in diameter. Thermal and hydrothermal treatments did not change the size nor the morphology of the FeZSM-5 particles.

The effects of alkali cations (Li, Na and K) on the size and morphology of FeZSM-5 were also investigated. Crystals of FeZSM-5 were grown in the presence of Li, Na and K nitrate salts in a manner analogous to that described for growth of large crystals of the aluminosilicate ZSM-5 (6). Figure 1 shows FeZSM-5 particles grown from unstirred gels with  $\text{SiO}_2/\text{Fe}_2\text{O}_3$ -ratio  $\simeq 50$  and (a) without alkali cations, (b) with Li cations, (c) with Na cations and (d) with K cations. As in the case of the aluminosilicate ZSM-5, addition of alkali cations results in larger particles. In the iron silicates a few percent of the particles are large ( $\geq 3\mu\text{m}$  long) single crystals but most of the particles are agglomerates of smaller single or intergrown crystals. These agglomerates increase in size as the size of the added cation increases from Li to Na but remains constant with K.

### Transmission Electron Microscopy

**Procedures** Both the bright field imaging and the high resolution imaging were performed in a JEOL 200CX microscope equipped with a high resolution objective lens, operating at its maximum accelerating voltage 200 kV. At the expense of image contrast, maximum accelerating voltage was used to minimize the electron beam induced damage of the zeolite structure by minimization of its ionization cross-section (7-11). Microdiffraction was performed on an analytical version of the JEOL 200CX operated at 200 kV in micro-microdiffraction mode using a 20 nm probe. To prevent specimen contamination under the intense probe (12), the specimen was cooled to liquid nitrogen temperature in a GATAN cold stage.

As-synthesized, calcined and steam-treated samples of FeZSM-5 grown from stirred and unstirred gels with  $\text{SiO}_2/\text{Fe}_2\text{O}_3$ -ratios  $\simeq 50$ , 90 and 200 were studied. The specimens consisted of uniformly thin (50-80 nm) sections of the iron silicate particles embedded in an acrylic resin and were prepared by ultramicrotomy, described in detail elsewhere (13, 14).

**Results and discussion** The cuboidal or spherical FeZSM-5 particles are actually aggregates of smaller FeZSM-5 crystallites. These crystallites have a bimodal size distribution, many are 50-100 nm in diameter and others are 100-200 nm wide and up to 500 nm long. When FeZSM-5 is grown from unstirred gels, the particles form with the small crystals in the center surrounded by the larger crystals; in the case of stirred gels the crystallites are randomly arranged in the particle agglomerates

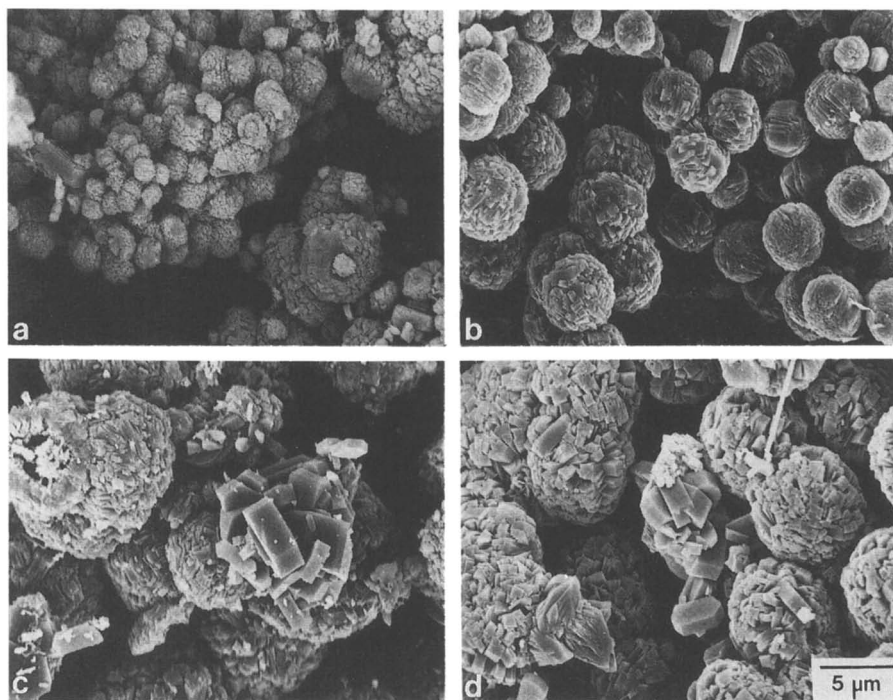


Figure 1--SEM image of iron silicate molecular sieve in the as-synthesized form, grown from an unstirred gel with  $\text{SiO}_2/\text{Fe}_2\text{O}_3$ -ratio  $\simeq 50$ , a-grown without alkali cations; b-grown with added Li; c-grown with Na cations; and d-grown with K cations.

without organization by shape or size. In and amongst these FeZSM-5 particles, no second phase material is detectable in either SEM or TEM images of the as-synthesized forms grown from stirred or unstirred gels.

Second phase particles ( $\leq 2.5$  nm) are detected after thermal treatment of samples with  $\text{SiO}_2/\text{Fe}_2\text{O}_3$ -ratio  $\simeq 50$  and in all FeZSM-5 samples after steam treatment at  $550^\circ\text{C}$  for 2 hours. In the calcined FeZSM-5 grown from stirred gel with high iron content, iron-rich second phase particles (15, 16) are observed along the outer edges of the particles; in corresponding samples grown from unstirred gels the second phase particles are found on edges of the crystallites in the middle of the FeZSM-5 particles and seldom near the FeZSM-5 particle outer edges.

Hydrothermal treatment of all samples grown from stirred gels produced homogeneous distributions of iron-rich second phase particles generally ranging in size from 1.5 to 5 nm for steaming times of 1, 2 or 4 h at  $550^\circ\text{C}$ . When the stirred FeZSM-5 samples are steamed at  $700^\circ\text{C}$  for 4 h, the second phase particles range in size from 2.5 to 15 nm. Particles 10 nm or larger are often found on the surfaces of the individual FeZSM-5 crystallites within the FeZSM-5 particle; whereas, the smaller second phase particles are homogeneously dispersed throughout the FeZSM-5. The number of iron-rich second phase particles increases with the iron content of the FeZSM-5 while their size increases with the duration and temperature of the steam treatment.

Prolonged steam treatment, 12 h at  $550^\circ\text{C}$ , of the FeZSM-5 also results in large second phase particles along grain boundaries and on the surfaces of the FeZSM-5 crystallites (Figure 2). Most probably during the long steam treatment, the larger particles on or near the FeZSM-5 internal and external surfaces grow at the expense of the smaller homogeneously distributed second phase particles since few small particles are visible after the 12 h treatment.

Molecular sieve particles grown from unstirred gels contain (6-15 nm) voids, some are sharply faceted; typically most of these voids are located in the small, iron-rich crystallites near the center of the FeZSM-5 particle (Figure 3) (15, 16). Many of the facets of these voids are rounded during steam treatment, the voids also provide sites for the nucleation and growth of second phase particles. Hydrothermal treatments for 1, 2 or 4 h at  $550^\circ\text{C}$  of the unstirred samples produces second phase particles, 2 to 6 nm diameter, whereas steaming at  $700^\circ\text{C}$  for 4 h results in particles 2.5 to 16 nm in size (Figure 4). The distribution of second phase particles in Figure 4 illustrates the effects of inhomogeneous iron distribution prior to steaming (15, 16). The iron-rich center of the FeZSM-5 particle contains a relatively uniform distribution of second phase particles (2.5 - 8 nm) but the second phase is sparsely distributed as larger (7 - 13 nm) particles throughout the larger silicon-rich FeZSM-5 crystallites at the particle edge.

Hydrothermal treatment of unstirred samples consistently resulted in larger second phase particles than did the same treatment of stirred samples. This is probably due to a combination of two contributing factors: a less homogeneous iron distribution in the as-synthesized form of the unstirred samples and enhanced diffusion during steam treatments. The latter is probably due to the voids decreasing the impedance to the movement of iron species.

**Microdiffraction and HREM imaging** The iron-rich second phase particles larger than 7.5 nm are crystalline but electron diffraction is very weak and diffuse due to their small size. Conventional selected area diffraction yields only the ZSM-5 framework structure spots. Microdiffraction, obtained by focusing a 20 nm electron probe onto the area from which diffraction is desired, applied to the second phase particles yields identifiable electron diffraction patterns (Figures 5 and 6). The patterns in Figure 5 are from well separated, larger particles in the FeZSM-5 sample, steamed for 4 h at  $700^\circ\text{C}$ , grown from a stirred gel with  $\text{SiO}_2/\text{Fe}_2\text{O}_3$ -ratio  $\simeq 200$ . In addition to these

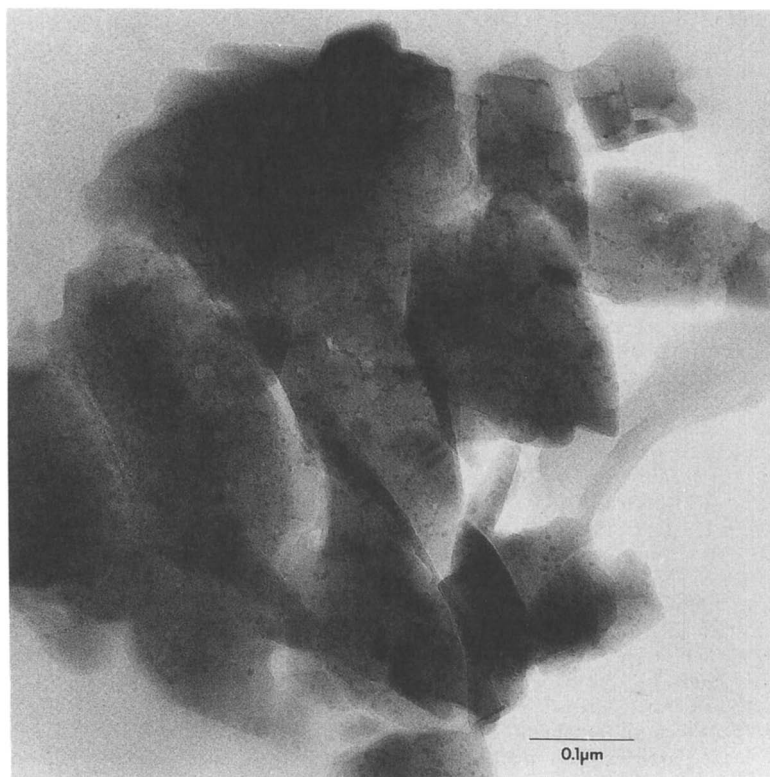


Figure 2--TEM image of FeZSM-5 particle aggregate grown from stirred gel with  $\text{SiO}_2/\text{Fe}_2\text{O}_3$ -ratio  $\simeq 50$ , after steam treatment for 12h at  $550^\circ\text{C}$ .



Figure 3--FeZSM-5 particle aggregate in as-synthesized form grown from an unstirred gel with  $\text{SiO}_2/\text{Fe}_2\text{O}_3$ -ratio  $\approx 200$ . The center of the FeZSM-5 particle (lower left area of the picture) consists of the small "hole" crystallites of FeZSM-5 and the outer edges are characterized by the larger FeZSM-5 crystals (upper right quadrant of the photograph).

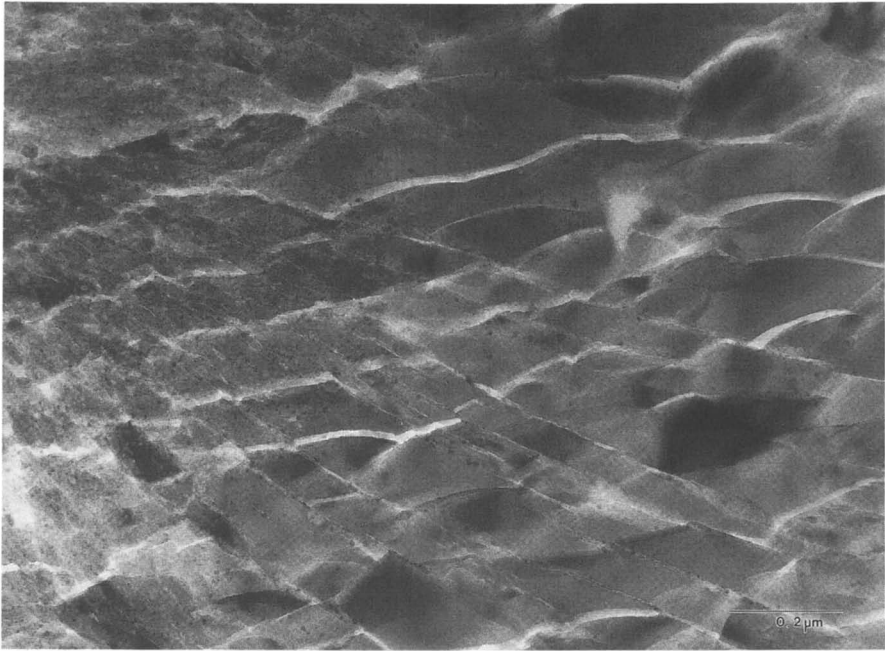


Figure 4--TEM image of part of a FeZSM-5 particle aggregate grown from an unstirred gel with  $\text{SiO}_2/\text{Fe}_2\text{O}_3$ -ratio  $\simeq 200$ , after steam treatment for 4h at  $700^\circ\text{C}$ . From the upper left corner to the lower right corner represents the center to the outer edge of the agglomerate.

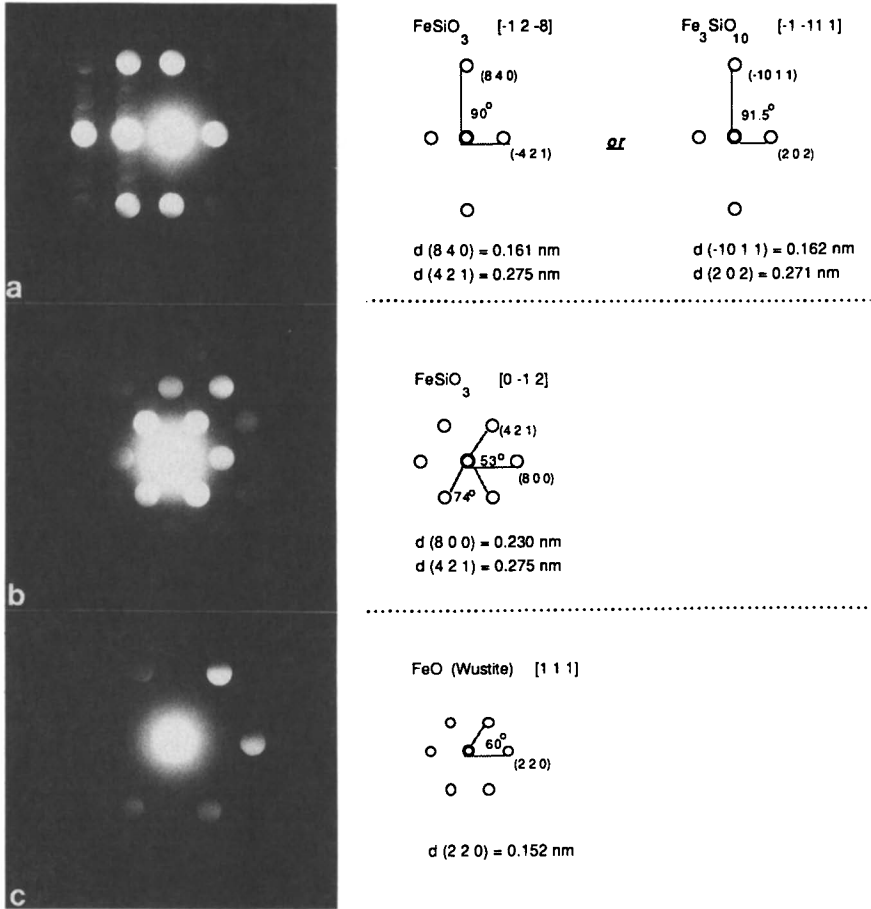
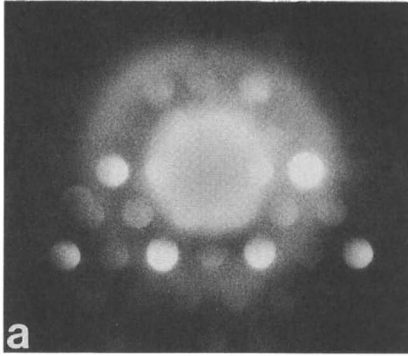
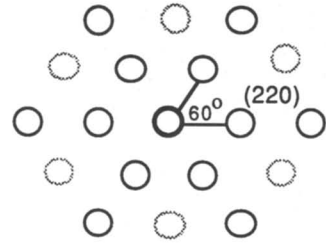


Figure 5--Microdiffraction patterns from three second phase particles, with most probable indexing, from some second phase particles in the steam treated (700 °C for 4h) FeZSM-5 particles grown from a stirred gel with  $\text{SiO}_2/\text{Fe}_2\text{O}_3$ -ratio  $\approx 200$ .

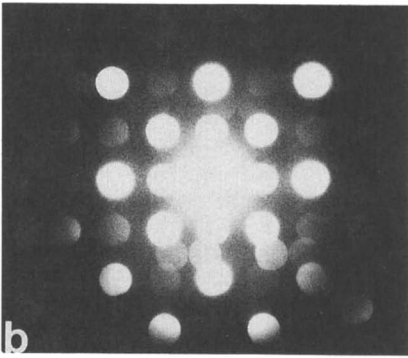


[111] face centered cubic

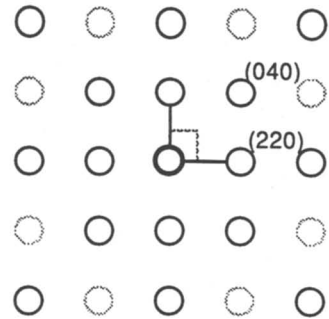


measured

$$d(220) = 0.285 \pm 0.01$$



[001] face centered cubic



measured

$$d(220) = 0.285 \pm 0.01$$

$$d(400) = 0.205 \pm 0.01$$

Figure 6--Indexed microdiffraction patterns from some of the iron-rich second phase particles in steam treated (700 °C for 4h) FeZSM-5 grown from a stirred gel with  $\text{SiO}_2/\text{Fe}_2\text{O}_3$ -ratio  $\simeq 50$ .



diffraction patterns, the sample grown from a stirred gel with  $\text{SiO}_2/\text{Fe}_2\text{O}_3$ -ratio  $\simeq 50$  after the same steam treatment also contains particles which produce the diffraction patterns in Figure 6. Microdiffraction on the small ( $\leq 5$  nm) iron-rich second phase particles shows only diffuse scattering, no Bragg spots, indicating that the small particles are amorphous. After prolonged hydrothermal treatment, however, the second phase particles (shown in Figure 2) show some weak diffraction spots but not any strong two dimensional patterns.

Since the steam treatments are performed on the ammonium form of the iron silicate, only iron oxides, hydroxides and iron silicate structures are considered as possible identities for the second phase particles. The pattern shown in Figure 5a may be indexed as the  $[\bar{1}\bar{1}\bar{1}]$  zone of  $\text{Fe}_3\text{SiO}_{10}$  if the weak spots between the transmitted beam and the  $\bar{1}\bar{0}\bar{1}\bar{1}$  spot are ignored. A more consistent indexing of this pattern is achieved using  $\text{FeSiO}_3$  in the  $[\bar{1}\bar{2}\bar{8}]$  zone; in this choice the weak spots consistently index as  $2\bar{1}0$  reflections. Figure 5b can be indexed only as  $\text{FeSiO}_3$  in the  $[0\bar{1}\bar{2}]$  direction which increases the confidence that the diffraction pattern in Figure 5a is correctly identified as  $[\bar{1}\bar{2}\bar{8}] \text{FeSiO}_3$ . For the pattern in Figure 5c only one solution seems possible, the  $[1\bar{1}\bar{1}]$  zone of wustite ( $\text{FeO}$ ).

After prolonged electron beam exposure, the molecular sieve structure is damaged and becomes amorphous, facilitating high resolution electron microscopy (HREM) images of the second phase particles. In Figure 7 two sets of lattice planes of the second phase particle with spacing 0.27 nm intersect with a  $74^\circ$  angle between them. This is the HREM image that would be expected for the  $[0\bar{1}\bar{2}]$  zone of  $\text{FeSiO}_3$ , adding confidence to the assignment of the  $\text{FeSiO}_3$  indexing to the diffraction pattern in Figure 5b.

The electron diffraction pattern in Figure 6a may be indexed as the  $[1\bar{1}\bar{1}]$  zone of face centered cubic  $\text{Fe}_2\text{SiO}_4$ ,  $\text{Fe}_3\text{O}_4$  (magnetite),  $\gamma\text{-Fe}_2\text{O}_3$  (maghemite) or as  $\text{Fe}(\text{OH})_3$ . These four structures can not be differentiated solely by electron diffraction since all four have very similar lattice parameters;  $a_0 = .8235$  nm ( $\text{Fe}_2\text{SiO}_4$ ),  $a_0 = .8396$  nm ( $\text{Fe}_3\text{O}_4$ ),  $a_0 = .8350$  nm ( $\gamma\text{-Fe}_2\text{O}_3$ ) and  $a_0 = .837$  nm ( $\text{Fe}(\text{OH})_3$ ). Figure 6b shows a  $[0\bar{0}\bar{1}]$  zone diffraction pattern that also can be identified as resulting from a face centered cubic material, either the iron silicate, the iron oxides or the iron hydroxide.

Although electron diffraction cannot distinguish between the oxide, hydroxide or silicate structures, other information can be used to eliminate some of the choices. It is well documented that hydroxide compounds and hydrated compounds change structure under the electron beam (17-20); typically they dehydrate to the oxide. On this basis, the  $\text{Fe}(\text{OH})_3$  can not be responsible for the diffraction patterns in Figure 6; microdiffraction requires a large electron flux to the specimen which would result in change of the iron hydroxide structure probably to an iron oxide (or amorphous) phase. By the same rational if maghemite is responsible for the diffraction patterns, then lepidocrocite,  $\text{FeO}(\text{OH})$ , may have been formed during the hydrothermal treatment and probably transformed to  $\text{Fe}_2\text{O}_3$  by dehydration under the intense electron beam.

Thermodynamic phase equilibria considerations allow for the formation of either of the iron oxides or the iron silicate (21, 22); however,  $\gamma\text{-Fe}_2\text{O}_3$  is metastable with respect to  $\alpha\text{-Fe}_2\text{O}_3$  and will rapidly transform at  $400^\circ\text{C}$  from light brown maghemite to dark red  $\alpha\text{-Fe}_2\text{O}_3$ , hematite (23). Therefore  $\gamma\text{-Fe}_2\text{O}_3$  would not be expected in the FeZSM-5 sample producing the diffraction patterns in Figure 6 since this sample had been steamed at  $700^\circ\text{C}$ . Subsequent heat treatment in air at  $450^\circ\text{C}$  confirms that maghemite is not present in this sample in sufficient quantity to cause a color change of the sample with its transformation to hematite. This argument

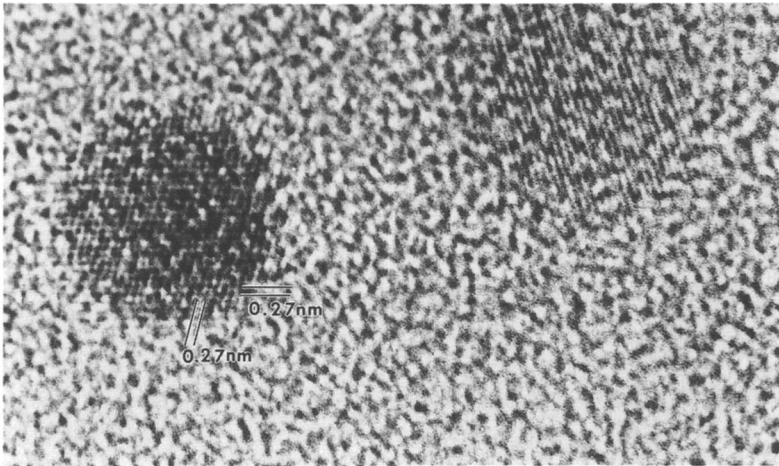


Figure 7--Second phase particles (lattice fringes) in molecular sieve matrix, FeZSM-5, after 4h steam treatment at 700 °C, SiO<sub>2</sub>/Fe<sub>2</sub>O<sub>3</sub>-ratio  $\approx$  90. Molecular sieve structure is amorphous due to electron beam damage.

alone is not sufficient to eliminate maghemite as the phase giving the diffraction patterns since the color of a phase containing iron depends on its particle size and its dispersion in addition to its concentration (23).

Since microdiffraction is specific and representative only of the individual particles probed, the statistics of the analysis are important. The microdiffraction patterns shown are representative only of the larger second phase particles, since the smaller ones produced diffraction patterns characteristic of amorphous material. In the 4 h 700 °C steamed FeZSM-5 sample grown from a stirred gel with SiO<sub>2</sub>/Fe<sub>2</sub>O<sub>3</sub> ratio  $\approx$  200, 41% of the large second phase particles probed by microdiffraction gave the pattern in Figure 5a, 32% gave that in Figure 5b and 5% gave the wustite pattern in Figure 5c. In the similarly steamed sample grown from a stirred gel with four times as much iron, 21% of the second phase particles gave the diffraction pattern in Figure 5a, 14% yielded that in Figure 5b, 7% gave Figure 5c, 14% gave Figure 6a and 21% gave Figure 6b. Other particles in both samples produced incomplete or overlapping diffraction patterns that could not be identified. In all, 78% of the patterns recorded by microdiffraction were identified, in reality these particles probably are characteristic of about 30% of the second phase particles, since most of the particles are smaller and amorphous; hence the identity of these smaller particles is unclear.

Both high resolution imaging and microdiffraction indicate that some of the second phase particles contain iron in the 2+ oxidation state, e.g., FeSiO<sub>3</sub> and FeO (and possibly Fe<sub>2</sub>SiO<sub>4</sub> and Fe<sub>3</sub>O<sub>4</sub>). This contradicts the Mössbauer data on these materials (4), which indicates the presence of iron in the 3+ oxidation state mostly ( $\sim$ 85%) in octahedral coordination and a small amount ( $\sim$ 15%) in tetrahedral environment. Since the smaller particles are a different structure and are generally more numerous, it is probable that the Mössbauer data is only sensitive to the larger volume fraction of the material in the smaller particles, as Mössbauer is a bulk technique. Thus the identification of some of the large second phase particles as structures containing iron in its 2+ oxidation state is valid although it is not corroborated by the Mössbauer results.

Although it would be valuable to positively identify the second phase particles formed by hydrothermal treatment so that a mechanism for their formation and growth could be understood, it is not essential to its use as a catalyst. Fischer-Tropsch reactions occur in a reducing atmosphere and the actual iron catalyst is probably a reduced iron compound that could only exist under the reaction conditions.

### Conclusions

Scanning electron microscopy has shown that stirring the gel during crystal growth results in small (0.5  $\mu$ m - 1  $\mu$ m) molecular sieve particle aggregates. Crystal growth without agitation produces some single crystals in addition to the micron or larger sized particle aggregates. The addition of alkali cations during unstirred crystal growth leads to larger particle agglomerates and generally more single crystals of FeZSM-5. In the stirred batches, the particle morphology changes from regular spheres to irregular spheres and "cauliflower-shapes" as the iron content increases; this is analogous to the effect of increasing the aluminum content in ZSM-5 zeolites.

Transmission electron microscopy imaging of a thin section of FeZSM-5 particles reveals that they are aggregates of smaller FeZSM-5 crystallites. Unstirred gels produce aggregates with small crystals in the center surrounded by larger crystals, while the agglomerates from stirred gels are formed without size or shape discrimination.

Thermal and hydrothermal treatments lead to the formation and growth of iron-rich second phase particles in the FeZSM-5 particles. Second phase particles

range in size from 1.5 nm to 6 nm for 1, 2 or 4 h 550 °C steam treatments and 5 nm to 16 nm for 4 h 700 °C treatments. These particles are homogeneously dispersed throughout the FeZSM-5 particles grown from stirred gels. Overall in the FeZSM-5 particle agglomerates grown from unstirred gels, the second phase particles are larger than in the stirred samples with the smaller second phase particles relatively uniformly distributed at the agglomerate center and the larger ones are predominately located between FeZSM-5 crystallites nearer to the aggregate edges.

Microdiffraction shows that the second phase particles larger than 7.5 nm are crystalline while smaller particles are amorphous. The identity of the particles differs with the temperature and duration of the steam treatments and probably on the amount of iron in the FeZSM-5 before steaming. Samples of FeZSM-5 steamed at 550 °C for 1, 2 or 4 h generally contain only amorphous second phase particles; after 12 hours at 550 °C some crystallinity is observed in the iron-rich second phase. Hydrothermal treatment at 700 °C leads to many crystalline second phase particles. Some of them are FeSiO<sub>3</sub> and FeO; and some Fe<sub>2</sub>SiO<sub>4</sub>, Fe<sub>3</sub>O<sub>4</sub>, γ-Fe<sub>2</sub>O<sub>3</sub> and γ-FeO(OH) are probably also present.

#### Acknowledgments

Sincere gratitude is expressed toward C.E. Lyman, V. Nair and R. Szostak for stimulating discussions and support, and toward C. Echer for helping with the microdiffraction work. The FeZSM-5 samples were prepared at Georgia Institute of Technology in the Zeolite Research Program; electron microscopy was performed at the Electron Microscopy Laboratories at the College of Letters and Sciences, University of California, Berkeley and at the National Center for Electron Microscopy, Lawrence Berkeley Laboratory. This work has been supported by the Director, Office of Energy Research, Office of Basic Energy Sciences, Materials Sciences Division, U.S. Department of Energy, under Contract DE-AC03-76SF00098.

#### Cited literature

1. Szostak, R., and Thomas, T.L., *J. Catal.* 1986, 100, 555.
2. Szostak, R., Nair, V., and Thomas, T.L., *J. Chem. Soc. Faraday* 1987, 83, 487.
3. Nair, V., PhD Thesis, Georgia Institute of Technology, Atlanta, GA, 1987.
4. Meagher, A., Nair, V. and R. Szostak, *Zeolites* 1988, 8, 3.
5. Csencsits, R., Gronsky, R., Nair, V. and Szostak, R., in *Microstructure and Properties of Catalysts*, Treacy, M.M.J., Thomas, J.M., and White, J.M., eds.; Mater. Res. Soc. Proc. 111, Pittsburgh, PA, 1988; p. 155.
6. Nastro, A. and Sand, L.B., *Zeolites* 1983, 3, 57.
7. Bursill, L.A., Lodge, E.A., and Thomas, J.M., *Nature* 1980, 286, 111.
8. Bursill, L.A., Thomas, J.M., and Rao, K.J., *Nature* 1981, 289, 157.
9. Treacy, M.M.J., and Newsam, J.M., *Ultramicroscopy* 1987, 23, 411.
10. Csencsits, R., and Gronsky, R., *Ultramicroscopy* 1987, 23, 421.
11. Csencsits, R., and Gronsky, R., *Zeolites* 1988, 8, 122.
12. Williams, D.B, *Practical Analytical Electron Microscopy in Materials Science*; Philips Electronic Instruments, Inc.: New Jersey, 1979; p. 122.
13. Csencsits, R., Schooley, C. and Gronsky, R., *J. Electr. Microsc. Tech.* 1985, 2, 643.
14. Csencsits, R., and Gronsky, R., in *Specimen Preparation for Transmission Electron Microscopy of Materials*, J.C. Bravman, M.L. McDonald and R. Anderson, eds.; Mater. Res. Soc. Proc. 115, Pittsburgh, PA, 1988; p. 103.
15. Csencsits, R., Lyman, C.E. and Gronsky, R., in *Proc. of the 46th Annual Electr. Microsc. Soc. of Amer. Meeting*, Milwaukee, WI, 1988, Bailey, G.W., eds.; San Francisco Press, San Francisco, CA, 1988; p. 712.

16. Csencsits, R., PhD thesis, University of California at Berkeley, 1988.
17. Hobbs, L.W., *Electr. Microsc. Soc. of Amer. Bulletin* 1985, 15, 51.
18. Hobbs, L.W., *Ultramicroscopy* 1987, 23, 339.
19. Dahmen, U., Kim, M.G., and Searcy, A.W., *Ultramicroscopy* 1987, 23, 365.
20. Van Landuyt, J., Van Tendeloo, G., and Amelinckx, S., *Ultramicroscopy* 1987, 23, 371.
21. Kingery, W.D., Bowen, H.K., and Uhlmann, D.R., *Introduction to Ceramics*; John Wiley and Sons, New York, 1976; pp. 283-300.
22. Garrels, R.M., and Christ, C.L., *Solutions, Minerals and Equilibria*, Freeman, Cooper and Company, San Francisco, 1965; pp. 146-151, 182-197.
23. Brindley, G.W., *X-ray Identification and Crystal Structures of Clay Minerals*; The Mineralogical Society, London, 1951; pp. 244-265.
24. Rossmann, G.R., *American Mineralogist* 1975, 60, 698.

RECEIVED January 10, 1989

## Chapter 34

# Mechanical and Physical Testing of Catalysts

Ralph J. Bertolacini

Research and Development, Amoco Oil Company, Naperville, IL 60566

Proper catalyst specifications for mechanical and physical properties are as important as activity and selectivity. Poor resistance to attrition and crushing can cause pressure drops and expensive unit shutdowns in refining and petrochemical operations. Setting reasonable specifications depends on the development of reliable test procedures and well-characterized reference materials for method development. Statistical control processes can be used to eliminate variations to reduce off-specification catalysts and contractual disputes. These important issues are reviewed and discussed, and subsequent papers in this symposium deal with the specific topics.

Catalytic activity, selectivity, and the rate of deactivation are the usual criteria for developing, evaluating, and recommending commercial industrial catalysts. These important catalyst properties, most often, are proprietary and determined by the catalyst user. However, while these catalyst properties are important for successful commercial performance, they are not the sole criteria and this is well recognized by the catalysis community. Catalyst stability (1), attrition resistance (2-3), and crushing strength (4-5) are equally as important as activity. These mechanical properties can supersede outstanding catalytic performance and often are the limiting factors for using, and regenerating, industrial catalysts. Mechanical and physical properties are usually tightly specified by the user.

Poor mechanical and physical properties are costly problems for the refining and chemical industries. Broken catalyst particles in fixed bed reactors increase pressure drop by bridging interstices between catalyst particles which can plug the bed with debris coming from above and in some cases facilitate coke formation which further increases the pressure drop. Fixed bed catalysts are prone to breakage when they are loaded into reactors. Loading can be performed by pneumatically lifting the

catalyst from ground level into the reactor or dropping the catalyst down a sleeve so the catalyst must be rugged. High pressures, high temperatures, and high velocity feed throughputs also exert a tremendous strain on the catalyst particles. To overcome some of these problems, catalysts are prepared in different shapes designed to resist fracture, spalling, and disintegration. Catalyst forms vary from pellets, rings, extrudates, geometric shapes, to fine powders. Each engineered to fit the process and each causing problems for measuring their mechanical properties.

Catalysts for ebullating bed reactors are subjected to attrition. Those used for resid hydroprocessing and coal liquefaction must resist turbulence, from high gas velocities as well as erosion by the ash and impurities in the feedstocks. Fluid catalytic cracking catalysts must have good fluidization properties to eliminate circulation problems and excess generation of catalyst fines which cause operational and environmental problems. Fluid bed catalytic cracking catalysts are also subjected to high temperature during steam stripping and regeneration, which further decrease their resistance to attrition.

Developing methods to prevent and eliminate catalyst breakage and attrition are as important as developing highly active and selective catalysts. Good diagnostic tests for accelerated aging and pseudoequilibration are used to simulate and predict catalyst in-service performance.

Two important tests used to measure potential catalyst breakage problems during operation are single pellet and bulk crushing strengths. Single pellet tests are applicable to pills, extrudates, and spheres. These tests measure the resistance to a compressive force and are used for quality control by the producer. The user usually specifies a range of strengths, for example 3-4 pounds/millimeter of length or diameter, or a specific percentage at some minimum strength, for example not more than 5% below 22 pounds total. This eliminates soft pellets which could pulverize during loading or reaction and lead to pressure drop problems.

Bulk crush measures the ability of the catalyst to support the weight of the catalyst bed. This is difficult to measure precisely and has not yet been standardized. This test is now done on a proprietary basis. The paper by S. A. Bradley, et al. (6) addresses a procedure now under consideration for standardization which, if adopted, should be valuable to catalyst users and producers for specification and quality control.

Similar to the importance of mechanical stability, physical properties such as surface area, pore size, and pore size distribution, metal dispersion, and surface acidity are important parameters, which the catalytic chemist or engineer considers when developing a catalytic system. The physical properties are optimized to fit the catalytic application. Measurement of these properties, while not all are fully standardized, have been widely published for specific catalytic systems. The most complete review of these procedures with examples for specific catalytic systems and references have been published (7-8).

Traditionally, for proprietary reasons, industrial catalytic researchers have not discussed or disclosed in-house methods for setting the mechanical and physical property specifications of industrial catalysts. However in 1974, the American Institute of Chemical Engineering at the June meeting in Pittsburgh, devoted a day-long symposium on measuring the mechanical and physical properties of catalysts (9). Beaver described a mechanically-driven piston apparatus which gave more reproducible results than previously described hand-operated devices for shaped catalysts (10). Dart described a procedure for measuring catalyst attrition resistance, i.e., abrasion loss for formed and shaped catalysts (11). Proper sampling procedures for developing standardized tests were addressed by Adams, et al. (12). They point out that proper sampling is an important factor in catalyst testing which is not often discussed when setting catalyst specifications. Often disputes between the vendor and purchaser are caused by poor sampling methods.

As a result of the 1974 American Institute of Chemical Engineering, the American Society for Testing Materials organized Committee D-32--Catalysts in January 1975. The early history and development of the Committee was reported by Kiovsky (13), Neal (14), and Bertolacini (15). Similar standardization groups have since been formed in Japan, United Kingdom, Europe, and the Soviet Union. Twenty-five standards have been developed by the American Society for Testing Materials Committee D-32--Catalysts including tests for attrition, crush strength, particle size distribution, and vibrated apparent packing density (16).

Standardization of catalyst test methods will help eliminate costly and unnecessary repeated testing because the analyses are done by the same method with measured precision and bias. This should help eliminate conflicts in maintaining quality control and specification requirements.

Quality assurance is an important consideration for the user and producer. Both aspects are discussed by Puls (17) in his symposium paper. Lot-to-lot variations in purchased catalyst can be minimized by a system of statistical process control by the catalyst producer, his supplier, and the user. The statistical process helps to minimize product quality variations by instituting corrective action on a real-time basis to prevent the production of off-specification material.

The development and standardization of reliable test procedures requires an ample supply of well-characterized reference materials. These samples are used for round-robin tests by participating laboratories in the method development. A reliable set of reference materials are available from the National Bureau of Standards. These special reference materials are described by Haines in this symposium series. The Bureau has packaged the materials in an appropriate size and secure container. Producer and user laboratories have these reference materials available to cross-check results and resolve differences in specification analyses. These reference standards are available at a reasonable cost.

The standardization of all of these procedures for analyzing catalysts has been the goal of ASTM Committee D-32. Reference



procedures have been established and supporting data may be obtained from ASTM.

By 1992, the free-world catalyst market could reach four billion dollars; and the United States projection is estimated to be two billion (18). It is difficult to estimate how much of an impact improved methods for engineering improved mechanical and physical properties will have on these figures, but we can expect that all catalysts will be checked to meet the specifications of the user and the quality control program of the producer.

#### LITERATURE CITED

1. National Petroleum Refiners Association, Questions and Answers Refining Technology, Farrar, G. L., Ed.; National Petroleum Refiners Association, Washington, DC, 1982, p 52.
2. Ibid., p 154, 1982.
3. Ibid., p 151, 1983.
4. Ibid., p 129, 1983.
5. Ibid., p 102, 1984.
6. Bradley, S.; Pretzer, E., Koves, W. J., Bulk Crush Testing of Catalysts, Prep. Am. Chem. Soc.,; Div. Pet. Chem. 1988, 33 (4), p 557-561.
7. Introduction to Characterization and Testing of Catalysts, Anderson, J. R. and Pratt, K. C., Academic Press, Inc., Florida, 1985.
8. "Characterization of Catalysts," Baker, A., Kohler, M. A., Handbook of Heat and Mass Transfer, Vol. 3, Catalysis, Kinetics, and Reactor Engineering, Cheremesenoff, N. P., Ed.; Gulf Publishing Co., Houston, Texas, 1989, p 3-62.
9. Weller, S. W., Standardization of Catalyst Test Methods, Vol 70, No. 143, AIChE Symposium Series, AIChE New York, 1974.
10. Beaver, E. R., Ibid., p 1-4.
11. Dart, J. C., Ibid., p 5-8.
12. Adams, C. R., Sartor, A. F., and Welch, J. G., Ibid., p 49-54.
13. Kivosky, J. R., Oral Communication, Proceedings of the International Symposium in the Relations Between Heterogenous and Homogeneous Catalytic Phenomena, Brussels, October 1974.
14. Neal, A. H., Preparation of Catalysts II, B. Delman, Ed.; Elsevier, Amsterdam, 1979, p 719.
15. Bertolacini, R. J., Neal, A. H., Preparation of Catalysts III, G. Poncelet, Grange, P., Jacobs, P. A., Eds.; Elsevier, 1983, p 767.
16. ASTM Standards on Catalyst; Third Edition, 1988 American Society for Testing Materials, Philadelphia.
17. Puls, F. H., Quality Assurance for Purchased Catalysts, Prep. Am. Chem. Soc., Div. Pet. Chem. 1988, 33 (4), p 568-71.
18. Chem Week; June 29, 1988; p.21.

RECEIVED April 27, 1989

## Chapter 35

# Quality Assurance for Purchased Catalysts

F. H. Puls

Exxon Chemical Company, Baton Rouge, LA 70821-2226

Analytical results of measuring particle sizes of catalyst pellets, depths of metal impregnation through electron microscope scans, and acidic properties through ammonia chemisorption, are presented here to illustrate the fact that some commercial catalyst replacement charges exhibit quite undesirable quality variations which are causing petrochemical operating costs to be higher than expected.

Statistical process control is being implemented by catalyst manufacturers to detect and eliminate, if possible, causes of variations in quality. As many departments, such as operating, technical, purchasing, and R&D, become involved in the pursuit of quality, a unified approach toward the implementation of total quality is being developed through an accreditation procedure for catalyst suppliers.

Petrochemical industries require many different types of catalysts and adsorbents in process applications. Major portions of such requirements are being met through purchases from commercial catalyst suppliers. The importance of catalysts to chemical and petrochemical industries cannot be overstated. Deviations in catalyst performance from expectations affect yields and feedstock utilization, generate undesirable side reactions and by-products, increase operating costs, and reduce capacity. The cost of such deviations from the expectations which were incorporated in the process design, are not always known and can easily exceed the cost of a new catalyst charge.

When catalyst charges are replaced, additional unloading, loading, and handling costs are incurred and valuable production capacity is being lost. Moreover, expectations for improved performances resulting from new catalyst replacement charges are not always being realized. Therefore, it is not surprising that in the quest for quality, which has touched much of US industry in the eighties (1) (2), catalysts were among the first products which were singled out for special attention.

From QC to SPC. A new quality control (QC) function for Exxon Chemical Company was established at one of the Exxon laboratories in 1980. Exxon Research and Development Laboratories at Baton Rouge, Louisiana was chosen, because a similar function already existed for refinery catalysts, and because analytical and professional capabilities at this location superbly met our needs.

In 1984, a standard quality control procedure was introduced for all purchased fixed bed catalysts and adsorbents, e.g. to be used at the discretion of all Exxon Chemical worldwide operating plants.

Finally, this year, a standard catalyst supplier accreditation procedure is being implemented. Primary emphasis is on the implementation of control charts and statistical process control (SPC) procedures in the manufacture of commercial catalysts in order to improve lot to lot consistencies (3) for purchased catalysts.

Fixed Bed Catalysts. Noble metal, base metal, and other types of catalysts, including alumina, silica, resins, clays, zeolites, and combinations thereof are used in almost every type of chemical and petrochemical business segment. There are many different process applications ranging from the generation of suitable feedstocks, actual chemical reactions, and purification of products to the treatment of by-product streams.

Petrochemical processes require smaller reactors than used in refineries. Chemical reactors are sized in the 50 to 250 cu.ft. range. Orders for replacement catalyst usually range from 10,000 to 50,000 lbs, but there are many different process applications. Catalyst quality is becoming more important than in recent years as many industries attempt to reduce the cost of nonconformance and improve the quality of manufactured goods. A chemical producer has a choice of either selecting an off-the-shelf catalyst available from usually several sources, or of developing a proprietary catalyst suited to his specific process and operating needs.

Fixed Bed Adsorbents. Similar quality requirements, as discussed for catalysts, apply to molecular sieves and other adsorbents. Instead of catalytic activity, adsorption capacities for certain materials, such as water, or linear paraffins, are important properties of aluminas, clays, and zeolites when used as adsorbents.

### User's Plant Problems

At some point in time, every operating plant must make the decision to replace an existing catalyst charge because it has aged due to feedstock poisons, its history of high temperatures and chemical reactions, mechanical and chemical degradation and so on (4). Expectations are created with every catalyst replacement decision that the new charge will perform better than the charge being replaced.

When the new catalyst charge does not meet these expectations, significant financial losses are incurred. Technical efforts are initiated to investigate the causes of nonconformance. Feedstock properties, start-up procedures, plant operations, and catalyst properties usually are being considered.

Changed Catalyst Properties. In several cases, changed plant performance could be traced to changed catalyst properties. The potential impact of such nonconformance on plant operations is shown in Table I.

Table I. Nonconforming Catalyst Replacement Charges

<u>Nonconformance</u>	<u>Impact on Operations</u>
Lower activity	Reduced throughput to maintain same conversion
Higher activity	Reduced throughput due to heat transfer limitation
Lower crush strength	Pressure drop; increased fines due to reduced physical integrity
Higher crush strength	Pressure drop; increased fines due to greater brittleness
Higher abrasion loss	Pressure drop; increased fines when handling, shipping, loading
Smaller particles	Bulk density; possibly channelling due to unequal size distribution
Larger particle size	Reduced activity and catalyst life
Larger crystallites	Reduced activity and catalyst life
Reduced selectivity	Higher losses; shorter cycle time; poor feedstock utilization
Lower sieve capacity	Reduced cycle time; shorter life of molecular sieve

Performance variations of different lots of the same brand of catalyst still are causes of significant plant problems in the industry. Such experiences justify efforts to develop effective quality control procedures for purchased catalysts. Obtaining a clear understanding of required catalyst properties is a first step. Plant problems and unusual events need to be recorded. The history of catalyst performance in the plant is most valuable to have in developing catalyst specifications.

### Purchase Specifications

General catalyst properties, sometimes called typical analyses, are usually being provided by vendors in sales literature. Nominal size and shape of catalysts, composition by major components, internal surface area and pore volume, bulk density, and average crushing strength are usually available. The name and designation of merchant catalysts is being highlighted. The suppliers of user-proprietary catalysts are required to use more explicit specifications. In either case, the chemical and petrochemical user of a purchased catalyst does well to make sure that catalyst quality needs are understood by both supplier and user.

Quality Requirements. One can state three principal quality requirements as follows: (1) the catalyst must have sufficient physical integrity to withstand the physical forces which are created when loading the catalyst into reactors and when subjecting the particles to process conditions of varying temperatures, pressures, vapor and liquid mass velocities, and to withstand chemical attack, (2) the catalyst must have the prescribed chemical properties needed to function in the desired chemical reaction and (3) physical and chemical properties in the interior of individual particles must permit access of the reactants on a bulk molecular scale and exhibit sufficient reactivity to meet the requirements set by the process design.

Specifications. Purchase specifications have to be defined first. Then, quality control of catalyst samples which are representative of the purchased catalyst lots, can be implemented to compare actual chemical and physical properties with the range of values stated in the purchase specifications.

Activity and selectivity of catalysts are sometimes included in specifications and can be monitored in small scale simulations of commercial reactors, such as in pilot plants using standard feed stocks or model compounds. The steam reforming test performed commercially by Catalyst Services Inc. of Shelbyville, Kentucky is mentioned as an example.

Information on purchased catalysts should include the lot numbers and dates of manufacture, and the amount of water and other volatile matter still contained on the catalyst. Specifications should provide data for chemical analyses, and physical-mechanical and physical-chemical properties. The latter information should include data concerning the average shape and sizes of particles, including oversized particles, fines content, and other measures of physical integrity. An example of information which could be included in purchase specifications for a fixed bed catalyst is shown in the following Table II.

Table II. Catalyst Purchase Specifications

Analyses	ASTM Method	Specified Values		
		Min.	Max.	Typical
Supplier Catalyst Designation		.....		
Lot No. & Date Manufactured		..... ..../.../..		
Shape and Nominal Sizes		to be reported:		
<b>CHEMICAL ANALYSES</b>				
Molybdenum, wt%	D 3943-86			
Nickel, wt%	D 4481-85			
Other Chemical Analyses, ppm				
<b>PHYSICAL PROPERTIES</b>				
		for instance:		
Crush Strength, lbs, radial	D 4179-82	12	25	15
Abrasion Resistance, % Loss	D 4058-87			
Packed Bulk Density	D 4699-87			
Pore Size Distribution,				
by Mercury Intrusion,	D 4284-83			
Nitrogen Desorption	D 4222-83			
Pore Volume, ml/g				
Surface Area, m <sup>2</sup> /g	D 3663-84			
Ammonia Chemisorption	D 4824-88			

### Quality Control Procedures

A catalyst manufacturer will have procedures in place to monitor the quality of catalyst lots as these are being manufactured. To a large extent, it will depend on the customer, how much information concerning catalyst properties and catalyst performance is being communicated.

In some cases, the catalyst manufacturer may have insufficient information concerning the intended use for the catalyst being sold. He will base his manufacturing specifications on his assumptions concerning possible catalyst uses.

The catalyst user may rely on the supplier's quality control, or he may have his own quality controls for catalysts received at the plant site.

Standard Quality Control Procedure. A standard quality control procedure was established in Exxon Chemical Company in 1984. Operating plants were offered in-house assistance for developing appropriate purchase specifications, and for monitoring the quality of lot samples of purchased commercial catalysts and adsorbents.

Representative Lot Samples and Analyses. Suppliers of catalyst and fixed bed adsorbent are being requested to supply representative lot samples and analytical certificates for each new purchase order at the time the catalyst is ready for shipment. The analytical results are being compared with updated purchase specifications.

QC Experience. When we applied quality controls to purchased catalysts within Exxon Chemical Company, we found

significant lot to lot variations in the quality of some catalysts. Sometimes, such variations were within the specifications, oscillating between maximum and minimum values in an unpredictable fashion, sometimes variations were caused by the absence of appropriate specifications. This is illustrated in the following three examples:

**Particle Size - Length of Extrudates.** A new reactor charge of a 3.2 mm (1/8 inch) extruded nickel oxide on alumina catalyst was compared with the previous charge, because the operating plant observed an increase in catalyst chips. These were thought to have contributed to pressure drop problems. Retained samples of the respective catalyst lots were examined. It was found that the replacement lot contained a higher percentage of smaller particles which resulted in reducing the length to diameter ratio of catalyst particles.

The test was conducted by taking a 125 ml random sample from each representative lot sample, sorting individual particles in each sample by length, and measuring groups of 25-50 particles of approximately equal size. Total number of particles ranged from 900 to 1200, respectively. These were divided into about 30 fractions.

The average particle length was calculated by dividing the length of a 260 mm long ruler by the number of pellets, counted for each fraction, which were lined up against the ruler. The data is summarized in the following table.

Table III. Particle Size Measurements

Particle Size Range Length in millimeters	Replacement Lot B	Previous Lot A
> 13.6	1 %	17 %
5.6 - 13.5	50 %	73 %
4.6 - 5.5	23 %	9 %
< 4.6	26 %	1 %
Average particle length	100 %	100 %
Diameter of extrudates	5.8 mm	9.4 mm
Average L/D ratio of extrudates	3.2 mm	3.2 mm
	1.8	2.9

These analyses were reviewed with the supplier. The size distribution and the length/diameter ratio of the catalyst were subsequently defined in purchase specifications to eliminate uncontrolled lot to lot variations.

**Depth of Palladium Penetration.** A new catalyst charge, consisting of 0.3 wt % palladium on alumina, exhibited higher activity and lower selectivity at given plant operating conditions. Chemical and physical properties of this charge were compared with the previous charge which had been operating satisfactorily.

Standard analytical procedures, including CO chemisorption, indicated that the new charge appeared to be of the same quality as previously used catalyst. Subsequently, electron probe scans led to the observation that the depth of palladium impregnation had changed. A comparison of typical palladium penetrations for the two charges is shown in Table IV and in Figures 1 and 2.

Subsequent activity tests with model compounds were consistent with the results shown in Table IV and proved to our satisfaction that the new catalyst was different.

Table IV. Electron Probe Pd Measurements

Scanning Electron Probe Traces of 3 mm Spheres In Cross Section (Averages)	Lot Y	Lot X
Depth of major Pd peak, microns	115	360
Total Pd penetration, microns	570	770

Catalyst Acidity by Ammonia Chemisorption. Plant performances below expectations were reported by two units, in which the original alumina based catalysts were replaced. Surface area specifications were 150-200 m<sup>2</sup>/g for both catalysts. Acidity was measured by ammonia chemisorption using a recording vacuum thermoanalyzer with a TGA sample holder, and was correlated with BET surface area, as shown in Table V.

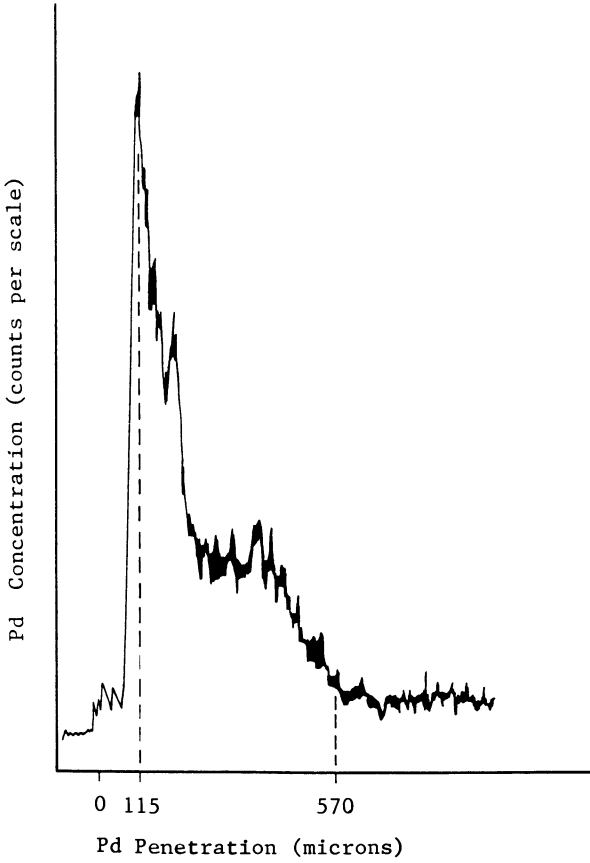
In one case, acidity needed for the reaction was maximized by changing the specification to 190-200 m<sup>2</sup>/g surface area. In the other case, undesirable side reactions, thought to be caused by excessive acidity of the carrier, were minimized by adopting a surface area of 150-160 m<sup>2</sup>/g as a new purchase specification.

Table V. Ammonia Chemisorption and Surface Area

Sample	BET Surface Area m <sup>2</sup> /g	Ammonia Chemisorption milliequivalents/gram
<b>High Acidity Alumina</b>		
New replacement	192	0.55
New specification	190-200	-
Replacement charge	147 (too low)	0.46
Previous charge	198	0.60
<b>Low Acidity Catalyst</b>		
New replacement	153	0.41
New manuf. target	150-160	-
Replacement charge	196 (too high)	0.56
Previous charge	150	0.40

Limitations of Quality Control. Quality control by detection is based on the inspection of finished catalyst before it is being shipped to the customer.





**Figure 1. Lower Depth of Impregnation.**

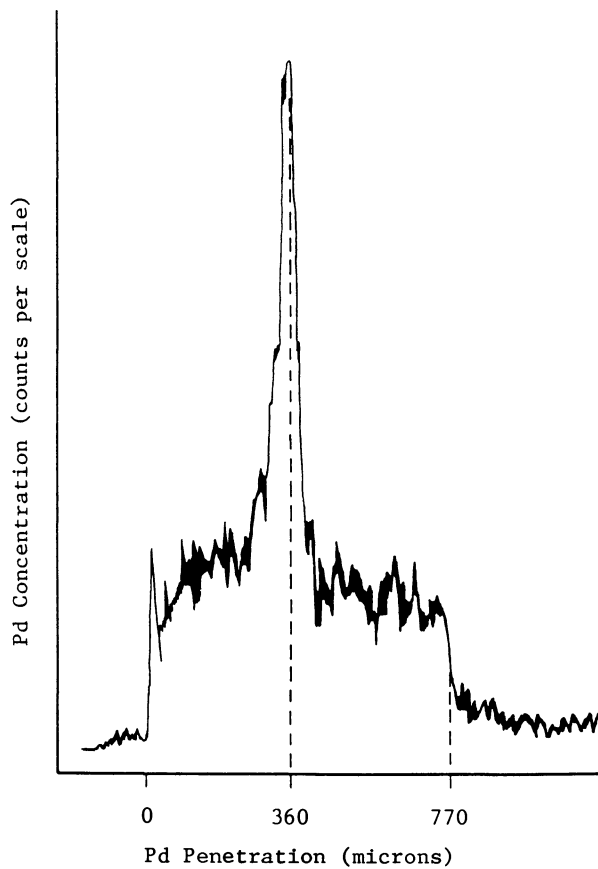


**Figure 2. Deeper Subsurface Impregnation.**

Product not meeting manufacturing specifications is either being recycled, separated for other uses, or discarded. After receiving the catalyst, the customer may apply his own quality control and may reject drums of catalysts which do not meet his inspection criteria.

Information developed during an inspection can be used only for the next catalyst order, assuming the purchaser will pass the information on to the supplier. Thus, quality control by detection is unsatisfactory, and is wasteful due to potential duplication of quality control efforts by both the supplier and the customer.

Quality control can only detect, but does not prevent, deviating and poorer quality from happening. In this situation, suppliers under-utilize catalyst performance data since users usually will not communicate such information. Users under-utilize the know-how in catalyst manufacture which suppliers carefully guard.

The way out of this situation is to introduce appropriate statistical process control procedures in the manufacturing processes of the supplier, his suppliers, and the user. Through these efforts, satisfactory as well as unsatisfactory performances of individual lots of catalysts can be determined, and lot to lot variations of catalyst quality can be identified.

#### Producers' Lot to Lot Variations

Fixed bed catalysts are manufactured in non-continuous processes. Variations in the quality have been observed from lot to lot and from pellet to pellet.

Catalyst Manufacture. Many batch and semicontinuous processing steps are required. A typical flow plan for a catalyst manufacturing plant includes the preparation and purification of raw materials, manufacture of catalyst support materials as powders, drying, sizing, forming, impregnation, calcining, reduction and stabilization, screening and packaging operations. Some of the operations are carried out in repetitive batches as small as 500 to 1,000 lbs.

Catalyst quality is affected in all of the operations. Adjustments being made to any of these processing steps affect other downstream operations. An adjustment being made to correct a single catalyst property will affect other properties. For instance, an increase in the crush strength through application of higher forming pressure will reduce the size of macro-pores. With these facts in mind, it is not surprising that catalyst properties usually vary in some way from one lot to the next.

#### Statistical Process Control

Statistical process control (SPC) is used in accordance with the principle of prevention instead of detection by measuring variables and attributes on a real-time basis.

This allows the manufacturer to take corrective actions as soon as statistically significant deviations from an aim are being detected during the manufacturing process.

The operator should not have to decide frequently to what values individual operating parameters should be adjusted, i.e. within ranges as being specified in the recipes, thus allowing for arbitrary variations to occur between many upper and lower control points.

Specific targets for manufacturing variables and for attributes of raw and intermediate materials can be defined through the application of control charts when the manufacturing process overall is balanced and in control. By using such targets, the operator can reduce start-up times for catalyst batches and can maintain, through SPC (5), a more steady operation, in which uncontrolled manufacturing variations will be minimized.

Essentially all catalyst manufacturers have taken steps in recent years to train laboratory and manufacturing personnel in the application of SPC, and to make modifications to the manufacturing facilities to improve Cpk, the process capability index (6). Data collection and analysis on control charts are usually first steps for implementing SPC.

**Catalyst User.** Analysis of consecutive lots of purchased catalyst is usually a first step which customers can take to determine how catalyst properties oscillate between upper and lower specification values. This is illustrated in Figures 3 and 4. The two control charts shown contain the values of reduced nickel content of consecutive lots of similar nickel catalysts. Both catalysts contain about 50 wt % NiO and are prereduced.

In the first figure, large lot to lot variations can be observed, although the catalyst meets its specifications of 40-60 wt % NiO and 40-60% reduction. However, its quality with respect to reduced Ni value could be considered to be out of control. An X-bar value of 29.0 wt % Ni is being calculated.

The second case represents more recent data. Here, quality with respect to reduced Ni value is in control through the probable application of appropriate targets for operating variables in catalyst manufacture. An X-bar value of 31.3 wt % Ni is being calculated.

Similar observations can be made concerning other chemical and physical catalyst properties. Not all variations in quality will adversely affect catalyst performance. However, the price of nonconformance, in many cases, is unknown.

**Catalyst Manufacturer.** The next step is for the manufacturer to generate control charts of individual data (such as X- or I- charts and R-charts) from which averages, upper and lower three-sigma limits and ranges between consecutive data can be determined. Manufacturing observations and events are also listed on these control

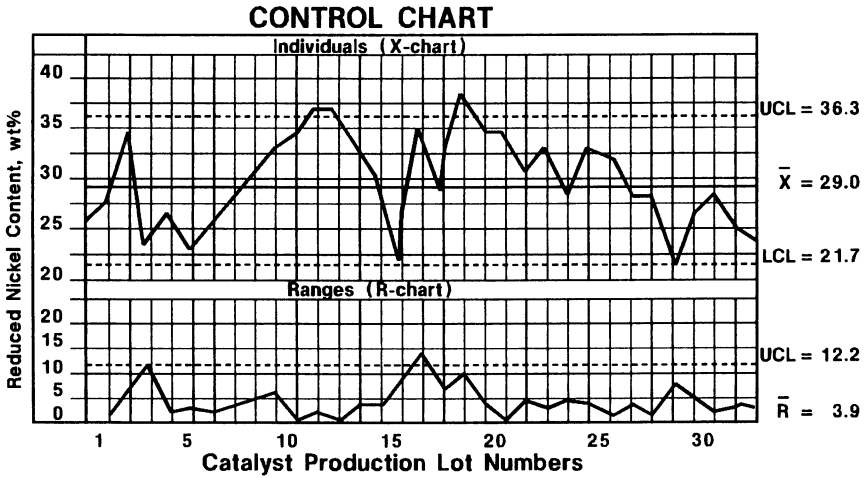


Figure 3. Lot to Lot Variations Within Specifications.

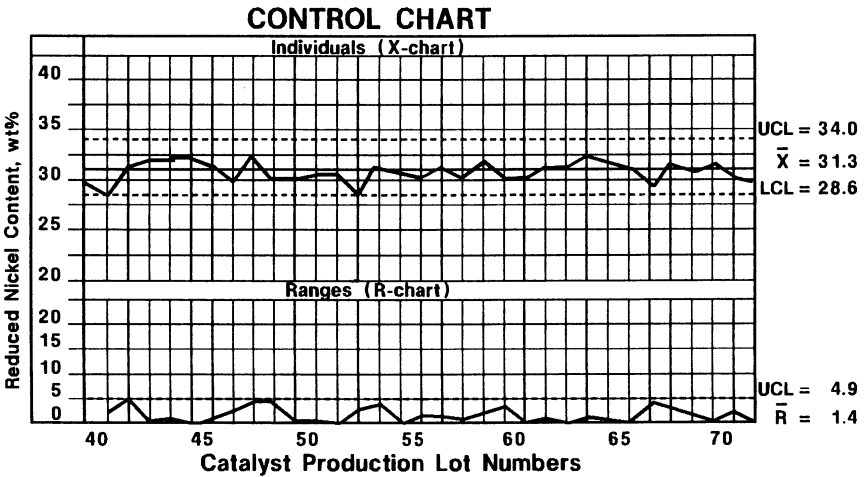


Figure 4. In Control Through Manufacturing Targets.

charts, in order to determine assignable causes of deviations. This leads to the development of corrective actions aimed at eliminating unwanted variations.

In addition to X-charts and R-charts, CUSUM charts are sometimes used. Trends can be detected sooner when using CUSUM charts. More recently, the use of EWMA, exponentially weighted moving averages, is being suggested as being easier to use on the factory floor.

Sources of process variance can be quantified and ranked through statistical design of experiments. Relations between variances of process input and output can be developed. In this way, the effect of laboratory analyses, as well as of parallel or sequential manufacturing steps, on the overall variance for a catalyst can be determined.

### Supplier Accreditation Procedure

The supplier-user or vendor-vendee relationship, as it pertains to quality, is well described in the American National Standard's ANSI/ASQC Q90-1987 to Q94-1987. The standards are technically equivalent to the ISO 9000 to ISO 9004 series of the international Quality Management and Quality Assurance Standards. The recommended quality system specifies quality policy, organization, authority, personnel, management review, and so on.

Twelve chemical producers recently cooperated with the American Society for Quality Control and issued a Manual of Good Practices. An extensive bibliography is included in the booklet (7).

Our current views on how to implement a catalyst supplier accreditation procedure are as follows. A team consisting of representatives of technical, analytical, plant operation and purchasing functions visits with the supplier's equivalent representatives prior to placing a major order, or at certain intervals. The meeting will have the following five part agenda:

Table VI. Supplier Accreditation

	<u>Agenda for Catalyst User and Supplier Visit Topic</u>
1.	Provide estimate of potential purchases
2.	Review previous analyses, catalyst performance, and catalyst specifications
3.	Review implementation of control charts and SPC
4.	Review previous total quality performance
5.	Notify supplier of evaluation results and provide finalized purchase specifications.

This supplier accreditation procedure is aimed at achieving programs of continued improvement in quality through SPC implementation in catalyst manufacture.

In working with catalyst suppliers we are led to the understanding that SPC procedures and control charts can be applied to the preparation of smaller batches of finished catalysts such as used in chemical industries.

Data collected for consecutive catalyst lots show that quality consistency has improved significantly after introducing control charts in catalyst manufacture.

Rewards for this course of action are seen in more consistent catalyst quality, eventually reduced analytical costs, and opportunities to develop preferred supplier status to meet the special needs of the customer's individual chemical unit.

### Conclusions

Lot to lot variations in the quality of purchased fixed bed catalysts are causing significant plant problems for petrochemical catalyst users.

Conventional quality control procedures fall short of current needs to improve the consistency of purchased catalyst quality and are being supplemented by the use of control charts and statistical process control.

Essentially all catalyst manufacturers have taken steps in these past couple of years to implement SPC in their manufacturing processes, in order to improve the consistency of catalyst properties.

The quality of purchased fixed bed catalysts and adsorbents is important. A supplier accreditation procedure is being implemented.

ASTM Methods for catalyst and zeolite analyses and American and International Standards for quality control and quality assurance form the cornerstones of the foundation upon which future catalyst supplier-catalyst user relationships will be constructed.

### Literature Cited

1. Garvin, David A. Managing Quality; The Free Press, Macmillan Inc.: New York, NY, 1988
2. Peters, Tom The New Masters of Excellence; Nightingale-Conant Corporation (Audiocassette Programs), Chicago, 1986
3. Crosby, Philip B. Quality is Free; New American Library, New York, 1979
4. Bartholomew, C. H. Chem. Eng. Nov 12, 1984, 91, 96.
5. Oakland, John S. Statistical Process Control, A Practical Guide; Heineman Professional Publishing Ltd: London, 1986
6. Small, Bonnie B. Statistical Quality Control Handbook, by Western Electric Co., Inc.: 1956; Eleventh Printing by Delmar Printing Company, Charlotte, NC, 1985
7. Quality Assurance for the Chemical and Process Industries, A Manual of Good Practices; American Society for Quality Control: Milwaukee, WI, 1987

## Chapter 36

# Bulk Crush Testing of Catalysts

Steven A. Bradley<sup>1</sup>, Emory Pitzer<sup>2,3</sup>, and William J. Kovacs<sup>1</sup>

<sup>1</sup>UOP Research Center, Des Plaines, IL 60017

<sup>2</sup>Phillips Petroleum Company, Bartlesville, OK 74004

The ASTM D-32 Committee on Catalysts has investigated the variables associated with bulk crush testing of formed catalyst and catalysts supports. The most critical parameters include packing density of the catalyst in the cell, the ratio of the height of the bed to the diameter of the bed, and moisture content of the catalyst. Because of the problems associated with obtaining identical packing densities in the cell, a new test cell was designed.

Catalysts have to be sufficiently strong to endure the rigors of handling and use. For example, the catalyst must be strong enough to withstand the loading into a reactor. The catalyst also cannot attrite or break-up due to the weight of the bed, gas flow, catalyst movement in continuous process or thermal expansion and contractions of the bed and container vessel. If a physical breakdown were to occur, the resulting fines formation can produce a pressure drop across the reactor as well as cause flow maldistribution. Channeling or maldistribution through the bed decreases reactor performance because of reduced catalyst contact and reduction of products of reaction. The commercialization or sales of a formed catalyst may require evaluation of the mechanical properties by both the user and producer and this necessitates the utilization of identical test methods.

To evaluate the mechanical properties of catalysts and catalyst precursors, the ASTM D-32 Committee on Catalysts has prepared several test methods that meet the criteria of acceptable inter-laboratory reproducibility. Some of these methods for evaluating the physical characteristics of a catalyst include attrition and abrasion (D4058), single pellet crush strength (D4179), vibrated packing density (D4180 and D4512), and particle size analysis (D4438, D4464 and D4513). One physical property determination that has proved most difficult to standardize has been the bulk crush strength of a catalyst bed. This paper will describe the experimental problems associated with this determination as well as the development of a new test cell that significantly improves the interlaboratory reproducibility. Bulk crush strength evaluation was anticipated to be more indicative of the physical failure which

<sup>3</sup>Retired consultant



might be experienced in a catalyst bed during usage. Furthermore the crushing strength would be expected to be less sensitive to the variations in catalyst diameter or length that has been reported for single pellet crushing [1]. There are two basic experimental approaches for measuring the crushing strength of a catalyst bed. Either a load is applied by pressing a plunger onto a bed that is constrained by the walls of a cylinder [2,3] or an isostatic load is utilized [4].

The procedure selected by the committee used a uniaxial piston load applied to the top of the bed (Figure 1). Samples were dried in air at 400°C for 3h because variations in moisture content are known to affect crush strength [2]. The load was applied at 5 psi/sec and then held at the test pressure for 60 seconds. The amount of fines was determined by sieving the total sample. Data was displayed as either amount of fines for a fixed force or the force necessary to produce a given amount of fines.

With this fixture design a strong and a weak catalyst could be differentiated (Figure 2). However, there was substantial data scatter among laboratories in the crushing strength required to produce 1% fines as this value for two different laboratories could vary by as much as a factor of two. For example, for a Norton 0.3 cm diameter spherical catalyst base the crushing strength average was 650±220kg. This wide variation was deemed unacceptable by the task group. A number of variables were then investigated. As would be expected, changing sieves from a No. 12 to a No. 8 size increased the amount of fines but this variable had little influence in interlaboratory data scatter. Reducing the bed height to bed diameter (L/D ratio) from 1 to 0.25 also had a significant effect on fines generation (Figure 3) and did have some improvement in interlaboratory reproducibility. This result was not unanticipated since the applied stress is rapidly transmitted to the walls of the cylinder by shear stress from the catalyst. The axial stress carried by the catalyst bed diminishes with distance from the applied load until at great distances the cylinder walls carry essentially all of the load. Figure 4 illustrates the influence of wall friction and L/D ratio on the axial stress carried by the catalyst. The results are plotted as the ratio of catalyst stress at the bottom of the test cup to the applied stress, versus length to diameter (L/D) ratio for several values of wall friction coefficient times the Janssen [5] stress ratio coefficient. The theory behind the curves is based on the method of differential slices as described by Walker [6], which may not be accurate for small L/D ratios; however, it is qualitatively correct.

For an L/D of 1 the theory predicts that the pressure at the bottom of the cup would be significantly reduced, depending on the catalyst friction properties. Paxton and Seddon [7] demonstrated this by monitoring effective loads transmitted by beds of varying depths. Thus with a large L/D ratio very few catalyst pellets will see a significant load. A double piston arrangement can double the number of pellets seeing a given stress level. However, depending upon how the bed is packed, some catalyst pellets will always stick above the bed and be initially crushed. In fact pellets that are above the rest of the bed can create the entire amount of fines. This initial crushing could also be noted in the load displacement

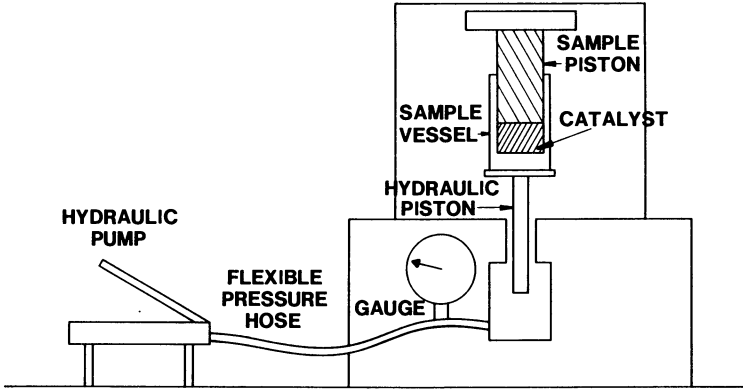


Figure 1. Configuration of uniaxial bulk crush tester.

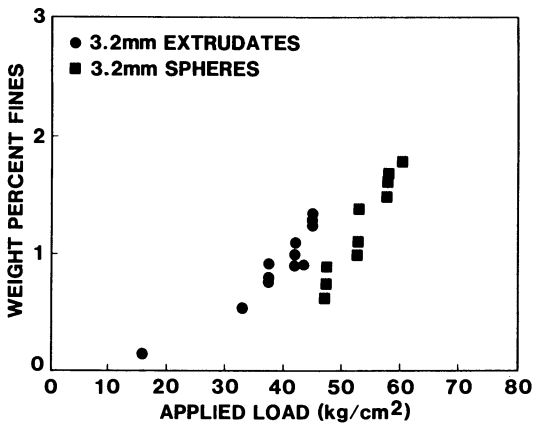


Figure 2. Bulk crushing characteristics of two different types of catalysts.

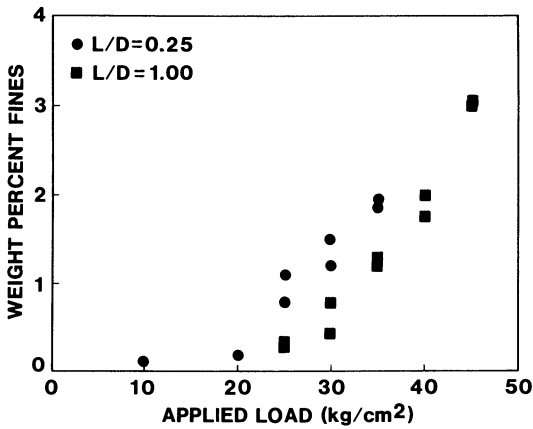


Figure 3. Effect of changing the amount of catalyst in cell, bed height (L)/bed diameter (D).

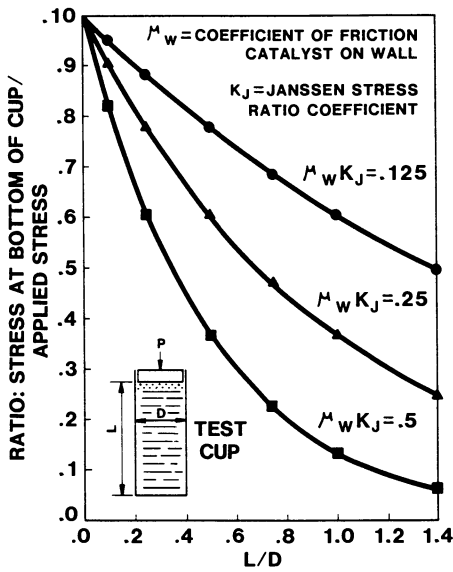


Figure 4. Influence of wall friction on axial stress.

curve (Figure 5). Several approaches can be used to minimize this problem. A rubber insert [2] or felt pad [3] in the piston has been suggested. Another possibility is to utilize steel balls at the top of the bed. These steel balls reduced the amount of fines for a given applied load; but uniform covering was difficult to achieve. Round robin evaluation was not pursued.

Even decreasing the L/D ratio to 0.25, using the same charge of catalyst to the cylinder, drying the catalyst to an identical moisture level, increasing the fines production requirement, calibrating load cells, and trying to pack the bed so that the top of the bed was of uniform height, still did not reduce the data scatter among laboratories. Data scatter could not be attributed to variations in fixtures such as wall or piston surface finish, as the exchange of piston and cylinder resulted in rather similar results when tested by a single individual (Figure 6). However, an investigation of operator controlled parameters revealed the necessity of achieving the same packing density of catalyst pellets (Figure 7). When all operators used the same vibratory method, similar fines production could be achieved for the given applied load.

Because of the criticality of achieving the same packing density, a new cell was designed that also incorporated many of the other important variables that had already been integrated into the method (Figure 8). The objective was to load a fixed volume of catalyst into the cell. To determine the amount of catalyst to add, the bulk density of the catalyst per ASTM D4180 was performed first. A similarly dried sample that would fill a 47 cm<sup>3</sup> volume was weighed and inserted into the fixed volume. Neoprene inserts at each end of the cell were utilized to prevent single pellets from crushing prematurely. Weight percent fines was then obtained after crushing the sample under various loads. Crushing strength was defined as the load required to produce one percent or some other pre-determined weight percent fines. To assure uniaxial loading a steel ball was placed on top of the piston.

To evaluate interlaboratory reproducibility, a round robin testing program was initiated. A 0.6 cm diameter spherical alumina base was supplied by Phillips Petroleum Company for this round robin test. The bulk density of as-received material was determined by ASTM D4180 and the loss of weight after a 2 hour heat treatment at 400°C was used to calculate the amount of dried catalyst base to be charged to the test cell. The variation in catalyst base loaded to the cell for all laboratories participating was less than 1.8%. After filling the cell with the appropriate amount of catalyst base that had been dried for 2 hours at 400°C, the load was applied to the cell at a rate of 10-20 kg/sec. The required load was maintained for 30 seconds. Weight percent fines were determined at loads of 817, 1135 and 1453 kg. The load required to produce 1% fines was then interpolated from the average of three runs for each loading. For the five laboratories participating in the program, the average crushing load required to produce 1% fines was 1150±90 kg. The standard deviation for this series of tests has been significantly reduced when compared to the previous round robin testing programs.

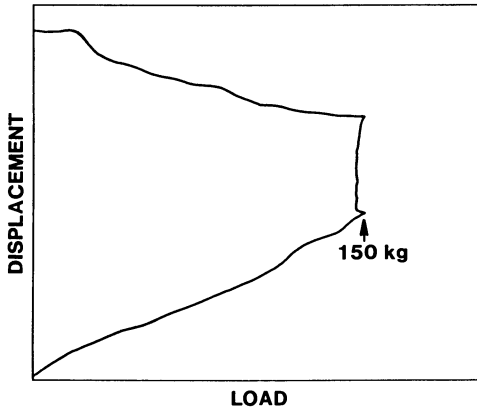


Figure 5. Load displacement curve for 3.2 mm diameter spheres.

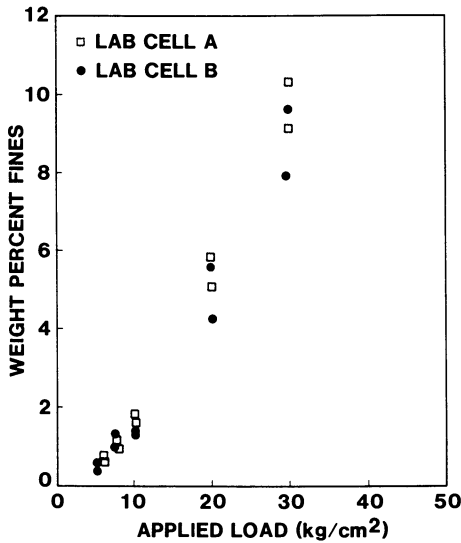


Figure 6. Minor variation in fine production from utilizing load cells fabricated by two different laboratories.

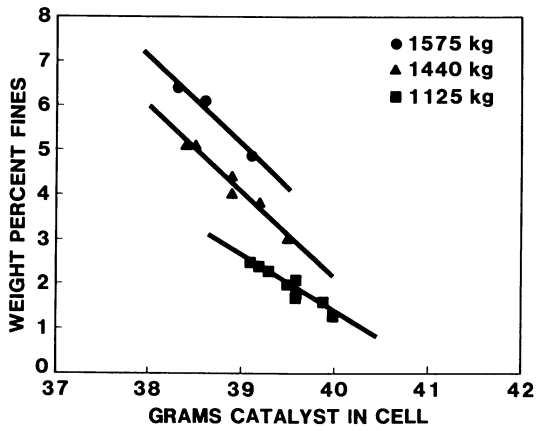


Figure 7. Effect of packing density on fines production.

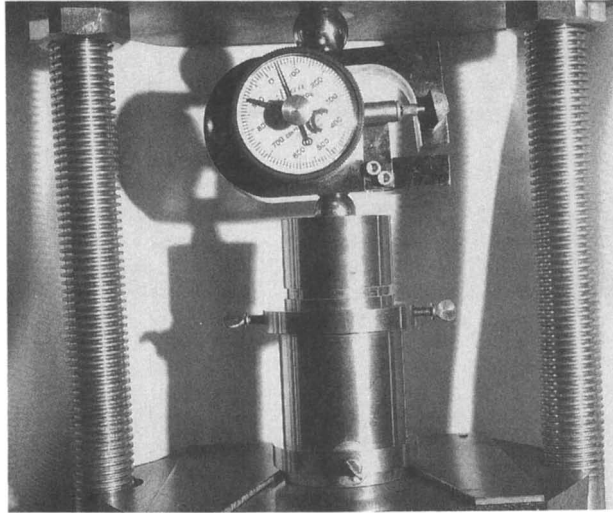


Figure 8. New test cell design.

### Conclusion

A test method for bulk crush testing of catalysts and catalyst bases has been developed that significantly reduces interlaboratory data scatter. For excellent interlaboratory reproducibility, identical packing density of the catalyst in the cell and moisture content of the catalyst must be maintained. The new cell design improves the uniformity of the applied load across the top of the bed and thus reduces the potential of premature fines formation.

### ACKNOWLEDGMENTS

Laboratories participating in these studies include Allied-Signal Engineered Materials Research Center, Phillips Petroleum, Akzo Chemie, Shell, Monsanto, Mallinckrodt, Haldor Topsoe, Nalco Chemical, American Cyanamid, Union Carbide, and Exxon Chemical.

### References

1. Hutchings, G.J.; J. Chem. Tech. Biotechnol., 1986 36, 255
2. Adams, A.R., Sartor, A.F. and Welch, J.G.; Chem. Eng. Prog., 1975 71, 35
3. Fulton, J.W.; Chem Eng., 1986 93(10), 71
4. Baillie, L.A.; U.S. Patent 4513603
5. Janssen, H.A.; Vereins Deutsch. Ing., 1845 39, 1045
6. Walker, D.M.; Chem. Eng. Sci., 1966 21, 957
7. Paxton, P.M. and Seddon, D.; Appl. Cat., 1984 12, 179

RECEIVED January 26, 1989



## Chapter 37

# Single-Pellet Crush Strength Testing of Catalysts

P. K. Brienza<sup>1</sup>

ASTM, 1916 Race Street, Philadelphia, PA 19103-1187

ASTM D-32 Committee on Catalysts has developed a standard test method for single pellet crush strength for formed catalyst shapes. This standard was issued under the fixed designation D-4179. The method is applicable to regular catalyst shapes such as tablets and spheres. Extrudates, granular materials and other irregular shapes are excluded. The committee continues to work on the development of a method for the single pellet crush strength testing of extrudates.

Single pellet crush testing has played an integral part in industry for many years. Pharmaceutical companies, for example, consider the mechanical strength of medicinal tablets to be an important property. (1)

With the development of catalytic processes such as reforming, hydrocracking and hydrotreating, which utilize formed particles, single pellet crush strength tests were devised by the manufacturers and users of such catalysts. These tests were developed in order to determine the ability of the catalyst particles to maintain integrity during use in catalytic reactors. (2)

Due to variations in sampling procedures, instrumentation, test methods and pretreatment conditions, there has been great difficulty in obtaining agreement among the tests performed in different laboratories. (2)

ASTM Committee D-32 on Catalysts was organized in order to standardize catalyst testing and a Task Group began working on single pellet crush methods with the formation of the committee.

Two round robin testing programs were carried out using spheres, tablets and extrudates. Testing conditions were controlled in order to minimize inter-laboratory variations; however, the use of

<sup>1</sup>Chairman of ASTM D32.02 Subcommittee on Physical-Mechanical Properties of ASTM D-32 Committee on Catalysts. Mailing address: 66 Emerson Avenue, Apt. B 18, Wall, NJ 07719

identical crush test instruments was not required. Test equipment used included load cell hardness testers, in-house designed computer operated systems and commercial crush test apparatus. Representative samples were provided and a test portion of 50 to 200 pellets was obtained by riffing or splitting. The samples were then heated at 400°C for 3 hours and cooled in a desiccator, since moisture absorption by hygroscopic catalytic materials has been shown to affect crushing strength. (3)

The compression testing device was required to have a calibrated gauge and a system that provided a uniform rate of force application in the range of 1 to 10 lbf/s.

The single catalyst pellets of spheres and tablets (in radial orientation) were placed between the flat anvils of the compression testing instrument by use of tweezers or other suitable device. Force was then applied at a uniform rate in the range of 1 to 10 lbf/s until the pellets crushed or collapsed. When all the pellets in the sample were tested, the average crush strength, standard deviation and 80% spread were reported. The 80% spread was defined as the range in which 80% of the individual pellet strengths are expected to fall, assuming that individual pellets form a normal distribution.

Results of the second round robin testing of spheres and tablets are shown in Tables I and II. These data are included in ASTM Research Report Number 1004 for Standard Test Method D-4179 for Single Pellet Crush Strength of Formed Catalyst Shapes.

Table I. Product Characteristics (lbs. force)

<u>Test Sample</u>	<u>Mean Crush Strength(1)</u>	<u>Within-Sample Variation</u>	
		<u>Std. Dev.(2)</u>	<u>Typical 80% Spread(3)</u>
1/8" Spheres (EAS-480)	19.27	6.75	10.6 to 27.9
1/8" Tablets (GSAT-480)	16.43	5.38	9.5 to 23.3

(1) Mean of 6 tests each by 6 laboratories.

(2) Average value of the within-sample standard deviation (S.D.) of the 36 tests.

(3) Based on: Mean Strength + 1.28 S.D. within sample.

Table II. Test Precision (lbs. force)

Test Sample	Within a Laboratory	Between Labs	
	95% Reliability of Mean of 100 Pcs. (1)	95% Overall Repeatability (2)	95% Spread of Laboratory Means
1/8" Spheres (EAS-480)	<u>+1.40</u>	<u>+1.47</u>	<u>+1.15 (4)</u>
1/8" Tablets (GSAT-480)	<u>+1.13</u>	<u>+1.34</u>	<u>+1.97</u>

- 1) Calculated as  $\pm 1.96 \times \text{S.D. within-sample} \sqrt{100}$
- 2) Includes Reliability of Mean of 100 pieces, plus within-day and day-to-day laboratory variation.
- 3) Calculated as  $\pm 1.96 \times \text{S.D. of laboratory means around grand mean of all laboratories.}$
- 4) Based on classifying one of the 6 reporting laboratories as an outlier. For all 6 laboratories, the figure here was +5.56.

Standard D-4179 specifically excludes the testing of granular materials, other irregular shapes and extrudates. It was never planned to include irregularly shaped materials within the scope of a single pellet crush test method; however, extrudate testing was included in the original procedure. This was done by modifying one of the flat anvils to form a 0.125 in. bar shaped cross section on the anvil and reporting results as lbf/0.125 in. (Figure 1)

The interlaboratory precision for extrudate crush strength testing was so poor in both of the round robins, that it was decided to publish the method for regular shapes only, and have the task group continue to work to improve extrudate testing.

A subsequent round robin, using three extruded alumina samples, showed not only multi-lab error but poor within-lab reproducibility as well (Table III).

The participating laboratories then responded to a detailed questionnaire regarding exact test methodology. It was discovered that three laboratories were using testing practices outside the method. Two of the labs were withdrawn from the round robin, one because the force application did not comply with the procedure requirements and a second because sample exposure was too long and testing was not repeated. The third laboratory repeated the test using the correct force application and data from an additional lab were

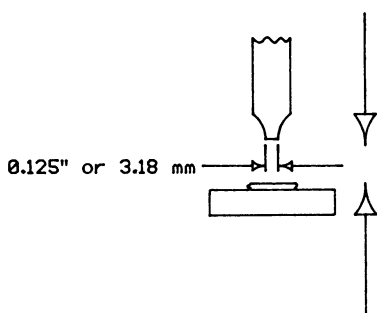


Figure 1. Method of test for radial crush strength of extruded catalyst shapes.

Table III. Extrudate Radial Crush Strength

Extrudate Designation	M-9			K-6		J-5	
	Lab	lbf	% of $\bar{X}$	lbf	% of $\bar{X}$	lbf	% of $\bar{X}$
Within sample variation (+ 2S)	B	+ .21	+4.6%	+ .90	+5.5%	+ .43	+5.6%
	D	+ .15	+2.3%	+ .75	+3.8%	+ .34	+3.7%
	F	+ .37	+5.0%	+1.22	+6.2%	+ .65	+6.3%
	J	+ .39	+4.3%	+1.41	+5.1%	+ .81	+5.6%
	E	+ .59	+5.2%	+1.45	+5.5%	+ .92	+5.6%
	Avg		+4.3%		+5.2%		+5.4%
TOTAL WITHIN LAB ERROR (+ 2S)	B	+ .33	+7.2%	+2.67	+16.4%	+ .98	+12.9%
	D	+ .97	+15.1%	+1.92	+9.6%	+ .90	+9.6%
	F	+1.82	+24.9%	+2.55	+13.1%	+ .82	+8.1%
	J	+2.00	+22.3%	+2.05	+7.4%	+1.30	+8.9%
	E	+3.50	+30.9%	+2.42	+9.2%	+2.58	+15.8%
	Avg		+20.1%		+11.1%		+11.1%
MULTI-LAB ERROR		+69.3%		+45.3%		+64.6%	

added. (Table IV). The revisions significantly reduced the differences among laboratories, however, the results remained unsatisfactory.

The Task Group then decided to conduct a round robin using pencil leads in an attempt to establish a non-hygroscopic (albeit non-catalytic) standard.

Results of this round robin (excluding laboratories using other than 0.125 in anvils), shown in Table V, still demonstrate a less than satisfactory inter-laboratory variation in crush results among nine laboratories using different pieces of crush strength apparatus. In addition, one of the laboratories conducted experiments which indicated moisture

Table IV. Extrudate Radial Crush Strength  
Summary of Revised Results

Extrudate Designation	M-9		K-6		J-5		
	LAB	lb/ $\bar{X}$	lb/ $\bar{X}$	% OF $\bar{X}$	lb/ $\bar{X}$	% OF $\bar{X}$	
100							
Within Sample Variation (+ 2S)	D	+ .15	+2.3%	+ .75	+3.8%	+ .34	+3.7%
	F	+ .37	+5.0%	+1.22	+6.2%	+ .65	+6.3%
	J	+ .39	+4.4%	+1.41	+6.0%	+ .81	+5.8%
	I	+ .44	+5.6%	+1.49	+6.0%	+ .77	+6.2%
	G	+ .35	+4.1%	+1.22	+5.3%	+ .70	+5.7%
	Avg	+ .34	+4.28%	+1.22	+5.46%	+ .65	+5.5%
TOTAL WITHIN LAB ERROR (+2S)	D	+ .97	+15.1%	+1.92	+9.6%	+ .90	+9.6%
	F	+1.82	+24.9%	+2.55	+13.1%	+ .82	+8.1%
	J	+2.00	+22.6%	+2.05	+8.7%	+1.30	+9.3%
	I	+0.96	+12.4%	+2.63	+10.6%	+1.37	+11.0%
	G	+2.08	+24.7%	+5.06	+22.4%	+3.58	+27.8%
	Avg	+19.9%			+13.6%		+13.2%
LAB-TO-LAB DIFFERENCES		+20.9%		+19.2%		+31.8%	
MULTI-LAB ERROR		+28.8%		+23.5%		+34.5%	

Table V. Crush Strength Round Robin  
Test on Pencil Leads

1. Grand Average and Mean Standard Deviations

LABORA- TORY CODES	PENCIL LEAD: B SOFT TYPE R		PENCIL LEAD: HB MEDIUM TYPE R		PENCIL LEAD: H MED HARDTYPE R	
	GRAND AVE (X) lbf.	MEAN STD. DEV.	GRAND AVE (X) lbf.	MEAN STD. DEV.	GRAND AVE (X) lbf.	MEAN STD. DEV.
A	10.73	2.09	11.92	2.00	16.53	3.25
B	10.76	0.48	10.78	0.48	14.18	0.638
C	11.39	0.77	11.89	0.87	15.71	1.44
D	14.00	0.92	15.47	1.40	20.87	2.34
F	13.12	1.83	14.06	1.46	16.95	2.54
G	10.07	1.16	10.53	1.09	13.45	1.63
H	11.39	1.40	12.46	1.44	15.62	2.15
I	14.07	1.43	15.23	1.30	20.40	2.48
J	13.78	1.75	14.20	1.67	18.85	3.410

absorption by the pencil leads, since crushing strength increased after drying for 3 hours at 100°C.

At a subsequent meeting of ASTM D-32 Committee on Catalysts, the Task Group decided to revise the extrudate test procedure to exclude the use of the 0.125 in. anvil. Instead, a procedure used in the laboratories of several members of the group, in which extrudate particles are measured for length and crushed between flat anvils, will be adopted. In addition, the method will include the use of a flow of dry nitrogen over the particles during the test. This alternate procedure will test the validity of the group's assumption that the two main causes of differences in test results are the variations caused by the anvil and by moisture absorption.

An additional round robin, utilizing several varieties of extruded alumina will be carried out.

### Conclusion

A test method for single pellet crush testing of catalytic spheres and tablets was developed by ASTM Committee D-32 on Catalysts. A procedure for the single pellet crush strength of extrudates that gives satisfactory interlaboratory variation is yet to be attained. An alternate method will test the assumption that the interlaboratory variations, seen in all round robins, were caused by moisture absorption during testing and the use of a specialized anvil in the test instrument.

### Acknowledgments

Laboratories participating in these studies include Allied-Signal Engineered Materials Research Center, Akzo Chemie, Shell, Monsanto, Exxon, Haldor-Topsoe, Union Carbide, Mallinckrodt, Norton, General Motors, W. R. Grace, Engelhard, American Cyanamid, Criterion, Arco, United Catalyst, Ashland, Filtrol, Gulf, Air Products, and Amoco.

### Literature Cited

1. Brook, D.B.; Marshall, K. J. Pharmaceutical Sciences 1968 57, 481.
2. Beaver, E.R. Chem. Eng. Prog. 1975, 71 44.
3. Adams, A.R.; Sartor, A.F.; Welch, J.G. Chem. Eng. Prog. 1975 71 35.

RECEIVED June 20, 1989

## Chapter 38

# Attrition- and Metal-Resistant Fluid Cracking Catalyst Prepared with Alumina Powder in the Matrix

L. A. Pedersen<sup>1</sup>, J. A. Lowe, and C. K. Matocha, Sr.

Alcoa Laboratories, Aluminum Company of America,  
Alcoa Center, PA 15069

Slurry rheological measurements, fluidized bed attrition studies, and microactivity tests (MAT) were used to evaluate fluid cracking catalyst formulations containing Alcoa's rehydration bondable CP alumina powder. When process variables, including viscosity, pH, batch holding time, and alumina particle size, are controlled, spray dried material incorporating CP alumina is more attrition resistant than an alumina-free reference. Macrostructure of the spheres is more uniform than that of some commercial catalysts. MAT results for the catalytic cracking of gas oil show that the ReY based catalyst has about 81 v/o conversion before and 54 v/o after Ni+V poisoning. This contrasts with values of 78 and 34 for the reference catalyst without the alumina. Before poisoning, selectivity for the gasoline fraction is comparable to a commercial catalyst.

Recent literature shows a growing trend to include free alumina in the formulation of fluid catalytic cracking (FCC) products. Over the last dozen years, FCC catalysts containing free alumina have been cited in the open and patent literature for benefits including: (1) enhanced catalyst reactivity and selectivity (1-3), (2) more robust operation in the presence of metals in the petroleum feedstock (4-7), (3) improved attrition resistance (8,9), (4) improved hydrothermal stability against steam deactivation during regeneration (2,8), (5) increased pore volume and decreased bulk density (8), and (6) reduction of SO<sub>x</sub> emissions (10).

Alumina promoted FCC catalysts are commercially viable if, and only if, the alumina component produces the desired properties without detrimentally affecting the attrition resistance and the cracking activity of the finished catalyst particle. Previous work (8,9,11) indicated that attrition resistant catalysts containing alumina could be formed only if a highly dispersed, pseudoboehmitic alumina was used. Other studies have demonstrated catalytic performance improvement without determining the attrition character of the catalyst (1-7).

Research into the properties and applications of Alcoa's rehydration bondable alumina powders (CP series) has been reported (12-14). The objective of this study was to determine if rehydration bondable aluminas could be successfully incorporated in the matrix of a conventionally formulated FCC catalyst. Success was based on meeting three criteria. First, addition of the alumina would not inhibit the fabrication of well-formed microspheres with diameters typical for FCC catalyst particles.

<sup>1</sup>Current address: Saint Vincent College, Latrobe, PA 15650



Second, the alumina would not cause a serious deterioration of the attrition resistance of the microspheres. Third, the alumina-containing material had to have reasonable cracking activity as measured by conversion and product selectivity.

To achieve these criteria, we needed to establish standard processing and characterization procedures for FCC catalysts. In particular, a process for making microspheres of controlled size distribution and shape, independent of composition, had to be defined. Also, an approach for obtaining the intrinsic attrition rate of commercial grade and experimental catalysts had to be adapted from a method for alumina. This paper describes these methods and shows that the substitution of CP alumina for part of the clay in a commercially viable FCC formulation can improve attrition behavior and enhance catalytic activity, especially in the presence of Ni+V poisoning.

### Experimental

**Catalyst Formulation.** The experimental samples were prepared following the method of Ostermaier and Elliott (15) and comprise two groups: (1) alumina-free reference catalysts, and (2) alumina-added catalysts. The reference catalysts contained about 2 wt%  $\text{Al}_2\text{O}_3$  as a result of buffering the hydrosol with acid alum. Group 1 materials were formulated to contain 17 wt% Y zeolite, 18 wt%  $\text{SiO}_2$ , 2 wt%  $\text{Al}_2\text{O}_3$ , and 63 wt% kaolin clay. Group 2 samples were prepared with a CP-x transition alumina or commercial pseudoboehmite additive and contain 20 wt% added  $\text{Al}_2\text{O}_3$  in place of a portion of the kaolin clay. Group 2 samples are identified as CP-formulated or pseudoboehmite-formulated catalysts. The CP-x alumina additives (x is the median particle size in microns) are X-ray indifferent, rehydration bondable powders produced by the Aluminum Company of America. (CP-25 was obtained by air classifying CP-100). The commercial pseudoboehmite was obtained from Vista Chemicals.

**Catalyst Preparation.** A silica sol was prepared by blending sodium silicate (Diamond Shamrock Grade 40) and acid alum in a high shear, in-line mixer. Then, a 0.4  $\mu\text{m}$  kaolin clay (Thiele RC-32) was dispersed in the vigorously agitated, fresh sol by gradual addition of the solid. Next, the Y zeolite and (optional) free alumina were added as acid dispersions. We used sodium Y zeolite (PQ Valfor CP300-66), prepared as a 16 wt%, pH 4 slurry, for attrition samples. MAT test samples were prepared with the same zeolite after 68% of its sodium was exchanged with  $\text{LaCl}_3$ . The alumina additives were prepared by dispersing the solids at 12.5 wt% in  $\text{H}_2\text{SO}_4$  water at pH 4. Addition of the clay, zeolite, and free alumina resulted in pH 3 spray dryer feed at 20 wt% solids. The slurry was pumped to a 7 ft diameter Bowen rotary atomized spray dryer. Disc velocity, feed rate, and temperature were adjusted for 60-80  $\mu\text{m}$  average particle diameter spheres. The spray dryer product was slurried at 10 wt% in hot water, decanted, reslurried, and aged at 80°C for 1 h. Ammonium hydroxide was added as needed to maintain the reslurry at pH 5. The hot water aged solids were filtered, rinsed, and oven dried.

**Catalyst Characterization.** Particle size distributions of oven dried products were determined with a Microtrac Particle Size Analyzer. PH, PM, and PS are the diameters corresponding to the 90th, 50th, and 10th percentiles, respectively, on the distribution curve. Particle microstructures were obtained with an ISI-SX-40 scanning electron microscope.

### Attrition Measurement.

**Apparatus.** The Attrition Index Analyzer (AIA) is shown in Figure 1. The instrument, a modification of the Forsythe and Hertwig design (16), was developed at Alcoa Laboratories to improve and standardize, within Alcoa, the measurement of attrition resistance for calcined and hydrate aluminas. The instrument and test

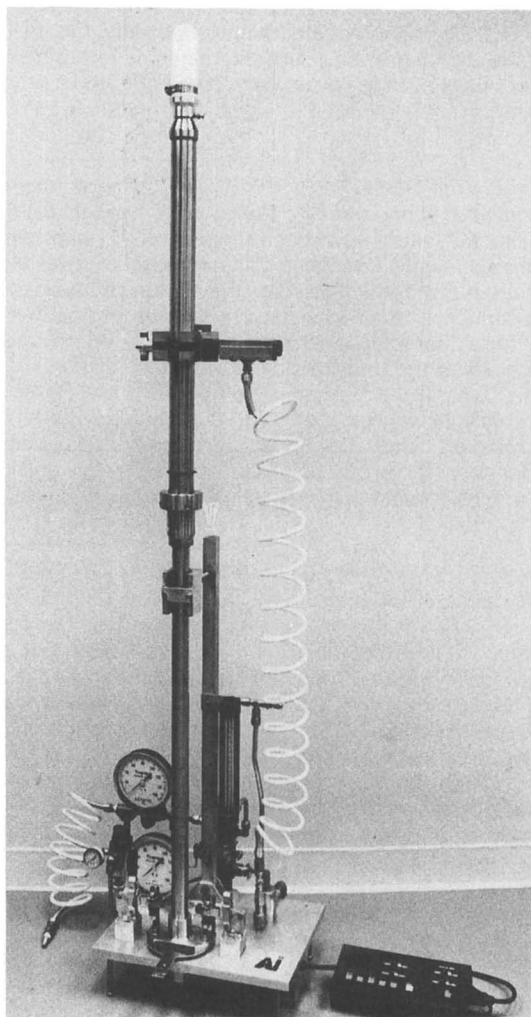


Figure 1. Attrition index analyzer.

procedure are unique in that both attrition and elutriation character can be investigated. The Elutriation Profile characterizes the generation of the material transported into the collector with time. Because of its small particle size (95% <20  $\mu\text{m}$  for calcined alumina) material collected is often referred to as dust. The two-stage column has a traditional 1.00-inch diameter attrition zone followed by a 1.50-inch diameter elutriation zone. Wall effects are minimized because the stainless steel tube is honed to a smooth finish, the tube is grounded to reduce electrostatic charge, and the column is automatically rapped during the test to dislodge particles which still accumulate on the wall of the tube. The development and use of the AIA instrument with alumina samples have been previously presented (17,18).

**Sample Preparation.** Seventy grams of sample, previously calcined at 538°C, was dispersed in about 125 mL of sodium metaphosphate solution and "wet screened" using a sieve stack of 250, 270 and 325 mesh, 8-inch diameter sieves. The sieves were washed with water until the effluent was free of any particulate and then rinsed with acetone to de-water. After air drying, the contents of each sieve were transferred to a porcelain dish and the material was recalcined at 538°C. Appropriate weights taken during this procedure allowed for the determination of percent moisture in the starting material and sieve analysis relative to the appropriate sieve fractions. The total +325 mesh material was recombined and mixed for the test.

**Measurement.** The operating parameters for the tests on commercial and experimental FCC catalysts are summarized in Table I.

Table I. Attrition Test Operating Parameters

Test Constant	Value
Sample	40.0 g +325 mesh Calcined at 538°C
Attriting/Media Flow Rate	Air, 70 psig 13.7 scfh (760 mm Hg, 0°C)
Attrition Tube Material Reaction Zone Expansion Zone	Two-staged, 60.0 in Stainless steel, honed bore 1.00-in i.d. X 30-in 1.50-in i.d. X 30-in
Orifice, diameter	0.0150-in
Time	90 min, interrupted each 15 min for Response Curve
Rapping	One-second on one min cycle
Elutriated Fines	Trapped and removed by Collector

The Elutriation Profile requires determination of the increase in the collector weight with time. To provide this information, the test is stopped at 15 minute intervals, the dust is allowed to settle, and the collector assembly is removed, weighed, and then repositioned. The test is continued for an accumulated attrition time of 90 minutes. After the last interval measurements, the total weight of the material collected is determined. The portion remaining inside the column, the bed

material, is also removed and weighed. A Ro-Tap sieve analysis is performed on this latter fraction using a sieve nest having the following mesh sizes: 150, 170, 200, 250, 270, and 325. The weight of the material in the collector is added to the weight of the -325 mesh fraction from the Ro-Tap analysis. The increase in the -325 mesh fraction due to attrition is divided by the weight of the +325 mesh material charged to the column and normalized for 60 minutes. This value is reported as the Attrition Index, AI. The standard deviation of this determination is 0.1 for samples with AI <12. Response Curves for the Elutriation Profile are generated by plotting the increase in collector weight for each 15 minute interval of the 90 minute test.

**Catalytic Cracking Test.** A standard microactivity test (MAT) was used to evaluate the conversion and selectivity of catalyst samples. The tests were done at the University of Pittsburgh's Applied Research Center (former Gulf Research Laboratory), a qualified laboratory for MAT evaluations. A standard method, developed by Gulf, was used without modification. A Cincinnati gas oil was cracked under the following conditions: cat/oil=3, 16 h<sup>-1</sup> WHSV, and 516°C. Prior to charging the reactor, all samples underwent a standard thermal pretreatment. Solids were first heat shocked for 1 h at 593°C. Next, selected materials were impregnated with 3000 ppm Ni and 6000 ppm V, as naphthenates. Then all samples were calcined for 10 h at 538°C. Finally, each material was steamed at 732°C for 14 h in a fluidized bed to produce a catalyst in a simulated equilibrium state.

## Results and Discussion

**Microsphere Formation.** Because the microspheres were fabricated using a batch process, we monitored the viscosity and pH of the catalyst slurry as it aged. Figure 2 shows that the viscosity of the slurry was dependent on both the age of the slurry and the additive type. The reference formula was stable for 3 h, but the CP-alumina and pseudoboehmite formulations thickened or gelled in the same time period. A typical batch starting at pH 3.0 increased to about pH 3.3 before the onset of thickening (about 100 cP). For CP formulations, the onset of thickening may be related to the median particle size of the powder.

We believe the effect of alumina additives on catalyst slurry viscosity is associated with the surface reactivity of the additive. OH<sup>-</sup> is a catalyst for polymerization and Si-O-Si bonding of uncondensed silanols; higher pH promotes conversion to a solid phase consisting of discrete silica particles (19). Ostermaier and Elliott (15) suggest that pH be carefully controlled at a value less than 3.5, or thickening occurs in the alumina-free reference formula.

Once the conditions for making a processible catalyst slurry were established, microspheres were generated using the reference formula with and without the different alumina powders. Table II summarizes particle size distributions for typical commercial FCC and our experimental catalysts. Two commercial samples (Catalysts V and VI) had particle sizes much higher than we could produce with our spray dryer. However, the size distributions of the experimental catalysts approximate those of the other four commercial grades.

Figures 3 and 4 illustrate the particle size distribution and shape of the commercial and experimental microspheres, respectively. In Figure 3, the 100X SEM micrographs demonstrate that a wide range of particle shape and size occur in the commercial materials. The variation in fines content, evident in these photographs, led us to develop an attrition method that was independent of the initial fines content. The experimental products in Figure 4 show a higher degree of sphericity and size uniformity than the commercial samples. Hence, the structure and quality of our microspheres did approximate known FCC catalysts. Also, no significant difference existed between alumina-containing and alumina-free particles. With these results, the first criterion for success was met.

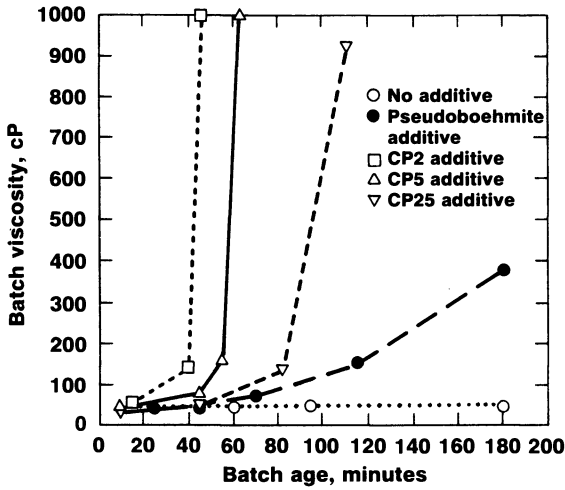
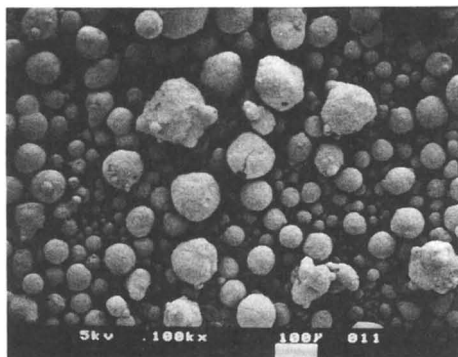
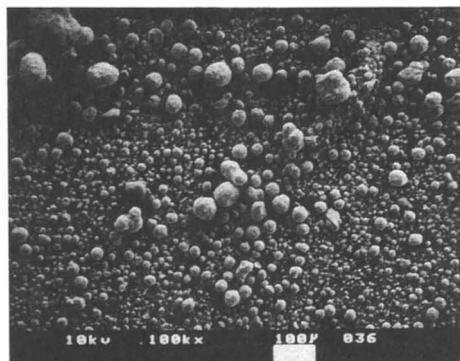


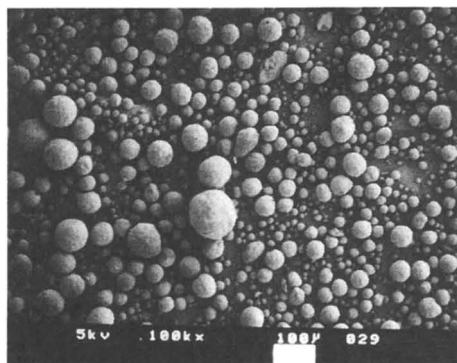
Figure 2. Effect of additive on viscosity of the catalyst slurry.



**(a) Catalyst I**

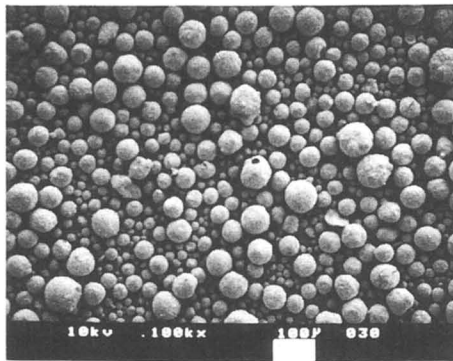


**(b) Catalyst II**

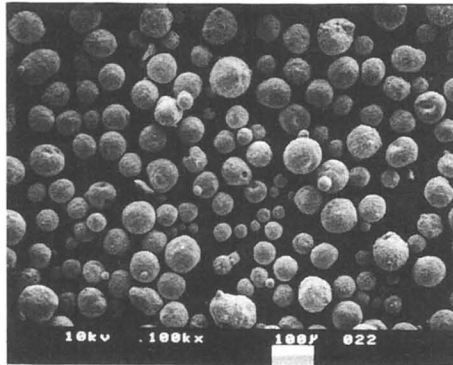


**(c) Catalyst IV**

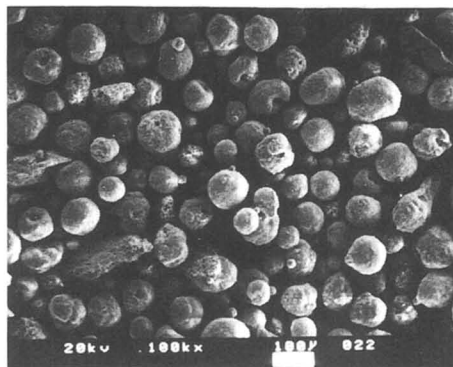
Figure 3. Commercial FCC catalysts at 100X.



(a) Reference (alumina-free)



(b) CP-2 additive



(c) CP-25 additive

Figure 4. Experimental FCC catalysts at 100X.

Table II. Particle Size Distributions of Catalyst Samples

Catalyst	Particle Size, $\mu\text{m}$		
	PH (90% $\leq$ )	PM (50% $\leq$ )	PS (10% $\leq$ )
<b>Commercial Samples</b>			
Catalyst I	132	72	37
Catalyst II	122	64	23
Catalyst III	130	82	48
Catalyst IV	125	70	38
Catalyst V	183	91	45
Catalyst VI	179	94	42
<b>Experimental Samples</b>			
Reference (1)	101	61	34
Reference (4)	136	81	45
CP-2 (1)	113	68	39
CP-2 (4)	128	74	43
CP-5 (1)	104	65	36
CP-25 (1)	117	68	41
Pseudoboehmite (1)	103	63	34

( ) Hours silica sol aged.

**Attrition.** To demonstrate acceptable attrition resistance of various catalysts, it is desirable to compensate for the variations in fine particle content of the samples. Forsythe and Hertwig empirically compensated for this dilution effect by reporting the increase in the -325 mesh material relative to the +325 mesh content of the starting material (16); most adaptations of their procedure do likewise (20). We suggest that a more universal and discriminating test for specifically evaluating attrition resistance is obtained by removal of the -325 mesh material prior to the test. A "wet sieve" procedure to remove the -325 mesh material prior to testing was adapted. The test, therefore, measured the intrinsic attrition resistance of the sample, thus allowing direct comparison.

The cumulative weight increases in the collector for the "15-Minute" intervals were used to construct a Response Curve for the generation of fines due to attrition. The Response Curve is a plot of time as the abscissa and the corresponding percent collector fines as the ordinate. The Response Curve concept was introduced and discussed in reference 18. Three types of Response Curves have been identified for alumina:

*Type 1* -- An initial rapid increase in Collector weight followed by a period in which the attrition and removal remain constant for the period of interest.

*Type 2* -- A linear response in which the attrition and removal remain constant for the period of interest.

*Type 3* -- A slow increase at the start before the attrition and removal become constant for the period of interest.

Type 3 Response Curves are typical of samples that have a low fines content and/or spherical particles that attrit at a rate represented by the slope of the near linear region. Since the -325 mesh fraction was removed, Type 3 Response Curves were anticipated.



Response Curves for two commercial and three experimental catalysts are shown in Figure 5. Inspection shows that the period of near linear response was from 45 through 75 minutes. This linear response appears to be associated with a period when the dynamics of the bed are in equilibrium. This behavior demonstrates that the maximum attrition time for this class of samples could be reduced to 75 minutes. The shape of the Response Curve and the rate the collector fines were generated (as represented by the slope of the near linear portion) have the potential to be correlated with the catalyst makeup rate in commercial applications.

The data in Figure 5 can be examined from three viewpoints. First, the curves of the Reference and CP-2 samples resemble that of a commercial material (Catalyst I) that has a low Attrition Index (5.3). Second, the CP-2 curve rises at a slower rate than the Reference. This indicates more attrition resistance in the CP-2 alumina formula. Finally, the pseudoboehmite formula produced fines much more rapidly than the CP-2 product. These findings suggest that the rehydratable alumina is a superior binder for some FCC formulations.

The effect of catalyst slurry and sol age time on the Attrition Indexes of the CP-formulated samples is seen in Table III. There is a trend toward greater attrition as the batch holding time increases for both CP-2 products. Concomitantly, the viscosity range becomes higher, as was observed previously. CP-5 also appears to lose attrition resistance as the age and viscosity of the slurry advance. On the other hand, the holding time does not impact the CP-25 Attrition Index. The CP-2(4) material, made with a sol aged 4 hours, exhibits lower AI values, and, perhaps, a longer useful batch lifetime.

Table III. Effect of Processing Conditions on Attritability of CP-Formulated Catalyst

Additive	Batch Age, min	Viscosity, cP	Attrition Index
CP-2 (1)	0-15	30-50	5.2
	15-45	<sup>a</sup> 50-200	11.7
	110-140	<sup>a</sup> 400-500	14.5
CP-2 (4)	0-35	20-30	3.5
	35-70	30-60	6.8
	70-95	60-230	12.7
CP-5 (1)	0-45	40-80	8.8
	45-70	80-1440	12.9
CP-25 (1)	0-45	30-50	10.7
	85-115	140-920	10.3

( ) Hours silica sol aged.

<sup>a</sup> Acid added.

When the slurry ages, the pH rises, and, consequently, the viscosity rapidly elevates, there appears to be a breakdown in the mechanism that binds the solid particles in the silica matrix. With a well-developed sol, this behavior is more controllable. We believe that, at longer aging times, the microgel development proceeds by mechanisms more favorable to a finely textured, fibrillar structure (19). Hence, catalysts bound with this gel are more attrition resistant. We suggest that the dependence of attrition on slurry age/viscosity may be a consequence of an inhibition to forming a strong matrix. The most important conclusion that can be drawn from

the data in Table III is that slurry viscosities must be kept low to have low attrition, CP-formulated products. This observation is independent of particle size. This condition can easily be achieved with a continuous process where slurry age and pH are controlled.

The trend to improved attrition resistance as the CP particle size decreases is illustrated in Figure 6. The bar graph plots the AI against median particle diameter of the aluminas. We suspect that CP-2 offers the most binding sites per unit volume of particles. Also, there are more nuclei of CP-2 than CP-25 in equivalent slurry volumes. Consequently, more surface functionality is available for condensation of the polysilicic acid moieties and the CP-2 material is the least attritable.

Table IV gives the Attrition Indexes for the commercial and experimental samples. These values are reported for microspheres that were spray dried before the viscosity of the slurry exceeded 100 cP. The data show, again, that sol age and particle size of the CP alumina affect attrition. Sol age also seems to reduce the influence of the CP-2 as a binder. The Reference (4) has an AI of about 3 which is comparable to the index for CP-2(4). The important point here is that the alumina particles can be incorporated into a standard FCC formula to change catalytic activity without a detrimental effect on attrition resistance.

Table IV. Attrition Indexes of Catalyst Samples

Catalyst	Attrition Index
Commercial Samples	
Catalyst I	5.3
Catalyst II	9.2
Catalyst III	9.1
Catalyst IV	11.0
Catalyst V	11.1
Catalyst VI	4.6
Experimental Samples	
Reference (1)	6.9
Reference (4)	3.0
CP-2 (1)	5.2
CP-2 (4)	3.5
CP-5 (1)	8.8
CP-25 (1)	10.7
Pseudoboehmite (1)	<sup>a</sup>

( ) Hours silica sol aged.

<sup>a</sup> Could not be quantified by this test.

The friability of the pseudoboehmite-formulated material is illustrated in Figure 7, which gives the 100X and 400X views for (a) the freshly spray dried product and (b) the product after 10 bed volumes of water were filtered through the sample. Severe cracking of the microspheres, which are already flawed as seen in (a), is induced by a less rigorous procedure than was routinely used to process spray dried particles and to prepare the attrition specimen. These photographs support the conclusion that the addition of pseudoboehmite, under the same conditions used for CP alumina, weakened the matrix. Although this contrasts with the Filtrol findings (7,8,11), the basic FCC formulation for this work was quite different from Filtrol's. There is little doubt that the specific chemistry of the catalyst synthesis significantly

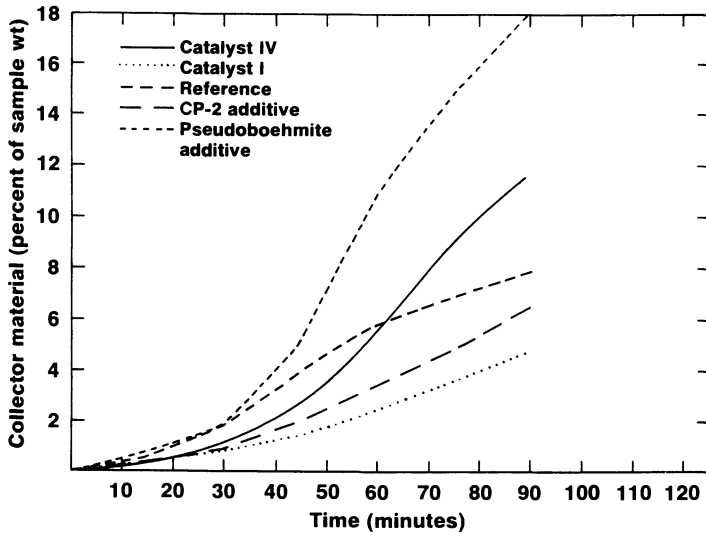


Figure 5. Typical response curves for commercial and experimental FCC catalysts.

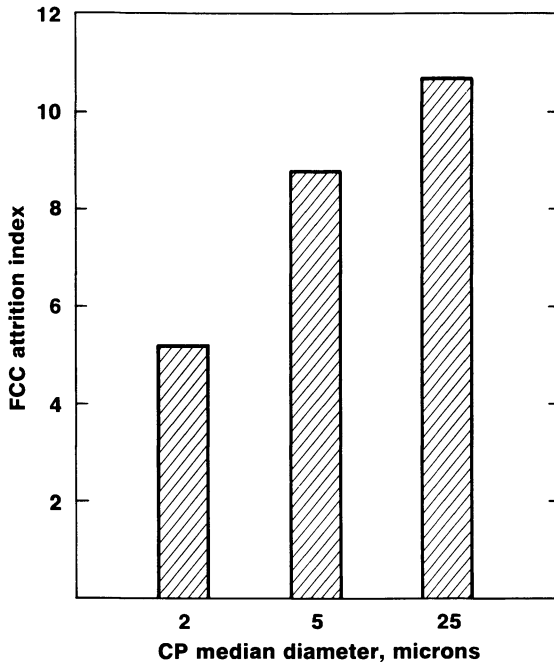


Figure 6. FCC attrition index vs particle size of CP alumina additive.

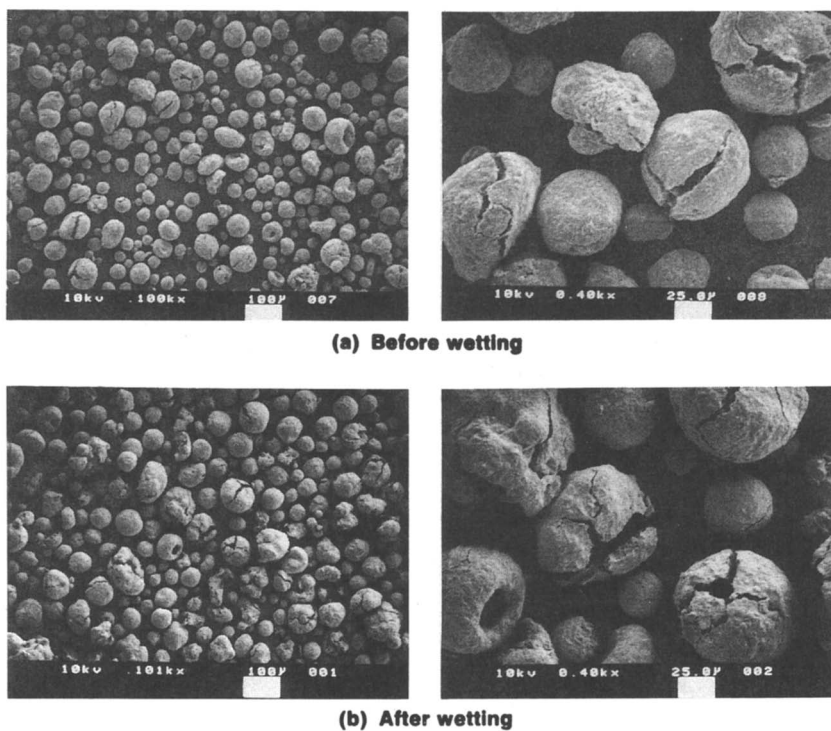


Figure 7. Microspheres with pseudoboehmite additive at 100X and 400X.

impacts the effect of the alumina additive. Hence, it is not possible, at this time, to compare our results with Filtrol's.

The data in Table IV show that CP-formulated samples have excellent intrinsic attrition resistance. The AI of 3.5 for CP-2(4) exceeds the performance of all six commercial samples tested; even 10.7 for CP-25 is within the range of AI values obtained for the commercial materials. With rehydratable alumina in the matrix, microspheres with superior attrition resistance can be manufactured. Thus, the second criterion for success was met.

Catalytic Activity. Table V gives the analytical output from MAT evaluations of Catalyst VI, a baseline sample, and from CP-2 and the Reference, before and after metals poisoning. The experimental samples were made using the formulations which produced the materials with the lowest AIs. Catalyst VI was selected for baseline data because the chemical composition was the best match between one of the commercial FCC catalysts and CP-2. Total rare earths were 2.76 wt% (La, Ce, Nd, and Pr) for Catalyst VI and 2.42 wt% (only La) for CP-2. Also, Catalyst VI had 48 wt%  $\text{Al}_2\text{O}_3$ , 46 wt%  $\text{SiO}_2$ , and 0.34 wt%  $\text{Na}_2\text{O}$ . Nominally, the CP-2 formulation consists of about 45 wt%  $\text{Al}_2\text{O}_3$ , 52 wt%  $\text{SiO}_2$ , and 0.9 wt%  $\text{Na}_2\text{O}$ . Catalyst VI had the highest alumina analysis; the other 5 commercial samples contained about 35 wt%  $\text{Al}_2\text{O}_3$ .

Inspection of the data in the table reveals several important observations. For the metals free tests, the two experimental samples have higher conversion than Catalyst VI. On the basis of 100% conversion, CP-2 yields more gasoline grade product than the Reference. Of the three materials, Catalyst VI is the most selective for  $\text{C}_5+$ . As expected (5), the alumina formulated catalyst has a high coke make. CP-2 also produces less light catalytic gas oil (LCGO) and heavy gas oil (HGO) fractions than Catalyst VI or the Reference. When the Reference and CP-2 catalysts are poisoned with Ni and V, conversion is significantly reduced. However, the effect is less severe for the alumina-added material. Others (5-7) have reported that free alumina in the matrix enhances the ability of the catalyst to withstand heavy metals poisoning.

Figure 8 provides a means to compare the performance of the CP-2 formulated material against that of the Reference (before and after metals poisoning) and of the commercial standard (no poisoning). The performance factors were developed from the FCC literature. To have an improved cracking catalyst, conversion, gasoline, and  $\text{iC}_4/\text{C}_3 + \text{C}_4$  olefins, ideally, should be higher. On the other hand, LCGO, HGO, light gases,  $\text{H}_2$  production, and coke are desired to be lower (21).

For metals free behavior, the CP-2 meets all of these criteria except coke make when contrasted with the Reference. Against the commercial catalyst, CP-2 fared very well except for coke. The gasoline cut was lower by 3 vol% on a 100% conversion basis.

Comparison of the selectivity of CP-2 with and without metals contamination shows that the poisoned sample had lower gasoline and higher LCGO, HGO, gas, and coke; i.e., it did not crack as well. This is not surprising. However, quantitatively, the results indicate that, although the degree of conversion may have been decreased substantially, the conversion efficiency to desired fractions was not significantly less for the catalyst treated with metals. For example, the normalized gasoline fraction was 79 vol% for CP-2 and 76 vol% for CP-2 (NiV).

After Ni/V poisoning, the performance of the CP-2 was superior to the cracking behavior of the Reference for conversion and LCGO and HGO production. Also, the poisoned CP-2 converts slightly more fresh feed to gasoline than the Reference. Although the alumina-added catalyst also makes more coke and light gases, the gain in conversion and gasoline production probably outweighs the disadvantages inherent when these byproducts are generated. The conclusion from the MAT evaluations is that poisoning is more detrimental to the alumina-free material. CP-2 still retains significantly more conversion and selectivity after contamination with Ni and V. The metals essentially deactivate the Reference.

Table V. Activity of FCC Catalysts Before and After Metals Contamination

Sample	Catalyst				
	VI	CP-2	Ref	CP-2	Ref
% V	0	0	0	0.6	0.6
% Ni	0	0	0	0.3	0.3
Conversion, vol% FF	74	81	78	54	34
Product Yields, vol% FF <sup>a</sup>					
Total C <sub>3</sub> 's	11.0	11.6	12.9	8.6	7.7
Propane	3.2	3.9	4.2	1.6	1.5
Propylene	7.8	7.7	8.7	7.0	6.2
Total C <sub>4</sub> 's	19.1	20.8	21.4	13.2	9.9
I-Butane	10.0	11.6	11.4	4.4	3.2
N-Butane	2.4	3.0	3.1	1.0	0.9
Total Butenes	6.7	6.1	7.0	7.8	5.9
C <sub>5</sub> -430 F (Gasoline)	83.4	79.1	77.8	75.5	74.2
430-650 F (LCGO)	23.6	16.7	18.1	43.7	77.2
650 F + DO (HGO)	11.3	7.1	9.7	42.7	121
Product Yields, wt% FF <sup>a</sup>					
Total C <sub>2</sub> and Lighter	2.5	2.4	2.9	3.1	3.6
H <sub>2</sub>	0.07	0.05	0.05	1.29	1.34
Carbon (Coke)	3.7	4.5	3.8	5.5	3.7

<sup>a</sup> Normalized to 100% conversion.

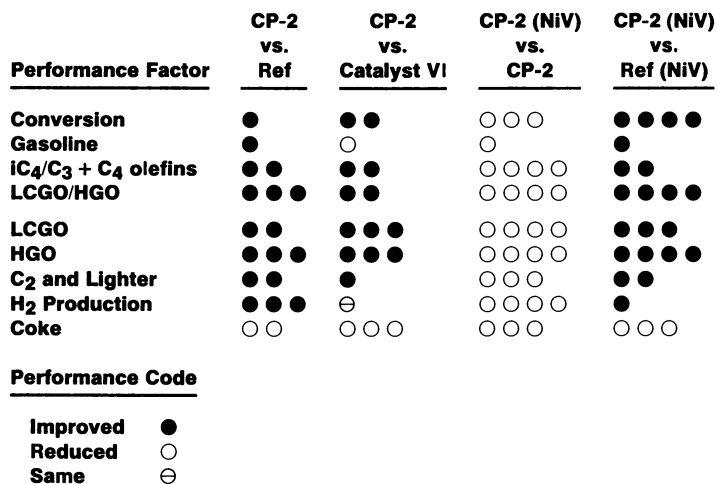


Figure 8. Relative performance of CP-2 formulated FCC catalysts.

With the catalytic cracking results, the third criterion for success was met. Indeed, the excellent activity of the metals-free CP-2 and the superior performance of the metals contaminated CP-2 samples suggest that the formulation would be an excellent candidate for a variety of cracking processes. It seems especially well suited for resid service formulations.

### Conclusions

Alcoa's rehydratable CP alumina powders can be used effectively to improve a viable FCC catalyst formulation. Well-formed microspheres which have superior attrition resistance can be fabricated by controlling the pH and viscosity of the FCC slurry. At this time, the preferred formulation uses CP-2 as the free alumina source and a silica sol which has aged at conditions conducive to the formation of chains of polysilicic acid aggregates. The addition of the rehydratable alumina can also have a beneficial effect on the cracking activity of the catalyst. The conversion and selectivity of a CP-2 formulated sample were comparable to a commercial grade catalyst and an experimental reference, which was alumina-free. After heavy metals poisoning, the CP-2 material had activity which was superior to the reference formulation.

### Literature Cited

1. Worldwide Catalyst Report, *Oil Gas J.* 1986, **84**, (41), 55.
2. Nishimura, Y.; Ogata, M.; Ida, T. U.S. Patent 4 636 484, 1987.
3. Gladrow, E. M.; Winter, W. E.; and Schuette, W. L. UK Patent Application GB 2 022 439 A, 1979.
4. Maselli, J. M.; Peters, A. W. *Catal. Rev. Sci. Eng.* 1984, **26** (3&4), 525.
5. Otterstedt, J. E.; Gevert, S. B.; Jaras, S. G.; Menon, P. G. *Appl. Cat.* 1986, **22**, 159.
6. Sato, G.; Ogata, M.; Ida, T. U.S. Patent 4 631 261, 1986.
7. Occelli, M. L.; Kennedy, J. V. UK Patent Application GB 2 116 062 A, 1982.
8. Lim J.; Stamires, D. U.S. 4 086 187, 1978.
9. Lim, J.; Stamires, D.; Brady, M. U.S. 4 206 085, 1980.
10. Albers, E. W.; Magee, J. S.; Ritter, R. E. UK Patent GB 2 007 107 B, 1978.
11. Secor, R. B.; Van Nordstrand, R. A.; Pegg, D. R. U.S. 4 010 116, 1977.
12. Pillai, G. C.; Stiles, A. B.; Pedersen, L. A. *Proc. 9th Mtg. No. Am. Cat. Soc.*, 1985, p 30.
13. Conner, W. C.; Weist, E. L.; Pedersen, L. A. In *Preparation of Catalysts IV*; Delmon B.; Grange, P.; Jacobs, P. A.; Poncelet, G. Eds.; Elsevier Science Publishers B.V.: Amsterdam, 1987; pp 323-332.
14. Pearson, A. U.S. Patent 4 574 839, 1986.
15. Ostermaier, J. J.; Elliott, Jr., C. H. U.S. Patent 3 957 689, 1976.
16. Forsythe, W. L.; Hertwig, W. R. *Ind. Eng. Chem.* 1949, **41**, 1200-1206.
17. Matocha, Sr., C. K.; Crooks, J. H. In *Light Metals 1987 Addendum*; The Metallurgical Society: Warrendale, PA, 1987; pp 875-879.
18. Matocha, Sr., C. K.; Crooks, J. H.; Plazio, P. P. In *Light Metals 1987*; Zabreznik, R. D., Ed.; The Metallurgical Society: Warrendale, PA, 1987; pp 129-137.
19. Iler, R. K. *The Chemistry of Silica*; John Wiley & Sons: New York, 1979; pp 62, 172-177.
20. *Particle Attrition, State-of-the-Art Review*; British Materials Handling Board, Series on Bulk Materials Handling; Trans. Tech.: Brookfield, VT, 1987, Vol. 5.
21. Scott, J. P. Presented at the 11th Australian Conference on Chemical Engineering, Brisbane, September 1983, paper 23.c.

## Chapter 39

# Characterization of Catalyst Materials as Reference Standards

Ruth A. Haines

National Institute of Standards and Technology, Gaithersburg, MD 20899

Through a series of round robin tests conducted by participating laboratories, ASTM Committee D-32 on Catalysts has characterized a variety of catalyst materials using standard test methods. Materials include fluid cracking catalysts, zeolites, silicas, aluminas, supported metals, and a gas oil feedstock. Properties characterized include surface area, crush strength, catalytic microactivity, particle size, unit cell dimensions and metal content. These materials are available from the National Institute of Standards and Technology as reference materials.

ASTM Committee D-32 on Catalysts was organized in the mid-seventies in response to a recognized need on the part of the catalyst producers and users for test methods and standards. The Committee is structured to bring together interests in measuring physical-chemical and physical-mechanical properties, catalytic properties and composition. Working groups are organized to develop specific standard test methods of interest to the membership using commercial catalysts or catalyst supports.

Key to the success of these working groups in establishing test methods is the availability of catalyst materials in large enough quantities to allow for extensive round robin testing of the methods within the Committee. In fact, adequate quantities exist to make these well characterized materials available for use as standards. Fearing loss of these materials in the warehouses of the many donor companies, the Committee has asked the National Institute of Standards and Technology (formerly the National Bureau of Standards) to distribute the samples. At the present time several catalyst materials are available from the National Institute of Standards and Technology and more will be made available in the near future. (1)

Using commercial materials donated by interested companies the members of D-32 have been able to test for a wide range of important properties of catalysts or catalyst supports. In most



cases a working group agrees on a tentative measurement procedure, asks participating laboratories to follow the procedure to characterize one or more materials, studies the findings, refines the procedure and frequently asks for another set of laboratory measurements. The results of the tests are treated statistically and reported in detail in research reports filed with the ASTM. The test methods appear in Volume 05.03 of the Annual Book of ASTM Standards (2) or in the special publication ASTM Standards on Catalysts. (3)

Table I lists the catalyst materials characterized and available for use as reference materials. For each property measured, the number of the ASTM Standard Test Method used in the determination is identified; the material is specified; the consensus mean value determined is listed; the interlaboratory reproducibility and the intralaboratory repeatability from round robin tests are presented; and the number of the ASTM research report describing the round robin data is listed. These round robins were conducted in accordance with ASTM E-691 -- Standard Practice for Conducting an Interlaboratory Study to Determine the Precision of a Test Method.

Table II summarizes the test methods used for the characterization of the catalyst samples. These methods have been subject to the balloting procedures of the ASTM after extensive review by task force members. The procedures specify equipment parameters when necessary. Limits in the application of the methods are outlined. In all cases the test method must be followed in order to assure comparability of the results to the values assigned. It should be noted that the official ASTM test method numbers have two more digits which represent the year of issue or revision of the standard.

#### Surface Area and Particle Size Reference Materials

Among the physical-chemical properties of most widespread use in the catalyst industry are surface area and particle size distribution. Three materials, a low surface area kaolin, a moderate surface area alumina and a high surface area silica-alumina, have been characterized for surface area using nitrogen gas or a nitrogen-helium flowing gas mixture. Several extensive round robin tests have been conducted using standard static and continuous flow test methods appropriate to catalysts or catalyst supports that have Type II or IV nitrogen adsorption isotherms. As a result these materials are recommended as reference materials by an industry funded ASTM Committee (S-21) responsible for standards for particle metrology. Because several techniques are frequently used in the industry to characterize particle size distribution, an FCC catalyst has been characterized using laser light scattering, electronic counting, and sieving in the 20 to 150- $\mu\text{m}$  equivalent spherical diameter range. Values for the consensus mean found with each type of test method are listed in Table I. Comparison of the various cumulative percent data from the three methods using the same materials has been reported by Flank. (4)

Table I. CATALYST MATERIALS CHARACTERIZED (2, 3,)

Property	Test Method	Test Material	Consensus Mean	2.77S(a). Percent of Consensus Mean		ASTM Research Report
				Interlaboratory Repeatability	Intralaboratory Repeatability	
Surface Area	D-3663(b)	Kaolin MI36384	10.9 sq m/g	17.6	12.2	D32-1006
		Alumina N10131	158 sq m/g	7.5	4.3	
		Silica Alumina R50475	291 sq m/g	6.1	2.8	
	D-4567	Kaolin MI36384	10.3 sq m/g	17.6	1.7	D32-1019
		Alumina N10131	1535 sq m/g	14.5	1.7	
		Silica Alumina R50475	278 sq m/g	16.8	1.6	
Crush Strength	D-4179(b)	Alumina EAS-480 Spheres	20.19 lbs-force	8.7	6.0	D32-1004
Median Diameter	D-4438(b)	Equilibrium FCC Catalyst CC-408	56.7 μm	6.4	3.2	D32-1011
	D-4464(b)	Equilibrium FCC Catalyst CC-408	64.4 μm	5.7	1.9	D32-1013
	D-4513	Equilibrium FCC Catalyst CC-408	64.3 μm	8.2	1.7	D32-1015
	D-4642	Pt/Alumina	0.578%	2.31	0.93	
Platinum, Wt %	D-4782	Pd/Silica-Alumina Molecular Sieve	0.539%	4.54	0.78	
	D-4365	FCC Catalyst AGZ-200	87.3 g/cm <sup>3</sup>	36.5	5.4	D32-1009
Zeolite Area						

Unit Cell Dimension	D-3942	FCC Catalyst AGZ-200	24.723Å	0.4	0.2	D32-1002
Relative Diffraction	D-3906(b,c)	FCC Catalyst AGZ-200	12.3%	71.2	7.3	D32-1010
		FCC Catalyst Bobcat 2	12.8%	34.5	8.6	
Percent Conversion	D-3907	RR-1 FCC Catalyst/ Gas Oil	59.39 wt%	8.7	4.3	D32-1016
		RR-2 FCC Catalyst/ Gas Oil	64.94	12.5	4.3	
		RR-3 FCC Catalyst/ Gas Oil	76.06	11.4	3.5	
		RR-4 FCC Catalyst/ Gas Oil	76.16	9.7	3.6	
		RR-5 FCC Catalyst/ Gas Oil	80.87	8.9	3.4	
		RR-6 FCC Catalyst/ Gas Oil	70.07	10.4	1.7	

(a) 2.77S is the 95% probability interval limit on the difference between two test results, and S is the appropriate estimate of standard deviation.

(b) Standard deviation not using weighted data reduction.

(c) This method employs a NaY zeolite standard reference material available from NIST.

Table II. SUMMARY OF METHODS FOR CATALYST CHARACTERIZATION

ASTM Method Number	Title	Summary of the Method
D-3363	Surface Area of Catalysts	Multi-point volumetric (BET) surface area by nitrogen adsorption
D-4567	Single-point Determination of the Specific Surface Area of Catalysts Using Nitrogen Adsorption by the Continuous Flow Method	Single-point surface area using continuous flowing nitrogen-helium gas mixture
D-4179	Single Pellet Crush Strength of Formed Catalyst Shapes	Strength of spherical or tablet shaped particles individually crushed between two flat surfaces
D-4438	Particle Size Distribution of Catalyst Material by Electronic Counting	Particle size distribution of catalyst particles (20 to 150 $\mu$ m equivalent spherical diameter) as determined by an electroconductive sensing method
D-4464	Particle Size Distribution of Catalytic Material by Laser Light Scattering	Particle size distribution of catalyst particles (20 to 150 $\mu$ m equivalent spherical diameter) as ascertained by laser light scattering
D-4513	Particle Size Distribution of Catalytic Material by Sieving	Particle size distribution of catalyst particles (20 to 420 $\mu$ m) as measured weight of sample passing through calibrated sieves

- |        |   |   |
|--------|---|---|
| D-4642 | Platinum in Reforming Catalysts   | Assay for platinum in a non-zeolitic reforming catalyst by dissolution of the catalyst and spectrophotometric absorbance for platinum |
| D-4782 | Palladium in Molecular Sieve Catalyst                                       | Potentiometric technique for determining about 0.5 weight percent palladium in molecular sieve containing fresh catalyst.             |
| D-4365 | Determining Zeolite Area of a Catalyst                                      | T-plot analysis of portion of total area attributed to zeolite fraction   |
| D-3942 | Determination of the Unit Cell Dimension of a Faujasite-type                | Unit cell dimension of synthetic faujasite type zeolite by x-ray diffraction  |
| D-3906 | Relative Zeolite Diffraction Intensities                                    | Relative fraction of zeolite as determined by comparing x-ray diffraction peak intensities  |
| D-3907 | Method for Testing Fluid Catalytic Cracking Catalysts by Microactivity Test | Activity of FCC catalysts as evaluated by percent conversion of gas oil using a fixed bed reactor                                     |

### Catalyst Activity

Of particular mention and of widespread interest throughout the petrochemical industry has been the Committee's success in obtaining round robin results on testing fluid cracking catalysts. Overcoming a natural desire not to share data or methods, industry representatives developed a standard method to determine the weight percent conversion of gas oil in a fixed bed microactivity unit. The test requires the use of a standard batch of gas oil as a feedstock and a set of equilibrium fluid cracking catalysts with consensus mean conversion values assigned in a reactor of specified design. The gas oil and the set of equilibrium cracking catalysts are useful reference materials. Conversion for any equilibrium or laboratory-deactivated fluid cracking catalyst can be measured and compared to a conversion calibration curve. Conversion is measured by the difference between the amount of feed used and the amount of unconverted material. The unconverted material is defined as all liquid product with a boiling point above 216°C.

### Other Physical and Chemical Properties

Although several standard test methods have been developed for the chemical analysis of catalysts only small samples of supported platinum and palladium reference materials are available. Zeolites have been characterized for zeolite area, unit cell dimensions, and relative x-ray diffraction intensity. The crush strength of alumina pellets has also been determined. As the needs of catalyst users and producers change so will the materials characterized. To the extent that adequate amounts of material can be donated, standard test methods developed, and round robin tests performed Committee D-32 on catalysts will continue to make them available through NIST as reference materials.

Special acknowledgment goes to Steve Bradley and the many D-32 members who worked on the characterization of the materials described in this paper.

### Literature Cited

1. NBS Standard Reference Materials Catalog; Seward, R. W., Ed.; 1988-89, NBS Special Publication 260.
2. Annual Book of ASTM Standards; ASTM: Philadelphia, PA, 1988; Vol. 05.03, p 569-654.
3. ASTM Standards on Catalysts; ASTM: Philadelphia, PA, (3rd Edition, 1988).
4. Flank, W. H.; Ind. Eng. Chem. Res. 1987, 26, 1750.

RECEIVED April 27, 1989

## Author Index

- Anderson, M. W., 40  
 Barr, Tery L., 180,203  
 Bauer, S. H., 328  
 Bell, A. T., 183  
 Bergna, Horacio E., 55  
 Bertolacini, Ralph J., 380  
 Bhattacharyya, Alak A., 46  
 Bouwens, S. M. A. M., 319  
 Bradley, Steven A., 274,342,398  
 Braunschweig, E. J., 65  
 Brienza, P. K., 407  
 Brinker, C. J., 251  
 Bunker, B. C., 65  
 Chiu, N.-S., 328  
 Cormier, William E., 46  
 Cotterman, R. L., 24  
 Csencsits, Roseann, 365  
 Datye, A. K., 65  
 Dautzenberg, Frits M., 99  
 Davis, B. H., 328  
 de Beer, V. H. J., 319  
 Flank, W. H., 92  
 Gallegos, D. P., 251  
 Gattuso, Mark J., xi  
 Graves, C. L., 251  
 Goodman, D. W., 191  
 Griffith, Stephen D., 17  
 Gronsky, Ronald, 365  
 Guohui, Z., 79  
 Haensel, Hertha Skala, 2  
 Haensel, Vladimir, 2  
 Haines, Ruth A., 430  
 Hartkamp, M. B., 135  
 Hicks, Robert F., 214  
 Hickson, D. A., 24  
 Hsu, Chen C., 234  
 Klier, Kamil, 12  
 Koningsberger, D. C., 319  
 Koves, William J., 398  
 Kugler, E. L., 354  
 Lambert, S. L., 262  
 Lee, W.-H., 328  
 Leonowicz, M. E., 303  
 Leta, D. P., 354  
 Levin, M. E., 183  
 Li, Yong-Xi, 328  
 Lowe, J. A., 414  
 Margolis, M. J., 120  
 Martinez, S. L., 65  
 Matocha, C. K., Sr., 414  
 McLean, J. B., 120  
 Mieville, R. L., 243  
 Moorehead, E. L., 120  
 Occelli, M. L., 40  
 O'Connor, P., 135  
 Peden, C. H. F., 65  
 Pedersen, L. A., 414  
 Peri, J. B., 222  
 Pitzer, Emory, 398  
 Prins, R., 319  
 Puls, F. H., 384  
 Reichmann, M. G., 243  
 Robota, Heinz J., 274  
 Rohrbaugh, Wayne J., 279  
 Sahimi, Muhammad, 158  
 Salmeron, M., 183  
 Seamans, J. D., 148  
 Scapan, M., 79  
 Shatlock, M. P., 24  
 Smith, D. M., 251  
 Somorjai, G. A., 183  
 Strohmaier, K. G., 303  
 Suib, S. L., 40  
 Targos, William M., 342  
 Tsotsis, Theodore T., 158  
 Vaughan, D. E. W., 303  
 Vuitel, C. A., 148  
 Welch, J. G., 148  
 Welsh, L. B., 262  
 Williams, K. J., 183  
 Woltermann, Gerald M., 46  
 Wu, Ellen L., 279  
 Yin, M. P., 203

## Affiliation Index

- Akzo, 135  
 Allied-Signal Engineered Materials  
   Research Center, 274  
 Aluminum Company of America, 414  
 Amoco Oil Company, 243,380  
 ASTM, 407  
 Catalyst Recovery, Inc., 148  
 Catalytica, 99  
 Center for Applied Energy Research, 328  
 Cornell University, 328  
 E. I. du Pont de Nemours and Company, 55  
 Engelhard Corporation, 120  
 Exxon Chemical Company, 384  
 Exxon Research and Engineering  
   Company, 303,354  
 W. R. Grace and Company, 24  
 Katalistiks International, 17,46  
 Lawrence Berkeley Laboratory, 183,365  
 Lehigh University, 12  
 Mobil Research and Development  
   Corporation, 279  
 National Institute of Standards  
   and Technology, 430  
 Northeastern University, 222  
 Oklahoma State University, 79  
 Phillips Petroleum Company, 398  
 Sandia National Laboratories, 65,251  
 Texas A&M University, 191  
 University of California—Berkeley, 183,365  
 University of California—Los Angeles, 214  
 University of Connecticut, 40  
 University of Massachusetts, 2  
 University of New Mexico, 65,251  
 University of Southern California, 158  
 University of Technology—Eindhoven, 319  
 University of Wisconsin—Milwaukee, 180,203  
 Unocal Corporation, 40  
 UOP, xi,92  
 UOP Research Center, 262,274,342,398  
 U.S. Army Chemical Research, Development,  
   and Engineering Center, 234

## Subject Index

### A

#### $\gamma$ -Alumina

- effect of sulfide treatment, 231,232f  
 NO spectra, 231,232f  
 Alumina-added fluid catalytic cracking  
   catalysts  
   attrition, 422–427  
   index, 424t,427  
   index vs. particle size of  
     additive, 424,426f  
     measurement, 415,416f,417t,418  
   catalytic activity, 427,428t,429  
   catalytic cracking test, 418  
   commercial catalysts, 418,420f  
   effect of additive on viscosity of  
     catalyst slurry, 418,419f  
   effect of processing conditions on  
     attritability, 423t,424  
   experimental catalysts, 418,421f  
   formulation, 418  
   microsphere formation, 418–422  
   particle size distributions, 418,422t  
   preparation, 418  
   relative performance, 427,428f,429  
   response curves, 422–423,425f

- Alumina-promoted fluid catalytic cracking  
   catalysts, commercial viability, 414  
 Analysis of testing responses  
   definition of sensitivity of result to  
     given variable, 94  
   problems, 95  
   uncertainty components, 95  
 Annular dark-field detection method,  
   detection of supported metal  
     crystallites, 346,348f  
 ARCO pilot riser plant tests  
   conditions, 138,139t  
   flow scheme, 144,146f  
 ASTM Committee D–32 on catalysts  
   function, 430  
   key to success, 430  
   list of catalyst materials available for  
     use as reference materials,  
     431,432–433t  
   list of test methods for catalyst  
     characterization, 431,434–435t  
   testing procedure, 430–431  
 Attrition measurement  
   apparatus, 415,416f,417  
   measurement, 417t,418  
   sample preparation, 417



## Affiliation Index

- Akzo, 135  
 Allied-Signal Engineered Materials  
   Research Center, 274  
 Aluminum Company of America, 414  
 Amoco Oil Company, 243,380  
 ASTM, 407  
 Catalyst Recovery, Inc., 148  
 Catalytica, 99  
 Center for Applied Energy Research, 328  
 Cornell University, 328  
 E. I. du Pont de Nemours and Company, 55  
 Engelhard Corporation, 120  
 Exxon Chemical Company, 384  
 Exxon Research and Engineering  
   Company, 303,354  
 W. R. Grace and Company, 24  
 Katalistiks International, 17,46  
 Lawrence Berkeley Laboratory, 183,365  
 Lehigh University, 12  
 Mobil Research and Development  
   Corporation, 279  
 National Institute of Standards  
   and Technology, 430  
 Northeastern University, 222  
 Oklahoma State University, 79  
 Phillips Petroleum Company, 398  
 Sandia National Laboratories, 65,251  
 Texas A&M University, 191  
 University of California—Berkeley, 183,365  
 University of California—Los Angeles, 214  
 University of Connecticut, 40  
 University of Massachusetts, 2  
 University of New Mexico, 65,251  
 University of Southern California, 158  
 University of Technology—Eindhoven, 319  
 University of Wisconsin—Milwaukee, 180,203  
 Unocal Corporation, 40  
 UOP, xi,92  
 UOP Research Center, 262,274,342,398  
 U.S. Army Chemical Research, Development,  
   and Engineering Center, 234

## Subject Index

### A

#### $\gamma$ -Alumina

- effect of sulfide treatment, 231,232f  
 NO spectra, 231,232f  
 Alumina-added fluid catalytic cracking  
   catalysts  
   attrition, 422–427  
   index, 424t,427  
   index vs. particle size of  
     additive, 424,426f  
     measurement, 415,416f,417t,418  
   catalytic activity, 427,428t,429  
   catalytic cracking test, 418  
   commercial catalysts, 418,420f  
   effect of additive on viscosity of  
     catalyst slurry, 418,419f  
   effect of processing conditions on  
     attritability, 423t,424  
   experimental catalysts, 418,421f  
   formulation, 418  
   microsphere formation, 418–422  
   particle size distributions, 418,422t  
   preparation, 418  
   relative performance, 427,428f,429  
   response curves, 422–423,425f

- Alumina-promoted fluid catalytic cracking  
   catalysts, commercial viability, 414  
 Analysis of testing responses  
   definition of sensitivity of result to  
     given variable, 94  
   problems, 95  
   uncertainty components, 95  
 Annular dark-field detection method,  
   detection of supported metal  
     crystallites, 346,348f  
 ARCO pilot riser plant tests  
   conditions, 138,139t  
   flow scheme, 144,146f  
 ASTM Committee D–32 on catalysts  
   function, 430  
   key to success, 430  
   list of catalyst materials available for  
     use as reference materials,  
     431,432–433t  
   list of test methods for catalyst  
     characterization, 431,434–435t  
   testing procedure, 430–431  
 Attrition measurement  
   apparatus, 415,416f,417  
   measurement, 417t,418  
   sample preparation, 417

- Attrition-resistant porous microspheres, illustration of preparation methods, 56,59f
- Attrition-resistant porous microspheres by spray drying  
determination of distribution of hardening phase, 57  
effect of acid leaching on scanning electron micrographs, 58,60–62f  
effect of poly(silicic acid) on resistance, 58,59f  
experimental procedure, 57  
materials, 56–57  
measurement of attrition resistance, 57  
scanning electron micrograph showing silicon distribution, 58,63f
- Attrition testing, description, 21
- Axial dark-field-imaging detection method, detection of supported metal crystallites, 346–347,348f
- B**
- Bimetallic catalysts, *See* Mixed-metal catalysts
- Brunauer–Emmett–Teller (BET) surface areas, measurements on Ni catalysts, 71,73t
- Bulk chemical analysis, description, 22–23
- Bulk crush test, description, 381
- Bulk crush testing of catalysts  
characteristics of two types of catalysts, 399,400f  
configuration of tester, 399,400f  
effect of changing amount of catalyst in cell, 399,401f  
effect of packing density on design of fines, 402,404f  
evaluation of interlaboratory reproducibility, 402  
influence of wall friction on axial stress, 399,401f  
load displacement curve, 399,402,403f  
new test cell design, 402,405f  
reasons for determination, 398–399  
variation in fine production from different load cells, 402,403f
- Bulk densities, measurements, 22
- C**
- Calcined dealuminated Y zeolites, characterization, 27t
- Calcined zeolites  
hexadecane cracking results, 30,31t  
molecular weight distribution from hexane cracking, 30,32f
- Catalysis research, goal, 12
- Catalyst(s)  
commercial importance, 17  
examination under reactor conditions, 278  
importance to chemical and petrochemical industries, 384  
quality assurance, 385–397  
strength requirements, 398  
tests for evaluation of physical characteristics, 398  
X-ray and electron microscopic analyses, 274–278
- Catalyst analysis  
description, 18–19  
techniques, 19–20
- Catalyst breakage problems, measurement tests, 381
- Catalyst characterization  
advantages, 12  
analysis, 18–20  
analysis of atomic and active species, 21  
analysis of electronic structure, 15  
breakthroughs and challenges, 3–5  
classification of methods, 13–16  
description, 18  
determination of catalyst phases, 20  
development of catalysts by design, 2  
evaluation, 18–19  
example of *n*-heptane hydrocracking, 9t,10f,11  
functions, 13  
goal, 2  
history, 5–6  
humorous recollections, 11  
imaging secondary-ion MS, 354–364  
microanalytical methods, 20–21  
multiple tasks, 12  
need for understanding and knowledge of entire system, 6–7  
need to diagnose and fix problems quickly, 7–8  
nitrogen physisorption methods, 20  
physical measurements, 20  
reactor studies, 15–16  
role of catalyst diagnostician, 2–3  
structural analysis, 14–15  
surface analysis, 13–14
- Catalyst characterization by IR spectroscopic methods  
advantages, 222–223  
applications, 225–232  
characterization  
metal sites on supported metal catalysts, 229,231,232f  
strained bonds on oxides and zeolites, 227,229,230f  
surface acid sites, 225–228,230  
surface groups on supports and catalysts, 225,226f

- Catalyst characterization by IR  
 spectroscopic methods—*Continued*  
 future prospects, 231,233  
 IR cell design, 223–224  
 pretreatment, 225  
 problems resulting from use of probes,  
 224–225  
 sample preparation, 223  
 spectrometer selection, 224
- Catalyst characterization by scanning  
 transmission electron microscopy  
 advantages, 342–343  
 annular dark-field detection method,  
 346,348f  
 apparatus, 343  
 axial dark-field-imaging detection method,  
 346–347,348f  
 commercial catalyst composition, 344,345r  
 deposition of carbon in area of beam  
 concentration, 350,352  
 determination of metal content, 346  
 identification of bimetallic crystallites,  
 347,349f  
 micrograph of platinum crystallites on  
 $\gamma$ -alumina, 344,345f,346  
 poisons, 350  
 problem in analyzing heterogeneously  
 distributed metal catalysts, 347  
 problem with beam sensitivity of  
 catalyst, 346  
 selection of model catalyst, 344  
 specimen preparation, 343  
 stability under beam exposure,  
 350,351f,352
- Catalyst deactivation  
 percolation models, 167–175  
 statistical modeling, 162–167  
 types, 162
- Catalyst development, goal, 214
- Catalyst evaluation  
 description, 18  
 techniques and equipment, 19
- Catalyst materials, characterization as  
 reference standards, 430–436
- Catalyst poisons, detection, 350
- Catalyst preparation  
 characteristics of final product, 18  
 procedure, 18
- Catalyst testing  
 catalyst tailoring, 113,115f  
 commercially available hydrometallation  
 catalysts, 113,115f  
 comparison of laboratory and industrial  
 reactors, 101,103f  
 criteria for isothermal operation,  
 104,108r  
 deviation in reaction rate at given  
 activation energy and temperature,  
 104,106f
- Catalyst testing—*Continued*  
 diagnostic test for interphase transport  
 limitation, 107,108f  
 diagnostic test for intraparticle  
 transport disguises, 107,110f  
 effect of flow pattern on rate analysis,  
 102,103f  
 Koros–Nowak tests for transport disguises,  
 109,110f  
 long-term deactivation during residue  
 desulfurization, 113,114f  
 reactor and catalyst gradient application  
 to heterogeneous catalyst, 104,106f  
 schematic representation of prototype  
 tube, 102,103f  
 statistical design vs.  
 one-variable-at-a-time approach, 101r  
 steps for ensuring plug-flow operation,  
 104,105r  
 ten guidelines, 99–116  
 Weisz window, 112,114f
- Catalyst testing program  
 attrition testing, 21–22  
 bulk chemical analysis, 22–23  
 bulk density measurements, 22  
 microactivity test, 21  
 particle size analysis, 22
- Catalytic activity, nickel-loaded titanates,  
 73–74,75–76f
- Catalytic properties, dealuminated Y  
 zeolites, 30–34
- Catalytic systems, characterization by using  
 spectroscopic techniques, 180–182
- Cerium dioxide, oxidation of  $\text{SO}_2$  to  $\text{SO}_3$ , 48
- Characterization of catalyst materials as  
 reference standards  
 catalyst activity, 436  
 list of materials characterized and  
 available for use as reference  
 materials, 431,432–433r  
 list of test methods, 431,434–435r  
 particle size reference materials, 431  
 physical and chemical properties, 436  
 surface area reference materials, 431  
 testing procedure, 430–431
- Characterization of catalytic systems  
 IR spectroscopy, 182  
 magic-angle-spinning NMR spectroscopy, 182  
 solid-state NMR spectroscopy, 182  
 X-ray photoelectron spectroscopy, 181
- Chemical analysis of catalysts, standard  
 test methods, 436
- Chemical dealumination, Y zeolites, 25
- Cobalt sulfide phase structure in Co–Mo–S  
 catalysts  
 activity per cobalt atom, 326  
 Co–S coordination distance, 325  
 Co–S coordination number, 325–326  
 Fourier-transform EXAFS spectra, 321,322f

- Cobalt sulfide phase structure in Co–Mo–S catalysts—*Continued*  
 material preparation, 320  
 structural parameters, 321,323t  
 XANES spectrum, 321,324f,325  
 X-ray absorption measurements, 320–321
- Cogel formation of  $MgAl(OH)_5$  and  $Mg_2Al_2O_5$ , magnesium aluminate spinel formation, 51
- Coke, chemical structure, 81
- Commercial industrial catalysts  
 criteria, 380  
 importance of mechanical and physical properties, 380–381  
 importance of methods to prevent and eliminate catalyst breakage and attrition, 381  
 market, 383
- Cu/Ru(0001) catalyst, model studies, 194
- D**
- Dealuminated Y zeolites  
 active-site distributions, 34  
 $^{27}Al$  MAS-NMR spectra, 28,29f,30  
 bulk elemental analyses, 26  
 calcination, 26  
 calculated octane numbers vs. gasoline yield, 36,37f  
 catalyst performance relationships, 35–36,37f  
 catalyst structural characteristics, 34–35  
 catalytic properties, 30–34  
 characterization, 26  
 characterization of starting materials, 25,26t  
 compositions, 27t  
 dependence of hexadecane cracking activity on framework composition, 35,37f  
 effect of coke selectivity on catalyst deactivation rate, 35  
 extraframework aluminum, 36  
 factors influencing gasoline selectivity, 35  
 gasoline composition from hexadecane cracking, 35–36  
 hexadecane cracking reactions, 26  
 light-gas compositions for hexadecane cracking, 34t  
 light-gas selectivities, 35  
 molecular weight distribution from hexane cracking, 30–31,32f  
 paraffin, olefin, naphthene, and aromatic component selectivities in gasoline fraction from hexadecane cracking, 31,33f  
 pore size distributions, 34–35
- Dealuminated Y zeolites—*Continued*  
 preparation, 24–25  
 presence of extraframework material, 34  
 relative first-order rate constants for hexadecane cracking, 30t  
 role of characteristics in hydrocarbon reactivity, 24  
 role of mesoporosity in catalytic behavior, 36  
 $^{29}Si$  MAS-NMR spectra, 28,29f,30  
 structural feature characterization, 24  
 unit cell sizes, 34
- Degree of branching of gasoline measurement, 138,140f  
 vs. branching, 138,149f  
 vs. olefinicity, 138,140f
- Density grading  
 effectiveness in separation of catalyst mixtures to enhance regeneration quality and possibility, 153  
 fractions produced, 153  
 function, 153  
 opportunities for regeneration and reuse of catalysts, 153  
 test case performed on cobalt–molybdenum catalyst, 155t  
 test case performed on nickel–molybdenum catalyst, 153,154t,155
- Drawing conclusions for testing  
 cautions and constraints, 95–96  
 examples, 96–98  
 reliability, 95
- E**
- ECR–1 zeolite  
 chemical properties, 304–305  
 determination of proposed structure, 304  
 electron diffraction patterns, 308,310f  
 hexane isotherms, 305,306f  
 high-resolution lattice imaging, 311–315  
 powder X-ray diffraction patterns, 308,309f  
 role of unit-cell constants in structure determination, 308  
 solution properties, 305,306f  
 spectroscopic analyses, 305,307f  
 structural modeling, 314,316f,317  
 synthesis, 304  
 thermogravimetric analyses, 305,306f
- Electron beam, catalyst analysis, 350,351f,352
- Electron density, distribution function, 280
- Electron diffraction, ECR–1 zeolite patterns, 308–310f
- Electron energy loss spectroscopy  
 analysis of light elements, 350  
 applications, 352

- Electron microscopy  
 evaluation of metal distribution, 276  
 microstructural study of iron silicate catalyst, 365–376  
 use in catalyst characterization, 276
- Electronic structure of catalysts  
 electron paramagnetic resonance, 15  
 scattered wave X- $\alpha$ , 15  
 spin-polarized XPS, 15  
 UV photoelectron spectroscopy, 15  
 valence band XPS, 15  
 XANES, 15
- Electronic transitions probed by X-ray  
 absorption spectroscopy, description, 275
- Energy balance of photoemission process, equations, 215,217
- Extended X-ray absorption fine structure (EXAFS)  
 description, 275–276  
 Pt–Sn–alumina catalysts, 332–339  
 structure determination of cobalt sulfide phase in Co–Mo–S catalysts, 319  
 use in catalyst characterization, 319
- Extractive decoking, principles, 80–82
- F
- Fix concept, description, 180–181
- Fixed-bed adsorbents, quality requirements, 385
- Fixed-bed catalysts  
 applications, 385  
 quality, 385
- Fluid catalytic cracking (FCC)  
 catalyst development for different applications, 120  
 differences among units, 120  
 test(s), 135–147  
 testing  
 ARCO pilot riser test conditions, 138,139t  
 aromatic formation, 141,143f  
 criteria for judging simulations, 136,138  
 establishment of good FCC simulation, 136,138–143  
 kinetics, 141,143f  
 microscale simulation test of FCC unit, 138,139t  
 strategy, 136  
 testing philosophies for evaluation of catalysts, 120–134
- Fluid catalytic cracking catalyst(s)  
 attrition, 422–427  
 indexes, 424t,427  
 measurement, 415,416f,417t,418  
 testing, 21
- Fluid catalytic cracking catalyst(s)—*Continued*  
 catalytic activity, 427,428t,f,429  
 catalytic cracking test, 418  
 characterization, 415  
 characterization by imaging secondary ion MS  
 cross section of bottoms conversion, 359,360–361f  
 cross section of old and new catalyst particles, 359,362–363f,364  
 cross section of typical gas oil conversion catalyst, 356,357–358f,359  
 experimental procedure, 355–356  
 ion image collection system, 355  
 commercial catalysts, 418,420f  
 experimental catalysts, 418,421f  
 formulation, 415  
 friability of pseudoboehmite-formulated material, 424,426f,427  
 microsphere formation, 418–422  
 particle(s)  
 composition, 354  
 problems with characterization of submicron phases, 354  
 particle size distributions, 418,422t  
 passivation of metal contaminants, 41  
 preparation, 415  
 response curves, 422–423,425f  
 testing, 436
- Fourier-transform IR spectroscopy, determination of light-off temperature of oxidation catalyst, 234–241
- G
- Gasoline  
 branching and degree of branching factor, 138,140f  
 degree of branching vs. olefinicity, 140f,141  
 vs. olefinicity, 141f
- H
- H<sub>2</sub> chemisorption, measurements on Ni catalysts, 71,73t
- Heavy hydrocarbons in supercritical fluids, effect of solvent on solubility, 82
- n-Heptane, hydrocracking, 9t,10f,11
- Heterogeneous catalytic-type systems, characterization of evolving chemistry, 180
- High-resolution electron microscopy, images for second-phase particles of iron silicate molecular sieve, 374,375f,376

- High-resolution electron spectroscopy for chemical analysis studies in catalysis of Pt metals  
 analysis of alumina support, 204–205,206f  
 bimetallic cases, 209,211f,212  
 effect of dopant, 203–204  
 example of Pt crystallite growth, 209,210f  
 experimental procedure, 204  
 increase in differentially charged Pd with increased basicity of alkaline dopant, 209,211f,212  
 overlay of valence bands, 205,206f  
 oxidized material, 205,207f  
 Pt(4d<sub>5/2</sub>) spectra, 205,207f  
 reduction and dispersion of metals, 205,208–209,210f
- High-resolution transmission electron microscopy lattice imaging  
 determination of zeolite structure, 311  
 ECR–1 connectivity model, 311,314,315f  
 image of crystal side view along ECR–1 laths, 311,312f  
 image of section normal to ECR–1 lath length, 311,313f
- Hydrocracking of *n*-heptane catalyst characterization, 9–11  
 product distribution, 9t  
 reactions, 9,10f
- Hydrothermal dealumination, Y zeolites, 25
- Hydrotreating catalysts  
 applications, 79  
 commercial demand, 80  
 deactivation mechanisms, 80  
 in situ regeneration, 79–88  
 operating conditions of processes, 80,81t  
 process description, 79
- Hydrous oxide ion exchangers of metals, use as catalyst substrates, 65
- Hydrous sodium titanate ion-exchange materials, use as catalyst supports, 65–76
- Hydroxide coprecipitation, magnesium aluminate spinel preparation, 49,50f,51,52f
- Hypothesis for testing design, 92–93  
 form, 92
- I
- Imaging secondary-ion MS, use in catalyst characterization, 354–364
- In situ regeneration of hydrotreating catalyst  
 advantages, 80  
 apparatus, 82  
 effect of CO<sub>2</sub> extraction on characterization, 83,85,86f
- In situ regeneration of hydrotreating catalyst—  
*Continued*  
 effect of extraction on characteristics, 85t  
 effect of pyridine extraction on hydrogenation, 85,86f,87  
 effect of pyridine extraction on hydronitrogenation, 85,87,88f  
 effect of SO<sub>2</sub>–pyridine extraction on characteristics, 87,88f  
 experimental conditions of extraction, 83,84t  
 experimental procedure, 82–83  
 use of supercritical fluid extraction, 80
- Industrial powders with high attrition resistance  
 example, 55  
 preparation, 55–56
- Interphase gradient, description, 104
- Intraparticle gradients, description, 104
- Intrareactor gradients, description, 104
- IR spectroscopic methods, catalyst characterization, 222–233
- IR spectroscopy  
 ECR–1 zeolite, 305,307f  
 use in characterization of catalytic systems, 182
- Iron silicate analogues of ZSM–5 zeolite  
 effect of alkali cations on size and morphology, 366  
 effect of iron concentration on morphology, 366  
 effect of steam treatment on size, 368–369f  
 effect of stirring and steam treatment on morphology, 368,371f  
 effect of stirring on morphology, 368,370f  
 high-resolution electron microscopic images, 374,375f,376  
 identification of crystallites, 366–368  
 indexed microdiffraction patterns, 368,373f,374  
 microdiffraction patterns, 368,372f,374  
 morphology vs. synthesis conditions, 366,367f  
 Mossbauer studies, 376  
 particle size vs. synthesis conditions, 366,367f  
 synthesis, 365
- K
- Ketjen microactivity test for development of fluid catalytic cracking  
 description, 136  
 simulation of FCC bed reactor, 136,137f

## L

## Length and density grading

- advantages, 157
- density grading, 153–156
- length grading, 149–154
- objective, 148
- regenerated naphtha re-forming catalyst, 155,156*r*
- separation of hydrocracking–hydrotreating catalyst mixture, 155,156*r*,157
- test case performed on cobalt–molybdenum catalyst, 155*r*
- test case performed on nickel–molybdenum catalyst, 153,154*r*,155

## Length grading

- applications, 153
- effectiveness in separation by length, 149,150*r*,151–152*f*
- example, 149,153,154*r*
- function, 149
- results from 110-in. catalyst, 149,152*r*

## Light elements, analysis by electron energy

- loss spectroscopy, 352

## Light-off temperature determination of

- oxidation catalyst by Fourier-transform IR spectroscopy

- activation energy of CO and CO<sub>2</sub> formation, 239*r*

- Arrhenius plot of CO on oxidation catalyst, 239,240*f*

- Arrhenius plot of CO<sub>2</sub> on oxidation catalyst, 239,241*f*

- experimental procedure, 235

- IR spectra at various temperatures, 235,237–238*f*,239

- materials, 235

- schematic representation of IR flow cell, 235,236*f*

- schematic representation of measurement system, 235,236*f*

- values for three-way automotive catalysts, 239*r*

## Lot-to-lot variations for catalysts, catalyst manufacture, 393

## M

- Magic-angle-spinning NMR spectroscopy, use in characterization of catalytic systems, 182

- Magnesium aluminate spinel(s), preparation methods, 48

- Magnesium aluminate spinel for SO<sub>x</sub> abatement
  - cerium impregnation, 47
  - material preparation, 46–47
  - preparation of Al<sub>2</sub>O<sub>4</sub> by cogel formation method, 47

- Magnesium aluminate spinel for SO<sub>x</sub> abatement—*Continued*

- preparation of MgAl<sub>2</sub>O<sub>4</sub>
  - cocondensation method, 47
  - coprecipitation method, 47
  - thermal studies, 47–48

## Magnesium aluminate spinel preparation

- cocondensation of oxides, 48–49,50*f*,*r*

- cogel formation, 50*r*,51,52–53*f*

- coprecipitation of hydroxides, 49,50*r*,51,52*f*

- physical and chemical properties, 49,50*r*

## Mechanical and physical testing of catalyst

- formation of standardization groups, 382

- importance of quality assurance, 382

- importance of standardization procedures, 382

- measurement procedures, 382

- need for ample supply of well-characterized reference materials, 382

## Mercury porosimetry

- accuracy, 251–252

- applications, 251

- description, 251

## Metal catalyst–support interactions

- development, 214

- implications from XPS studies, 219–220

- photoemission from insulators, 215,216*f*,217

- photoemission from small metal clusters on insulators, 217,218*f*,219

## Metal crystallites, identification

- techniques, 277

## Metal distribution, evaluation by electron microscopy, 276

## Metal oxide overlayers, surface

- characterization, 183

## Metal reduction and dispersion,

- high-resolution electron spectroscopy for chemical analysis, 205,208–209,210*f*

Metal sites on supported metal catalysts, characterization by IR spectroscopic methods, 229,231,232*f*

## Microactivity test, description, 21

## Microactivity test for development of fluid catalytic cracking

- advantages and disadvantages, 135

- modifications, 136,137*f*

- problems with simulation of commercial operating conditions, 135,137*r*

## Microactivity test of catalysts for

- fluid catalytic cracking

- alternate approaches, 127,129*r*,130

- coke selectivity, 130,133*f*

- comparison to steaming procedures, 127,129–134

- dry-gas selectivity, 130,132*f*

- equilibrium comparison, 134*r*

- Microactivity test of catalysts for  
 fluid catalytic cracking—*Continued*  
 gasoline selectivity, 130,131f  
 light-cycle-oil selectivity, 130,132f  
 process flow scheme, 127,128f  
 summary of procedures, 127,129t  
 wet-gas selectivity, 130,131f
- Microdiffraction, patterns for iron silicate  
 analogues of ZSM-5 zeolite,  
 368,372-373f,374
- Microscale simulation test for development  
 of fluid catalytic cracking  
 description, 144  
 flow scheme, 144,145f  
 gasoline composition, 141,142f  
 RON and MON predictions, 141,143f  
 simulation of FCC unit, 138,139t  
 test conditions, 141,142t,147
- Mixed-metal catalysts  
 commercial success, 191  
 surface properties, 191-200
- Molecular catalysis, use of spectroscopic  
 analysis, 181
- N**
- Near-edge X-ray absorption fine structure,  
 (NEXAFS), Pt-Sn-alumina catalysts,  
 331-332
- New zeolites, determination of structural  
 topology, 303-304
- Ni(II) hydrolysis, chemistry, 68,69f,70
- Nickel-loaded catalysts, effect of loading  
 conditions on degree of dispersion,  
 70-71
- Nickel on hydrous sodium titanate catalyst  
 supports  
 BET surface areas, 71,73t  
 catalytic activity, 73-74,75-76f  
 dissolved Ni species concentrations vs.  
 pH, 70,72f  
 experimental procedure, 67  
 H<sub>2</sub> chemisorption measurements, 71,73f  
 ion-exchange behavior of sodium titanate,  
 67-68,69f  
 material preparation, 66-67  
 Ni(II) hydrolysis chemistry, 68,69f,70  
 nickel-loaded catalysts, 70-71,72f,75f  
 nickel-loading experiments, 70,72f  
 rate of *n*-butane hydrogenolysis, 74,75f  
 selectivity for hydrocarbon formation,  
 74,76f  
 transmission electron microscopy,  
 71,72f,75f
- Nitrogen adsorption and condensation  
 advantages and disadvantages, 252-253  
 determination of specific surface areas  
 and pore size distributions, 252
- Nu-13  
 deconvolution of XRD powder pattern,  
 292,296f,297  
 electron microscopy data, 292,295f,297
- O**
- Oxidation catalysts  
 determination of light-off temperature,  
 234-241  
 techniques for performance evaluation, 234
- Oxide cocondensation, magnesium aluminate  
 spinel preparation, 48-49,50f,t
- P**
- Particle size analysis, description, 22
- Particle size reference materials,  
 examples, 431
- Percolation models of catalyst deactivation  
 applications, 169  
 assumptions, 170-171  
 average pore radius, 168-169  
 concentration of poisoned sites, 167-168  
 effective radius, 168  
 identification of process, 167  
 mapping of porous medium, 170  
 normalized reaction rate vs. time,  
 171,173f  
 overall reaction rate, 167  
 plugging time vs. average coordination  
 number, 171,172f  
 total number of fragments vs. time,  
 171,174f,175
- Percolation theory, determination of  
 network and percolation effects, 252
- Petroleum catalysts  
 factors influencing demand, 17  
 preparation and characterization, 17-18
- Philosophy for testing, *See* Testing  
 philosophy
- Photoemission from insulators  
 energy balance of process, 215,217  
 schematic representation of energy levels  
 from large metal particle on  
 insulator, 215,216f  
 schematic representation of energy levels  
 from metal sample, 215,216f
- Photoemission from small metal clusters on  
 insulators  
 factors influencing binding energies,  
 217,218f,219  
 role of support, 217,218f,219
- Poly(silicic acid), definition, 57
- Pore structure characterization of catalyst  
 supports via low-field NMR  
 advantages, 253



- Pore structure characterization of catalyst supports via low-field NMR—*Continued*  
 alumina pore size distributions, 259f  
 background for conventional methods, 251–253  
 calculation of NMR pore size distributions, 258f,259  
 determination of surface interaction parameter, 254  
 experimental materials, 254–255  
 experimental procedure, 255  
 magnetization vector vs. time, 254  
 network and percolation effects, 251–252  
 nitrogen adsorption and condensation, 252–253  
 NMR spin–lattice relaxation inversion recovery experiments, 251  
 NMR theory, 253–254  
 plots of surface area vs. solid concentration, 256,257f  
 pore volumes, 255,256r  
 reciprocal values of bulk fluid relaxation decay constant, 256r  
 silica aerogel pore size distributions, 259,260f  
 values of surface interaction parameters, 256r
- Porous media in catalysis  
 characterization, 160  
 examples, 159  
 pore-plugging phenomenon, 160
- Powder X-ray diffraction  
 applications, 274–275  
 ECR–1 zeolite patterns, 308,309f
- Protocol for testing  
 establishment of relevant variables, 93  
 steps, 93  
 types of risks, 93–94
- Pt re-forming catalysts  
 characterization techniques, 243  
 temperature-programmed desorption, 243–250
- Pt–Sn–alumina catalysts  
 evidence for development of metallic Pt and Pt–Sn alloy, 339  
 EXAFS, 332–339  
 experimental procedure, 329,331  
 metallic content, 329,330r  
 NEXAFS, 331–332  
 procedure for X-ray spectrum measurements, 329,331  
 radial distribution functions from fluorescence intensities  
 at Pt edge, 333,335f  
 at Sn edge, 336,338f  
 reduced radial distribution peaks  
 at Pt edge, 333,334r  
 at Sn edge, 336,337r,339  
 review of reported structures, 339–340  
 state of tin, 339
- Pt–Sn–alumina catalysts—*Continued*  
 theoretical analysis of XANES profiles, 339
- Pt–Sn bimetallic catalysts  
 roles in petroleum processing, 328  
 structural characterization, 328–340
- Purchase specifications for catalysts  
 factors, 387  
 quality requirements, 387  
 specifications, 387,388r
- Q
- Quality assurance for purchased catalysts  
 fixed-bed adsorbents, 385  
 fixed-bed catalysts, 385  
 lot-to-lot variations, 393  
 purchase specifications, 387,388r  
 quality control procedures, 388–393  
 quality control to statistical process control, 385  
 statistical process control, 393–394,395f,396  
 supplier accreditation procedure, 396r,397  
 user's plant problems, 386
- Quality control procedures for catalysts  
 activity determination by ammonia chemisorption, 390r  
 limitations, 390,393  
 palladium penetration depth measurements, 389,390r,391–392f  
 particle size measurements, 389r  
 quality control experience, 388–389  
 representative lot samples and analyses, 388  
 standard procedure, 388
- R
- Reactor studies of catalysts  
 function, 16  
 hardness and attrition-resistance tests, 16  
 pore structure analysis, 16
- Regeneration of spent catalyst, length and density grading, 148–156
- Responses of testing  
 cause-and-effect relationships, 94  
 evaluation methodology, 94  
 relevance, 94
- S
- Scanning electron microscopy, image of iron silicate molecular sieve, 366,367f

- Scanning transmission electron microscope, advantages, 342–343
- Single pellet crush strength testing of catalysts  
 crush strength round-robin test on pencil leads, 411,412r,413  
 extrudate radial crush strength, 409,410–411r  
 method of test for radial crush strength of extruded catalyst shapes, 409,410f  
 procedure of round-robin testing program, 407–408  
 product characteristics from round-robin testing of spheres and tablets, 408r  
 reasons for development, 407  
 revision of test procedure, 413  
 test precision for round-robin testing of spheres and tablets, 408,409r
- Single-pellet tests, description, 381
- SO<sub>x</sub>  
 catalyst design for effective removal, 46–53  
 definition, 46
- Sodium-23 magic angle spinning NMR, characterization of Y zeolites, 262–271
- Sodium titanate, ion-exchange behavior, 67–68,69f
- Sodium titanate powders, solution properties, 66–76
- Solid-state NMR spectroscopy, use in characterization of catalytic systems, 182
- Spent catalyst, recovery and reuse as viable options, 148
- Spray drying, attrition-resistant porous particles, 56–63
- Statistical modeling of catalyst deactivation  
 activity decline due to deactivation, 164–165  
 coke content of particle, 166  
 deactivating rate constant, 164  
 development, 163–164  
 early efforts, 162–163  
 percolation-type phenomenon, 166–167  
 probability that a site is covered with coke, 165–166  
 reaction rate, 164
- Statistical modeling of catalytic and noncatalytic reactive porous media, approaches, 160–161
- Statistical process control for catalysts  
 catalyst manufacturer, 394,396  
 catalyst user, 394,395f  
 description, 393–394
- Steam deactivation of fluid catalytic cracking catalysts  
 alternate approaches, 127,129r,130  
 coke selectivity, 130,133f
- Steam deactivation of fluid catalytic cracking catalysts—*Continued*  
 comparison to microactivity test procedures, 127,129–134  
 dry-gas selectivity, 130,132f  
 effect of steaming conditions on physical and chemical characteristics of catalyst, 122  
 effect of steaming conditions on equilibration of unit-cell size, 124,125f  
 effect of steaming on microactivity conversion and surface area, 124,125f  
 effect of steaming severity on zeolite surface area, 124,126f  
 equilibrium comparison, 134r  
 gasoline selectivity, 130,131f  
 light-cycle-oil selectivity, 130,132f  
 summary of steaming conditions, 122,123r,124  
 use of several steaming procedures for different catalyst, 124  
 wet-gas selectivity, 130,131f
- Steamed dealuminated Y zeolites, characterization, 27,28r
- Steamed zeolites  
 hexadecane cracking results, 30,31r  
 molecular weight distribution from hexane cracking, 31,32f
- Strained bonds on oxides and zeolites, characterization by IR spectroscopic methods, 227,229,230f
- Structural analysis of catalysts  
 atomic resolution transmission electron microscopy, 14  
 electron spectroscopy for chemical analysis, 15  
 EXAFS, 15  
 Fourier-transform IR spectroscopy, 15  
 laser Raman spectroscopy, 15  
 low-energy electron diffraction crystallography, 15  
 MAS solid-state NMR, 14  
 X-ray crystallography, 14  
 X-ray powder diffraction, 14
- Structure, definition, 12
- Structure factor, description
- Structure modeling  
 comparison of experimental X-ray diffraction pattern vs. that for model, 316f,317  
 procedure, 314,316f,317
- Supercritical fluid extraction  
 applications, 82  
 decoking and regeneration of hydrotreating catalyst, 80–88
- Supplier accreditation for catalysts, procedure, 396r,397
- Surface acid sites, characterization by IR spectroscopic methods, 225–228,230

Surface analysis of catalysts  
 atomic force microscopy, 14–15  
 Auger spectroscopy, 13  
 chemisorption, 14  
 electron microscopy, 13  
 high-resolution electron energy loss spectroscopy, 14  
 IR spectroscopy, 14  
 scanning tunneling microscopy, 14–15  
 secondary-ion MS, 13  
 temperature-programmed desorption, 13  
 XPS, 13

Surface area reference materials, examples, 431

Surface characterization of metal oxide overlayers  
 atomic emission spectroscopic intensity vs. titania evaporation time, 183,184f,185  
 CO chemisorption capacity vs. titania coverage, 185,186f  
 effects of titania deposits on ethane hydrogenolysis, 189  
 experimental procedure, 183  
 hydrocarbon product selectivity vs. coverage, 185,188f  
 ISS intensity vs. titania evaporation time, 183,184f,185  
 methanation rate on  $\text{TiO}_x$ -Rh foil vs.  $\text{TiO}$  coverage, 185,188f  
 percentage of metal after CO hydrogenation, 185,189r  
 XPS spectra of Ti(2p) region, 185,187f

Surface groups on supports and catalysts, characterization by IR spectroscopic methods, 225,226f

Surface properties of mixed-metal catalysts apparatus, 192  
 catalytic activity of Ni vs. Ni coverage, 198f,199  
 CO adsorption vs. Ni coverage, 197  
 comparison of strained-metal overlayer systems, 200r  
 effect of Cu addition  
 attaining steady-state reaction rates, 196–197  
 CO hydrogenation rates, 191  
 cyclohexane dehydrogenation, 196,198f  
 effect of  $\text{H}_2$  spillover on specific activity, 194,196  
 effect of Ni coverage on ethane hydrogenolysis, 199f  
 relative importance of ensemble vs. electronic effects in modification of properties, 192  
 temperature-programmed desorption of multilayer Cu, 192,193f,194  
 temperature-programmed desorption vs. Cu coverage, 194,195f

## T

Temperature-programmed desorption, surface properties of mixed-metal catalysts, 192–195

Temperature-programmed desorption of CO on Pt re-forming catalysts  
 coverage variation, 246,247f  
 effect of calcination temperature with different reductions, 244,245f,246  
 effect of particle size, 246,247f  
 effect of predrying and partial desorption on IR spectra of absorbed CO, 249f,250  
 effect of predrying temperature, 246,249f  
 effect of Pt dispersion, 246,248f  
 effect of Pt loading, 246,248f  
 effect of sample amount, 246,247f  
 experimental procedure, 244  
 spectra of catalyst with different activities, 246,248f  
 spectra of CO with and without  $\text{CO}_2$  trap, 244,245f

Ten guidelines for catalyst testing  
 diagnosis and minimization of transport disguises, 107,108f,109,110f  
 early assessment of catalyst stability, 113,114–115f  
 ensuring of isothermal conditions, 104,106f,107,108r  
 establishment of ideal flow pattern, 102,103f,104,105r  
 following of good experimental practice, 113–116  
 gathering of meaningful catalyst performance data, 111–113,114f  
 providing of perspectives on results, 116  
 selection of appropriate laboratory reactor, 101–102,103f  
 specification of objective, 99–100  
 use of effective strategy, 100,101r

Testing philosophies for evaluation of fluid catalytic cracking catalysts  
 comparison of steaming and microactivity testing procedures, 127,129–134  
 experimental procedures, 121  
 fresh-catalyst properties, 121,123r  
 laboratory evaluation procedures, 121  
 microactivity testing, 127,128f,129r  
 objective, 120–121  
 steaming, 122–126

Testing philosophy  
 analysis of responses, 94–95  
 drawing conclusions, 95–98  
 hypothesis, 92–93  
 protocol, 93–94  
 responses, 94

Tin passivation, vanadium contaminants in model fluid cracking catalysts, 41–42,43r,44

- Transmission electron microscopy  
 identification of crystallites in iron silicates, 366,368  
 image of iron silicate particle aggregate after steam treatment, 368,369f  
 image of iron silicate particle aggregate after steam treatment of unstirred gel, 368,371f  
 procedures, 366
- U
- Ultramicrotomy, identification of impurities on catalysts, 277
- Ultrastable Y zeolites, formation, 25
- V
- V<sub>2</sub>O<sub>5</sub>, generation during calcination of catalysts, 40
- Vanadium-contaminated fluid cracking catalysts  
 electron paramagnetic resonance studies, 42,43r,44  
 existence, 40  
 experimental procedure, 41–42  
 luminescence data, 42,43r,44  
 material preparation, 41  
 Mossbauer spectrometry, 43r,44  
 tin passivation, 42,44  
 X-ray powder diffraction, 42,44
- Vanadium species, role in catalyst deactivation, 40–41
- W
- Weisz window, description, 112
- X
- X-ray absorption near-edge structure (XANES)  
 description, 275  
 structure determination of cobalt sulfide phase in Co–Mo–S catalysts, 321–326
- X-ray absorption spectroscopy  
 description, 275  
 structural studies, 275
- X-ray analytical methods  
 analytical role in characterization and development of catalysts, 274  
 application approaches, 274
- X-ray diffraction (XRD)  
 advantages for use in catalyst research and development, 279
- X-ray diffraction (XRD)—*Continued*  
 expression for diffracted X-ray intensity from crystallographic plane, 280,281f,282  
 factors affecting zeolite patterns, 284–298  
 line broadening, 282,283f,284  
 locations of cations in zeolites, 263  
 present and future, 297,299f,300  
 theory, 280,281f,282  
 use of peak widths and areas for average crystallite size and weight percent, 282,283f,284
- X-ray photoelectron spectroscopy (XPS)  
 advantages, 214  
 investigation of metal–support interactions, 214–220  
 use in characterization of catalytic systems, 181
- Y
- Y zeolite(s)  
 ability to distinguish types of sodium cations, 263–264  
 chemical dealumination, 25  
 CO<sub>2</sub> spectra, 227,228f  
 hydrothermal dealumination, 25  
 techniques for cation location determination, 263
- Y zeolite characterization with sodium-23 magic-angle-spinning NMR  
 acquisition, processing, and simulation of sodium-23 NMR spectra, 264  
 comparison of spectra of dehydrated and cation-exchanged zeolites, 268,270f,271  
 comparison of spectra of hydrated and cation-exchanged zeolites, 266,268,269f  
 determination of sodium-23 line origin, 264,266  
 molarities of cation-exchanged samples, 264,265r  
 reasons for study, 262–263  
 sample preparation, 264  
 spectra of lanthanum-exchanged zeolites, 266,267f
- Yield, definition, 112
- Z
- Zeolite(s), new. *See* New zeolites
- Zeolite X-ray diffraction powder patterns  
 comparison of conventional and synchrotron patterns, 297,299f,300

Zeolite X-ray diffraction powder patterns—  
*Continued*  
 deconvolution of pattern for Nu-13,  
 292,296f,297  
 effect of cations, 287,291f  
 effect of changes in ordered stacking  
 sequence, 284,286f,287  
 effect of changes in structural symmetry,  
 284,285f  
 effect of crystal morphology,  
 292,293–294f  
 effect of diffraction geometry, 297,298f  
 effect of directing agents, 287,290f  
 effect of extraframework material,  
 287,289,291f  
 effect of framework structure, 284–288

Zeolite X-ray diffraction powder patterns—  
*Continued*  
 effect of impurities, 292,295–296f,297  
 effect of instrumentation, 297,298f  
 effect of physical preparation of sample,  
 292,294f  
 effect of preferred orientation, 292,293f  
 example of disordered stacking faults,  
 287,288f  
 influencing factors, 284–298  
 ZSM-5 zeolite  
 CO<sub>2</sub> spectra, 227,228f  
 effects of rehydration on deuteroyl  
 bands, 227,230f  
 hydroxyl spectra, 225,226f,227

*Production: Rebecca Hunsicker*  
*Indexing: Deborah H. Steiner*  
*Acquisition: Robin Giroux*

*Elements typeset by Hot Type Ltd., Washington, DC*  
*Printed and bound by Maple Press, York, PA*

*Paper meets minimum requirements of American National Standard*  
*for Information Sciences—Permanence of Paper for Printed Library*  
*Materials, ANSI Z39.48–1984* 